energies

Volume 2

Optimization Methods Applied to Power Systems

Edited by
Francisco G. Montoya and Raúl Baños Navarro

Printed Edition of the Special Issue Published in *Energies*

www.mdpi.com/journal/energies

Optimization Methods Applied to Power Systems

Optimization Methods Applied to Power Systems

Volume 2

Special Issue Editors

Francisco G. Montoya
Raúl Baños Navarro

MDPI • Basel • Beijing • Wuhan • Barcelona • Belgrade

Special Issue Editors
Francisco G. Montoya
University of Almería
Spain

Raúl Baños Navarro
University of Almería
Spain

Editorial Office
MDPI
St. Alban-Anlage 66
4052 Basel, Switzerland

This is a reprint of articles from the Special Issue published online in the open access journal *Energies* (ISSN 1996-1073) from 2018 to 2019 (available at: https://www.mdpi.com/journal/energies/special_issues/optimization)

For citation purposes, cite each article independently as indicated on the article page online and as indicated below:

LastName, A.A.; LastName, B.B.; LastName, C.C. Article Title. *Journal Name* **Year**, *Article Number*, Page Range.

Volume 2
ISBN 978-3-03921-156-2 (Pbk)
ISBN 978-3-03921-157-9 (PDF)

Volume 1-2
ISBN 978-3-03897-154-8 (Pbk)
ISBN 978-3-03897-155-5 (PDF)

Contents

About the Special Issue Editors

Francisco G. Montoya, professor at the Engineering Department and the Electrical Engineering Section in the University of Almeria (Spain), received his M.S. from the University of Malaga and his Ph.D. from the University of Granada (Spain). He has published over 70 papers in JCR journals and is the author or coauthor of books published by MDPI, RA-MA, and others. His main interests are power quality, smart metering, smart grids and evolutionary optimization applied to power systems, and renewable energy. Recently, he has become passionately interested in Geometric Algebra as applied to Power Theory.

Raúl Baños Navarro is an associate professor at the Department of Engineering, University of Almeria (Spain). He received his first Bachelor's degree in Computer Science at the University of Almeria and his second Bachelor's degree in Economics by the National University of Distance Education (UNED). He wrote his Ph.D. dissertation on computational methods applied to optimization of energy distribution in power networks. His research activity includes computational optimization, power systems, renewable energy systems, and engineering economics. The research is being carried out at Napier University (Edinburgh, UK) and at the Universidade do Algarve (Portugal). As a result of his research, he has published more than 150 papers in peer-reviewed journals, books, and conference proceedings.

Preface to "Optimization Methods Applied to Power Systems"

Power systems are made up of extensive complex networks governed by physical laws in which unexpected and uncontrolled events can occur. This complexity has increased considerably in recent years due to the increase in distributed generation associated with increased generation capacity from renewable energy sources. Therefore, the analysis, design, and operation of current and future electrical systems require an efficient approach to different problems such as load flow, parameters and position finding, filter designing, fault location, contingency analysis, system restoration after blackout, islanding detection, economic dispatch, unit commitment, etc. The evolution is so frenetic that it is necessary for engineers to have sufficiently updated material to face the new challenges involved in the management of new generation networks (smart grids).

Given the complexity of these problems, the efficient management of electrical systems requires the application of advanced optimization methods for decision-making processes. Electrical power systems have so greatly benefited from scientific and engineering advancements in the use of optimization techniques to the point that these advanced optimization methods are required to manage the analysis, design, and operation of electrical systems. Considering the high complexity of large-scale electrical systems, efficient network planning, operation, or maintenance requires the use of advanced techniques. Accordingly, besides classical optimization techniques such as Linear and Nonlinear Programming or Integer and Mixed-Integer Programming, other advanced techniques have been applied to great effect in the study of electrical systems. Specifically, bio-inspired meta-heuristics have allowed scientists to consider the optimization of problems of great importance and obtain quality solutions in reduced response times thanks to the increasing calculation power of the current computers.

Therefore, this book includes recent advances in the application optimization techniques that directly apply to electrical power systems so that readers may familiarize themselves with new methodologies directly explained by experts in the field.

Francisco G. Montoya, Raúl Baños Navarro
Special Issue Editors

energies

MDPI

Article

Hybrid Imperialist Competitive and Grey Wolf Algorithm to Solve Multiobjective Optimal Power Flow with Wind and Solar Units

Jalel Ben Hmida [1,*], Mohammad Javad Morshed [2], Jim Lee [1] and Terrence Chambers [1]

[1] Department of Mechanical Engineering, University of Louisiana at Lafayette, Lafayette, LA 70504, USA; jlee@louisiana.edu (J.L.); tlchambers@louisiana.edu (T.C.)
[2] Department of Electrical and Computer Engineering, University of Louisiana at Lafayette, Lafayette, LA 70504, USA; morshed@louisiana.edu
* Correspondence: jalel@louisiana.edu; Tel.: +1-337-482-6622

Received: 24 September 2018; Accepted: 21 October 2018; Published: 24 October 2018

Abstract: The optimal power flow (OPF) module optimizes the generation, transmission, and distribution of electric power without disrupting network power flow, operating limits, or constraints. Similarly to any power flow analysis technique, OPF also allows the determination of system's state of operation, that is, the injected power, current, and voltage throughout the electric power system. In this context, there is a large range of OPF problems and different approaches to solve them. Moreover, the nature of OPF is evolving due to renewable energy integration and recent flexibility in power grids. This paper presents an original hybrid imperialist competitive and grey wolf algorithm (HIC-GWA) to solve twelve different study cases of simple and multiobjective OPF problems for modern power systems, including wind and photovoltaic power generators. The performance capabilities and potential of the proposed metaheuristic are presented, illustrating the applicability of the approach, and analyzed on two test systems: the IEEE 30 bus and IEEE 118 bus power systems. Sensitivity analysis has been performed on this approach to prove the robustness of the method. Obtained results are analyzed and compared with recently published OPF solutions. The proposed metaheuristic is more efficient and provides much better optimal solutions.

Keywords: multiobjective optimization; optimal power flow; metaheuristic; wind energy; photovoltaic

1. Introduction

Optimal power flow (OPF) is the mathematical tool used to find the optimal settings of the power system network [1]. The main target of the OPF problem is to optimize a specific objective function while satisfying feasibility and security constraints [2]. OPF has been broadly used in previous studies [3], and has served as a substantial optimization test problem because it is characterized as multidimensional, large-scale nonlinear nonconvex, and highly constrained [4,5]. Several OPF formulations have been developed during the last few decades in order to optimize the operation of an electric power system subject to physical constraints [6]. The emerging optimization problem uses different names and different objective functions [7]. A lot of OPF solution approaches have been developed, each with distinct mathematical characteristics and computational requirements [8,9]. In recent years, OPF optimization problems have regained importance due to the rapid adoption of distributed energy resources in the network [10]. The integration of distributed and intermittent renewable energy sources, such as photovoltaic (PV) systems and wind energy (WE), into modern power systems has introduced new types of challenges for operating and managing the power grid [11]. The stochastic nature of WE and PV units must be taken into consideration to ensure successful

implementation of these intermittent energy sources to the network [12]. Solving the OPF problem has become more complicated with massive incorporation of renewable resources that impose volatile dynamics to the power grid because of their uncertainty.

Conventional optimization methods, like linear (LP) and nonlinear programming (NLP) [13], quadratic programming (QP) [14], interior point method (IPM), and Newton's method [15] showed excellent convergence characteristics in solving OPF problems; however, they use theoretical assumptions not suitable for practical systems having non-differentiable, non-smooth, and nonconvex objective functions. Sometimes, the preceding approaches fail to represent the main characteristics of the fuel cost as a convex function [16]. Such a situation emerges when piecewise quadratic cost, valve points, and prohibited operating zones characteristics are presented [17]. Usually, multiple trials and accurate adjustment of associated parameters are needed to achieve the optimal solution for a specific problem. As a result, we need a faster and more robust algorithm to solve realistic OPF problems. Recently, many publications have focused on metaheuristics to solve hard optimization problems. Metaheuristics, based on a common set of principles which make it possible to design solution algorithms, may be used to overcome the abovementioned weaknesses. Most metaheuristics have the following features: they are inspired from nature, they do not use the objective function's Hessian or gradient matrix, they make use of stochastic components, and they have many parameters that need to be adapted to the problem [18]. The following artificial intelligence based optimization methods have been successfully used to solve OPF problems: moth swarm algorithm, MSA [19]; modified particle swarm optimization, MPSO [20]; modified differential evolution, MDE [21]; moth-flame optimization, MFO [22]; flower pollination algorithm, FPA [23]; adaptive real coded biogeography-based optimization, ARCBO and real coded biogeography-based optimization, RCBBO [24]; grey wolf algorithm, GWO and differential evolution, DE [25]; modified Gaussian bare bones imperialist competitive algorithm, MGBICA and Gaussian bare bones imperialist competitive algorithm, GBICA [26]; artificial bee colony, ABC [27]; simulated annealing and hybrid shuffle frog leaping algorithm [28]; Lévy mutation teaching-learning-based optimization, LTLBO [29]; teaching learning-based optimization, TLBO [30]; hybrid MPSO and shuffle frog leaping algorithms, HMPSOSFLA, and particle swarm optimization, PSO [31]; Gbest-guided artificial bee colony, GABC [32]; differential search algorithm, DSA [33]; efficient evolutionary algorithm, EEA and eclectic genetic algorithm, EGA [34]; particle swarm optimization with aging leader and challengers, ALCPSO [35]. The above optimization approaches have been developed to solve simple and multiobjective OPF problems. These algorithms performed better than traditional mathematical programming techniques in solving multiobjective optimization problems because they are less affected by the Pareto front shape, and are capable of finding the optimal solutions sets in one run [36]. The assessment of these metaheuristics is commonly based on experimental comparisons.

The objective of this research is to develop an original metaheuristic called hybrid imperialist competitive and grey wolf algorithm (HIC-GWA) to solve twelve different cases of simple and multiobjective OPF problems for hybrid power systems that includes PV and WE sources, in order to find effective, faster, and better solutions. The potential and efficiency of the HIC-GWA are presented and evaluated on two standard test systems: IEEE 30 and IEEE 118 bus power systems. Simulation results are compared with the abovementioned optimization approaches. The proposed HIC-GWA is a combination of two algorithms: the imperialist competitive algorithm (ICA) and the grey wolf optimization (GWO). ICA is a sociopolitically inspired optimization strategy that has been proposed to handle tough optimization problems [37]. This approach exhibits good performance in terms of convergence rate and improved global optimum [38,39]. The GWO algorithm is an original swarm intelligence technique stimulated by the leadership hierarchy and hunting structure of grey wolves. This robust algorithm has been used in different complex problems because of the reduced number of random parameters and a faster convergence due to continuous reduction of search space [40,41]. Each optimization technique, ICA and GWO, possesses certain specific intelligence to search for the solution of a problem. Therefore, a collection of such abilities enhances the power of the proposed metaheuristic.

2. OPF Problem Formulation

2.1. Objective Functions

OPF research seeks to compute a steady state operating point that reduces cost, emission, loss, etc., while maintaining good system performance. The general OPF problem usually contains discrete and continuous control variables. It is a large-scale, nonconvex, and nonlinear optimization problem. OPF seeks to optimize the generation, transmission, and distribution of electric power with no disruption of flow, operating limits, or constraints. Similar, to other power flow analysis techniques, OPF also allows the determination of system's state of operation, that is, the injected power, voltage, and current throughout the electric power system. In this context, a large array of OPF formulations and solution methods have been developed. Furthermore, OPF research is growing, due to contemporary electricity markets and integration of renewable energy sources.

The following objective functions are minimized by the proposed HIC-GWA:

2.1.1. Wind Cost Function

Wind energy is increasingly being integrated into the power grid due to its rapidly declining cost and emission free nature. The WE power cost function can be modeled as

$$C_{d,w,i} = d_{w,i} P_{w,i} \tag{1}$$

Wind power operators get penalized if they fail to provide the scheduled amount of wind energy. Penalty costs consists of two parts: (1) underestimation cost which should be considered when available power of wind farm is not utilized, (2) overestimation cost which is calculated for buying power from alternate sources (reserves) or load shedding. These costs can be modeled as follows [12]:

$$C_{ue,w,i} = K_{ue,w,i} \int_{P_{w,i}}^{P_{w,r,i}} (P - P_{w,i}) f(P) dP \tag{2}$$

$$C_{oe,w,i} = K_{oe,w,i} \int_{0}^{P_{w,i}} (P_{w,i} - P) f(P) dP \tag{3}$$

where $i = 1, 2, \ldots, n_w$ and $f(P)$ symbolizes the probability density function (PDF) of WE output power.

The WE total cost is given by the following function:

$$F_1 = \sum_{i=1}^{n_w} COST_{w,i} = \sum_{i=1}^{n_w} C_{d,w,i} + C_{ue,w,i} + C_{oe,w,i} \tag{4}$$

To model the unpredictable nature of wind speed, we use the Weibull distribution with PDF $f(V_w)$ and cumulative distribution function (CDF), $F(V_w)$, defined as follows [12]:

$$f(V_w) = \frac{K}{C} \left(\frac{V_w}{C} \right)^{K-1} e^{-(V_w/C)^K}, \quad V_w > 0 \tag{5}$$

$$F(V_w) = 1 - e^{-(V_w/C)^K}, \quad V_w > 0 \tag{6}$$

The generated power of WE is computed as

$$P_w(V_w) = \begin{cases} 0 & V_w < V_{w,in}, V_w > V_{w,out} \\ \frac{P_{w,r}}{V_{w,r} - V_{w,in}} V_w - \frac{V_{w,in} \cdot P_{w,r}}{V_{w,r} - V_{w,in}} & V_{w,in} \le V_w \le V_{w,r} \\ P_{w,r} & V_{w,r} \le V_w \le V_{w,out} \end{cases} \tag{7}$$

where

V_w and $V_{w,r}$ symbolizes speed and rated speed of WE generators,
$V_{w,in}$ and $V_{w,out}$ symbolizes cut-in and cut-out speed of WE generators,
K, C symbolizes shape and scale parameters of the Weibull distribution.

2.1.2. PV Cost Function

Photovoltaic systems are gaining popularity as a clean energy source due to their affordable cost and simple design. PV characteristics are highly dependent on various factors, including irradiance level, shades, and temperature, which makes it hard to accurately forecast its power production. The generation and penalty costs for PV power can be calculated as follows:

$$C_{d,pv,i} = d_{pv,i} P_{pv,i} \tag{8}$$

$$C_{ue,pv,i} = K_{ue,pv,i} \int_{P_{pv,i}}^{P_{pv,r,i}} (P - P_{pv,i}) f(P) dP \tag{9}$$

$$C_{oe,pv,i} = K_{oe,pv,i} \int_{0}^{P_{pv,i}} (P_{pv,i} - P) f(P) dP \tag{10}$$

where $i = 1, \ldots, n_v$ and $f(P)$ represent the PDF of the PV unit's output power.

The total cost of PVs is given by the following function:

$$F_2 = \sum_{i=1}^{n_v} COST_{PV,i} = \sum_{i=1}^{n_v} C_{d,pv,i} + C_{ue,pv,i} + C_{oe,pv,i} \tag{11}$$

The PDF of the ith PVs' output power is calculated as follows:

- Solar cells or PV cells are hypersensitive to the amount of solar radiation. The PDF of solar radiation $f(R)$ can be modeled by a beta distribution [12]:

$$f(R) = \frac{\Gamma(\alpha + \beta)}{\Gamma(\alpha)\Gamma(\beta)} R^{\alpha - 1} (1 - R)^{\beta} \tag{12}$$

  where $\Gamma(.)$ is the gamma function, α and β are parameters of the beta distribution, and R is the solar radiation.
- The relation between power output of PV and output power of solar cell generator which is related to the solar radiation can be calculated as follows:

$$P_{pv}(R) = \begin{cases} P_{pv,r}\left(\frac{R^2}{R_C R_{STD}}\right) & 0 \le R \le R_C \\ P_{pv,r}\left(\frac{R}{R_{STD}}\right) & R_C \le R \le R_{STD} \\ P_{pv,r} & R_{STD} \le R \end{cases} \tag{13}$$

  where R_C and R_{STD} are solar radiation in W/m^2. Usually, a typical solar radiation point is set to 150 W/m^2, and it is set to 100 W/m^2 under standard conditions.

2.1.3. Basic Fuel Cost Function

The basic fuel cost is OPF's most common objective function. A power plant's fuel cost is commonly modeled as a quadratic function [42]:

$$F_3 = \sum_{i=1}^{n_G} a_i + b_i P_{Gi} + c_i P_{Gi}^2 \tag{14}$$

where i represents the ith power plant and n_G is the number of power plants. a_i, b_i, and c_i are cost coefficients for the ith power plant. P_{Gi} is power of ith power plant.

2.1.4. Piecewise Quadratic Fuel Cost Function

For a given operating range, power plants usually use the most economical available fuel option. Such a system has piecewise quadratic fuel cost function

$$F_4 = \sum_{i=1}^{n_G} f_i(P_i) \tag{15}$$

Each quadratic piece of the fossil fuel cost can be calculated using the following function:

$$f_i(P_i) = \sum_{k=1}^{n_f} a_{i,k} + b_{i,k}P_{Gi} + c_{i,k}P_{Gi}^2 \tag{16}$$

where n_f is the number of fossil fuel options for ith power plant and $a_{i,k}$, $b_{i,k}$, $c_{i,k}$, are coefficients for the cost of ith power plant for kth fuel option.

2.1.5. Piecewise Quadratic Fuel Cost with Valve Point Loading

The generator cost is a convex function with an incremental heat rate curve, subjected to discontinuities caused by the steam admission valves in large turbines. The valve point effect must be included in order to have an accurate cost for each generating unit [43]:

$$F_5 = \sum_{i=1}^{n_G} a_i + b_iP_{Gi} + c_iP_{Gi}^2 + \left|e_i sin\left(f_i\left(P_{Gi}^{min} - P_{Gi}\right)\right)\right| \tag{17}$$

where e_i and f_i are valve point cost coefficients of ith power plant.

2.1.6. Emission Cost Function

To produce electricity, a fossil fuel power station burns natural gas, petroleum, or coal. Significant amounts of emission are produced during the burning process. In this paper, the emission level of the two important pollutants, nitrogen oxides (NOx) and sulfur oxides (SOx), are modeled by the following function [19]:

$$F_6 = \sum_{i=1}^{n_G} \alpha_i + \beta_iP_{Gi} + \gamma_iP_{Gi}^2 + \zeta_i e^{(\theta_i P_{Gi})} \tag{18}$$

where, α_i, β_i, ζ_i, and θ_i are emission coefficients of ith power plant.

2.1.7. Power Loss Cost Function

To reduce the active power loss of transmission lines, the following power loss function has to be minimized [27]:

$$F_7 = \sum_{i=1}^{n_l} \sum_{\substack{j=1 \\ j \neq i}}^{n_l} G_{ij}V_i^2 + B_{ij}V_j^2 - 2V_iV_j\cos\delta_{ij} \tag{19}$$

where n_l is the number of transmission lines, $(G_{ij}$,$B_{ij})$ are (real, imaginary) of ith jth components of the admittance matrix, δ_{ij} is the angle separating the ith bus from the jth bus, and V_i is the ith bus voltage.

2.1.8. Fuel Cost and Active Power Loss Cost Function

This function model two simple objectives: fuel cost and active power loss.

$$F_8 = F_3 + \beta_1 F_7 \tag{20}$$

where β_1 is a weighting factor.

2.1.9. Fuel Cost and Voltage Deviation

One of the valuable quality and security indices is the voltage magnitude fluctuation from the specified reference value at each load bus. This function models both fuel cost and voltage deviation (VD).

$$F_9 = F_3 + \beta_2 \sum_{i=1}^{n_L} |1 - V_{Li}| \tag{21}$$

where n_L is the number of load buses, V_{Li} is the ith voltage of load buses, and β_2 is a weighting factor.

2.1.10. Fuel Cost and Voltage Stability Enhancement

Voltage stability is the ability of a power system to sustain stable voltages at each bus within acceptable level after being exposed to a disruption. It is represented by indices like the L index, which has been introduced to evaluate the stability limit [19]. The L index is a quantitative measure of how close a point is to the system stability limit. Reducing the value of the L index is very important in power system planning and operations.

This function models the fuel cost and the L index maximum.

$$F_{10} = F_3 + \beta_3 L_{max} \tag{22}$$

where β_3 is a weighting factor.

The nodal admittance relates system voltages and currents as

$$I_{bus} = Y_{bus} \times V_{bus} \tag{23}$$

Equation (23) can be reformulated by separating the PQ bus—active and reactive power; and the PV bus—active power and voltage magnitude.

$$\begin{bmatrix} I_L \\ I_G \end{bmatrix} = \begin{bmatrix} Y_1 & Y_2 \\ Y_3 & Y_4 \end{bmatrix} \begin{bmatrix} V_L \\ V_G \end{bmatrix} \tag{24}$$

The L index is calculated by

$$L_j = \left| 1 - \sum_{i=1}^{G_N} \gamma_{ji} \frac{V_i}{V_j} \right| \quad j = 1, 2, \cdots, N_L \tag{25}$$

$$\gamma_{ji} = -[Y_1]^{-1} \times [Y_2] \tag{26}$$

where Y_1 and Y_2 are the system Y bus submatrices.

$$L_{max} = \max(L_j) \quad j = 1, 2, \cdots, nb \tag{27}$$

2.1.11. Fuel Cost and Voltage Stability Enhancement during Contingency Condition

Transmission lines outages are used to replicate a contingency condition. This function models both fuel cost and enhancement of voltage stability.

$$F_{11} = F_3 + \beta_4 (max(L_i)) \tag{28}$$

where β_4 is a weighting factor.

2.1.12. Fuel Cost, Emission, Voltage Deviation, and Active Power Loss

This function models fuel cost, emission, voltage deviation, and active power loss.

$$F_{12} = F_3 + \beta_5 F_6 + \beta_6 \sum_{i=1}^{n_L} |1 - V_{Li}| + \beta_7 F_7 \tag{29}$$

where β_5, β_6, and β_7 are weighting factors.

2.2. Constraints

The OPF optimization problem should satisfy the following constraints:

(1) Active and reactive power balances

$$\begin{aligned} P_{Gi} - P_{Di} &= \sum_{j=1}^{n} V_i V_j \left(G_{ij} cos\delta_{ij} + B_{ij} sin\delta_{ij}\right) \;\; i = 1, \ldots, n \\ Q_{Gi} - Q_{Di} &= \sum_{j=1}^{n} V_i V_j \left(G_{ij} sin\delta_{ij} - B_{ij} cos\delta_{ij}\right) \;\; i = 1, \ldots, n \end{aligned} \tag{30}$$

where the number of power system bus is represented by n. P_{Gi}, Q_{Gi}, and P_{Di}, Q_{Di} are active and reactive power of generators and load, respectively, at the ith bus.

(2) The voltage magnitude of the power plant

$$V_i^{min} \le V_i \le V_i^{max}, \;\; i = 1, 2, \ldots, n_G \tag{31}$$

where V_i^{min} and V_i^{max} are minimum and maximum limit of ith bus voltage of power plants V_i.

(3) Prohibited operating zones

There is a risk of machine or accessory failure when a power plant operates outside acceptable ranges, as shown in Equations (32)–(41).

$$\begin{cases} P_{Gi}^{min} \le P_{Gi} \le P_{Gi,1}^{l} \\ P_{Gi,k-1}^{u} \le P_{Gi} \le P_{Gi,k}^{l} \quad k = 1, 2, \ldots, z \\ P_{Gi,z}^{u} \le P_{Gi} \le P_{Gi}^{max} \end{cases} \tag{32}$$

where $P_{Gi,k}^{l}$ and $P_{Gi,k}^{u}$ are lower and upper bounds of the kth POZ of ith unit. P_{Gi}^{min} and P_{Gi}^{max} are active power boundaries of ith generator.

(4) Active and reactive power

$$\begin{matrix} P_{Gi}^{min} \le P_{Gi} \le P_{Gi}^{max} \\ Q_{Gi}^{min} \le Q_{Gi} \le Q_{Gi}^{max} \end{matrix} \quad , i = 1, 2, \ldots, n_G \tag{33}$$

where Q_{Gi}^{min} and Q_{Gi}^{max} are boundaries' reactive power of ith traditional generator.

(5) Phase shifter and transformer tap

$$PS_i^{min} \le PS_i \le PS_i^{max}, \;\; i = 1, 2, \ldots, N_{phase} \tag{34}$$

$$T_i^{min} \le T_i \le T_i^{max}, \;\; i = 1, 2, \ldots, N_{tap} \tag{35}$$

T_i^{min} and T_i^{max} are boundaries of ith tap changer transformer T_i, PS_i^{min}, and PS_i^{max} are boundaries of ith phase shifter transformer PS_i, and N_{tap}, N_{phase}, are the number of tap changer and installed phase shifter to the network.

(6) Shunt compensator

$$Q_{c,i}^{min} \leq Q_{c,i} \leq Q_{c,i}^{max} \quad i = 1, 2, \ldots, N_{cap} \tag{36}$$

where $Q_{c,i}^{min}$ and $Q_{c,i}^{max}$ are the ith shunt compensator $Q_{c,i}$ limits. N_{cap} represents the number of capacitors linked to the network.

(7) Transmission line loading

$$|S_i| \leq S_i^{max} \quad i = 1, 2, \ldots, N_l \tag{37}$$

where S_i^{max} is MVA's maximum. N_l is the number of lines.

(8) Active power of WE

$$0 \leq P_{w,i} \leq P_{w,r,i} \tag{38}$$

Each wind turbine is equipped with a squirrel cage induction generator modeled as PQ buses [44].

$$P_{w,i}^2 + Q_{w,i}^2 + \frac{V_{ww,i}^2 Q_{w,i}}{X_i} = 0 \tag{39}$$

$$\frac{-V_{ww,i}^2}{2X_i} \leq Q_{w,i} \leq 0 \tag{40}$$

where X_i is the sum of the leakage reactance of the stator and rotor of the ith wind turbine. $V_{ww,i}$ and $Q_{w,i}$ represents the voltage and the reactive power of the associated bus of the ith wind generator.

(9) Active power of photovoltaic

$$0 \leq P_{pv,i} \leq P_{pv,r,i} \tag{41}$$

3. New Hybrid Optimization Algorithm

In this research, a new metaheuristic HIC-GWA is considered to solve twelve cases of simple and multiobjective OPF problems. This approach is a combination of two algorithms: ICA and GWO. Each of such optimization techniques, ICA and GWO, possesses certain specific heuristics to search for the solution of a problem. Therefore, a collection of such abilities enhances the power of the proposed metaheuristic.

3.1. Imperialist Competitive Algorithm (ICA)

The ICA is stimulated by the sociopolitical aspect of imperialistic competition between countries in the same population. Countries can be colonies or imperialists. Powerful countries are selected to be imperialists. Colonies are distributed among imperialists based on imperialist's power. Empires are formed with imperialist states and their colonies. Imperialistic competition between empires converge to one imperialist state which represent the optimum point of the ICA [37–39].

3.1.1. Creation of Initial Empires

A country is usually represented by an N_{var}-dimensional array of variables that should be optimized.

$$\text{country} = [P_1, P_2, \ldots, P_{N\ var}] \tag{42}$$

The cost of each country is inversely proportional to its power.

The cost function f is given by

$$\text{cost} = f\ (\text{country}) = f\ (P_1, P_2, \ldots, P_{N\ var}) \tag{43}$$

In the initialization process, the algorithm produces $N_{Country}$ initial countries. A certain number of empires, N_{imp}, are formed with the most powerful countries. The remaining countries, N_{col}, become colonies of the empires.

The cost of the nth imperialist is

$$C_n = c_n - \underset{i}{max}\{c_i\} \tag{44}$$

The power of the nth imperialist is

$$p_n = \left| \frac{C_n}{\sum_{i=1}^{N_{imp}} C_i} \right| \tag{45}$$

The nth empire's initial number of colonies is

$$NC_n = round\{p_n \times N_{col}\}$$

where N_{col} is the total number of original colonies.

3.1.2. Assimilation

To absorb their colonies, the imperialist states use different sociopolitical axes to make colonies move toward themselves. This movement can be modeled using different optimization axes. In a two-dimensional problem, colonies are absorbed by the imperialist using language and culture. Colonies will move toward the imperialist among these two axes. This acclimatization, modeled by approaching the colonies to the imperialist, will continue until all colonies are fully assimilated. This motion is represented by a uniform distribution:

$$x \sim U(0, \beta \times d) \tag{46}$$

where $\beta > 1$. d represents the distance separating the colony to the imperialist state.

A random deviation θ is added to the direction of movement to increase the search space around the imperialist. θ is represented by a uniform distribution.

$$\theta \sim U(-\gamma, +\gamma) \tag{47}$$

where γ accommodates the fluctuation from the initial direction.

3.1.3. Revolution

Revolution is simulated to denote a shift in sociopolitical institutions that prohibits the convergence of a country to a local minimum which increases the exploration of this approach.

3.1.4. Exchanging Positions of a Colony and the Imperialist

The colony and the imperialist countries will change positions if the colony reaches a position with higher power than the imperialist.

3.1.5. Union of Empires

While moving toward the optimum solution, two imperialists may merge into one empire if they are too close to each other. Their colonies become colonies of the new empire which take the position of one of the two imperialists.

3.1.6. Total Empire Power

An empire's total power is highly correlated to the power of the imperialist country, but it is slightly affected by the power of the colonies. An empire's total cost is modeled as

$$TC_n = Cost(imperialist_n) + \xi mean\{Cost(colonies\ of\ empire_n)\} \tag{48}$$

where ξ is a positive small weight factor.

3.1.7. Imperialistic Competition

This competition is built on the total power of the empires. Empires try to take control of each other's colonies to expand their territory. Every empire will have the possibility of possessing colonies that it is competing for. Powerful empires will control weaker colonies. The weakest colony of the weakest empire will be selected in the initiation process of the competition. An empire's possession probability (PP) is proportional to the empire's total power.

Empire's normal total cost:

$$NTC_n = TC_n - max_i\{TC_i\} \tag{49}$$

Empire's possession probability:

$$P_{P_n} = \left| \frac{NTC_n}{\sum_{i=1}^{N_{imp}} NTC_i} \right| \tag{50}$$

The algorithm will stop after a predetermined number of iterations which represents maximum number of decades.

3.2. Grey Wolf Optimizer (GWO)

The GWO is a conventional swarm intelligence algorithm stimulated by the leadership hierarchy and hunting structure of grey wolves. This algorithm has been used in diverse complex problems because of its simplicity and robustness. The wolf colony (N_w) is divided into four clusters: alpha (α), beta (β), delta (δ), and omega (Ω). The hunting mechanism involves three main steps: searching and approaching the prey, encircling and harassing the prey, and attacking the prey [40,41].

3.2.1. Social Hierarchy

The leaders α are mostly responsible for making decisions about hunting. They are considered as the fittest solution. The second-best candidates are the β wolves, based on the democratic behavior of the colony. Consequently, the δ wolves take place after the β wolves. The rest are assumed to be the ωwolves. The optimization (hunting) process is guided by α, β, and δ, with the ω wolves tracking them.

3.2.2. Encircling Prey

Hunting in groups is another compelling social behavior of grey wolves. A grey wolf can revise its position neighboring the prey in any random place using the following equations [40]:

$$\vec{D} = \left| \vec{C} \times \vec{X}_p(t) - \vec{X}(t) \right| \tag{51}$$

$$\vec{X}(t+1) = \vec{X}_p(t) - \vec{A} \times \vec{D} \tag{52}$$

where $\vec{X}_p$ represent the prey's location vector, $\vec{X}$ indicates the wolf's location vector, t represents the current iteration; and $\vec{A}$ and $\vec{C}$ are coefficient vectors:

$$\vec{A} = 2\vec{a} \times \vec{r_1} - \vec{a} \tag{53}$$

$$\vec{C} = 2 \times \vec{r_2} \tag{54}$$

where $\vec{r_1}$ and $\vec{r_2}$ are random vectors in [0, 1], and vector $\vec{a}$ components vary from 2 to 0, linearly, throughout the iterations.

3.2.3. Hunting

The α, β, and δ type wolves have better awareness about the possible prey's position. Consequently, the initial three best solutions are saved. The other search agents should update their locations according to the position of the leading search agents [40] using Equations (55)–(61).

$$\vec{D_\alpha} = \left| \vec{C_1} \times \vec{X_\alpha} - \vec{X} \right| \tag{55}$$

$$\vec{D_\beta} = \left| \vec{C_2} \times \vec{X_\beta} - \vec{X} \right| \tag{56}$$

$$\vec{D_\delta} = \left| \vec{C_3} \times \vec{X_\delta} - \vec{X} \right| \tag{57}$$

$$\vec{X_1} = \vec{X_\alpha} - \vec{A_1} \times (\vec{D_\alpha}) \tag{58}$$

$$\vec{X_2} = \vec{X_\beta} - \vec{A_2} \times (\vec{D_\beta}) \tag{59}$$

$$\vec{X_3} = \vec{X_\delta} - \vec{A_3} \times (\vec{D_\delta}) \tag{60}$$

$$\vec{X}(t+1) = \frac{\vec{X_1} + \vec{X_2} + \vec{X_3}}{3} \tag{61}$$

3.2.4. Attacking Prey (Exploitation)

When attacking the prey, the value of $\vec{a}$ is reduced, which decreases the variation of $\vec{A}$. If $|A| < 1$, then, the next location of the search agent will be closer to the prey.

3.2.5. Search for Prey (Exploration)

The search is guided according to the α, β, and δ type grey wolves' positions. They go in different directions to search for prey, and gather again to attack it. This divergence is modeled using $|A| > 1$, which allows the GWO to search all over the space by forcing the search agent to get away from the prey. The $\vec{C}$ vector is another constituent of the GWO that helps exploration. It contains random values between 0 and 2 inclusive. This parameter provides random weights for prey to emphasize $(C \geq 1)$ or deemphasize $(C < 1)$ the effect of prey in determining the distance in Equation (51). Consequently, the GWO exhibits a random behavior during optimization to avoid local optima and promote exploration. The GWO intentionally requires $\vec{C}$ to provide random values to accentuate exploitation/exploration during initial and final iterations. This helps if there is a stagnation of the local optima. C is not linearly decreased in comparison to A.

3.3. Hybrid IC-GWA Optimization Approach

Hybrid algorithms are created to increase the performance of an optimization algorithm. They combine the advantages of two or more algorithms. The HIC-GWA is a combination of two evolutionary algorithms where the GWO is used to enhance the exploration ability of the ICA as shown in Figure 1.

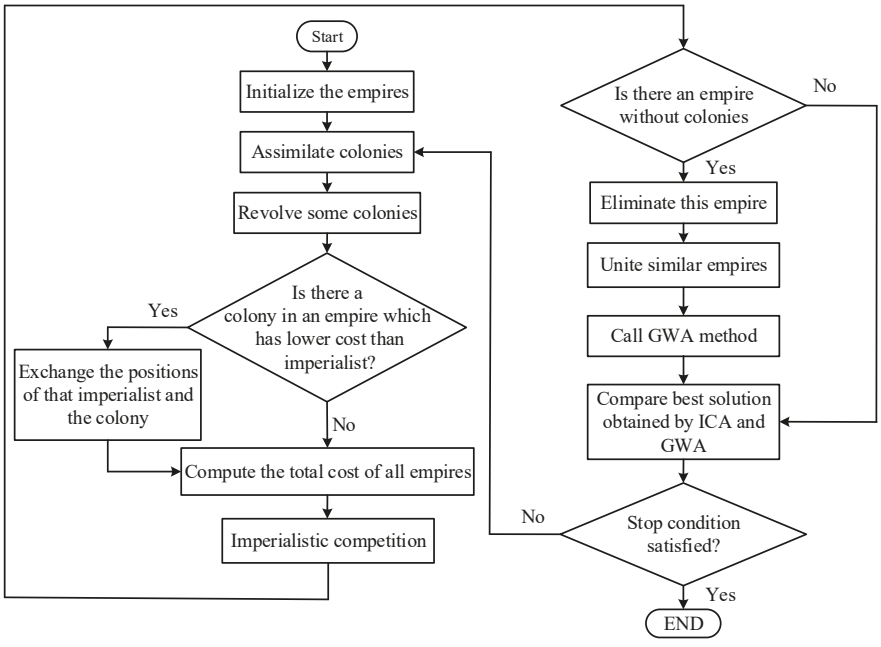

Figure 1. Flowchart of the proposed hybrid imperialist competitive and grey wolf algorithm (HIC-GWA).

In this proposed approach, ICA is initialized first to solve the OPF optimization problem. The assimilation and revolution of colonies, imperialist competition, elimination, and uniting empires are performed. The best solution of ICA is calculated as an initial condition of the GWA. The solution of the GWA is saved as the best value if it is less than the ICA's solution. The simulation continue until the stop condition is satisfied. The converged answer is achieved after termination of the algorithm.

The following steps show how to use the HIC-GWA to solve the OPF problem:

i. The power system data is specified. The HIC-GWA parameters are determined.
ii. Initialize the countries randomly, calculate their costs, and use assimilation.
iii. Revolution.
iv. Exchange positions between imperialist and colony if it has a lower cost.
v. Unite similar empires.
vi. Calculate the total cost of all empires.
vii. Imperialist competition.
viii. Discard powerless empires.
ix. Use solution obtained by ICA as initial condition for GWA.
x. The lower solution between ICA and GWA is saved as best solution.
xi. Go to step (ii) if the stop condition is not satisfied, otherwise, finish simulation.

4. Simulation Results

The HIC-GWA has been applied on the IEEE 30 and 118 bus power systems to solve 12 different cases of OPF problems. The maximum number of iterations is 500 for IEEE 118 bus power system, and 100 for the IEEE 30 bus power systems. Power systems parameters are given in Table 1. The setting of the proposed HIC-GWA approach can be found in Table 2. MATLAB 8.3 (R2014a) has been used to implement simulations on a personal computer with i7 CPU 3.0 GHz 8.0 GB RAM [45,46].

Table 1. Power system's parameters.

Characteristics	IEEE 30		IEEE 118	
Buses	30	[47]	118	[48]
Branches	41		186	
Load voltage	24	[0.95, 1.05]		[0.94, 1.06]
Control variables (N_{var})		24		130

Table 2. Setting of the proposed HIC-GWA approach.

ICA Parameters						GWA Parameters	
ξ	$N_{Country}$		β	N_{imp}		N_w	
	30 bus	118 bus		30 bus	118 bus	30 bus	118 bus
1.02	15	100	0.90	5	20	5	10

The initial population is represented by $N_{country}$. Each population contains one vector with N_{var} components, including bus voltage and active power of the power plant, transformer tap changers, and shunt power injection compensator. The parameter N_{var}, given in Table 1 is different for each case.

Solutions using the proposed approach will be compared with recently published OPF solutions using different optimization methods and objective functions shown in Table 3.

Table 3. Recently published approaches to solve OPF problems.

Acronym	Reference	Simple Objective	Multiobjective	Fuel Cost	Emission	P_{loss}	VD	L Index
MSA	[19]	✓	✓	✓	✓	✓	✓	✓
MPSO	[20]	✓	✓	✓	✓	✓	✓	✓
MDE	[21]	✓	✓	✓	✓	✓	✓	✓
MFO	[22]	✓	✓	✓	✓	✓	✓	✓
FPA	[23]	✓	✓	✓	✓	✓	✓	✓
ARCBBO	[24]	✓		✓	✓	✓	✓	✓
RCBBO	[24]	✓		✓	✓	✓	✓	✓
GWO	[25]	✓	✓	✓		✓		
DE	[25]	✓	✓	✓		✓		
MGBICA	[26]	✓	✓	✓	✓			
ABC	[27]	✓	✓	✓	✓	✓	✓	✓
HSFLA-SA	[28]	✓		✓	✓	✓	✓	✓
LTLBO	[29]	✓		✓	✓	✓	✓	
TLBO	[30]	✓		✓	✓	✓	✓	
HMPSO-SFLA	[31]	✓	✓	✓	✓			
PSO	[31]	✓	✓	✓	✓	✓		
GABC	[32]	✓		✓	✓	✓	✓	✓
DSA	[33]	✓	✓	✓	✓	✓	✓	✓
EEA	[34]	✓	✓	✓		✓		✓
EGA	[34]	✓	✓	✓		✓		✓
ALC-PSO	[35]	✓		✓		✓	✓	

4.1. IEEE 30 Bus Test System

This power test system is used to exhibit the efficiency of the HIC-GWA. The details for busses and line data are shown in [43]. The system active and reactive power are 283.4 MW and 126.2 MVAR.

4.1.1. Simple Objective OPF

The first five case studies have been used to solve simple objective OPF problems.

Case 1: Fuel Cost

This first single objective function considers minimizing the total fuel cost of power generation. It is modeled by the quadratic cost curve given in Equation (14). Simulation results, illustrated in Table 4, show that the fuel cost using the HIC-GWA is 798.20 ($/h).

Table 4. Optimal solution of IEEE 30 bus power system for case studies 1 to 5.

Solutions	Case 1	Case 2	Case 3	Case4	Case 5
Fuel cost ($/h)	798.20	645.85	902.25	959.54	1000.30
Emission (t/h)	0.37	0.28	0.45	0.20	0.21
P_{loss} (MW)	8.86	6.59	11.18	2.67	2.61
VD (p.u.)	1.15	1.25	0.96	1.68	1.41
L index	0.13	0.13	0.17	0.13	0.12

Compared with solutions from state-of-the-art existing optimization approaches in Table 5, the proposed HIC-GWA has significantly reduced the total fuel cost.

Table 5. Comparison of HIC-GWA with the literature for case study 1.

Algorithm	Fuel Cost ($/h)	Emission (t/h)	P_{loss} (MW)	VD (p.u.)	L Index
MSA	800.51	0.37	9.03	0.90	0.14
MPSO	800.52	0.37	9.04	0.90	0.14
MDE	800.84	0.36	808365.00	0.78	0.14
MFO	800.69	0.37	9.15	0.76	0.14
FPA	802.80	0.36	9.54	0.37	0.15
ARCBO	800.52	0.37	9.03	0.89	0.14
HSFLA-SA	801.79				
HIC-GWA	798.20	0.37	8.86	1.15	0.13

The convergence curve of the total cost ($/h) for case 1 is shown in Figure 2. Note that it converged in less than 30 iterations.

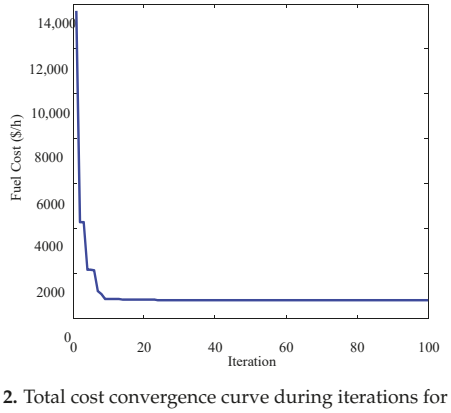

Figure 2. Total cost convergence curve during iterations for case 1.

Case 2: Piecewise quadratic fuel cost

Thermal generators produce electricity by burning fuels such as coal, petroleum, or natural gas. The model for the fuel cost curve is given by Equation (15). Simulation results, illustrated in

Table 4, show that the fuel cost using the proposed approach is 645.85 ($/h). Compared with existing optimization methods in Table 6, HIC-GWA has significantly reduced the total fuel cost.

Table 6. Comparison of HIC-GWA with the literature for case study 2.

Algorithm	Fuel Cost ($/h)	Emission (t/h)	P_{loss} (MW)	VD (p.u.)	*L* Index
MSA	646.84	0.28	6.80	0.84	0.14
MPSO	646.73	0.28	6.80	0.77	0.14
MDE	650.28	0.28	6.98	0.58	0.14
MFO	649.27	0.28	7.29	0.47	0.14
FPA	651.38	0.28	7.24	0.31	0.15
LTLBO	647.43	0.28	6.93	0.89	
TLBO	647.92		7.11	1.42	0.12
HIC-GWA	645.85	0.28	6.59	1.25	0.13

In cases 1 and 2, the proposed metaheuristic has a better convergence than recently published optimization methods.

Case 3: Piecewise quadratic fuel cost with valve point loading

The valve point loading effect is included in the cost function of Equation (17). Simulation results, illustrated in Table 4, show that the fuel cost using HIC-GWA is 902.25 ($/h). Compared with existing optimization methods in Table 7, HIC-GWA has significantly reduced the fuel cost in this case.

Table 7. Comparison of HIC-GWA with the literature for case study 3.

Algorithm	Fuel Cost ($/h)	Emission (t/h)	P_{loss} (MW)	VD (p.u.)	*L* Index
MSA	930.74	0.43	13.14	0.45	0.16
MPSO	952.30	0.30	7.30	0.72	0.14
MDE	930.94	0.43	12.73	0.45	0.16
MFO	930.72	0.44	13.18	0.47	0.16
FPA	931.75	0.43	12.11	0.47	0.15
HIC-GWA	902.25	0.45	11.18	0.96	0.17

Case 4: Emission

The objective, in this case, is to reduce the emission level of important air pollutants like NOx and SOx, using the emission function described in Equation (18). Simulation results, illustrated in Table 4, show that the emission using HIC-GWA is 0.2009 (ton/h). Compared with existing optimization methods in Table 8, HIC-GWA has significantly reduced the emission level.

Table 8. Comparison of HIC-GWA with the literature for case study 4.

Algorithm	Fuel Cost ($/h)	Emission (t/h)	P_{loss} (MW)	VD (p.u.)	*L* Index
MSA	944.50	0.2048	3.24	0.87	0.14
MPSO	879.95	0.2325	7.05	0.57	0.14
MDE	927.81	0.2093	4.85	0.40	0.15
MFO	945.46	0.2049	3.43	0.71	0.14
FPA	948.95	0.2052	4.49	0.43	0.14
ARCBO	945.16	0.2048	3.26	0.86	0.14
MGBICA	942.84	0.2048			
GBICA	944.65	0.2049			
ABC	944.44	0.2048	3.25	0.85	0.14
DSA	944.41	0.2583	3.24		0.13
HMPSO-SFLA		0.2052			
HIC-GWA	959.54	0.2009	2.67	1.68	0.13

Case 5: Active power loss

To reduce transmission lines active power loss, we use the objective function given in Equation (19). Simulation results, illustrated in Table 4, show that the power loss using HIC-GWA is 2.61 (MW). Compared with existing optimization methods in Table 9, HIC-GWA has significantly reduced the power loss.

Table 9. Comparison of HIC-GWA solutions with the literature for case study 5.

Algorithm	Fuel Cost ($/h)	Emission (t/h)	P_{loss} (MW)	VD (p.u.)	L Index
MSA	967.66	0.2073	3.10	0.89	0.14
MPSO	967.65	0.2073	3.10	0.96	0.14
MDE	967.65	0.2073	3.16	0.77	0.14
MFO	967.68	0.2073	3.11	0.92	0.14
FPA	967.11	0.2076	6.57	0.39	0.14
ARCBO	967.66	0.2073	3.10	0.89	0.14
GWO	968.38		3.41		
DE	968.23		3.38		
ABC	967.68	0.2073	3.11	0.90	0.14
DSA	967.65	0.2083	3.09		0.13
EEA	952.38		3.28		
EGA	967.93		3.24		
ALC-PSO	967.77		3.17		
HIC-GWA	1000.30	0.2080	2.61	1.41	0.12

In cases 3, 4, and 5, the proposed metaheuristic showed a better exploration than recently published optimization methods that appear to be stuck at a local minimum.

4.1.2. Multiobjective OPF

In the next five cases, we used the proposed metaheuristics to find better solutions for multiobjective OPF problems. Table 10 summarizes the best solutions of the simulation results using the HIC-GWA approach for cases 6–10.

Table 10. Optimal solution of IEEE 30 bus power system for case studies 6 to 10.

Solutions	Case 6	Case 7	Case 8	Case 9	Case 10
Fuel cost ($/h)	856.99	802.45	797.80	802.00	817.59
Emission (t/h)	0.23	0.36	0.37	0.36	0.27
P_{loss} (MW)	4.04	9.95	8.75	9.67	5.29
VD (p.u.)	1.78	0.10	1.98	1.97	0.23
L index	0.12	0.13	0.11	0.11	0.15

Case 6: Fuel cost and active power losses

Cases 1 and 5 have been combined to reduce the fuel cost and the active power losses using the multiobjective function given in Equation (20). Simulation results show that the fuel cost and power loss using HIC-GWA are 856.99 ($/h) and 4.04 (MW). Compared with MSA, MDE, MPSO, FPA, and MFO approaches in Table 11, HIC-GWA has significantly reduced the fuel cost and power loss.

Table 11. HIC-GWA solutions compared with the literature for case 6.

Solutions	MSA	MDE	MPSO	FPA	MFO	HIC-GWA
Fuel cost ($/h)	859.19	868.71	859.58	855.27	858.58	856.99
Emission (t/h)	0.23	0.23	0.23	0.23	0.23	0.23
P_{loss} (MW)	4.54	4.39	4.54	4.80	4.58	4.04
VD (p.u.)	0.93	0.88	0.95	1.01	0.90	1.78
L index	0.14	0.14	0.14	0.14	0.14	0.12
Total cost	1040.81	1044.05	1041.22	1055.72	1041.67	1018.45

Case 7: Fuel cost and voltage deviation

Voltage profile management is essential to ensure system security. Voltage profile improvement reduces the deviation of load bus voltage. A multiobjective function is presented in Equation (21) to reduce the voltage deviations and fuel cost simultaneously. Simulation results show that the fuel cost and voltage deviations using the proposed approach are 802.45 ($/h) and 0.10 (p.u), respectively. Compared with MSA, MDE, MPSO, FPA, and MFO approaches in Table 12, HIC-GWA has significantly reduced the fuel cost and voltage deviations.

Table 12. Comparison of the proposed approach with different approaches for this case.

Solutions	MSA	MDE	MPSO	FPA	MFO	HIC-GWA
Fuel cost ($/h)	803.31	803.21	803.98	803.66	803.79	802.45
Emission (t/h)	0.36	0.36	0.36	0.37	0.36	0.36
P_{loss} (MW)	9.72	9.60	9.92	9.93	9.87	9.95
VD (p.u.)	0.11	0.13	0.12	0.14	0.11	0.10
L index	0.15	0.15	0.15	0.15	0.15	0.13
Total cost	814.15	815.86	816.00	817.32	814.35	812.05

Case 8: Fuel cost with voltage stability improvement

The L index describes the system stability by measuring the distance of the actual state of the system to the stability limit. We are using the objective function given in Equation (22) to reduce both fuel cost and voltage stability. Simulation results, illustrated in Table 13, show that the fuel cost and L index using the proposed approach are 797.80 ($/h) and 0.11 (p.u), respectively. Compared with MSA, MDE, MPSO, FPA, and MFO approaches in Table 13, HIC-GWA has significantly reduced the fuel cost and L index.

Table 13. Comparison of the proposed approach with different approaches for case 8.

Solutions	MSA	MDE	MPSO	FPA	MFO	HIC-GWA
Fuel cost ($/h)	801.22	802.10	801.70	801.15	801.67	797.80
Emission (t/h)	0.36	0.35	0.36	0.37	0.34	0.37
P_{loss} (MW)	8.98	9.06	9.20	9.32	8.56	8.75
VD (p.u.)	0.93	0.89	0.83	0.88	0.84	1.98
L index	0.14	0.14	0.14	0.14	0.14	0.11
Total cost	814.94	815.84	815.44	814.91	815.43	808.38

Case 9: Fuel cost with voltage stability improvement during contingency condition

We consider the previous case with disruption of line (2–6) to simulate N - 1 contingency. Best solutions for the fuel cost and the L index using HIC-GWA are 802.00 ($/h) and 0.11 (p.u), respectively. Compared with MSA, MDE, MPSO, FPA, and MFO approaches illustrated in Table 14, HIC-GWA has significantly reduced the fuel cost and L index during contingency condition.

Table 14. Comparison of the proposed approach with different approaches for case 9.

Solutions	MSA	MDE	MPSO	FPA	MFO	HIC-GWA
Fuel cost ($/h)	804.48	806.67	807.65	805.54	804.56	802.00
Emission (t/h)	0.36	0.37	0.36	0.36	0.36	0.36
P_{loss} (MW)	9.95	10.72	10.76	10.18	9.95	9.67
VD (p.u.)	0.92	0.57	0.43	0.45	0.91	1.97
L index	0.14	0.14	0.14	0.14	0.14	0.11
Total cost	832.32	834.63	835.75	833.84	832.43	823.06

Case 10: Fuel cost, voltage deviation, emission, and power loss

The multiobjective function defined by Equation (24) combines three previous cases: 4, 5, and 7 to minimize fuel cost, voltage deviation, emission, and power loss simultaneously. Simulation results, illustrated in Table 15, show that HIC-GWA has significantly reduced the fuel cost, emission, power loss, and voltage deviation compared with MSA, MDE, MPSO, FPA, and MFO approaches

Table 15. Comparison of the proposed approach with different approaches for case 10 of IEEE 30.

Solutions	MSA	MDE	MPSO	FPA	MFO	HIC-GWA
Fuel cost ($/h)	830.6	829.1	833.7	835.4	830.9	817.6
Emission (t/h)	0.3	0.3	0.3	0.2	0.3	0.3
P_{loss} (MW)	5.6	6.1	6.5	5.5	5.6	5.3
VD (p.u.)	0.3	0.3	0.2	0.5	0.3	0.2
L index	1.5	0.1	0.1	0.1	0.1	0.1
Total cost	965.3	973.6	986.0	971.9	965.8	944.0

In cases 6–10, the proposed metaheuristic showed a better exploration than recently published optimization methods that appear to be stuck at a local minimum.

The total cost convergence curve for case 10 is displayed in Figure 3. The HIC-GWA approach converged in less than 50 iterations.

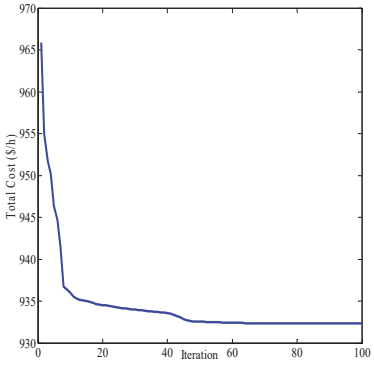

Figure 3. Total cost convergence curve for case 10.

Convergence curves of the fuel cost, voltage deviation, power loss, and emission are shown in Figure 4.

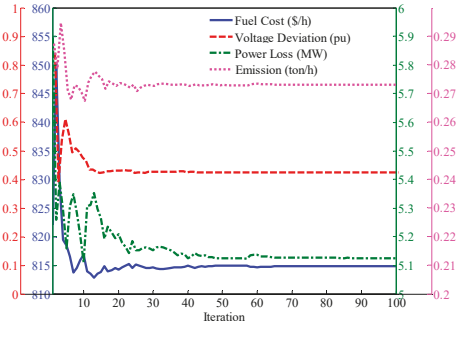

Figure 4. Total cost components convergence curves for case 10.

4.2. The IEEE 118 Bus Power System

The IEEE 118 bus test system [44], has been used for the next two cases to confirm the effectiveness of the HIC-GWA approach. The active and reactive power demand are 4242 MW and 1439 MVAR.

Case 11: Fuel cost

The function modeled by the quadratic cost curve given in Equation (14) is considered to minimize the total fuel cost of power generation. The simulation results, illustrated in Table 16, show that the HIC-GWA has significantly reduced the fuel cost compared with MSA, MDE, MPSO, FPA, and MFO approaches.

Table 16. Comparison of HIC-GWA results with the literature for case study 11.

Solutions	MSA	MDE	MPSO	FPA	MFO	HIC-GWA
Fuel cost ($/h)	129640.72	130444.57	132039.21	129688.72	129708.08	129633.70
P_{loss} (MW)	73.26	71.64	112.85	74.32	74.71	76.80
VD (p.u.)	3.07	1.31	1.15	2.54	2.38	3.13
L index	0.06	0.07	0.07	0.06	0.06	0.06

In this case, the proposed metaheuristic has a better convergence than recently published optimization methods.

Case 12: Fuel cost with renewable energy sources (Wind/PV)

The objective in this case is to use the HIC-GWA to minimize the fuel cost (F_1), wind cost (F_2), and PV cost (F_3) for a system that includes renewable sources like WE and PV. The conventional power plants 12, 31, 66, 72, and 100 are replaced by five wind power units, and the conventional power plants 34, 36, 46, and 62 are replaced by four PV units. The simulation results are illustrated in Table 17.

Table 17. Optimal solution of IEEE 118 bus power system for case study 12.

Fuel cost ($/h)	112,545.51
Wind cost ($/h)	5340.42
PV cost ($/h)	4211.38
P_{loss}(MW)	76.64
VD (p.u.)	3.13
L index	0.06

The total cost convergence curve for case 12 is presented in Figure 5. The proposed HIC-GWA approach converged in less than 100 iterations.

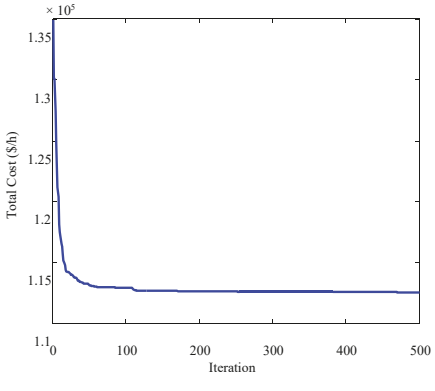

Figure 5. Total cost convergence curve for case 12.

4.3. HIC-GWA Robustness Analysis

Robustness analysis, which is a non-empirical form of confirmation, is an indispensable procedure in studying complex phenomena. A sensitivity analysis for case studies 1 and 11 has been performed to evaluate the robustness of the considered metaheuristic. Each parameter of the HIC-GWA has been perturbed by changing the values up and down. Likewise, optimization parameters values have been changed also to check the global effect of parameter's variations on the solution of the OPF problem. The equivalent Pareto solutions are illustrated in Table 18. The deviation ratio between normal and perturbed solutions is calculated using the following equation:

$$Deviation\ (\%) = \frac{Normal\ Solution - Perturbed\ Solution}{Normal\ Solution} \times 100, \tag{62}$$

Table 18. Sensitivity analysis for IEEE 30 bus and 118 bus power systems.

Parameters	30 Bus Power System		Parameters	118 Bus Power System	
	Cost ($/h)	Deviation (%)		Cost ($/h)	Deviation (%)
Normal Solution	798.20	0.0	Normal Solution	129,633.70	0.0
$N_{Country} = 15 + 5$	797.38	+0.1017	$N_{Country} = 200 + 30$	129,631.93	+0.00137
$N_{Country} = 15 - 5$	799.07	−0.1102	$N_{Country} = 200 - 30$	129,636.79	−0.00238
$N_{imp} = 5 + 2$	797.33	+0.1082	$N_{impw} = 40 + 10$	129,632.44	+0.00098
$N_{imp} = 5 - 2$	797.00	+0.1491	$N_{impw} = 40 - 10$	129,630.66	+0.00235
$N_w = 5 + 2$	797.12	+0.1341	$N_w = 10 + 3$	129,631.77	+0.00149
$N_w = 5 - 2$	798.98	−0.0984	$N_w = 10 - 3$	129,634.92	−0.00094
All (up)	797.06	+0.1420	All (up)	129,630.94	+0.00213
All (Down)	799.08	−0.1110	All (Down)	129,645.84	−0.00936

Small deviations affirm the robustness of the HIC-GWA to variation of parameters in solving OPF problems.

To confirm the robustness of the HIC-GWA, we compare best and worst fuel cost averages to recently published OPF optimization methods in Table 19. The proposed HIC-GWA has consistently better solutions over 30 trial runs.

Table 19. Comparisons of the results obtained for case 2.

Algorithm	Best Cost ($/h)	Worst Cost ($/h)	Average Cost ($/h)
MSA	646.84	648.03	646.86
MPSO	646.73	656.23	649.86
MDE	650.28	653.40	651.26
MFO	649.27	650.62	649.89
FPA	651.38	654.33	652.96
LTLBO	647.43	647.86	647.47
ABC	649.09	659.77	654.08
GABC	647.03	647.12	647.08
HIC-GWA	645.85	647.03	645.87

Table 20 shows the convergence speed of the HIC-GWA compared to recently published optimization methods. With 14.34 (s), HIC-GWA is second fastest to MFO by one hundredth of a second.

Table 20. Case 2 simulation time.

Algorithm	Time (s)
MICA-TLA	30.74
LTLBO	22.78
HMPSO-SFLA	19.06
MPSO	16.05
MDE	15.63
MSA	14.91
FPA	14.79
HIC-GWA	14.34
MFO	14.33

5. Conclusions

A novel hybrid optimization method combining imperialist competitive and grey wolf algorithm, HIC-GWA, has been proposed, developed, and applied successfully to solve twelve different test cases of single and multiobjective OPF problems in two IEEE test power systems with a mixture of wind energy and photovoltaic units. The results show that this metaheuristic is found to be very effective for large-scale applications, due to fast convergence and very few chances to get stuck at local minima. Analysis of the obtained solutions, along with a comparative study with recently published OPF optimization algorithms, proved the validity, effectiveness, and robustness of the HIC-GWA in precisely providing a set of stable optimal solutions, computed under realistic conditions, for a hybrid power system. This is very important in managing modern power systems, which are incorporating an ever-increased number of alternative energy sources. The proposed metaheuristic outperformed current well known and powerful algorithms in the literature, which confirms its superiority and potential to find valid and accurate solutions for multiobjective optimization. Indeed, the proposed paradigm may be used as a tool to answer many specific features of large-scale complex systems in general, thereby motivating further studies.

Author Contributions: Conceptualization, J.B.; Methodology, J.B.; Software, J.B., and M.M.; Validation, J.B., and M.M.; Formal Analysis, J.B.; Investigation, J.B.; Resources, J.B.; Data Curation, J.B.; Writing-Original Draft Preparation, J.B.; Writing-Review & Editing, J.B., J.L., and T.C.; Visualization, J.B., M.M.; J.L.; and T.C.; Supervision, J.L., and T.C.; Project Administration, J.L., and T.C.; Funding Acquisition, T.C.

Funding: This research received no external funding.

Conflicts of Interest: The authors declare no conflict of interest.

Nomenclature

$C_{d,i}$	direct cost of WE and PV(\$/h)
$C_{ue,i}$	underestimating penalty cost of ith WE and PV (\$/h)
$C_{oe,i}$	overestimating penalty cost of ith WE and PV (\$/h)
$COST_i$	total cost of ith WE and PV (\$/h)
$d_{w,i}$	direct cost coefficient of WE and PV (\$/MW)
$K_{ue,i}$	underestimating coefficient cost of ith WE and PV (\$/MW)
$K_{oe,i}$	overestimating coefficients cost of $i$thWE and PV (\$/MW)
$P_{w,i}$	power of the ith WE (MW)
$P_{pv,i}$	power of the ith PV (MW)
$P_{w,r,i}$	rated power of the ith WE (MW)
$P_{pv,r,i}$	rated power of the ith PV(MW)
n_w	number of WEs
n_v	number of PVs

References

1. Carpentier, J. Optimal power flows. *Int. J. Elect. Power Energy Syst.* **1979**, *1*, 3–15. [CrossRef]
2. Momoh, J.A.; Koessler, R.J.; Bond, M.S.; Stott, B.; Sun, D.; Papalexopoulos, A.; Ristanovic, P. Challenges to optimal power flow. *IEEE Trans. Power Syst.* **1997**, *12*, 444–447. [CrossRef]
3. Capitanescu, F.; Martinez Ramos, J.L.; Panciatici, P.; Kirschen, D.; Platbrood, L.; Wehenkel, L. State-of-the-art challenges and future trends in security constrained optimal power flow. *Elect. Power Syst. Res.* **2011**, *81*, 1731–1741. [CrossRef]
4. Low, S.H. Convex Relaxation of Optimal Power Flow: Parts I & II. *IEEE Trans. Control Netw. Syst.* **2014**, *1*, 15–27.
5. Panciatici, P.; Campi, M.; Garatti, S.; Low, S.; Molzahn, D.; Sun, A.; Wehenkel, L. Advanced optimization methods for power systems. In Proceedings of the 18th Power Systems Computation Conference (PSCC), Wroclaw, Poland, 18–22 August 2014; pp. 1–18.

6. Cain, M.B.; O'Neill, R.P.; Castillo, A. History of Optimal Power Flow and Formulations. Available online: https://www.ferc.gov/industries/electric/indus-act/market-planning/opf-papers/acopf-1-history-formulation-testing.pdf (accessed on 18 June 2018).
7. Molzahn, D.K.; Dorfler, F.; Sandberg, H.; Low, S.H.; Chakrabarti, S.; Baldick, R.; Lavaei, J. A survey of distributed optimization and control algorithms for electric power systems. *IEEE Trans. Smart Grid* **2017**, *8*, 2941–2962. [CrossRef]
8. Frank, S.; Steponavice, I.; Rebennack, S. Optimal power flow: A bibliographic survey parts I and II. *Energy Syst.* **2012**, *3*, 221–289. [CrossRef]
9. Baydar, B.; Gozde, H.; Taplamacioglu, M.C.; Kucuk, A.O. Resilient Optimal Power Flow with Evolutionary Computation Methods: Short Survey. In *Power Systems Resilience*; Mahdavi, T.N., Ed.; Springer: Cham, Switzerland, 2019.
10. Thomson, M.; Infield, D. Network power-flow analysis for a high penetration of distributed generation. *IEEE Trans. Power Syst.* **2007**, *22*, 1157–1162. [CrossRef]
11. Bonface, O.N.; Hideharu, S.; Tsuyoshi, F. Optimal power flow considering line-conductor temperature limits under high penetration of intermittent renewable energy sources. *Int. J. Electr. Power Energy Syst.* **2018**, *101*, 255–267.
12. Morshed, M.J.; Ben Hmida, J.; Fekih, A. A probabilistic multiobjective approach for power flow optimization in hybrid wind-PV-PEV systems. *Appl. Energy* **2018**, *211*, 1136–1149. [CrossRef]
13. Pourakbari-Kasmaei, M.; Sanches, J.R. Logically constrained optimal power flow: Solver-based mixed-integer nonlinear programming model. *Int. J. Electr. Power Energy Syst.* **2018**, *97*, 240–249. [CrossRef]
14. Momoh, J.A.; Adapa, R.; El-Hawary, M.E. A review of selected optimal power flow literature to 1993. I. Nonlinear and quadratic programming approaches. *IEEE Trans. Power Syst.* **1999**, *14*, 96–104. [CrossRef]
15. Momoh, J.A.; El-Hawary, M.E.; Adapa, R. A review of selected optimal power flow literature to 1993. II. Newton linear programming and interior point methods. *IEEE Trans. Power Syst.* **1999**, *14*, 105–111. [CrossRef]
16. Ghasemi, M.; Ghavidel, S.; Akbari, E.; Vahed, A.A. Solving non-linear, non-smooth and non-convex optimal power flow problems using chaotic invasive weed optimization algorithms based on chaos. *Energy* **2014**, *73*, 340–353. [CrossRef]
17. Ghasemi, M.; Ghavidel, S.; Aghaei, J.; Gitizadeh, M.; Falah, H. Application of chaos-based chaotic invasive weed optimization techniques for environmental OPF problems in the power system. *Chaos Solitons Fractals* **2014**, *69*, 271–284. [CrossRef]
18. Boussaïd, I.; Lepagnot, J.; Siarry, P. A survey on optimization metaheuristics. *Inf. Sci.* **2013**, *237*, 82–117. [CrossRef]
19. Mohamed, A.A.; Mohamed, Y.S.; El-Gaafary, A.A.M.; Hemeida, A.M. Optimal power flow using moth swarm algorithm. *Electr. Power Syst. Res.* **2017**, *142*, 190–206. [CrossRef]
20. Karami, A. A fuzzy anomaly detection system based on hybrid pso-k means algorithm in content-centric networks. *Neurocomputing* **2015**, *149*, 1253–1269. [CrossRef]
21. Dos Santos Coelho, L.; Mariani, V.C.; Leite, J.V. Solution of Jiles-Atherton vector hysteresis parameters estimation by modified Differential Evolution approaches. *Expert Syst. Appl.* **2012**, *39*, 2021–2025. [CrossRef]
22. Mirjalili, S. Moth-flame optimization algorithm: A novel nature-inspired heuristic paradigm. *Knowl. Based Syst.* **2015**, *89*, 228–249. [CrossRef]
23. Yang, X.S. Flower Pollination Algorithm for Global Optimization. In *Unconventional Computation and Natural Computation*; Springer: Berlin, Germany, 2012; pp. 240–249.
24. Kumar, A.R.; Premalatha, L. Optimal power flow for a deregulated power system using adaptive real coded biogeography-based optimization. *Int. J. Electr. Power Energy Syst.* **2015**, *73*, 393–399. [CrossRef]
25. El-Fergany, A.A.; Hasanien, H.M. Single and multiobjective optimal power flow using grey wolf optimizer and differential evolution algorithms. *Electr. Power Compon. Syst.* **2015**, *43*, 1548–1559. [CrossRef]
26. Ghasemi, M.; Ghavidel, S.; Ghanbarian, M.M.; Gitizadeh, M. Multiobjective optimal electric power planning in the power system using Gaussian bare-bones imperialist competitive algorithm. *Inf. Sci.* **2015**, *294*, 286–304. [CrossRef]
27. Adaryani, M.R.; Karami, A. Artificial bee colony algorithm for solving multiobjective optimal power flow problem. *Int. J. Electr. Power Energy Syst.* **2013**, *53*, 219–230. [CrossRef]

28. Niknam, T.; Narimani, M.R.; Azizipanah, A.R. A new hybrid algorithm for optimal power flow considering prohibited zones and valve point effect. *Energy Convers. Manag.* **2012**, *58*, 197–206. [CrossRef]
29. Ghasemi, M.; Ghavidel, S.; Gitizadeh, M.; Akbari, E. An improved teaching-learning-based optimization algorithm using Lévy mutation strategy for non-smooth optimal power flow. *Int. J. Electr. Power Energy Syst.* **2015**, *65*, 375–384. [CrossRef]
30. Bouchekara, H.; Abido, M.A.; Boucherma, M. Optimal power flow using teaching-learning-based optimization technique. *Electr. Power Syst. Res.* **2014**, *114*, 49–59. [CrossRef]
31. Narimani, M.R.; Azizipanah, A.R.; Zoghdar, M.S.B.; Gholami, K. A novel approach to multiobjective optimal power flow by a new hybrid optimization algorithm considering generator constraints and multi-fuel type. *Energy* **2013**, *49*, 119–136. [CrossRef]
32. Roy, R.; Jadhav, H.T. Optimal power flow solution of power system incorporating stochastic wind power using Gbest guided artificial bee colony algorithm. *Int. J. Electr. Power Energy Syst.* **2015**, *64*, 562–578. [CrossRef]
33. Abaci, K.; Yamacli, V. Differential search algorithm for solving multiobjective optimal power flow problem. *Int. J. Electr. Power Energy Syst.* **2016**, *79*, 1–10. [CrossRef]
34. Reddy, S.S.; Bijwe, P.R.; Abhyankar, A.R. Faster evolutionary algorithm based optimal power flow using incremental variables. *Int. J. Electr. Power Energy Syst.* **2014**, *54*, 198–210. [CrossRef]
35. Singh, R.P.; Mukherjee, V.; Ghoshal, S.P. Particle swarm optimization with an aging leader and challenger's algorithm for the solution of optimal power flow problem. *Appl. Soft Comput.* **2016**, *40*, 161–177. [CrossRef]
36. Coello Coello, C.A. A Comprehensive Survey of Evolutionary-Based Multiobjective Optimization Techniques. *Knowl. Inf. Syst.* **1999**, *1*, 269–308. [CrossRef]
37. Khabbazi, A.; Atashpaz, G.E.; Lucas, C. Imperialist competitive algorithm for minimum bit error rate beamforming. *Int. J. Bio-Inspired Comput.* **2009**, *1*, 125–133. [CrossRef]
38. Kaveh, A. Imperialist Competitive Algorithm. In *Advances in Metaheuristic Algorithms for Optimal Design of Structures*; Springer: Cham, Switzerland, 2017.
39. Ardalan, A.; Karimi, S.; Poursabzi, O.; Naderi, B. A novel imperialist competitive algorithm for generalized traveling salesman problems. *Appl. Soft Comput.* **2015**, *26*, 546–555. [CrossRef]
40. Mirjalili, S.; Mirjalili, S.M.; Lewis, A. Grey wolf optimizer. *Adv. Eng. Softw.* **2014**, *69*, 46–61. [CrossRef]
41. Zhang, X.; Miao, Q.; Liu, Z.; He, Z. An adaptive stochastic resonance method based on grey wolf optimizer algorithm and its application to machinery fault diagnosis. *ISA Trans.* **2017**, *71*, 206–214. [CrossRef] [PubMed]
42. Hooshmand, R.A.; Morshed, M.J.; Parastegari, M. Congestion management by determining optimal location of series FACTS devices using hybrid bacterial foraging and Nelder-Mead algorithm. *Appl. Soft Comput.* **2015**, *28*, 57–68. [CrossRef]
43. Zimmerman, R.D.; Murillo-Sánchez, C.E. Matpower. Available online: http://www.pserc.cornell.edu/matpower (accessed on 18 June 2018).
44. Shi, L.; Wang, C.; Yao, L.; Ni, Y.; Bazargan, M. Optimal power flow solution incorporating wind power. *IEEE Syst. J.* **2012**, *6*, 233–241. [CrossRef]
45. Atashpaz-Gargari, E. Available online: https://www.mathworks.com/matlabcentral/fileexchange/22046-imperialist-competitive-algorithm-ica (accessed on 18 June 2018).
46. Mirjalili, S. Available online: https://www.mathworks.com/matlabcentral/fileexchange/44974-grey-wolf-optimizer-gwo (accessed on 18 June 2018).
47. Ghasemi, M.; Ghavidel, S.; Ghanbarian, M.M.; Gharibzadeh, M.; Azizi Vahed, A. Multiobjective optimal power flow considering the cost, emission, voltage deviation and power losses using multiobjective modified imperialist competitive algorithm. *Energy* **2014**, *78*, 276–289. [CrossRef]
48. Electrical and Computer Engineering Department. Available online: http://motor.ece.iit.edu/data/ (accessed on 18 June 2018).

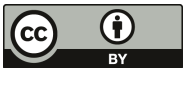

energies

MDPI

Article

A Novel Integrated Method to Diagnose Faults in Power Transformers

Jing Wu [1,*], Kun Li [1], Jing Sun [1] and Li Xie [2]

[1] School of Automation Science and Electrical Engineering, Beihang University, Beijing 100191, China; jackli5288@gmail.com (K.L.); jing.sun@buaa.edu.cn (J.S.)

[2] China Electric Power Research Institute, Beijing 100192, China; xieli@epri.sgcc.com.cn

* Correspondence: wujing06@buaa.edu.cn; Tel.: +86-10-82317304

Received: 10 September 2018; Accepted: 15 October 2018; Published: 5 November 2018

Abstract: In a smart grid, many transformers are equipped for both power transmission and conversion. Because a stable operation of transformers is essential to maintain grid security, studying the fault diagnosis method of transformers can improve both fault detection and fault prevention. In this paper, a data-driven method, which uses a combination of Principal Component Analysis (PCA), Particle Swarm Optimization (PSO), and Support Vector Machines (SVM) to enable a better fault diagnosis of transformers, is proposed and investigated. PCA is used to reduce the dimension of transformer fault state data, and an improved PSO algorithm is used to obtain the optimal parameters for the SVM model. SVM, which is optimized using PSO, is used for the transformer-fault diagnosis. The diagnostic-results of the actual transformers confirm that the new method is effective. We also verified the importance of data richness with respect to the accuracy of the transformer-fault diagnosis.

Keywords: smart grid; transformer-fault diagnosis; principal component analysis; particle swarm optimization; support vector machine

1. Introduction

Several advanced technologies can be used to monitor power-equipment, and the large amount of status data of used equipment helps make the power grid "smarter". Power transformers are expensive and important components of the smart grid, and hub devices for power transformation and transmission [1–4]. Because various faults, such as discharge and overheating, can occur during the operation of transformers, many characteristics corresponding to the faults can be affected like dissolved gases (H_2, CH_4, C_2H_6, C_2H_4, C_2H_2, CO, etc.), organic compounds (methanol, ethanol and 2-furfural), as well as the current and power of the transformers [5]. The dissolved gas analysis (DGA) is a common tool for monitoring and identifying transformer's faults. IEEE C57.104. and IEC 60599 provide different methods such as key gases, Doernenburg Ratio, Rogers, three basic gas ratio, Duval triangle, and so on. However, due to the complexity of the working environment and the process structure of the transformers, these methods are not enough to make a right judgement and cannot judge fault fuzzy boundary. According to [6], their accuracy rates are about in 60%, which means the ratio methods cannot account for the diagnostic criteria completely [7]. In addition, the concentrations of cellulose chemical markers in oil, such as methanol, ethanol and 2-furfural, are used as a determination mark for diagnosing transformer insulation failure, which still present many challenges for an accurate interpretation in real transformers [8].

To improve the accuracy of fault diagnosis, artificial intelligence and machine learning algorithm were added to the field of transformer-fault diagnosis (TFD), including fuzzy sets [9], artificial neural networks (ANN) [10], artificial immune networks [11], probabilistic neural networks [12], rough sets [13], and support vector machines (SVM) [14]. These algorithms provide ways to develop new TFD technologies. However, these algorithms have some disadvantages. For example, it is difficult to

determine the selection of parameters of fuzzy sets, artificial immune networks and probabilistic neural networks, ANNs are easier to fall into local minimum, and the fault-tolerant ability and generalization ability of rough set are weak.

SVM is usually used as a classification tool. From early 2-category techniques, multi-class SVM have been developed and are more suitable for TFD. The accuracy of multi-class SVM is determined by the parameters of its kernel function and penalty factor. In order to improve the efficiency of SVM in processing large amounts of input fault data, principal component analysis (PCA) will be used. Moreover, to reduce the influence of human experience and subjective judgment on these parameters, a new Particle Swarm Optimization (PSO) is borrowed to search the optimized parameters. This way, the most suitable SVM parameters within the effective input data reflecting the transformer's fault will be found. SVM integrated with PCA and PSO can improves the speed and accuracy of TFD considerably. This paper is organized as follows. Section 2 introduces the complete TFD procedure implemented by improved SVM; In Section 3, we compare the accuracy of transformer-fault diagnosis using different methods. We then verify the effectiveness of the proposed method, and analyze the effect of data richness on the accuracy of the fault diagnosis. Section 4 summarizes all results.

2. TFD Model Based on SVM Integrated with PCA and PSO

TFD model based on SVM integrated with PCA and PSO is shown in Figure 1. It includes two main parts. One is that a set of transformer fault data (Data set) such as the densities of the dissolved gases is preprocessed by PCA. The other is that the parameters of SVM model are searched and optimized by PSO.

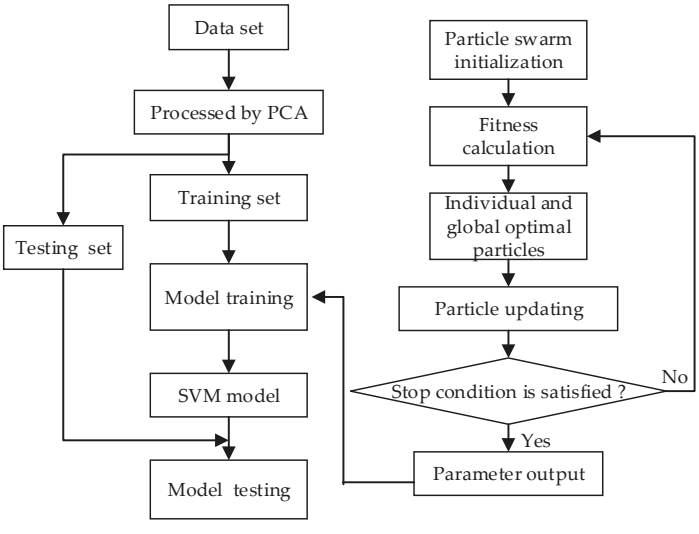

Figure 1. Transformer-fault diagnosis (TFD) model based on support vector machines (SVM) integrated with principal component analysis (PCA) and particle swarm optimization (PSO).

2.1. Data Set Preprocessed by PCA

TFD is a complicated task. In order to improve the operating efficiency of the SVM when there are many transformer fault data, the data needs to be pre-processed before they are used to train the SVM model. PCA aims to reduce the dimensions of fault data and replaces them with fewer uncorrelated and unoverlapped data (called principal components). The number of principal components is selected by variance contribution rate indicating how much information is included.

Suppose the data set X has n groups and each group has p fault data and they construct an original data observation matrix:

$$X_{n\times p} = \begin{pmatrix} x_{11} & x_{12} & \cdots & x_{1p} \\ x_{21} & x_{22} & \cdots & x_{2p} \\ \vdots & \vdots & \ddots & \vdots \\ x_{n1} & x_{n2} & \cdots & x_{np} \end{pmatrix} \tag{1}$$

To solve the principal components, it needs to find $i(i \leq p)$ linear functions: $y_{ji} = A_i^T X_j$, where $j = 1, \cdots, n$, $X_j = (x_{j1}, x_{j2}, \cdots, x_{jp})^T$, and $A_i = (a_{1i}, a_{2i}, \cdots, a_{pi})^T$ is unknown. The amount of information of $\boldsymbol{x}$ is proportional to its variance. Letting $Y_{ji} = (y_{1i}, y_{2i}, \cdots, y_{ni})^T$ and to avoid $\mathrm{var}(Y_{ji}) \to \infty$, $\|A_i\|^2 = 1$ Therefore, to obtain the maximum variance, the following equations of conditional extremes are formed:

$$\begin{cases} \max \mathrm{var}(Y_{ji}) = \max A_i^T \sum A_i \\ A_i^T A_i = 1 \end{cases} \tag{2}$$

where $\sum$ represents the covariance matrix.

Here Lagrange multiplier method is used to solve (2). The Lagrangian objective function is expressed as:

$$Q(A_i) = A_i^T \sum A_i - \lambda_j (A_i^T \sum A_i - 1) \tag{3}$$

where the Lagrange multiplier λ_j is the characteristic root of $\sum$ and A_i is the corresponding eigenvector. Because $A_i \neq 0$ and $A_i^T \sum A_i = \mathrm{var}(A_i^T X_j) > 0$, $\sum$ is positive definite and all characteristic roots are positive. Assuming that:

$$\lambda_{j1} \geq \lambda_{j2} \geq \cdots \geq \lambda_{jp} \geq 0 \tag{4}$$

In the practical applications, only p' principal components will be selected, which satisfies $\sum_{k=1}^{p'} \lambda_{jk} / \sum_{i=1}^{p} \lambda_{ji} \geq 0.85$. The k-th principal component for the j-th group is $y_{jk} = A_k^T X_j$. All the principal components form a vecor $Y_j = (y_{j1}, y_{j2}, \cdots, y_{jp'})^T$.

2.2. Support Vector Machine

Suppose the j-th group of principal component Y_j reflects the fault type z_j. We divide n groups of fault data into two sets. One set is the training set including l groups and the other set is the testing set including (n-l) groups. The training set is used to solve the parameters of SVM.

TFD is usually a multi-class problem to classify the categories in d ($d \geq 2$). The one-versus-one (OVO) method is adopted to extend 2-category SVM to multi-class SVM in this paper. This means it need to build SVM classifiers for any two different fault types F_1 and F_2 ($F_1, F_2 \in \{z_j\}$), and there are a total of $d(d-1)/2$ classifiers. Assume a hyperplane function $\omega^T \varphi(Y) + b = 0$ can accurately separate F_1 and F_2 whose category labels are marked in -1 and 1. Here ω is the normal vector of the hyperplane, b is the offset, and $\varphi(\boldsymbol{y})$ is nonlinear transformation function. For the optimal classification hyperplane, the following conditions should be satisfied:

$$\begin{cases} \omega^T \varphi(Y_j) + b \geq 1, H_j = 1 \\ \omega^T \varphi(Y_j) + b \leq -1, H_j = -1 \end{cases} \tag{5}$$

and $H_j \in \{F_1, F_2\}$ is the classification of Y_j. In this case, Y_j is mapped into a high-dimensional space.

The maximum margin between the plane and the nearest data is $1/\|\omega\|$. The greater it is, the better the classification confidence is. To increase the misclassification tolerance of SVM, a non-negative variable e_j is introduced. Then the problem can be described as:

$$\begin{cases} \min\left(\frac{1}{2}\|\omega\|^2 + C\sum\limits_{j=1}^{l} e_j\right) \\ H_j\left(\omega^T\varphi(Y_j) + b\right) \geq 1 - e_j \\ e_j \geq 0 \end{cases} \tag{6}$$

where C is a constant named penalty factor and controls the punishment degree for misclassified data. Lagrange multiplier method is also used to solve (6). The corresponding Lagrangian function is:

$$L(\omega, \sigma, e_j, \alpha_j, \beta_j) = \frac{1}{2}\|\omega\|^2 + C\sum_{j=1}^{l} e_j - \sum_{j=1}^{l} \alpha_j\left[H_j\left(\omega^T\varphi(Y_j) + b\right) - 1 + e_j\right] - \sum_{j=1}^{l} \beta_j e_j \tag{7}$$

where $\alpha_j > 0$ and $\beta_j > 0$ are the Lagrangian multipliers. After $\alpha_j (j = 1, \cdots, l)$, ω and b are solved, the final SVM classification function is:

$$f(Y_r') = \mathrm{sgn}(\sum_{j=1}^{l} \alpha_j H_j K(Y_r', Y_j) + b) \tag{8}$$

where Y_r' $(r = l+1, \cdots, n)$ is the r-th group data in testing set, $K(Y_r', Y_j) = \varphi(Y_r') \cdot \varphi(Y_j)$ is the kernel function and we choose Gaussian radial basis function:

$$K(Y_r', Y_j) = \exp\left(-\frac{\|Y_r' - Y_j\|^2}{\sigma^2}\right) \tag{9}$$

where σ is the parameter of kernel function.

2.3. Parameter Optimization in SVM Using Improved PSO

As mentioned before, when using SVM for fault diagnosis, we first need to determine the parameter σ in kernel function (9) and penalty factor C in (6). σ affects the optimal classification performance and generalization ability of the SVM. C is required to balance the learning machine's complexity and empirical risk when determining the minimization of the objective function. Therefore, σ and C should be optimized. We use an improved PSO algorithm for optimization.

Assuming that in a 2-dimensional search space, there is a swarm including S particles, $q_s = (q_{s1}, q_{s2})$ $(s = 1, \cdots, S)$. Each particle represents a potential solution and corresponds to a point in the 2-dimensional search space. Its velocity is $v_s = (v_{s1}, v_{s2})^T$ and optimal position is $P_s = (P_{s1}, P_{s2})^T$. The optimal position within the S-particle population represents the global extremum, and it is set to $P_g = \left(P_{g1}, P_{g2}\right)^T$. The position-updating method for the particle's velocity is expressed as:

$$v_{sd}(t+1) = wv(t) \cdot v_{sd}(t) + c_1(t)r_1(t)(P_{sd}(t) - q_{sd}(t)) + c_2(t)r_2(t)\left(P_{gd}(t) - q_{sd}(t)\right), d = 1, 2 \tag{10}$$

$$q_{sd}(t+1) = q_{sd}(t) + v_{sd}(t+1) \tag{11}$$

where $c_1(t)$ and $c_2(t)$ are acceleration constants, $r_1(t)$ and $r_2(t)$ obey the (0,1)-uniform distribution, $wv(t)$ is the speed update inertia weight representing the effect of the previous generation's particles on the next generation particles' velocity during the particle updating process.

Generally, the algorithm has relatively strong global optimization capability when $wv(t)$ is large, and a relatively strong local optimization capability when $wv(t)$ is small. However, the linear weight-adjustment method is single, and thus limits the optimization of the search ability. Aiming to

change to single adjustment mode and better adapt to the complex environment, we present a new scheme for the stochastic inertia weight:

$$\begin{cases} wv(t) = \alpha_1 + \varepsilon/2.0, k \geq 0.05 \\ wv(t) = \alpha_2 + \varepsilon/2.0, k < 0.05 \end{cases} \tag{12}$$

$$k = \frac{\text{fit}(t) - \text{fit}(t\text{-}10)}{\text{fit}(t\text{-}10)} \tag{13}$$

where fit(t) represents the optimal fitness value of the t-th generation and fit$(t$-10$)$ is the optimal fitness value of the (t-10)-th generation, α_1 and α_2 are set to 0.5 and 0.4, respectively, reflecting the search ability in different situations, and ε is a random value between 0 and 1. The acceleration constants $c_1(t)$ and c_2 are modified in:

$$\begin{cases} c_1(t) = c_{11} + (c_{12} - c_{11})\frac{t}{T} \\ c_2(t) = c_{21} + (c_{22} - c_{21})\frac{t}{T} \end{cases} \tag{14}$$

where $c_1(t)$ decreases linearly from the initial value c_{11} to the final value c_{12}, while $c_2(t)$ increases linearly from c_{21} to c_{22}.

3. Verification and Discussion

Based on the above mentioned SVM-diagnosis model, optimized using PSO, a code is made in MATLAB in which SVM algorithm is implemented directly by MATLAB toolkit [15]. Some real TFD examples are analyzed.

3.1. TFD Example 1

We analyze the dissolved-gas data for the existing 157 groups of transformers under normal and other fault conditions. The dissolved-gas data were detected from 6 types of real transformer faults: low-energy discharge fault (LE-D), high-energy discharge fault (HE-D), high temperature overheat fault (HT), medium temperature overheating fault (MT), medium and low temperature overheating failure (ML-T), and low temperature overheating fault (LT). 112 groups of data were selected as training samples, and the remaining 45 groups were used for testing. The distribution of the various faults and normal state samples are shown in Table 1.

Table 1. Statistics of samples for training and testing, corresponding to various types of real faults.

Fault Type	Training Sample	Test Sample	Total
Normal	17	7	24
LE-D	23	10	33
HE-D	20	8	28
HT	23	10	33
MT	7	2	9
ML-T	13	5	18
LT	9	3	12
Total	112	45	157

In this analysis, the particle swarm number is 20, the maximum iteration number is 200, and the search intervals for parameters C and σ are [0.01, 1000] and [0.01, 1000], respectively. Furthermore, C = 15.8823 and σ = 50.1658.

The fault diagnostic results of both the training set and the testing set are shown in Figure 2. Only one group of samples shows diagnosis errors among 112 groups of training samples (LE-D fault is diagnosed as HT fault), while 3 out of 45 samples yield diagnosis errors which are marked by circles. The accuracy reaches 93.33%. Diagnostic errors are either normal (diagnosed as HE-D), or LE-D

fault (diagnosed as HE-D), or MT fault (diagnosed as HE-D). The results indicate that this method is relatively accurate and capable of realizing the aim of TFD.

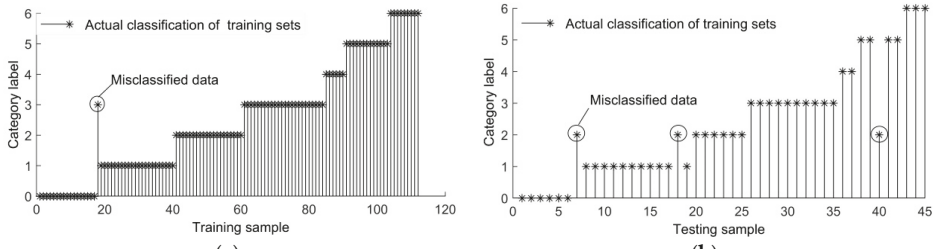

(**a**) (**b**)

Figure 2. Results of the transformer-failure diagnosis: (**a**) training sets; (**b**) testing sets.

We adopt the three-ratio method, Duval triangle method, back propagation neural network (BPNN), and SVM methods to diagnose the testing data set for comparison. The same set of data was used for all methods. During the test, BPNN selected a network structure with 13 hidden nodes.

Table 2 shows the fault-diagnosis accuracy for different methods, when testing the same sample of transformer. The Duval triangle method shows the lowest accuracy. The three ratio method's accuracy is better than The Duval triangle method, however, worse than other methods. Both of three-ratio and Duval triangle methods are obtained from typical accidents, and they will fail when dealing with some complicated faults. The accuracy of the neural-network algorithm (BPNN) is 60% and it will be improved if there are a lot of data. Compared with the BPNN and IEC methods, the SVM method shows a relatively good diagnosis. When the SVM parameters are optimized, the accuracy of the fault diagnosis improves substantially.

Table 2. Accuracy rate for the different diagnostic methods of transformer.

Method	Three-Ratio	Duval Triangle	BPNN	SVM	This Paper
Accuracy rate	51.111%	42.222%	60.000%	75.556%	93.333%

3.2. TFD Example 2

This section uses SVM optimized by PSO to analyze the fault and normal states from the 132 groups of data detected from real transformers. The data were from the oil-dissolved gas and SCADA. We also verified the impact of data richness on the results. The dissolved gases in the oil include C_2H_2, C_2H_4, C_2H_6, CH_4, CO, CO_2, H_2 and total hydrocarbon. The SCADA data include maximum current, minimum current, average current, maximum active power, minimum active power, average active power, maximum reactive power, minimum reactive power, and average reactive power. SVM optimized by PSO is used to diagnose the faults for three kinds of data: using only the dissolved gas data in oil, using only the SCADA data, and using all data. We used 112 groups as the training set and 20 groups as the testing set, and then judged the effect of data types on fault diagnosis.

In this experiment, the number for the particle swarm is 20, the maximum iteration number is 200, and the search interval of parameters C and σ are [0.01, 1000] and [0.01, 1000], respectively. The optimized parameter values and accuracy rate of different data types are shown in Table 3.

Table 3. Fault-diagnostic results of transformer of different methods.

Types	Data	C	σ	Accuracy Rate
1	Dissolved gas data in oil only	5.023	0.709931	80%
2	SCADA data only	26.5631	7.3787	65%
3	Both above data	36.6918	0.074581	95%

For TFD results using only the dissolved gas in the oil, four out of 20 groups of normal data are misdiagnosed as fault state. However, the fault state is diagnosed correctly, and so the accuracy can reach 80% in general. The TFD results of using only SCADA data, as shown in Table 3, has many errors in the non-fault diagnosis. 13 out of 20 groups were correctly evaluated, and the accuracy is as high as 65%. For the TFD results using the dissolved gas in oil and the SCADA data as input data of SVM optimized by PSO, only 1 out of 20 groups of test data is erroneous (the non-fault condition is misdiagnosed as fault state). Hence, the accuracy of the fault diagnosis is 95%.

Comparing the diagnostic results for the above three data types, type 1 and type 2 can be used to diagnose most of the transformer states, but there errors are different, when diagnosing non-fault states. This is because each data type can reflect the fault states of the transformer to some extent, including part of the transformers' state changes—but not completely. By combining these two kinds of data, more state information can be considered. The SVM optimized by PSO can learn the rich information from the data, thus improving the accuracy of the transformer-fault diagnosis.

4. Conclusions

A new fault-diagnosis technology for transformers, SVM optimized using PSO, was proposed in this paper, and it fully combines the advantages of the SVM and PSO. We used the dissolved-gas data in oil as the characteristic quantity and compared it with traditional methods as three-ratio, Duval triangle, and the artificial intelligence and machine learning algorithms as BPNN and SVM. The results showed that the proposed technology greatly improves the accuracy of the fault diagnosis. We also analyzed the effect of different data types of transformer on the TFD results. The data types included the dissolved-gas data in the transformer oil only, the SCADA data only, and both of them. The combination of the dissolved-gas data and SCADA data can improve the accuracy of the new technology substantially. This also testifies the importance of having sufficient data to perform an accurate transformer fault diagnosis.

The proposed method can be applied to prognostics and health management system in smart substations. It is noted that, if the amount of fault data is very big, it will take a long time to perform the fault diagnosis and it is inappropriate for on-line diagnosis; if the amount of fault data is not enough, its accuracy will be limited. The balance between the data amount and accuracy in its real applications needs further discussion.

Author Contributions: Conceptualization, K.L., J.S., J.W. and L.X.; Methodology, K.L., J.W., J.S. and L.X.; Software, K.L.; Validation, K.L. and J.W.; Data resources, L.X.; Writing—original draft preparation, K.L.; Supervision, J.W.; Project administration, J.S. and J.W.; All authors have read and approved the final manuscript.

Funding: This work was supported in part by National Natural Science Foundation of China, grant number 51207004.

Conflicts of Interest: The authors declare no conflict of interest.

References

1. Zhao, Z.Y.; Tang, C.; Zhou, Q. Identification of Power Transformer Winding Mechanical Fault Types Based on Online IFRA by Support Vector Machine. *Energies* **2017**, *10*, 2022. [CrossRef]
2. Kari, T.; Gao, W.S.; Zhao, D.B.; Zhang, Z.W.; Mo, W.X. An Integrated Method of ANFIS and Dempster-Shafer Theory for Fault Diagnosis of Power Transformer. *IEEE Trans. Dielectr. Electr.* **2018**, *25*, 360–371. [CrossRef]
3. Wang, Y.Y.; Gong, S.L.; Grzybowski, S. Reliability evaluation method for oil-paper insulation in power transformers. *Energies* **2011**, *4*, 1362–1375. [CrossRef]
4. Tenbohlen, S.; Coenen, S.; Djamali, M.; Müller, A.; Samimi, M.H.; Siegel, M. Diagnostic measurements for power transformers. *Energies* **2016**, *9*, 347. [CrossRef]
5. Zheng, H.B.; Liao, R.J.; Grzybowski, S.; Yang, L.J. Fault diagnosis of power transformers using multi-class least square support vector machines classifiers with particle swarm optimization. *IET Electr. Power Appl.* **2011**, *5*, 691–696. [CrossRef]

6. Zhao, A.X.; Zhang, C.T. DGA fault diagnosis based on the counter propagation neural network optimized by parallel genetic algorithm. In Proceedings of the 2013 IEEE International Conference of IEEE Region 10 (TENCON 2013), Xi'an, China, 22–25 October 2013; pp. 1–5.
7. Ghoneim, S.S.M.; Taha, I.B.M.; Elkalashy, N.I. Integrated ANN-based proactive fault diagnostic scheme for power transformers using dissolved gas analysis. *IEEE Trans. Dielectr. Electr. Insul.* **2016**, *23*, 1838–1845. [CrossRef]
8. Jalbert, J.; Lessard, M.C.; Ryadi, M. Cellulose chemical markers in transformer oil insulation part 1: Temperature correction factors. *IEEE Trans. Dielectr. Electr. Insul.* **2013**, *2013. 20*, 2287–2291. [CrossRef]
9. Arispe, J.C.G.; Mombello, E.E. Power transformer diagnosis using FRA and Fuzzy Sets. *IEEE Latin Am. Trans.* **2015**, *13*, 2991–2997. [CrossRef]
10. Seifeddine, S.; Khmais, B.; Abdelkader, C. Power transformer fault diagnosis based on dissolved gas analysis by artificial neural network. In Proceedings of the 2012 First International Conference on Renewable Energies and Vehicular Technology, Hammamet, Tunisia, 26–28 March 2012; pp. 230–236.
11. Xiong, H.; Sun, C.X. Artificial immune network classification algorithm for fault diagnosis of power transformer. *IEEE Trans. Power Deliv.* **2006**, *22*, 930–935.
12. Li, S.; Li, X.Y.; Wang, W.X. Fault Diagnosis of Transformer Based on Probabilistic Neural Network. In Proceedings of the Fourth International Conference on Intelligent Computation Technology and Automation, Shenzhen, China, 28–29 March 2011; Volume 1, pp. 128–131.
13. Su, P.; Yuan, J.S.; An, X.L.; Li, Z.; Shen, T. Diagnosis method of transformer faults based on rough set theory. *Electr. Power Sci. Eng.* **2008**, *24*, 56–59.
14. Bigdeli, M.; Vakilian, M.; Rahimpour, E. Transformer winding faults classification based on transfer function analysis by support vector machine. *IET Electr. Power Appl.* **2012**, *6*, 268–276. [CrossRef]
15. Hsu, C.W.; Lin, C.J. A comparison of methods for multiclass support vector machines. *IEEE Trans. Neural Netw.* **2002**, *13*, 415–425. [PubMed]

energies

MDPI

Article

Intelligent Regulation Method for a Controllable Load Used for Improving Wind Power Integration

Jia-Jue Li [1], Bao-Zhu Shao [1], Jun-Hui Li [2,*], Wei-Chun Ge [3], Jia-Hui Zhang [2] and Heng-Yu Zhou [2]

[1] Electric Power Research Institute of State Grid Liaoning Electric Power Co. Ltd., Shenyang 110006, China; en-sea@163.com (J.-J.L.); shaobaozhu@gmail.com (B.-Z.S.)
[2] School of Electrical Engineering, Northeast Electric Power University, Jilin City 132012, China; m13364392991_2@163.com (J.-H.Z.); zhouhengyu1994@163.com (H.-Y.Z.)
[3] State Grid Liaoning Electric Power Co. Ltd., Shenyang 110004, China; gwc@ln.sgcc.com.cn
* Correspondence: lijunhui@neepu.edu.cn; Tel.: +86-139-4420-3007

Received: 6 October 2018; Accepted: 31 October 2018; Published: 8 November 2018

Abstract: Improving the safety and stability of power systems by adjusting the controllable load to improve the wind power integration has become a hot research topic. However, the methodology of accurately controlling the load and fundamentally improving the wind power integration capacity has yet to be studied. Therefore, this paper proposes an intelligent regulation method for a controllable load. This method takes the new energy consumption assessment as feedback, and it combines the wind power acceptance assessment and scheduling plan to form the internal and external loop control structure, and it derives the controllable load intelligent regulation architecture. The load curve is decomposed by an interactive load observer, and the load curve is adjusted by the interactive load controller according to a given standard, thereby improving the new energy acceptance capability. Finally, based on the actual grid operation data of a provincial power grid in Northeastern China, the source grid load balancing process and the interactive load regulation model of the wind power system are simulated. The above method verifies the validity and rationality of the proposed method.

Keywords: wind power; integration assessment; interactive load; considerable decomposition; controllable response

1. Introduction

In recent years, the scale of wind power has increased significantly. In the first half of 2018, China's installed capacity for wind power reached 171.6 million kW, but the annual abandonment of wind power has reached 18.2 billion kWh [1], and some of the "three north" areas have an abandoned wind rate of 30% [2]. The volatility and intermittent nature of wind power also pose great challenges to the safety, stability, and reliability of power systems. The consumption of renewable energy, such as wind power, has become a worldwide problem [3,4].

At present, energy storage technology has become a popular wind power consumption method [5–7]. Gupta et al. [8] used mixed integer programming and battery energy storage systems to build security constrained unit commitment models in order to solve intermittent wind power generation problems. In [9,10], a capacity allocation strategy was proposed for a battery energy storage system from the viewpoint of schedule ability and economy. In [11], a comparative analysis method was proposed for the suitability of multi-attribute and multi-objective energy storage conditions in order to obtain an optimal energy storage configuration scheme for different application scenarios for power systems. The method in [12] used energy storage system bidirectional power conversion and storage algorithms to improve the utilization of renewable energy. The method in [13–15] used a battery energy storage system to solve the intermittence and volatility problems of wind power and improve the grid's ability to accept wind power.

However, several current energy storage technologies that are relatively mature have presented short-term economic costs. So far, no energy storage technology has developed "high security, low cost and long life" [16]. In addition, system resources from the power supply side are used to stabilize wind power uncertainty, thus achieving a grid frequency/peak balance. However, in a power grid with a high wind power penetration rate, the development of the adjustable capacity of a power side has gradually reached a bottleneck [17]. The deterministic identification and adjustment on the load side is one of the effective methods for furthering the acceptance of large-capacity renewable energy [18,19].

So far, a large amount of research has been done on the use of control loads to improve wind power integration [20]. In [21], a method was proposed to divide the demand-side resources that are involved in the interaction into a load-reducing load, a translatable load, and a transferable load, according to the user response characteristics, and to make the three types of interactive loads cooperate with each other. Not only can the load curve be reasonably adjusted, but the new energy output can also be effectively eliminated in order to achieve system economic operation. However, there are still certain difficulties in the process of regulating the load. The method in [22,23] selected an air conditioning load with a large proportion of the urban load to study, and proposed a load schedule ability potential evaluation method suitable for the proposed model. Vrakopoulou et al. [24] developed a multi-period opportunity-constrained optimal power flow model for scheduling the generation and reserves of generators and controllable power load sets. In [25], using a particle swarm optimization algorithm combined with a controllable load, an isolated three-level expansion planning method for a micro grid was proposed in order to meet the load demand. The method in [26,27] improved the stability of the grid voltage through a controllable load.

In order to improve the wind power integration, this paper proposes an interactive load generalized observer and controller design method by establishing a mathematical model of the interactive load observation and the control, combined with a wind power integration assessment and scheduling plan. Then, the internal and external loop control structure is formed and an interactive load intelligent control architecture is obtained. Through this method, the power system load curve can be changed in a responsive manner, thereby greatly improving the wind power receiving capability.

The paper is organized as follows. Wind power acceptance assessment model was established in Section 2. Analysis of key factors affecting wind power acceptance in Section 3. An interactive load observer and controller are designed in Section 4. A case study was carried out in Section 5. Finally, Section 6 concludes the paper.

2. Wind Power Integration Assessment Model

For an intelligent control method of the controllable load of wind power, in order to intuitively reflect the improvement of wind power integration and to ensure the safety of the grid dispatching operation after the wind power is connected to the grid, it is necessary to establish a wind power integration assessment model according to the actual situation of the grid operation and the ability of the grid to accept wind power under the current conditions.

2.1. Grid Power Balance Model

The real-time balance of power supply and demand power is the physical premise of the safe and stable operation of power systems. Since the system contains many uncertain variables, especially for the wind power generation and the load side power, it is necessary to provide a certain amount of adjustment to maintain the power balance. When considering the key variables of the three sides of the source grid load, the power balance equation for the wind power system is constructed, as follows:

$$\begin{cases} P_{\mathrm{Gmax}}(t_i) = \overline{P}_L(t_i) + \overline{R}_G \\ P_{\mathrm{Gmin}}(t_j) = \underline{P}_L(t_j) - \underline{R}_G \\ P_L(t) = P_{L,a}(t) + P_{L,na}(t) \end{cases} \tag{1}$$

where $P_{G\max}(t_i)$ is the maximum adjustable output of the system power supply side at the peak of the load, $P_{G\min}(t_j)$ is the minimum adjustable output of the system power supply side at the time of the low load, $\overline{R}_G$ is the system upgrade standby, $\underline{R}_G$ is the system downgrade standby, $P_L(t)$ is the grid power supply load that is divided into two categories, $P_{L,a}(t)$ is the controllable load, and $P_{L,na}(t)$ is the uncontrollable load, $\overline{P}_L(t)$ is the maximum power supply load of the grid, and $\underline{P}_L(t)$ is the minimum power supply load of the grid.

$$\begin{bmatrix} P_{G\max}(t) \\ P_{G\min}(t) \end{bmatrix} = \begin{bmatrix} P_{\max} \\ P_{\min} \end{bmatrix} [1-\alpha]^T \tag{2}$$

$$\begin{cases} P_{\max} = \left(P_{f\max}(t), P_{h\max}(t), P_{n\max}(t), P_{w\max}(t), P_{c\max}(t)\right) \\ P_{\min} = \left(P_{f\min}(t), P_{h\min}(t), P_{n\min}(t), P_{w\max}(t), P_{c\min}(t)\right) \\ \alpha^T = \begin{bmatrix} \beta_f & \beta_h & \beta_n & \beta_w & a \end{bmatrix}^T \end{cases} \tag{3}$$

where $P_{f\max}(t)/P_{f\min}(t)$ is the maximum/minimum output of the coal-fired unit, $P_{h\max}(t)/P_{h\max}(t)$ is the maximum/minimum output of the hydropower unit, $P_{n\max}(t)/P_{n\min}(t)$ is the maximum/minimum output of the nuclear power unit, $P_{w\max}(t)/P_{w\min}(t)$ is the maximum/minimum output of the wind power, $P_{c\max}(t)/P_{c\min}(t)$ is the maximum/minimum power of the tie line exchange, β_f is the power rate for his thermal power plant, β_h is the power consumption rate of the hydropower unit, β_n is the plant power consumption rate of the nuclear power unit, β_w is the power consumption rate of the wind turbine, and a is the grid loss rate. $P_{\max}$ and $P_{\min}$ are the row vectors of the maximum/minimum output of the power supply and α is the coefficient vector of the power output.

2.2. Wind Power Integration Assessment

According to the power balance equation of the wind power system, when considering the variables of the system's multi-power supply, grid backup, and tie line constraints, an evaluation index of the integration capability of the wind power system is proposed.

2.2.1. Grid Backup Margin

Combined with the power balance equation, the system standby relationship equation in the initial state of the system is established, and the relationship between the system's up/down standbys is further analyzed. The expression is as follows:

$$\begin{cases} \overline{R}_G = P^0_{G\max}(t) - \overline{P}_L(t) \\ P^0_{G\min}(t) = g\left(P^0_{G\max}(t)\right) \\ \underline{R}_G = \underline{P}_L(t) - g\left(\overline{R}_G + \overline{P}_L(t)\right) \end{cases} \tag{4}$$

where $g(\bullet)$ is the relationship function between the maximum boot capacity and the minimum boot mode, and it can also be understood as the peak shaving depth on the system power side, $P^0_{G\max}(t)$ is the maximum boot capacity, and $P^0_{G\min}(t)$ is the minimum boot capacity.

According to Equation (4), since the power system spike standby involves the system safety and stability margin, the power grid up-regulation standby $\overline{R}_G$ usually takes 3–5% of the peak load, and the model is given as the study boundary condition value. Equation (4) is subjected to recursive analysis, and $\underline{R}_G$ is positively correlated with the trough load, positively correlated with the peak shaving depth, and negatively correlated with the up-regulation standby and the peak load.

2.2.2. Wind Power Acceptability

Based on the above alternate derivation model, the calculation formula for the maximum adjustable margin of the trough is given below. Starting from the physical process, the downward

adjustment of the grid has the maximum adjustable margin of the grid, as shown in the following equation:

$$\Delta P_s = \underline{R}_G = \underline{P}_L(t_j) - P^0_{\mathrm{Gmin}}(t_j) \tag{5}$$

where ΔP_s is the wind power acceptance capability of the grid.

The large-scale wind power integration capability index includes the maximum adjustable margin of the valley, the power consumption rate of the wind power plant, and the grid loss rate. The equation is as follows:

$$P_w = \Delta P_s/(1-\beta_w)(1-a) \tag{6}$$

where P_w is the indicator of wind power integration capability.

3. Analysis of the Key Factors Affecting Wind Power Integration

3.1. Essential Factor of Integration

In the process of the coordinated operation and integration of the source grid, there are many measures used to improve the integration ability, and each research result is reflected in the current research field. The power supply side promotes the integration capabilities, including the thermal power unit deep peak shaving, large capacity battery energy storage, pumped storage power station, and electric heat storage. The grid side promotion integration includes a cross-regional integration of the interconnected power grids and ultra high vacuum power grid wind power delivery. The load side facilitation integration includes interruptible loads, transferable loads, and translational loads, etc. However, according to the power balance equation described in Section 2.1 of this paper, under the premise of satisfying the security and stability constraints, the essential process of the integration capability is to up-regulate the process of maximizing the standby minimization and down-regulating the standby. Therefore, the overall objective function accepted by the wind power system is as shown in Equation (7):

$$\begin{cases} \min \overline{R}_G \\ \max \underline{R}_G \end{cases} \tag{7}$$

3.2. The Influence of the Source Grid Load Coordination on the Integration

The integration demand period is determined, the source grid load integration contribution index is defined, and the contribution of the source grid load to the integration amount is calculated. Figure 1 is a schematic diagram of the wind power integration. In this paper, the minimum allowable output of the wind power in the system is defined to be greater than the period in which the load is located. The time period of integration is shown in Figure 1 as the period t_1~t_2.

The influence of the source grid load on the admission is solved quantitatively, and the source grid load integration contribution index is given, as shown in Equation (8):

$$\delta_x = \frac{\int_{t_1}^{t_2}\{P_{x,av} - P_x\}}{\sum\limits_x \int_{t_1}^{t_2}\{P_{x,av} - P_x\}} \tag{8}$$

where P_x is the power value of the source grid load with different variables and the load is treated as a negative virtual generator. $P_{x,av}$ is the full-time average power of each variable, δ_x is the acceptance contribution of each variable: δ_f is the acceptance ability of thermal power units,δ_h is the acceptance ability of the hydropower unit, δ_n is the acceptance ability of nuclear power plants, δ_c is the acceptance contribution of the tie line connection, and δ_l is the acceptance capacity of the load.

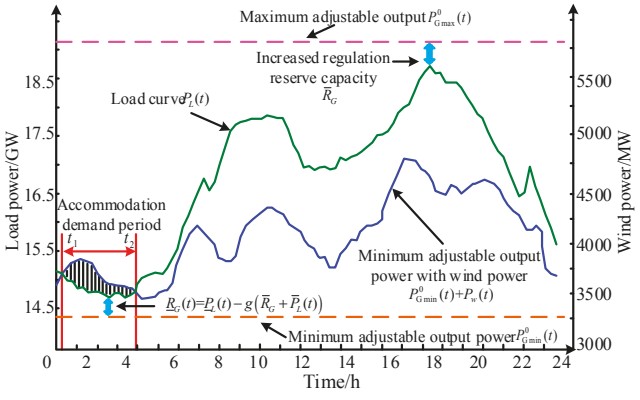

Figure 1. Schematic diagram of wind power acceptance principle.

4. Interactive Load Observer and Controller Design

Through the specific analysis of the load curve, the interactive load observer and controller are designed. The specific design flow is shown in Figure 2:

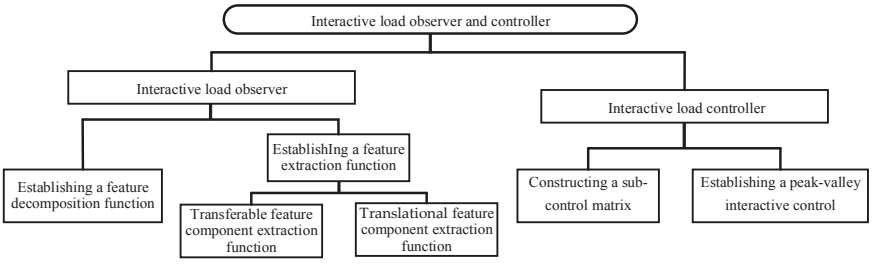

Figure 2. Construction chart of interactive load observer and controller.

4.1. Interactive Load Observer Design

It can be seen from the above argument that the development and utilization of the load side has a high amount of characteristics in the source grid load coordination integration. The big data mining is carried out for the uncertain load characteristic curve, and the design method of the interactive load observer is proposed. The load curve is characterized and the feature extraction function is established.

4.1.1. Feature Decomposition Function

The load curve is decomposed into three feature quantities, and the decomposition formula is as follows:

$$P_L(t) = \sum_{n=1}^{n} P_n(t) = \sum_{m=1}^{m} P_{m,tran}(t) + \sum_{i=1}^{i} P_{i,shift}(t) + \sum_{j=1}^{n-m-i} P_{j,wait}(t) \quad (9)$$

where $P_{m,tran}(t)$ is a transferable feature component, m is the total number of observation points of the transferable characteristic load, $P_{i,shift}(t)$ is a translatable feature component, i is the total number of observation points of the translatable feature load, $P_{j,wait}(t)$ is the feature component to be modeled, and n is the total number of observation points for all loads.

4.1.2. Feature Extraction Function

Transferable feature component extraction function:

$$P_{m,tran}(t) = \left\{ P(t) \left| \frac{\int_{t_i}^{t_j} P(t)}{\int_0^{24} P(t)} \geq \frac{(t_i - t_j) \times n}{24}, [t_i, t_j] \in T \right. \right\} \tag{10}$$

The function indicates that the average load in t_i~t_j continuous time is n times the average load of the entire day. Generally, the t_i~t_j takes 8 h in continuous time, and n takes a value according to the characteristic demand (this article takes n = 2.25). The load with this feature is defined herein as a transferable feature load.

Translational feature component extraction function:

The typical intermittent step load is selected. For the typical load curve, the gray correlation analysis is used, the correlation is used as the index in order to extract a load similar to a typical load curve, and the feature extraction function is as follows:

$$\begin{cases} P_{i,shift}(t) = \left\{ P(t) \middle| R_{P_a,P_i} \geq z \right\} \\ R_{P_a,P_i} = \frac{1}{n} \sum_{k=1}^{n} L_{P_a,P_i}(k) \\ L_{P_a,P_i}(k) = \frac{(\Delta\min + \rho\Delta\max)}{(\Delta_{ai}(k) + \rho\Delta\max)} \end{cases} \tag{11}$$

where P_a is a typical intermittent step load. In this paper, the load curve of a central air conditioning load is taken as a typical intermittent step load. $\Delta_{ai}(k)$ represents the absolute difference between the typical reference sequence P_a and the comparison sequence P_i at time k, that is, $\Delta_{ai}(k) = |P_a(k) - P_i(k)|$. Δmin and Δmax represent the maximum and minimum values, respectively, of the absolute differences of all the comparison sequences at each time. ρ is 0.5, $L_{P_a,P_i}(k)$ is the correlation coefficient, R_{P_a,P_i} is the correlation degree, n is the load value sampling point, and z is the translatable feature component extraction threshold, which represents the similarity between the comparison load sequence and the typical intermittent step coincidence sequence, the value range is 0–1 and z = 0.9.

The feature component to be modeled:

$P_{j,wait}(t)$ is the feature load to be modeled, which needs to be continuously studied by big data technology, and that will gradually decompose various features of the load part to be modeled. In this paper, the intelligent control method of the controllable load is not studied further, and its characteristic component values are as follows:

$$P_{j,wait}(t) = P_L(t) - P_{m,tran}(t) - P_{i,shift}(t) \tag{12}$$

4.2. Interactive Load Controller Design

After the load curve is decomposed by the observer, it is necessary to further control the observable load characteristics, establish a sub-control matrix, propose a peak-valley interactive control model, and control the discriminant characteristic load in order to form an interactive load controller.

4.2.1. Constructing a Sub-Control Matrix

The construction of the sub-control matrix is as follows:

$$P(t) = \begin{bmatrix} P_i(t) & \cdots & 0 \\ \vdots & \ddots & \vdots \\ 0 & \cdots & P_n(t) \end{bmatrix} \tag{13}$$

$$K_{ctr}(t) = \begin{bmatrix} k_{ctr,i}(t) \\ \vdots \\ k_{ctr,n}(t) \end{bmatrix} \tag{14}$$

$$k_{pr}(t) = \begin{bmatrix} k_{pr,i}(t) & \cdots & 0 \\ \vdots & \ddots & \vdots \\ 0 & \cdots & k_{pr,n}(t) \end{bmatrix} \tag{15}$$

where $P_n(t)$ is the load's n-type decomposition matrix, $K_{ctr}(t)$ is the control matrix of the characteristic load, and the control word $K_{ctr,n}$ is the nth type characteristic load controllable belonging to the 0–1 variable, where 0 is uncontrollable and 1 is controllable. In this paper, the translatable feature component and the transferable feature component are controllable components, and the feature component to be modeled is an uncontrollable component. $K_{pr}(t)$ is the control weight matrix of the feature load, $K_{pr,n}$ is the control weight value of the nth type characteristic load, and the weight value needs to be verified according to factors, such as the compensation pricing of the load.

The sub-control rules are defined as follows:

$$Z_n(t) = [P_n(t) \cdot k_{ctr}(t)]^T \cdot k_{pr}(t) \tag{16}$$

where $Z_n(t)$ is a controllable quantity matrix for various characteristic loads.

4.2.2. Establishing a Peak-Valley Interactive Control Model

It can be seen from the characteristic load controllable quantity matrix defined above that the matrix includes the translatable characteristic load control amount and the transferable characteristic load control quantity, so that $Z_n(t)$ is converted into the following form:

$$Z_n(t) = \left[z_i(P_{i,shift}(t)), z_j(P_{j,tran}(t)), 0 \right] \tag{17}$$

The peak load interaction constraints are as follows. In the peak period, the load is interactively controlled to ensure that the total amount of electricity used during the peak period is constant and load shifting. The interactive model looks like this:

$$\begin{cases} z_i(P_{i,shift}(t)) \le P_{L_k,op} - P_{L_k,ini}(t) \\ S = S', [t_1, t_2] \cup [t_1', t_2'] \in T_k \\ S = \int_{t_1}^{t_2} \left(P_{L_k,ini}(t) - P_{L_k,op} \right) \\ S' = \int_{t_1'}^{t_2'} \left(P'_{L_k,op}(t) - P_{L_k,ini}(t) \right) \end{cases} \tag{18}$$

where $P_{L_k,ini}$ is the load of the peak period in the total load curve and $P_{L_k,op}$ is the reference limit of the translatable load during the peak period of the total load curve, which is 80% of the peak load.

The low load period load interaction constraints are as follows. In the low valley period, the load interaction control is attained. When the transferable load control quantity satisfies the calling condition, the corresponding policy/economic incentive low load is adopted in order to increase the power load during the low valley period, and the load interaction regulation conditions are as follows:

$$z_j(P_{j,tran}(t)) \ge P_{L_v,op} - P_{L_v,ini}(t), t \in T_v \tag{19}$$

where $P_{L_v,ini}$ is the load of the trough period in the total load curve and $P_{L_v,op}$ is the reference limit of the transferable load in the trough period of the total load curve, which is 20% of the peak load.

The schematic diagram of the interactive load peak-valley interactive control model is shown in Figure 3.

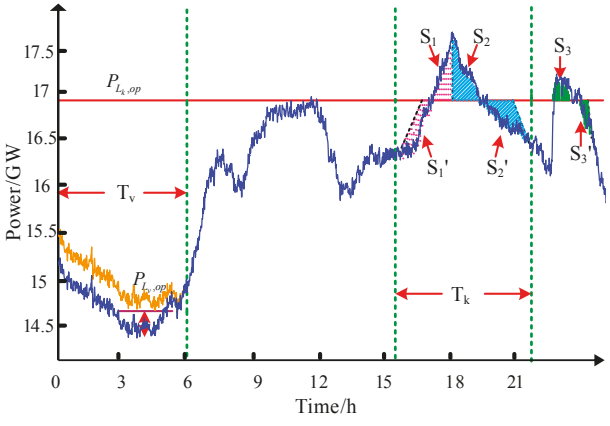

Figure 3. Schematic diagram of the peak-valley control for the interaction load.

4.3. Interactive Load Intelligent Control Architecture

Combining the theoretical design of the observer and the controller with the interactive load, the intelligent control architecture of the interactive load is constructed and designed into the inner and outer loop control model.

The model principle of the intelligent control inner loop design of the interactive load is shown in Figure 4. First, the observer is used as a feedback link, and the series connection in the link includes the load curve decomposition, the feature component extraction, and the feature component accumulation. Second, the ideal given load curve is compared with the initial accumulated curve. Finally, the controller acts to determine the interactive characteristic load and then performs a flat-point regulation of the peak and the low-level excitation regulation. The inner loop input is the load expectation curve and the output is the control corrected load curve.

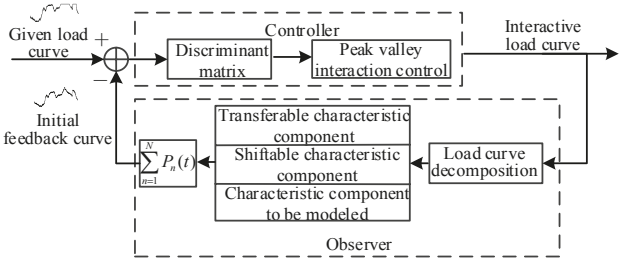

Figure 4. Diagram of the inner control loop for the interaction load.

The model principle of the intelligent control outer loop design of the interactive load is shown in Figure 5. Section 2.2 of this paper proposes a wind power integration capability assessment model as a feedback link, accepts the demand as the input given link, adjusts the power generation plan according to the interactive load curve of the inner loop output, and reduces the maximum amount of space of the output. Combined with the interactive control intelligent control inner loop design, this can form an intelligent control architecture of the interactive load.

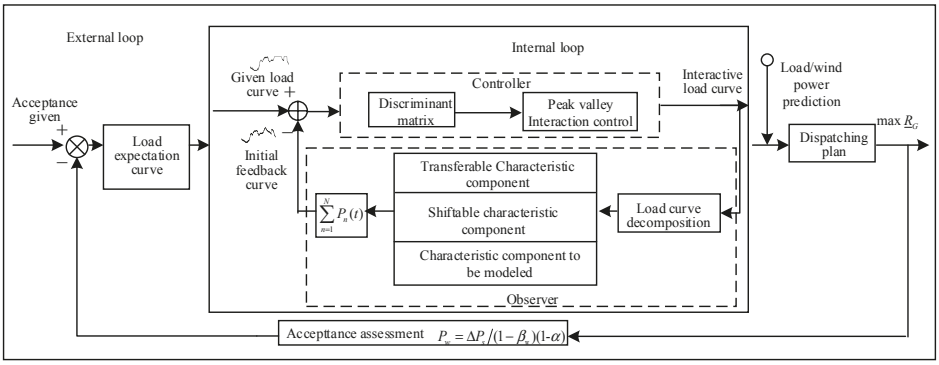

Figure 5. Block Diagram of the inner–outer control loop for the interaction load.

Through the intelligent control method proposed in this paper, the peak value of the load is first reduced, thereby reducing the maximum adjustable output value of the power supply, and the maximum starting capacity of the unit is reduced, so that the minimum adjustable output value of the power supply is also reduced. Secondly, the method increases the load low value, so that the difference between the load low value and the minimum adjustable output value of the power supply increases, thereby improving the wind power receiving capability.

5. Instance Grid Verification

5.1. Evaluating the Wind Power Integration Capability of the Instance Grid

Based on the actual trend data for the power grid in a specific area, the capacity of the thermal motor assembly machine in the region is 20 GW, the installed capacity of the hydropower (including pumping) is 3 GW, the nuclear power is 4.4 GW, and the wind power is 4.5 GW. The system's running curve is shown in Figure 6:

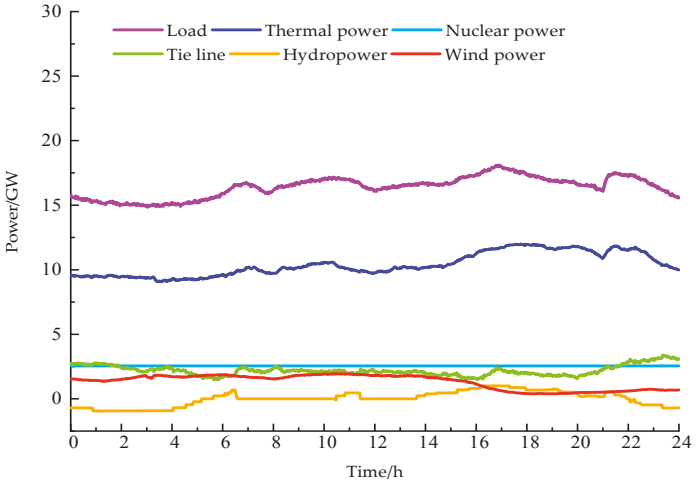

Figure 6. Curve of a real example system's operation.

According to the integration index of the Equation (6), the integration ability of the current system is calculated, and the calculation result is shown in Table 1.

Table 1. Result of the accommodation capability evaluation.

Operational Variable	$P^0_{G\max}$	$P_{L\min}$	$P^0_{G\min}$	β_w	a	P_w
Calculated (MW)	19,020	14,830	12,550	0.5	0.2	2450

5.2. Source Grid Load Factor Contribution Ratio

According to the source grid load integration capability index of Equation (8), the integration demand period is [00:00, 05:00], and the integration contribution capacities of the thermal power, hydropower, nuclear power, tie line, and trough transfer load in the current system are calculated. The calculation results are shown in Table 2.

Table 2. Result of the participatory evaluation for the source-grid-load accommodation.

Source-Grid-Load Variable	δ_f	δ_h	δ_n	δ_c	δ_L
Contribution Degree	0.36	0.29	0	−0.07	0.42

According to the statistics of the classic daily operation data, the total amount of the transferred load in the trough integration period is 2.7 GW. According to the above calculation results, in the integration demand period of wind power integration, the relative contribution capacity of the diverted load is 0.42, the thermal power unit is 0.36, and the hydropower unit (including the pumped storage) is 0.29. The baseband of the nuclear power belt does not participate in peak shaving, and the tie line of the power grid is reversed peak-adjusting due to the delivery of wind power in the adjacent area. It can be concluded that, if there is no such transfer load in the valley period, then the wind power acceptance will be reduced by 2.7 GW. Therefore, this paper proves the strong proportion of the trough characteristic load for wind power integration through the proposed index Equation (8), which can greatly increase the receiving space through the load side interaction.

5.3. Intelligent Control Method for the Interactive Load

Using the interactive load observer Equations (9)–(11), the feature extraction of the grid load operation data of the region is carried out to determine the observable load.

After the characteristic curve of the load curve is decomposed, the characteristic load curve of the trough is extracted as the transferable load for the load interaction control of the load trough period. The characteristic load curve of the air conditioning and the intermittent characteristic load curve are extracted for the load interaction regulation of the load peak period, and the peak characteristic load curve is extracted as the load to be modeled.

The observed solution of the load observer is shown in Figure 7.

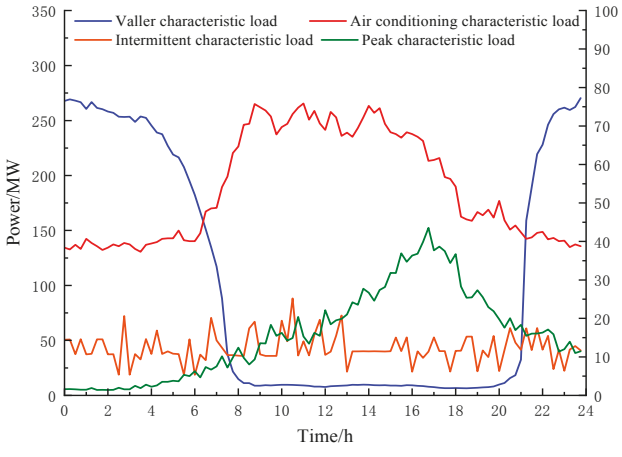

Figure 7. The solution of the interaction load observer.

According to the characteristic load that was observed by the above interactive load observer, according to Equations (13)–(19), the interactive load controller can be used for control. In the peak period, the intermittent characteristic load and the air conditioning characteristic load are controlled by A, and the reference limit is B = 17.65 GW. The trough period has the transfer load to the trough characteristics, and C is the variable policy control, the reference limit is D = 15.22 GW, through the peak-valley interactive control model in this paper, the control solution E of the transferable load and the translatable load can be obtained. The result is shown in Figure 8.

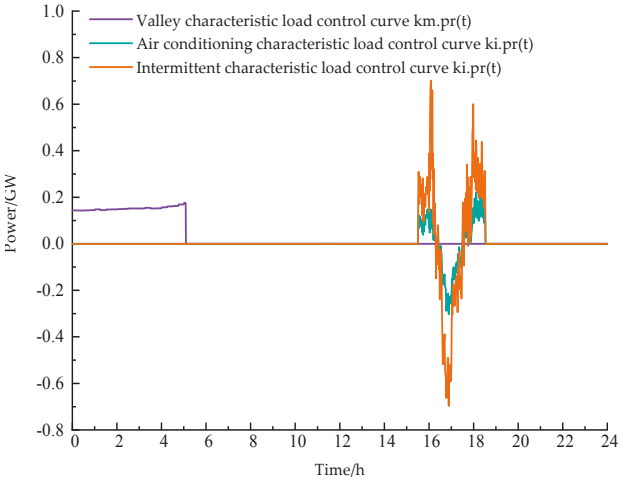

Figure 8. Characteristic load control solution curve in interactive load controller.

Through the solution of the interactive load observer and controller, the interaction load curve is obtained, and the method in this paper is compared with the original method in [19], and the load curve comparison chart is obtained, as shown in Figure 9:

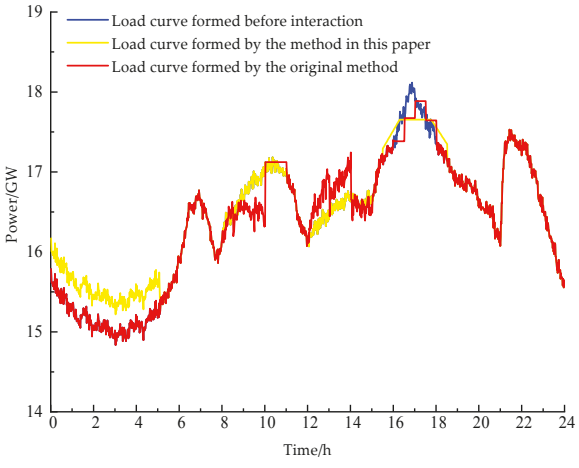

Figure 9. Contrast curve of the original load and the interaction load.

After the correction of the inner loop of the load curve proposed in this paper, the control outer loop is entered and the optimized power generation plan is dispatched. Table 3 shows the operating parameters of the system before and after the method is used. Through the wind power acceptance capability assessment, it is estimated that the wind power acceptance capacity will increase by 900 MW.

Table 3. Result of the accommodation capability evaluation.

Operational Variable (MW)	P^0_{Gmax}	P_{Lmin}	P^0_{Gmin}	β_w	a	P_w
Before Interaction	19,020	14,830	12,550	0.5	0.2	2450
Original Method	18,620	14,830	12,300	0.5	0.2	271
Method of this Paper	18,420	15,330	12,200	0.5	0.2	3350

It can also be seen from Table 3 that the maximum adjustable output is reduced and the corresponding minimum adjustable output is reduced from 12.55 GW to 12.2 GW. This shows that, after the load interaction control, the adjustment capability of the power supply side of the grid is significantly improved. In addition, the minimum load output value increased from 14.83 GW to 15.33 GW, which significantly improved the wind power integration capacity during the grid load period. The wind power accepted by this method is 640 MW more than the original method.

The example grid verification shows that this method optimizes the source grid load operation mode and effectively improves the wind power integration capability through load interaction observation and control.

6. Conclusions

This paper analyzes how to accurately control the load, and proposes an intelligent control method for the controllable load. The main conclusions are as follows:

(1) This paper has established a wind power acceptance capability evaluation index and quantitatively solves the target power system's ability to accept wind power. The key factors of the source network load coordination process and the source network load acceptance ability index have been combined to quantitatively calculate the relative extent of the source network load different variables contributing to the grid wind power acceptance.

(2) In order to improve the acceptance of the wind power, an intelligent regulation method for the controllable load has been constructed. The internal and external control loops have been

designed through the theoretical model of the interactive load observer and controller, so that an interactive load intelligent control structure has been constructed.

(3) This paper has applied the proposed theory and method to the Liaoning regional power grid. Firstly, for the typical day of winter reception, the contribution of wind power acceptance capacity and source network load to the admission process has been quantitatively calculated. Then, the method that is proposed in this paper has been used, and the load curve has been corrected through feature observation and interactive control, which effectively improves the acceptance ability of the regional power grid.

The method proposed in this paper is scientific and reasonable and has strong applicability. In addition, it effectively validates the fact that load side transparency interaction is the key technology for the new energy-friendly power grid.

Author Contributions: J.-J.L. and B.-Z.S. are responsible of designing the proposed method and performing the simulation works. J.-H.L. and J.-H.Z. is responsible for the design and preparation of the framework of the thesis. All the authors have reviewed and approved this paper.

Funding: This work is supported by The State Grid Corporation Science and Technology Project of China (Research and application of grid dispatching support technology based on new energy integration), the National Natural Science Foundation of China (No. U1766204) and Industrial Innovation of Jilin Province Development and Reform Commission (2017C017-2).

Acknowledgments: We would like to thank LetPub (www.letpub.com) for providing linguistic assistance during the preparation of this manuscript.

Conflicts of Interest: The authors declare no conflict of interest.

References

1. National Energy Administration of China. *Wind Power Grid-Connected Operation in the First Half of 2018*. Available online: http://www.nea.gov.cn/2018-07/30/c_137357453.htm (accessed on 27 July 2018).
2. Li, J.H.; Xing, Z.T.; Mu, G.; Fan, X.K.; Yan, G.G.; Ge, Y.F. Analysis of wind abandonment of power grids under peak cooling during heating period. *J. Sol. Energy* **2018**, *39*, 596–602. (In Chinese)
3. Shu, Y.B.; Zhang, Z.G.; Guo, J.B.; Zhang, Z.L. Research on key factors of new energy consumption and research on solving measures. *Chin. J. Electr. Eng.* **2017**, *37*, 1–9. (In Chinese)
4. Xue, Y.S.; Lei, X.; Xue, F.; Yu, C.; Dong, C.Y.; Wen, F.S.; Qu, P. Review on the influence of wind power uncertainty on power system. *Chin. J. Electr. Eng.* **2014**, *34*, 5029–5040. (In Chinese)
5. Li, X.J.; Wang, S.W.; Hui, D. Overview and prospect of operation control and application methods of battery energy storage system. *Power Syst. Technol.* **2017**, *41*, 3315–3325. (In Chinese)
6. Li, J.L.; Tian, L.T.; Lai, X.K. The prospect of power storage technology under the background of energy internet. *Autom. Electr. Power Syst.* **2015**, *39*, 15–25. (In Chinese)
7. Li, J.; Ma, Y.; Mu, G.; Feng, X.; Yan, G.; Guo, G.; Zhang, T. Optimal configuration of energy storage system coordinating wind turbine to participate power system primary frequency regulation. *Energies* **2018**, *11*, 1396. [CrossRef]
8. Gupta, P.P.; Jain, P.; Sharma, S.; Bhaker, R. Security constrained unit commitment in a power system based on battery energy storage with high wind penetration. In Proceedings of the 2018 International Conference on Power, Instrumentation, Control and Computing (PICC), Thrissur, India, 18–20 January 2018. [CrossRef]
9. Yang, D.Y.; Wen, J.X.; Chen, J.R.; Cai, G.W. Predictive control strategy for energy storage system for improving the dispatch ability of wind farms. *High Volt. Eng.* **2017**, *43*, 1043–1048. (In Chinese)
10. Xu, G.D.; Cheng, H.Z.; Fang, S.; Ma, Z.L.; Zhang, J.P.; Zhu, Z.L. Optimization model of battery energy storage configuration for improving the operation efficiency of wind farms. *Autom. Electr. Power Syst.* **2016**, *40*, 62–70. (In Chinese)
11. Li, J.H.; Zhang, J.H.; Hu, D.C.; Li, J.L.; Ma, H.M. Comparison and Analysis of Multi-Attribute and Multi-Objuctive Energy Storage System Working Conditions Suitability. *Electr. Power Constr.* **2018**, *39*, 2–8. (In Chinese)

12. Gök, G.; Kaya, S.; Aydemir, E.; Demir, H.; Alişar, İ. Development of a prototype of renewable source(wind) prediction-based modular multi-purpose energy conversion system with energy storage. In Proceedings of the 2018 6th International Istanbul Smart Grids and Cities Congress and Fair (ICSG), Istanbul, Turkey, 25–26 April 2018. [CrossRef]
13. Rodriguez, R.H.L.; Vechiu, I.; Jupin, S.; Bacha, S.; Tabart, Q.; Pouresmaeil, E. A new energy management strategy for a grid connected wind turbine-battery storage power plant. In Proceedings of the 2018 IEEE International Conference on Industrial Technology (ICIT), Lyon, France, 20–22 February 2018. [CrossRef]
14. Sano, S.; Ito, Y.; Hirose, Y.; Takeuchi, H.; Aone, S. Development of long cycle life valve-regulated lead-acid battery for large-scale battery energy storage system to utilize renewable energy, In Proceedings of the 2015 IEEE International Telecommunications Energy Conference (INTELEC), Osaka, Japan, 18–22 October 2015.
15. Li, J.H.; Mu, G.; Cui, X.Z.; Ge, Y.F.; Gao, F.J.; Jin, P. Design of control strategy for dual lithium battery-capacitor hybrid energy storage system. *High Volt. Eng.* **2015**, *41*, 3224–3232. (In Chinese)
16. Li, J.L.; Ma, H.M.; Hui, D. The status quo and development trend of energy storage technology fusion distributed renewable energy. *Trans. China Electrotechn. Soc.* **2016**, *31*. (In Chinese) [CrossRef]
17. Zeng, B.; Yang, Y.Q.; Duan, J.H.; Zeng, M.; Ouyang, S.J.; Li, C. Key issues of demand side response in new energy power system and future research prospects. *Autom. Electr. Power Syst.* **2015**, *39*, 10–18. (In Chinese)
18. Committee of Development and Reform of the People's Republic of China. *Notice of the National Development and Reform Commission of the Ministry of Finance on Improving the Electric Power Emergency Mechanism and Doing a Comprehensive Pilot Work on the Power Demand Side Management City*. Available online: http://www.sdpc.gov.cn/zcfb/zcfbtz/201504/t20150409_677004.html (accessed on 14 May 2018).
19. Wang, W.; Yao, J.G.; Yao, L.Z.; Yang, S.C.; Yan, T.Y. Summary of Research on Power Flexible Load Scheduling. *Autom. Electr. Power Syst.* **2014**, *38*, 127–135. (In Chinese)
20. Hossain, E.; Perez, R.; Padmanaban, S.; Siano, P. Investigation on the development of a sliding mode controller for constant power loads in microgrids. *Energies* **2017**, *10*, 1086. [CrossRef]
21. Sun, C.; Wang, L.J.; Xu, H.L. User interaction load model and its application of micro-grid economic dispatch. *Power Syst. Technol.* **2016**, *40*, 2009–2016. (In Chinese)
22. Zhu, Y.C.; Wang, J.X.; Cao, X.Y. Direct control strategy of central air conditioning load and its dispatching potential evaluation. *Electr. Power Autom. Equip.* **2018**, *38*, 227–234. (In Chinese)
23. Wang, Y.Z.; Tong, Y.B.; Huang, M.Y.; Yang, L.; Zhao, H.G. Study on virtual energy storage model of air conditioning load based on demand side response. *Power Syst. Technol.* **2017**, *41*, 394–401. (In Chinese)
24. Vrakopoulou, M.; Li, B.; Mathieu, J.L. Chance constrained reserve scheduling using uncertain controllable loads. *IEEE Trans. Smart Grid* **2017**. [CrossRef]
25. Wang, Z.J.; Chen, Y.; Mei, S.W.; Huang, S.W.; Xu, Y. Optimal expansion planning of isolated microgrid with renewable energy resources and controllable loads. *IET Renew. Power Gener.* **2017**, *11*, 931–940. [CrossRef]
26. Mazhari, I.; Parkhideh, B. DC-bus voltage regulation for DC distribution system with controllable DC load. In Proceedings of the 2017 IEEE 8th International Symposium on Power Electronics for Distributed Generation Systems (PEDG), Florianopolis, Brazil, 17–20 April 2017.
27. Yang, H.M.; Zhang, S.M.; Qiu, D.; Zhao, J.H.; Lai, M.Y.; Dong, Z.Y.; Dong, Z.H. Distributionally Robust Optimal Bidding of Controllable Load Aggregators in the Electricity Market. *IEEE Trans. Power Syst.* **2017**, *33*, 1089–1091. [CrossRef]

energies

MDPI

Article

SOCP Relaxations of Optimal Power Flow Problem Considering Current Margins in Radial Networks

Yuwei Chen [1], Ji Xiang [1,*] and Yanjun Li [2]

[1] College of Electrical Engineering, Zhejiang University, Hangzhou 310027, China; chenyuwei@zju.edu.cn
[2] School of Information and Electrical Engineering, Zhejiang University City College, Hangzhou 310030, China; liyanjun@zucc.edu.cn
* Correspondence: jxiang@zju.edu.cn

Received: 23 October 2018; Accepted: 7 November 2018; Published: 15 November 2018

Abstract: Optimal power flow (OPF) is a non-linear and non-convex problem that seeks the optimization of a power system operation point to minimize the total generation costs or transmission losses. This study proposes an OPF model considering current margins in radial networks. The objective function of this OPF model has an additional term of current margins of the line besides the traditional transmission losses and generations costs, which contributes to thermal stability margins of power systems. The model is a reformulated bus injection model with clear physical meanings. Second order cone program (SOCP) relaxations for the proposed OPF are made, followed by the over-satisfaction condition guaranteeing the exactness of the SOCP relaxations. A simple 6-node case and several IEEE benchmark systems are studied to illustrate the efficiency of the developed results.

Keywords: SOCP relaxations; optimal power flow; current margins

1. Introduction

The Optimal power flow (OPF) problem is widely researched in the many fields of power systems, such as energy management, economic dispatch, congestion management, demand response, etc. [1]. In Carpentier's research about economic dispatch, this optimization problem is firstly raised [2]. Dommel and Tinney make the contribution of making OPF a complete optimization model [3].

Constrained by Kirchhoff's law, the OPF problem is a nonlinear mathematical program, being non-convex and NP-hard [4]. Myriad algorithms for solving OPF have been proposed in recent years. Linearized power flow equations have been used extensively in practice, often called DC OPF, see [5–8]. It approximates the AC power flow in a mathematical format resembling DC power flow. The model is simpler in a linear format and makes the simulation faster. However, the solution cannot be exactly correct due to unavoidable errors. In [9], OPF is solved with the Newton-method. After that, many methods according to Newton-method and gradient-algorithm are proposed, see [10–12]. In these methods, the optimization point is found with iterations in the specific direction. However, the problem is that it is very slow to reach convergence near the optimal point. Besides, when there are many local optimal solutions, it is hard to get the global optimization point. With the rapid development of computer science, the artificial intelligence algorithm makes great progress in searching the optimal solution. Many algorithms are therefore applied in solving OPF, see [13–18]. However, these methods occupy much space of storage and the operational time depends very much on the performance of the CPU.

In order to ensure a global optimization solution, people tend to model OPF through convex optimization problems. Some familiar ways are to relax the nonconvex constraints of bus injection model by a semidefinite program (SDP) or the branch flow model's constraints by a second order cone program (SOCP). Ref. [19] firstly transforms the power flow model in a quadric format with SDP

relaxations. This model processes superlinear convergence but it is not exactly equal to the original problem. Ref. [20] reveals that SDP relaxation is exact only if the duality gap is zero. This method is based on the bus injection model, relaxing the nonconvex rank-1 constraint of network's voltage matrix. The bus injection model is established on the relationship of the node voltage, voltage product of the connected nodes and apparent power, of which the physical meaning is easy to understand. However, the rank-1 solution cannot be obtained for some cases. Exact SOCP relaxations are demonstrated in [21,22]. By relaxing the constraints of apparent power, branch current and node voltage, the OPF is shown in a convex optimization model. The SOCP method can use short operation time and does not have much relations with the network scale. It calculates faster than the SDP method with colossal matrices. In this model, the physical relationship is no longer clear due to the squared algorithm of the power flow equation and the direction in which the line should be defined.

The objective functions in OPF are often about transmission losses and generator's active power costs. Due to practical requirements, there can be some other constraints or objectives of OPF in addition to these two objectives. Ref. [23] considers an emission and voltage stability enhancement index in the objective functions. Ref. [24] focuses on voltage deviation and emission objective. Ref. [25] solves OPF under security consideration. It adds operating limits in both pre-contingency and post-contingency conditions. The OPF in [26] has additional voltage stability constraints. It puts constraints on voltage difference. From the perspective of stability, people always put constraints on the maximum transmission power or current and maximum voltage difference. The margin of transmission current influences the thermal stability greatly. When the current margin is relatively large, the system will obtain strong robustness to the transient current burst. Current margins seem to be more important with high penetration of renewable energies that will lead to large power flow changes due to inherent fluctuations.

In this paper, we propose an OPF problem considering current margins in radial networks. We use different weight coefficients to make the current margins, active power losses and generation costs an objective function. It concentrates on enough current margins on each branch, smallest transmission losses and generators' costs. The OPF model is derived from the bus injection model and with some branch variables accounting for the current margins. SOCP relaxations are made for rank-1 constraints of voltage matrix of each branch. The complex variables are decoupled into real ones so as to formulate the OPF into a real convex optimization problem whose theory is self-contained nowadays and can be solved in polynomial time with a global optimal solution. One theorem with the over-satisfaction condition is presented to guarantee the exactness of the relaxations.

The paper is organized as follows: In Section 2, we introduce the notations in this paper and the original OPF problem. Also, the basic OPF problem is elaborated from objective functions to equality and inequality constraints. The objective functions here consider the current margins. In Section 3, we solve OPF by two steps of relaxations. After two steps, the OPF is reformulated as a convex optimization problem. In Section 4, we discuss the exactness of relaxations and propose one condition to guarantee the exactness. In Section 5, a 6-node system and IEEE benchmark systems are applied to test the algorithm. In Section 6, we conclude the paper, summarizing the main contributions of this manuscript.

2. Problem Formulation

2.1. Notations

In this paper, we use the following notations:

1. *Indices and Sets*

$\mathbb{R}$	*the set of real numbers*	$\mathbb{C}$	*the set of complex numbers*
$Re(a)$	*the real parts of a*	$Im(a)$	*the imaginary parts of a*

a^H	*the conjugate form of a*	E	*the set of connected lines*
N^0	*the set of all the nodes*	$\boldsymbol{i}$	*the imaginary number constant*
N	*the set of nodes without slack node*	G	*the set of generators' node*
$i \sim j$	*the branch from i to j*	k	*serial number of each node*

2. *Parameters*

For each bus node $i \in N^0$, the variables are in capital letters, and the subscripts of them represent the bus node numbers. U_i denotes the voltage in node i, I_i denotes the injection current of node i. We define P_{Gi} and P_{Di} for a node i, where P_{Di} denotes the active power of node i demanded, P_{Gi} denotes the active power which node i generated. Similarly, we define Q_{Gi} and Q_{Di} the generated and demanded reactive power of node i. For the injection power of each node $S_i = (P_{Gi} - P_{Di}) + \boldsymbol{i}(Q_{Gi} - Q_{Di})$ denotes the complex power of node i, and $Y_i = G_i - \boldsymbol{i}B_i$ denotes the admittance to ground.

For each line $(i, j) \in E$, let I_{ij} denote the current from i to j and I_{ijmax} denote the maximum transferred current of each line. Let $S_{ij} = P_{ij} + \boldsymbol{i}Q_{ij}$ denote the transmission power from i to j, and $S_{ji} = P_{ji} + \boldsymbol{i}Q_{ji}$ denote the transmission power from j to i. $Y_{ij} = G_{ij} - \boldsymbol{i}B_{ij}$ denotes the admittance of the line. $Z_{ij} = R_{ij} + \boldsymbol{i}X_{ij}$ denotes the line impedance and $Y_{ij} = \frac{1}{Z_{ij}}$. In the AC network, U, Y, Z, I, S are all complex variables, P, Q, G, B, R, X are all real variables.

Some notations are illustrated in Figure 1.

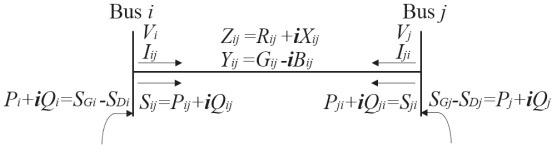

Figure 1. Summary of notations.

2.2. Optimal Power Flow Problem and Assumptions

An OPF problem can be stated mathematically as

$$\begin{aligned} \text{Minimize} \quad & f(x) \\ \text{s.t.} \quad & g(x) = 0 \\ & h(x) \leq 0. \end{aligned} \tag{1}$$

This is an optimization format where the objective function is described as $f(x)$ here and $g(x)$ represents all the equality constraints of the variable x. $h(x)$ means the inequality constraints. The word "s.t." is the abbreviation of the phrase "subject to". As summarized in Equation (1), we make the problems by minimizing the value of $f(x)$ when the equality constraints $g(x)$ and inequality constraints $h(x)$ are satisfied and x is the optimization variable.

2.2.1. Objective Functions

The objective function $f(x)$ in OPF generally focuses on the transmission power losses or total generators' costs. The power loss can be formulated with the square of transmission current or the square voltage of bus nodes. The generators' cost function can be described with the non-negative thermal plants' coefficients c_i and the generators' active power P_G. It can be shown as

$$f(I_{ij}, P_{Gi}) = \sum_{(i,j)\in E} I_{ij}^2 R_{ij} + \sum_{i \in G} c_i P_{Gi}, \tag{2}$$

The total power loss is represented with $\sum I_{ij}^2 R_{ij}$ here. $\sum c_i P_{Gi}$ is the total generators' cost. In this paper, our objective functions involve a new term of current margin considering the thermal stability limit.

In a power system, there is always a specific limit for the apparent power or current that can be transferred from one node to another. This constraint only considers the maximum transforming limit rather than margins of the branch. For a specific line, the percentage of transmission current and limit current constructs the current margins. Let $\varphi_{ij} = \frac{I_{ij}}{I_{ijmax}}$ be an index variable where I_{ijmax} represents the maximum transferred current of each line (i, j) which is greater than 0. If each of branch is labeled with $i_k j_k$ where in radial network k ranges from 1 to n, there is $\varphi_{i_1 j_1}, \varphi_{i_2 j_2}, \ldots, \varphi_{i_n j_n}$ individually for every line where $(i_1, j_1), (i_2, j_2), \ldots, (i_n, j_n) \in E$. With a relative small and similar value on $\varphi_{i_k j_k}$, enough current margins will be acquired on all lines. For the connected lines, it goes as follows:

$$0 < \varphi_{i_1 j_1} = \varphi_{i_2 j_2} = \cdots = \varphi_{i_n j_n} < 1 \tag{3}$$

To simplify the notations, $\varphi_{i_k j_k}$ will be abbreviated to φ. To obtain the uniform current margins, (3) should be added as a constraint in OPF. However, this cannot be strictly satisfied considering different situations of operation. Our targets are to get the relatively similar current margins which means to approach (3) instead of exactly being at (3). We prefer small difference in φ of neighboring branches. Due to the Cauchy-Buniakowsky-Schwarz inequality theorem [27], it is known (3) can be obtained when the lower bound of $\sum \varphi^2$ is acquired under the condition that the sum of φ is fixed, and $0 < \varphi < 1$. Therefore, we put the $\sum \varphi^2$ in the objective functions. The objective functions considering current margins will be shown as:

$$f(I_{ij}, P_{Gi}) = \kappa \sum_{(i,j)\in E} I_{ij}^2 R_{ij} + \beta \sum_{i \in G} c_i P_{Gi} + \iota \sum_{(i,j)\in E} \frac{I_{ij}^2}{I_{ijmax}^2}, \tag{4}$$

where β, κ, ι are the weight coefficients here.

2.2.2. Equality Constraints

The equality constraints $g(x)$ in OPF are about load flow equations which are governed by the Kirchhoff's law and power balance's law. For two bus nodes i and j in a connected branch as shown in Figure 1, the formulation goes as follows:

$$S_{ij} = U_i I_{ij}^H, \tag{5a}$$

$$I_{ij} = (U_i - U_j) Y_{ij}, \tag{5b}$$

$$\Sigma S_{ij} = (P_{Gi} - P_{Di}) + \boldsymbol{i}(Q_{Gi} - Q_{Di}). \tag{5c}$$

Equation (5) shows the load flow equations of each line. Equation (5a) demonstrates the relations of the node voltage, transmission current and complex power. The Equation (5b) describes the relationship of transmission current and voltage difference. Equation (5c) means each node's power is governed by the power balance law.

2.2.3. Inequality Constraints

The inequality constraints $h(x)$ refer to limit of transmission power and current, limits for voltage and capacity power considering system's stable and safe operation. Let P_{Gimin}, P_{Dimin} and P_{Gimax}, P_{Dimax} denote lower and upper bounds of the generated and demanded active power, Q_{Gimin}, Q_{Dimin} and Q_{Gimax}, Q_{Dimax} denote lower and upper bounds of the generated and demanded reactive power. For a load node, the bounded values of P_{Gi} and Q_{Gi} are regulated 0. For the non-dispatchable load, the value of P_{Dimin} and P_{Dimax}, Q_{Dimin} and Q_{Dimax} will remain the same as its demand value respectively. Then $P_{Gi}, P_{Di}, Q_{Gi}, Q_{Di}$ can be constrained as:

$$P_{Gimin} \leq P_{Gi} \leq P_{Gimax}, \tag{6a}$$
$$Q_{Gimin} \leq Q_{Gi} \leq Q_{Gimax}, \tag{6b}$$
$$P_{Dimin} \leq P_{Di} \leq P_{Dimax}, \tag{6c}$$
$$Q_{Dimin} \leq Q_{Di} \leq Q_{Dimax}. \tag{6d}$$

In the power system, the voltage of each node should not fluctuate much from the sending point to the receiving point. The limits are usually ±5% within the base voltage value. U_{imin} and U_{imax} represents the minimum and maximum voltage value respectively. U_i gets the following constraints:

$$U_{imin} \leq U_i \leq U_{imax}. \tag{7}$$

The nodes following Equation (7) are the ones that do not connect to the main grid, that is to say $i \in N$. While for the slack bus which connects to the grid, the power limits of active power and reactive power can vary from $-\infty$ to ∞. However, we always regulate its voltage to be $1 + 0i$ under unitary or regulate with a fixed voltage U_0^{ref}.

For a transmission line from i to j, there are some constraints for the thermal limit to make sure that the transmission line operates safely and stably. It can be shown as follows:

$$|I_{ij}| \leq I_{ijmax} \tag{8}$$

where I_{ijmax} denotes the maximum limit of the transmission current. Usually, it depends on the transmission line's length and materials. We may use (8) for each line separately in different occasions.

2.2.4. OPF Problem and Assumptions

The OPF problem can be represented according to the above formulations:

$$\begin{aligned} &\text{Minimize} \quad (4) \\ &\text{s.t.} \quad (5), (6), (7), (8) \end{aligned} \tag{9}$$

In this paper, we make the following assumptions:

1. The network graph $\mathcal{G}$ in network topology is connected.
2. The OPF in (9) is feasible.

3. OPF in Conic Format

Due to the nonlinear equality constraints in (5a), OPF is a nonlinear and nonconvex program problem which is hard to find the global optimal solution. To make OPF solvable in polynomial time and the optimal operation point found, we change OPF problem into a convex optimization format. In this part, we aim to solve OPF problem (9) through two steps of relaxations. After the fist step, the current variables in OPF problem will be wade away. In the second step, the quadric equations will be relaxed with SOCP relaxations. The OPF problem can be solved thus by convex optimizations and the global optimum can be obtained successfully. The structure of this section is summarized in Figure 2.

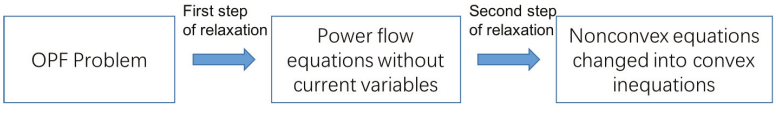

Figure 2. The structure of this section schematic.

3.1. First Step

The first step of relaxation is to handle with the current variables. By eliminating the current variables, the non-convexitiy in power flow constraints (5a) will be changed. In the transformation, we introduce the variables S_{ij} and S_{ji} at the same time for a transmission line i, j. S_{ij} denotes the direction of current form i to j and S_{ji} denotes the power transformed form j to i. Please note that on the transmission line $i \sim j$, the current from i to j equals to the value of $-I_{ji}$. However, due to the voltage difference, the transmission power S_{ij} does not equal to $-S_{ji}$. By eliminating the variables I_{ij} and I_{ji}, the power flow formulation becomes:

$$\Sigma S_{ij} = (P_{Gi} - P_{Di}) + \boldsymbol{i}(Q_{Gi} - Q_{Di}), \tag{10a}$$

$$S_{ij} = Y_{ij}^H U_i U_i^H - Y_{ij}^H U_i U_j^H, \tag{10b}$$

$$S_{ji} = Y_{ij}^H U_j U_j^H - Y_{ij}^H U_j U_i^H. \tag{10c}$$

We define the variables as:

$$\begin{aligned} V_i &= U_i U_i^H, \qquad i \in N \\ V_{ij} &= U_i U_j^H. \quad (i,j) \in E \end{aligned} \tag{11}$$

where $V_i \in \mathbb{R}$ and $V_i \geq 0, V_{ij} \in \mathbb{C}$. Through the transformation, the following power flow formula can be obtained by substituting variables:

$$\Sigma S_{ij} = (P_{Gi} - P_{Di}) + \boldsymbol{i}(Q_{Gi} - Q_{Di}), \tag{12a}$$

$$S_{ij} = Y_{ij}^H V_i - Y_{ij}^H V_{ij}, \tag{12b}$$

$$S_{ji} = Y_{ij}^H V_j - Y_{ij}^H V_{ij}^H, \tag{12c}$$

where $i \in N, i, j \in E$.

With the transformation, there is relationship for the voltage of each line. It can be shown as:

$$|V_{ij}|^2 = V_i V_j. \tag{13}$$

Equation (12) together with (13) is the new power flow constraints that indicate the current, voltage and power balance in each branch of a power system topology. It is the power flow constraints instead of the (5).

From Equation (12) above, we can see that V_{ij} and V_{ij}^H exist at the same time. For a convex optimization problem, all the equality constraints should be affine, the objective functions and inequality constraints should be convex functions. The Equation (12b) combining with (12c) together are no longer affine functions due to the non-affine relationship between V_{ij} and V_{ij}^H. Therefore we change the power flow constraints in the real number filed and replace V_{ij} and V_{ij}^H with new variables in real number field.

Below we decouple the active and reactive power, real and imaginary parts of voltage and current totally; the complex problem is changed into a real convex problem. More details about convex optimization can be seen in [28]. The active and reactive power balance equation can be described as

$$P_{Gi} - P_{Di} = \Sigma P_{ij}, \tag{14a}$$

$$Q_{Gi} - Q_{Di} = \Sigma Q_{ij}, \tag{14b}$$

where $i \in N$ and $(i, j) \in E$. P_{Gi} and P_{Di} are always equal or larger than zero. The equations above means the total power of node i is the sum power of all connecting branches. The real and imaginary part of V_{ij} is defined as a_{ij} and b_{ij}. That is to say,

$$V_{ij} = a_{ij} + b_{ij}\boldsymbol{i}. \tag{15}$$

Then the relations of P_{ij},P_{ji},Q_{ij},Q_{ji} can be shown as follows:

$$P_{ij} = G_{ij}(V_i - a_{ij}) + B_{ij}b_{ij}, \tag{16a}$$
$$P_{ji} = G_{ij}(V_j - a_{ij}) - B_{ij}b_{ij}, \tag{16b}$$
$$Q_{ij} = -G_{ij}b_{ij} + B_{ij}(V_i - a_{ij}), \tag{16c}$$
$$Q_{ji} = G_{ij}b_{ij} + B_{ij}(V_j - a_{ij}). \tag{16d}$$

The Equation (13) can be represented as

$$a_{ij}^2 + b_{ij}^2 = V_i V_j, \tag{17}$$

because of (15).

Since there are no more variables as I_{ij} in the power flow constraints, the objective functions should be reformulated correspondingly.

For (4), the power loss of $i \sim j$ can be represented with the sum of P_{ij} and P_{ji}. The active power loss is consumed by the resistance of the line. For φ^2 here, we can describe as

$$\varphi_{ij}^2 = \frac{(P_{ij} + P_{ji})}{R_{ij} I_{ijmax}^2} \qquad (i,j) \in E$$

The objective function (4) can be shown as:

$$g(P_{ij}, P_{ji}, P_{Gi}) = \sum_{(i,j)\in E} \alpha_{ij}[P_{ij} + P_{ji}] + \beta \sum_{i \in G} f(P_{Gi}), \tag{18}$$

where

$$\alpha_{ij} = \kappa + \frac{\iota}{R_{ij} I_{ijmax}^2}. \tag{19}$$

The objective function is concerned with the active power of each line which can be written as:

$$\text{Minimize} \quad g\,(P), \tag{20}$$

where P refers to (P_{ij}, P_{ji}, P_{Gi}). It should be noted the objective functions here can get the same value of (4). For the voltage constraint, it will be for the new variables V_i instead of U_i.

$$\begin{aligned} &U_{min}^2 \le V_i \le U_{max}^2, \qquad i \in N \\ &V_0 = U_{ref}^2. \end{aligned} \tag{21}$$

U_{ref} denotes the reference voltage of the slack node.

For the inequality constraints (8), the constraints for I_{ij} can be represented with the variables P_{ij} since $P_{ij} = I_{ij}^2 R_{ij}$ and R_{ij} is a constant variable. For the line $i \sim j$, the maximum transmission value of I_{ij} is same as that of $-I_{ji}$, which both represents the current limit of the line (i,j). The constraints (8) can be represented as:

$$\begin{aligned} -R_{ij} I_{ijmax}^2 \le P_{ij} \le R_{ij} I_{ijmax}^2, \\ -R_{ij} I_{ijmax}^2 \le P_{ji} \le R_{ij} I_{ijmax}^2. \end{aligned} \tag{22}$$

With the variables P_{ij} and P_{ji}, we have the following constraints considering the actual physical meanings.

$$P_{ij} + P_{ji} \ge 0. \tag{23}$$

When the value of I_{ij} is positive, the value of I_{ji} must be negtive and vice versa. The sum of P_{ij} and P_{ji} represents the power loss of the transmission line which should be positive.

After the first step of relaxation, the relaxed OPF problem is like this:

$$\begin{aligned} &\text{Minimize } g(P) \\ &\quad \text{s.t.} \quad (14), (16), (17), (6), (21), (22), (23) \end{aligned} \tag{24}$$

The objective functions $g(P)$ in a convex function of variables. The equality constraints (14a)–(14b) and (16a)–(16d) are totally linear and affine and in a simple form. The equality constraints (17) are in quadratic form. The inequality constraints (6), (21), (22) and (23) are all convex. Besides all the variables are in real format. To make this problem a convex optimization, we need to do with the non-affine equality constraints (17). This will be done in the next step.

3.2. Second Step

SOCP relaxations are applied to quadratic equations to convexify the OPF problem in this subsection.

The quadric Equation (17) is converted into an inequality constraint after the relaxation. The quadratic equation is changed into a rotating cone when relaxing the sign of equality into the sign of inequality.

$$a_{ij}^2 + b_{ij}^2 \leq V_i V_j. \tag{25}$$

This Equation (25) can be presented as a cone in a 2-norm form.

$$\left\| \begin{array}{c} 2a_{ij} \\ 2b_{ij} \\ V_i - V_j \end{array} \right\|_2 \leq V_i + V_j. \tag{26}$$

This way, the inequality constraints are in conic format. The OPF (24) becomes a convex optimization problem in real field after the second step of relaxation:

$$\begin{aligned} &\text{Minimize } g(P) \\ &\quad \text{s.t.} \quad (14), (16), (25), (6), (21), (22), (23). \end{aligned} \tag{27}$$

To guarantee the correctness of the solution, it is expected that the final result exists on the bound of the cone. If we get the solution when the formulation (26) acquires the equal sign, the relaxation is what we call it an exact relaxation. When (26) gets the exact relaxations, the relaxed problem is equal to (24) then. The exactness of the relaxation will be illustrated in the next section.

3.3. Relaxation Discussions

It is (27) that is the final presenting form in this paper. It is in a standard convex optimization format, which ensures global optimality. The objective function considering power loss and current margins here are linear independent with variables P_{ij} and P_{ji}. In addition, the generators' cost objective is a convex function with variables P_{Gi}. Therefore, it is regarded as a convex objective function in OPF problem. The nonconvexity in the power flow constraints changes into convex constraints after two steps of relaxations. Then, all the variables above are in $\mathbb{R}$, the equality constraints are in affine format, and the inequality constraints are convex functions. From the formulation, we can know that the optimization problem is about variables $P_{Gi}, P_{Di}, Q_{Gi}, Q_{Di}, V_i, a_{ij}, b_{ij}$ and $P_{ij}, P_{ji}, Q_{ij}, Q_{ji}$ are the intermediate variables.

Compared with the SDP relaxation method mentioned in [20], we transform the positive semidefinite matrix of the voltage into some 2*X*2 ones, the number of which depend on branches' amount. We improve the operational efficiency this way. Furthermore, with the bus injection model adding branch variables, we make the current margin as a part of objective functions under thermal stability consideration. The optimal solution of this objective function will leave enough margins to

branches and contribute to the power system's stable operation. Compared with the SOCP relaxation method proposed in the branch flow model in [21], we do not use the current variables in the model. Instead, we use voltage variables. In addition, for each branch, we focus on the branch itself. In branch flow OPF, when building up model for node i, it regulates the direction of transmission such as $k \sim i$ and $i \sim j$. In the above method, we split the power system with nodes and there is no need to regulate the transforming direction for the branches.

The OPF solutions of voltage U can be recovered from square root calculations of V_i and division operations of $a_{ij} + b_{ij}\boldsymbol{i}$. With the solutions of V_i, a_{ij}, b_{ij}, we present the following Algorithm 1 to recover voltage of each node. In this algorithm, we first make the value of U_0 equal to U_0^{ref} and initialize the set M_{stay} with number 0. When the set M_{stay} is not equal to the set N^0, the algorithm runs into the loop. In this loop, we will get the voltage value of the node and update the M_{stay} at the same time. When the set M_{stay} is same as the set N^0, the loop will end.

Algorithm 1: Recover U from V_i, a_{ij} and b_{ij}

Input:(V_i, a_{ij}, b_{ij}) that satisfies Lemma 1
Output:U
1. $U_0 \leftarrow U_0^{ref}$;
2. $M_{stay} \leftarrow 0$;
3. **while** $M_{stay} \neq N^0$ **do**
   find $i \rightarrow j$ that $i \in M_{stay}$ and $j \notin M_{stay}$;
   compute $U_j \rightarrow \frac{a_{ij} - bij\boldsymbol{i}}{U_i^H}$;
   $M_{stay} \rightarrow M_{stay} \cup j$;
   end while

Lemma 1. *Let $V_i \in \mathbb{R}$ for $i \in N^0$, let a_{ij} and $b_{ij} \in \mathbb{R}$ for $(i,j) \in E$.*
If 1. *$V_0 = U_0^{ref}[U_0^{ref}]^H$ for $U_0^{ref} \in \mathbb{C}$;*
2. *V_i is nonzero for $i \in N^0$;*
3. *$V_i V_j = a_{ij}^2 + b_{ij}^2$;*
then the above algorithm computes the unique U_i that satisfies

$$U_0 = U_0^{ref} \tag{28a}$$
$$V_i = (U_i)(U_i)^H \quad i \in N, \tag{28b}$$
$$a_{ij} + b_{ij}\boldsymbol{i} = U_i U_j^H \quad (i,j) \in E. \tag{28c}$$

Proof of Lemma 1. We will proof this with the recursive algorithm. The total recursive time is denoted by the postive interger T. Let t indicate the recursive time where $t = 1, 2, \ldots, T$. Let $M_{(0)} = 0$, M_t represent the set M_{stay} after the t recursion.

In the algorithm, for node 0 we simplify name one of the nodes connecting to it with number 1. When $t = 0$, it is easy to know:

$$V_0 = (U_0)(U_0)^H, \tag{29a}$$
$$V_1 \neq 0, \tag{29b}$$
$$a_{01}^2 + b_{01}^2 = V_0 V_1. \tag{29c}$$

Because of Algorithm 1, it can be obtained:

$$U_0 = U_0^{ref} \tag{30a}$$
$$a_{01} - b_{01}\boldsymbol{i} = U_1 U_0^H. \tag{30b}$$

It satisfies (28a) naturally due to (30a). Combining (29) and (30b) together, we will get the following equations:

$$a_{01} + b_{01}\boldsymbol{i} = U_0 U_1^H, \tag{31a}$$
$$V_1 = U_1 U_1^H. \tag{31b}$$

It satisfies (28b) and (28c) at the same time. Therefore, Lemma 1 is satisfied for node 0 and the branch connecting to node 0. Assume Lemma 1 holds for the node k and the branch $(k-1,k)$ after the t recursion where $k-1 \in M_t, k \in M_t, 1 < t < T-1$. Therefore for one of the nodes connecting to k which is denoted as k_1 and $k_1 \notin M_t$, we can know:

$$V_k = U_k U_k^H, \tag{32a}$$
$$V_{k_1} \neq 0, \tag{32b}$$
$$a_{k,k_1}^2 + b_{k,k_1}^2 = V_k V_{k_1}. \tag{32c}$$

Similarly, applying Algorithm 1 in the $t+1$ recursion, we can get:

$$a_{k,k_1} - b_{k,k_1}\boldsymbol{i} = U_{k_1} U_k^H. \tag{33}$$

Combining (32) and (33), we can get

$$a_{k,k_1} + b_{k,k_1}\boldsymbol{i} = U_k U_{k_1}^H, \tag{34a}$$
$$V_{k_1} = U_{k_1} U_{k_1}^H. \tag{34b}$$

(28) is satisfied for the node k_1 and the connecting branch $k \sim k_1$. Therefore, Lemma 1 holds for $t+1$ recursion. This completes the proof that Algorithm 1 computes a U that satisfies (28). □

Please note that such recursion holds on condition that the network topology is radial. In radial networks, introducing a new node will only lead to one new branch. While in mesh networks, a new node introduced will construct more than one branch when the node is in a circle. This makes it no more sufficient in the recursion.

Lemma 1 offers a way to recover the OPF solution of (9) from the solution of (27) under the condition that the second step of relaxation is exact.

For constraints, the solution of (27) with variables $P_{Gi}, Q_{Gi}, P_{Di}, Q_{Di}, a_{ij}, b_{ij}$ satisfy the equality and inequality constraints in (27). The Algorithm 1's recovered variables $P_{Gi}, Q_{Gi}, P_{Di}, Q_{Di}, U_i$ can be proved to satisfy the constraints (5)–(8) by putting (28) and (14), (16), (17), (6), (21), (22), (23) into the formula. This implies that when the second step of relaxation is exact, the relaxed OPF constraints can accord with primal OPF constraints equivalently.

For objective functions in (9) and (27), we can get some $f(I_{ij}, P_{Gi}) = g(P_{ij}, P_{ji}, P_{Gi})$ here. In the first step of relaxation above, we can see the first step is done by introducing variables V_i, a_{ij} and b_{ij} satisfying $V_i = U_i U_i^H$ and $U_i U_j^H = a_{ij} + b_{ij}\boldsymbol{i}$. With each I_{ij} and U_i, we can get the corresponding V_i, a_{ij}, b_{ij}, P_{ij} and P_{ji}. Thus,

$$f(I_{ij}, P_{Gi}) \leq g(P_{ij}, P_{ji}, P_{Gi}). \tag{35}$$

Due to Lemma 1, with Algorithm 1 we can recover U_i and I_{ij}. Subsequently,

$$g(P_{ij}, P_{ji}, P_{Gi}) \geq f(I_{ij}, P_{Gi}). \tag{36}$$

Then,

$$f(I_{ij}, P_{Gi}) = g(P_{ij}, P_{ji}, P_{Gi}). \tag{37}$$

Since solving (27) gets a global optimal solution of $g(P_{ij}, P_{ji}, P_{Gi})$, the recovered solution will be the global optimum of $f(I_{ij}, P_{Gi})$. Therefore, the recovered solution of relaxed OPF in Algorithm 1 is the optimal solution of OPF problem.

4. Exactness of the Relaxation

As is shown before, we call the relaxation is exact if the optimal solution is where the formulation (26) gets the equality sign. In this section, we will give one theorem to guarantee the exactness of relaxation.

Theorem 1. *If there is no upper bound on P_{Dmax} and Q_{Dmax} , the relaxation is exact then.*

Proof of Theorem 1. Assume we get a group of optimal solutions, a_{ij}, b_{ij}, V_i and V_j . In addition, we get exact solutions on line $i \sim j$ where $i, j \neq 0$ except the particular line $k \sim l$. That is to say, $\{i, j\} \cap \{k, l\} \neq \emptyset$ and

$$\begin{aligned} a_{ij}^2 + b_{ij}^2 &= V_i V_j \qquad when \quad \{i, j\} \neq \{k, l\}, \\ a_{ij}^2 + b_{ij}^2 &< V_i V_j \qquad when \quad \{i, j\} = \{k, l\}. \end{aligned} \tag{38}$$

On the line $k \sim l$, we define

$$\begin{aligned} a_{kl}^* &= \sqrt{V_k V_l - b_{kl}}, \\ b_{kl}^* &= b_{kl}, \\ V_k^* &= V_k, \\ V_l^* &= V_l. \end{aligned} \tag{39}$$

We define the following variables with $a_{kl}^*, b_{kl}^*, V_k^*, V_l^*$,

$$\begin{aligned} P_{kl}^* &= G_{kl}(V_k^* - a_{kl}^*) + B_{kl} b_{kl}^*, \\ P_{lk}^* &= G_{kl}(V_l^* - a_{kl}^*) - B_{kl} b_{kl}^*, \\ Q_{kl}^* &= -G_{kl} b_{kl}^* + B_{kl}(V_k^* - a_{kl}^*), \\ Q_{lk}^* &= G_{kl} b_{kl}^* + B_{kl}(V_l^* - a_{kl}^*). \end{aligned} \tag{40}$$

Since $a_{kl}^2 + b_{kl}^2 < V_k V_l$, a_{kl}^* is larger than a_{kl}. Then

$$P_{kl}^* - P_{kl} = G_{kl}(V_k^* - a_{kl}^*) + B_{kl} b_{kl}^* - G_{kl}(V_k - a_{kl}) - B_{kl} b_{kl} = G_{kl}(a_{kl}^* - a_{kl}) < 0, \tag{41}$$

$$Q_{kl}^* - Q_{kl} = -G_{kl} b_{kl}^* + B_{kl}(V_k^* - a_{kl}^*) + G_{kl} b_{kl} - B_{kl}(V_k - a_{kl}) = B_{kl}(a_{kl}^* - a_{kl}) < 0. \tag{42}$$

The Equations (41) and (42) represent the difference of the transmission power on branch $k \sim l$. For the injected active power at node k and l, we can get

$$\begin{aligned} P_{Gk}^* - P_{Dk}^* &= P_{kl}^* + \Sigma_{k*\sim i} P_{ki}^* \\ &= P_{kl}^* + \Sigma_{k*\sim i} P_{ki} < P_{Gk} - P_{Dk} \\ P_{Gl}^* - P_{Dl}^* &= P_{lk}^* + \Sigma_{l*\sim i} P_{li}^* \\ &= P_{lk}^* + \Sigma_{l*\sim i} P_{ki} < P_{Gl} - P_{Dl} \\ Q_{Gk}^* - Q_{Dk}^* &= Q_{kl}^* + \Sigma_{k*\sim i} Q_{ki}^* \\ &= Q_{kl}^* + \Sigma_{k*\sim i} Q_{ki} < Q_{Gk} - Q_{Dk} \\ Q_{Gl}^* - Q_{Dl}^* &= Q_{lk}^* + \Sigma_{l*\sim i} Q_{li}^* \\ &= Q_{lk}^* + \Sigma_{l*\sim i} Q_{ki} < Q_{Gl} - Q_{Dl} \end{aligned} \tag{43}$$

When the demanded active power at node k and l remains unchanged, $P_{Gk}^* < P_{Dk}$ and $P_{Gl}^* < P_{Dl}$. When the demanded reactive power at node k and l remains unchanged, $Q_{Gk}^* < Q_{Dk}$ and $Q_{Gl}^* < Q_{Dl}$.

If the value of P_G and Q_G has already reached the lower bound of P_{Gmin} and Q_{Gmin}, we can change the value of P_{Di} and Q_{Di} due to the fact there is no upper bound for P_{Dmax} and Q_{Dmax}. The value of P_{Gi} and Q_{Gi} will remain unchanged then which will satisfy the constraint (6). According to the objective functions of power cost are strictly increasing in variables P_G, the objective function with the variable P_G will have a smaller value or the same value. Besides,

$$P_{kl}^* + P_{lk}^* - (P_{kl} + P_{lk}) = G_{kl}(V_k^* - V_k + V_l^* - V_l - 2a_{kl}^* + 2a_{kl}) < 0. \tag{44}$$

Then, the objective function with $P_{ij} + P_{ji}$ has a smaller value.

For this set of solutions $a_{kl}^*, b_{kl}^*, V_k^*, V_l^*$, we can know that this satisfies (14) and (16) according to (40) and (43). Obviously, this set of solution satisfies (25), (6), (21), (22),(23). Therefore, the solutions satisfy the constraint (14) and (6). In addition, it is definitely a solution of (24) and has a better value on objective functions. The optimal solution is such that every inequality sign in Equation (26) achieves equality sign. This concludes the proof. □

Please note that there is no upper bound on the active and reactive demand power means for a node i, we can supply more power than it originally needed, this can be called load over-satisfaction condition. This condition has been mentioned in ref. [20] and ref. [21]. From the proof above, we can know that if the relaxation is not exact, we can always find a better optimal solution which contradicts the global optimum. Therefore, we can get the exact solutions under this over satisfaction condition. Besides, the proof has no relation with the network structure. This works for the mesh network as well.

From all above, the proposed two step relaxation can be summarized by the following Figure 3.

Figure 3. The structure of relaxing and recovering schematic.

5. Case Study

The novel OPF formulation is tested in some cases in this section. One is a six-node system as an example and the other is the standard IEEE benchmark systems which helps to verify whether the relaxations are exact. The case studies are evaluated on a computer whose CPU is Intel Core 5 at 2.9 GHz with 8 G RAM. The operation system is Mac OS 10.13. The YALMIP [29] is used to depict the variables of the model in Matlab 2016a. In addition, the CPLEX [30] solver is used to solve the convex relaxation problems.

5.1. A 6-Node Small System Example

In the simple radial network, there are six nodes and five branches in total as shown in Figure 4. In this system, the node 1 refers to the default slack bus. The node 3 and 5 represent the generator node, and the node 2, 4 and 6 is the adjustable load nodes with controllers. The specific parameters are summarized in the below Tables 1 and 2, and all the values are in per unit quantities (100MVA Base).

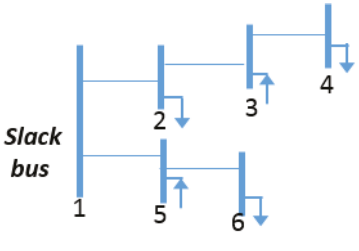

Figure 4. A 6-node small system example.

Table 1. 6-Node System Bus Parameters.

Bus Parameters							
Node	**P**	**Q**	**Vmin**	**Vmax**	c_0	c_1	c_2
1	∞	∞	1	1	0.22	2.5	0.11
2	−2.4	−3.2	0.8	1.2	0	0	0
3	limit	limit	0.8	1.2	0.25	2.4	0.85
4	−3.5	−1.8	0.8	1.2	0	0	0
5	limit	limit	0.8	1.2	0	2.4	0.25
6	−2.5	0	0.8	1.2	0	0	0

Table 2. 6-Node System Line Parameters.

Line Parameters					
From to Node	**r**	**x**	**b**	p_{lim}	q_{lim}
1–2	0.05	0.20	0.030	7.5	4.5
1–5	0.10	0.20	0.040	7.5	4.5
2–3	0.05	0.075	0.070	7.5	4.5
3–4	0.01	0.01	0.030	7.5	4.5
5–6	0.01	0.01	0.04	7.5	4.5

The OPF problems can be formulated with Equation (27). Therefore, each branch is constrained with 7 formulations, 3 of which are inequality constraints and 4 of which are equality equations. For the nodes, considered on the limit, two equality constraints and five inequality constraints are applied for each node.

Our optimization objective of this system is to minimize the total cost, transmission loss and to the best of uniform current margin of the system. We firstly make the objective function $g = P_{ij} + P_{ji} + f(P_{Gi})$ focusing on transmission loss and power cost and denote it as LC. Moreover, we choose objective function as $g = (1 + \frac{1}{R_{ij} I_{ijmax}^2})(P_{ij} + P_{ji}) + f(P_{Gi})$ and denote it as LCC. In these two models, the weight coefficients are all equal to 1. Applying the data in Tables 1 and 2, we get the corresponding result as follows in Table 3. The transmission loss of each branch here is denoted with $P_{ij} + P_{ji}$, and we calculate the value of φ in each branch. All the values are in per unit quantities (100MVA Base).

Table 3. Branch value.

Objective Function	**LC**		**LCC**	
Branch No.	$P_{ij} + P_{ji}$	φ	$P_{ij} + P_{ji}$	φ
1–2	0.047295	0.30	0.055648	0.47
2–3	0.7975	0.88	0.76391	0.82
3–4	0.11632	0.55	0.11632	0.55
1–5	0.0019792	0.38	0.02467	0.49
5–6	0.061718	0.95	0.071718	0.82
Total power loss	1.025		1.032	

We list the corresponding bus value in Table 4. The value of P_{Gi} is the active power generated. In addition, V here is the square amplitude of node voltage.

Table 4. Bus value.

Objective Function	LC		LCC	
Bus No.	P_{Gi}	V	P_{Gi}	V
1	0.72371	1	0.9011	1
2	0	0.88	0	0.87
3	6.0817	0.94	5.8975	0.95
4	0	0.94	0	0.93
5	2.6266	1.2	2.6334	1.2
6	0	0.92	0	0.91
Total power cost	22.71		22.73	

Comparing the results above, we can see with current margin considered in OPF, there will be changes to the value of φ in each branch. As is shown in in Table 3, the φ of branch 2–3 and 5–6 are so large in LC. However, it becomes less somehow in LCC then. Similarly, the value of φ of branch 2–3 and 5–6 becomes larger in LCC than LC. In addition, at the cost of considering current margin, the active power generated will be more in LCC than LC as shown in Table 4. It can be seen the φ is not uniform when the weight coefficients equal to one. Further increasing the weight coefficients, we make the objective function as $F = (1 + \frac{100}{R_{ij} I_{ijmax}^2})(P_{ij} + P_{ji}) + f(P_{Gi})$ and denote it as LCBC. This way we make the weight of current margin bigger than power loss and generators' cost. We get the corresponding branch results as follows in Table 5.

Table 5. Branch value of LCBC.

Branch No.	$P_{ij} + P_{ji}$	φ
1–2	0.068284	0.56
2–3	0.68128	0.60
3–4	0.11632	0.55
1–5	0.002786	0.54
5–6	0.046313	0.61

The corresponding bus value is listed in Table 6, where the value of P_{Gi} is the generated active power and V is the square amplitude of node voltage.

From the results we can see different φ are in the tendency of accordance. The values of φ are around 0.5 then. With bigger weight of current margin objective, we obtain the relative uniform φ.

Table 6. Bus value of LCBC.

Bus No.	P_{Gi}	V
1	1.672	1
2	0	0.78
3	5.2342	1.1
4	0	0.97
5	2.6352	1.2
6	0	0.82

5.2. Test Results in IEEE Benchmark

In the standard IEEE benchmark, the test networks are modified in the Matlab toolbox matpower. Since the IEEE systems are meshed, we split the circles of five systems for simulation. Our optimization objective function focuses on the active power loss, which is the sum of P_{ij} and P_{ji}. The operation time is compared in two different models. The first model is proposed in [31] and we use the relaxed OPF 3 model metioned in the paper of which the SDP relaxations have been changed into SOCP ones. We denote this model as BIMR. The second model is according to (27) and denote this model as BIMBR.

The comparison results are shown in Table 7. The unit of time is in second and all the values are in per unit quantities (100MVA Base)

Table 7. Two Relaxation Tests in IEEE Benchmark Systems.

Relaxation	System	Power Loss	Operation Time
BIMR	IEEE 9	2.548	0.0262
	IEEE 14	13.574	0.0367
	IEEE 30	7.359	0.0486
	IEEE 57	19.482	0.0521
	IEEE 118	62.6212	0.1321
BIMBR	IEEE 9	2.548	0.0251
	IEEE 14	13.574	0.0334
	IEEE 30	7.359	0.0354
	IEEE 57	19.482	0.0425
	IEEE 118	62.6212	0.0905

It can be seen from Table 7 that the proposed relaxation makes OPF a convex and solvable optimization problem. The computation speed of the optimization is counted on the topology and scale of system. The optimal value of the objective functions is the same in two models. This shows that both of the relaxation is exact and tight. The model mentioned in [31] is in a complex number field and our model is illustrated in a real number filed, and as is shown in Table 7, the model proposed in this paper calculates faster than the bus injection model with SOCP relaxation of each branch, which is especially obvious in the large systems.

5.3. Discussions

From the case study above, it can be seen that this kind of method is applicable in both small networks and standard IEEE benchmark systems whose networks are transformed in radial formats. When the loads have not reached the maximum capacity, our relaxations can be proved to be exact. With our methods, the current margins of testing cases tend to be more uniform. Besides, compared with the relaxed SDP method, our method shows a better efficiency.

6. Conclusions

In this paper, we propose an OPF power flow formulation considering current margins in radial networks. With current margins in objective function, we obtain OPF solutions with relatively similar and enough margins of each branch. This OPF model makes it possible to consider the current margins under thermal stability consideration with new branch variables added to bus injection model. Applying the SOCP relaxations, the OPF is convex and solvable. With branch variables added into bus injection model, the proposed method is not sensitive to the system scale and has no need to define transmission directions. Moreover, we propose one sufficient condition to guarantee the exactness of relaxations. In the case studies, the simple 6-node network model shows relatively uniform current margins and the tests in standard IEEE benchmark systems using achieve a higher efficiency.

Author Contributions: Y.C. conducted analysis and simulations. J.X. provided guidance and gave final approval of the version to be submitted. Y.L. provided guidance.

Funding: This research was funded by [National Key R&D Program of China] grant number [2018YFB0904800], [National Natural Science Foundation of China] grant number [61573314, 61773339], and the science and technology project of SGCC [5211SX16000J], the Open Research Project of the State Key Laboratory of Industrial Control Technology [ICT180038].

Acknowledgments: The authors would like to thank anonymous reviewers for their valuable comments and insights.

Conflicts of Interest: The authors declare no conflicts of interest.

References

1. Sakis, A.P.; Xia, F. Optimal Power Flow Application to Composite Power System Reliability Analysis. In Proceedings of the Joint International Power Conference Athens Power Tech, Athens, Greece, 5–8 September 1993; pp. 185–190.
2. Carpentier, J. Contribution to the economic dispatch problem. *Bull. Soc. Franc. Electr.* **1962**, *3*, 836–845.
3. Dommel, H.W.; Tinney, W.F. Optimal Power Flow Solutions. *IEEE Trans. Power Appar. Syst.* **1968**, *PAS-87*, 1866–1876. [CrossRef]
4. Shyamasundar, R.K. *Introduction to Algorithms*; MIT Press: Cambridge, MA, USA, 2010; pp. 14–24.
5. Dvijotham, K.; Molzahn, D.K. Error bounds on the DC power flow approximation: A convex relaxation approach. In Proceedings of the 2016 IEEE 55th Conference on Decision and Control, Las Vegas, NV, USA, 12–14 December 2016; pp. 2411–2418.
6. Stott, B.; Jardim, J.; Alsac, O. DC Power Flow Revisited. *IEEE Trans. Power Syst.* **2009**, *24*, 1290–1300. [CrossRef]
7. Yang, Z.; Zhong, H.; Xia, Q.; Bose, A.; Kang, C. Optimal power flow based on successive linear approximation of power flow equations. *IET Gener. Transm. Distrib.* **2016**, *10*, 3654–3662. [CrossRef]
8. Babu, M.R.; Harini, D. LP based solution for Security Constrained Optimal Power Flow. In Proceedings of the International Conference on Science Technology Engineering and Management, Chennai, India, 30–31 March 2016; pp. 355–359.
9. Sasson, A.M.; Viloria, F.; Aboytes, F. Optimal Load Flow Solution Using the Hessian Matrix. *IEEE Trans. Power Appar. Syst.* **1973**, *PAS-92*, 31–41. [CrossRef]
10. Tinney, W.F.; Hart, C.E. Power Flow Solution by Newton's Method. *IEEE Trans. Power Appar. Syst.* **2007**, *PAS-86*, 1449–1460. [CrossRef]
11. Li, X.; Sun, D.; Toh, K.C. An efficient linearly convergent semismooth Netwon-CG augmented Lagrangian method for Lasso problems. *Siam J. Optim.* **2016**, *28*, 433–458. [CrossRef]
12. Raviprabakaran, V. Enhanced ant colony optimization to solve the optimal power flow with ecological emission. *Int. J. Syst. Assur. Eng. Manag.* **2016**, *9*, 58–65. [CrossRef]
13. Li, M.S.; Tang, W.J.; Tang, W.H.; Wu, Q.H.; Saunders, J.R. Bacterial Foraging Algorithm with Varying Population for Optimal Power Flow. *Biosystems* **2010**, *100*, 185–197. [CrossRef] [PubMed]
14. Sivasubramani, S.; Swarup, K.S. Sequential quadratic programming based differential evolution algorithm for optimal power flow problem. *IET Gener. Transm. Distrib.* **2011**, *5*, 1149–1154. [CrossRef]
15. Radosavljević, J.; Jevtić, M.; Arsić, N.; Klimenta, D. Optimal power flow for distribution networks using gravitational search algorithm. *Electr. Eng.* **2014**, *96*, 335–345. [CrossRef]
16. Kahourzade, S.; Mahmoudi, A.; Mokhlis, H.B. A comparative study of multi-objective optimal power flow based on particle swarm, evolutionary programming, and genetic algorithm. *Electr. Eng.* **2015**, *97*, 1–12. [CrossRef]
17. King, R.T.F.A.; Tu, X.; Dessaint, L.A.; Kamwa, I. Multi-contingency transient stability-constrained optimal power flow using multilayer feedforward neural networks. In Proceedings of the Electrical and Computer Engineering, Vancouver, BC, Canada, 15–18 May 2016; pp. 1–6.
18. Shilaja, C.; Ravi, K.; Shilaja, C.; Ravi, K. Optimal Power Flow Using Hybrid DA-APSO Algorithm in Renewable Energy Resources. *Energy Procedia* **2017**, *117*, 1085–1092. [CrossRef]
19. Bai, X.; Wei, H.; Fujisawa, K.; Wang, Y. Semidefinite programming for optimal power flow problems. *Int. J. Electr. Power Energy Syst.* **2008**, *30*, 383–392. [CrossRef]
20. Lavaei, J.; Low, S.H. Zero Duality Gap in Optimal Power Flow Problem. *IEEE Trans. Power Syst.* **2012**, *27*, 92–107. [CrossRef]
21. Farivar, M.; Low, S.H. Branch flow model: Relaxations and convexification. In Proceedings of the 2012 IEEE 51st IEEE Conference on Decision and Control (CDC), Maui, HI, USA, 10–13 December 2012; pp. 3672–3679.
22. Chen, Y.; Li, Y.; Xiang, J.; Shen, X. An Optimal Power Flow Formulation with SOCP Relaxation in Radial Network. In Proceedings of the 2018 IEEE 14th International Conference on Control and Automation (ICCA), Anchorage, AK, USA, 12–15 June 2018; pp. 921–926.
23. Niknam, T.; Narimani, M.R.; Aghaei, J.; Azizipanah-Abarghooee, R. Improved particle swarm optimisation for multi-objective optimal power flow considering the cost, loss, emission and voltage stability index. *IET Gener. Transm. Distrib.* **2012**, *6*, 515–527. [CrossRef]

24. Varadarajan, M.; Swarup, K.S. Solving multi-objective optimal power flow using differential evolution. *IET Gener. Transm. Distrib.* **2008**, *2*, 720–730. [CrossRef]
25. Zhang, R.; Dong, Z.; Xu, Y.; Wong, K.; Lai, M. Hybrid computation of corrective security-constrained optimal power flow problems. *IET Gener. Transm. Distrib.* **2014**, *8*, 995–1006. [CrossRef]
26. Rabiee, A.; Nikkhah, S.; Soroudi, A.; Hooshmand, E. Information gap decision theory for voltage stability constrained OPF considering the uncertainty of multiple wind farms. *IET Renew. Power Gener.* **2017**, *11*, 585–592. [CrossRef]
27. Rooin, J.; Inequality, K.F.; Inequality, B. *Inequalities and Applications*; Birkhäuser Verlag: Basel, Switzerland, 2009; p. i.
28. Boyd, S.; Vandenberghe, L.; Faybusovich. Convex Optimization. *IEEE Trans. Autom. Control* **2006**, *51*, 1859.
29. Johan, L. YALMIP: A toolbox for modeling and optimization in MATLAB. *Skelet. Radiol.* **2011**, *41*, 287–292.
30. Z/Os, I.C.O.F. *IBM ILOG CPLEX Optimizer*; IBM Corporation: Armonk, NY, USA, 2013.
31. Sojoudi, S.; Lavaei, J. Physics of power networks makes hard optimization problems easy to solve. In Proceedings of the Power and Energy Society General Meeting, San Diego, CA, USA, 22–26 July 2012; pp. 1–8.

energies

MDPI

Article

Interval Power Flow Analysis Considering Interval Output of Wind Farms through Affine Arithmetic and Optimizing-Scenarios Method

Weijie Cheng [1], Renli Cheng [1], Jun Shi [1], Cong Zhang [2], Gaoxing Sun [3] and Dong Hua [3,*]

[1] Shenzhen Power Supply Bureau Co., Ltd., Shenzhen 518000, China; chengweijie@sz.csg.cn (W.C.); chengrenli@sz.csg.cn (R.C.); shijun@sz.csg.cn (J.S.)
[2] College of Electrical and Information Engineering, Hunan University, Changsha 410000, China; zcong@hnu.edu.cn
[3] School of Electric Power, South China University of Technology, Guangzhou 510000, China; 201721014448@mail.scut.edu.cn
* Correspondence: z.c25@mail.scut.edu.cn; Tel.: +86-150-1871-6275

Received: 11 October 2018; Accepted: 14 November 2018; Published: 15 November 2018

Abstract: Wind power belongs to sustainable and clean energy sources which play a vital role of reducing environment pollution and addressing energy crisis. However, wind power outputs are quite difficult to predict because they are derived from wind speeds, which vary irregularly and greatly all the time. The uncertainty of wind power causes variation of the variables of power grids, which threatens the power grids' operating security. Therefore, it is significant to provide the accurate ranges of power grids' variables, which can be used by the operators to guarantee the power grid's operating security. To achieve this goal, the present paper puts forward the interval power flow with wind farms model, where the generation power outputs of wind farms are expressed by intervals and three types of control modes are considered for imitating the operation features of wind farms. To solve the proposed model, the affine arithmetic-based method and optimizing-scenarios method are modified and employed, where three types of constraints of wind control modes are considered in their solution process. The former expresses the interval variables as affine arithmetic forms, and constructs optimization models to contract the affine arithmetic forms to obtain the accurate intervals of power flow variables. The latter regards active power outputs of the wind farms as variables, which vary in their corresponding intervals, and accordingly builds the minimum and maximum programming models for estimating the intervals of the power flow variables. The proposed methods are applied to two case studies, where the acquired results are compared with those acquired by the Monte Carlo simulation, which is a traditional method for handling interval uncertainty. The simulation results validate the advantages, effectiveness and the applicability of the two methods.

Keywords: affine arithmetic; interval variables; optimizing-scenarios method; power flow; wind power

1. Introduction

Wind power belongs to sustainable and clean energy sources, which play a vital role in reducing environment pollution and addressing the energy crisis. However, wind power outputs are quite difficult to predict because they are derived from wind speeds, which always vary irregularly and greatly [1]. Therefore, the output power of wind farms belongs to uncertainties existing in power systems. Uncertainties of power grids cause the parameters of a power grid, such as active line power flows, bus angles, and bus voltages, to vary, which may threaten the power grids' operating security. It makes essential sense to acquire the ranges of power flow results over which the power

grid could operate safely when considering the uncertainties from wind farms. Operators then are able to use these obtained ranges to clarify the quantity of wind power generation to incorporate into the power grid, so as to safeguard the operating security of power systems. Accordingly, the following introduction section will discuss the state-of-the-art methods for dealing with the uncertainty of wind power in power flow models.

At present, there are mainly two kinds of approaches for handling uncertainty of wind power in power flow equations: the probabilistic power flow [2–16] and the interval power flow [17–30]. As for probabilistic power flow, the uncertainty of output generation from a wind farm can be defined as random with description of some probabilistic distributions, which will be utilized to build the probabilistic power flow model of power grids. Three methods are generally used for dealing with the probabilistic power flow model, i.e., the analytical method [2–6], the point estimate method [7–12], and Monte Carlo simulation (MCS) [13–16]. Monte Carlo simulation produces a series of samples and obtains the load flow results under every single sample. Accordingly, this method is able to acquire the corresponding variables' distributions. The MCSs' sampling efficiency is enhanced through consideration of relationships among random variables utilizing Latin hypercube sampling [15]. However, MCSs still require huge computational time, and they perform poorly in terms of obtaining accurate results, especially when solving a large-scale test system [16]. The point estimate method aims at acquiring random output variables' statistical features through refining some important statistical information from the random input data. Point estimate methods are divided by two methods considering utilization of different orders of moments, i.e., the three-point method [21] and two-point method [12]. Despite the efficiency of the point estimate method being higher than that of MCSs, it is unable to compute the load flow variables' accurate distribution functions. Analytical methods aimed at obtaining variables' probability distribution results by employing different theoretic instruments from mathematics include: the approximation expansions and cumulants, which includes the Cornish−Fisher expansion [8], Gram−Charlier expansion [16], and the fast Fourier transform [14]. In solution procedures of the aforementioned approaches, they require linearizing the nonlinear load flow equations by usage of linear diffusion methods. The transformation and linearization including in linear diffusion methods will give rise to approximation errors and reduce flexibility. In conclusion, the aforementioned approaches are employed for solving probabilistic power flow models aimed at acquiring the critical statistical information or probability distribution functions of the power flow results of probabilistic power flow models. This information, however, is always crude since the parameters of random variables' distribution functions are inaccurate, and the probabilistic power flow methods always underestimate power flow results due to their inherent limited sampling space.

To overcome this problem, the interval power flow approach uses intervals, whose bound information is easily acquired, to model the uncertainties, thus building the interval power flow model and obtaining the conventional ranges of the power flow variables. Three kinds of interval power flow methods have been proposed to solve the interval power flow model, i.e., interval arithmetic-based method [17–19], affine arithmetic (AA)-based method [21–24], and the optimizing-scenarios method (OSM) [25,26]. The interval arithmetic-based methods are aimed to solve the interval power flow model through conventional nonlinear equation iteration methods such as Newton iteration [17], Gauss−Seidel iteration [18], and Krawczyk−Moore method [19], by incorporating the interval arithmetic computation. However, these methods are too conservative due to dependency problems among interval calculations [20], and their convergence depends on the choice of initial intervals. To solve this problem, the AA-based methods propose the usage of affine arithmetic to realize interval computation instead of the interval arithmetic, thus avoiding the interval dependency problem. Besides, the AA-based methods introduce the domain-contracting process to replace the iteration process in interval arithmetic-based methods, so as to overcome the convergence problem. Although the AA-based methods provide an effective way for solving the interval power flow model, they still overestimate the ranges of power flow variables because of approximation errors produced by affine arithmetic computation of nonlinear functions [20]. The OSM acquires the ranges of each

variable of the interval power flow through its corresponding optimization models directly, where the uncertainties are regarded as variables varying in their own intervals arbitrarily. It considers any possible scenario during the interval uncertainty bounds. It has previously been demonstrated to be the most accurate method for obtaining results of the interval power flow models in theory. In conclusion, the interval power flow methods outperform the probabilistic power flow methods in terms of simplicity of modelling and accuracy of obtained results. However, it is much easier to consider the models of wind farms in the probabilistic power flow methods, due to their simple computational processes. Accordingly, lots of navigations have been conducted regarding the probabilistic power flow considering wind farms [27–29]. As for the interval power flow methods, although some researchers have considered wind power in their power flow models [30], the specific models of wind farms are neglected. Therefore, the present paper first uses intervals to describe the uncertainties of generation from a wind farm and proposes a model of interval power flow considering wind farm (IPFWF) models. To solve the IPFWF model, the AA-based method and the OSM are therefore modified for considering the models of wind farms, and thereby employed to acquire results of the interval power flow variables. To accomplish this target, in the present paper, we conducted the relevant work listed below.

- We first proposed the IPFWF model, during which the uncertainties of generation from a wind farm were expressed by intervals. This model is aimed at obtaining the ranges of the power flow results of power grids incorporating wind farms with interval power generation. Considering differences among the wind farms' operation conditions, we considered three types of wind farms in the proposed model.
- We modified the AA-based method and employed it to handle the proposed model. The AA-based method is a previously proposed method for solving the interval power flow model without considering wind farms. Here, the relationship between the reactive power and active power generation of wind farms is considered in the affine arithmetic computation. To solve the IPFWF model, minimum and maximum optimization models are established to contract the noise elements in affine arithmetic forms, and thus the results of load flow variable intervals are acquired.
- The OSM was employed here to acquire the intervals of the variables from the IPFWF model. The OSM builds two types of optimization models to acquire ranges of the load voltage magnitudes, bus angles, as well as the active line power flows of the IPFWF model. Three types of constraints of wind control modes were considered in the optimization models of the OSM, so as to imitate the operation features of wind farms. Meanwhile, the voltage recovery processes and limits of reactive power of generators were considered.
- We compared the results acquired using the AA-based method and OSM in two case studies with those acquired by the MCS, to demonstrate the advantages and effectiveness of the proposed methods, as well as validating their applicability of solving larger systems.

As far as the following contents of this paper are concerned, they are arranged as follows. Mathematical formulations of the IPFWF model are described in Section 2. Introduction of the AA-based method and OSM procedures, which are employed for solving the proposed model, are given in Section 3. Analysis and discussions related to simulation results are introduced in Section 4. The contributions as well as conclusions of the work are introduced in Section 5.

2. Mathematical Formulations of the Problem

2.1. Wind Farm Models

2.1.1. Modeling of the Output Wind Power Generation

Regarding modeling of the wind generators, two kinds of control modes are mainly used for modelling the wind turbines, i.e., fixed speed/constant frequency (FSCF) control and variable

speed/constant frequency control (VSFC) [31–33]. Variable speed/constant frequency control modes are classified as the constant voltage control mode (CVCM) and the constant power factor control mode (CPFCM) [34–37]. However, despite the wind turbine's control types, its output active power should be generally described by functions which vary with wind speeds [38,39]. Generally, a wind farm usually contains numerous wind turbines, whose spatial placement is quite similar because of similarity of landforms. This feature makes the active power outputs of wind turbines in one wind farm show a quite high degree of similarity [40]. Meanwhile, in practice, considering design requirements, relevant control modes are usually employed to control the wind farm's wind turbines. As a result, a wind farm is able to be regarded as a model of wind turbine if neglecting spacing between turbines, turbulence, and the wake effect [41–43].

As is discussed in Reference [44], the output power of wind turbines can be assumed as a function closely related to wind speeds. Numerous expressions have been proposed to present the function relationship between wind speed and output wind power generation, such as quadratic function [44] and cubic function forms [39]. In practice, however, it makes sense to pay more attention to the characteristics of the output power based on the actual operating conditions of wind turbines, rather than the function relationship. Therefore, the cut-out (v_{co}), cut-in (v_{ci}), and rated (v_r) wind speeds should be taken into account when using power generation functions of a wind turbine. Here, we use a formulation proposed in Reference [44], where the output active wind power generation P_W is expressed by a function of wind speeds, and it is given as follows.

$$P_W = \begin{cases} (A_0 + A_1 v + A_2 v^2) P_r, v_{ci} \le v < v_r \\ P_r,\ v_r \le v < v_{co} \\ 0,\ \ v < v_{ci}\, or\, v \ge v_{co} \end{cases} \tag{1}$$

where P_r represents rated output active wind power generation and coefficients A_0, A_1, and A_2 are given as follows. The relationship between wind power output and wind speeds is presented Figure 1.

$$\begin{cases} A_2 = \dfrac{1}{(v_{ci} - v_r)^2}\left[2 - 4\left(\dfrac{v_{ci} + v_r}{2v_r}\right)^3\right], \\ A_1 = \dfrac{1}{(v_{ci} - v_r)^2}\left[4(v_{ci} + v_r)\left(\dfrac{v_{ci} + v_r}{2v_r}\right)^3 - (3v_{ci} + v_r)\right], \\ A_0 = \dfrac{1}{(v_{ci} - v_r)^2}\left[v_{ci}(v_{ci} + v_r) - 4v_{ci}v_r\left(\dfrac{v_{ci} + v_r}{2v_r}\right)^3\right]. \end{cases} \tag{2}$$

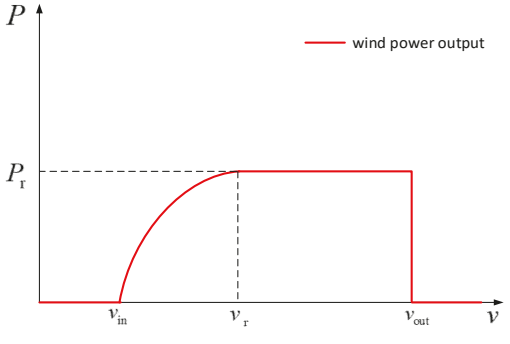

Figure 1. Relationship between wind power output and wind speeds according to Equation (1).

We observe from Equation (1) and Figure 1 that $P_W = 0$ when $v < v_{ci}$ or $v \ge v_{co}$, and can be written as a quadratic function related to v when $v_{ci} \le v < v_r$. However, P_W is a constant value P_r

when $v_r \leq v < v_{co}$, due to well adjustable ability of pitch angles of wind turbines. Notice here that v is regarded as a random, and it is with a Weibull distribution:

$$f(v) = \frac{k}{c}\left(\frac{v}{c}\right)^{k-1} \exp\left[-\left(\frac{v}{c}\right)^{k}\right], \tag{3}$$

where c and k, respectively, represent the scale and shape parameters. Therefore, P_W varies in an interval expressed as $[0, P_r]$.

2.1.2. Fixed Speed and Constant Frequency Control

In the initial stage of designing wind turbines, technologies were unable to adjust the speed of impellers for various wind speeds. The active power of wind turbines, therefore, was produced in an asynchronous mode and only over a quite narrow wind speed range. Meanwhile, the PQ and RX nodes were frequently employed by load flow analysis rather than FSCF. Here, Equation (4) will be used for modelling the reactive power consumption of the PQ bus in the FSCF wind turbines.

$$Q = V^2 \frac{\mathrm{X_c} - \mathrm{X_m}}{\mathrm{X_c X_m}} + \mathrm{X}\frac{V^2 + 2\mathrm{R}P_W}{2(\mathrm{R}^2 + \mathrm{X}^2)} - \mathrm{X}\frac{\sqrt{(V^2 + 2\mathrm{R}P_W)^2 - 4{P_W}^2(\mathrm{R}^2 + \mathrm{X}^2)}}{2(\mathrm{R}^2 + \mathrm{X}^2)}, \tag{4}$$

where V stands for the bus voltage magnitude, P_W represents the active wind power generation calculated by (1), R represents the total of the rotor and stator resistance values, X represents the combination of rotor and stator leakage reactance values, $\mathrm{X_m}$ stands for excitation reactance, and $\mathrm{X_c}$ stands for the capacitance of shunt capacitors. The principle of power generation is illustrated in Figure 2.

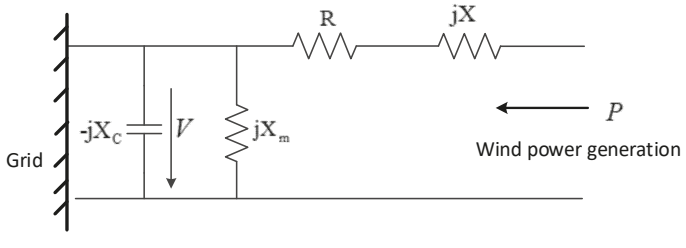

Figure 2. Simplified circuit of fixed speed/constant frequency type wind turbines.

With the development of control technology for wind turbines, FSCF modes became outdated and gradually were substituted by VSCF modes.

2.1.3. Constant Power Factor Control Mode

Constant power factor control mode is a special type of variable speed/constant frequency control mode, and its schematic is illustrated in Figure 3. Here, the current transformer and crowbar resistance are used to realize control of constant power factors. Meanwhile, a resistance here is used to prevent the current from overrunning, and a step-up transformer converts bus voltage to that of the connected grid. As for the reactive power consumption of CPFCM, it is calculated by

$$Q = P_W \times \tan\varphi, \tag{5}$$

where φ is the angle of power factor $\cos\varphi$ and P_W is the active power generation.

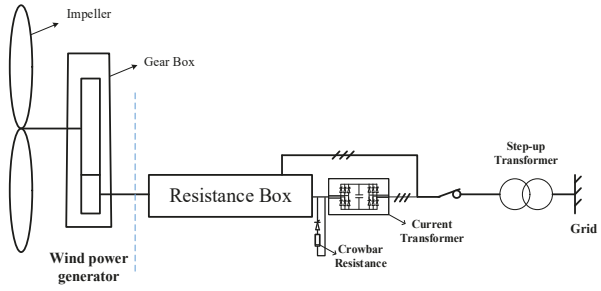

Figure 3. Schematic of a constant power factor control mode wind turbine.

2.1.4. Constant Voltage Control Mode

Constant voltage control mode is another type of variable speed/constant frequency control mode, and its layout is presented in Figure 4. Here, the wind turbine's voltage can be controlled using the full-power converter operating similar to the thermal generator. In addition, it is able to control its reactive power consumption and is modelled by a PV node.

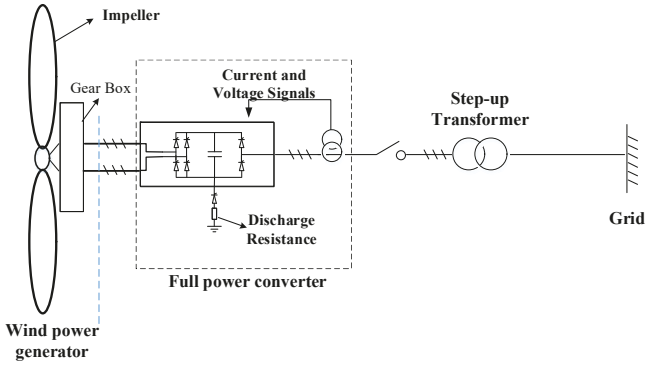

Figure 4. Schematic of a constant voltage control mode wind turbine.

Based on preceding discussions, the wind turbines in three control modes can be discriminated through distinct reactive power consumption modes. That is, the CVCM is able to control its reactive power output, while the reactive power outputs of FSCF and CPFCM can be calculated through Equations (4) and (5), respectively.

2.2. Interval Power Flow with Wind Farms Model

Regardless of the consideration of wind power, the load flow model of a power grid is expressed as

$$P_{Gi} - P_{Li} - P_i = 0,\ i \in \{\text{generator buses}\}, \tag{6}$$

$$-P_{Li} - P_i = 0,\ i \in \{\text{load buses}\}, \tag{7}$$

$$Q_{Ci} - Q_{Li} - Q_i = 0,\ i \in \{\text{load buses}\}, \tag{8}$$

where

$$Q_i = V_i \sum_{j \in S} V_j (G_{ij} \sin\theta_{ij} - B_{ij} \cos\theta_{ij}), \tag{9}$$

$$P_i = V_i \sum_{j \in S} V_j (G_{ij} \cos\theta_{ij} + B_{ij} \sin\theta_{ij}). \tag{10}$$

where S is the set of indices of system buses, P_{Gi} is the ith generator's active output power, Q_{Li} and P_{Li}, respectively, represent reactive and active power load demand of the ith bus, Q_{Ci} stands for the output of reactive power compensator at the ith bus, $\theta_{ij} = \theta_i - \theta_j$, where θ_i represents the bus angle of the ith bus, and they should regard the slack bus's angle value as the reference, V_i is the voltage magnitude of the ith bus, B_{ij} and G_{ij} respectively represent the imaginary and real portions of Y_{ij}, where $Y = \{Y_{ij}\}$ is the nodal admittance matrix.

However, if the wind power is taken into consideration, equations of buses related to wind farms should make changes. An obvious change is that all the real power generation of buses with farms should be substituted by intervals, marked as $\hat{P}_{Gi} = [\underline{P}_{Gi}, \overline{P}_{Gi}]$, where $\underline{P}_{Gi}$ and $\overline{P}_{Gi}$ represent minimum and maximum of wind power generation, respectively. Accordingly, the equations of buses correlated to wind farms can be rewritten based on three reactive power control modes in the following. For FSCF wind power control, based on Equation (4), their load flow equations can be rewritten as

$$Q_{Gi} = V_i^2 \frac{X_{ci} - X_{mi}}{X_{ci} X_{mi}} + X_i \frac{V_i^2 + 2R_i \hat{P}_{Gi}}{2(R_i^2 + X_i^2)} - X_i \frac{\sqrt{(V_i^2 + 2R_i \hat{P}_{Gi})^2 - 4\hat{P}_{Gi}^2 (R_i^2 + X_i^2)}}{2(R_i^2 + X_i^2)}, \tag{11}$$

$$\hat{P}_{Gi} - P_{Li} - P_i = 0, \tag{12}$$

$$\hat{Q}_{Gi} - Q_{Li} - Q_i = 0, \tag{13}$$

the power flow equations of CPFCM control are given by

$$\hat{Q}_{Gi} = \hat{P}_{Gi} \times \tan \varphi, \tag{14}$$

$$\hat{P}_{Gi} - P_{Li} - P_i = 0, \tag{15}$$

$$\hat{Q}_{Gi} - Q_{Li} - Q_i = 0, \tag{16}$$

regarding CVCM control buses, it only needs to replace P_{Gi} of Equation (6) with $\hat{P}_{Gi}$:

$$\hat{P}_{Gi} - P_{Li} - P_i = 0. \tag{17}$$

The solution of this interval computation problem will be introduced in the following sections.

3. Solution to the IPFWF Model

3.1. Solution of the IPFWF Model by AA-Based Method

In this section, the AA-based method is employed and modified to solve the IPFWF model [17]. The AA-based method uses the affine arithmetic to realize the interval computation instead of the interval arithmetic, so as to reduce the conservatism of the interval computing results.

3.1.1. Introduction of AA

The affine arithmetic uses a series of noises to express the interval $\hat{x} = [\underline{x}, \overline{x}]$, which can be written as

$$\hat{x} = x_0 + x_1 \varepsilon_1 + x_2 \varepsilon_2 + \cdots + x_p \varepsilon_p, \tag{18}$$

where ε_i stands for a noise element and is valued as interval $[-1, 1]$; x_i represents the coefficient corresponding to ε_i, and it reflects the influence of ε_i on the interval $\hat{x}$; x_0 is the midpoint of $\hat{x}$; p is the number of noise element. The AA form (18) can be easily switched to interval arithmetic form by using formulation

$$\hat{x} = [x_0 - \sum_{i=1}^{p} |x_i|, \; x_0 + \sum_{i=1}^{p} |x_i|]. \tag{19}$$

where p is the number of noise element, and $|x_i|$ represents absolute value of x_i. Based on the definition (18), the minus/plus and scalar multiplication operators of AA are respectively defined in the following:

$$\hat{x} \pm \hat{y} = (x_0 \pm y_0) + (x_1 \pm y_1)\varepsilon_1 + (x_2 \pm y_2)\varepsilon_i + \cdots + (x_p + y_p)\varepsilon_p, \tag{20}$$

$$\alpha\hat{x} = (\alpha x_0) + (\alpha x_1)\varepsilon_1 + (\alpha x_2)\varepsilon_i + \cdots + (\alpha x_p)\varepsilon_p, \tag{21}$$

where α is a constant. AA-based interval computation is more accurate because the relevance on intervals is considered. For example, $\hat{x} = [-1, 1]$, then $\hat{x} - \hat{x} = [-1, 1] - [-1, 1] = [-2, 2]$ according to interval arithmetic, while affine arithmetic leads to computing result as $\hat{x} - \hat{x} = (x_0 - x_0) + (x_1 - x_1)\varepsilon_1 = 0$. Here, $x_0 = 0$, $x_1 = 1$ and ε_1 is the unique noise element.

However, AA requires more complicated computations on the nonlinear operations. To realize the nonlinear computation, AA needs to linearize the nonlinear functions and introduces new noise elements. If we assume a nonlinear function as $\hat{z} = f(\varepsilon_1, \varepsilon_2, \cdots, \varepsilon_p)$, then its linear affine arithmetic form can be expressed as

$$f^a(\varepsilon_1, \varepsilon_2, \cdots, \varepsilon_p) = \varepsilon_0 + z_1\varepsilon_1 + z_2\varepsilon_2 + \cdots + z_p\varepsilon_p + z_k\varepsilon_k, \tag{22}$$

where $z_i (i = 1, 2, \ldots, p)$ represents the coefficient of noise element ε_i of linear AA form of $\hat{z}$; ε_k is a new noise element; z_k stands for the approximation error caused by linearization of $\hat{z}$, and it satisfies the following constraint

$$\max\left\{\left|f(\varepsilon_1, \varepsilon_2, \cdots, \varepsilon_p) - f^a(\varepsilon_1, \varepsilon_2, \cdots, \varepsilon_p)\right| : \varepsilon_i \in [-1, 1]\right\} \leq z_k. \tag{23}$$

In fact, different linear approximation methods always have different approximation errors, and the Chebyshev function approximation is supposed as the best linear approximation method because it minimizes the approximation errors. Therefore, it is commonly used by AA to compute the intervals of nonlinear function.

3.1.2. Solution of the IPFWF through AA

According to the affine arithmetic theory, the AA-based method is used to solve the IPFWF model. It should be noticed that the FSCF wind farms are not considered in the AA-based method, because it is outdated and is unable to realize affine arithmetic due to complex relationships (11) between active and reactive power. The AA-based method mainly includes three steps, which are introduced in the following.

Step (1) Express the voltage magnitudes of load buses and bus angles of non-slack buses as the following affine forms:

$$V_i = V_{i,0} + \sum_{j \in CVCM} V_{i,j}^{\mathrm{P}} \varepsilon_{\mathrm{P}j} + \sum_{j \in CPFCM} V_{i,j}^{\mathrm{P}} \varepsilon_{\mathrm{P}j} + \sum_{j \in CPFCM} V_{i,j}^{\mathrm{Q}} \varepsilon_{\mathrm{Q}j}, \ \text{for } i \in \mathrm{S_L}, \tag{24}$$

$$\theta_i = \theta_{i,0} + \sum_{j \in CVCM} \theta_{i,j}^{\mathrm{P}} \varepsilon_{\mathrm{P}j} + \sum_{j \in CPFCM} \theta_{i,j}^{\mathrm{P}} \varepsilon_{\mathrm{P}j} + \sum_{j \in CPFCM} \theta_{i,j}^{\mathrm{Q}} \varepsilon_{\mathrm{Q}j}, \ \text{for } i \in \mathrm{S_G} \cup \mathrm{S_L}, \tag{25}$$

where coefficients $V_{i,j}^{\mathrm{P}}$, $V_{i,j}^{\mathrm{Q}}$, $\theta_{i,j}^{\mathrm{P}}$, $\theta_{i,j}^{\mathrm{Q}}$ are partial deviations corresponding to noise elements $\varepsilon_{\mathrm{P}j}$, $\varepsilon_{\mathrm{Q}j}$. Here, these coefficients should be enlarged by an amplification to ensure (24) and (25) include the real ranges of bus angles and load voltage magnitudes. $V_{i,0}$ and $\theta_{i,0}$ are load voltage magnitude and bus angle results at nominal point. Because CPFCM wind farms satisfy constraint (14), then $\varepsilon_{\mathrm{Q}j} = \varepsilon_{\mathrm{P}j} \times \tan\varphi_j$. Therefore, (24) and (25) are rewritten as

$$V_i = V_{i,0} + \sum_{j \in CVCM} V_{i,j}^{\mathrm{P}} \varepsilon_{\mathrm{P}j} + \sum_{j \in CPFCM} (V_{i,j}^{\mathrm{P}} + V_{i,j}^{\mathrm{Q}} \tan\varphi_j) \varepsilon_{\mathrm{P}j}, \ \text{for } i \in \mathrm{S_L}. \tag{26}$$

$$\theta_i = \theta_{i,0} + \sum_{j \in CVCM} \theta_{i,j}^{\mathrm{P}} \varepsilon_{\mathrm{P}j} + \sum_{j \in CPFCM} (\theta_{i,j}^{\mathrm{P}} + \theta_{i,j}^{\mathrm{Q}} \tan \varphi_j) \varepsilon_{\mathrm{P}j}, \text{ for } i \in \mathrm{S_G} \cup \mathrm{S_L}. \tag{27}$$

Step (2) Substitute the affine forms of voltage magnitude and bus angles into power flow equations, thus compute the affine forms of injected active power and reactive power, which are written as

$$\hat{P}_i = P_{i,0} + \sum_{j \in CVCM \cup CPFCM} P_{i,j}^{\mathrm{P}} \varepsilon_{\mathrm{P}j} + \sum_{h \in nN} P_{i,h} \varepsilon_h, \text{ for } i \in \mathrm{S_G} \cup \mathrm{S_L}, \tag{28}$$

$$\hat{Q}_i = Q_{i,0} + \sum_{j \in CVCM \cup CPFCM} Q_{i,j}^{\mathrm{P}} \varepsilon_{\mathrm{P}j} + \sum_{h \in nN} Q_{i,h} \varepsilon_h, \text{ for } i \in \mathrm{S_L}, \tag{29}$$

where $Q_{i,0}$ and $P_{i,0}$ are respective the injected reactive and active power for buses without wind farms, for buses with wind farms,

$$P_{i,0} = \frac{\underline{P}_{\mathrm{G}i} + \overline{P}_{\mathrm{G}i}}{2} (i \in \mathrm{CVCM} \cup \mathrm{CPFCM}) \tag{30}$$

and

$$Q_{i,0} = \frac{\underline{P}_{\mathrm{G}i} + \overline{P}_{\mathrm{G}i}}{2} \tan \varphi_i (i \in \mathrm{CPFCM}). \tag{31}$$

nN is the set of new noise variables caused by affine approximation computations, which include multiplication and Chebyshev linear approximation for sine and cosine functions. Here, the approximation computation is conducted according to the constraint (23).

Step (3) Construct linear programming problems to contract the ranges of noise symbols $\varepsilon_{\mathrm{P}i}$. Based on the affine forms expressed by (28) and (29), we can acquire the following matrix form:

$$f(X) = AX + B, \tag{32}$$

where

$$X = [\varepsilon_1 \, \varepsilon_2 \, \cdots \, \varepsilon_N]^T, \tag{33}$$

$$f(X) = \begin{bmatrix} \hat{\boldsymbol{P}} \\ \hat{\boldsymbol{Q}} \end{bmatrix}, \tag{34}$$

$$\hat{\boldsymbol{Q}} = [\hat{Q}_1 \, \hat{Q}_2 \cdots \hat{Q}_{nQ}]^T, \tag{35}$$

$$\hat{\boldsymbol{P}} = [\hat{P}_1 \, \hat{P}_2 \cdots \hat{P}_{nP}]^T, \tag{36}$$

$$A = \begin{bmatrix} P_{1,1}^P & \cdots & P_{1,N}^P \\ \cdots & \cdots & \cdots \\ P_{nP,1}^P & \cdots & P_{nP,N}^P \\ Q_{1,1}^P & \cdots & Q_{1,N}^P \\ \cdots & \cdots & \cdots \\ Q_{nQ,1}^P & \cdots & Q_{nQ,N}^P \end{bmatrix}, \tag{37}$$

$$B = \begin{bmatrix} P_{1,0} \\ \cdots \\ P_{nQ,0} \\ Q_{1,0} \\ \cdots \\ Q_{nP,0} \end{bmatrix} + \begin{bmatrix} P_{1,1} & \cdots & P_{1,nN} \\ \cdots & \cdots & \cdots \\ P_{nP,1} & \cdots & P_{nP,nN} \\ Q_{1,1} & \cdots & Q_{1,nN} \\ \cdots & \cdots & \cdots \\ Q_{nQ,1} & \cdots & Q_{nQ,nN} \end{bmatrix} \begin{bmatrix} \varepsilon_1 \\ \cdots \\ \cdots \\ \cdots \\ \cdots \\ \varepsilon_{nN} \end{bmatrix}, \tag{38}$$

nP and nQ are the element number of sets $\mathrm{S_G} \cup \mathrm{S_L}$ and $\mathrm{S_L}$. Here, X represents the vector of noise elements that should be contracted, and the initial value of each dimension is set as the interval $[-1,1]$; A is a matrix that consists of calculated real parameters; B is an interval vector computed by the new

noise elements. Because the newly produced noise element ε_h varies within a fixed interval [−1,1] and cannot be contracted, and they stand for the internal noise elements introduced by the nonlinear function's AA computational process.

Since the ranges of (32) will contain the ranges of the real ranges of injected nodal power, due to multiplication of amplification coefficients on the partial deviations of voltage magnitude and bus angles affine forms in step (1), as well as usage of affine approximation computations in step (2). Therefore, the intervals of load flow variables are acquired through compressing the ranges of vector X such that

$$AX + B = f^{SP}, \tag{39}$$

where f^{SP} represents a vector valued by intervals, which are defined by the fixed ranges of reactive and active power inputs. To contract the vector X, the "min" and "max" linear programming problems are established as follows, respectively:

$$\begin{aligned} &\min \varepsilon_{Pj} \text{ or } \max \varepsilon_{Pj}, \text{ for } j \in \text{CVCM} \cup \text{CPFCM} \\ &s.t. \begin{cases} -1 \le \varepsilon_{Pj} \le 1 \\ \inf(C_i) \le \sum\limits_{j \in CVCM \cup CPFCM} A_{ij} \varepsilon_{Pj} \le \sup(C_i), i = 1, 2, \cdots, nP + nQ \end{cases} \end{aligned} \tag{40}$$

where $C = f^{SP} - B$; $\inf(\cdot)$ and $\sup(\cdot)$ are infimum and supremum functions. By solving (32), the accurate ranges of bus angles and voltage magnitudes are acquired as follows:

$$\begin{cases} V_i = V_{i,0} + \sum\limits_{j \in CVCM} V_{i,j}^{\mathrm{P}} [\varepsilon_{\mathrm{P}j,\min}, \varepsilon_{\mathrm{P}j,\max}] + \sum\limits_{j \in CPFCM} (V_{i,j}^{\mathrm{P}} + V_{i,j}^{\mathrm{Q}} \tan \varphi_j)[\varepsilon_{\mathrm{P}j,\min}, \varepsilon_{\mathrm{P}j,\max}], \text{ for } i \in \mathrm{S_L} \\ \theta_i = \theta_{i,0} + \sum\limits_{j \in CVCM} \theta_{i,j}^{\mathrm{P}} [\varepsilon_{\mathrm{P}j,\min}, \varepsilon_{\mathrm{P}j,\max}] + \sum\limits_{j \in CPFCM} (\theta_{i,j}^{\mathrm{P}} + \theta_{i,j}^{\mathrm{Q}} \tan \varphi_j)[\varepsilon_{\mathrm{P}j,\min}, \varepsilon_{\mathrm{P}j,\max}], \text{ for } i \in \mathrm{S_G} \cup \mathrm{S_L} \end{cases} \tag{41}$$

After the three steps, the intervals of voltage magnitudes and bus angles are obtained. To obtain (28) and (29), some affine approximation computations like multiplication and Chebyshev approximation need to be done, and detailed information about how to do these approximation computations can be found in Reference [20]. To make it easier to understand the AA-based method, a simple case study is employed and introduced in detail in the Appendix A section.

3.2. Solution of the IPFWF Model by OSM

In this section, the solution process of the proposed IPFWF model through the OSM is discussed. The OSM is mainly proposed through the extreme value theorem [32]. To make a comprehension of the OSM, introduction of extreme value theorem as well as two vital viewpoints are given as follows.

(**Extreme Value Theorem**): Assume that f is a real-valued continuous function bounded in a closed interval $[a, b]$, then f must obtain at least one minimum and one maximum. In other words, there are real numbers d and c in $[a, b]$ satisfying $f(d) \le f(x) \le f(c)$ for arbitrary $x \in [a, b]$.

Then, for brevity, we express the IPFWF model as $\boldsymbol{h}(\boldsymbol{x}) = [\boldsymbol{h}^{\mathrm{L}}, \boldsymbol{h}^{\mathrm{U}}]$, where $\boldsymbol{h}^{\mathrm{L}}$ and $\boldsymbol{h}^{\mathrm{U}}$, respectively, represent lower and upper bounds of the injected power, for the buses without wind farms $\boldsymbol{h}^{\mathrm{L}} = \boldsymbol{h}^{\mathrm{U}}$, and $\boldsymbol{x}$ are power flow variables including bus angles and load voltage magnitudes. According to the extreme value theory, the two key points can be expressed as follows.

Viewpoint 1: For each scenario $\boldsymbol{\xi} \in [\boldsymbol{h}^{\mathrm{L}}, \boldsymbol{h}^{\mathrm{U}}]$, there exists a fixed $\boldsymbol{x}$ which corresponds to $\boldsymbol{\xi}$, and this relationship is established by load flow equations. That is to say, $\boldsymbol{x}$ varies with uncertain $\boldsymbol{\xi}$.

Viewpoint 2: For every dimension x_i of $\boldsymbol{x}$, there is a selected scenario $\boldsymbol{\xi}_{\max}^{(i)}$ making x_i maximum for arbitrary scenario $\boldsymbol{\xi} \in [\boldsymbol{h}^{\mathrm{L}}, \boldsymbol{h}^{\mathrm{U}}]$. Meanwhile, there exists a specific scenario $\boldsymbol{\xi}_{\min}^{(i)}$, which makes minimum. If we respectively mark the maximum and minimum values as $x_i^{\max}$ and $x_i^{\min}$, then $[x_i^{\min}, x_i^{\max}]$ is the varying interval of x_i under the active wind power generation data interval $[\boldsymbol{h}^{\mathrm{L}}, \boldsymbol{h}^{\mathrm{U}}]$, this is because the function $\boldsymbol{y} = \boldsymbol{h}(\boldsymbol{x})$ is continuous and the extreme theorem takes effects here.

It is known from Viewpoint 2 that the solution of the IPFWF model is reduced to searching the extreme scenarios $\boldsymbol{\xi}_{\max}^{(i)}$ and $\boldsymbol{\xi}_{\min}^{(i)}$ for every x_i. Accordingly, we can regard $\boldsymbol{\xi}$ as variables bounded by interval $[\boldsymbol{h}^{\mathrm{L}}, \boldsymbol{h}^{\mathrm{U}}]$, and establish two optimization models to obtain the variation interval of x_i. Based on the extreme value theorem, the OSM establishes the maximum and minimum programming models to acquire intervals of the power flow results of the IPFWF model, and they can be formulated as follows.

$$\text{minimize } x_i \text{ or maxmum } x_i \tag{42}$$

s.t.

$$\begin{cases} P_{\mathrm{G}i} - P_{\mathrm{L}i} - P_i = 0,\ i \in \{\text{generator buses}\} \\ -P_{\mathrm{L}i} - P_i = 0,\ i \in \{\text{load buses}\} \\ Q_{\mathrm{C}i} - Q_{\mathrm{L}i} - Q_i = 0,\ i \in \{\text{load buses}\} \end{cases} \tag{43}$$

and

$$\begin{cases} \xi_i - P_{\mathrm{L}i} - P_i = 0,\ i \in \{\text{FSFT or CPFCM or CVCM}\} \\ Q_{\mathrm{G}i} - Q_{\mathrm{L}i} - Q_i = 0,\ i \in \{\text{FSFT or CPFCM}\} \\ Q_{\mathrm{G}i} = V_i^2 \dfrac{\mathrm{X}_{ci} - \mathrm{X}_{\mathrm{m}i}}{\mathrm{X}_{ci}\mathrm{X}_{\mathrm{m}i}} + \mathrm{X}_i \dfrac{V_i^2 + 2\mathrm{R}_i \hat{P}_{\mathrm{G}i}}{2(\mathrm{R}_i^2 + \mathrm{X}_i^2)} - \mathrm{X}_i \dfrac{\sqrt{(V_i^2 + 2\mathrm{R}_i \hat{P}_{\mathrm{G}i})^2 - 4\hat{P}_{\mathrm{G}i}^2(\mathrm{R}_i^2 + \mathrm{X}_i^2)}}{2(\mathrm{R}_i^2 + \mathrm{X}_i^2)},\ i \in \{\text{FSFT}\} \\ Q_{\mathrm{G}i} = \hat{P}_{\mathrm{G}i} \times \tan\varphi,\ i \in \{\text{CPFCM}\} \\ \underline{P}_{\mathrm{G}i} \le \xi_i \le \overline{P}_{\mathrm{G}i},\ i \in \{\text{FSFT or CPFCM or CVCM}\} \end{cases} \tag{44}$$

where x_i represents the variables of power flow equations, which can be V_i or θ_i, and ξ_i is a variable constrained in the interval $[\underline{P}_{\mathrm{G}i}, \overline{P}_{\mathrm{G}i}]$. If the ranges of the active transmission power flow are considered, the expression

$$P_{ij} = V_i V_j (G_{ij} \cos\theta_{ij} + B_{ij} \sin\theta_{ij}) - G_{ij} V_i^2 \tag{45}$$

should replace x_i in Reference (18), where P_{ij} represents the active line power transmitted from bus i to bus j. Here, the real portion of the shunt admittances is neglected for simplifying the computation of P_{ij}. In addition, if we consider limits on the voltage recovery processes and reactive power generation of the generators within these programs, and these constraints are listed as

$$V_i - V_{\mathrm{G}i} - V_{ai} + V_{bi} = 0,\ i \in \{\text{generator buses}\}, \tag{46}$$

$$(Q_{\mathrm{G}i} - Q_{\mathrm{G}i}^{\min}) V_{ai} = 0,\ i \in \{\text{generator buses}\}, \tag{47}$$

$$(Q_{\mathrm{G}i}^{\max} - Q_{\mathrm{G}i}) V_{bi} = 0,\ i \in \{\text{generator buses}\}, \tag{48}$$

$$Q_{\mathrm{G}i} = Q_{\mathrm{L}i} + Q_i,\ i \in \{\text{generator buses}\}, \tag{49}$$

$$Q_{\mathrm{G}i}^{\min} \le Q_{\mathrm{G}i} \le Q_{\mathrm{G}i}^{\max},\ i \in \{\text{generator buses}\}, \tag{50}$$

$$V_{ai}, V_{bi} \ge 0,\ i \in \{\text{generator buses}\}. \tag{51}$$

where V_{bi} and V_{ai} represent the slack variables for tracking the variation of the voltage magnitudes, $V_{\mathrm{G}i}$ stands for the initial point value of the voltage at the generator bus i, $Q_{\mathrm{G}i}^{\max}$ and $Q_{\mathrm{G}i}^{\min}$ are the upper and lower limitations of the reactive power generation $Q_{\mathrm{G}i}$, respectively.

The solution models expressed by Equations (42)–(44) are all nonlinear optimization models, and they could be solved efficiently using the interior point method (IPM) [45]. According to the established optimization models, we illustrate the procedure for solving the IPFWF model in Figure 5. Here, the input data include network parameters, injected active power and voltage of the generator buses, and injected power of load buses. Parameters of the wind farms mainly consist of their cut-in, cut-out, rated wind speeds, rated output power, as well as the Weibull distribution information of wind speeds. Parameters of IPM contain the iteration precision and the central parameter.

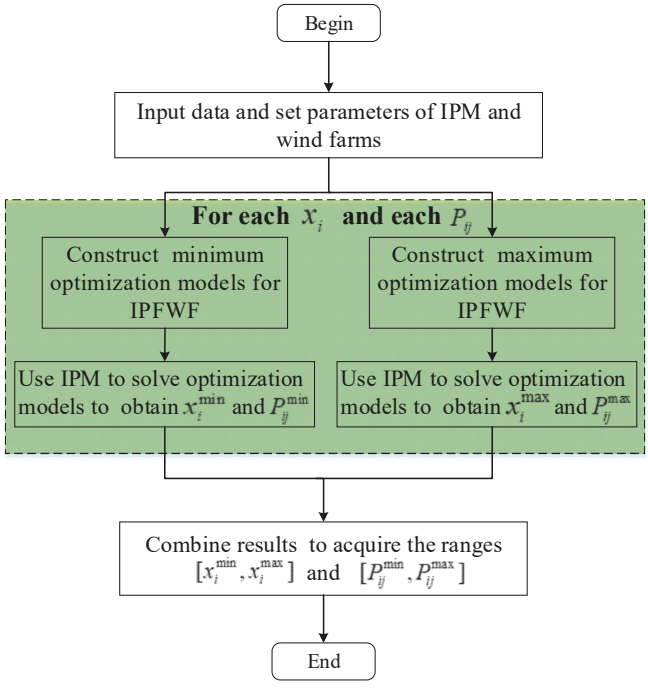

Figure 5. Solution process of solving the interval power flow considering wind farm (IPFWF) model based on the optimizing-scenarios method (OSM).

4. Simulation Results

Two test cases will be navigated in this section, including the IEEE 30-bus and IEEE 118-bus systems. Case one will simulate the IEEE 30-bus system, and results acquired using the AA-based method and OSM are compared with those obtained suing the MCS method in this case, thus demonstrating the advantages and effectiveness of the proposed two methods. The second case is used to demonstrate the applicability of the proposed methods for handling larger systems, where the IEEE 118-bus will be simulated and analyzed. Network parameters of IEEE 118-bus and IEEE 30-bus systems are introduced in detail elsewhere [46]. One-hundred MV A was selected as the test systems' basic power, and all parameters and data were computed in per-unit (p.u.) system. The constant power factor of CPFCM was $\cos\varphi = 0.95$. To facilitate an easier description of the results, all the bus orders of the test systems were rearranged with the reference (slack) bus first, followed in order by the buses connected to the CVCM wind farm, conventional generator buses, load buses (capacitor buses prior), and finally buses combined with the CPFCM wind farm. The order of all branches was also rearranged, the rear bus number of the branch was set larger than that of its front bus number. The whole branches were arranged in an ascending order based on the number of the front bus, where, if the number of the front bus in two branches were identical, the branch with a bigger rear bus number would be set in a front order. Accordingly, real transmission power was calculated from its front bus to its rear bus. The IPM's central parameter was set as 0.1, and iteration precision was chosen as 10^{-6}. Sampling numbers of MCS in two cases were both set as 5000, and this number was large enough for ensuring the accuracy of sampling results. To show the possible fluctuations of the power system state as a function of uncertain wind farms generation, the "base scenario" was given in all figures which describes the variables' intervals of IPFWF models. Here, the base scenario was defined as the

obtained power flow results when the wind power outputs of wind farms equals to the midpoint of their variation intervals.

4.1. IEEE 30-Bus System

The IEEE 30-bus system was modified and tested here to demonstrate the advantages and effectiveness of the OSM in addressing the IPFWF model by comparing with the MCS. This system contains 37 transmission lines, five generators, two capacitors, four transformers, and two wind farms, see Figure 6. Here, the generator at bus No. 2 and load bus No. 30 were modified as wind farms. The positions of the wind farms in CPFCM and CVCM control modes were respectively located on buses No. 2 and No. 30. Intervals of input power data of the CPFCM and CVCM wind farms were given as [0, 0.2756] (p.u.) and [0, 1.04] (p.u.), respectively. Limits of reactive power of the generators were given as [−0.5, 1] (p.u.). The active power generation of power compute through (1)–(3), and the Weibull distribution parameters of wind speeds as well as the operational parameters of the wind turbines are presented in Table 1.

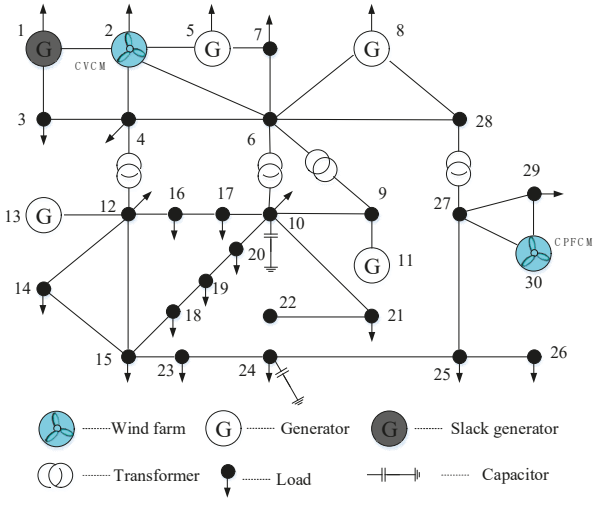

Figure 6. Layout of IEEE 30-bus system incorporating constant power factor control mode (CPFCM) and constant voltage control mode (CVCM) wind farms.

Table 1. Wind farm rated power and wind speed parameters.

Type	P_r (MW)	c	k	v_{co} (m/s)	v_r (m/s)	v_{ci} (m/s)
CPFCM	27.56	7.5	2	20	14	5
CVCM	104	8	2	24	16	4

CPFCM and CVCM respectively stands for the wind farms in constant voltage control mode and the constant power factor control mode.

According to the aforementioned parameters and input data, the proposed IPFWF model is solved by the MCS, AA-based method, and OSM. The load voltage, bus angle, and active transmission power results are exhibited in Figures 7–9, respectively. Notice that load flow variable results acquired using the OSM and the AA-based method are broader than those acquired through the MCS. This is because the MCS is unable to consider the whole scenarios when producing samples. However, the AA-based method mainly relies on affine arithmetic computation, which represents a kind of self-validated computation, and it always obtains more conservative results than "real" results due to approximation errors produced by affine arithmetic computation of nonlinear functions. The OSM

considers all probable scenarios due to usage of the interval, which includes the whole extreme scenarios described through the upper and lower bounds, and it was proven to acquire the most accurate interval results [25]. To show this inclusion relationship of these three methods more clearly, the sampling results of bus angles at bus No. 30 and bus No. 2 are exhibited in Figure 10. Observe that all MCS samples bounded in intervals acquired using the OSM, while interval bounds of OSM reside in those of in the AA-based method. In Figures 7 and 8, it shows that load voltage at bus No. 30, bus angle at bus No. 2, and bus angle of bus No. 30 all display huge fluctuations because bus No. 2 and bus No. 30 are related to wind farms. In Figure 9, the transmission power of branch No. 1 also fluctuates widely because it connects bus No. 1 (the slack bus) with bus No. 2, which is related with a CVCM wind farm.

The results and analysis of this case demonstrate that the OSM and the AA-based method could provide an effective approach to addressing the IPFWF model. Meanwhile, the comparing results indicate that results acquired by the OSM are more accurate than those obtained using the MCS and the AA-based method.

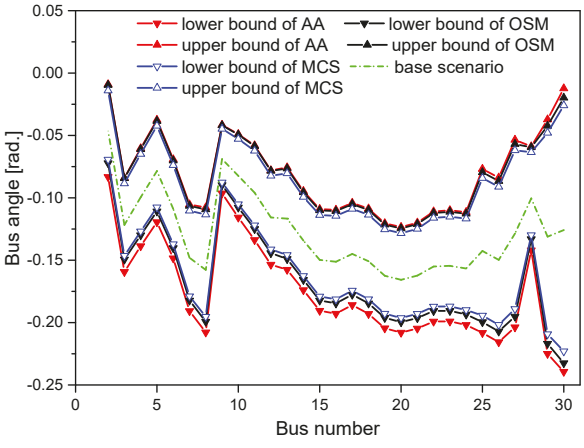

Figure 7. Ranges of bus angles acquired by three different methods.

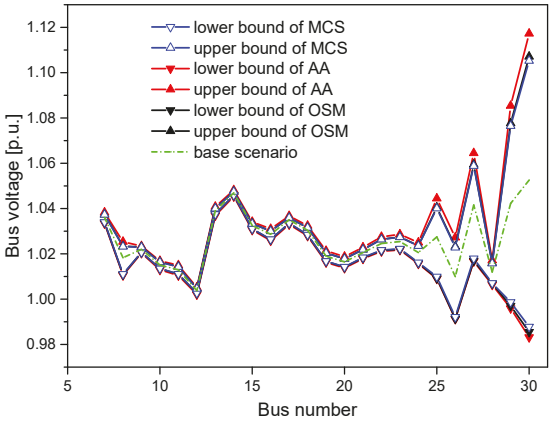

Figure 8. Ranges of load voltages acquired by three different methods.

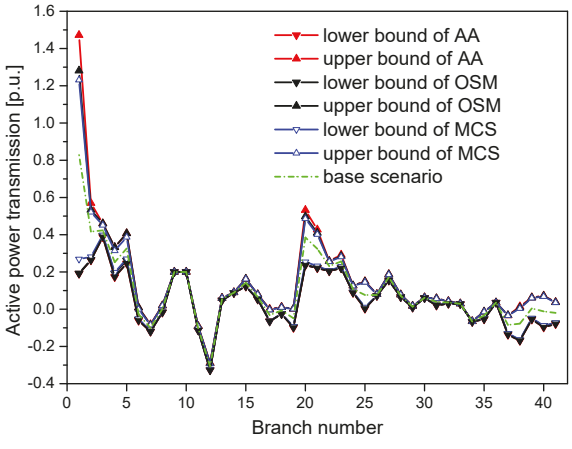

Figure 9. Ranges of active transmission power by three different methods.

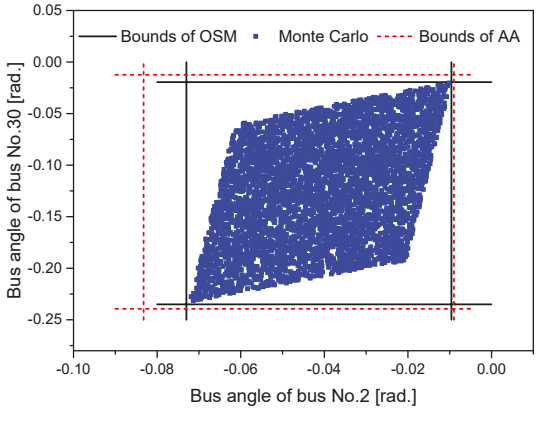

Figure 10. Sampling results of bus angles at bus No. 2 and bus No. 30.

4.2. IEEE 118-Bus System

The IEEE 118-bus contains 169 lines, 9 transformers, 54 generator buses, and 9 capacitors (see Figure 11). To account for the wind farms, the IEEE 118-bus system is modified and connected to CVCM and CPFCM wind farms. Here, generators at bus Nos. 1, 4, 6, 8, and 10 are set as CVCM wind farms and load bus Nos. 109, 114, 115, 117, and 118 are transformed as CPFCM wind farms, and their parameters are listed in Table 2. This table includes the information of bus positions, control types, wind speeds, rated output power, and parameters of their Weibull distributions.

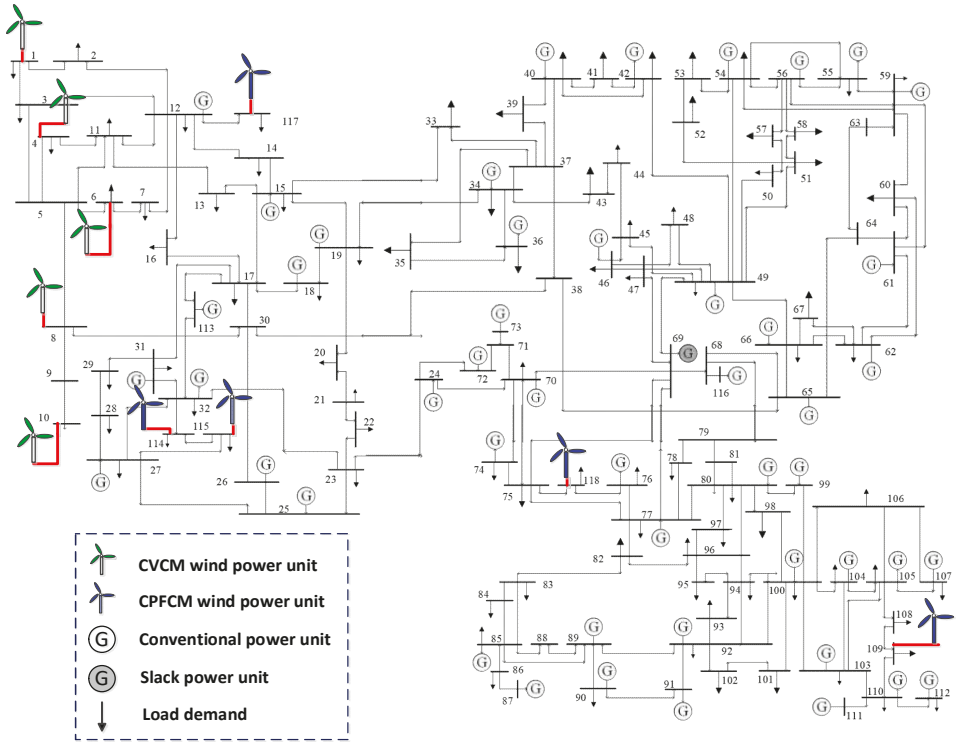

Figure 11. Layout of the IEEE 118 bus system with different wind power farms.

Table 2. Parameters of wind speed and wind farms in the IEEE 118-bus system.

Bus Position	Type	v_{ci} (m/s)	v_r (m/s)	v_{co} (m/s)	P_r (MW)	k	c
1	CVCM	5	14	20	50	2	7.5
4	CVCM	6	15	24	50	3	8
6	CVCM	4	16	21.5	50	2.5	8.0
8	CVCM	4	17	23	50	2.5	7.5
10	CVCM	4	15	24	50	2	8.5
109	CPFCM	5	14	21	21.2	2	7.5
114	CPFCM	4	16	22	21.2	2.5	6.5
115	CPFCM	6	16	23	21.2	2	8.5
117	CPFCM	5.5	16	24	21.2	2.5	7.5
118	CPFCM	5	15	20	21.2	3	7.0

Based on the aforementioned data and parameters, the IEEE 118 bus system is solved by the OSM, AA-based method, and MCS. The bus angles, load voltages, and the active transmission powers are respectively presented in Figures 12–14. In Figure 14, the branches are reordered according to the midpoint values of the active transmission power intervals. Observe from the data and figures that the interval results acquired by these three methods still hold the inclusion relationship in Case one, which furthermore validates the explanations for different accuracy. Besides, greater fluctuations on the bus angles, voltage magnitudes, as well as the transmission power usually occur on the buses with farms or the branches connected to buses with wind farms. This is expected because fluctuations on injected power of buses is bound to cause the fluctuations on bus angles, bus voltages, and transmission power rated to these buses. This case validates the applicability of the proposed methods to large bus systems.

Regarding the required computational time, both cases were tested through MATLAB 2016b on a 3.2 GHz CPU and 4 G RAM. Testing of the modified IEEE 30-bus system by the AA-based method, OSM, and MCS, respectively, required 4 s, 5 s, and 20 s, while IEEE 118-bus system needed 15 s, 25 s, and 50 s. It indicates that the computational efficiency of the AA-based method and the OSM is much less than that of MCS. To show the applicability of the AA-based method and the OSM to real systems, we tested the Polish 2383-bus system. We found that the AA-based method was able to solve the Polish 2383-bus system within 1 h, whereas the OSM could not work out results in one day. This is because the solution models of the OSM are non-convex nonlinear programming problems, which are time-consuming especially when the scale of the problem grows large.

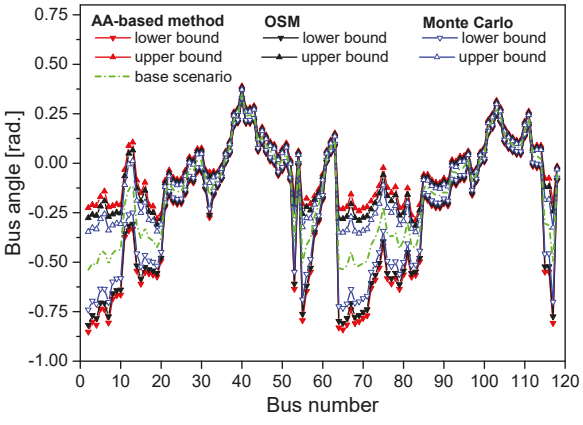

Figure 12. Bus angle results obtained by different methods.

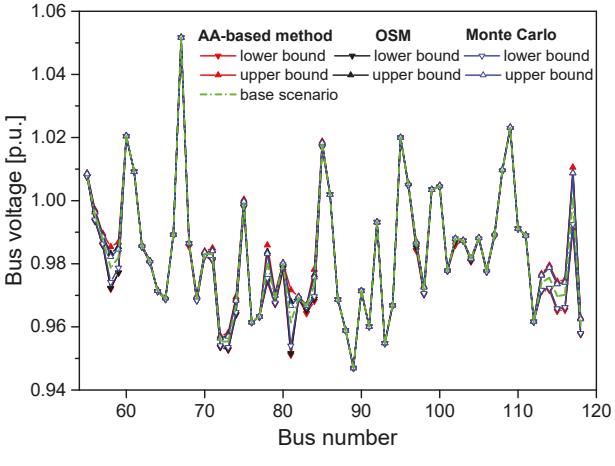

Figure 13. Load voltage magnitude results obtained by different methods.

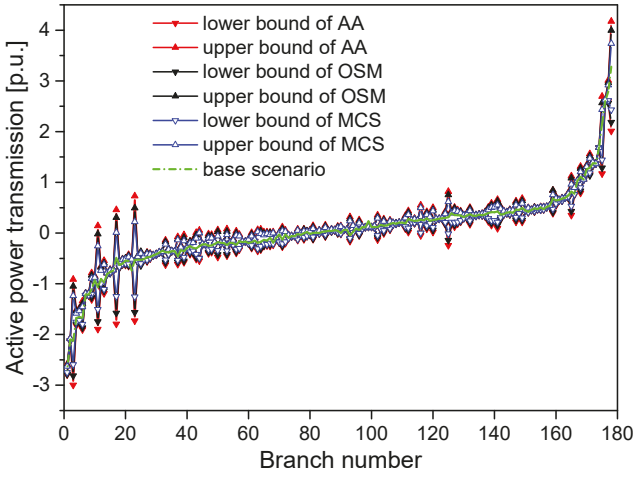

Figure 14. Results of active transmission power obtained by different methods.

5. Conclusions

This paper used intervals to express the active power outputs of wind farms, and accordingly proposed the IPFWF model for obtaining load flow results of power grids incorporating uncertain wind power. Meanwhile, the IPFWF model uses three different formulations to describe three control modes of wind farms. The OSM and the AA-based method were employed to solve the proposed IPFWF model. The AA-based method expressed the wind power data intervals as affine arithmetic forms, and constructs optimization models to contract the affine arithmetic forms and obtain the accurate intervals of power flow variables. The OSM solved the IPFWF model through switching its solution to two types of optimization models that could be efficiently addressed using the IPM. To show the advantages, effectiveness, and applicability of the proposed methods for solving the IPFWF model, the IEEE 30-bus and IEEE 118-bus test systems were tested. Results of testing the IEEE 30-bus system indicate that the AA-based method and the OSM were effective for solving the IPFWF model, and it also demonstrated that the OSM can obtain more accurate results than the MCS method and AA-based method. The case of testing the IEEE 118-bus system showed that the OSM and the AA-based method outperformed the MCS in terms of required computational time, which demonstrates the proposed two methods' good applicability to larger systems.

The ranges obtained by the AA-based method are always wider than the "real" ranges of the IPFWF model, because its solution process includes Chebyshev approximation errors when computing affine forms of nonlinear functions. However, the approximation errors can be further reduced through defining higher orders of affine forms. The OSM is able to obtain the accurate results of the IPFWF model, but the optimization models established in its solution process belong to nonlinear programmes, and its solution obtained by the IPM is not necessary to be global solution, which may cause the underestimation of the interval results of the IPFWF model. Therefore, further work is needed to relax the nonlinear programmes to convex problems, so as to seek more reliable but accurate solutions to the IPFWF model.

Author Contributions: Conceptualization, W.C., J.S., and R.C.; Methodology, W.C. and J.S.; Software, J.S.; Validation, R.C.; Formal Analysis, R.C.; Investigation, R.C.; Resources, C.Z.; Data Curation, J.S.; Writing-Original Draft Preparation, D.H.; Writing-Review & Editing, G.S., R.C.; Visualization, C.Z.; Supervision, J.S.; Project Administration, D.H.; Funding Acquisition, D.H.

Funding: This research was funded by Scientific Project of Shenzhen Power Supply Bureau Co., Ltd. grant number [D9180090].

Conflicts of Interest: The authors declare no conflict of interest.

Appendix A

To make it easier to comprehend the AA-based method, a three-bus system, which is derived from Reference [25], will be tested and its solution process will be introduced in the following. The layout of this case is exhibited in Figure A1. For simplification, wind farms are not considered here.

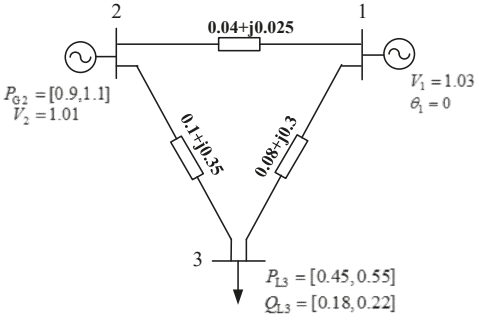

Figure A1. Layout of the three-bus system.

According to Figure A1, the interval power flow (IPF) model in rectangle form can be established in the following:

$$\begin{cases} P_3 = -e_3 \sum\limits_{j=1}^{3} (G_{3j}e_j - B_{3j}f_j) - f_3 \sum\limits_{j=1}^{3} (G_{3j}f_j + B_{3j}e_j) = [0.45, 0.55], \\ Q_3 = -f_3 \sum\limits_{j=1}^{3} (G_{3j}e_j - B_{3j}f_j) + e_3 \sum\limits_{j=1}^{3} (G_{3j}f_j + B_{3j}e_j) = [0.18, 0.22], \\ P_2 = -e_2 \sum\limits_{j=1}^{3} (G_{3j}e_j - B_{3j}f_j) - f_2 \sum\limits_{j=1}^{3} (G_{3j}f_j + B_{3j}e_j) = [0.9, 1.1], \\ V_2^2 = e_2^2 + f_2^2 = 1.01^2. \end{cases} \tag{A1}$$

where bus Nos. 1 to 3 respectively represent the slack bus, generator bus, and load bus. $e_1 = 1.03$, $f_1 = 0$, and the real and imaginary portions of the admittance matrices are respectively computed as

$$\boldsymbol{G} = \begin{bmatrix} 18.81 & -17.98 & -0.83 \\ -17.98 & 18.73 & -0.75 \\ -0.83 & -0.75 & 1.58 \end{bmatrix}, \tag{A2}$$

and

$$\boldsymbol{B} = \begin{bmatrix} -14.35 & 11.24 & 3.11 \\ 11.24 & -13.88 & 2.64 \\ 3.11 & 2.64 & -5.75 \end{bmatrix}. \tag{A3}$$

Notice that the power flow equations are expressed in the rectangle coordinate system, so as to avoid complex Chebyshev approximation computation for sine and cosine functions. Procedure for solving model (A1) is described in the following:

Step (1) Solve the conventional power flow model of Figure A1 at the midpoints of the power intervals, i.e., $P_{G2}^0 = 1.0$, $P_{L3}^0 = 0.5$, $Q_{L3}^0 = 0.2$. By doing this, we can obtain the power flow results $e_{2,0} = 1.0066$, $e_{3,0} = 0.9594$, $f_{2,0} = 0.0826$, $f_{3,0} = -0.0349$ and the Jacobi matrix.

$$J = \begin{bmatrix} \frac{\partial P_2}{\partial e_2} & \frac{\partial P_2}{\partial e_3} & \frac{\partial P_2}{\partial f_2} & \frac{\partial P_2}{\partial f_3} \\ \frac{\partial P_3}{\partial e_2} & \frac{\partial P_3}{\partial e_3} & \frac{\partial P_3}{\partial f_2} & \frac{\partial P_3}{\partial f_3} \\ \frac{\partial Q_3}{\partial e_2} & \frac{\partial Q_3}{\partial e_3} & \frac{\partial Q_3}{\partial f_2} & \frac{\partial Q_3}{\partial f_3} \\ \frac{\partial V_2}{\partial e_2} & \frac{\partial V_2}{\partial e_3} & \frac{\partial V_2}{\partial f_2} & \frac{\partial V_2}{\partial f_3} \end{bmatrix} = \begin{bmatrix} 18.564 & -0.542 & 17.228 & -2.721 \\ -0.8161 & 1.208 & -2.508 & 5.692 \\ -2.508 & 5.238 & 0.8161 & -2.234 \\ 2.013 & 0 & 0.165 & 0 \end{bmatrix} \tag{A4}$$

Step (2) Construct the initial affine forms of the IPF variables. According to (26) and (27), the initial form of IPF model can be written as

$$\begin{cases} e_2 = 1.0066 + e^{\mathrm{P}}_{2,2}\varepsilon_{\mathrm{P}2} + e^{\mathrm{P}}_{2,3}\varepsilon_{\mathrm{P}3} + e^{\mathrm{Q}}_{2,3}\varepsilon_{\mathrm{Q}3}, \\ e_3 = 0.9594 + e^{\mathrm{P}}_{3,2}\varepsilon_{\mathrm{P}2} + e^{\mathrm{P}}_{3,3}\varepsilon_{\mathrm{P}3} + e^{\mathrm{Q}}_{3,3}\varepsilon_{\mathrm{Q}3}, \\ f_2 = 0.0826 + f^{\mathrm{P}}_{2,2}\varepsilon_{\mathrm{P}2} + f^{\mathrm{P}}_{2,3}\varepsilon_{\mathrm{P}3} + f^{\mathrm{Q}}_{2,3}\varepsilon_{\mathrm{Q}3}, \\ f_3 = -0.0349 + f^{\mathrm{P}}_{3,2}\varepsilon_{\mathrm{P}2} + f^{\mathrm{P}}_{3,3}\varepsilon_{\mathrm{P}3} + f^{\mathrm{Q}}_{3,3}\varepsilon_{\mathrm{Q}3}. \end{cases} \tag{A5}$$

where $\varepsilon_{\mathrm{P}2}$, $\varepsilon_{\mathrm{P}3}$, and $\varepsilon_{\mathrm{Q}3}$ are noise elements, and their corresponding coefficients can computed through the inverse of the Jacobi matrix.

$$J^{-1} = \begin{bmatrix} \frac{\partial e_2}{\partial P_2} & \frac{\partial e_2}{\partial P_3} & \frac{\partial e_2}{\partial Q_3} & \frac{\partial e_2}{\partial V_2} \\ \frac{\partial e_3}{\partial P_2} & \frac{\partial e_3}{\partial P_3} & \frac{\partial e_3}{\partial Q_3} & \frac{\partial e_3}{\partial V_2} \\ \frac{\partial f_2}{\partial P_2} & \frac{\partial f_2}{\partial P_3} & \frac{\partial f_2}{\partial Q_3} & \frac{\partial f_2}{\partial V_2} \\ \frac{\partial f_3}{\partial P_2} & \frac{\partial f_3}{\partial P_3} & \frac{\partial f_3}{\partial Q_3} & \frac{\partial f_3}{\partial V_2} \end{bmatrix} = \begin{bmatrix} e^{P}_{2,2} & e^{P}_{2,3} & e^{Q}_{2,3} & e^{V}_{2,2} \\ e^{P}_{3,2} & e^{P}_{3,3} & e^{Q}_{3,3} & e^{V}_{3,2} \\ f^{P}_{2,2} & f^{P}_{2,3} & f^{Q}_{2,3} & f^{V}_{2,2} \\ f^{P}_{3,2} & f^{P}_{3,3} & f^{Q}_{3,3} & f^{V}_{3,2} \end{bmatrix} = \begin{bmatrix} -0.0056 & -0.0027 & 0 & 0.5477 \\ 0.0007 & 0.0683 & 0.1751 & 0.2529 \\ 0.0688 & 0.0327 & 0.0004 & -0.6216 \\ 0.0297 & 0.1752 & 0.165 & 0 \end{bmatrix} \tag{A6}$$

To ensure the initial affine form (A4) includes the "real" ranges of the IPF model, J^{-1} is multiplied by an amplitude of 1.05 and thus (A4) can be rewritten as

$$\begin{cases} e_2 = 1.0066 - 0.0059\varepsilon_{\mathrm{P}2} - 0.0028\varepsilon_{\mathrm{P}3}, \\ e_3 = 0.9594 + 0.0007\varepsilon_{\mathrm{P}2} + 0.0718\varepsilon_{\mathrm{P}3} + 0.1751\varepsilon_{\mathrm{Q}3}, \\ f_2 = 0.0826 + 0.0722\varepsilon_{\mathrm{P}2} + 0.0344\varepsilon_{\mathrm{P}3} + 0.0005\varepsilon_{\mathrm{Q}3}, \\ f_3 = -0.0349 + 0.0311\varepsilon_{\mathrm{P}2} - 0.0392\varepsilon_{\mathrm{P}3} - 0.2615\varepsilon_{\mathrm{Q}3}. \end{cases} \tag{A7}$$

Step (3) Compute the affine forms of nodal power of the IPF model. By substituting (A5) to (A1) and applying the affine operations expressed by (20), (21), and (23) we obtain

$$\begin{cases} P_3 = 0.5 + 0.105\varepsilon_{\mathrm{P}2} + 0.001\varepsilon_1 + 0.0006\varepsilon_2 + 0.105\varepsilon_4 + 0.0005\varepsilon_6, \\ Q_3 = 0.2 + 0.0525\varepsilon_{\mathrm{P}3} + 0.0001\varepsilon_2 + 0.0525\varepsilon_5, \\ P_2 = 1.0 + 0.0211\varepsilon_{\mathrm{Q}3} + 0.0005\varepsilon_2 + 0.0001\varepsilon_3 + 0.0002\varepsilon_6, \\ V_2^2 = 1.01^2 + 0.0001\varepsilon_1. \end{cases} \tag{A8}$$

where ε_1, ε_2, ε_3, ε_4, ε_5, and ε_6, respectively, represent new noise elements produced by $\varepsilon^2_{\mathrm{P}2}$, $\varepsilon^2_{\mathrm{P}3}$, $\varepsilon^2_{\mathrm{Q}3}$, $\varepsilon_{\mathrm{P}2} \cdot \varepsilon_{\mathrm{P}3}$, $\varepsilon_{\mathrm{P}2} \cdot \varepsilon_{\mathrm{Q}3}$, and $\varepsilon_{\mathrm{P}3} \cdot \varepsilon_{\mathrm{Q}3}$, and they are all valued as interval $[-1,1]$. Here, the multiplication of two affine forms is also introduced in Reference [31].

Step (4) Construct optimization models for contracting the noise elements. Based on (39) and (40), we substitute ε_1 to ε_6 in (A6) by interval $[-1,1]$, and construct the optimization models for contracting $\varepsilon_{\mathrm{P}2}$, $\varepsilon_{\mathrm{P}3}$, and $\varepsilon_{\mathrm{Q}3}$ in the following:

$$\begin{aligned} &\min\left(\varepsilon_{\mathrm{P}2}, \varepsilon_{\mathrm{P}3}, \varepsilon_{\mathrm{Q}3}\right) \text{ or } \max\left(\varepsilon_{\mathrm{P}2}, \varepsilon_{\mathrm{P}3}, \varepsilon_{\mathrm{Q}3}\right), \\ &\begin{cases} -0.2065 \le 0.105\varepsilon_{\mathrm{P}2} \le 0.2065, \\ -0.1027 \le 0.0525\varepsilon_{\mathrm{P}3} \le 0.1027, \\ -0.0208 \le 0.0211\varepsilon_{\mathrm{Q}3} \le 0.0208, \\ -0.0001 \le 0 \le 0.0001, \\ -1 \le \varepsilon_{\mathrm{P}2}, \varepsilon_{\mathrm{P}3}, \varepsilon_{\mathrm{Q}3} \le 1. \end{cases} \end{aligned} \tag{A9}$$

By solving optimization models in (A7), the contracted noise elements are written as $[\varepsilon_{P2}^{min}, \varepsilon_{P2}^{max}] = [-1, 1]$, $[\varepsilon_{P3}^{min}, \varepsilon_{P3}^{max}] = [-1, 1]$, $[\varepsilon_{Q3}^{min}, \varepsilon_{Q3}^{max}] = [-0.9896, 0.9896]$.

Step (5) Calculate the intervals of power flow variables of the IPF model. By substituting the contracted noise elements ε_{P2}, ε_{P3}, and ε_{Q3} to (A5), we obtain

$$\begin{cases} e_2 = 1.0066 - 0.0059 \cdot [-1, 1] - 0.0028 \cdot [-1, 1] = [1.0059, 1.0074], \\ e_3 = 0.9594 + 0.0007 \cdot [-1, 1] + 0.0718 \cdot [-1, 1] + 0.1751 \cdot [-0.9896, 0.9896] = [0.9521, 0.9667], \\ f_2 = 0.0826 + 0.0722 \cdot [-1, 1] + 0.0344 \cdot [-1, 1] + 0.0005 \cdot [-0.9896, 0.9896] = [0.0736, 0.0915], \\ f_3 = -0.0349 + 0.0311 \cdot [-1, 1] - 0.0392 \cdot [-1, 1] - 0.2615 \cdot [-0.9896, 0.9896] = [-0.048, -0.0218]. \end{cases} \tag{A10}$$

Therefore, the intervals of the bus voltage of bus No. 3, bus angle of bus No. 2, and bus angle of bus No. 3 are respectively computed as

$$V_3 = \sqrt{e_3^2 + f_3^2} = \sqrt{[0.9521, 0.9667]^2 + [-0.048, -0.0218]^2} = [0.9523, 0.9679], \tag{A11}$$

$$\theta_2 = \arg\tan \frac{f_2}{e_2} = \arg\tan \frac{[0.0736, 0.0915]}{[1.0059, 1.0074]} = [0.0729, 0.0907], \tag{A12}$$

$$\theta_3 = \arg\tan \frac{f_3}{e_3} = \arg\tan \frac{[-0.048, -0.0218]}{[0.9521, 0.9667]} = [-0.0503, -0.0225]. \tag{A13}$$

Other variables like active power transmission and reactive power generation can also be calculate using (A8) through the interval arithmetic computation.

By applying the aforementioned five steps, a solution procedure for the IPF model by the AA-based method is introduced in detail.

References

1. Li, Z.; Ye, L.; Zhao, Y.; Song, X.; Teng, J.; Jin, J. Short-term wind power prediction based on extreme learning machine with error correction. *Prot. Control Mod. Power Syst.* **2016**, *1*, 1–8. [CrossRef]
2. Chen, Y.; Wen, J.; Cheng, S. Probabilistic load flow method based on Nataf transformation and Latin hypercube sampling. *IEEE. Sustain. Energy* **2013**, *4*, 294–301. [CrossRef]
3. Zhou, G.; Bo, R.; Chien, L.; Zhang, X.; Yang, S.; Su, D. GPU-Accelerated Algorithm for On-line probabilistic power flow. *IEEE Trans. Power Syst.* **2018**, *33*, 1132–1135. [CrossRef]
4. Hong, Y.Y.; Lin, F.J.; Yu, T.H. Taguchi method-based probabilistic load flow studies considering uncertain renewables and loads. *IET Renew. Power Gener.* **2016**, *10*, 221–227. [CrossRef]
5. Yuan, Y.; Zhou, J.; Ju, P. Probabilistic load flow computation of a power system containing wind farms using the method of combined cumulants and Gram-Charlier expansion. *IET Renew. Power Gener.* **2011**, *5*, 448–454. [CrossRef]
6. Fan, M.; Vittal, V.; Heydt, G.T. Probabilistic power flow studies for transmission systems with photovoltaic generation using cumulants. *IEEE Trans. Power Syst.* **2012**, *27*, 2251–2261. [CrossRef]
7. Williams, T.; Crawford, C. Probabilistic load flow modeling comparing maximum entropy and Gram-Charlier probability density function reconstructions. *IEEE Trans. Power Syst.* **2013**, *28*, 272–280. [CrossRef]
8. Xiao, Q.; He, Y.; Chen, K.; Yang, Y.; Lu, Y. Point estimate method based on univariate dimension reduction model for probabilistic power flow computation. *IET Gener. Trans. Distrib.* **2017**, *11*, 3522–3531. [CrossRef]
9. Saunders, C.S. Point estimate method addressing correlated wind power for probabilistic optimal power flow. *IEEE Trans. Power Syst.* **2014**, *29*, 1045–1054. [CrossRef]
10. Liu, C.; Sun, K.; Wang, B. Probabilistic power flow analysis using multi-dimensional Holomorphic embedding and generalized cumulants. *IEEE Trans. Power Syst.* **2018**, *33*, 7132–7142. [CrossRef]
11. Zhang, L.; Cheng, H.; Zhang, S. A novel point estimate method for probabilistic power flow considering correlated nodal power. In Proceedings of the 2014 IEEE PES General Meeting | Conference & Exposition, National Harbor, MD, USA, 27–31 July 2014; pp. 1–5.

12. Aien, M.; Khajeh, M.G.; Rashidinejad, M. Probabilistic power flow of correlated hybrid wind-photovoltaic power systems. *IET Renew. Power Gener.* **2014**, *8*, 649–658. [CrossRef]
13. Zuluaga, C.D.; Alvarez, M.A. Bayesian probabilistic power flow analysis using Jacobian approximate Bayesian computation. *IEEE Trans. Power Syst.* **2018**, *33*, 5217–5225. [CrossRef]
14. Yu, H.; Rosehart, B. Probabilistic power flow considering wind speed correlation of wind farms. In Proceedings of the 17th Power Systems Computation Conference, Stockholm, Sweden, 22–26 August 2011; pp. 1–7.
15. Hajian, M.; Rosehart, W.D.; Zareipour, H. Probabilistic power flow by Monte Carlo simulation with Latin supercube sampling. *IEEE Trans. Power Syst.* **2013**, *28*, 1550–1559. [CrossRef]
16. Baghaee, H.R.; Mirsalim, M.; Gharehpetian, G.B. Fuzzy unscented transform for uncertainty quantification of correlated wind/PV microgrids: Possibilistic–probabilistic power flow based on RBFNNs. *IET Renew. Power Gener.* **2017**, *11*, 867–877. [CrossRef]
17. Melhorn, A.C.; Dimitrovski, A. Three-phase probabilistic load flow in radial and meshed distribution networks. *IET Gener. Trans. Distrib.* **2015**, *9*, 2743–2750. [CrossRef]
18. Wang, Z.; Alvarado, F.L. Interval arithmetic in power flow analysis. *IEEE Trans. Power Syst.* **1992**, *7*, 1341–1349. [CrossRef]
19. Mori, H.; Yuihara, A. Calculation of multiple power flow solutions with the Krawczyk method. In Proceedings of the 1999 IEEE International Symposium on Circuits and Systems VLSI (Cat. No.99CH36349), Orlando, FL, USA, 30 May–2 June 1999; pp. 94–97.
20. De Figueiredo, L.H.; Stolfi, J. Affine arithmetic: Concepts and applications. *Numer. Algorithm.* **2004**, *37*, 147–158. [CrossRef]
21. Vaccaro, A.; Canizares, C.; Villacci, D. An affine arithmetic-based methodology for reliable power flow analysis in the presence of data uncertainty. *IEEE Trans. Power Syst.* **2010**, *25*, 624–632. [CrossRef]
22. Pirnia, M.; Canizares, C.A.; Bhattacharya, K.; Vaccaro, A. An affine arithmetic method to solve the stochastic power flow problem based on a mixed complementarity formulation. In Proceedings of the 2012 IEEE Power and Energy Society General Meeting, San Diego, CA, USA, 22–26 July 2012; pp. 1–7.
23. Vaccaro, A.; Cañizares, C.A.; Bhattacharya, K. A range arithmetic-based optimization model for power flow analysis under interval uncertainty. *IEEE Trans. Power Syst.* **2013**, *28*, 1179–1186. [CrossRef]
24. Zhang, C.; Chen, H.; Ngan, H.; Yang, P.; Hua, D. A mixed interval power flow analysis under rectangular and polar coordinate system. *IEEE Trans. Power Syst.* **2017**, *32*, 1422–1429. [CrossRef]
25. Zhang, C.; Chen, H.; Shi, K.; Qiu, M.; Hua, D.; Ngan, H. An interval power flow analysis through optimizing-scenarios method. *IEEE Trans. Smart Grid* **2018**, *9*, 5217–5226. [CrossRef]
26. Zhang, C.; Chen, H.; Guo, M.; Wang, X.; Liu, Y.; Hua, D. DC power flow analysis incorporating interval input data and network parameters through the optimizing-scenarios method. *Int. J. Electr. Power Energy Syst.* **2018**, *96*, 380–389. [CrossRef]
27. Ran, X.; Miao, S. Three-phase probabilistic load flow for power system with correlated wind, photovoltaic and load. *IET Gener. Transm. Distrib.* **2016**, *10*, 3093–3101. [CrossRef]
28. Li, X.; Cao, J.; Lu, P. Probabilistic load flow computation in power system including wind farms with correlated parameters. In Proceedings of the 2nd IET Renewable Power Generation Conference (RPG 2013), Beijing, China, 9–11 September 2013; pp. 1–4.
29. Jaoued, I.B.; Guesmi, T.; Abdallah, H.H. Power flow solution for power systems including FACTS devices and wind farms. In Proceedings of the IEEE International Conference on Sciences and Technology of Automatic Control and Computer Engineering, Sousse, Tunisia, 7 April 2014; pp. 136–139.
30. Vaccaro, A.; Canizares, C.A. An affine arithmetic-based framework for uncertain power flow and optimal power flow studies. *IEEE Trans. Power Syst.* **2016**, *32*, 274–288. [CrossRef]
31. Zhang, C.; Chen, H.; Ngan, H. Reactive power optimisation considering wind farms based on an optimal scenario method. *IET Gener. Transm. Distrib.* **2016**, *10*, 3736–3744. [CrossRef]
32. Jin, X.; Zhang, C.; Chen, H.; Xu, X. Optimal reactive power dispatch considering wind turbines. In Proceedings of the 2014 IEEE PES Asia-Pacific Power and Energy Engineering Conference (APPEEC), Hong Kong, China, 7–10 December 2014; pp. 1–5.
33. Castro, L.M.; Fuerte-Esquivel, C.R.; Tovar-Hernandez, J.H. A unified approach for the solution of power flows in electric power systems including wind farms. *Electr. Power Syst. Res.* **2011**, *81*, 1859–1865. [CrossRef]

34. Feijoo, A.; Villanueva, D. Wind farm power distribution function considering wake effects. *IEEE Trans. Power Syst.* **2017**, *32*, 3313–3314. [CrossRef]
35. Shi, L.B.; Weng, Z.X.; Yao, L.Z. An analytical solution for wind farm power output. *IEEE Trans. Power Syst.* **2014**, *29*, 3122–3123. [CrossRef]
36. Priyadharshini, P.; Mohamed, T.A.M. Modeling and analysis of wind farms in load flow studies. In Proceedings of the 2015 International Conference on Computation of Power, Energy, Information and Communication (ICCPEIC), Chennai, India, 22–23 April 2015; pp. 364–372.
37. Feijoo, A.; Villanueva, D. Four parameter models for wind farm power curves and power probability density functions. *IEEE Trans. Sustain. Energy* **2017**, *8*, 1783–1784. [CrossRef]
38. Eminoglu, U.; Ayasun, S. Modeling and design optimization of variable-speed wind turbine systems. *Energies* **2014**, *7*, 402–419. [CrossRef]
39. Eminoglu, U. A new model for output power calculation of variable-speed wind turbine systems. In Proceedings of the 2015 International Aegean Conference on Electrical Machines & Power Electronics (ACEMP), Side, Turkey, 2–4 September 2015; pp. 141–146.
40. Sulaeman, S.; Benidris, M.; Mitra, J. A method to model the output power of wind farms in composite system reliability assessment. In Proceedings of the 2014 North American Power Symposium (NAPS), Pullman, WA, USA, 7–9 September 2014; pp. 1–6.
41. Yu, H.; Rosehart, W.D. An optimal power flow algorithm to achieve robust operation considering load and renewable generation uncertainties. *IEEE Trans. Power Syst.* **2012**, *27*, 1808–1817. [CrossRef]
42. Merizalde, Y.; Bonilla, L.M.; Hernández-Callejo, L.; Duque-Perez, O. Wind turbine maintenance. A review. *DYNA-Ingeniería e Industria* **2018**, *93*, 435–441. [CrossRef]
43. Tian, J.; Su, C.; Soltani, M. Active power dispatch method for a wind farm central controller considering wake effect. In Proceedings of the IECON 2014—40th Annual Conference of the IEEE Industrial Electronics Society, Dallas, TX, USA, 29 October–1 November 2014; pp. 5450–5456.
44. Ghosh, S.; Kamalasadan, S.; Senroy, N. Doubly fed induction generator (DFIG)-based wind farm control framework for primary frequency and inertial response application. *IEEE Trans. Power Syst.* **2016**, *31*, 1861–1871. [CrossRef]
45. Liu, M.; Tso, S.K.; Cheng, Y. An extended nonlinear primal-dual interior-point algorithm for reactive-power optimization of large-scale power systems with discrete control variables. *IEEE Trans. Power Syst.* **2002**, *17*, 982–991. [CrossRef]
46. Power Systems Test Case Archive. Available online: http://www.ee.washington.edu/research/pstca/ (accessed on 3 January 2018).

energies

MDPI

Article

Decentralized and Collaborative Scheduling Approach for Active Distribution Network with Multiple Virtual Power Plants

Xiangyu Li [1], Dongmei Zhao [1] and Baicang Guo [2,*]

[1] School of Electrical and Electronic Engineering, North China Electric Power University, Beijing 102206, China; ak_1235@sina.com (X.L.); zhao-dm@ncepu.edu.cn (D.Z.)

[2] Transportation College, Jilin University, Changchun 130012, China

* Correspondence: m18646323411@163.com; Tel.: +86-010-6341-6550

Received: 4 October 2018; Accepted: 12 November 2018; Published: 19 November 2018

Abstract: In order to build an active distribution system with multi virtual power plants (VPP), a decentralized two-stage stochastic dispatching model based on synchronous alternating direction multiplier method (SADMM) was proposed in this paper. Through the integration of distributed energy and large-scale electric vehicles (EV) in the distribution network by VPP group, coordinative complementarity, and global optimization were realized. On the premise of energy autonomy management of active distribution network (AND) and VPP, after ensuring the privacy of stakeholders, the power of tie-line was taken as decoupling variable based on SADMM. Furthermore, without the participation of central coordinators, the optimization models of VPPs and distribution networks were decoupled to achieve fully decentralized optimization. Aiming at minimizing their own operating costs, the VPPs aggregate distributed energy and large-scale EVs within their jurisdiction to interact with the upper distribution network. On the premise of keeping operation safe, the upper distribution network formulated the energy interaction plan with each VPP, and then, the global energy optimization management of the entire distribution system and the decentralized autonomy of each VPP were achieved. In order to improve the stochastic uncertainty of distributed renewable energy output, a two-stage stochastic optimization method including pre-scheduling stage and rescheduling stage was adopted. The pre-scheduling stage was used to arrange charging and discharging plans of EV agents and output plans of micro gas turbines. The rescheduling stage was used to adjust the spare resources of micro gas turbines to deal with the uncertainty of distributed wind and light. An example of active distribution system with multi-VPPs was constructed by using the improved IEEE 33-bus system, then the validity of the model was verified.

Keywords: active distribution system; virtual power plant; stochastic optimization; decentralized and collaborative optimization

1. Introduction

1.1. Motivation

The clean transformation of energy brings great challenges to traditional power dispatching. In recent years, in order to relieve the pressure of energy shortage and environmental deterioration, many countries have accelerated the development of distributed energy resources (DER) and electric vehicles (EV) and other active loads. In the future, active distribution network (ADN) will be an important form of intelligent distribution network, which manages power flow through flexible network topology and can actively control and manage the local DER. However, many kinds of distributed new energy have randomness and volatility, and the strong uncertainty of its output brings challenges to the economic operation of power grid.

Besides, large-scale EVs access to the grid will generate a new round of load growth, which will aggravate the peak–valley load difference of the grid, and as a kind of mobile load, it will increase the difficulty of grid operation control. VPP provides a new solution for the above problems. VPP does not change the way of interconnecting all kinds of distributed energy, but aggregates all kinds of distributed energy and EV groups through advanced coordinated control technology, intelligent measurement technology, and communication technology. Coordinated and optimized operation is achieved through coordinated control on the upper level, so as to promote rational and optimal allocation and utilization of resources [1]. With the help of VPP aggregated EV and distributed renewable energy, the coordinated and optimized scheduling of large-scale EV and distributed renewable energy is carried out by utilizing the characteristics of distributed energy storage unit of power battery devices in EVs. This can effectively alleviate the adverse effects on the power grid caused by the disordered charging and discharging of EVs and the uncertainty of distributed renewable energy output.

1.2. Literature Survey

There are mainly three modeling methods for the uncertainty of distributed new energy output: stochastic programming, scenario method and robust optimization. Wang et al. [2] proposed a rolling scheduling model based on chance constrained programming to reduce the impact of the stochasticity of new energy output. Considering the maximum and minimum limit scenarios of new energy output, a two-stage scheduling model based on the limit scenario set is proposed [3]. Furthermore, Qiu et al. proposed a two-stage robust scheduling model for AC/DC hybrid microgrids [4].

Currently at home and abroad, there are many studies on the economic dispatch of single ADN, VPP, and EV groups. In the aspect of ADN scheduling, the second-order cone programming (SOCP) convex relaxation technique was proposed [5], which laid an important theoretical foundation for the global optimization of optimal power flow in distribution network. On the basis of [5], Liu et al. [6] studied the multi-period economic dispatch problem of active and reactive power coordination in ADN. Also, Li et al. [7] established a convex optimization model of SOCP for distribution network with high proportion photovoltaic. In [8], the OPF problem in AC/DC grids was studied to address the non-convexity problem. In the aspect of VPP scheduling, Dong et al. [9] studied the cooperative game strategy between VPP and distribution companies in the market environment. Pandzic et al. [10] considered the uncertainties of market price and distributed new energy output, then the medium-term dispatching model of VPP was established. In the aspect of EVs' participation in scheduling, Zhuang et al. [11] established the economic scheduling model of micro-grid under the condition of EV charging and discharging mode. Zhang et al. [12] took EV quantity as charge and discharge power constraint, and an economic scheduling model was established. Furthermore, clustering according to the characteristics of EV itself, Huang and Yang et al. participated in power distribution in the form of EV group [13,14]. Therefore, with the popularity of EV, due to its mobile storage and transferable load characteristics, the large-scale EV will play an important role in grid operation.

However, there are relatively few researches on the scheduling problem of VPP or ADN with EV and distributed new energy. Aiming at the problem of VPP bidding strategy with large-scale EV, a robust scheduling model of VPP joint bidding in day-ahead energy market was established [15]. Considering the impact of VPP on the environment, a multi-objective VPP scheduling model with EV participation was established by Arslan et al. [16]. Moreover, Shaaban et al. studied the coordinated charging and discharging problem of AC/DC hybrid distribution network with EV [17]. Therefore, if DER and large-scale EV are connected to the active distribution system in the form of virtual power plants, they will carry out energy interaction with the distribution network according to their respective interests. This will break through the traditional mode of operation and management, and bring new challenges to the safe and economic operation of power distribution system.

In the environment of active distribution system with multi VPP in electricity market, ADN, and VPP agents have the characteristics of decentralization and autonomy, thus, the traditional centralized operation and management mode will no longer be applicable. However, the decentralized modeling

method can model ADN and VPP as different stakeholders, which is more realistic. Lagrange relaxation method [18,19] is the most widely used decentralized scheduling method at present, while augmented Lagrange function method [20,21] improves the convergence performance by adding the boundary coupling constraint quadratic term. The augmented Lagrange function method mainly includes the auxiliary problem principle method [20] and the alternating direction method of multipliers (ADMM) [21]. Zhang et al. presented a decentralized scheduling method for micro-grid based on ADMM, but it requires the participation of higher-level coordinators [22]. In contrast, synchronous ADMM (SADMM) only needs to exchange information between adjacent regions in iteration instead of a higher-level coordinator. Therefore, all stakeholders can achieve completely decentralized autonomy [23]. Furthermore, Erseghe proposed a decentralized optimal power flow method for transmission networks based on SADMM [24]. However, there are few studies on decentralized scheduling models for active power distribution systems with multi VPP.

In this paper, distributed generators and large-scale EV were integrated by virtual power plants in distribution network to realize the coordination and complementarity of multiple distributed energy sources and the overall optimization. After that, a decentralized cooperative scheduling model of active distribution system with multiple virtual power plants was established based on the synchronous alternating direction multiplier method. Then, interactive power was taken as a decoupling variable to decouple the optimization model of virtual power plants and active distribution network. While ensuring the privacy of all stakeholders, the global energy optimization management and decentralized autonomy of the entire distribution system can be achieved.

1.3. Contributions

The contributions of this paper can be summarized as follows:

(1) At present, the application of SADMM in power system optimal operation is few. Aiming at solving distributed day ahead scheduling problem, the SADMM was used in the distributed active distribution system with multiple VPPs. On the premise of autonomous energy management of ADN and VPPs, decoupling the optimization models of virtual power plants and distribution networks without the participation of central coordinators was realized to achieve fully decentralized optimization. Compared with the traditional centralized optimization methods, the method proposed in this paper has good convergence performance. It can achieve the scheduling independence of each agent, protect the data privacy of each agent, and is more suitable for the environment of the power market.

(2) This paper integrated distributed energy and large-scale EVs in distribution network through VPP cluster, and adopts two-stage stochastic optimization method including pre-scheduling stage and re-scheduling stage to deal with the stochastic uncertainty of distributed wind and light outputs, so as to realize the collaborative complementarity and overall optimization of the whole distribution system. Compared with the independent optimization mode of distributed energy and EV and the traditional deterministic scheduling method without considering the uncertainty of wind and light, the model in this paper can make full use of the advanced coordinated control technology of VPP to aggregate the distributed energy and EV groups. Furthermore, it can make full use of the mobile energy storage characteristics of EVs, then the adverse effects of disorderly charging and discharging of EVs and uncertainties of distributed wind and light power outputs on dispatching operation of active distribution network were alleviated.

(3) The simulation results showed that the proposed decentralized optimization method based on SADMM has good convergence performance, it can converge to almost the same running cost as centralized optimization by 16 iterations. When the discharge loss cost of power battery is high, VPP will not reduce the operation cost because of V2G reverse discharge of EV. However, under the incentive of electricity price policy, the EV charging load during peak load period is transferred to the low load valley to charge, which effectively reduces the operation cost and peak–valley load difference. The proposed two-stage stochastic optimization method can ensure that the

day-ahead scheduling plan can be transferred to various error conditions smoothly. Although the operation cost has increased, it can effectively deal with the uncertainty of distributed scenery.

1.4. Organization

The remainder of this paper is arranged as follows. The scheduling model of active distribution system with multi virtual power plants are presented in Section 2. Section 3 proposes the distributed collaborative model based on SADMM. The simulations are described in Section 4, and the conclusions follow in Section 5.

2. Scheduling Model of Active Distribution System with Multi Virtual Power Plants

In this paper, considering the advanced coordinated control technology of VPP, VPP aggregate with large-scale EV and DER was utilized to participate in the economic operation of ADN. VPP would provide subsidies to EV users to encourage more EV registrations as schedulable VPP with dual functions of serving EV users' distribution networks. Load forecasting, distributed new energy output forecasting, and EV centralized controller charging and discharging power were integrated by VPP to optimize scheduling. Then, a power generation plan, a EV charging and discharging plan and a power exchange plan with the distribution network were formulated.

For active distribution systems with multiple VPP, geographically close DER and load interact with the distribution network in the form of VPP, which coordinate the power interaction with the distribution network by arranging the DER output plan rationally. Therefore, each VPP and distribution network will act as different stakeholders, have different optimization objectives, and realize coupling operation through power interaction on the tie line. About the research objects of this paper, the active distribution network is a radial network, including conventional load, diesel generator (*DG*), and static var compensator (*SVC*). Moreover, the virtual power plant is composed of conventional load, photo voltaic photo voltaic (*PV*), wind turbine (*WT*), micro turbine (*MT*), and EV groups. EV is controlled by charging and discharging facilities to play its auxiliary energy storage role and help solve the uncertainty of the output of distributed PV and wind energy.

The centralized controller in VPP is the interface between EV and distribution network, which is able to serve EV users and distribution network. VPP coordinated control center integrates load forecasting, distributed new energy output forecasting, and optimal dispatching of charging and discharging power of EV centralized controller. Then the generation plan of generator set, charging and discharging plan of EV centralized controller and power exchange plan with distribution network were formulated. The dispatching instructions issued by the control center can charge and discharge the dispatchable EVs in an orderly manner, so as to overcome the adverse effects of the disorderly charging and discharging of large-scale EVs on the economic operation of the ADN. For the dispatchable EV in EV agent, it must be connected to the charging pile under the jurisdiction of the VPP centralized controller within the agreed time period, and the dispatching arrangement of the VPP is obeyed. The interaction framework of VPPs and ADN is shown in Figure 1.

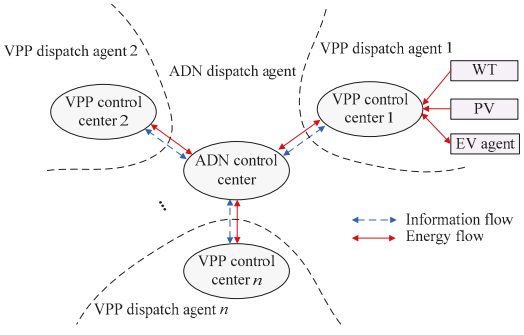

Figure 1. Interaction framework of VPPs and ADN.

2.1. Active Distribution Network Scheduling Model

2.1.1. Objective Function

The optimization objective of ADN is to minimize the sum of the generation cost of *DG*, the power interaction cost with each VPP and the ADN loss cost.

$$\min \sum_{t\in T} \left[\sum_{g\in\Omega^{DG}} \left(c^{DG} P_{gt}^{DG} + c^{SU} v_{gt}^{DG} \right) + \sum_{j\in\Omega^{N}} \sum_{i\in e(j)} c_t^{loss} r_{ij} L_{ijt} + \sum_{k\in\Omega^{VPP}} \left(c_t P_{kt}^{ADN} \right) \right] \tag{1}$$

where c_t, c^{DG}, c^{SU}, and c_t^{loss} respectively denote market price, operation and maintenance cost of *DG* and startup cost and network loss cost of DG. P_{gt}^{DG} and v_{gt}^{DG} respectively denote the output and starting action of *DG*. Ω^N, Ω^{DG}, and Ω^{VPP} respectively denote the set of internal nodes in the distribution network, the set of *DG* nodes and the set of VPP nodes. P_{kt}^{ADN} is the active interaction power between distribution network and VPP, while electricity purchase is positive and electricity sales is negative. r_{ij} is the three-phase resistance for branch ij. L_{ijt} is the square of the current amplitude of the branch ij. $e(j)$ is the branch end node set with j as the terminal node.

2.1.2. Constraints

(1) Constraints of *DG* outputs limitation

$$\begin{cases} -u_{gt} RD_g^{DG} \le P_{gt}^{DG} - P_{gt-1}^{DG} \le u_{gt-1} RU_g^{DG} \\ u_{gt} \underline{P}_g^{DG} \le P_{gt}^{DG} \le u_{gt} \overline{P}_g^{DG} \\ Q_{gt}^{DG} = P_{gt}^{DG} \tan\varphi \end{cases} \tag{2}$$

(2) Constraints of *DG* start/stop state and start/stop action

$$\begin{cases} \left(T_{gt-1}^{on} - \underline{T}_g^{on} \right) \left(u_{gt-1} - u_{gt} \right) \ge 0 \\ \left(T_{gt-1}^{off} - \underline{T}_g^{off} \right) \left(u_{gt-1} - u_{gt} \right) \ge 0 \\ v_{gt} - y_{gt} = u_{gt} - u_{gt-1} \\ v_{gt} + y_{gt} \le 1 \end{cases} \tag{3}$$

(3) Constraints of *SVC* operation

$$-\overline{Q}_i^{SVC} \le Q_{it}^{SVC} \le \overline{Q}_i^{SVC} \tag{4}$$

(4) Constraints of node voltage safety

$$\begin{cases} V^{ref}(1-\varepsilon) \le V_{it} \le V^{ref}(1+\varepsilon) \\ V_{2t} = V^{ref} \end{cases} \tag{5}$$

(5) Constraints of interaction power among tie lines of VPP

$$\begin{cases} P_{it}^{ADN} = P_{it}^{ADN,buy} - P_{it}^{ADN,sell} \\ 0 \le P_{it}^{ADN,buy} \le \overline{P}_i^{ADN} \alpha_{it}^{buy} \\ 0 \le P_{it}^{ADN,sell} \le \overline{P}_i^{ADN} \alpha_{it}^{sell} \\ \alpha_{it}^{buy} + \alpha_{it}^{sell} \le 1 \\ -\overline{Q}_i^{ADN} \le Q_{it}^{ADN} \le \overline{Q}_i^{ADN} \end{cases} \tag{6}$$

(6) Constraints of branch network load flow

Active power and reactive power are coupled in distribution network. Active and reactive power flow will affect line loss and voltage quality. In this paper, branch power flow model of distribution network was used to describe branch power flow of ADN.

$$\sum_{i \in e(j)} \left(P_{ijt} - \frac{(P_{ijt})^2 + (Q_{ijt})^2}{(V_{it})^2} r_{ij} \right) = P_{jt} + \sum_{k \in f(j)} P_{jkt} \tag{7}$$

$$\sum_{i \in e(j)} \left(Q_{ijt} - \frac{(P_{ijt})^2 + (Q_{ijt})^2}{(V_{it})^2} x_{ij} \right) = Q_{jt} + \sum_{k \in f(j)} Q_{jkt} \tag{8}$$

$$(V_{it})^2 = (V_{jt})^2 + 2(r_{ij}P_{ijt} + x_{ij}Q_{ijt}) - \left[(r_{ij})^2 + (x_{ij})^2 \right] \frac{(P_{ijt})^2 + (Q_{ijt})^2}{(V_{it})^2} \tag{9}$$

$$P_{jt} = \begin{cases} P_{jt}^{ADN,L} - P_{jt}^{DG}, & j \notin \Omega^{VPP} \\ P_{jt}^{ADN,L} - P_{jt}^{DG} - P_{jt}^{ADN}, & j \in \Omega^{VPP} \end{cases} \tag{10}$$

$$Q_{jt} = \begin{cases} Q_{jt}^{ADN,L} - Q_{jt}^{MT}, & j \notin \Omega^{VPP} \\ Q_{jt}^{ADN,L} - Q_{jt}^{DG} - Q_{jt}^{ADN}, & j \in \Omega^{VPP} \end{cases} \tag{11}$$

Considering the nonconvexity of constraints (7)–(9), it is difficult to obtain the optimal solution and the efficiency is low, so SOC relaxation technique [5] was adopted to solve this problem. Then, the square U_{it} of node voltage amplitude and the square L_{ijt} of branch current amplitude are defined in Equation (12).

$$\begin{cases} U_{it} = (V_{it})^2 \\ L_{ijt} = \frac{(P_{ijt})^2 + (Q_{ijt})^2}{(V_{it})^2} \end{cases} \tag{12}$$

According to [5], Equation (12) can be transformed into Equation (13)

$$L_{ijt} \ge \frac{(P_{ijt})^2 + (Q_{ijt})^2}{U_{it}} \tag{13}$$

Then, Equation (13) is written as a standard two order cone as Equation (14).

$$\left\| 2P_{ijt} \quad 2Q_{ijt} \quad L_{ijt} - U_{it} \right\|_2^T \le L_{ijt} + U_{it} \tag{14}$$

Therefore, branch flow constraints (7)–(9) can be deformed into Equation (15)

$$\begin{cases} \sum\limits_{i \in u(j)} \left(P_{ijt} - L_{ijt} r_{ij} \right) = P_{jt} + \sum\limits_{k \in v(j)} P_{jkt} \\ \sum\limits_{i \in u(j)} \left(Q_{ijt} - L_{ijt} x_{ij} \right) = Q_{jt} + \sum\limits_{k \in v(j)} Q_{jkt} \\ U_{it} = U_{jt} + 2\left(r_{ij} P_{ijt} + x_{ij} Q_{ijt} \right) - \left[\left(r_{ij} \right)^2 + \left(x_{ij} \right)^2 \right] L_{ijt} \\ \left\| 2P_{ijt} \quad 2Q_{ijt} \quad L_{ijt} - U_{it} \right\|_2^T \le L_{ijt} + U_{it} \end{cases} \tag{15}$$

where x_{ij} is the three-phase reactance of branch ij. V^{ref} is the reference value of node voltage. P_{ijt} and Q_{ijt} respectively denote the three phase active and reactive power flows from node i to node j. $P_{jt}^{ADN,L}$ and $Q_{jt}^{ADN,L}$ respectively denote the active and reactive load of node j. $f(j)$ is the branch terminal node set with j as the leading end node.α_{it}^{buy} and α_{it}^{sell} are the 0 1 variables. φ is power factor angle. Q_{jt}^{ADN} is the reactive power interaction between distribution network and VPP. $P_{it}^{ADN,buy}$ and $P_{it}^{ADN,sell}$ respectively denote the purchase and sale of electricity from VPP. $\overline{P}_i^{ADN}$ and $\overline{Q}_i^{ADN}$ respectively denote the active power limits and reactive power limits of the distribution network to VPP. Q_{gt}^{DG} is the *DG* reactive power outputs. ε is the allowable deviation percentage of node voltage. $\overline{P}_g^{DG}$ and $\underline{P}_g^{DG}$ respectively denote the upper and lower limits of *DG*. $\underline{T}_g^{on}$ and $\underline{T}_g^{off}$ respectively denote the minimum boot time and minimum shutdown time of *DG*. RU_g^{DG} and RD_g^{DG} respectively denote the climbing and landslide rates of *DG*. Q_{it}^{SVC} and $\overline{Q}_i^{SVC}$ respectively denote regulated power and maximum power of SVC. u_{gt} is start stop state of *DG* and y_{gt} is shutdown action identification of *DG*. T_{gt-1}^{on} and T_{gt-1}^{off} respectively denote the continuous boot time and continuous shutdown time from *DG* to time $t-1$.

2.2. Two-Stage Stochastic Schedule Model for Virtual Power Plant

VPP coordinates the distribution of internal DER outputs to meet the load demand inside and maintain firm outputs. However, the distributed new energy outputs in the VPP is highly uncertain, which leads to some deviation between the scheduling plan formulated by the VPP and the actual operation. Therefore, when formulating a scheduling plan, VPP should take full account of the uncertainty of distributed new energy outputs. In addition, when the number of schedulable EVs in the EV centralized controller is large, the problem of dimensionality disaster will occur when a single EV is used as the scheduling object. Therefore, the EV centralized controller is considered as an EV agent to participate in the scheduling operation.

The established two-stage VPP stochastic scheduling model consists of pre-scheduling stage and prescheduling stage. The prescheduling stage is used to arrange the charging and discharging plan of EV agent and the base point of the outputs plan of *MT*. The decision-making results of the prescheduling stage are suitable for all *PV* and wind energy outputs in the rescheduling stage. The rescheduling stage is used to adjust the reserve resources of *MT* to cope with the uncertainty of *PV* and wind energy. The decision result of the rescheduling stage is the decision of all real-time operation scenarios based on the decision of the prescheduling stage, which is used to correct the imbalance of supply and demand in the real-time operation scenario. In the prescheduling stage, the *PV* and wind energy outputs—which may appear in the real-time operation—had been considered. By optimizing the *MT* outputs adjustment in the rescheduling stage, the *PV* and wind energy outputs which can be realized in any set are guaranteed to meet the safe and stable operation requirements of VPP.

2.2.1. Objective Function

The operation cost of VPP is composed of prescheduling stage cost and rescheduling stage cost. Prescheduling cost includes penalty cost for abandoning *PV* and wind energy, *MT* generation cost, purchase and sale cost from distribution network, and the owners' battery loss cost which compensated by V2G services. The cost of rescheduling is adjustment expenses of MT outputs.

$$\begin{aligned}\min \sum_{t\in T} \quad & \left[c^{PV}\left(\overline{P}_{it}^{PV}-P_{it}^{PV}\right)+c^{WT}\left(\overline{P}_{it}^{WT}-P_{it}^{WT}\right)+c^{MT}P_{it}^{MT}\right. \\ & \left.+c_t P_{it}^{VPP}+c_t^{V2G}P_{it}^{EV,dis}+\sum_{s\in S}\rho_s c^{adj}\left|r_{ist}^{U}-r_{ist}^{D}\right|\right]\end{aligned} \tag{16}$$

where c^{MT}, c_t^{V2G}, c^{WT}, c^{PV}, and c^{adj} respectively denote operation and maintenance cost of *MT*, service compensation cost of V2G, punishment cost of abandoning wind, punishment cost of abandoning light, adjustment cost of *MT* outputs. *S* is the total number of PV and wind energy. r_{ist}^{U} and r_{ist}^{D} respectively denote positive reserve adjustment and negative reserve adjustment of MT in VPP *i* under condition *s*. ρ_s is the implementation probability of condition *s*. $\overline{P}_{it}^{PV}$ and $\overline{P}_{it}^{WT}$ respectively denote the active power prediction value of PV and WT. $P_{it}^{EV,dis}$ is the power of V2G service provided by EV agent. P_{it}^{MT} is the outputs of *MT*. P_{it}^{VPP} is the interaction power between VPP *i* and distribution network, the electricity purchase is positive while the sale of electricity is negative.

2.2.2. Constraint Conditions in Prescheduling Phase

(1) Restriction constraint of *EV* agent charging and discharging power

$$\begin{cases} P_{it}^{EV}=P_{it}^{EV,ch}-P_{it}^{EV,dis} \\ 0\le P_{it}^{EV,dis}\le \overline{P}_{i}^{EV,dis}\beta_{it}^{dis} \\ 0\le P_{it}^{EV,ch}\le \overline{P}_{i}^{EV,ch}\beta_{it}^{ch} \\ \beta_{it}^{dis}+\beta_{it}^{ch}\le 1 \end{cases} \tag{17}$$

(2) Restriction constraint of *EV* agent residual power

$$\begin{cases} E_{it+1}=E_{it}+P_{it}^{EV,ch}\eta^{ch}\Delta t-\frac{P_{it}^{EV,dis}}{\eta^{dis}}\Delta t \\ \underline{E}_i\le E_{it}\le \overline{E}_i \\ \overline{E}_i-E_{it}\ge P_{it}^{EV,ch}\eta^{ch}\Delta t \\ E_{it}\ge \frac{P_{it}^{EV,dis}}{\eta^{dis}}\Delta t \end{cases} \tag{18}$$

(3) Constraint of *VPP* power balance

$$\begin{cases} P_{it}^{MT}+P_{it}^{PV}+P_{it}^{WT}+P_{it}^{VPP}-P_{it}^{EV}=P_{it}^{VPP,L} \\ Q_{it}^{MT}+Q_{it}^{PV}+Q_{it}^{WT}+Q_{it}^{VPP}=Q_{it}^{VPP,L} \end{cases} \tag{19}$$

(4) Restriction constraint of *MT* outputs

$$\begin{cases} RD_i^{MT}\le P_{it}^{MT}-P_{it-1}^{MT}\le RU_i^{MT} \\ \underline{P}_i^{MT}\le P_{it}^{MT}\le \overline{P}_i^{MT} \\ Q_{it}^{MT}=P_{it}^{MT}\tan\varphi \\ P_{it}^{MT}+R_{it}^{U}\le \overline{P}_i^{MT} \\ P_{it}^{MT}-R_{it}^{D}\ge \underline{P}_i^{MT} \end{cases} \tag{20}$$

(5) Restriction constraint of *PV* outputs

$$\begin{cases} 0 \le P_{it}^{PV} \le \overline{P}_{it}^{PV} \\ Q_{it}^{PV} = P_{it}^{PV} \tan\varphi \end{cases} \tag{21}$$

The interaction power constraint with ADN is similar to Equation (6), and *WT* output constraint is similar to PV. There is no need to repeat.

Where P_{it}^{MT}, P_{it}^{PV}, P_{it}^{WT} and P_{it}^{VPP} respectively denote active power of *MT*, active outputs of PV, active output of *WT* and interaction active power between VPP *i* and ADN. Q_{it}^{MT}, Q_{it}^{PV}, Q_{it}^{WT} and Q_{it}^{VPP} respectively denote reactive power of *MT* reactive power output of PV, reactive power outputs of *WT* and reactive power interaction between VPP *i* and ADN. β_{it}^{dis} and β_{it}^{ch} are 01 variables. η^{ch} and η^{dis} respectively denote charging and discharging efficiency of EV agents. $\overline{P}_i^{dis}$ and $\overline{P}_i^{ch}$ respectively denote maximum charging and discharging power of EV agents. $\underline{E}_i$ and $\overline{E}_i$ respectively denote minimum and maximum power limits for EV agents. E_{it} is the power of EV agents. $P_{it}^{VPP,L}$ and $Q_{it}^{VPP,L}$ respectively denote the active load and reactive load values of VPP *i*. $\overline{P}_i^{MT}$ and $\underline{P}_i^{MT}$ respectively denote the upper and lower limited outputs of *MT*. RU_i^{MT} and RD_i^{MT} respectively denote the climbing speed and landslide rate of *MT*. R_{it}^{U} and R_{it}^{D} respectively denote the positive reserve and negative reserve regulation of *MT*.

2.2.3. Constraints of Rescheduling Phase

(1) Restriction constraint of PV output conditions

$$\begin{cases} 0 \le P_{ist}^{PV} \le \overline{P}_{ist}^{PV} \\ Q_{ist}^{PV} = P_{ist}^{PV} \tan\varphi \end{cases} \tag{22}$$

(2) Constraint of *MT* climbing speed and landslide speed

$$RD_i^{MT} \le P_{ist}^{MT} - P_{ist-1}^{MT} \le RU_i^{MT} \tag{23}$$

(3) Constraint of the two-stage correlation

Two-stage correlation constraints represent the relationship between the scenario value of *MT* outputs in the rescheduling phase and the planned outputs base value and standby value of *MT* in the prescheduling phase, as shown in Equation (24).

$$\begin{cases} P_{ist}^{MT} = P_{it}^{MT} + r_{ist}^{U} - r_{ist}^{D} \\ 0 \le r_{ist}^{U} \le R_{it}^{U} \\ 0 \le r_{ist}^{D} \le R_{it}^{D} \end{cases} \tag{24}$$

where P_{ist}^{MT} and P_{ist}^{PV} respectively denote the active output of MT and the active output of PV under the conditions.

The *WT* scenario constraint is similar to PV, there is no need to repeat.

2.2.4. Boundary Coupling Characteristics between Virtual Power Plant and Active Distribution Network

The interaction power between ADN and VPP should be kept equal to represent the consistency of the whole interconnected system, so as to ensure the feasibility of the scheduling solution of the

whole active distribution system with multiple VPP. The boundary coupling characteristic equation is shown in Equation (25).

$$\begin{cases} P_{it}^{ADN} + P_{it}^{VPP} = 0 \\ Q_{it}^{ADN} + Q_{it}^{VPP} = 0,\ \forall i \in \Omega^{VPP},\ \forall t \end{cases} \tag{25}$$

3. Distributed Collaborative Model Based on SADMM

Under the background of power market, the scheduling participants of VPP and ADN in active distribution system with multiple VPPs belong to different stakeholders. Traditional centralized dispatching is no longer applicable. Therefore, decentralized collaborative model is needed to solve the problem in order to coordinate the interests of each stakeholder.

3.1. Basic Principles of Standard ADMM Algorithm

For an active distribution system with a VPP, its standard ADMM form can be expressed as Equation (26).

$$\begin{cases} \min \quad \boldsymbol{F}_1(\boldsymbol{x}_1) + \boldsymbol{F}_2(\boldsymbol{x}_2) \\ s.t. \quad \boldsymbol{A}\boldsymbol{x}_1 = \boldsymbol{B}\boldsymbol{x}_2 \end{cases} \tag{26}$$

where $\boldsymbol{F}_1$ and $\boldsymbol{F}_2$ respectively denote objective function of VPP and ADN. A and B respectively denote the coupling coefficient matrix of VPP and ADN.

To solve the optimization problem iteratively, the newest value of ADN optimization is substituted into VPP and the multiplier vector $\boldsymbol{\lambda}$ is updated by the upper coordinator. The $\tau + 1$ iteration process can be expressed in Equation (27).

$$\begin{cases} \boldsymbol{x}_1^{\tau+1} = & \operatorname{argmin}[\boldsymbol{F}_1(\boldsymbol{x}_1) + (\boldsymbol{\lambda}^{\tau})^T(\boldsymbol{A}\boldsymbol{x}_1 - \boldsymbol{B}\boldsymbol{x}_2^{\tau}) + \\ & \frac{\beta}{2}\|\boldsymbol{A}\boldsymbol{x}_1 - \boldsymbol{B}\boldsymbol{x}_2^{\tau}\|^2] \\ \boldsymbol{x}_2^{\tau+1} = & \operatorname{argmin}[\boldsymbol{F}_2(\boldsymbol{x}_2) + (\boldsymbol{\lambda}^{\tau})^T\left(\boldsymbol{A}\boldsymbol{x}_1^{\tau+1} - \boldsymbol{B}\boldsymbol{x}_2\right) + \\ & \frac{\beta}{2}\|\boldsymbol{A}\boldsymbol{x}_1^{\tau+1} - \boldsymbol{B}\boldsymbol{x}_2\|^2] \\ \boldsymbol{\lambda}^{\tau+1} = & \boldsymbol{\lambda}^{\tau} + \beta\left(\boldsymbol{A}\boldsymbol{x}_1^{\tau+1} - \boldsymbol{B}\boldsymbol{x}_2^{\tau+1}\right) \end{cases} \tag{27}$$

where the first and second is the update formula of the internal variable. The third formula is the renewal formula of multiplier vectors, and β is a larger positive number.

3.2. The Basic Principle of SADMM Algorithm

Based on the above, the first and second terms of the augmented Lagrange function can be derived in Equation (28).

$$\begin{aligned} (\boldsymbol{\lambda}^{\tau})^T\left(\boldsymbol{A}\boldsymbol{x}_1 - \boldsymbol{B}\boldsymbol{x}_2^{\tau}\right) + \tfrac{\beta}{2}\|\boldsymbol{A}\boldsymbol{x}_1 - \boldsymbol{B}\boldsymbol{x}_2^{\tau}\|^2 = \\ \tfrac{\beta}{2}\|\boldsymbol{A}\boldsymbol{x}_1 - \boldsymbol{B}\boldsymbol{x}_2^{\tau} + \tfrac{1}{\beta}\boldsymbol{\lambda}^{\tau}\|^2 - \tfrac{1}{2\beta}\|\boldsymbol{\lambda}^{\tau}\|^2 \end{aligned} \tag{28}$$

where $\frac{1}{2\beta}\|\boldsymbol{\lambda}^{\tau}\|^2$ is constant and can be omitted. Set $\boldsymbol{\mu}^{\tau} = \frac{1}{\beta}\boldsymbol{\lambda}^{\tau}$, then the Equation (28) can be changed into Equation (29).

$$\begin{cases} \boldsymbol{x}_1^{\tau+1} = \operatorname{argmin}\left[\boldsymbol{F}_1(x_1 + \ \tfrac{\beta}{2}\|\boldsymbol{A}\boldsymbol{x}_1 - \boldsymbol{B}\boldsymbol{x}_2^{\tau} + \boldsymbol{\mu}^{\tau}\|^2)\right] \\ \boldsymbol{x}_2^{\tau+1} = \operatorname{argmin}\left[\boldsymbol{F}_2(\boldsymbol{x}_2) + \tfrac{\beta}{2}\|\boldsymbol{A}\boldsymbol{x}_1^{\tau+1} - \boldsymbol{B}\boldsymbol{x}_2 + \boldsymbol{\mu}^{\tau}\|^2\right] \\ \boldsymbol{\mu}^{\tau+1} = \boldsymbol{\mu}^{\tau} + \left(\boldsymbol{A}\boldsymbol{x}_1^{\tau+1} - \boldsymbol{B}\boldsymbol{x}_2^{\tau+1}\right) \end{cases} \tag{29}$$

Then the average value of the boundary coupling variables which correspond to the last iteration result of VPP and ADN optimization problems is obtained.

$$\boldsymbol{x}_{F1}^{\tau} = \boldsymbol{x}_{F2}^{\tau} = \frac{\boldsymbol{A}\boldsymbol{x}_1^{\tau} + \boldsymbol{B}\boldsymbol{x}_2^{\tau}}{2} \tag{30}$$

Substituting Equation (30) in Equation (29).

$$\begin{cases} \mathbf{x}_1^{\tau+1} = \text{argmin}\left[\mathbf{F}_1(\mathbf{x}_1) + \frac{\beta}{2}\|\mathbf{A}\mathbf{x}_1 - \mathbf{x}_{F1}^{\tau} + \boldsymbol{\mu}_1^{\tau}\|^2\right] \\ \boldsymbol{\mu}_1^{\tau+1} = \boldsymbol{\mu}_1^{\tau} + \left(\mathbf{A}\mathbf{x}_1^{\tau+1} - \mathbf{x}_{F2}^{\tau+1}\right) \\ \mathbf{x}_2^{\tau+1} = \text{argmin}\left[\mathbf{F}_2(\mathbf{x}_2) + \frac{\beta}{2}\|\mathbf{B}\mathbf{x}_2 - \mathbf{x}_{F2}^{\tau} + \boldsymbol{\mu}_2^{\tau}\|^2\right] \\ \boldsymbol{\mu}_2^{\tau+1} = \boldsymbol{\mu}_2^{\tau} + \left(\mathbf{B}\mathbf{x}_2^{\tau+1} - \mathbf{x}_{F1}^{\tau+1}\right) \end{cases} \tag{31}$$

The penalty term is the deviation between the interaction power of VPP and ADN and the optimal average value of the last boundary node in all VPP and ADN. As the iteration proceeds, the interactive power gradually tends to the last value, and finally the interactive power of all tie lines is consistent in each VPP and ADN. In SADMM-based decentralized optimization, the iterative variables of each VPP and ADN can be calculated independently without central coordinator and can be implemented in parallel. Detailed proof of convergence is detailed in [24].

3.3. The Solving Process

Based on the ADMM algorithm, each VPP and ADN agent respectively solves their economic scheduling plans until the convergence conditions shown in Equation (32) are satisfied.

$$\begin{cases} \left|P_{it}^{ADN}(\tau+1) + P_{it}^{VPP}(\tau)\right| \le \zeta \\ \left|Q_{it}^{ADN}(\tau+1) + Q_{it}^{VPP}(\tau)\right| \le \zeta \end{cases}, \ \forall i \in \Omega^{VPP}, \ \forall t \tag{32}$$

where ζ is the convergence precision.

The steps of solving the model are as follows:

(1) Set the iteration number $\tau = 1$, initialize the algorithm parameters of SADMM.
(2) Independently solve the ADN and VPP economic dispatch models in a decentralized manner.
(3) To judge whether Equation (32) is satisfied, if yes, the iteration ends, or continue the next step.
(4) $\tau = \tau + 1$, update the tie line interaction power according to the Equations (30) and (31), and turn to step (2).

4. Example Analysis

The decentralized cooperative scheduling model of active distribution system with multiple VPPs is solved in a PC of which CPU is Intel core i5-8250U and memory is 8 GB. The test platform is MATLAB R20115a and the solver is Guribo 8.0.

4.1. Basic Data

An active distribution system with three VPPs is constructed by connecting one VPP to the nodes 13, 22, and 31 of the IEEE 33 node distribution network and named VPP 1, VPP 2, and VPP 3 respectively. Each VPP contains 1 EV agents, *MT*, *PV*, and *WT*. Three *DG* are connected to nodes 7, 12 and 27 of the ADN, and three SVC are connected to nodes 4, 14, and 30 of the ADN respectively, as shown in Figure 2. Assuming that *PV* or *WT* in three VPP have the same predictive power, the predictive errors of *PV* and *WT* obey the normal distribution with the standard deviation of 20% of the predictive value. The predictive power and output interval of each *PV* and *WT* are shown in Figure 3. The combination of 10 *PV* and *WT* output conditions generated in this interval is also shown in Figure 3, and each scenario combination has the same probability of occurrence. The market electricity price and the total active load of ADN refer to [25]. The load of 3 VPP is ADN total load one-third. Assuming that the power factor of each node is fixed, the reactive load of ADN node and three VPP can be obtained by the power factor of each node. The network loss cost coefficient is the same as the market price. The reference value of network node voltage is 12.66 kV. The allowable voltage deviation ratio is 0.05 p.u. The upper limit of active and reactive power between VPP and ADN is 1 MW and

1 Mvar. Suppose that the upper charge limit of a single EV is 20 kWh, the lower discharge limit is 4 kWh, the maximum charge-discharge power is 5 kW, and the charge–discharge efficiency is 90%. The number of registered schedulable EVs in VPP 1, VPP 2, and VPP 3 is 50, 75, and 100 respectively, and it is assumed that the registered EVs are subject to scheduling arrangements. The *MT*, *PV*, and *WT* characteristics of each VPP are the same. The rated capacities of *MT*, *PV*, and *WT* are 600 kW, and the power factor is cos φ = 0.95. The *DG* rated capacity of ADN is 1000 kW, the minimum startup and shutdown time is 3 h, and the compensation range of SVC is [−1, 1] Mvar. The slope climbing and landslide rates of *MT* and *DG* in VPP and ADN are 30% of the rated capacity, and the operation and maintenance costs are 0.04 USD/kW, and the penalty cost of abandoning scenery is 0.04 USD/kW. *MT* output adjustment cost is 0.06$/kW, EV provides V2G services with a compensation price of 0.1$/kW. The convergence coefficient of SADMM algorithm is 0.01, and the initial values of active and reactive power transmitted between VPP and ADN are 0, β = 30,000.

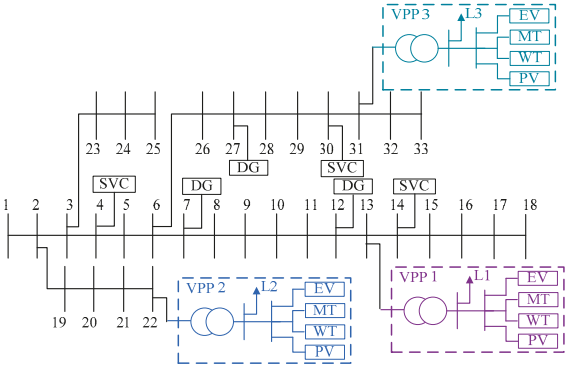

Figure 2. Diagram of ADN system with three VPPs.

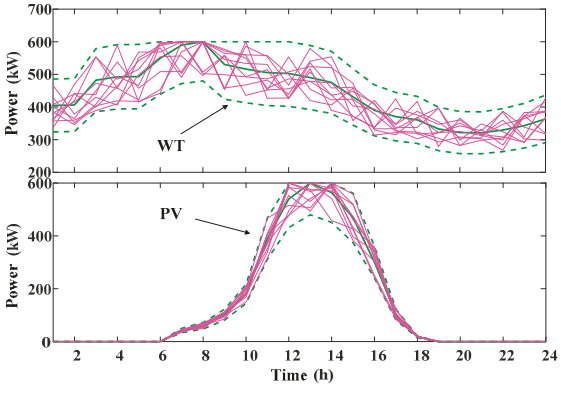

Figure 3. Output interval and scenarios of *WT*/*PV*.

4.2. Result Analysis

The influence of the traditional day-ahead scheduling method without considering the uncertainty of the PV and wind energy and the two-stage stochastic scheduling method with the uncertainty of the scenery were analyzed. The results were compared as shown in Table 1 and Figure 4. As shown in Table 1, the total operation cost of traditional day-ahead scheduling without considering the stochasticity of scenery is less than that of two-stage stochastic scheduling method. This is because the two-stage stochastic scheduling considers the revision of the day-ahead scheduling plan corresponding

to the predicted scenario in the prescheduling by the error scenario in the rescheduling process, which increases the running cost. However, it can ensure that the day-ahead scheduling plan can be smoothly transferred to various error scenarios, that is, two-stage stochastic scheduling can make decisions before uncertainty occurs. Moreover, the decision-making process incorporates the consideration of uncertainties, which can consider whether the optimization problem still has a feasible solution after the uncertainties are realized.

Table 1. Impact of different dispatch approaches on the operating costs

Scheduling Methods	Prescheduling Cost/$	Rescheduling Cost/$	Total Cost/$
Deterministic day ahead scheduling	2118	0	2118
Two-stage stochastic scheduling	2079	282	2361

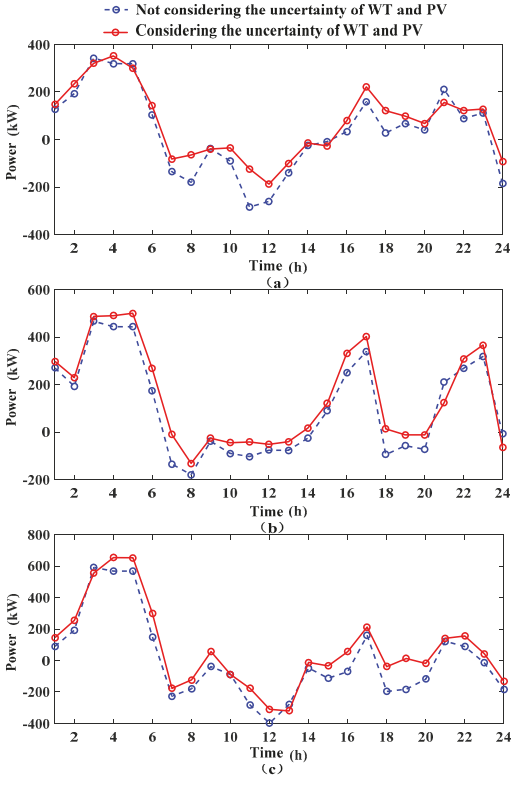

Figure 4. The interactive active power of the ADN and VPPs (**a**) VPP 1-ADN; (**b**) VPP 2-ADN; (**c**) VPP 3-ADN.

As can be seen in Figure 4, in most scheduling times, VPP purchases more electricity from ADN than without considering the uncertainty of wind and light. The electricity sales to ADN are less than those without considering the uncertainty of wind and light. It shows that the controllable power generation in VPP will be reduced when the uncertainty of wind power is considered, and the electricity purchased from ADN will be increased to cope with the uncertainty of wind and light. That is to say, two-stage stochastic scheduling will sacrifice part of the operating economy to improve the ability to deal with stochastic wind and light, so it has higher operational security. In the two-stage scheduling stage, the scenario of possible errors in the real time operation stage has been considered in

the prescheduling stage. By optimizing the adjustable outputs of controllable power supply in the rescheduling stage, any possible wind and light condition in the error condition set can be guaranteed to meet the operation requirements.

The charging and discharging power of EV intelligent agent is shown in Figure 5. The charging power of EV agents are mainly affected by the electricity price. In the period of low market price, which is also the period of large *WT* output, each VPP will purchase electricity from ADN to supply load demand while charging EV. When the compensation cost of V2G service provided by VPP is 0.1 \$/kW, which means the compensation cost of V2G service is higher than the market price at any time, then EV only participates in the V2G reverse discharge in 18–20 period. Because of the high load in the VPP and ADN, the controllable power supply cannot increase its output due to its output limitation, and the total output of the wind and light in this period is the least time of the day. Therefore, VPP will transfer EV with higher cost of V2G service to reverse discharge, and help meet the higher load requirements in the system and avoid load shedding. In other words, when the discharge loss cost of power battery is high, VPP will not reduce its operation cost because of the V2G reverse discharge of EV. However, with the advancement and development of battery technology, the compensation cost of V2G service provided by VPP will also be reduced when the loss cost of power battery is significantly reduced. Moreover, in the peak load period with high electricity price, the V2G reverse discharge from the EV agent to the VPP will increase, that can reduce the power purchasing from the VPP to the distribution network in the period of high electricity price, and reduce the operation cost of the VPP. In addition, although under the current V2G service compensation cost, EV almost does not carry out V2G reverse discharge but participate in system balance only as a similar reserve resource. However, under the incentive of electricity price policy, the EV charging load during peak load period is transferred to the low load period, which makes full use of the low price during the low load period. It also reduced the high price of VPP in the peak load period, and can effectively reduce the operation cost and load peak–valley difference of VPP and ADN.

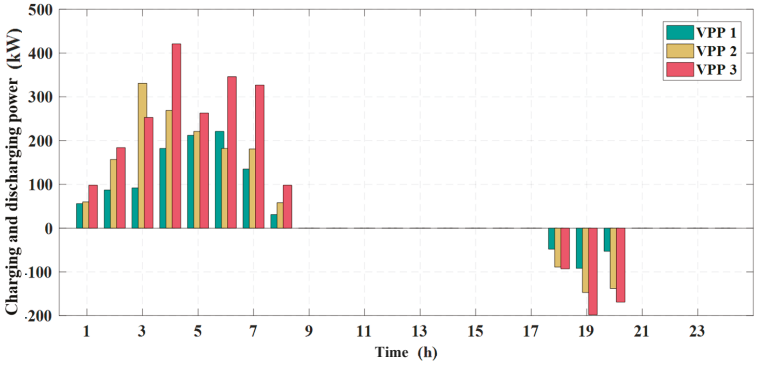

Figure 5. The charge–discharge power of EV agent.

The node voltage level in the ADN area is shown in Figure 6. Since this paper supposed that node 2 is the reference node, the voltage of node 2 remains at 12.66 kV. When the regional load level is relatively low, the node voltage is on the high side, which will make the voltage difference of the network larger. However, the voltage level of each node is kept in the safe operation range of (0.95, 1.05) p.u., so that the whole system can operate safely.

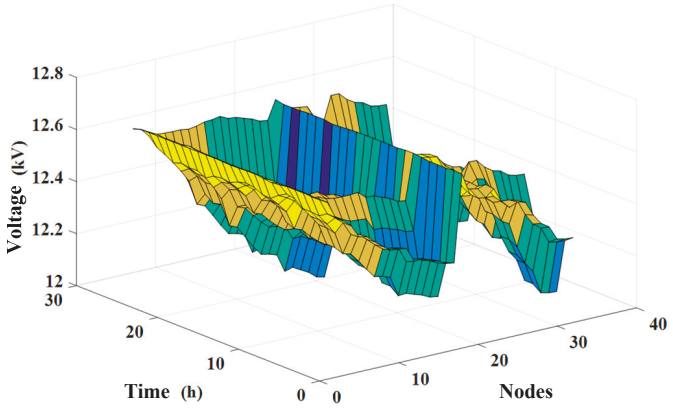

Figure 6. Node voltage level of AND.

Taking the typical time periods 3, 9, 15, and 20 as examples, the convergence performance of the dispatching method that proposed in this paper was analyzed. Active power interaction between ADN and VPP converged after 16 iterations, as shown in Figure 7. The total operation cost of traditional centralized two-stage stochastic scheduling was compared with that of decentralized two-stage stochastic scheduling, as shown in Figure 8. It can be seen that the total operation cost of centralized two-stage stochastic scheduling is 2303$. After 16 iterations, the total cost of decentralized two-stage stochastic scheduling converges to 2361$. This shows that the calculation effect of decentralized two-stage stochastic optimization based on ADMM is very close to centralized optimization and can converge after finite iterations.

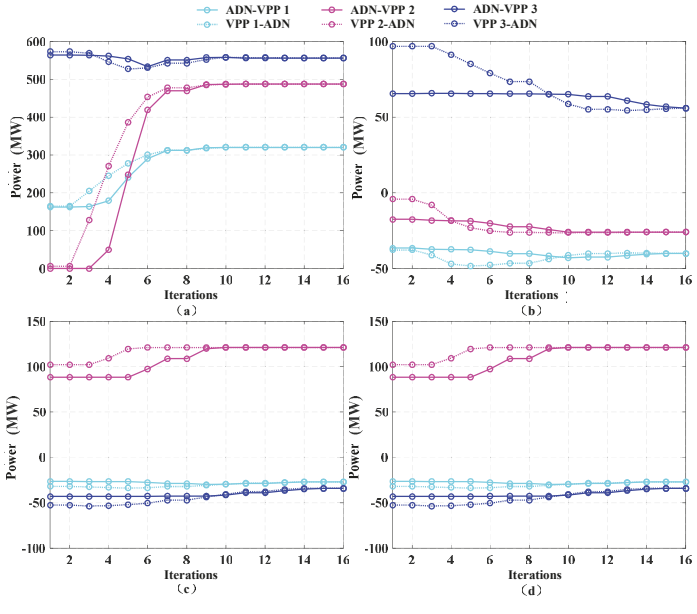

Figure 7. Iteration curve of active power of ADN and VPPs (**a**) 3rd period; (**b**) 9th period; (**c**) 15th period; (**d**) 20th period.

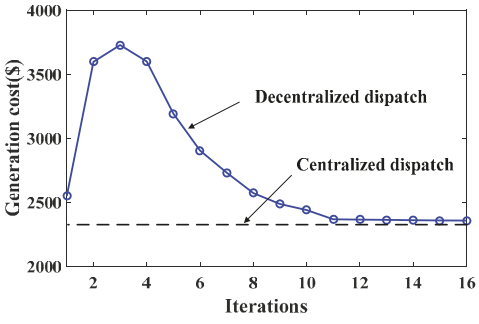

Figure 8. Convergence of total generation cost.

In order to verify the effectiveness of the decentralized two-stage stochastic optimization model for active distribution systems with multi-virtual power plants proposed in this paper, the following four comparison situations are set up.

Case 1: Without considering the stochastic uncertainty of distributed wind and light power output, the traditional centralized scheduling method is used to solve the problem.

Case 2: Considering the stochastic uncertainty of distributed wind and light power output, the traditional centralized scheduling method is used to solve the problem.

Case 3: Regardless of the stochastic uncertainty of distributed wind and light power output, a distributed scheduling method based on ADMM is adopted to solve the problem.

Case 4: Considering the stochastic uncertainties of distributed wind and light power output, a distributed scheduling method based on ADMM is adopted to solve the problem, i.e., the two-stage stochastic optimization method proposed in this paper.

The results of the four cases are shown in Table 2.

Table 2. Comparisons of four typical cases

Case	Model	Algorithm	Total Generation Cost ($)	Iterations	Calculation Time (s)
1	Deterministic	Centralized	2287	1	3.5
2	Two-stage stochastic	Centralized	2303	1	20.6
3	Deterministic	Decentralized	2336	14	102.7
4	Two-stage stochastic	Decentralized	2361	16	192.4

For centralized and decentralized optimization results, the total cost of case 3 is only 49 $ more than case 1, and the total cost of case 4 is only 58 $ more than case 2. It shows that the results of decentralized optimization are very close to those of centralized optimization, that is, the decentralized optimization in this paper can converge to the global optimal solution after finite iterations. The computation time of case 3 and case 4 is larger than case 1 and case 2. However, it needs to be pointed out that the model in this paper is to perform computational tasks on a single computer, and the decentralized optimization algorithm is not used to improve the computational speed, but to achieve the scheduling independence of ADN and VPPs, protect the data privacy of each agent, and more suitable for the future power market environment. In addition, when the proposed decentralized optimization method is applied in practice, the generation planning of each dispatching agent will be carried out separately by computers distributed in different geographical locations, and the computing speed advantage of decentralized optimization will gradually be reflected.

For the two-stage stochastic optimization model considering the stochastic uncertainty of distributed wind and light power output and the traditional deterministic model without considering the stochastic uncertainty of wind and light power output, the total cost of case 4 was 1.1% more than case 3, and the total cost of case 2 was 0.7% more than case 1. This showed that the total operating

cost of the system was greater than that of the system without considering the stochastic wind and light power output when considering the influence of the stochastic distributed wind and light power output on the power generation plan in the model. The reason was that when considering the stochastic uncertainty of wind power output, the error scenario of the second stage will correct the MT output plan obtained in the first stage, resulting in an increase in total operating costs. In the first stage scheduling, wind and light output scenarios that have been considered in the real-time operation stage have been considered. By optimizing the output adjustment of the second stage micro-gas turbine, it ensured that any possibility in the error situation set can meet the requirements. Then the first day scheduling plan can be transferred to the error situation smoothly. In addition, case 2 and case 4, which considered the randomness of wind power output, were much longer than case 1 and case 3, which did not consider the randomness of wind power output. This is because the situations considering the randomness of wind power include the calculation of 10 error situations, resulting in a significant increase in computing time, and the greater the number of error situations, the higher the computational complexity.

5. Conclusions

This paper presents a decentralized two-stage stochastic dispatching method for active distribution system with multiple VPPs based on the SADMM algorithm. The main bodies of VPPs interact with the upper distribution network by aggregating distributed energy and large-scale EVs within their jurisdiction. Without the participation of the central coordinator, the decentralized optimization was realized on the premise of autonomous energy management of active distribution network and VPPs. Then a two-stage stochastic optimization method including pre-scheduling stage and re-scheduling stage was adopted to deal with the uncertainty of wind and light output, and to reduce its adverse impact on the economic operation of the system. The proposed decentralized optimization method can realize the decentralized autonomy of dispatching agents and has good convergence performance. By aggregating distributed energy sources and EVs in VPPs, the adverse effects of disorderly charging and discharging of EVs and uncertainties of distributed wind and light power output on active distribution network dispatching and operation can be effectively alleviated.

For the next research plan, the following two aspects are mainly carried out:

Firstly, the uncertainties of charging and discharging behavior of EVs were not considered in this paper. With the large-scale network entry of EV, how to effectively deal with the uncertainties of charging and discharging behavior of EV will be of great significance.

Secondly, this paper studied a decentralized day-ahead scheduling method based on synchronous alternating direction multiplier method. How to enhance the convergence performance and computing speed of the algorithm as much as possible and further apply it to real-time operation conditions of power systems will become the future research direction.

Author Contributions: Conceptualization, X.L. and D.Z.; methodology, X.L.; software, X.L.; validation, X.L., D.Z. and B.G.; formal analysis, X.L.; investigation, X.L.; resources, X.L.; data curation, X.L.; writing—original draft preparation, X.L.; writing—review and editing, B.G.; visualization, X.L.; supervision, D.Z.; project administration, D.Z.; funding acquisition, D.Z., corresponding author, B.G.

Funding: This research was funded by Fundamental Research Funds for the Central Universities, grant number 2017XS019 and National Key Research and Development Program Funded Projects, grant number 2017YFB0902600.

Conflicts of Interest: The authors declare no conflict of interest.

References

1. Wei, Z.; Yu, S.; Sun, G.; Sun, Y.; Yuan, Y.; Wang, D. Concept and development of virtual power plant. *Autom. Electr. Power Syst.* **2013**, *37*, 1–9.
2. Wang, Y.; Zhao, S.; Xu, Y.; Yin, J. Rolling dispatch of wind/thermal/storage system based on chance constrained goal programming. *Power Syst. Technol.* **2017**, *41*, 187–194.

3. Gao, H.; Liu, J.; Wei, Z.; Cao, Y.; Wang, W.; Huang, S. A security-constrainted dispatching model for wind generation units based on extreme scenario set optimization. *Power Syst. Technol.* **2013**, *37*, 1590–1595.
4. Qiu, H.; Zhao, B.; Gu, W.; Bo, R. Bi-level two-stage robust optimal scheduling for AC/DC hybrid multi-microgrids. *IEEE Trans. Smart Grid* **2018**, *9*, 5455–5466. [CrossRef]
5. Gan, L.; Li, N.; Topcu, U. Exact convex relaxation of optimal power flow in radial networks. *IEEE Trans. Autom. Control* **2015**, *60*, 72–87. [CrossRef]
6. Liu, Y.; Wu, W.; Zhang, B.; Li, Z.; Li, Z. A mixed integer second-order cone programming based active and reactive power coordinated multi-period optimization for active distribution network. *Proc. CSEE* **2014**, *34*, 2575–2583.
7. Li, Q.; Ayyanar, R.; Vittal, V. Convex optimization for DES planning and operation in radial distribution systems with high penetration of photovoltaic resources. *IEEE Trans. Sustain. Energy* **2016**, *7*, 985–995. [CrossRef]
8. Bahrami, S.; Therrien, F.; Wong, V.W.; Jatskevich, J. Semidefinite Relaxation of Optimal Power Flow for AC–DC Grids. *IEEE Trans. Power Syst.* **2017**, *32*, 289–304. [CrossRef]
9. Dong, W.; Wang, Q.; Yang, L. A coordinated dispatching model for a distribution utility and virtual power plants with wind/photovoltaic/hydro generators. *Autom. Electr. Power Syst.* **2015**, *39*, 75–81.
10. Pandzic, H.; Kuzle, I.; Capuder, T. Virtual power plant mid-term dispatch optimization. *Appl. Energy* **2013**, *101*, 134–141. [CrossRef]
11. Zhuang, H.; Wu, H.; Liu, H. Multi-objective economic dispatch of microgrid system considering electric vehicles. *Tran. China Electrotech. Soc.* **2014**, *29* (Suppl. 1), 365–373.
12. Zhang, Q.; Liu, C.; Zhou, L. A bi-level economy dispatch model considering temporal and spatial optimal distribution of electric vehicles. *Autom. Electr. Power Syst.* **2014**, *38*, 40–45.
13. Huang, Y.; Guo, C.; Wang, L.; Bao, Y.; Dai, S.; Ding, Q. A cluster-based dispatch strategy for electric vehicles considering user satisfaction. *Autom. Electr. Power Syst.* **2015**, *39*, 183–191.
14. Pan, Z.; Zhang, X.; Yu, T.; Wang, D. Hierarchical real-time optimized dispatching for large-scale clusters of electric vehicles. *Autom. Electr. Power Syst.* **2017**, *17*, 014.
15. Yang, J.J.; Zhao, J.H.; Wen, F.S.; Xue, Y.S.; Li, L.; Lv, H.H. Development of bidding strategies for virtual power plants considering uncertain outputs from plug-in electric vehicles and wind generators. *Autom. Electr. Power Syst.* **2014**, *38*, 92–102.
16. Arslan, O.; Karasan, O.E. Cost and emission impacts of virtual power plant formation in plug-in hybrid electric vehicle penetrated networks. *Energy* **2013**, *60*, 116–124. [CrossRef]
17. Shaaban, M.F.; Eajal, A.A.; El-Saadany, E.F. Coordinated charging of plug-in hybrid electric vehicles in smart hybrid AC/DC distribution systems. *Renew. Energy* **2015**, *82*, 92–99. [CrossRef]
18. Wang, Z.; Chen, B.; Wang, J.; Begovic, M.M.; Chen, C. Coordinated energy management of networked microgrids in distribution systems. *IEEE Trans. Smart Grid* **2015**, *6*, 45–53. [CrossRef]
19. Zhao, W.; Liu, M.; Zhu, J. A bi-level decomposition and coordination economic dispatch method for power plants/network considering stochastic wind generation. *Power Syst. Technol.* **2015**, *39*, 1847–1854.
20. Zhou, M.; Wang, M.; Li, J.; Li, G. Multi-area generation-reserve joint dispatch approach considering wind power cross-regional accommodation. *CSEE J. Power Energy Syst.* **2017**, *3*, 74–83. [CrossRef]
21. Boyd, S.; Parikh, N.; Chu, E.; Peleato, B.; Eckstein, J. Distributed optimization and statistical learning via the alternating direction method of multipliers. *Found. Trends Mach. Learn.* **2010**, *3*, 1–122. [CrossRef]
22. Zhang, Y.; Giannakis, G.B. Efficient decentralized economic dispatch for microgrids with wind power integration. In Proceedings of the Sixth Annual IEEE Green Technologies Conference, Corpus Christi, TX, USA, 3–4 April 2014.
23. Peijie, L.; Yong, L.; Xiaoqing, B.; Hua, W. Decentralized optimization for dynamic economic dispatch based on alternating direction method of multipliers. *Proc. CSEE* **2015**, *35*, 2428–2435.
24. Erseghe, T. Distributed optimal power flow using ADMM. *IEEE Trans. Power Syst.* **2014**, *29*, 2370–2380. [CrossRef]
25. Zhang, C.; Xu, Y.; Dong, Z.Y.; Wong, K.P. Robust coordination of distributed generation and price-based demand response in microgrids. *IEEE Trans. Smart Grid* **2017**, *9*, 4236–4247. [CrossRef]

energies

MDPI

Article

Grounding System Cost Analysis Using Optimization Algorithms

Jau-Woei Perng [1], Yi-Chang Kuo [1,2,*] and Shih-Pin Lu [2]

[1] Department of Mechanical and Electro-Mechanical Engineering, National Sun Yat-sen University, Kaohsiung 80424, Taiwan; jwperng@faculty.nsysu.edu.tw

[2] Taiwan Power Company Southern Region Construction Office, Kaohsiung 81166, Taiwan; u596864@taipower.com.tw

* Correspondence: a0917689485@gmail.com; Tel.: +886-07-357-2268

Received: 3 October 2018; Accepted: 6 December 2018; Published: 13 December 2018

Abstract: In this study, the concept of grounding systems is related to the voltage tolerance of the human body (human body voltage tolerance safety value). The maximum touch voltage target and grounding resistance values are calculated in order to compute the grounding resistance on the basis of system data. Typically, the grounding resistance value is inversely proportional to the laying depth of the grounding grid and the number of grounded copper rods. In other words, to improve the performance of the grounding system, either the layering depth of the grounding grid or the number of grounded copper rods should be increased, or both of them should be simultaneously increased. Better grounding resistance values result in increased engineering costs. There are numerous solutions for the grounding target value. Grounding systems are designed to find the combination of the layering depth of the grounding grid and the number of grounded copper rods by considering both cost and performance. In this study, we used a fuzzy algorithm on the genetic algorithm (GA), multi-objective particle swarm optimization (MOPSO) algorithm, Bees, IEEE Std. 80-2000, and Schwarz's equation based on a power company's substation grounding system data to optimize the grounding resistance performance and reduce system costs. The MOPSO algorithm returned optimal results. The radial basis function (RBF) neural network curve is obtained by the MOPSO algorithm with three variables (i.e., number of grounded copper rods, grounding resistance value, and grounding grid laying depth), and the simulation results of the electrical transient analysis program (ETAP) system are verified. This could be a future reference for substation designers and architects.

Keywords: genetic algorithm; multi-objective particle swarm optimization algorithm; artificial bee colony; IEEE Std. 80-2000; Schwarz's equation; fuzzy algorithm; radial basis function; neural network; ETAP

1. Introduction

The harmful effects of electric current on the human body can be broadly categorized as electric shock and electrical injury. The harmful effects on the normal functions of the heart, lungs, and nervous system when an electric current flows through the human body can be referred to as electric shock. Such effects can include numbness, paralysis, difficulty in breathing, and even respiratory and/or cardiac arrest and ventricular fibrillation. Low-voltage electrocution can occur if the heart is unable to function. Most electricity-induced deaths are caused by electric shocks from low-voltage power systems.

Electrical injuries, also known as electrical burns, refer to localized damage to human tissue due to the thermal, chemical, or mechanical effects of current flowing through the body. Such electrical burns can harm the skin, muscles, blood vessels, bones, internal organs, and the nervous system. In a high-voltage power system, faulty operation can cause severe burns. Strong electric arcs can be produced by high-voltage discharges, harming humans near the charged equipment. The temperature

of electric arcs can reach 8000 °C, which can cause large and deep burns; severe arc burns can be lethal. When a current-carrying conductor comes into contact with the human body for a period of time, the skin at the contact site hardens and forms an imprint-like lump called an "electric imprint" due to the chemical and mechanical effects of the current. In addition, when splashed, metal particles penetrate the skin by chemically reacting with it, and the skin becomes rough and hard. This condition, which is commonly observed with arc burns, is referred to as "skin metallization".

The human body suffers different degrees of harm when an electric current flows through vital organs. The extent of damage depends on the duration, amplitude, and frequency of the current. Ventricular fibrillation, which causes the heart to stop beating, is among the most severe types of damage [1]. Previous studies have indicated that humans are easily affected by alternating current (AC) at frequencies of 50–60 Hz. At such frequencies, a current of approximately 0.1 A can be fatal. However, the human body can tolerate frequencies that are slightly higher than 25 Hz, which represents an intensity that is approximately five times that of direct current (DC). At this frequency, DC is five times more intense than AC at a frequency of 50–60 Hz [2]. A stronger current can be tolerated between 3 and 10 kHz [3]. The effects of current flowing through the human body can be expressed in increments of current flow: muscle contraction, unconsciousness, cardiac fibrillation, respiratory obstruction, and burning.

Various algorithms that are designed for optimizing the grounding resistance, improving grounding efficiency, and reducing engineering costs have been proposed. For example, Alik et al. proposed a genetic algorithm optimization (GAO) based on the safety and cost-effectiveness of the grounding system design of the Ain El-Melh substation in M'Sila, Algeria [4]. Here, the primary objective was to minimize the cost function of the grounding system in accordance with the requirements of the American National Standards Institute (ANSI)/IEEE Std. 80-2000. The variables that were involved in their cost function model included the number and size of the grounding conductors, the number and length of the grounding bars, and the total area of the grounding grid. They demonstrated that their GAO achieved a cost-effective grounding system design. They also proposed a method to minimize the grounding system costs of the Labreg Power Plant located in Khenchela (400 km east of Algiers). The grounding system was designed using particle swarm optimization (PSO), GAO, and hybrid particle swarm genetic algorithm optimization (HPSGAO). Their objective was to implement the number of iterations and convergence times of PSO, GAO, and HPSGAO, as well as the cost function of the grounding system, to evaluate the effectiveness of cost reduction [5].

This study presents the grounding prediction line in different regions that was drawn up using the grounding resistance divided by the grounding resistance coefficient in the study area, and multiplied by the grounding resistance coefficient in the replacement area (i.e., by replacing the grounding resistance of the area). The grounding prediction line and relative grounding material cost can serve as additional design references for the grounding system designers. In addition, previous studies have combined PSO and genetic optimization algorithms to compare the convergence time and the number of iterations. Using modern computers, these algorithms can be processed quickly. Therefore, in this study, we have focused on an algorithm to reduce the material costs of grounding systems and to maintain good grounding resistance performance. In this study, we compared the advantages and disadvantages of the fuzzy system in the grounding system of each algorithm, and the simulation results of the ETAP system were verified. The remainder of this study is organized in the following manner. Section 2 recalls the representation of the grounding system material cost function to prevent electric shocks, and Section 3 details the system structure. The simulation results are shown and analyzed in Section 4, and the conclusions are summarized in Section 5.

2. Representation of the Grounding System Material Cost Function to Prevent Electric Shocks

Current can be categorized relative to its effect [6].

(1) Current that causes a slight tingling sensation when it passes through the fingertips is called a perception current [7]. The minimum current that can be felt is known as the perception current threshold. Note that the threshold is not related to the duration of the current flow.

The American National Standards Institute (ANSI) Std. 80 identifies the perception current threshold as 1 mA [3], and the International Electrotechnical Commission (IEC) sets the threshold at 0.5 mA (IEC 479-1) [6].

(2) Current that causes discomfort but does not hinder muscle control is referred to as a let-go current. As the current increases, heat and tingling sensations increase, and when the current reaches a certain level, the muscles contract, causing muscle spasms, and the current-carrying body becomes unable to let go of the contact point. Generally, let-go currents do not cause adverse effects. The let-go current threshold represents the current value that a human body can tolerate without adverse effects. The ANSI Std. 80 sets the let-go current threshold for women and men at 6 and 9 mA, respectively, and the IEC sets the threshold value at 10 mA for both men and women. When the current exceeds this threshold, people may panic and experience unbearable pain. Depending on the duration, currents that exceed the threshold may result in a coma, suffocation, and even death.

(3) The current that causes a rapid disorganized electrical activity in the heart is called a ventricular fibrillation current. The heart functions in humans are controlled by an internal electrical system, and when an external current exceeds the let-go threshold and continues to increase, the heart's normal electrical signals become disturbed and myocardial vibration is induced (i.e., ventricular fibrillation occurs). If the heart cannot pump blood normally, death can occur within minutes.

In order to avoid injuries or death, a safe grounding system must be designed to keep the current below the current threshold. According to Dalziel et al., the human body's tolerance can be represented by the following energy relationship [8,9]:

$$S_B = (I_B)^2 t_s, \tag{1}$$

where I_B is the maximum current (unit: ampere) that the human body can tolerate, t_s is the duration of current flow through the body (unit: seconds), and S_B is the experimentally known energy constant that 99.5% of people can safely withstand without experiencing ventricular fibrillation; it is also the ratio of energy absorbed by the body to the body's resistance in joules per ohm. Assuming that S_B holds, from Equation (1), it can be deduced that the magnitude and duration of the current are expressed as follows:

$$I_B = \frac{k}{\sqrt{t_s}}. \tag{2}$$

By the corollary of Equation (1) (i.e., $k = \sqrt{S_B}$), it can be inferred the human body absorbs the energy. Dalziel et al. found that, for people weighing approximately 50 kg, $S_{B50} = 0.0135$; therefore, $k_{50} = 0.116$ [6]. Thus, the relationship between human-safe current and duration is expressed as follows:

$$I_{B50} = \frac{k}{\sqrt{t_s}} = \frac{0.116}{\sqrt{t_s}}. \tag{3}$$

Dalziel and Lee found that, based on Equations (1) and (2), for people weighing 70 kg, $k_{70} = 0.157$ and $S_{B70} = 0.0246$ [10,11]. Therefore, we obtain the following:

$$I_{B70} = \frac{k}{\sqrt{t_s}} = \frac{0.157}{\sqrt{t_s}}. \tag{4}$$

Conservative grounding grid models are often used when assessing human safety. Typically, workers at the target AC substation weigh more than 50 kg; thus, the human-safe current is calculated using Equation (3). Therefore, the grounding design is most easily overlooked; however, it is one of the most important parts of power system safety. In substation systems, in addition to protecting the power system from the effects of grounding malfunctions, grounding grids protect substation maintenance personnel. Current grounding grid designs, including touch voltage, step voltage, surge voltage, ground resistance, and other parameters, are determined by IEEE Std. 80TM [3]. However, in the

design of the overall grounding grid, grounding resistivity is significantly influenced by earth resistivity. According to IEEE Std. 80TM, a single average calculation is used to determine earth resistivity. After construction is complete, the measured grounding value is frequently greater than the calculated grounding value in multilayered complex geology [12]. Blindly increasing the number of grounding grids and grounding copper rods would be uneconomical.

The Taiwan Power Company's Electric Power Construction Unit designs grounding grids and grounding rods, and selects grounding conductors to achieve lower ground resistance on the basis of several factors, including the location of various equipment, the building configuration, and the land size of the substation. The grounding resistance value is also calculated using grounding system data in order to ensure that it does not exceed the target value. To ensure the safety of human life and property, as well as stable and reliable power system operation, uncharged parts of machinery, iron frames, and low-voltage loops, among others, should be grounded so that the ground current will not cause abnormal voltages when a grounding malfunction occurs. The calculation of the grounding resistance target value assumes that the touch voltage [$E_{touch50}$ in Equation (5)] should not exceed the allowable value when a grounding malfunction occurs. Assuming that the touch voltage is calculated using a ratio of a safety factor to the ground potential rise (GPR), this GPR value is divided by the ground current [I_g in Equation (6)] to obtain the required grounding resistance target value [R_e in Equation (7)] and the correlation factor for the ground resistance target value. The earth surface resistance coefficient (ρ_s), based on a 20 cm-thick gravel layer, is 3000 Ω-m. Here, the malfunction clearing time (t) is calculated as 0.5 s. (I_f) is the single-phase fault current of the final stage for the substation. The power system split rate $K = \frac{I_f - I_g}{I_f}$ depends on the power line transmission method. Without connection station in substation K = 0.8. With connection station in substation K = 0.7. All lines are cables K = 0.9. All lines are overhead cables K = 0.7. The safety coefficient α = 5.

$$E_{touch50} = (1000 + 1.5\rho_s)\frac{0.116}{\sqrt{t_s}}, \tag{5}$$

$$I_g = (1 - K)I_f, \tag{6}$$

$$R_e = \alpha\frac{E_{touch50}}{I_g}. \tag{7}$$

The grounding system contains grounding grids, grounding rods, and grounding lead. The grounding grids comprise horizontal copper conductors, where the distance between wires is 8–10 m outside the indoor substation building, and less than 6 m inside the house. Relative to buildings, the grounding grid must be laid on the base layer of the underground excavation to obtain low grounding resistance. The area of the grounding grid outside the house should be as large as possible (within 1 m from the fence). If metal structures are used in fences, the distance between the grounding grid and the fence must not be less than 1 m, and the fence should be grounded separately. The grounding rod cooperates with the ground network node, and every two grounding nodes have one grounding rod. Ideally, each rod should be installed at the corner zone of the grounding grid. In addition, major equipment, such as iron towers, iron structures, transformers, and surge arresters, requires more rods to improve performance. The indoor substation must include copper strips to connect its grounding grid to the outdoor substation. Here, there should be at least two copper strips per wall, and an additional passage should be employed for walls exceeding 45 m in length (one passage for a wall that is less than 20 m). In order to keep the building and grounding grid at the same potential, the grounding grid must be connected to the building's rebar via iron plates welded at four corners.

The designed grounding resistance values are obtained according to Schwarz's formula [13] using the following equations:

$$\text{Mesh electrode grounding resistance } (\Omega): \ R_{11} = \frac{\rho[\text{In}\frac{2L}{a'} + \frac{LK1}{\sqrt{A}} - K2]}{\pi L}. \tag{8}$$

$$\text{Rod electrode grounding resistance } (\Omega): \ R_{22} = \frac{\rho[\text{In}\frac{2\iota}{r1} + \frac{2\iota K1}{\sqrt{A(\sqrt{n}-1)^2}} - 1]}{2\pi n\iota}. \tag{9}$$

$$\text{Mesh and rod combined grounding resistance } (\Omega): \ R_{12} = \frac{\rho[\text{In}\frac{2L}{\iota} + \frac{LK1}{\sqrt{A}} - K2 + 1]}{\pi L}. \tag{10}$$

$$\text{Synthesis resistance } (\Omega): \ R_g = \frac{R_{11}R_{22} - {R_{12}}^2}{R_{11} + R_{22} - 2R_{12}}. \tag{11}$$

Here, ρ is the earth resistance coefficient (Ω-m), r is the grounding line radius (m), and z is the grounding rod depth (m); thus, $a' = \sqrt{(2rz)}$. r1 is the grounding rod radius (m), L is the total length of the grounding grid (m), ι is the length of the grounding rod (m), n is the number of grounding rods, and A is the mesh electrode area (m^2). K1 = 1.41 − 0.04 L/W and K2 = 5.5 + 0.15 L/W [where L is the grounding grid length (m) and W is the grounding grid width (m)].

A schematic calculation of the designed grounding resistance value (according to the IEEE Std. 80-2000 formula) is given by

$$R_g = \rho\left[\frac{1}{L_T} + \frac{1}{\sqrt{20A}}\left(1 + \frac{1}{1 + h\sqrt{\frac{20}{A}}}\right)\right], \tag{12}$$

where A is the mesh electrode area (m^2), L_T is the total length of the grounding line and grounding rods, and h is the grounding grid depth.

Regardless of which calculation (i.e., the IEEE Std. 80-2000 formula or Schwarz's formula) is used to obtain the grounding resistance value, R_g (designed value) < R_e (target value) must hold.

3. System Structure

In this section, we introduce the design flow and function of the fuzzy system in the grounding system of each algorithm along with the function of the RBF neural network. This section can be structured as follows: Section 3.1 introduces the structure of the grounding prediction system; Section 3.2 introduces the grounding resistance design flow; Section 3.3 introduces the design flow of the grounding system with GAO; Section 3.4 introduces the design flow of the grounding system with MOPSO; Section 3.5 introduces the design flow of the grounding system with artificial bee colony algorithm optimization; Section 3.6 introduces the membership function of the fuzzy Integral; and Section 3.7 introduces the function of the RBF neural network.

3.1. Grounding Prediction System

The grounding prediction system employed in this study can help evaluate grounding resistance and grounding system costs in any area. The system design is shown in Figure 1. Figure 1 shows designs for lightning protection systems of high-rise constructions in various regions of the world and the grounding system resistance value plus the grounding system cost planning required for transient elimination of high-energy currents, such as fault currents or lightning strikes at power company facilities. The substation design parameters are optimized by grounding systems using various algorithms, such as genetics algorithm (GA), multi-objective particle swarm optimization (MOPSO), and bee swarm algorithm (BA). The adaptive function used is dominated by the Schwarz equation to solve the grounding resistance value R_g, grounding cost, where the net grounding depth h

= 0.6 m. The result is then compared to the IEEE Std. 80-2000 at h = 0.6 cm to evaluate the effectiveness. However, the grounding resistance is typically inversely proportional to the grounding grid depth and the number of grounding copper rods. In other words, in order to achieve better grounding system performance, either the grounding grid depth or the number of grounding copper rods must be increased (or both). Note that a better grounding resistance value will result in higher relative engineering costs. Based on this characteristic, the fuzzy membership function is used to establish the integral to identify the best algorithm. The fuzzy membership function identified MOPSO as the optimal algorithm from among GA and Bee. Therefore, the depth of the grounding network is optimized at 0.4–0.6 m to find the best grounding resistance value and number of grounding copper rods in a radial basis function (RBF) prediction module.

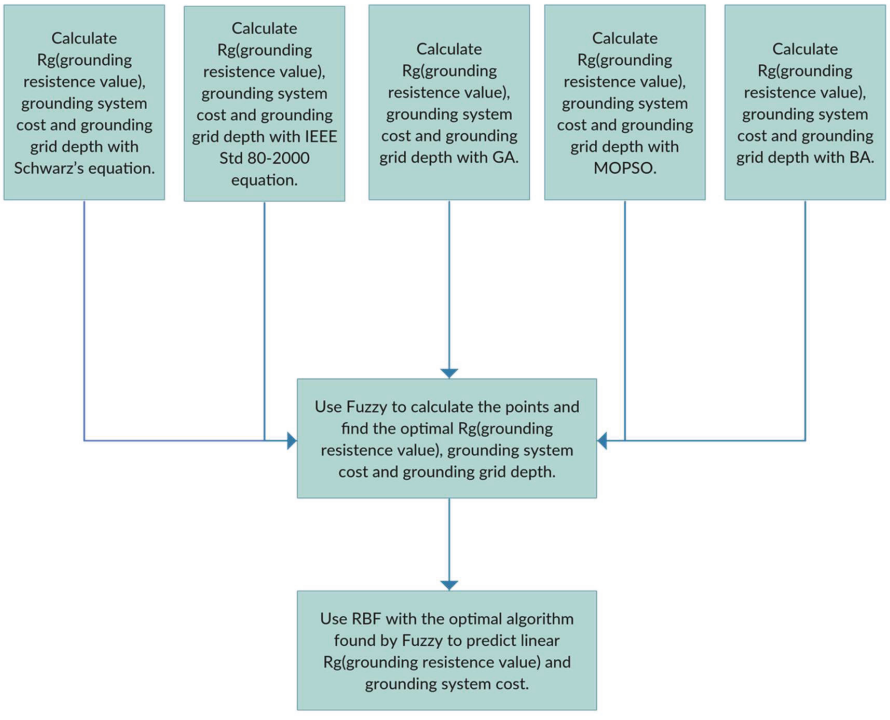

Figure 1. Grounding prediction system.

3.2. Grounding Resistance Design

The current design of the grounding system, used by Taiwan Electric Power Co., Ltd., calculates the maximum allowable touch voltage and the grounding resistance target value according to the grounding design criterion (i.e., the safe voltage that the human body can withstand). In addition, the design calculates the grounding resistance using the grounding system data in the guideline that has been stated by the Taiwan Power Company's Electric Power Construction Unit. As stated previously, the value must be less than the target value. Calculations of the grounding resistance in the grounding design criteria are based on the planned area of the grounding grid associated with the ground network node. IEEE Std. 80-2000 is used to calculate the grounding resistance (R_g designed value) of E_m, E_s, E_{touch}, E_{step}, GPR, the total number of grounding rods, the measurement report of the depth resistivity of the base of Taipower Institute of Research, as well as the area, length, and width of the grounding grid. Simultaneously, the grounding resistance is calculated precisely using Schwarz's equation, where the value must be less than the target value. At present, the surface resistivity

coefficient is gravel 3000, and the ground network is buried at a depth of 0.6 m. The company uses Microsoft Excel 2010 to design the grounding system to perform calculations for item (2) IEEE Std. 80-2000. The ground resistance design flow is illustrated in Figure 2.

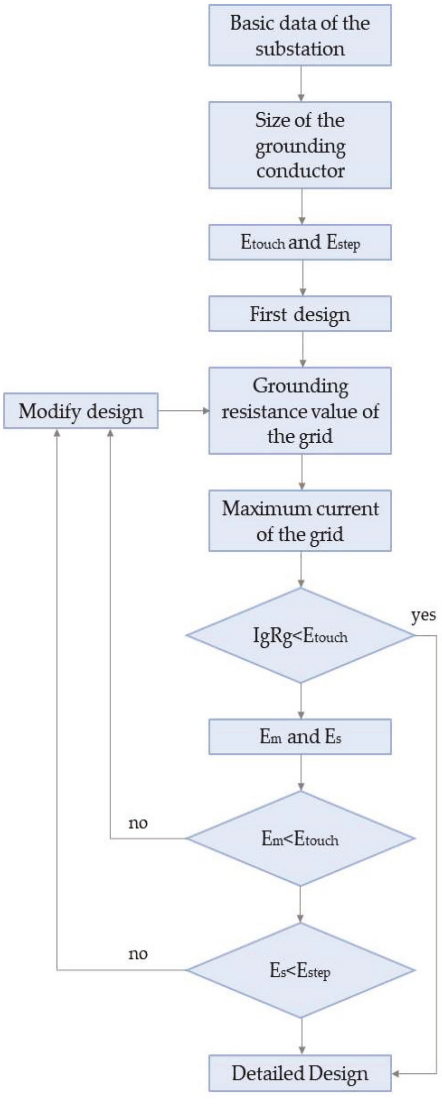

Figure 2. Grounding resistance design flow.

3.3. GA Optimization Flow Chart

The flow chart of the grounding system designed using GA optimization [14] is shown in Figure 3. According to the grounding resistance design process, the number of grounded copper rods required to solve the grounding resistance design value is used as the chromosome mother number. Since there are numerous grounding system data items collected by the grounding target value, it is necessary to determine the search range, by designing the number of grounded copper rods, and to use Schwarz's equation in an adaptive function calculation.

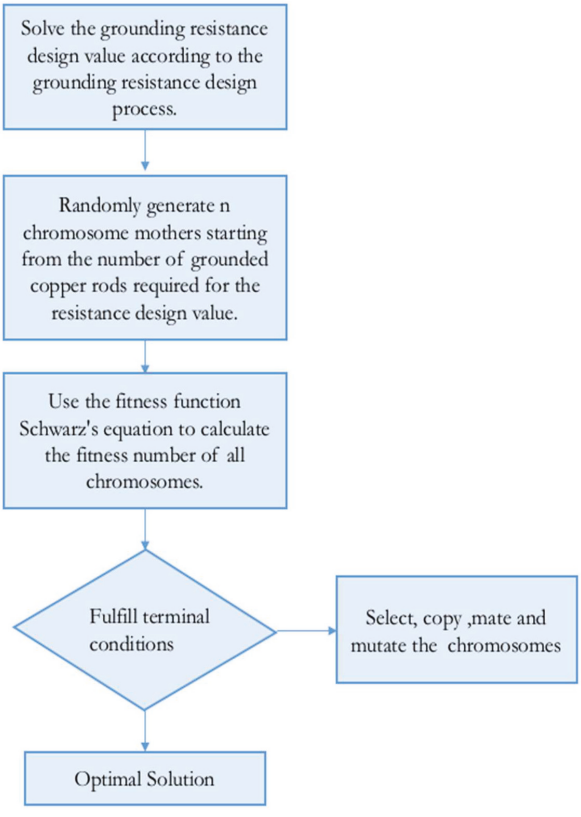

Figure 3. Flow of the grounding system with GAO.

3.4. MOPSO Flow Chart

In the MOPSO flow chart [15–17], the number of grounding copper rods required to ground the resistance design value is calculated on the basis of the ground resistance design flow chart. There are many grounding system data items collected by the grounding target value; thus, it is necessary to determine the search range by determining an effective number of grounding copper rods for optimization, and to use Schwarz's equation as the adaptive function, as shown in Figure 4.

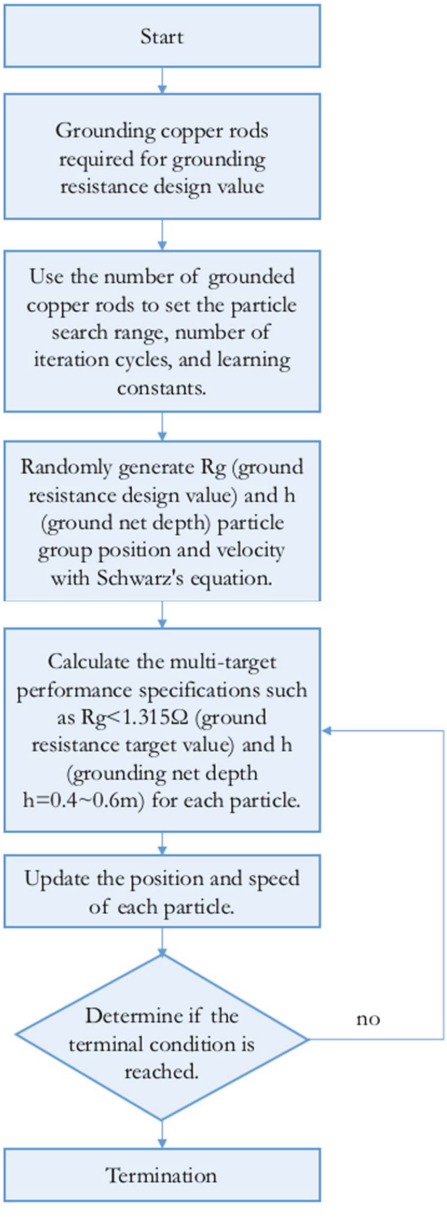

Figure 4. Flow of the grounding system with MOPSO.

3.5. Artificial Bee Swarm Algorithm Flowchart

As for the grounding system that employs the artificial bee colony algorithm [18], the number of grounded copper rods is used as the initial value for the grounding resistance design. Furthermore, the search solution m is divided into a local search using the adaptation function of the Schwarz's function as a local search. The optimal solution e is determined from an m local search; further, the optimal global solution is updated until the terminal condition is reached, as depicted in Figure 5.

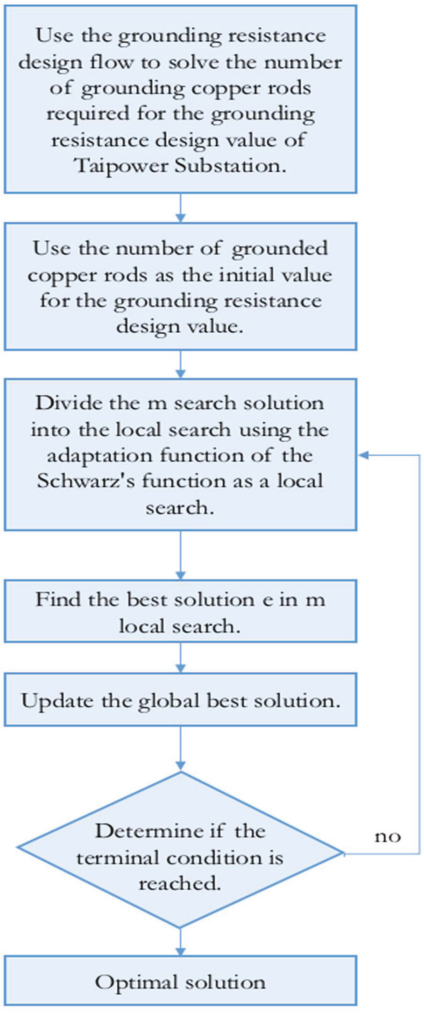

Figure 5. Flow of the grounding system with artificial bee colony algorithm optimization.

3.6. Fuzzy Integral

The fuzzy rule [19] semantic notation is summarized as follows: If (x is A) and (y is B), then (z is α), and if (x is A) or (y is C), then (z is β); this expression represents the Fuzzy logic grammar. This study employs a fuzzy membership function. The two established inputs are R_g (grounding resistance) and tip (engineering cost), as depicted in Figure 6. Further, the conditions can be given as follows:

If (R_g is bad i.e., R_g (designed value) > Re (target value) = 1.315 Ω) or (tip is high), then (performance is poor). (13)

If (R_g is significant), then (performance is good). (14)

If (R_g is significant) and (tip is low), then (performance is excellent). (15)

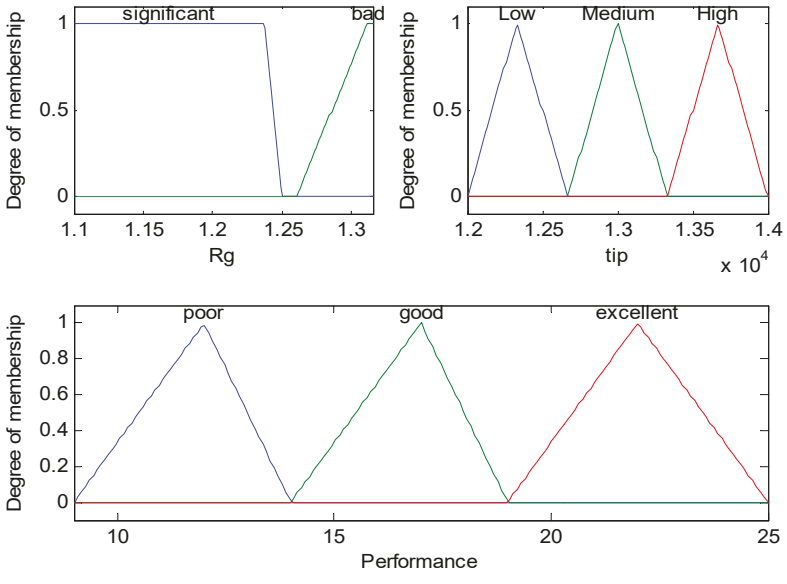

Figure 6. Membership functions of inputs R_g (ground resistance) and tip (project cost) and the output performance.

3.7. RBF Neural Network

The RBF neural network [20] is the first function to use the real multivariate interpolation method. Its main structure can be divided into three layers. The first layer is the input layer with input dimension p, and the second layer is the hidden layer, that is, a nonlinear transformation from the input layer space to the hidden layer space, which is an application of high-dimensional space. The third layer is the output layer, which is converted by the activation function of the network. The output of the third layer has linearly-segmentable features. To predict the grounding resistance value of the soil layer in any area, the number of grounding copper rod, grounding depth of the grounding grid, and other grounding parameters, the three variable values of the grounding parameter are input into nine neurons of every input variable of the hidden layer along with the three output variables. The RBF neural network of the hidden layer neurons (i.e., the basis function used by the neuron output) is dominated by a Gaussian function, and its mathematical representation is expressed as follows:

$$\phi_j(x) = \exp\left(\frac{|x - m_j|^2}{2\sigma_j{}^2}\right). \tag{16}$$

4. System Simulation

Typically, the grounding resistance value is inversely proportional to the laying depth of the grounding grid and the number of grounded copper rods. In order to achieve a better grounding system performance, the laying depth of the grounding grid and the number of grounded copper rods should be either alternatively or simultaneously increased. A better grounding resistance value results in a higher relative engineering cost. The fuzzy algorithm is more suitable to comparatively evaluate the degree of goodness and weakness of the entire system with various algorithms. The grounding resistance value and grounding system engineering cost are taken as fuzzy input/disadvantage scores to identify the best algorithm relative to outputting the fuzzy integral score (Table 1). Among the various algorithms used, the MOPSO integral of 19.9989 was the highest input, as shown in Table 1.

Therefore, MOPSO was used as the input module for subsequent prediction of the grounding system data.

Table 1. Fuzzy integrals of grounding data for each algorithm in the fixed network laying depth.

Parameters of the Grounding-Parameter Algorithm	Grounding Copper Rod (n)	Ground Network Excavation Depth (m)	Grounding Resistance (Ω)	Project Cost	Fuzzy Integral
Schwarz's equation	82	0.6	1.24	13,136.76 USD	15.0000
IEEE Std. 80-2000	82	0.6	1.19	13,136.76 USD	15.0000
GA	61	0.6	1.25	12,832.05 USD	15.0000
MOPSO	28	0.6	1.24	12,353.22 USD	19.9989
Bees	139	0.6	1.14	13,963.83 USD	13.2965

Grounding copper rod price: approx. 14.51 USD. Grounding network excavation cost: 7.24 USD/m (total ground line length: approximate 1650.13 m). Ground net area: 75 × 67 m; target value < 1.315 Ω.

MOPSO is the most suitable algorithm for the grounding system relative to predicting various grounding data. In order to quickly establish the prediction line of the grounding system, MOPSO's adaptation function (i.e., Schwarz's equation) is replaced by IEEE Std. 80-2000, which has a small value gap, as a prediction line adaptation function. The trend of grounding rods used and the grounding resistance value simulating grounding grid depth at 0.1–0.6 m is shown in Figure 7. Here, after MOPSO simulated-result for h = 0.35 m, R_g = 1.3482 Ω exceeded the design target value R_g = 1.315 Ω of this substation. Thus, we used h = 0.4–0.6 m as a sample for the input of the ground resistance prediction line simulation. The follow-up MOPSO simulation results are given in Table 2. The data in Table 2 were used to create a three-dimensional (3D) space curve, as shown in Figure 8. To construct a general model of grounding parameters, such as the grounding resistance value, grounding copper rods, and ground net depth for any region, any of the three variable values of the parameters in Table 2 is inputted into RBF neural networks. The constructed neural network can input any grounding resistance, grounding copper rod, and grounding grid depth parameter values. After the RBF neural network process, the results mostly pass through the prediction line of the IEEE Std. 80-2000 adaptation function calculated by MOPSO, as shown in Figure 9.

Table 2. Simulation results of the adaptation function for IEEE Std. 80-2000 by MOPSO at grounding grid depths of h = 0.4–0.6 m.

Laying Depth of Grid (m)	Grounding Copper Rod (n)	Grounding Resistance R_g (Ω)
h = 0.4 m	101	1.1897
h = 0.425 m	53	1.1949
h = 0.45 m	34	1.1967
h = 0.475 m	33	1.1960
h = 0.5 m	34	1.1950
h = 0.525 m	34	1.1942
h = 0.55 m	34	1.1934
h = 0.575 m	33	1.1927
h = 0.6 m	28	1.1926

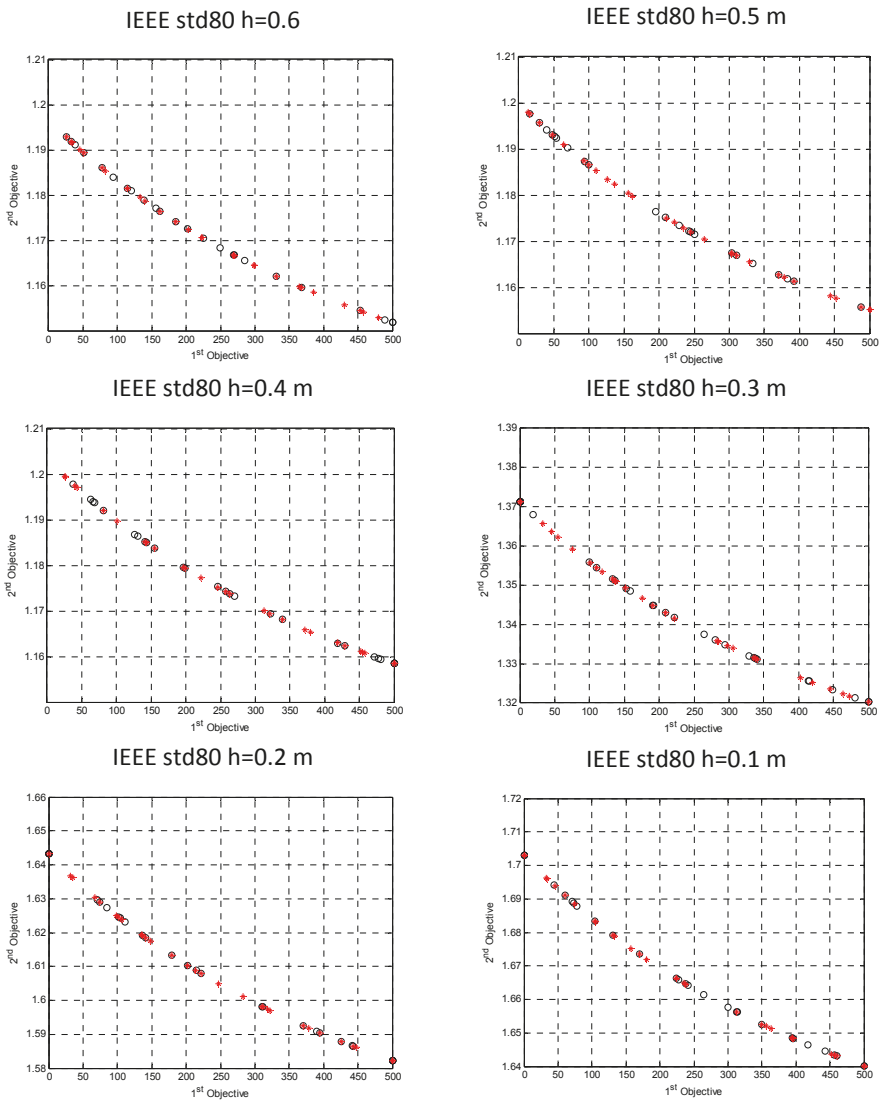

Figure 7. IEEE Std. 80-2000 adaptation function calculated by MOPSO at grounding grid depths of 0.1–0.6 m. The first objective is the number of grounding copper rods; the second objective is the trend of grounding resistance value (Ω) (red stars represent the local l best; black circles represent the global best).

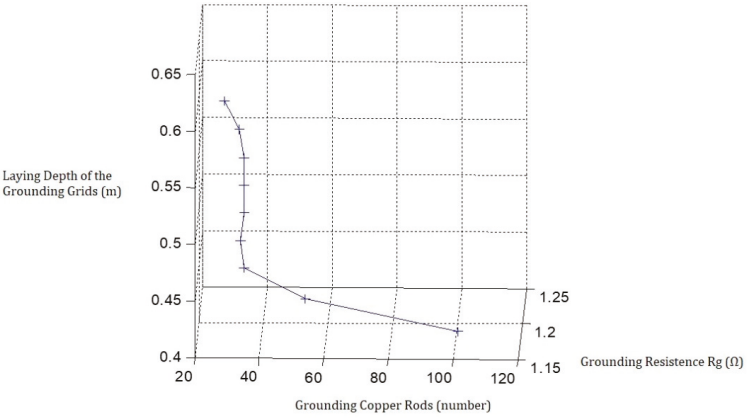

Figure 8. Prediction line of the IEEE Std. 80-2000 adaptation function by MOPSO for h = 0.4–0.6 m.

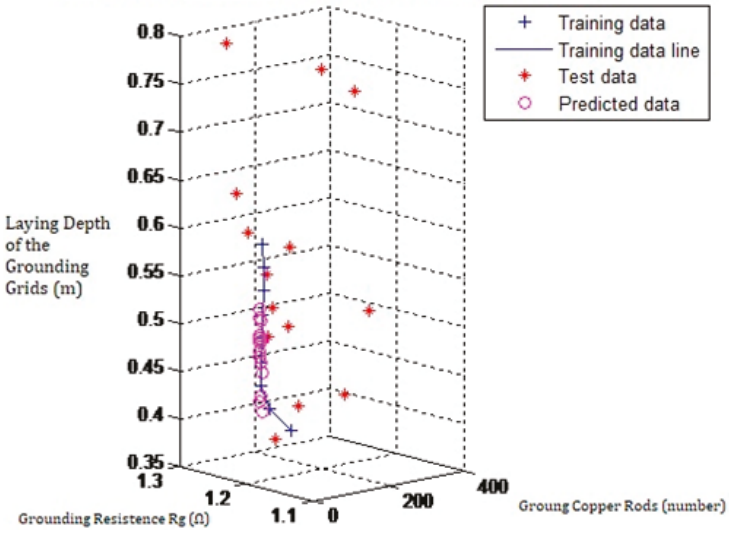

Figure 9. Prediction line calculation results by an RBF neural network.

After the MOPSO calculation, the best result of the IEEE Std. 80-2000 adaptation function was at a grounding depth h = 0.6 m, grounding resistance 1.1926 Ω, and 28 grounded copper rods (the other related parameter data are given in Appendix A). ETAP [21] ver. 4.0.0. is a simulating software. We use the finite element method (FEM) of the ETAP toolbox to construct the grounding copper rod, grounding depth of the grounding grid, and other grounding parameters that are required to perform the simulation [22], as depicted in Figure 10. The simulation results of the best grounding parameters for the prediction line of the RBF neural network grounding system comply with E_m = 686.3 V < $E_{touch50}$ = 775.8 V, E_s = 593.9 V < E_{step50} = 2611 V, and GPR = 4096.2 V > $E_{touch50}$ = 775.8 V, with a considerable safety margin (Figure 11). The result of ETAP simulating a 50 kg human body using I_f was R_g = 1.19 Ω, which is similar to the set of ground resistance values obtained by the MOPSO algorithm at a grounding grid depth of 0.4–0.6 m. Figures 12–14 show 3D plots of the step voltage, touch voltage, and absolute voltage for the ETAP simulations, respectively.

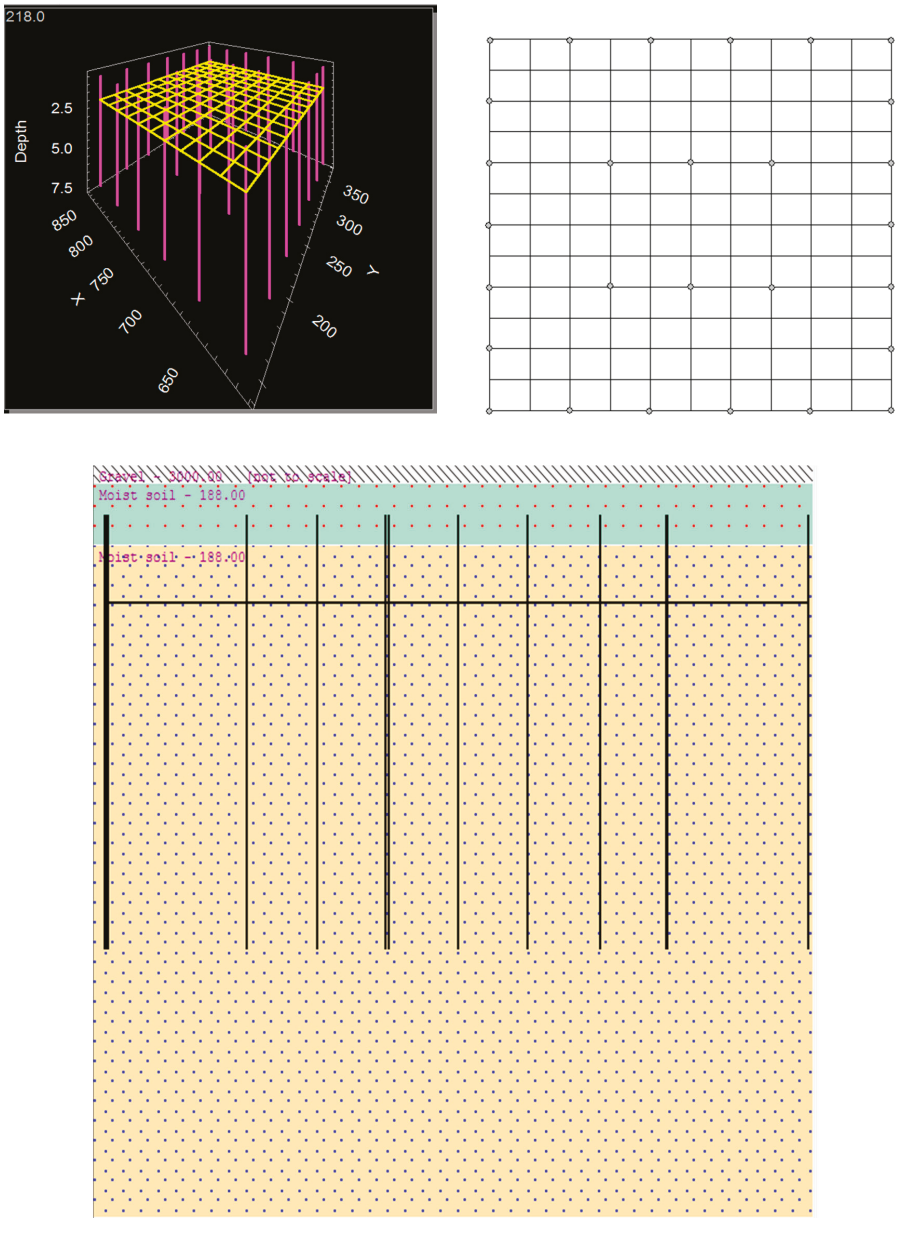

Figure 10. FEM mode grounding network completion diagram.

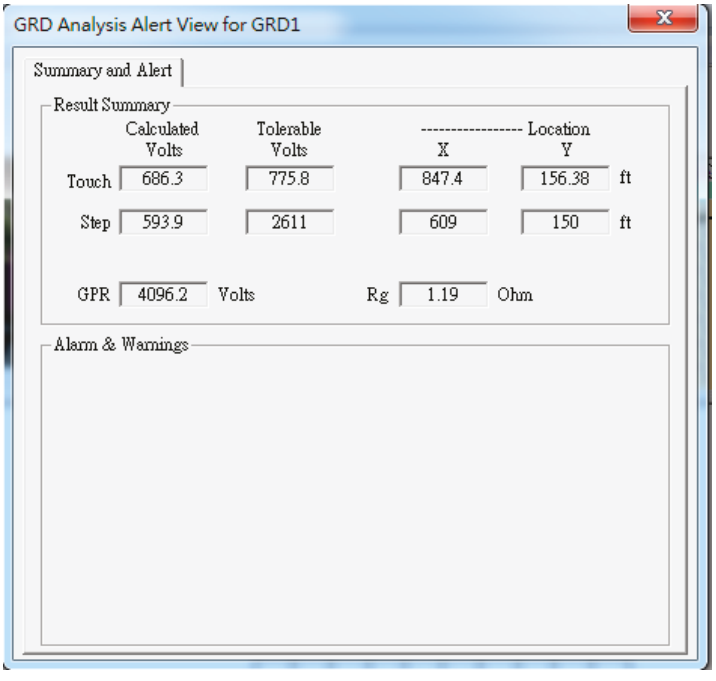

Figure 11. FEM simulation results with the best ground grid parameters predicted by the RBF neural network.

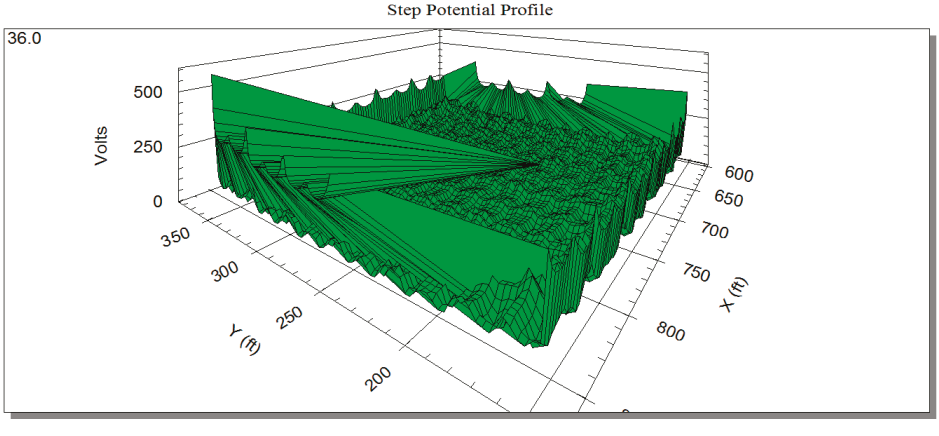

Figure 12. 3D plots of FEM mode step voltage.

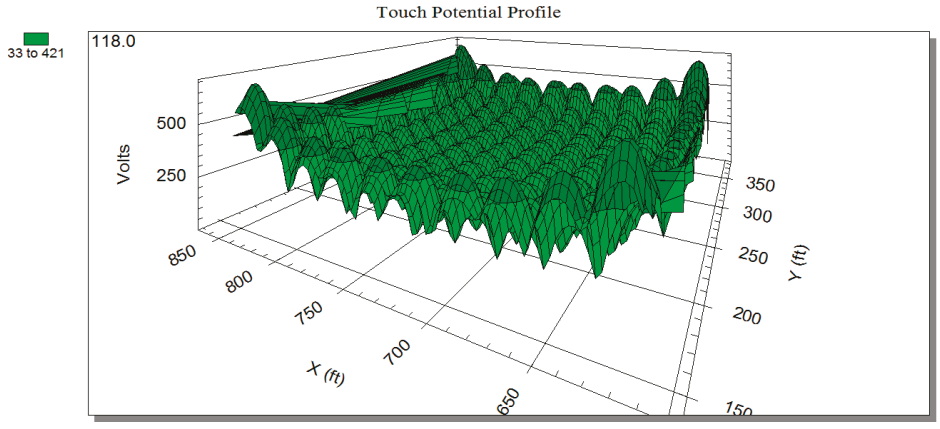

Figure 13. 3D plots of FEM mode touch voltage.

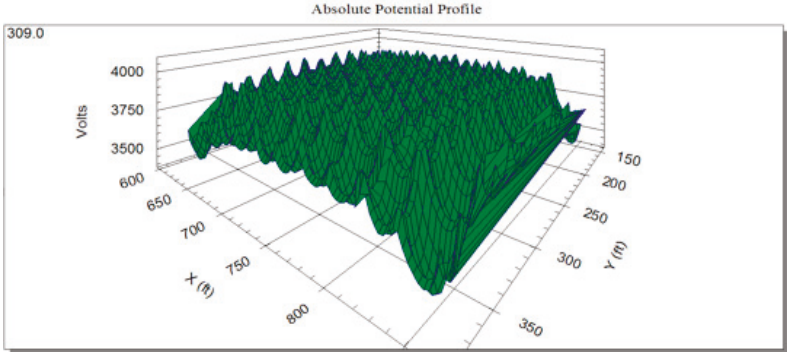

Figure 14. 3D plots of FEM mode absolute voltage.

5. Conclusions

The contributions of this paper may be summarized as follows.

(1) The grounding system data were optimized with numerous set solutions for GA, MOPSO, and Bees for same grounding target values.
(2) By establishing a fuzzy integral table to count the score of the optimization algorithms, IEEE Std 80-2000, and Schwarz, we identified a suitable algorithm for optimizing the grounding system.
(3) Using the RBF neural network as the prediction line of the grounding system is conducive to different soil layer resistivity in different regions, and it can predict the optimal grounding resistance and grounding system cost.

In future, these approaches can be optimized using optimization algorithms for uniform and non-uniform grounding grids as research directions.

Author Contributions: J.-W.P. conceived of the presented idea and designed the project. Y.-C.K. designed the project, carried out the project and wrote the article. S.-P.L. provided basic concepts regarding the topic.

Funding: This study was funded by a grant from Ministry of Science and Technology, Taiwan, under Grant no. MOST 107-2218-E-110-007.

Acknowledgments: The authors appreciate the contributions provided from Taiwan Power Company Research Institute.

Conflicts of Interest: The authors declare no conflict of interest.

Appendix A

A. Target Value of Grounding Resistance		
1. Maximum single-phase grounding malfunction current If		34.3 kA
2. Main neutral point shunt In		0 kA
3. Grounding current shunt rate at fault K		0.9
4. Maximum allowable touch voltage value (consider surface resistance coefficient = 3000 Ω-m) Et = 902 V		
5. Safety coefficient (the fence is not connected to the ground network) α = 5		
6. Target value of grounding resistance (R_e)		
(a) Fault current flowing into the earth through the ground network is Ie = (If − In) × (1 × k)		3430 A
(b) Ground network allowable maximum voltage rise value V = Et × α, 902 × 5 = 4510 V		
(c) $R_e = \frac{V}{Ie}$	1.315 Ω	
B. Design Data		
1. Earth resistance coefficient	176 Ω-m	
2. Grounding wire of the grid	80 cm^2	1650 m
3. Laying area of the grid	75 × 27 = 5025 m^2	
4. Grounding copper rod (diameter:14mm ϕ length: 2.4 m)	82 pieces	
C. Formulas		
$R_{11} = \frac{\rho[\ln\frac{2L}{d} + \frac{LK1}{\sqrt{A}} - K2]}{\pi L}$.		
$R_{22} = \frac{\rho[\ln\frac{2L}{n1} + \frac{2(K1)}{\sqrt{A}(\sqrt{n}-1)} - 1]}{2\pi nL}$.		
$R_{12} = \frac{\rho[\ln\frac{2L}{L} + \frac{LK1}{\sqrt{A}} - K2 + 1]}{\pi L}$.		
$R_g = \frac{R_{11}R_{22} - R_{12}^2}{R_{11} + R_{22} - 2R_{12}}$.		
D. Calculation Results		
Laying depth of grids	0.6 m	
R_{11}	1.25 Ω	
R_{22}	1.72 Ω	
R_{12}	1.17 Ω	
Synthetic resistance R_g	1.238 Ω (design value ≤ target value)	

References

1. IEEE. *Std 80TM-2013: Revision of IEEE Std 80-2000, IEEE Guide for Safety in AC Substation Grounding*; American National Standards Institute (ANSI): Washington, DC, USA, 2015.
2. Dalziel, C.F.; Mansfield, T.H. Effect of frequency on perception currents. *Trans. Am. Inst. Electr. Eng.* **1950**, *69*, 1161–1168. [CrossRef]
3. Dalziel, C.F.; Ogden, E.; Abbott, C.E. Effect of frequency on let-go currents. *Trans. Am. Inst. Electr. Eng.* **1943**, *62*, 745–750. [CrossRef]
4. Alik, B.; Teguar, M.; Mekhaldi, A. Optimization of grounding system of 60/30 kV substation of Ain el-Melh using GAO. In Proceedings of the 4th International Conference on Electrical Engineering (ICEE), Boumerdes, Algeria, 13–15 December 2015.
5. Alik, B.; Teguar, M.; Mekhaldi, A. Minimization of grounding system cost using PSO, GAO, and HPSGAO techniques, IEEE Trans. *Power Deliv.* **2015**, *30*, 2561–2569. [CrossRef]
6. IEC TS 60479-1(1994-09), Effect of Current Passing through Human Body—Part I: General Aspects. Available online: https://webstore.iec.ch/publication/16330 (accessed on 29 September 1994).
7. Dalziel, C.F. Dangerous electric currents. *Trans. Am. Inst. Electr. Eng.* **1946**, *65*, 579–585. [CrossRef]
8. Dalziel, C.F.; Massoglia, F.P. Let-go currents and voltages. *AIEE Trans. Part II Appl. Ind.* **1956**, *75*, 49–56. [CrossRef]
9. Dalziel, C.F.; Lagen, J.B.; Thurston, J.L. Electric shock. *Trans. Am. Inst. Electr. Eng.* **1941**, *60*, 1073–1079. [CrossRef]
10. Dalziel, C.F. Electric Shock Hazard. *IEEE Spectr.* **1972**, *9*, 41–50. [CrossRef]
11. Dalziel, C.F.; Lee, W.R. Reevaluation of lethal electric currents. *AIEE Trans. Ind. Gen. Appl.* **1968**, *IGA–4*, 467–476.
12. El-Tous, Y.; Alkhawaldeh, S.A. An efficient method for earth resistance reduction using the Dead Sea water. *Energy Power Eng.* **2014**, *6*, 47–53. [CrossRef]
13. Schwarz, S.J. Analytical expressions for the resistance of grounding systems. *Trans. Am. Inst. Electr. Eng. Part III Power Appar. Syst.* **1954**, *73*, 1011–1016.
14. Holland, J. *Adaptation in Natural and Artificial System*; University of Michigan Press: Ann Arbor, MI, USA, 1975.

15. Kennedy, J.; Eberhart, R. Particle swarm optimization. In Proceedings of the Fourth IEEE International Conference on Neural Networks, Perth, Australia, 27 November–1 December 1995; pp. 1942–1948.
16. Shi, Y.; Eberhart, R.C. A modified Particle swarm optimization. In Proceedings of the IEEE International Conference on Evolutionary Computation (ICEC), Anchorage, Alaska, 4–9 May 1998; pp. 69–72.
17. Hu, X.; Shi, Y.; Eberhart, R.C. Recent advances in particle swarm. In Proceedings of the IEEE Congresson Evolutionary Computation, Portland, OR, USA, 19–23 June 2004; Volume 2, pp. 90–97.
18. Pham, D.T.; Ghanbarzadeh, A.; Koc, E.; Otri, S.; Rahim, S.; Zaidi, M. *"The Bees Algorithm," Technical Note*; Manufacturing Engineering Centre, Cardiff University: Cardiff, UK, 2005.
19. Zadeh, L.A. Fuzzy sets. *Inform. Control* **1965**, *8*, 338–353. [CrossRef]
20. Chang, Y.W.; Hsieh, C.J.; Chang, K.W.; Ringgaard, M.; Lin, C.J. Training and testing low-degree polynomial data mappings via linear SVM. *J. Mach. Learn. Res.* **2010**, *11*, 1471–1490.
21. Tabatabaei, N.M.; Mortezaeei, S.R. Design of grounding systems in substations by ETAP intelligent software. *Int. J. Tech. Phys. Probl. Eng. (IJTPE)* **2010**, *2*, 45–49.
22. Lee, H.S.; Kim, J.H.; Dawalibi, F.P.; Ma, J. Efficient ground designs in layered soils. *IEEE Trans. Power Deliv.* **1998**, *13*, 745–751.

energies

MDPI

Article

Two States for Optimal Position and Capacity of Distributed Generators Considering Network Reconfiguration for Power Loss Minimization Based on Runner Root Algorithm

Anh Viet Truong [1], Trieu Ngoc Ton [1,2], Thuan Thanh Nguyen [3,*] and Thanh Long Duong [3]

[1] HCMC University of Technology and Education, Ho Chi Minh City 71307, Vietnam; anhtv@hcmute.edu.vn (A.V.T.); tonngoctrieu@gmail.com (T.N.T.)
[2] Thu Duc College of Technology, Ho Chi Minh City 71307, Vietnam
[3] Department of Electrical Supply, Faculty of Electrical Engineering Technology, Industrial University of Ho Chi Minh City, Ho Chi Minh City 71408, Vietnam; thanhlong802003@yahoo.com
* Correspondence: thuan.dap@gmail.com; Tel.: +084-0916-664-414

Received: 27 November 2018; Accepted: 24 December 2018; Published: 29 December 2018

Abstract: Although the distributed generator (DG) placement and distribution network (DN) reconfiguration techniques contribute to reduce power loss, obviously the former is a design problem which is used for a long-term purpose while the latter is an operational problem which is used for a short-term purpose. In this situation, the optimal value of the position and capacity of DGs is a value which must be not affected by changing the operational configuration due to easy changes in the status of switches compared with changes in the installed location of DG. This paper demonstrates a methodology for choosing the position and size of DGs on the DN that takes into account re-switching the status of switches on distribution of the DN to reduce power losses. The proposed method is based on the runner root algorithm (RRA) which separates the problem into two states. In State-I, RRA is used to optimize the position and size of DGs on closed-loop distribution networks which is a mesh shape topology and power is delivered through more than one line. In State-II, RRA is used to reconfigure the DN after placing the DGs to find the open-loop distribution network which is a tree shape topology and power is only delivered through one line. The calculation results in DN systems with 33 nodes and 69 nodes, showing that the proposed method is capable of solving the problem of the optimal position and size of DGs considering distribution network reconfiguration.

Keywords: distributed generations (DGs); distribution network reconfiguration; runner-root algorithm (RRA)

1. Introduction

The distribution system has a radial or mesh configuration but operates in radial state. The power flow in this case flows from the system through the distribution network to the load. Therefore, the transmission of power from the power plant to the consumer will generate losses on the transmission and distribution network. With the new distribution grid structure, due to the involvement of DGs, power flow is not only flowing from the transmission system but also circulating between parts of the distribution network back to the transmission grid. With the involvement of DGs, the distribution network performs better in the task of providing electricity to the consumer, assuring the quality of power, the reliability of the power supply as well as reduced load on the network, improved voltage, reduced power losses, reduced power losses and support grid.

DGs are linked to the electric distributed system. Because of their huge economical benefit and energy security, the appearance of DGs on distribution systems has been rising quickly [1,2].

In addition, for large-capacity DGs using renewable energy sources such as wind and solar cells are often connected to the transmission network. As unfavorable environmental conditions such as a lack of wind or sun can lead to power shortages on the transmission network for supplying to th distribution network, finding solutions to compensate for this shortfall of power are very importance for DG suppliers, especially in the competitive electricity market. One of the most effective solutions to this problem is the installation of small-capacity DGs based on diesel fuel, heavy oil, fuel cell, natural gas, etc. in the DN to compensate for the shortfall of power. Therefore, selection of the optimal installation position for these types of DG to reduce power losses and improve the efficiency of the DN is important. There are several studies which have been proposed for the problem of positioning and size with the goal of reducing losses on the network. The main method based on analytical approaches such as the improved analytical method [3–5] or meta-heuristic algorithms like genetic algorithm (GA) [6,7], particle swarm optimization algorithm (PSO) [8,9] the hybrid big bang-big crunch algorithm (HBB-BC) [10], hybrid teaching–learning-based optimization (HTLBO) [11], invasive weed optimization (IWO) [12], cuckoo search algorithm (CSA) [13], fireworks algorithm (FWA) [14], harmony search algorithm (HSA) [15], and adaptive weighted improved discrete particle swarm optimization (AWIDPSO) [16]. In [3–12], the authors only focused on optimizing the position and capacity of DGs on the DN without considering configuration of the DN which is also an effective technique for reduction power loss in the DN system. This technique called distribution network reconfiguration (DNR) is performed by changing the closed/open status of sectionalizing and tie switches while respecting system constraints [17]. Merlin and Back [18] were the first authors proposed the DNR problem and solved it by the discrete branch-and-bound type heuristic technique. The switch exchange method for loss reduction was proposed by Civanlar et al. [19]. Due to the based on heuristics methods, it is difficult to reach an optimal solution. In recent, new methods based on meta-heuristic have been proposed for finding an optimal network configuration. In [20], the DNR problem for minimizing power loss and enhancing system reliability is solved by an enhanced genetic algorithm. In the study, the crossover and mutation operations have been improved to determine the opened switches. In [21], a binary gravitational search algorithm was proposed for the multi-objective DNR problem. In [22], a binary group search optimization was applied to solve the DNR problem for power loss reduction. In [23], a fireworks algorithm has been performed to reduce power loss and enhance voltage of nodes. In [24], a shuffled frog leaping algorithm was used for minimizing the cost of power loss and power of distributed generators. In [8], a discrete artificial bee colony has presented for the DNR problem. In [25], a particle swarm optimization was presented to handle the DNR problem with multi-objective functions. In [26], a reconfiguration method based on adapted ant colony optimization was proposed for minimization of power loss.

On the DN system-integrated DGs, the operating configuration of the DN system will be changed by using the DNR technique. As the network configuration changes, the location of the DGs which is defined before that can be unsuitable to reduce losses and promote voltage stability or the unsuitable capacity of the DGs will cause large losses on the DN. Therefore, in recent years, some studies have combined both the DG placement problems and distribution network reconfiguration to enhance the effectiveness of the electric distribution system [13–16]. Although both techniques contribute to reduce power loss, obviously the DG placement problem is a design problem of the distribution network which is used for a long-term purpose while the distribution network reconfiguration problem is an operational problem of the distribution network which is used for a short-term purpose. In this situation, the optimal value of position and capacity of DGs is a value which must be not affected by the changing of operational configuration because changing the status of switches is easier than changing the location of DG as they are installed. This requirement is unnecessary by solving simultaneously both problems because the optimal position and size of DG will be change when the location of open switches on the DN change. In addition, by solving combined problems, the parameters of the optimization algorithm will be become more complex than those of solving individual problems.

An illustration for this point can be seen in that the control variables will be lengthier and it will take more time and more iterations for finding optimal solution.

Therefore, in this article we propose the method of determining the position and size of the DGs on the DN, considering the problem of distribution network reconfiguration with the goal of reducing power losses. The proposed method of determining the optimal location and size of DGs and operational configurations are implemented in two states based on the runner-root algorithm (RRA). In State-I, RRA is used to identify the optimal position and capacity of the DGs on the closed-loop distribution network. In State-II, the RRA is used to find the optimal operating configuration of the system. By using the proposed method for the combined problem of placement of the DG and re-switching, in the obtained results, the position and size of the DG is not affected by the location of open switches. It means that the design problem which is the placement DG problem is not be depended by the operational problem which is the re-switching problem. In addition, by solving individual problems, it also helps the optimization algorithms be more effective at finding the optimal solution in two states. The comparison results on 33 and 69 nodes systems with the method of solving simultaneously the combined problem and other studied methods have shown that the proposed method is capable of solving the problem of the optimal position and size of DGs considering distribution network reconfiguration. In the following section, the proposed distribution network reconfiguration method for the optimal location and size of the DG considering network reconfiguration for power loss is presented. The overview of RRA for the problem is demonstrated in Section 3. Section 4 presents the calculated results of the suggested algorithm and the conclusion are presented in Section 5.

2. Problem Formulation

The distribution networks are usually designed in a mesh structure but they are operated in open status. The change of power loss when they are transferred from the mesh status to the radial status is described as follows:

The distribution network reconfiguration problem will be demonstrated by the simple network shown in Figure 1. If the switch MN is closed, the system is operating in the mesh network configuration. Calling the current on the branch ith is I_i (i = 1, . . . , nbr). When the switch MN is opened, assuming that the current on the branches of the OM decreases by I_{MN}, the current on the branches of ON will increase by I_{MN}. Then, power loss of the mesh network (ΔP^{mesh}) and power loss of the radial network (ΔP^{radial}) are expressed by Equations (1) and (2) respectively.

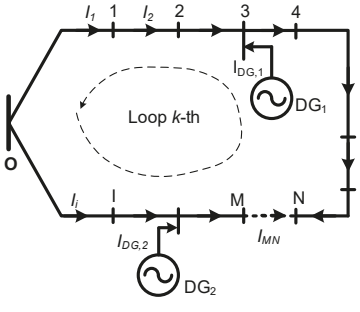

Figure 1. One loop distribution network.

$$\Delta P^{mesh} = \sum_{i \in OM}^{nbr} R_i I_i^2 + R_{MN} I_{MN}^2 + \sum_{i \in ON}^{nbr} (-I_i)^2 R_i \quad (1)$$

$$\Delta P^{radial} = \sum_{i \in OM}^{nbr} R_i (I_i - I_{MN})^2 + \sum_{i \in ON}^{nbr} R_i (I_i + I_{MN})^2 \quad (2)$$

The effect of the reconfiguration (change in power losses in the loop) can be obtained by using (3):

$$\begin{aligned} \Delta P^{radial} - \Delta P^{mesh} &= \sum_{i \in OM}^{nbr} R_i \left(I_i^2 - 2 I_{MN} I_i + I_{MN}^2\right) + \sum_{i \in ON}^{nbr} R_i \left(I_i^2 + 2 I_{MN} I_i + I_{MN}^2\right) \\ &- \sum_{i \in OM}^{nbr} R_i I_i^2 - R_{MN} I_{MN}^2 - \sum_{i \in ON}^{nbr} (I_i)^2 R_i \end{aligned} \quad (3)$$

$$\begin{aligned} \Delta P^{radial} - \Delta P^{mesh} &= \sum_{i \in OM}^{nbr} R_i \left(-2 I_{MN} I_i + I_{MN}^2\right) + \sum_{i \in ON}^{nbr} R_i \left(2 I_{MN} I_i + I_{MN}^2\right) - R_{MN} I_{MN}^2 + R_{MN} I_{MN}^2 \\ &- R_{MN} I_{MN}^2 \end{aligned} \quad (4)$$

Short (4), resulting in (5):

$$\begin{aligned} \Delta P^{radial} - \Delta P^{mesh} &= I_{MN}^2 \left(\sum_{i \in OM}^{nbr} R_i + R_{MN} + \sum_{i \in ON}^{nbr} R_i \right) \\ &- 2 I_{MN} \left(\sum_{i \in OM}^{nbr} R_i I_i + R_{MN} I_{MN} - \sum_{i \in ON}^{nbr} R_i I_i \right) \end{aligned} \quad (5)$$

Set $R_{Loop} = \sum_{i \in OM}^{nbr} R_i + R_{MN} + \sum_{i \in ON}^{nbr} R_i$ and short (5), resulting in (6):

$$\Delta P^{radial} - \Delta P^{mesh} = I_{MN}^2 R_{Loop} - 2 I_{MN} \left(\sum_{i \in OM}^{nbr} R_i I_i + R_{MN} I_{MN} - \sum_{i \in ON}^{nbr} R_i I_i \right) \quad (6)$$

On the other hand, due to the power flow on the radial network, the current on the branches does not depend on the impedance of the branches, it only depends on the consumed power at the nodes. So it can be assumed that there exists a network with impedance of branches replaced by corresponding branch resistance, and the power loss of this network still is calculated as a normal network by (2). Therefore, when closing the switch MN, according to the Kirchhoff's second law:

$$\sum_{i \in OM}^{nbr} R_i I_i + R_{MN} I_{MN} - \sum_{i \in ON}^{nbr} R_i I_i = 0 \quad (7)$$

So (6) will be become:

$$\Delta P^{radial} - \Delta P^{mesh} = I_{MN}^2 R_{Loop} \quad (8)$$

It can be seen from (8), the power loss in the mesh network is the most minimum. In the mesh network, if there exists a branch whose current is zero ($I_{MN} = 0$) then opening this branch the power loss in the system will be minimal and the mesh network will become a radial network. However, this case is impossible because it is difficult to maintain power flow in the mesh network that the current of one of the branches is zero. Therefore, only by minimizing power loss of the radial network does this value drop nearly to the value of power loss in the mesh network. Reality has shown that in the distribution network reconfiguration problem for power loss reduction, in the obtained optimal configuration, the open switches are usually located on the branches with very small currents if these switches are closed again.

Similarly, in a distribution network integrating DG, once the optimal location and size of DG have been identified on the mesh network for minimizing power loss; the value of power loss in this case will be the smallest that the system can achieve. Then, if the branches with the smallest current

are identified for opening, the mesh network will become a radial network and the power loss is approximately equal to the power loss in the mesh network with DG. Therefore, the problem can be divided into two states. The first state will determine the optimal position and capacity of the DG on the mesh network to minimize power loss. The second state determine the switches with minimum currents for opening to maintain radial topology. The result obtained from the second state are also the result of the distribution network reconfiguration for minimizing power loss. Furthermore, on the complex network with multiple loops, it is difficult to determine the branches with minimum currents due to the mutual effects among the loops and the order of the switch operation. So, in the second state the problem of re-switching provides a way to find out the radial network configuration for minimizing power loss.

In addition, in order for the position and capacity of DG to be not affected by changing the configuration of network, the problem of optimizing the location and capacity of the DG for power loss minimization are implemented in the mesh network. Once the optimal position and capacity of the DG have been determined on the mesh network, the identification of the open switches will be performed to maintain the radial operation condition. Implementing the two separate optimal phases not only helps the long-term design problem (optimization problem of location and capacity of DG) to not be affected by the short-term problem (problem of reconfiguration) but also supports the optimal algorithms solving the problem in a simpler way because they do not have to perform optimally at the same time as many variables which are different characters.

Therefore, the problem of determining the position and size of DGs considering network reconfiguration is divided to two stages as follows:

The first stage (State-I): determine the position and size of DGs to minimize power losses on the mesh network;

The second stage (State-II): determine the radial operating configuration of after installing DGs on the mesh network.

The objective function for the two stages is shown in (9):

$$P_{loss} = \sum_{i=1}^{nbr} R_i \times \left(\frac{P_i^2 + Q_i^2}{V_i^2} \right) \tag{9}$$

There are three constraints of the problem as follows:

(1) The voltage at each node and the current at each branch must be in their acceptable limit for each stage:

$$V_{min} \le V_i \le V_{max};\ \mathrm{i} = 1, 2, \ldots, nbus \tag{10}$$

$$0 \le I_i \le I_{max,i};\ \mathrm{i} = 1, 2, \ldots, nbr \tag{11}$$

(2) The radial configuration of electric distribution system must be satisfied and load nodes must be connected to the power for the second stage.

(3) Distributed generation capacity limits must be maintained for the first stage:

$$0 \le P_{DGi} \le P_{DGmax,i};\ \mathrm{i} = 1, 2, \ldots, ndg \tag{12}$$

3. Runner Root Algorithm (RRA)

The RRA is a recently developed algorithm based on ideas from the plants bred via runners and roots [27]. In this work RRA has outperformed other algorithms via 25 benchmark functions. In RRA, two tools for exploitation is equipped consist of the roots mechanism and the elite selection mechanism. The former is designed to search around the best solution of current generation. The latter is designed to ensure the best solution of current generation is transferred to the next generation. For exploration, RRA is also equipped two tools consist of random jump of mother plants and re-initialization. In the former, each candidate solution is a random change to jump to any point in the search space. In the

latter, the algorithm will be restarted after no considerable improvement in the fitness function after certain number of generations. Two tools equipped for exploitation and exploration mechanisms help RRA to be efficient at finding a global solution. In addition, in recently RRA has been applied for solving the network reconfiguration problem and it has demonstrated the advantages compared to other methods [28]. To implement the algorithm, reference [27] has used the following three rules:

— The mother plants are generated the daughter plants in new locations through their runners to explore new resources.
— The plants generate roots (runner) and root hairs (root) randomly to exploit new resources in new locations.
— The daughter plants grows rapidly and produce more new plants at rich resources. Otherwise, if the daughter plants move toward poor resources, they will die.

Based on the three rules, the RRA method is implemented for optimizing of position and capacity of DGs considering network reconfiguration as follows.

3.1. State-I: Optimizing of Position and Capacity of DGs in the Mesh Electric Distribution Network Using RRA

Step 1: Initialization

In the first stage, position and capacity of DGs is considered as a mother plant. Therefore, the mother plants are randomly initialized at the starting point of the algorithm as follows:

$$X_{mother,k}\ (\mathrm{i}) = \left\{ round[2 + rand \times (\mathrm{Lo}_{max,d} - 2)], P_{min,d} + rand \times (P_{max,d} - P_{min,d}) \right\} \tag{13}$$

where $k = 1, \ldots, N, i = 1, \ldots,\ Iter_{1,max}$ and $d = 1, \ldots, ndg$.

From the population of mother plants which are location and the size of DGs, the bus data of the DN is updated, and the power flow is run by using the Newton–Raphson method to obtain power loss, node voltages and branch currents. Then, the value of the fitness function is calculated by using (9). The best plant (X_{best}) of the population is determined.

Step 2: Generation of daughter plants

In this step, each daughter plant is generated by corresponding the mother plant. Noted that, the first plant is renewed by the best plant of the early generation. In the case of the first iteration, the first plant is the best mother plant of the randomly initialized population.

$$X_{daughter,k}(i) = \begin{cases} X_{best}\ (\mathrm{i}-1) & ,k = 1 \\ X_{mother,k}(i) + d_{runner} \times rand, & k = 2, \ldots, N \end{cases} \tag{14}$$

Then, the control variables represented for the location of DG are rounded to the integer values and the bus data of the DN is updated and the power flow is run by using the Newton–Raphson method to obtain power loss, node voltages and branch currents. The value of the fitness function is calculated by using (9). The best plant (X_{best} (i)) is determined again.

Step 3: Narrow search using big and small distance from the best plant

In step 3, if there are not a considerable improvement of the best plant in two iterations (i − 1)th and ith which is presented by a *RI* index, which is calculated by Equation (15). This step will be performed to generate new plants round the current best plant. Hence, the best plant is updated as follows:

$$X_{daughter,k}(i) = \begin{cases} X_{best}\ (\mathrm{i}-1) & ,k = 1 \\ X_{mother,\,k}(i) + d_{runner} \times rand, & k = 2, \ldots, N \end{cases} \tag{15}$$

where $f(X_{best}(i-1))$ and $f(X_{best}(i))$ are the fitness function value of the best plant in the generation (i − 1)th and the generation ith.

Narrow the search with large distance: in this procedure N_{DG} new plants are generated by adjusting the current best plant based on (16):

$$X_{perturbed,d} = round[vec\{1, 1 \ldots, 1, 1, 1 + d_{runner} \times rand_d, 1, \ldots, 1\} \times X_{best}(i)] \quad (16)$$

where $d = 1, \ldots, N_{DG}$; $vec\{1, 1 \ldots, 1, 1, 1 + d_{runner} \times rand, 1, \ldots, 1\}$ is a vector with the dth element is updated by $1 + d_{runner} \times rand_d$ and the remaining elements are equal to 1.

Narrow search with small distance: In this step, there are also N_{DG} new plants produced by using (17):

$$X_{perturbed,d} = round[vec\{1, 1 \ldots, 1, 1, 1 + d_{root} \times rand_d, 1, \ldots, 1\} \times X_{best}(i)] \quad (17)$$

From the $2 \times N_{DG}$ new daughter plants, the bus data of the DN is updated and the power flow is run by using the Newton–Raphson method to obtain the fitness function value based on (9). At the end of the step, the best solution (X_{best} (i)) is renewed again.

Step 4: Generation of new population of plants for next iteration

At the end step of each generation, the new mother plants for the next iteration are selected from the plants generated in step 3 based on the roulette wheel technique.

Step 5: Avoiding the local optimal solution

In this step, if there is not a considerable improvement of the best plant after the number of predefined iterations ($stall_{max}$), the RRA is restarted by generating random mother plants similar to step 1, otherwise it jumps to step 2.

3.2. Stage-II: Network Reconfiguration after Installing Distributed Generators (DGs) Using RRA

In the second stage, each radial configuration of the DN which is presented by position of open switches. Therefore, the position of open switches is considered as a mother plant and the mother plants are randomly generated as follows:

$$X_{mother,k}(\mathrm{i}) = round\left[X_{low,d} + rand \times \left(X_{high,d} - X_{low,d}\right)\right] \quad (18)$$

where $d = 1, \ldots, N_{SW}$, $X_{low,d} = 1$ and $X_{high,d}$ is the number of switches in the mesh loop dth of the DN. Noted that each fundamental loop contains the number of switches that is formed by that loop.

Similar to the step 2 of the stage-I, each daughter plant is generated by corresponding the mother plant as (19). It is noticed that due to the daughter plant population being represented by open switches all of daughter plants are rounded to integer value. Then the line data of the DN is updated and the power flow is run to obtain the fitness function value based on (9). At the end of the step, the best solution (X_{best} (i)) is renewed again.

$$X_{daughter,k}(i) = \begin{cases} X_{best}\ (\mathrm{i} - 1) & , k = 1 \\ round[X_{mother,k}(i) + d_{runner} \times rand], k = 2, \ldots, N \end{cases} \quad (19)$$

Similar to step 3 of state-I, in the second state, $2 \times N_{sw}$ new plants are generated if this step will be performed by Equations (20) and (21). From Equations (20) and (21), it can be seen that all control variables are also rounded to the nearest integer to represent open switches.

$$X_{perturbed,d} = round[vec\{1, 1 \ldots, 1, 1, 1 + d_{runner} \times rand_d, 1, \ldots, 1\} \times X_{best}(i)] \quad (20)$$

$$X_{perturbed,d} = round[vec\{1, 1 \ldots, 1, 1, 1 + d_{root} \times rand_d, 1, \ldots, 1\} \times X_{best}(i)] \quad (21)$$

The step of production of mother plants for next iteration and step of escaping the local solution are definitely similar to them in the first stage. The flowchart of the proposed RRA for the problem

of optimization of the position and capacity of DGs considering re-switching problem is presented in Figure 2.

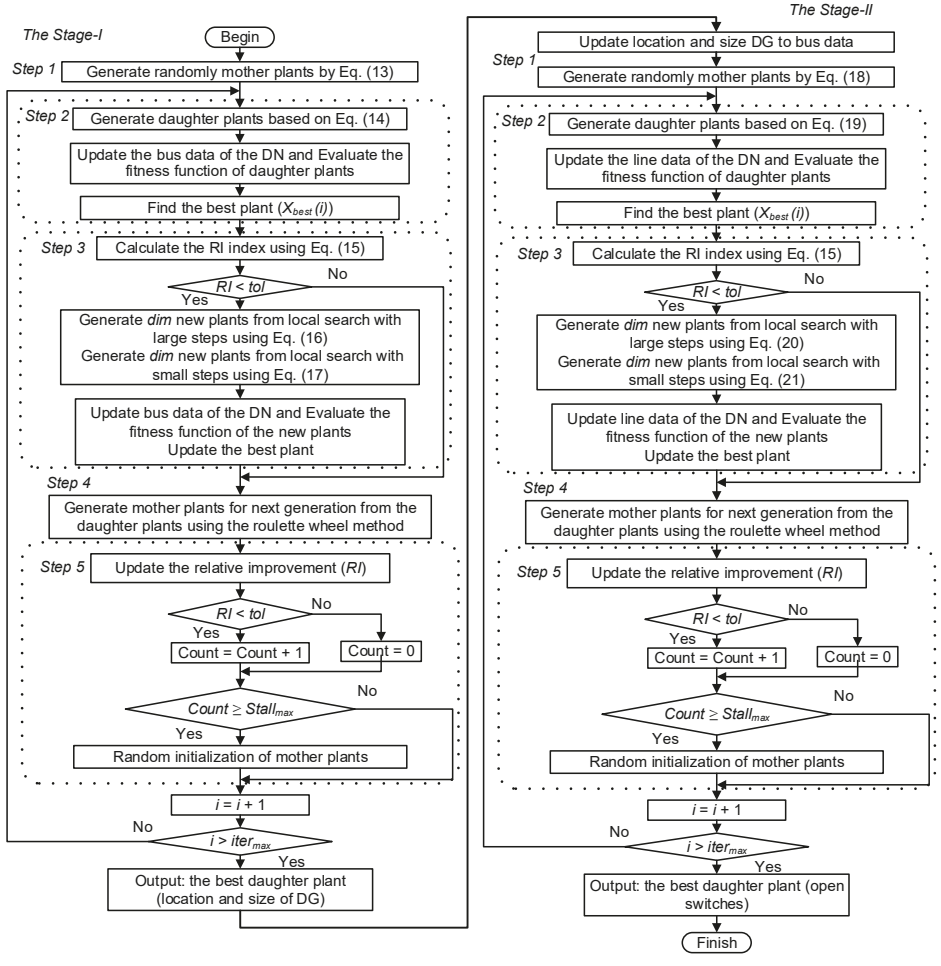

Figure 2. The flowchart for determining the position and capacity of distributed generators (DGs) in the mesh electric distribution considering re-switching problem based on the runner root algorithm (RRA) method.

4. Numerical Results

The proposed method has been evaluated on two electric distribution networks including of 33 nodes and 69 nodes. In each system, three DGs with maximum capacity of 2 MW are installed. The proposed method is implemented in Matlab software on a personal computer with CPU Intel Core i3 4160 @ 3.6 GHz, 1 CPU, 8 GB, Windows 7 SP1 (64-bit). To show the superiority of the proposed method, the method of installation of DGs and reconfiguration of network simultaneously based on RRA is also implemented and compared with the proposed method using two states. The parameters of the RRA, which are determined by numerous trial executions and applied for two systems are presented in Table 1.

Table 1. The parameters of the RRA for the 33 nodes and 69 nodes distribution network system.

System	The 33 and 69 Nodes		
Item	State-I	State-II	Simultaneous
Mother plants	30	30	30
Maximum iterations	300	150	1000
Dimension	6	5	11
d_{runner}	4	4	4
d_{root}	2	2	2
$stall_{max}$	50	50	50

4.1. The 33 Nodes System

The 33 nodes system presented in Figure 3, consists 5 tie switches and 37 branches [29]. In a normal operation, switches {33, 34, 35, 36, and 37} are opened.

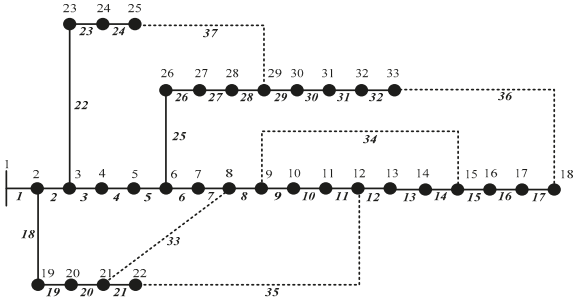

Figure 3. The 33 nodes distribution system.

From Table 2, power loss is decreased from 202.68 kW in the initial configuration to 41.9051 kW and 53.3129 kW using State-I and the State-II, respectively. The result from State-I shows that, the power loss is minimum because this is power loss caused by the mesh network. After using State-I to find the position and capacity of DGs in the mesh network, State-II is used to determine the open switches for radial operation, in which the open switches gained in the optimal configuration are {33, 34, 11, 30, 28}. So, the power loss is increased to 53.3129 kW compared with 41.9051 kW in State-I. However, compared with the method of simultaneous reconfiguration and placing DGs, these results are nearly the same as the results gained by the simultaneous reconfiguration and placing DGs method. The minimum power loss obtained by the simultaneous reconfiguration and placing DGs method is 50.825 kW which is only 2.4879 kW lower than the power loss caused by the optimum solution gained from the proposed method. In addition, the proposed method takes 34.39 seconds to execute the problem for both states, which is 46.39 seconds shorter than the simultaneous reconfiguration and placing DGs method. Moreover, it can be also be seen from Table 2 that the average values of the fitness function in State-I and State-II are closer the minimum value of the fitness function than that in the simultaneous reconfiguration and placing DGs method. This demonstrates that the proposed method also helps the RRA easily determine the optimal result for the problem.

The convergence behaviors for State-I and the State-II are presented Figures 4 and 5. The voltage profiles of the initial, State-I, State-II and the simultaneous reconfiguration and placing DGs method are presented in Figure 6. As shown in the figure, the voltage magnitude at all nodes has been advanced after using the suggested method and the voltage profile of State-II is nearly the same with the voltage profile of the simultaneous reconfiguration and placing DGs method.

Table 2. Performance of the suggested technique on the 33-node system.

Item	Initial	Proposed Method Based on RRA		Simultaneous Rec. and DG Based on RRA
		State-I	State-II	
Switches opened	33, 34, 35, 36, 37	None	33, 34, 11, 30, 28	33, 34, 11, 30, 28
Capacity of DG in MW (Bus number)	None	1.1326 (25), 0.8146 (32), 1.1011 (8)	1.1326 (25), 0.8146 (32), 1.1011 (8)	1.12095 (25), 0.87689 (18), 0.969711 (7)
Power loss (kW)	202.68	41.9051	53.3129	50.825
% Loss reduction	-	79.32	73.70	74.92
Max of fitness	-	46.2885	59.5526	64.0135
Mean of fitness	-	42.6949	55.4702	56.0123
Standard deviation (STD) of fitness	-	1.17681	2.50883	3.20373
CPU time (second)	-	25.0779	9.3156	80.7789
Average iterations	-	245.2	18.5	751.9

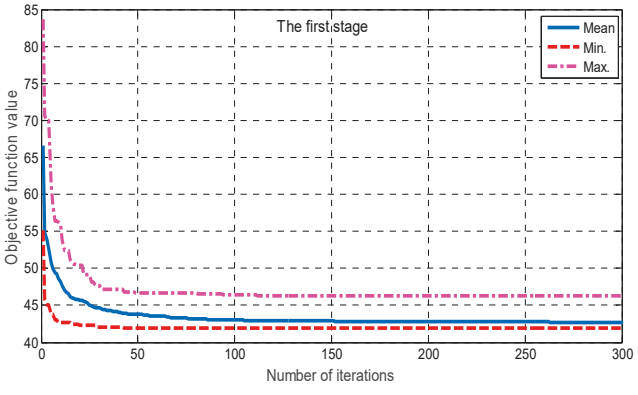

Figure 4. The convergence of RRA in the first stage over 50 independent runs for the 33-node system.

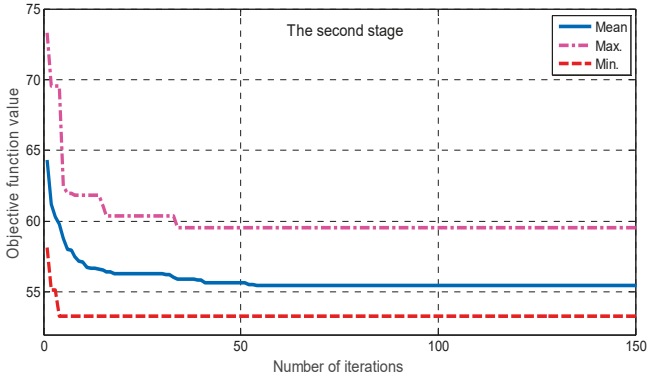

Figure 5. The convergence of RRA in the second stage over 50 independent runs for the 33-node system.

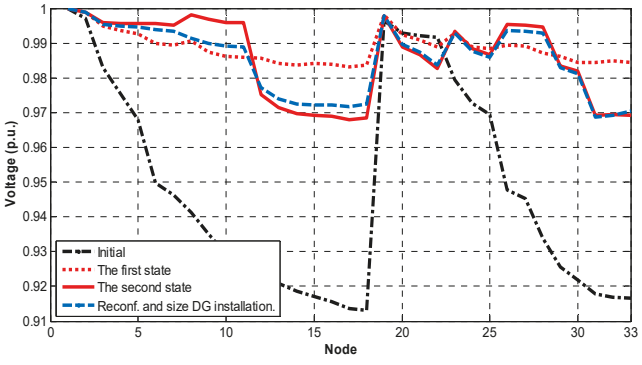

Figure 6. Voltage profiles in four cases of the 33-node system.

Comparison results with some of the methods are presented in Table 3. From the table, the loss reduction in percentage for the proposed method based on RRA is 0.05 higher than the result gained by CSA and 0.57 higher than the result gained by AWIDPSO, which is the method of solving the reconfiguration and simultaneous position and capacity of DGs. However, the performance of the proposed RRA is better than HSA and FWA. The percentage loss reduction for RRA, FWA and HSA is 73.70, 66.89 and 63.95, respectively. Note that the methods based on FWA and HSA have used different methods to pre-select the nodes for DGs installation on the initial radial network before optimization of the size of the DGs and reconfiguration.

Table 3. Comparison of results on the 33-node system with the different methods.

Item	Proposed Method—RRA	CSA [13]	FWA [14]	HSA [15]	AWIDPSO [16]
Switches opened	33, 34, 11, 30, 28	33, 34, 11, 31, 28	7, 14, 11, 32, 28	7, 14, 10, 32, 28	7, 10, 13, 28, 32
Capacity of DG (in MW) (Bus number)	1.1326 (25), 0.8146 (32), 1.1011 (8)	0.8968 (18), 1.4381 (25), 0.9646 (7)	0.5367 (32), 0.6158 (29), 0.5315 (18)	0.5258 (32), 0.5586 (31), 0.5840 (33)	1.1215 (22), 1.3816 (23), 0.6425 (05)
Power loss (kW)	53.3129	53.21	67.11	73.05	52.15
% Loss reduction	73.70	73.75	66.89	63.95	74.27

4.2. The 69 Nodes System

The 69 nodes distribution system shown in Figure 7 includes 73 branches and 5 tie switches [30]. The performance of the proposed approach on the 69 nodes system is presented in Table 4.

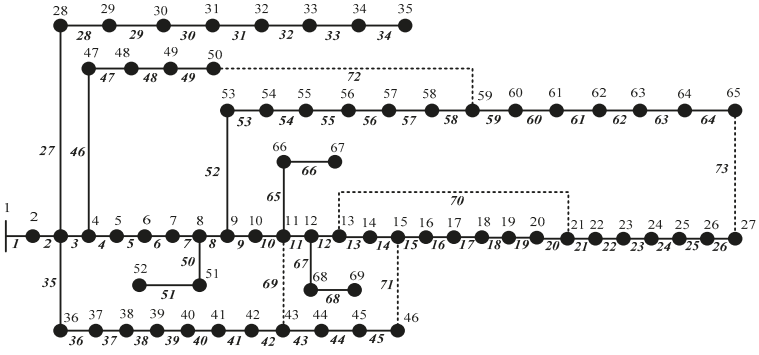

Figure 7. The 69 nodes distribution system.

Table 4. Performance of the suggested technique on the 69 nodes system.

Item	Initial	Proposed Method Based on RRA		Simultaneous Rec. and DGs Based on RRA
		State-I	State-II	
Switches opened	69, 70, 71, 72, 73	None	69, 70, 12, 55, 63	69, 70, 14, 55, 61
Size of DG (in MW) (Bus number)	None	1.6175 (61), 0.7710 (50), 0.6752 (21)	1.6175 (61), 0.7710 (50), 0.6752 (21)	0.516112 (64), 1.45167 (61) 0.53696 (11)
Power loss (kW)	224.89	28.8875	39.31	35.1929
% Loss reduction	-	87.15	82.52	84.35
Max of fitness	-	31.3996	42.8777	48.622
Mean of fitness	-	29.3798	40.5443	40.3116
STD of fitness	-	0.7229	1.46845	3.25004
CPU time (second)	-	32.9654	27.2612	244.4863
Average iterations	-	240.15	71.05	807.15

From the table, in the initial configuration, power loss is 224.89 kW, which is decreased to 28.8875 kW, and 39.31 kW using State-I and the State-II, respectively. It can be seen that compared with the method of simultaneous reconfiguration and placing DGs, these results are nearly the same as the results gained by the simultaneous reconfiguration and placing DGs method. The minimum power loss obtained by the simultaneous reconfiguration and placing DGs method is 35.1929 kW which is only 4.1171 kW lower than the result obtained from the proposed method. In addition, in terms of CPU times, the proposed method takes 60.23 s to obtain the results for both states, which is 184.26 seconds lower than the simultaneous reconfiguration and placing DGs method. In addition, Table 4 show that the average values of the fitness function in State-I and the State-II are closer to the minimum value of the fitness function than that in the simultaneous reconfiguration and placing DGs method.

The convergence behaviors for State-I and State-II are presented Figures 8 and 9. The voltage profiles of four cases are contrasted and shown in Figure 10. As illustrated in this figure, it is observed that the voltage magnitude at all nodes has been advanced after using the suggested method, and the voltage profile of State-II is nearly the same with the voltage profile of the simultaneous reconfiguration and placing DGs method.

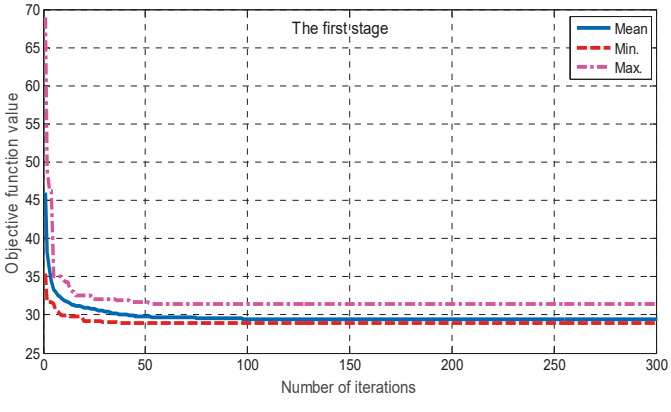

Figure 8. The convergence of RRA in the first stage over 50 independent runs for the 69-node test system.

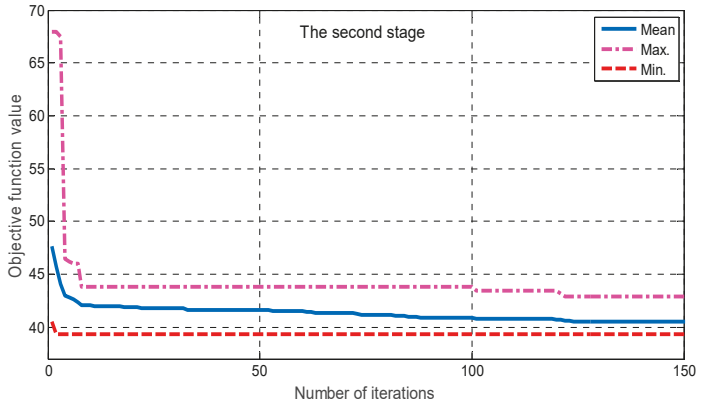

Figure 9. The convergence of RRA in the second stage over 50 independent runs for the 69-node test system.

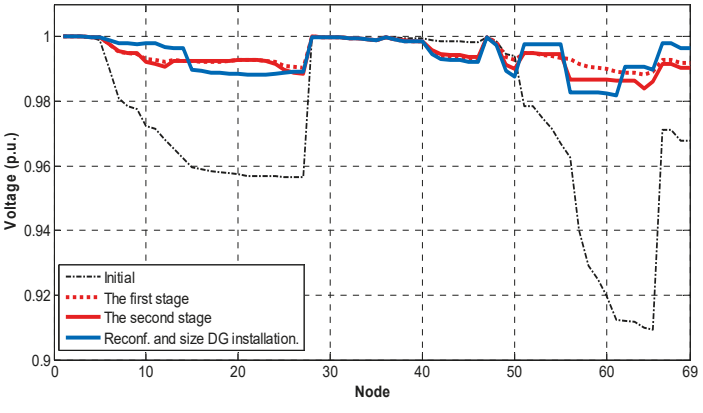

Figure 10. Voltage profiles in four cases of the 69 nodes system.

Comparison results with FWA and HSA are presented in Table 5. The results showed that in the 69 nodes network system, the percentage loss reduction for RRA method is 1.02 higher than the result gained by CSA and these results are nearly to the same with the results gained by the FWA method with 82.55% and compared with HSA, it is better.

Table 5. Comparison results on the 69 nodes system with the different methods.

Item	Proposed Method	CSA [13]	FWA [14]	HSA [15]
Switches opened	69, 70, 12, 55, 63	69, 70, 14, 58, 61	69, 70, 13, 55, 63	69, 17, 13, 58, 61
Size of DG (in MW) (Bus number)	1.6175 (61), 0.7710 (50), 0.6752 (21)	0.5413 (11), 0.5536 (65), 1.7240 (61)	1.1272 (61) 0.2750 (62) 0.4159 (65)	1.0666 (61) 0.3525 (60) 0.4257 (62)
Power loss (kW)	39.31	37.02	39.25	40.3
% Loss reduction	82.52	83.54	82.55	82.08

5. Conclusions

In this article, the method based on RRA has been successfully applied for optimizing the position and capacity of DGs taking into account reconfiguration of the network reconfiguration. The objective function is to minimize the power loss of the system. The main idea of the proposed method divided

the problem into two states which consist of the optimization of the position and size of DGs on closed-loop distribution networks and the optimization of the operating structure of the DN after placing the DGs. In the both states, the RRA is used to determine the best solution. The calculated results show that the suggested method is capable of determining an optimal solution and is better than compared techniques in literature. The comparison results with the method of solving simultaneously the combined problem show that the power loss obtained from the proposed method is very close to that from the method of solving simultaneously the combined problem. Although the optimal results obtained by proposed method are slightly worse than those from method of solving simultaneously the combined problem but using the proposed method, the results of the location and size of the DG obtained, which is the design problem, are not affected by the results of the location of open switches on the DN, which is the operation problem. In addition, the calculated results have also shown that the proposed method can solve the problem faster compared with the method of reconfiguration and simultaneous position and capacity of DGs. Therefore, the suggested method is worthy of consideration for solving the position and capacity of DGs considering the network reconfiguration problem.

Author Contributions: Conceptualization, A.V.T.; Methodology, T.T.N.; Project administration, A.V.T.; Software, T.T.N.; Validation, T.N.T. and T.T.N.; Writing—original draft, T.N.T.; Writing—review and editing, T.T.N. and T.L.D.

Conflicts of Interest: The authors declare no conflict of interest.

Nomenclature

round	round a number to the nearest integer
$Lo_{max,d}$	maximum bus in the system which is able to install DG
$P_{min,d}$	minimum power of DG *d*th
$P_{max,d}$	maximum power of DG *d*th
rand	random figure in the range between 0 and 1
N	population of plant
$Iter_{1,max}$	maximum figure of iterations in the first stage
N_{SW}	number of open switches which form a radial configuration of network.
X_{best}	best daughter plant in population of plant
d_{runner}	length of the runner
d_{root}	length of the root
tol	relative improvement of a best plant in two iterations
nbr	number of branches
nbus	number of buses
ndg	number of DGs connected to the system

References

1. Hung, D.Q.; Mithulananthan, N.; Bansal, R.C. An optimal investment planning framework for multiple distributed generation units in industrial distribution systems. *Appl. Energy* **2014**, *124*, 62–72. [CrossRef]
2. Doagou-Mojarrad, H.; Gharehpetian, G.B.; Rastegar, H.; Olamaei, J. Optimal placement and sizing of DG (distributed generation) units in distribution networks by novel hybrid evolutionary algorithm. *Energy* **2013**, *54*, 129–138. [CrossRef]
3. Hung, D.Q.; Mithulananthan, N. Multiple distributed generator placement in primary distribution networks for loss reduction. *IEEE Trans. Ind. Electron.* **2013**, *60*, 1700–1708. [CrossRef]
4. Acharya, N.; Mahat, P.; Mithulananthan, N. An analytical approach for DG allocation in primary distribution network. *Int. J. Electr. Power Energy Syst.* **2006**, *28*, 669–678. [CrossRef]
5. Gözel, T.; Hocaoglu, M.H. An analytical method for the sizing and siting of distributed generators in radial systems. *Electr. Power Syst. Res.* **2009**, *79*, 912–918. [CrossRef]
6. Silvestri, A.; Berizzi, A.; Buonanno, S. Distributed generation planning using genetic algorithms. In Proceedings of the International Conference on PowerTech Budapest 99. (Cat. No.99EX376), Budapest, Hungary, 29 August–2 September 1999; p. 257.

7. Esmaeilian, H.R.; Fadaeinedjad, R. Energy Loss Minimization in Distribution Systems Utilizing an Enhanced Reconfiguration Method Integrating Distributed Generation. *IEEE Syst. J.* **2014**, *9*, 1430–1439. [CrossRef]
8. Kansal, S.; Kumar, V.; Tyagi, B. Optimal placement of different type of DG sources in distribution networks. *Int. J. Electr. Power Energy Syst.* **2013**, *53*, 752–760. [CrossRef]
9. Kayal, P.; Chanda, C.K. Placement of wind and solar based DGs in distribution system for power loss minimization and voltage stability improvement. *Int. J. Electr. Power Energy Syst.* **2013**, *53*, 795–809. [CrossRef]
10. Sedighizadeh, M.; Esmaili, M.; Esmaeili, M. Application of the hybrid Big Bang-Big Crunch algorithm to optimal reconfiguration and distributed generation power allocation in distribution systems. *Energy* **2014**, *76*, 920–930. [CrossRef]
11. Quadri, I.A.; Bhowmick, S.; Joshi, D. A hybrid teaching—Learning-based optimization technique for optimal DG sizing and placement in radial distribution systems. *Soft Comput.* **2018**. [CrossRef]
12. Prabha, D.R.; Jayabarathi, T. Optimal placement and sizing of multiple distributed generating units in distribution networks by invasive weed optimization algorithm. *Ain Shams Eng. J.* **2016**, *7*, 683–694. [CrossRef]
13. Nguyen, T.T.; Truong, A.V.; Phung, T.A. A novel method based on adaptive cuckoo search for optimal network reconfiguration and distributed generation allocation in distribution network. *Int. J. Electr. Power Energy Syst.* **2016**, *78*, 801–815. [CrossRef]
14. Mohamed Imran, A.; Kowsalya, M.; Kothari, D.P. A novel integration technique for optimal network reconfiguration and distributed generation placement in power distribution networks. *Int. J. Electr. Power Energy Syst.* **2014**, *63*, 461–472. [CrossRef]
15. Rao, R.S.; Ravindra, K.; Satish, K.; Narasimham, S.V.L. Power Loss Minimization in Distribution System Using Network Reconfiguration in the Presence of Distributed Generation. *IEEE Trans. Power Syst.* **2013**, *28*, 1–9. [CrossRef]
16. Subramaniyan, M.; Subramaniyan, S.; Veeraswamy, M.; Jawalkar, V.R. Optimal reconfiguration/distributed generation integration in distribution system using adaptive weighted improved discrete particle swarm optimization. *COMPEL-Int. J. Comput. Math. Electr. Electron. Eng.* **2018**. [CrossRef]
17. Nguyen, T.T.; Truong, A.V. Distribution network reconfiguration for power loss minimization and voltage profile improvement using cuckoo search algorithm. *Int. J. Electr. Power Energy Syst.* **2015**, *68*, 233–242. [CrossRef]
18. Merlin, A.; Back, H. Search for a minimal loss operating spanning tree configuration in an urban power distribution system. In Proceedings of the 5th power Syst. Computation conference (PSCC), Cambridge, UK, 1–5 September 1975; pp. 1–18.
19. Civanlar, S.; Grainger, J.J.; Yin, H.; Lee, S.S.H. Distribution feeder reconfiguration for loss reduction. *IEEE Trans. Power Deliv.* **1988**, *3*, 1217–1223. [CrossRef]
20. Duan, D.L.; Ling, X.D.; Wu, X.Y.; Zhong, B. Reconfiguration of distribution network for loss reduction and reliability improvement based on an enhanced genetic algorithm. *Int. J. Electr. Power Energy Syst.* **2015**, *64*, 88–95. [CrossRef]
21. Esmaeilian, H.R.; Fadaeinedjad, R. Distribution system efficiency improvement using network reconfiguration and capacitor allocation. *Int. J. Electr. Power Energy Syst.* **2015**, *64*, 457–468. [CrossRef]
22. Teimourzadeh, S.; Zare, K. Application of binary group search optimization to distribution network reconfiguration. *Int. J. Electr. Power Energy Syst.* **2014**, *62*, 461–468. [CrossRef]
23. Mohamed Imran, A.; Kowsalya, M. A new power system reconfiguration scheme for power loss minimization and voltage profile enhancement using Fireworks Algorithm. *Int. J. Electr. Power Energy Syst.* **2014**, *62*, 312–322. [CrossRef]
24. Arandian, B.; Hooshmand, R.; Gholipour, E. Decreasing activity cost of a distribution system company by reconfiguration and power generation control of DGs based on shuffled frog leaping algorithm. *Int. J. Electr. Power Energy Syst.* **2014**, *61*, 48–55. [CrossRef]
25. Haghifam, M.R.; Olamaei, J.; Andervazh, M.R. Adaptive multi-objective distribution network reconfiguration using multi-objective discrete particles swarm optimisation algorithm and graph theory. *IET Gener. Transm. Distrib.* **2013**, *7*, 1367–1382.

26. Swarnkar, A.; Gupta, N.; Niazi, K.R. Adapted ant colony optimization for efficient reconfiguration of balanced and unbalanced distribution systems for loss minimization. *Swarm Evol. Comput.* **2011**, *1*, 129–137. [CrossRef]
27. Merrikh-Bayat, F. The runner-root algorithm: A metaheuristic for solving unimodal and multimodal optimization problems inspired by runners and roots of plants in nature. *Appl. Soft Comput.* **2015**, *33*, 292–303. [CrossRef]
28. Nguyen, T.T.; Nguyen, T.T.; Truong, A.V.; Nguyen, Q.T.; Phung, T.A. Multi-objective electric distribution network reconfiguration solution using runner-root algorithm. *Appl. Soft Comput.* **2017**, *52*, 93–108. [CrossRef]
29. Baran, M.E.; Wu, F.F. Network reconfiguration in distribution systems for loss reduction and load balancing. *IEEE Trans. Power Deliv.* **1989**, *4*, 1401–1407. [CrossRef]
30. Chiang, H.D.; Jean-Jumeau, R. Optimal network reconfigurations in distribution systems: Part 2: Solution algorithms and numerical results. *IEEE Trans. Power Deliv.* **1990**, *5*, 1568–1574. [CrossRef]

energies

MDPI

Article

Applications of a Strong Track Filter and LDA for On-Line Identification of a Switched Reluctance Machine Stator Inter-Turn Shorted-Circuit Fault

Li Xiao [1,*], Hexu Sun [2], Liyi Zhang [1], Feng Niu [3], Lu Yu [1] and Xuhe Ren [1]

[1] College of Information Engineering, Tianjin University of Commerce, Tianjin 300134, China; Zhangliyi@tjcu.edu.cn (L.Z.); yulu@tjcu.edu.cn (L.Y.); renxuhe@tjcu.edu.cn (X.R.)
[2] College of Control Science and Engineering, Hebei University of Technology, Tianjin 300130, China; hxsun@hebut.edu.cn
[3] College of Electrical Engineering, Zhejiang University, Hangzhou 310027, China; niufeng@hebut.edu.cn
* Correspondence: xiaoli@tjcu.edu.cn; Tel.: +86-022-2666-7577

Received: 4 September 2018; Accepted: 19 September 2018; Published: 1 January 2019

Abstract: Reliability is pivotal significance for switched reluctance machine drives (SRD) applied to safety essential transportation and industrial fields. An inter-turn shorted-circuit fault (ISCF) could incite the machine to operate in unbalanced status, resulting in the noise increases. In the event such a fault remains untreated, the fault will further destroy the rest of the normal phases, even leading to a tragic incident for the entire drive application. To improve the reliability of SRD, an efficient on-line fault diagnosis method for ISCF should be proposed. This paper is focused on employing the strong track filter (STF) to achieve real-time phase resistance differences between before and after ISCF, which are used as features to diagnose the fault occurrence and the fault phase. Furthermore, a classification namely as linear discriminant analysis (LDA) is selected to estimate fault severity. Finally, simulation and experiments correspond to various running statuses are executed and their results can verify that the diagnosis method has accuracy and robustness.

Keywords: inter-turn shorted-circuit fault (ISCF); strong track filter (STF); linear discriminant analysis (LDA); switched reluctance machine (SRM)

1. Introduction

In the past decade, switched reluctance machines and their drives have obtained a great deal of regards and have been applied to transportation and industrial applications, including aerospace, power traction, hybrid vehicles [1]. Switched reluctance machines' (SRM) structure is simple, without any permanent magnets and windings on the rotors [2]. It is very favorable for machine running in the rigorous circumstance owing to its remarkable fault tolerance, superior efficiency and wonderful reliability. The switched reluctance machine drives (SRD) has the capability of fault tolerance naturally, but is not absolutely fault free [3]. In the case where the SRM operates perennially, faults will possibly occur in the motor and its power convert. For SRM, the inter-turn shorted-circuit fault (ISCF) generally leads to unbalanced magnetic pull, high torque ripples, over-current, and lower load ability, yet would not influence the operation of the rest normal phases in the case where a small number of windings failed, due to the independence of excitation and control mode between windings of each phase. Thus, the ISCF is often overlooked, which results in a higher temperature and further damage the insulation system of the motor. Regarding this issue, it is essential to elevate the SRM with a certain ability to diagnose the ISCF. Thus, the progressive diagnosis method plays an important role for heightening safe operation and reliability for SRMs, which is the main issue of this paper.

In regard to detecting the ISCF, many methods have been reported. All the methods could be classified into two types: feature extraction and intelligent recognition. For the feature extraction

method, the distinctive between normal and fault machine performance can be presented by the amplitudes or frequencies of extracted signatures, which is used to realize the fault detection. As well as the common fault features include current, voltage, and vibration. In [4], the forward and backward rotating currents were measured, and their negative sequence components were extracted to detect inter-turn faults powerfully for induction motors. For permanent magnet synchronous motor, a combination of the values of the voltages and the stator currents obtain by wavelet transform was considered as the fault feature to diagnose the inter-turn faults in the literature [5]. In [6], the external vibration coupled with the stray magnetic field was analyzed to receive the vibration spectrum distinctions of healthy and faulty motor to implement non-invasive diagnosis for the rotor windings fault of the synchronous machine. Additionally, a number of intelligent recognition diagnosis methods have been used for the ISCF identification, such as neural networks, genetic algorithm, and support vector machines [7–9].

Comparing to other types of motors, the ISCF for SRMs has been investigated insufficiently. The fault mechanism was introduced in [1–3,10]. Recently, a modeling method for the ISCF with one shorted coil in SRM was presented in [11]. Fault diagnosis methods were investigated in [12–14]. A diagnosis technology based on tracking the maximum current point was presented to detect the fault occurrence and faulty degree by [12]. However, the diagnosis method is just applied to the fault occurring in only one phase winding. In [13], the fundamental components were extracted to reconstruct based on spectrum analysis, and components of reconstructed current were treated as the features to detect fault. In [14], an extended Kalman filter (EKF) was used to achieve a precise response in initial moments after inter-turn winding failure. In fact, the diagnosis method proposed in literature [13,14] could only detected the fault occurrence, but the detection of faulty phase and severity have not been implemented.

Indeed, the EKF can quickly confirm the fault appearance, so it has been already related to applications in fields of fault monitoring and diagnosing [15,16]. However, the EKF is similar to the open-loop system, which leads to the tracking results are not desired even divergent in certain case, such as in the mutation state [17]. Comparing to the tracking performance of EKF, the strong track filter (STF) is more robust for the uncertain faulty model, better tracking especially in the mutation state, and less complex for calculation. Hence, the STF algorithm is substituted for the EKF algorithm to use in the fault diagnose scheme in this paper.

Additionally, the developing of diagnosis mode always lack enough samples since the fault samples are obtained difficultly in industrial processes. This may cause the overfitting problem in case the model is developed by nonlinear methods [18]. However, linear discriminant analysis (LDA) has the capability of dimensionality reduction and supervised classification. Using LDA based on grabbling for the vintage discriminant direction of the samples, the data between different classes can be separated maximumly and robustly. Thus, LDA has been successfully utilized in detecting and monitoring for industrial applications [19,20]. In [21], it is suggested that LDA is not only used to diagnose fault type but also suitable to estimate the faulty severity. In this paper, LDA is especially adopted to estimate the fault severity.

The rest of the paper is arranged as follows: In Section 2, a faulty SRM model and the failure mechanism are elaborated. In Section 3, the STF procedure utilized in the faulty SRM is analyzed. In Section 4, the ISCF detection schemes, including the fault occurrence, faulty phases are explained in detail. Additionally, the major conception of LDA and how it is employed for the fault severity identification are also described in this section. Finally, to demonstrate effectiveness and evaluate the robustness of the diagnostic method, simulation results as well as online experimental results corresponding to different scenarios are all presented in Section 5.

2. Model of Switched Reluctance Machine (SRM) and the Failure Mechanism Analysis

2.1. Model of the Healthy SRM

The structure of the SRM utilized in this paper is described in Figure 1 which is a four-phase 8/6 motor. For SRMs, when the coil of a phase is excited, the magnetic flux always closes along the path with the minimized magnetic reluctance. The electromagnetic torque is produced by the energy conversion in a coil.

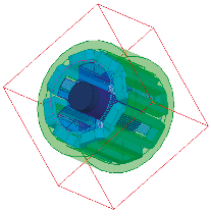

Figure 1. The structure of switched reluctance machine (SRM).

Each phase voltage involved two parts: the resistive voltage drop and the derivative of the flux linkage, that can be given by:

$$U_n = R_n i_n + \frac{d\psi_n}{dt} \tag{1}$$

where U_n is the phase voltage, i_n is the phase current, and ψ_n and R_n are, separately, the flux linkage and the resistance for each phase. Parameter n expresses the number of phase (n = A, B, C, D).

The flux linkage is expressed in Equation (2):

$$\psi_n = L_n(i_n, \theta) i_n \tag{2}$$

where L_n (i_n, θ) is the inductance per phase. Because the term L_n (i_n, θ) contains parameters i_n and θ. Equation (1) can be replaced with:

$$U_n = R_n i_n + \frac{d\theta}{dt}\frac{dL_n(i_n, \theta)}{d\theta} i_n + L_n(i_n, \theta)\frac{di_n}{dt} \tag{3}$$

The rotational velocity ω is shown in the following equation:

$$\omega = \frac{d\theta}{dt} \tag{4}$$

Hence, both sides of the Equation (3) are simultaneously multiplied by the phase current i_n, the power balance is found by:

$$U_n i_n = R_n {i_n}^2 + \frac{dL_n(i_n, \theta)}{d\theta} {i_n}^2 \omega + i_n L_n(i_n, \theta)\frac{di_n}{dt} \tag{5}$$

When the winding is energized, if the losses of the phase winding can be ignored, a part of the input power is used to make the energy storage in the winding increased, and the other part is converted to output mechanical power. Hence, the electromagnetic torque per phase is found by:

$$T_n = \frac{1}{2} i_n^2 \frac{dL_n(i_n, \theta)}{d\theta} \tag{6}$$

The Newton motion law for the SRM is given by:

$$J\frac{d\omega}{dt} = \sum_{n=1}^{4} T_n - T_L - F\omega \tag{7}$$

where J, F, T_L are respectively moment inertia, damping coefficient and the load torque. Therefore, Equation (7) can be replaced with:

$$J\frac{d\omega}{dt} + F\omega = \frac{1}{2}\sum_{n=1}^{4} i_n^2 \frac{dL_n(i_n, \theta)}{d\theta} - T_L \tag{8}$$

2.2. The Failure Mechanism Analysis

The equivalent circuit of the faulty coil is illustrated in Figure 2. ISCF could be cause by the insulation of windings. Due to the ISCF, a route with a certain resistance should be produced between the two turns.

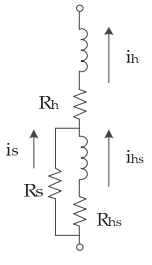

Figure 2. The equivalent circuit of the coil.

The voltage equation of the fault phase is found by:

$$U_n = i_h R_n + i_s R_s + (N_h - N_s)\frac{d\psi_s}{dt} + N_h \sum_{n}^{4} \frac{d\psi_n}{dt} \tag{9}$$

where U_n is the supplied voltage of the fault phase. Parameters R_n is the resistance in healthy turns, parameters R_{hs} is the resistance in shorted turns, as well as R_s is the resistance of the short-circuit route, which amplitude is very small. Parameters N_h is the number of healthy turns, and N_s is the short-circuit turn number. ψ_n is the magnetic flux of a healthy pole, ψ_s is the magnetic flux of a short-circuit pole. Parameters i_h, i_{hs} and i_s are currents, respectively flowing in healthy turns of the faulty pole, the shorted turns, and the short-circuit route. The relationship between three parameters is as follows:

$$i_h = i_{hs} + i_s \tag{10}$$

Moreover, the voltage drop of the resistance of the short-circuit route, $R_s i_s$ is denoted by:

$$R_s i_s = R_{hs} i_{hs} + N_s \frac{d\psi_s}{dt} \tag{11}$$

Therefore, the current flowing in shorted turns can be obtained from Equations (10) and (11):

$$i_{hs} = \frac{R_s i_h}{R_s + R_{hs}} - \frac{N_s(d\psi_s/dt)}{R_s + R_{hs}} \tag{12}$$

The current flowing in the shorted turns could be represented by:

$$i_p = -\frac{N_s(d\psi_s/dt)}{r\left(\frac{R_s}{r} + N_s\right)} \tag{13}$$

where r is assumed as the resistance of each turn.

3. The STF Procedure

The state equation of the SRD is described as follows:

$$x(k+1) = A(k, x(k)) \cdot x(k) + u(k) \tag{14}$$

where the vector x(k) as a variable, is estimated by STF, and defined as:

$$x(k) = [i_1(k) i_2(k)\ i_3(k)\ i_4(k)\ \theta(k)\ \omega(k)\ R(k)\ T_L]^T \tag{15}$$

Thus, the model of the SRM in the discrete-time state-space is described by the Equations (16)–(23), which include four currents, angular position, rotor angular position, phase resistance and load torque.

$$f_1 = i_1(k+1) = i_1(k) + \left[u_1(k) - R_1(k) i_1(k) - \frac{dL_1(i_1, \theta)}{d\theta} \cdot i_1(k) \cdot \omega(k)\right] \cdot \frac{t_s}{L_1[\theta(k)]} \tag{16}$$

$$f_2 = i_2(k+1) = i_2(k) + \left[u_2(k) - R_2(k) i_2(k) - \frac{dL_2(i_2, \theta)}{d\theta} \cdot i_2(k) \cdot \omega(k)\right] \cdot \frac{t_s}{L_2[\theta(k)]} \tag{17}$$

$$f_3 = i_3(k+1) = i_3(k) + \left[u_3(k) - R_3(k) i_3(k) - \frac{dL_3(i_3, \theta)}{d\theta} \cdot i_3(k) \cdot \omega(k)\right] \cdot \frac{t_s}{L_3[\theta(k)]} \tag{18}$$

$$f_4 = i_4(k+1) = i_4(k) + \left[u_4(k) - R_4(k) i_4(k) - \frac{dL_4(i_4, \theta)}{d\theta} \cdot i_4(k) \cdot \omega(k)\right] \cdot \frac{t_s}{L_4[\theta(k)]} \tag{19}$$

$$f_5 = \theta(k+1) = \theta(k) + \omega(k) \cdot t_s \tag{20}$$

$$f_6 = \omega(k+1) = \omega(k) + \frac{1}{J} \cdot \left[\frac{1}{2} \sum_{n=1}^{4} i_n^2(k) \frac{dL_n(i_n, \theta)}{d\theta} - T_L - F \cdot \omega(k)\right] \cdot t_s \tag{21}$$

$$f_7 = R_1(k+1) = R_1(k) \tag{22}$$

$$f_8 = T_L(k+1) = T_L(k) \tag{23}$$

In order to govern the relationship among above state vectors, the transition matrix A is required which is defined as:

$$A(k, x(k)) = \begin{bmatrix} a_{11} & 0 & 0 & 0 & 0 & a_{16} & a_{17} & 0 \\ 0 & a_{22} & 0 & 0 & 0 & a_{26} & 0 & 0 \\ 0 & 0 & a_{33} & 0 & 0 & a_{36} & 0 & 0 \\ 0 & 0 & 0 & a_{44} & 0 & a_{46} & 0 & 0 \\ 0 & 0 & 0 & 0 & a_{55} & a_{56} & 0 & 0 \\ a_{61} & a_{62} & a_{63} & a_{64} & 0 & a_{66} & 0 & a_{68} \\ 0 & 0 & 0 & 0 & 0 & 0 & a_{77} & 0 \\ 0 & 0 & 0 & 0 & 0 & 0 & 0 & a_{88} \end{bmatrix} \tag{24}$$

Additionally, each element in transition matrix A are acquired as:

$$a_{11} = \frac{\partial f_1}{\partial i_1} = 1 - \left[R_1(k) + \frac{dL_1(\theta(k))}{d\theta} \cdot \omega(k)\right] \cdot \frac{t_s}{L_1(\theta(k))} \tag{25}$$

$$a_{16} = \frac{\partial f_1}{\partial \omega} = -\frac{dL_1(\theta(k))}{d\theta} \cdot \frac{i_1(k)}{L_1(\theta(k))} \cdot t_s \tag{26}$$

$$a_{17} = \frac{\partial f_1}{\partial R_1} = -\frac{i_1(k)}{L_1(\theta(k))} \cdot t_s \tag{27}$$

$$a_{22} = \frac{\partial f_2}{\partial i_2} = 1 - \left[R_2(k) + \frac{dL_2(\theta(k))}{d\theta} \cdot \omega(k)\right] \cdot \frac{t_s}{L_2(\theta(k))} \tag{28}$$

$$a_{26} = \frac{\partial f_2}{\partial \omega} = -\frac{dL_2(\theta(k))}{d\theta} \cdot \frac{i_2(k)}{L_2(\theta(k))} \cdot t_s \tag{29}$$

$$a_{33} = \frac{\partial f_3}{\partial i_3} = 1 - \left[R_3(k) + \frac{dL_3(\theta(k))}{d\theta} \cdot \omega(k)\right] \cdot \frac{t_s}{L_3(\theta(k))} \tag{30}$$

$$a_{36} = \frac{\partial f_3}{\partial \omega} = -\frac{dL_3(\theta(k))}{d\theta} \cdot \frac{i_3(k)}{L_3(\theta(k))} \cdot t_s \tag{31}$$

$$a_{44} = \frac{\partial f_4}{\partial i_4} = 1 - \left[R_4(k) + \frac{dL_4(\theta(k))}{d\theta} \cdot \omega(k)\right] \cdot \frac{t_s}{L_4(\theta(k))} \tag{32}$$

$$a_{46} = \frac{\partial f_4}{\partial \omega} = -\frac{dL_4(\theta(k))}{d\theta} \cdot \frac{i_4(k)}{L_4(\theta(k))} \cdot t_s \tag{33}$$

$$a_{55} = \frac{\partial f_5}{\partial \theta} = 1 \tag{34}$$

$$a_{56} = \frac{\partial f_5}{\partial \omega} = t_s \tag{35}$$

$$a_{62} = \frac{\partial f_6}{\partial i_2} = \frac{1}{J} \cdot i_2(k) \cdot \frac{dL_2(\theta(k))}{d\theta} \cdot t_s \tag{36}$$

$$a_{63} = \frac{\partial f_6}{\partial i_3} = \frac{1}{J} \cdot i_3(k) \cdot \frac{dL_3(\theta(k))}{d\theta} \cdot t_s \tag{37}$$

$$a_{64} = \frac{\partial f_6}{\partial i_4} = \frac{1}{J} \cdot i_4(k) \cdot \frac{dL_4(\theta(k))}{d\theta} \cdot t_s \tag{38}$$

$$a_{66} = \frac{\partial f_6}{\partial \omega} = 1 - \frac{F}{J} \cdot t_s \tag{39}$$

$$a_{68} = \frac{\partial f_6}{\partial T_L} = -\frac{1}{J} \cdot t_s \tag{40}$$

$$a_{77} = \frac{\partial f_7}{\partial R_1} = 1 \tag{41}$$

$$a_{88} = \frac{\partial f_8}{\partial T_L} = 1 \tag{42}$$

Since the transition matrix A(k, x(k)) contains the variable state vector x(k), the STF is employed to obtain the estimated resistance based on easily measured outputs in order to eliminate negative impacts caused by load disturbance or inaccurate model. The STF is organized as follows.

The measurement equation is shown as:

$$\begin{cases} x(k+1) = f(k, x(k), u(k)) + \sigma(k) \\ y(k+1) = h(k+1, x(k+1), u(k+1)) + \varpi(k) \end{cases} \tag{43}$$

where f( ) is the state transition function and h( ) is the nonlinear transformation function. u(k) is the control variable, σ(k) is the process noise. Q(k) is symmetric and positive definite matrix. R(k) is a covariance matrix, which is symmetric positive definite. ϖ(k) is the matrix of the measurement noise, which are all irrelevant to initial value of state variable x(0).

The estimated value with one procedure of the state variable is given as:

$$\hat{x}(k+1|k) = f(k, \hat{x}(k|k), u(k)) \tag{44}$$

The residual matrix and the gain matrix are respectively defined as Equations (45) and (46):

$$\Upsilon(k+1) = y(k+1) - \hat{y}(k+1) = y(k+1) - h(k+1, \hat{x}(k+1|k)) \tag{45}$$

$$\begin{gathered} K(k+1) = P(k+1|k)H^T(k+1, \hat{x}(k+1|k)) \cdot \\ (H(k+1, \hat{x}(k+1|k))P(k+1|k) \cdot H^T(k+1, \hat{x}(k+1|k)) + R(k))^{-1} \end{gathered} \tag{46}$$

Calculating the predicted error covariance matrix:

$$P(k+1|k) = \lambda(k+1)F(k, \hat{x}(k|k), u(k)) \cdot P(k|k)F^T(k, \hat{x}(k|k), u(k)) + Q(k) \tag{47}$$

The state estimated error covariance matrix is calculated by:

$$P(k+1|k) = [I - K(k+1) \cdot H(k+1, \hat{x}(k+1|k))]P(k+1|k) \tag{48}$$

The steps of calculating the fading factor can be summarized as Equations (49)–(53):

$$\lambda(k+1) = \begin{cases} c_i\lambda_0 \, , c_i\lambda_0 \geq 1 \\ 1, c_i\lambda_0 < 1 \end{cases} \tag{49}$$

where c_i is the predetermined constant, and λ_0 can be obtained by Equations (50)–(52):

$$\lambda_0 = \frac{tr[N(k+1)]}{tr[M(k+1)]} \tag{50}$$

$$N(k+1) = V(k+1) - H(k+1, \hat{x}(k+1|k)) \cdot Q(k)H^T(k+1, \hat{x}(k+1|k)) - \beta R(k) \tag{51}$$

$$M(k+1) = H(k+1, \hat{x}(k+1|k))F(k, \hat{x}(k|k), u(k)) \cdot P(k|k)F^T(k, \hat{x}(k|k), u(k)) \cdot H^T(k+1, \hat{x}(k+1|k)) \tag{52}$$

$$V(k+1) = \begin{cases} \Upsilon(1)\Upsilon^T(1), & k = 1 \\ \frac{\rho V(k) + \Upsilon(k+1)\Upsilon^T(k+1)}{1+\rho}, & k > 1 \end{cases} \tag{53}$$

where β is a given weakening factor, satisfying $\beta \geq 1$. ρ is the forgetting factor, satisfying $0 < \rho \leq 1$. Based on Equations (44)–(46), the estimated value of state variable:

$$\hat{x}(k+1|k+1) = \hat{x}(k+1|k) + K(k+1) + \Upsilon(k+1) \tag{54}$$

Additionally, the process of the STF could be summarized as:

Step 1: Determoning the state estimation variable of the fault diagnosis system and selecting the initial value $\hat{x}(0|0)$, $P(0|0)$. Simultaneously, the weakening factor β and the forgetting factor ρ are respectively given appropriately based on the training experience.

Step 2: The state variable $\hat{x}(k+1|k)$ should be calculated by Equation (44), then the residual matrix $\Gamma(k+1)$ is also obtained by Equation (45).

Step 3: Calculating the fading factor λ(k+1) based on Equations (49)–(53).

Step 4: The matrix $P(k+1|k)$ and $K(k|k)$ can be obtained by Equations (46) and (47) respectively. Finally, the estimated value $\hat{x}(k+1|k+1)$ can be obtained by Equation (54).

Step 5: Comparing the estimated value $\hat{x}(k+1|k+1)$ and the target value x_0. The residual obtained from the comparison would be sent to the comparator of diagnostic system.

4. The Proposed Fault Diagnosis Method for Inter-Turn Shorted-Circuit Fault (ISCF)

The measurement variables included the measured rotor angles and the real-time four phase currents should be required to send the STF. While the resistance of the machine's phase windings, can be calculated by STF. The schematic of the proposed detection method is shown in Figure 3. It can be noted that the whole diagnosis program contains detection of the fault occurrence, identifying the faulty phase and estimation of faulty severity.

4.1. Detecting the Occurrence of ISCF

The proposed diagnostic method depends on the estimation of phase winding resistances. According to explanations in Section 2 and Reference [15], the conclusion that the faulty phase winding resistance must be decrease, has been already confirmed. However, in the SRM's normal operation, the phase winding resistances always increase with the temperature of winding goes up. Thus, the variation of the winding resistance can be tracked by the STF to diagnose the fault occurrence. The specific process is as follows.

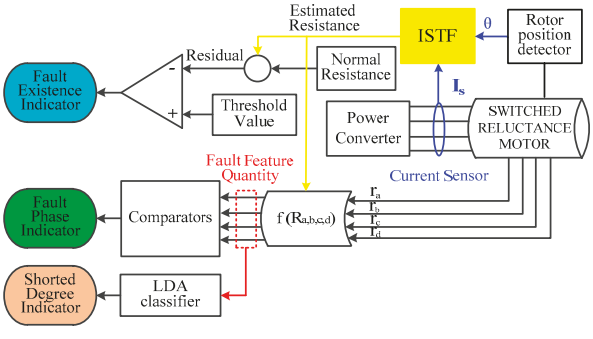

Figure 3. The schematic of the proposed detection method. STF: strong track filter; LDA: linear discriminant analysis.

The rotor position and four phase currents are applied to obtain the normalized estimated resistance R_e based on the algorithm STF. Comparing R_e and the normalized normal resistance R_r to generate the residual Υ. Any important differences between the resistance R_e and R_r indicates that the ISCF occurs in the machine's winding. The diagnostic feature quantity q is defined as follows:

$$q = \begin{cases} 1, \text{ if } |\Upsilon| > R_{ref} \\ 0, \text{ if } |\Upsilon| \leq R_{ref} \end{cases} \tag{55}$$

In the experimental tests, R_e and R_r present some differences, even during normal operation. A part of these differences results from transient phenomena, as well as another part is brought from signal noises enrolled by sensors. To avoid a wrong fault diagnosis caused by above undesirable effects, a threshold value R_{ref} is considered. In any situations, R_{ref} must be clearly higher than the maximum absolute value of Υ.

When q is equal to 1, it means that absolute value of Υ is higher than R_{ref}. This scenario occurs if the ISCF in one or more phase windings. When q is equal to 0, it means that Υ lies in the normal range, that can indicate the normal operation of SRM.

4.2. Identifying the Faulty Phase

The voltage for each phase is expressed by Equation (56) during the phase is in the turn-on region.

$$U_n = \begin{cases} U_s, \text{ upper-switch close\&\&lower-switch close} \\ 0\ , \text{ upper-switch open\&\&lower-switch close} \end{cases} \quad (56)$$

where U_s represents the dc voltage. When the two switches of one phase on the power converter are all close, the normal phase voltage U_n is equal to the U_s.

Once the ISCF occurs, the amplitude of the faulty phase current is surely higher than the normal value, yet currents of the remaining normal phases should be not influenced by the ISCF due to the independence of each phase winding, which results that the amplitude of $R_r \cdot i_n$ is also greater than the normal phase voltage U_n during the faulty phase is in the turn-on region. Thus, the characteristic of phase voltage, which of the faulty phase in the turn-on region can be used to diagnose the shorted phase. The diagnostic variables g_n and e_n are introduced to identify the faulted phase, which can be defined as:

$$g_n = \begin{cases} \left| \frac{U_s}{R_r \cdot i_n} \right|, \ i_n \neq 0 \text{ and } U_s \neq 0 \\ 1\ , \ i_n = 0 \text{ or } U_s = 0 \end{cases} \quad (57)$$

where n = A, B, C, D. To identify easily, the diagnostic variables g_n would be set as the value of 1 during the phase n in the turn-off region. The diagnostic variable e_n is Boolean, installed as:

$$e_n = \begin{cases} 0, \text{ if } g_n \geq 1 \\ 1, \text{ if } 0 < g_n < 1 \end{cases} \quad (58)$$

When e_n is equal to 1, the phase n is indicated as the shorted phase. However, this only concerned if the variable q is also equal to 1 simultaneously, as shown in Table 1.

Table 1. Diagnostic variable for identifying the faulty phase.

Diagnostic Variable						Phase Winding Status	Faulty Phase
q	e_A	e_B	e_C	e_D	$\sum e_n$		
1	1	0	0	0	1	ISCF	A
1	0	1	0	0	1	ISCF	B
1	0	0	1	0	1	ISCF	C
1	0	0	0	1	1	ISCF	D
0	-	-	-	-	-	Normal	-

ISCF: inter-turn shorted-circuit fault.

If there is only one e_n variable would be equal to 1, then just one phase is faulty. More than one e_n variable presents the value 1, which means the number of faulty phases is greater than 1. In other words, the number of e_n variable presented the value 1 can indicate the number of the faulty phase. The variables for multiphase ISCF are presented in Table 2 by taking faulty phase C as an example.

Table 2. Diagnostic variable for the phase winding short-circuit.

Diagnostic Variable						Faulty Number	Faulty Phase
q	e_A	e_B	e_C	e_D	$\sum e_n$		
1	0	0	1	0	1	1	C
1	1	0	1	0	2	2	A C
1	1	1	1	0	3	3	A B C
1	1	1	1	1	4	4	A B C D

4.3. Estimation of Fault Severity

It is necessary to estimate the fault degree, after the fault and its type are all identified. The LDA classifier is applied to detect the faulty degree. In the LDA classifier, samples from the faulted prototype with different severities are involved in the sample space, where the space is divided into k classes. A certain number of samples within the same condition are classified into the same class. Each class is related to the weighting coefficient, which is utilized to compute the corresponding linear discriminant function (LDF) [21]. The LDF for the kth class is expressed by:

$$C_k(X_i) = \alpha_{1k}x_{i1} + \alpha_{2k}x_{i2} + L + \alpha_{Nk}x_{iN} + \alpha_{(N+1)k} \quad (59)$$

where $[\alpha_{1k}, \alpha_{2k}, \ldots, \alpha_{(N+1)k}]$ is the coefficient matrix of the kth class. and the N dimensional vector for the sample X_i is represented by $X_i = [x_{i1}, x_{i2}, \ldots, x_{iN}]$.

For each iterative process, the weighting coefficient matrices can be resolved during the samples training. The $k \times N$ matrix is firstly guessed arbitrarily and the weighting coefficient matrix should be revised in each iteration. The class k of the training sample X_i is known, yet the coefficients are always adjusted till that the LDF C_k (X_i) for the kth class is bigger than for the other classes. In case the training procedures are all finished, as well as the matrix C has been achieved, the discriminant functions for the unclassified sample are computed to obtain the optimal coefficient. If the LDF for one sample is bigger than any other LDF, then this sample vector could be classified to a specific class. An unknown sample vector i can be classified to the class j if:

$$C_j(X_i) \geq C_k(X_i) \forall j \neq k \quad (60)$$

To verify the effectiveness of the presented method over the widespread running range, but not just at special case, the sampling space resistance is abounded to contain different operation speeds and currents in this section. The training matrix contains seven classes, respectively representing different faulty degrees (0–60%). In each class, the space includes 30 samples, corresponding to currents with different levels (5A,10A,15A). Each current level includes 10 samples, which are created by varying the amplitude of the speed from 600 r/min to 1500 r/min in the step of 100 r/min. Thus, the training matrix is generated by the overall 210 samples. The association of the estimated resistance at different rotor positions from 0–30° are utilized to classify the faulty severity by LDA. The full structure of training matrix for different shorted degree is shown in Figure 4a. The structure of the training matrix for healthy case is shown in Figure 4b.

Additionally, the leave-one-out method is used to verify the faulty degree estimated method. Firstly, only one sample is chosen and taken as the leftover sample. The other samples are used to calculate the coefficient matrix. Afterwards, the chosen sample is classified by the trained well coefficients. Then this classification procedure is duplicated for each sample. Thus, the coefficients are recomputed and the left-out sample is classified by these coefficients again and again. The accuracy of estimated faulty degree for each class could be expressed as:

$$\text{degree}(\%) = \frac{N_{\text{correct}}}{N_{\text{all}}} \times 100\% \quad (61)$$

where degree (%) indicates the percentage of the correct classification for every class, N_{correct} is the number of the classified correctly samples, N_{all} is the total number of samples.

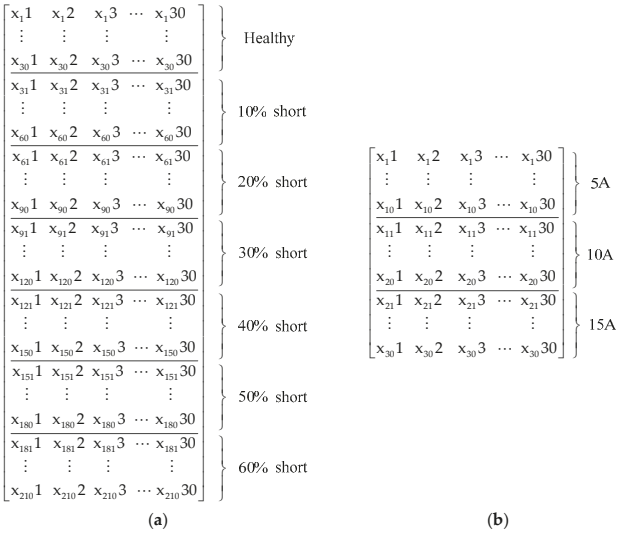

Figure 4. The structure of training matrix (**a**) full training matrix for different degree faults; and (**b**) training matrix for healthy case.

5. Simulation and Experimental Results

5.1. Simulation Analysis

A simulation model for the fault diagnosis method was built based on Ansys Maxwell and Matlab/Simulink. The SRM model is set up in Ansys/Maxwell based on Finite Element Analysis (FEA) while the control part and fault diagnostic part are all found in Matlab/Simulink. Different shorted-circuit turns of the phase winding can be easily sited in Maxwell. The flow diagram for the diagnosis algorithm is shown in Figure 5.

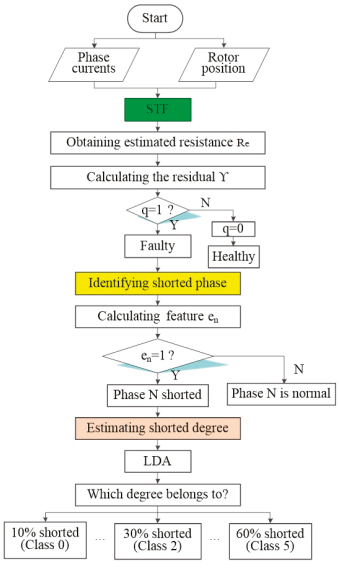

Figure 5. Flow diagram for the inter-turn shorted-circuit fault (ISCF) diagnosis and identification.

To confirm the performance of the ISCF diagnostic method, a lot of simulation and experiments were carried out corresponding to different speed and load running status. For this purpose, the unfavorable scenarios are considered, which correspond to the no-load and loading operations. Moreover, different scenarios including only one phase failure and multiphase failure are, respectively, discussed and tested in this section. The SRM characteristics are detailed in Table 3.

Table 3. Switched reluctance machine (SRM) characteristics.

Parameter	Value	Parameter	Value
Number of phases	4	rated voltage of the supply	220 V
Number of stator poles	8	number of rotor poles	6
Resistance of normal phase	4 Ω	turn number of each phase	120 turns
Rated power	1500 W	rated speed	1500 r/min

Figure 6 presents the simulation results for 30% turns shorted in which 120 turns of the phase winding are faulty. Four phase currents, the normalized residual, the normalized resistance and diagnostic variables g_n are respectively shown in this figure, which correspond to the 600r/min steady-state and no-load operation. At 0.25 s, 30% turns fault related to phase C was imitated. After the ISCF occurrence, the magnetization of shorted turns for phase C is not possible anymore, and phase C current immediately goes up. Then, it is registered an obvious difference between R_e and R_r, and the normalized residual γ changes from 0 till 0.3 (Figure 6b), which is higher than the threshold value R_{ref}, as well as the normalized resistance decreases from 1 to about 0.7 (Figure 6c). According to Equation (55), the variable q is equal to 1, indicating a possible ISCF appearance.

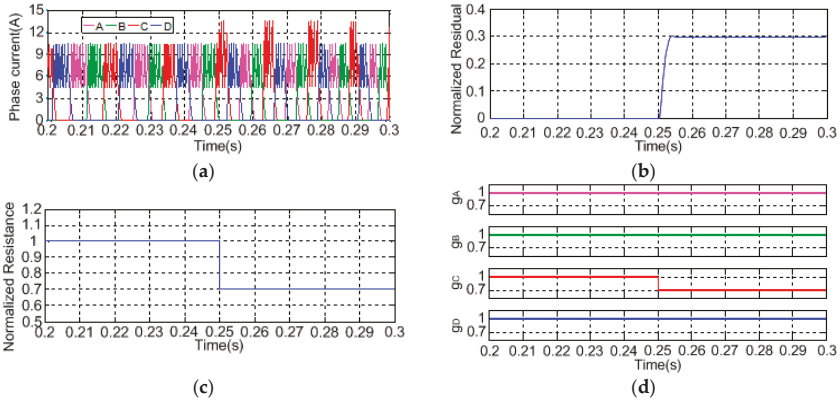

Figure 6. Simulation results in case of 30% turns fault of the SRM winding at low speed and no-load (**a**) four-phase currents; (**b**) normalized residual; (**c**) normalized resistance; and (**d**) diagnostic variables g_n.

Simultaneously, the variable g_C presents sudden change at 0.25 s, while diagnostic variables g_A, g_B, g_D are all throughout equal to 1 (Figure 6d). According to Equation (58), the diagnostic variables $e_A = e_B = e_D = 0$, $e_C = 1$ and $\sum e_n = 1$. Therefore, the ISCF associated to phase C is quickly diagnosed due to $e_C = 1$ and it is only variable equal to 1. In the fault diagnostic procedure, the threshold value R_{ref} is especially important. In this paper, R_{ref} is defined as 0.05 based on several experimental tests.

The applicability and extendibility of the proposed fault diagnostic method for more than one phase failure was tested exposing the SRD with the speed at 1500 r/min and loading 3 N·m. Figure 7 presents simulation results for windings of phase B and D respectively with 30% and 50% turns fault. The winding of phase B failure occurs at 0.45 s, soon afterwards the winding of phase D shorted at 0.47 s. After the fault occurrence, the magnetization of shorted turns for phase B and D vanish, and

currents of phase B and D also increase (Figure 7a). Moreover, there is an obvious difference between R_e and R_r, resulting in generating the normalized residual Γ of phase B and D, that are all higher than the threshold value R_{ref} (Figure 7b). Then the normalized resistance of phase B decreases from 1 to about 0.7 and the normalized resistance of phase D decreases from 1 to about 0.5 (Figure 7c). Thus, the diagnostic variable q is equal to 1, proving an ISCF occurrence. Meanwhile, it can be noted that the variables g_B, g_D present sudden change respectively at 0.45 s and 0.47 s, yet the variables g_A, g_C remain unchanged (Figure 7d), thereby the variables $e_A = e_C = 0$, $e_B = e_D = 1$ and $\sum e_n = 2$. Thus, the ISCF associated to phase B and phase D can be quickly diagnosed.

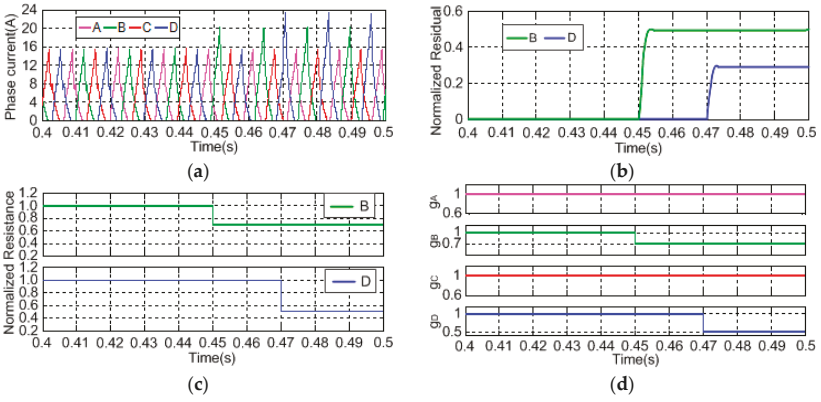

Figure 7. Simulation results in case of multiphase ISCF with high speed and variable loading. (**a**) four-phase currents; (**b**) normalized residual; (**c**) normalized resistance; and (**d**) diagnostic variable g_n.

5.2. Experimental Results

To verify the advanced diagnostic method by experimental teats, an experimental platform was set up, as shown in Figure 8. Experiments were developed on the prototype. An asymmetric half-bridge converter is employed. The control procedure based on current chopping control (CCC) and angle position control (APC), as well as the diagnostic program, is executed in the DSP TM320F2812. This digital signal processor is utilized as the primary control chip corresponding with high speed logic circuit.

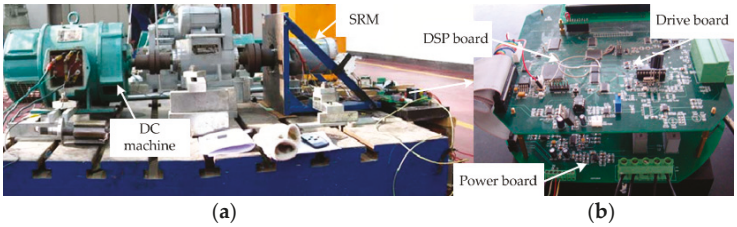

Figure 8. Experimental platform: (**a**) overall test bench; and (**b**) drive control and fault diagnosis sections.

Figure 9 shows the phase current i_C, the normalized residual, diagnostic variables g_C and the real-time speed before and after 30% turns of the phase C failure, at 600 r/min, with no-load. The resistance R_e is generated on phase currents and rotor positions by the STF algorithm. Due to the ISCF, there is an obvious difference between R_e and R_r, leading to the amplitude of normalized residual goes up suddenly and the variable g_C is smaller than the value of 1, that means $q = 1$, $e_C = 1$ and $\sum e_n = 1$. Therefore, the ISCF only associated to phase C can be quickly diagnosed at 1.08 s.

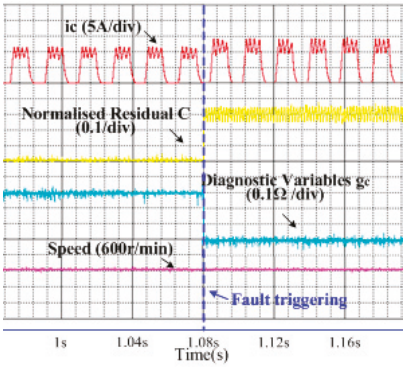

Figure 9. Experimental results for 30% turns of the motor winding faulty at low speed and no-load.

Figure 10 presents the phase currents, normalized residual, diagnostic variables and the real-time speed before and after 30% turns winding of phase B and 50% turns winding of phase D failure. An angle position control algorithm is conducted during the high speed operation. To verify the robustness of the advanced method, the load changes from 0 N·m to 3 N·m suddenly at 3.1 s and the speed is 1500 r/min. After 3.1 s, the phase currents B and D almost raise from 8 A to 16 A due to the load rising, while the normalized residual B and D are still approximately keep the value of 0 and diagnostic variables g_B, g_C, and g_D are all approximately 1 because the phase windings are healthy. However, at 3.3 s, the amplitude of phase current i_b changes to about 24 A, and the normalized residual B and the variable g_B also vary substantially. Subsequently, the amplitude of the current i_d also increases to about 24 A at 3.4 s. The normalized residual D goes up and the variable g_D decreases suddenly at the same time. Actually, at high speed and variable load, an ISCF also causes a significant difference between R_e and R_r. Diagnostic variables $q = 1$, $e_A = e_C = 0$, $e_B = e_D = 1$ and $\sum e_n = 2$, that are exported to diagnostic results. It is clearly indicated that the ISCF appears in the phase B and D.

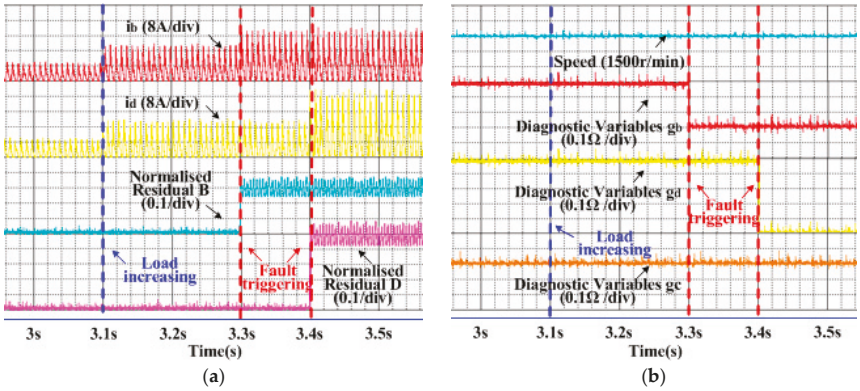

Figure 10. Experimental results in the case of a multiphase winding fault of the SRM at high speed and variable loading (**a**) phase currents i_b and i_d, normalized residual of phase B and D; and (**b**) diagnostic variables g_B, g_C and g_D.

After diagnosing the fault occurrence and faulty phase, it is necessary to estimate the severity by LDA.

The simulation and experimental results of faulty severity for the SRM with different loads are shown in Table 4. From the results, it is obvious that LDA can also validate the occurrence of the ISCF

and estimate the faulty severity, as well as the accuracy reaches up to above 95%. But, some of the samples related to the 10% ISCF are not classified precisely, not only the simulation results but also the experimental results.

Table 4. Results of identifying fault degree by linear discriminant analysis (LDA) classification.

Faulty Degree	Correct Classification			
	Simulation Results		Experimental Results	
	No-Load	50% Full Load	No-Load	50% Full Load
Healthy	100%	100%	100%	100%
10%	97%	97%	95%	95%
20%	100%	99%	97%	97%
30%	100%	100%	99%	99%
40%	100%	100%	100%	100%
50%	100%	100%	100%	100%
60%	100%	100%	100%	100%

6. Conclusions

Safety and reliability are the most significant property indicators for SRD-based electric vehicle applications. In this article, a new diagnosis method of stator ISCF was proposed for SRMs. To improve the detection preciseness further, the resistance of the phase windings was chosen as the diagnostic feature. Since the STF has the superior tracking performance, the diagnosis scheme used the STF to track the real-time resistance of the phase windings, so as to obtain the resistance differences between the healthy phase winding and the faulty phase winding. Then, the resistance differences comparing with the threshold were utilized to detect the fault occurrence and the faulty phase, as well as the number of faulty phases could be also diagnosed. Specifically, LDA was employed to estimate the faulty severity but not identify the faulty type based on the resistances corresponding to different phase currents and rotor positions with the severity from 0% to 60%. Finally, a large number of simulation studies and experiments were executed to validate the robustness and accuracy of the presented method. Whether the SRM was running at low speed or high speed, the accurate diagnostic results can be received with one current period. As further work, the performance of the advanced method in the event of a sudden load change suddenly has been discussed. The results can certify the accuracy and rapidity of the advanced diagnosis method in this case, while the future work is to further improve the precision of the estimating severity by the improved Linear Discriminant Analysis.

Author Contributions: L.X. and H.S. provided the key discussions and ideas for the paper. L.Y. and X.R. built the setup and experimental implementations, the script was composed by L.X., H.S., L.Z., and F.N. revised and reviewed the script.

Funding: This work is supported by Natural Science Foundation of Tianjin (16JCQNJC04200), the National Natural Science Foundation of China (51637009 and 51707174), the National Natural Science Foundation for nurturing of Tianjin University of Commerce (No. 160123), and the University Students Innovation and Entrepreneurship Training Program of China (201810069019 and 201810086136).

Conflicts of Interest: The authors declare no conflict of interest.

References

1. Bruno, L.; Suresh, G.; Avoki, M.O. Winding short circuits in the switched reluctance drive. *IEEE Trans. Ind. Appl.* **2005**, *41*, 1178–1184.
2. Suresh, G.; Avoki, M.O.; Bruno, L. Classification and remediation of electrical Faults in the switched reluctance drive. *IEEE Trans. Ind. Appl.* **2006**, *42*, 479–486.
3. Rareş, T.; Ioana, B. Effects of winding faults on the switched reluctance machine's working performances. In Proceedings of the 3rd IEEE International Symposium on Logistics and Industrial Informatics, Budapest, Hungary, 25–27 August 2013.

4. Dorrell, D.G.; Makhoba, K. Detection of Inter-Turn Stator Faults in Induction Motors Using Short-Term Averaging of Forward and Backward Rotating Stator Current Phasors for Fast Prognostics. *IEEE Trans. Magn.* **2017**, *53*, 1–7. [CrossRef]
5. Obeid, N.H.; Boileau, T.; Nahid-Mobarakeh, B. Modeling and Diagnostic of Incipient Inter-turn Faults for a Three-Phase Permanent Magnet Synchronous Motor. *IEEE Trans. Ind. Appl.* **2016**, *52*, 4426–4434. [CrossRef]
6. Cuevas, M.; Romary, R.; Lecointe, J.P.; Jacq, T. Non-Invasive Detection of Rotor Short-Circuit Fault in Synchronous Machines by Analysis of Stray Magnetic Field and Frame Vibrations. *IEEE Trans. Magn.* **2016**, *52*, 1–4. [CrossRef]
7. Jawadekar, A.; Paraskar, S.; Jadhav, S.; Dhole, G. Artificial neuralnetwork-based induction motor fault classifier using continuous wavelet transform. *Syst. Sci. Control Eng.* **2014**, *2*, 684–690. [CrossRef]
8. Rodríguez, P.V.J.; Arkkio, A. Detection of stator winding fault in induction motor using fuzzy logic. *Appl. Soft Comput.* **2007**, *8*, 1112–1120. [CrossRef]
9. Abiyev, R.; Kaynak, O. Fuzzy wavelet neural networks for identification and control of dynamic plants-a novel structure and a comparative study. *IEEE Trans. Ind. Electron.* **2008**, *55*, 3133–3140. [CrossRef]
10. Li, X.; Sun, H. Analysis and research of short-circuit fault for SRD based on Maxwell and simplorer. In Proceedings of the 4th International Conference on Manufacturing Science and Engineering, Dalian, China, 30–31 March 2013.
11. Chen, H.; Han, G.; Yan, W.; Lu, S.; Chen, Z. Modeling of a Switched Reluctance Motor Under Stator Winding Fault Condition. *IEEE Trans. Appl. Supercond.* **2016**, *26*, 1–6.
12. Torkaman, H. Intern-turn short-circuit fault detection in switched reluctance motor utilizing MCPT test. *Int. J. Appl. Electromagn. Mech.* **2014**, *46*, 619–628.
13. Hoseini, S.R.K.; Farjah, E.; Ghanbari, T.; Givi, H. Extended Kalman filter-based method for inter-turn fault detection of the switched reluctance motors. *IET Electr. Power Appl.* **2016**, *10*, 714–722. [CrossRef]
14. Xiao, L.; Sun, H.; Gao, F.; Hou, S.; Li, L. A New Diagnostic Method for Winding Short-Circuit Fault for SRM Based on Symmetrical Component Analysis. *Chin. J. Electr. Eng.* **2018**, *4*, 74–82.
15. Aubert, B.; Regnier, J.; Caux, S.; Alejo, D. Kalman-Filter-Based Indicator for Online Inter turn Short Circuits Detection in Permanent-Magnet Synchronous Generators. *IEEE Trans. Ind. Electron.* **2015**, *62*, 1921–1930. [CrossRef]
16. Nadarajan, S.; Panda, S.K.; Bhangu, B.; Gupta, A.K. Online Model-Based Condition Monitoring for Brushless Wound-Field Synchronous Generator to Detect and Diagnose Stator Windings Turn-to-Turn Shorts Using Extended Kalman Filter. *IEEE Trans. Ind. Electron.* **2016**, *63*, 3228–3241. [CrossRef]
17. Liu, M.; Zhou, D.H. Normalized residuals based strong tracking filter and its application. *Proc. CSEE* **2005**, *25*, 71–75.
18. Yu, W.; Zhao, C. Sparse Exponential Discriminant Analysis and Its Application to Fault Diagnosis. *IEEE Trans. Ind. Electron.* **2018**, *65*, 5931–5940. [CrossRef]
19. Mbo'o, C.P.; Hameyer, K. Fault Diagnosis of Bearing Damage by Means of the Linear Discriminant Analysis of Stator Current Features from the Frequency Selection. *IEEE Trans. Ind. Appl.* **2016**, *52*, 3861–3868. [CrossRef]
20. Li, W.; Zhao, C.; Gao, F. Linearity evaluation and variable subset partition based hierarchical process modeling and monitoring. *IEEE Trans. Ind. Electron.* **2018**, *65*, 2683–2692. [CrossRef]
21. Reemon, Z.H.; Elias, G.S. On the Accuracy of Fault Detection and Separation in Permanent Magnet Synchronous Machines Using MCSA/MVSA and LDA. *IEEE Trans. Energy Convers.* **2016**, *31*, 924–934.

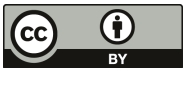

energies

MDPI

Article

Intelligent Energy Management Algorithms for EV-charging Scheduling with Consideration of Multiple EV Charging Modes

Tian Mao [1], Xin Zhang [2,*] and Baorong Zhou [1]

[1] State Key Laboratory of HVDC, Electric Power Research Institute, China Southern Power Grid, Guangzhou 510663, China; maotian@csg.cn (T.M.); zhoubr@csg.cn (B.Z.)
[2] School of Electrical and Electronic Engineering, Nanyang Technological University, 50 Nanyang Avenue, Singapore 639798, Singapore
* Correspondence: jackzhang@ntu.edu.sg; Tel.: +65-6790-5419

Received: 30 November 2018; Accepted: 10 January 2019; Published: 16 January 2019

Abstract: Electric vehicles (EVs) are now attracting increasing interest from both industries and countries as an environmentally friendly and energy efficient mode of travel. Therefore, the EV charging and/or discharging issue has become an important challenge and research topic in power systems in recent years. An advanced and economic EV charging process, however, should employ smart scheduling, which depends on effective and robust algorithms. To that end, a comprehensive intelligent scatter search (ISS) algorithm within the frame of a basic scatter search has been designed with both unidirectional and bidirectional charging considered. The ISS structure also supports both a flexible and constant charging power rate by respectively employing filter-SQP (sequential quadratic programming) and mixed-integer SQP as local solvers with module control. The detailed design of ISS is presented and the objectives of smoothing the daily load profile and minimizing the charging cost have been tested. Compared with methods based on GS (global search), GA (genetic algorithm), and PSO (particle swarm optimization), the outcome-verified ISS can produce attractive results with a significantly short computational time. Moreover, to handle a large scale EV charging scenario, a hybrid method comprised of a GA and ISS approach has been further developed. Simulation results also verified its prominent performance, plus superbly low computational time.

Keywords: charging/discharging; electric vehicle; energy management; genetic algorithm; intelligent scatter search

1. Introduction

The prominent advantages of electric vehicles (EVs) lie in their high energy transfer efficiency and lack of carbon dioxide (CO_2) and other air pollutant emissions. The transition to replace petrol vehicles by EVs, however, is never an easy task. From the aspect of power systems, conventional power distribution networks are typically designed for non-mobile loads, meaning that current power system infrastructures may not be resilient enough to accommodate the integration of EVs [1]. For instance, the daily load peak could be amplified by the aggregated load of unregulated EVs [2,3], which is certainly a threat for power grids. Other potential adverse impacts including voltage drops, frequency oscillations, network congestions, power imbalances, etc., as well concern for power system operators [4,5]. In addition, the implementation of V2G (Vehicle-to-grid) also affects the dynamics and performance of the entire power grid [6,7].

Reinforcing power infrastructures is a typical approach for addressing the above challenges, yet such a method appears to be inefficient and environmentally unfriendly. Meanwhile, it is also impossible to upgrade current power facilities for the accommodation of EV penetration, due to the

expensive investment. As a more economical and attractive alternative, smart scheduling strategies can be employed to postpone the construction of power infrastructures to support EV charging demand, through which the goal of wise load regulation as well as economic benefits can be reached [8–10]. Nevertheless, owing to the differences in operational characteristics between EV and the power system, smart EV scheduling becomes a rather complex task that must rely on an efficient and robust charging algorithm [11]. In general, the operation of EVs should take into account, but not be limited to, a charging and/or discharging power rate limit, initial state of charge (SOC), customer travelling habits, final energy demand, and battery capacity. On the other hand, the operation of a power system is constrained from the limitations of generation units, network structure, transformer capacities, voltage and frequency requirements, etc. In addition, power grids themselves are dynamic networks with unpredictable internal complexities and volatilities, indicating that real-time charging schemes are more practical and superior than merely day-ahead negotiation. As of now, several algorithms using combinations of different solving techniques have also been developed to solve real-time EV scheduling problems [12,13]. With all the above considerations, the demand for powerful algorithms to perform intelligent EV charging scheduling is apparent [14].

As of now, several approaches or algorithms attempting to regulate EV charging have been designed and reported. Typically, the constraint functions related to EV scheduling are usually, or particularly, linear. For example, the EV charging/discharging power should be bounded within the lower and upper limits, whereas the aggregated load must be constrained by the power supply. In the meantime, the objective functions (e.g., cost minimization, load smoothing) can be also formed or reformulated as convex functions. Hence, the EV scheduling issue can be modeled as a convex optimization problem and solved through CVX [15], GAMS [16] or CPLEX [17]. However, these tools come with license concerns, i.e., one must pay for their license to legally use these tools. On the other hand, many conventional methods, such as the alternating direction method of multipliers [18] and tree-based dynamic programming [19], have also been employed to solve the intractable issues of EVs.With multi-constraints and multi-objectives, this kind of approach often dividesthe problem into several sub-problems, thereafter solving them over each stage. When the number of EVs is increased, however, these methods can get stuck, due to "curse of dimensionality" [20].This can limit their usage in large-scale EV charging.Furthermore, some heuristic algorithms inspired from nature process such as a particle swarm optimization (PSO) [21], CRO (chemical reaction optimization) [22], and genetic algorithm (GA) [23,24] have also been utilized. These artificial intelligent algorithms, as verified, can outperform conventional methods in terms of computation overhead, with promising results. For example, the PSO approach in [21] for implementing EVs demand response is almost 2700 times faster than the MINLP (mixed integer nonlinear programming) technique under different scenarios. The deficiency of such methods is that they are intrinsically stochastic and can stagnate prematurely into local optima.

Although many algorithms have been utilized for scheduling EV charging, the emerging approaches are limited in a sense that the methods either only consider EV charging by assigning its states at an arbitrary value from 0 to a specified charging power limit (flexible power rate charging) [10,21], can just manage the EV charging pattern through adjusting the charging status (constant power rate charging) [25], or focus merely on unidirectional charging. Nevertheless, in the long run, both V2G and a flexible charging rate can occur simultaneously with unidirectional charging and a constant power charging rate, due to the fact that the future smart grid will accommodate various applications and services [26]. All the above issues indicate that a generic algorithm is desirable to meet the current EV charging demand and also support future bidirectional charging.

Hence, the aim of this work is to design a comprehensive and universal algorithm that can fit multiple charging modes and diverse charging rate scenarios for distribution-side management. With such complex considerations, an intelligent scatter search (ISS) algorithm framework has been designed. In principal, this novel method is essentially a hybrid SS (scatter search) framework, integrated with sequential quadratic programming (SQP), based local solvers. SS in nature is a population-based

evolutionary approach [27]. Instead of depending on massive random components and traditional evolution techniques, like mutation and crossover, SS only concentrates on a small solution set. Besides, SS is attractive for its well-designed flexibility, enabling various local search methods to complete different optimization tasks. In the design, SQP techniques are chosen as the local solvers to cope with different charging power rates, since they are efficient in solving nonlinear constrained problems. More specifically, a trust-region SQP method based on a filter technique (filter-SQP) [28] is adopted for solving the flexible power rate charging, while the MISQP (Mixed-integer SQP) technique evolved in [29] is in charge of constant power rate charging.

The main contributions of this work lie in: the general SS framework is redefined and adapted to be a new algorithm framework; for the scheduling of EV charging, two algorithms are proposed and applied, i.e., an ISS framework to deal with single EV charging, and a GA-ISS method comprised of GA theory and the proposed ISS approach for massive EV charging; and the proposed algorithms can support both V2G and G2V (grid-to-vehicle) for different power rate configurations.

For comprehensive comparison, various algorithms are compared in the simulation part, specifically:

(1) For the ISS framework, GA, PSO, and global search (GS) are compared;
(2) For the GA-ISS framework, three methods are compared, including: a global control that calculates all the variables and constraints through CVX; DCM (dumbing control method) that charges all EVs as soon as they are plugged in; and a GA-PSO hybrid method.

The following paper is organized as follows: the modeling of the constraints and objective functions for the optimization of EV charging is described in Section 2, the detail designs of the proposed algorithms are presented in Section 3, simulation results to demonstrate and verify the effectiveness of the proposed ISS and GA-ISS are described in Section 4, and finally, a conclusion is given in Section 5.

2. Modelling for the Optimization of EV Charging

2.1. Assumptions

Normally, an EV completes its charging within a certain time window, rather than a whole day. Within this time frame, the charging status (either charging, discharging, or idling) together with the charging power rate, are required to be determined for each timeslot. The following assumptions have been made for the algorithm development:

(1) All participated EVs are with the ideal charging/discharging efficiency of 100%.
(2) The charging price and discharging tariffs follow the spot prices of basic load at each timeslot.
(3) The time period of study starts from 8:00AM to 8:00AM of following day with 15 min per interval. Therefore, the time window is divided into 96 timeslots.

2.2. Definition of Charging Modes

Since both unidirectional and bidirectional charging, combined with either flexible or constant charging power rate, are considered, to better elaborate the design, four charging modes are herein defined:

(1) CD-F mode: charging/discharging with a flexible charging rate,
(2) CD-C mode: charging/discharging with a constant charging rate,
(3) C-F mode: charging only with a flexible charging rate,
(4) C-C mode: charging only with a constant charging rate.

The detailed comparisons for the different charging modes are listed in Table 1. Based on the type of variables, the charging problems can be transformed into NLP (nonlinear programming) or MINLP sub-problems, which will be introduced later.

Table 1. Comparisons for the four charging modes.

Charging Modes	Charging Rate Range (Normalized Value)	Variables Type	Sub-Problem
CD-F	[−1,1]	Continuous	NLP
CD-C	[−1,1]	Discrete	MINLP
C-F	[0,1]	Continuous	NLP
C-C	[0,1]	Discrete	MINLP

2.3. Constraints

With practical considerations, EV scheduling is subjected to its charging power limit, battery capacity, and customer demand, while the total load is constrained by the supply capacity of power grid.

(1) Charging power limit

Generally, the value of $P_{EV,j}^{\max}$ is equal to the battery nominal charging power rate, $P_{EV,j}^{\min}$ is set to be zero for charging only cases while set to be same as $P_{EV,j}^{\max}$ when V2G is permitted, i.e.,

$$-P_{EV,j}^{\min} \le P_{EV,j}^{i} \le P_{EV,j}^{\max} \quad \forall i \in \mathrm{ST}, \forall j \in \mathrm{SE}. \tag{1}$$

(2) Restriction of the battery capacity

For the sake of prolonging the lifetime of EV batteries, $Soc_{j,i}$ is often limited between $Soc_{j,\min}$ and $Soc_{j,\max}$. Take commonly used Li-ion batteries as an example, the range $Soc_{j,\min}$ and $Soc_{j,\max}$ are normally set to be 20% and 90% of their nominal state-of-charge (SOC) $E_{RC,j}$, respectively [30]. Therefore, the following constraints are considered:

$$Soc_{j,\min} \le Soc_{j,i} \le Soc_{j,\max} \le E_{RC,j}, \tag{2}$$

$$Soc_{j,i} = Soc_{j,start} + \frac{1}{C_{EV,j}} \sum_{i=start}^{current} P_{EV,j}^{i}. \tag{3}$$

(3) SOC expectation level for journey requirement

To fulfill the journey requirement, the final energy state $Soc_{j,\mathrm{end}}$ of the battery must reach $E_{\mathrm{exp},j}$, i.e.,

$$Soc_{j,\mathrm{end}} = Soc_{j,start} + \frac{1}{C_{EV,j}} \sum_{i=start}^{end} P_{EV,j}^{i} = E_{\mathrm{exp},j}. \tag{4}$$

(4) Capacity constraint of power grid

To ensure normal operation of the power grid, the total load cannot exceed the maximum capacity of generation units, i.e.,

$$P_{total}^{i} \le P_{g}^{i}, \tag{5}$$

$$P_{total}^{i} = P_{ld}^{i} + \sum_{j \in SE} P_{EV,j}^{i}. \tag{6}$$

2.4. Objective Functions

In terms of optimization objectives, the emerging applications for EV regulation normally consider: (i) load curve flattening, (ii) energy cost minimization, (iii) running cost reduction for the power system, (iv) benefit maximization for aggregators, (v) reduction of CO_2 emissions, and (vi) combinations of the above. The goal of multiple purpose optimizations can be set by utilizing weight factors, based on the

emphases of different entities. For exemplification's sake, only the first two objectives are considered to verify the proposed scheduling algorithm.

(1) Load curve flattening

This optimization objective aims to minimize the power load fluctuation, and the standard deviation of load profile can be utilized for this purpose:

$$\text{Minimize} \quad F_{obj,1} = \left[\frac{1}{n-1} \sum_{i \in ST} \left(P^i_{total} - P^{Ave}_{total} \right)^2 \right]^{1/2}, \tag{7}$$

where P^{Ave}_{total} denotes the daily load mean value and calculated as:

$$P^{Ave}_{total} = \frac{1}{n} \sum_{i \in ST} P^i_{total}. \tag{8}$$

(2) Energy cost minimization

The objective function to minimize power energy cost is given as:

$$\text{Minimize} \quad F_{obj,2} = \sum_{i \in ST} P^i_{total} C^i_e \tag{9}$$

The two mostly studied pricing strategies, namely time-of-use (TOU) price and real-time price, will be used for the simulation to determine the electricity price. The former usually sets the price C^i_{TOU} for different timeslots, while the latter determines an electricity tariff strictly according to time and load demand. For convenient purposes, the linear-price (LP) given in Equation (10) is adopted to model the dynamic real-time price. By incorporating Equation (10) into Equation (9), the final form of the function for cost minimization with the LP price is obtained and given in Equation (11), which is in a quadratic polynomial form.

$$C^i_{LP} = \psi P^i_{total} + \gamma \tag{10}$$

$$\begin{aligned} \text{Minimize} \quad F_{obj,2} = \sum_{i \in ST} P^i_{total} C^i_{LP} = & \sum_{i \in ST} P^i_{total} (\psi P^i_{total} + \gamma) \\ & = \sum_{i \in ST} (\psi {P^i_{total}}^2 + \gamma P^i_{total}) \end{aligned} \tag{11}$$

As can be seen, the optimization objectives in Equations (7), (9), and (11) are in three different forms, which will be separately simulated.

2.5. Transform the EV Charging into NLP/MINLP Problem

As previously introduced, the constraints considered for EV charging are nonlinear. Therefore, the EV charging cases are transformed into NLP or MINLP optimization problems [16,31], which consist of an objective function, some box bound constraints, several equal, and unequal constrained functions. Generally, the NLP problem has the form:

$$\text{subject to :} \quad \begin{array}{c} \text{minimize } F_{obj}(x), \\ H_{eq}(x) = 0 \\ G_{ieq}(x) \leq 0 \\ l_b \leq x \leq u_b \end{array} \tag{12}$$

where x represents the controllable vectors, $F_{obj}(x)$ denotes the objective function, $H_{eq}(x)$ and $G_{ieq}(x)$ represent the equality and inequality constraints, and l_b and u_b are the lower and upper box limits respectively, all with compatible dimensions.

In this work, the issue of flexible charging rate (CD-F and C-F mode) is therefore transformed into an NLP problem. For the condition of constant charging rate (CD-C and C-C mode), only the charging status of EVs needs to be settled, and the Equation (1) thus evolves into Equation (13), and the optimization model turns into MINLP.

$$P^i_{EV,j} = P^i_{EV,j} S^i_{EV,j} \quad \forall i \in \mathrm{ST}, \forall j \in \mathrm{SE}$$
$$S^i_{EV,j} = \begin{cases} 1, & \text{charging} \\ -1, & \text{discharging, if permitted} \\ 0, & \text{otherwise} \end{cases} \tag{13}$$

3. Proposed ISS and GA-ISS Algorithm Frameworks

There are two algorithms proposed in this work: ISS for single EV charging and GA-ISS for massive EV charging. The proposed ISS algorithm is based on a basic scatter search (SS) framework with advanced local solvers. Therefore, to better understand the proposed algorithms, the principle of SS and the utilized local search solvers will first be described, followed by the ISS framework, and the hybrid method GA-ISS handling massive EVs.

3.1. Basics of Scatter Search (SS)

SS is a novel evolutionary-based method, since it normally avoids too many random components (e.g., mutation or crossover operators), which other methods, such as GA, rely on [27]. It has been reported that SS has been successfully applied in a variety of continuous and discrete optimization problems [27,32–34]. One prominent feature of a scatter search lies in its flexible structure, where a variety of ways and degrees of sophistication can be deployed for its elements [27]. Moreover, instead of operating on massive populations, SS concentrates only on a small set denoted herein as *RefSet* [32–34]. It obtains an optimum through balancing diversification (robustness) and intensification (efficiency) for *RefSet* systematically. The whole process of basic SS is shown in Figure 1.

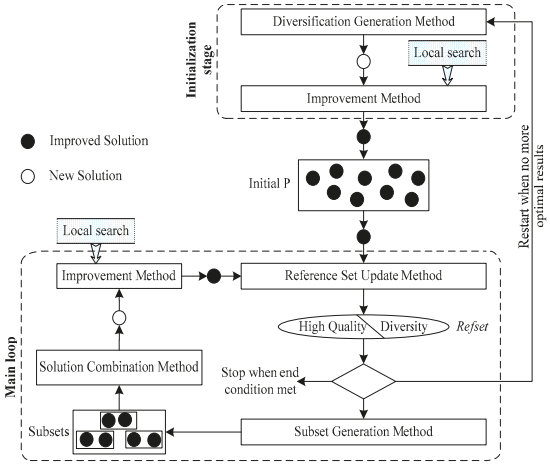

Figure 1. Schematic of a standard scatter search (SS) template.

In general, SS contains five strategies in total [27]: (i) a diversification generation method is used for generating an original population *P*, (ii) an improvement method wherein local search procedures can be embedded to examine the trial individuals and acquire high quality solutions, (iii) a reference set update method to initialize and maintain *RefSet*, normally resulting in a high quality subset $RefSet_1$ with best fitness value and a diversified subset $RefSet_2$ with optimal diverse

value ($RefSet = RefSet_1 + RefSet_2$), (iv) a subset generation method operates on $RefSet$, via which subsets are created and then utilized for producing combined vectors, and (v) a solution combination method for computing new testing vectors (one or more) from the results obtained from the subset generation method.

Optionally, a restart phase can be scheduled to rebuild the solutions. However, the SS framework described above is just a generic structure and all the five methods will be clearly defined in the latter designed ISS method.

3.2. The Utilized Local Search Solvers

As previously introduced, different SQP techniques, including filter-SQP and MISQP, are chosen as local solvers to complete different tasks. The process of the filter-SQP, as shown in Figure 2, essentially follows the procedure described in [28]. At each iteration, the sub-problem is replaced and solved as the trust-region sub-problem $TRQP(x_k, \Delta_k)$, with Δ_k denoting the trust-region radius. For trust-region methods, however, a common problem lies in the difficulty of tuning penalty coefficients. A filter technique is hence incorporated to determine whether the solution outperforms the previous one and also guarantee the acceptability. The acceptance of the basic filter is defined by comparing the violation function value $h(x_k)$ and fitness value $f(x_k)$:

$$h(x_k) \le \beta h_{\mathcal{F}} \ \ or \ \ f(x_k) \le f_{\mathcal{F}} - \lambda h_{\mathcal{F}} \ \text{for all} \ (h_{\mathcal{F}}, f_{\mathcal{F}}) \in \mathcal{F}, \tag{14}$$

where $0 < \lambda < \beta < 1$, $\mathcal{F}$ represents the filter set, $h_{\mathcal{F}}$ and $f_{\mathcal{F}}$ are the respective violation and fitness values of the element in the set. Additionally, with the aim of improving feasibility and optimality, a novel non-monotone technique for setting the filter criteria is also implemented [28]. In essence, it sets the filter by dividing the trail step d_k into a quasi-normal part d_k^n and a tangential part d_k^t.

Filter-SQP optimization process

Input: Parameters of the problem

Output: The best solution

Step 1) Initialization for the variables, initial region radius $\Delta_0 \ge \Delta_{\min} > 0$, Hessian matrix, $\mathcal{F} = \{(h_0, f_0)\}$;

Step 2) Solve the $TRQP(x_k, \Delta_k)$, stop if terminal condition is met

Step 3) Calculate d_k^n and d_k^t, obtain $d_k = d_k^n + d_k^t$;

Step 4) Judge whether $x_k + d_k$ is acceptable to $\mathcal{F}$. If yes, execute step 5, otherwise enter into step 6;

Step 5) When d_k is unacceptable, enter into step 7, else execute step 6;

Step 6) Adjust Δ_k, back to step 3;

Step 7) Update $x_{k+1} = x_k + d_k$ and $\mathcal{F}$, update Δ_{k+1}, Hessian matrix. Loop back to step 2 (for next iteration).

Figure 2. Pseudo code of filter- sequential quadratic programming (SQP).

For CD-C and C-C charging modes, the problem turns out to be far more complex, since no explicit available criterion can be utilized to approach the optimal solution, nor can the optimal positions of the integers be effectively captured from relevant corresponding continuous solutions. The MISQP technique in [29] is therefore employed for solving the MINLP model in the proposed framework. Three key techniques are employed to achieve the tasks and they are: (i) a trust region technique with second-order amendments to stabilize the algorithm, (ii) a quasi-Newton formula to update the Hessian matrix, and (iii) a branch-and-bound skill to handle the sub-problems.

3.3. The Proposed ISS Algorithm for Single EV Charging

The implementation of the proposed ISS algorithm follows the generic framework of SS as shown in Figure 1. Several techniques have been introduced to enhance the overall performance.

(1) Initialization and restart mechanism

A diversification generation method is implemented with Latin hypercube uniform sampling [33]. The initial results are then filtered as the original population P, of which half ($RefSet_1$) are top-ranking solutions with better fitness values, while another half ($RefSet_2$) are arbitrarily selected from the rest of the diverse vectors. On top of this, a restart mechanism that aims to escape from local minima is also designed when improvement cannot be obtained after the subset updating step. For this process, while leaving the subset $RefSet_1$ unchanged, additional solutions are first created with the diversification generation method, and the subset $RefSet_2$ is reconstructed in the manner of subsequent updating method.

(2) Improvement procedure

The improvement procedure embedded with local search solvers is utilized to improve the results obtained from the diversification or the combination methods. Since different objectives and price types are considered for both NLP and MINLP problems, an intelligent module is designed to conduct the optimizations, as shown in Figure 3. The data will be categorized into different types, including: power rate type, charging type, price type selection, and objective selection, with which the charging power rate, charging type, price category and objective function would be determined respectively. All this information is then collected by the joint units where different local solvers are allocated.

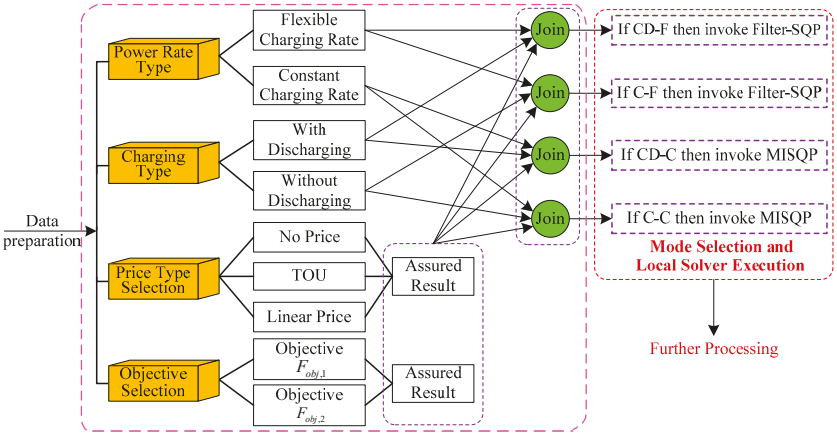

Figure 3. The intelligent module for executing the local solvers of the intelligent scatter search (ISS).

(3) Population updating

For the update of the solutions, a new solution can only enter into $RefSet_1$ upon the following criteria: (i) the individual occupies a fitness value superior to the worst one in $RefSet_1$, or (ii) the individual has a diverse value larger than the worst one in $RefSet_2$. The diverse value is assessed according to the Euclidean distance $d(x,z)$ between the candidate and the individuals in $RefSet_1$. The new solution that maximize $d_{min}(x)$ will be selected to update $RefSet_2$:

$$d_{min}(x) = \min_{z \in RefSet_1} \{ d(x,z) \}. \tag{15}$$

(4) Subset generation and combination

A common strategy considering all pairs of the individual solutions is adopted to generate the basis for creating combined solutions. Instead of using simple linear combination, an improved hyper-rectangle based skill proposed in [34] has been chosen for this task. For each pairwise member, a bias of their relative position is utilized to define the hyper-rectangles for leading the solutions to approach "better" ones and move away from "bad" ones. This method can help to extend the search region and also expand the exploring directions without an additional memory term. Meanwhile, the "go-beyond" strategy from the same paper is also employed to enhance the intensification. The principle of this technique is to search the potential directions of the best generated individual and its parents continuously, in order to produce new individuals within two generations. Since the search area in this process is extended, the strategy promotes a diversity of solutions and accelerates convergence.

To further confine each element x_k^r of the solution vector within the correct search region, the repair strategy given below is employed:

$$\begin{array}{ll} \text{if} & x_k^r > u_b^r, \quad \text{then } x_k^r = u_b^r \\ \text{if} & x_k^r < l_b^r, \quad \text{then } x_k^r = l_b^r \end{array} \tag{16}$$

where l_b^r and u_b^r are respective lower and upper limits.

3.4. The Proposed GA-ISS Method for Massive EV Charging

When massive EV charging is simultaneously considered, the computation burden is enormous. Neither traditional deterministic techniques nor intelligent meta-heuristics can easily produce the optimized result, since: (i) the CPU may run out of memory due to large data demand, and (ii) long computation time is expected because of its complexity. For instance, a whole day is required to solve a single EV charging case that comes with 96 variables. Accordingly, there are 96 box constraints for Equation (1); 1 equality constraint for Equation (4), and 96 × (2 + 1) inequality constraints for Equations (2) and (5). Therefore, it is desirable to have an efficient algorithm to deliver accurate solutions.

To handle large-scale EV charging, a hybrid method integrating GA and ISS is proposed, as shown in Figure 4.

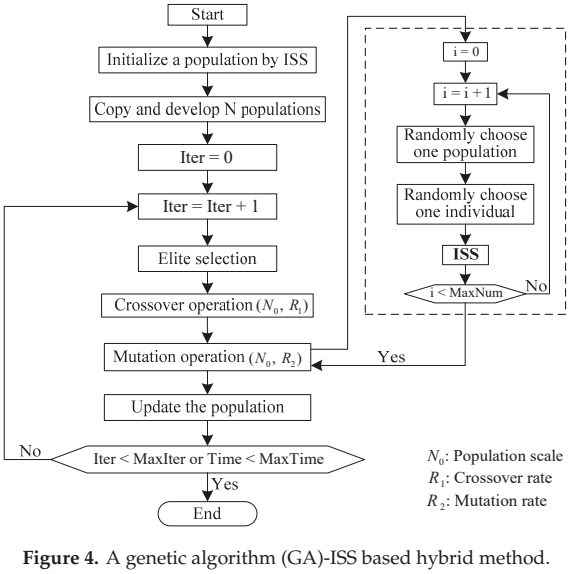

Figure 4. A genetic algorithm (GA)-ISS based hybrid method.

In Figure 4, N_0, R_1 and R_2 denote the population scale, crossover, and mutation rate, respectively. The proposed method (GA-ISS) expects to benefit from the gist of both algorithms, for which GA processes present a strong global search ability and robustness, while the ISS structure is prominent in searching capability and quick convergence. During the procedure, a single EV state is determined by ISS, whilst the entire fleet co-evolves to the optimum and relies on the mutation and crossover procedures from GA.

To speed up the process, the initialization of population is first processed by ISS and copied into the N_0 populations, which will then be optimized in the main loop. The mutation operation takes the speed and optimization advantage of the ISS, through which individuals from the previous population are refined. As previous individuals are utilized as the starting points of the ISS, the time spent for refining the individuals will be substantially reduced, since the old ones have already been optimized to approach their optimal positions.

4. Simulation and Results

4.1. Parameter Setting

A case of overnight charging in a typical residential area where EV charging occurs during the night is considered in the simulations. The TOU price modeled from [35] is set on a rolling hourly basis, and the price curve as well as the tested basic daily load profile is shown in Figure 5. The LP rate coefficients are chosen to be $\psi = 2 \times 10^{-4}$ and $\gamma = 0.22$. In addition, the maximum generation capacity is limited to be 20% above the daily peak load.

A single EV is used to illustrate the effectiveness of the ISS. The battery parameters and charging behavior are given in Table 2. It is also assumed that the minimum allowed SOC of the battery is 20%.

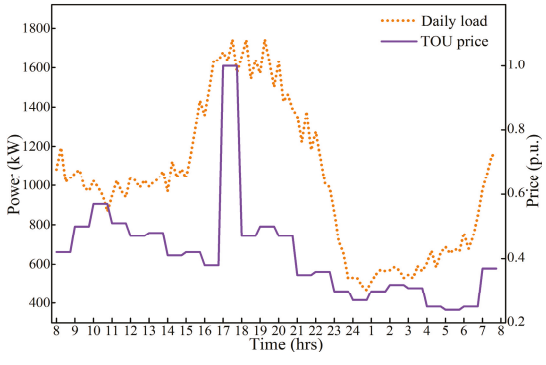

Figure 5. Data profile for simulation.

Table 2. Parameters for the single electric vehicle (EV).

Capacity	Initial SOC	Rated Charging Power	Start Time	End Time	Desired SOC
24 (kWh)	58.59%	3.3 kW	21:15	6:30	90%

To test the GA-ISS method, an EV fleet with 100 vehicles is simulated. As EVs arrive and depart at the charging points in a random manner, the arriving time, departure time, rated capacity, rated plugging power, and the initial SOC of the test fleet are defined based on truncated normal distribution [36]. In Table 3, the standard deviation (Std.), minimum, maximum, and mean values of the EV fleet are listed. It should be noted that the parameters of EVs in this work are just adopted for demonstration purposes, and there is no restriction on the power and capacity of EV batteries for the proposed algorithms.

Table 3. Parameters for the fleet with 100 EVs.

Parameter	Minimum	Maximum	Mean	St. Dev
Arriving Time (h)	18:00	22:00	20:00	1:30
Departure Time (h)	5:45	7:45	7:00	0:45
SOC (%)	20	90	50	20
Capacity (kWh)	10	30	18	6.93
Plugging power (kW)	2	10	3.54	1.48

4.2. Simulation Results

The algorithm is coded on the MATLAB Platform (R2012a) and executed on a PC with 2.66-GHz Quad CPU (Intel Core 2), 4GB RAM and Windows 7 64-bit system. The performance of the ISS is first tested with the single EV, followed by the testing for a GA-ISS with an EV fleet.

(1) Single EV charging

For a single EV case, the algorithm can help the user determine the charging schedule to reduce the charging cost, or to better cooperate with the system operator to smooth the load profile. In order to evaluate the performance of ISS:

(a) Two other commonly used heuristic algorithms, GA [37] and PSO [38], have been tested for flexible charging rate modes. And the GS method is utilized to produce the best reference result, since it explores all possible solutions [39].
(b) Since a GS is unable to solve MINLP problems, only a GA and PSO [40] have been tested for constant charging rate.
(c) The population number of the ISS is set to 30, while its iteration number of local solvers is limited to 10. The population member of the GA and PSO are set to 100. In addition, the total iteration numbers for all the above methods are set to 100.

Three different objective functions are used for the evaluation: (i) OF1—load curve flattening, refer to Equation (7), (ii) OF2—cost minimization with TOU price, refer to Equation (9), and (iii) OF3—cost minimization with LP price, refer to Equation (11).

For each condition, 50 simulations have been carried out, and Table 4 gives the mean values of the simulation results for all methods for comparison. It can be seen that the mean values for all the methods under different charging scenarios appear to be similar, however, an ISS can give slightly better performances compared with the heuristic GA and PSO algorithms for all three objective functions.

Table 4. Mean values of the methods for single EV charging.

Objectives	Type	GS	GA	PSO	Proposed ISS
OF1 (standard deviation, kW)	CD-F	368.19	368.91	368.30	368.21
	CD-C	N/A	368.40	368.40	368.36
	C-F	368.71	368.96	368.77	368.74
	C-C	N/A	369.00	368.80	368.80
OF2 (normalized value, p. u.)	CD-F	44,277.19	44,278.55	44,278.04	44,277.22
	CD-C	N/A	44,278.63	44,278.19	44,277.69
	C-F	44,280.23	44,281.59	44,281.34	44,280.45
	C-C	N/A	44,280.65	44,280.42	44,280.39
OF3 (normalized value, p. u.)	CD-F	40,457.35	40,459.66	40,459.15	40,457.39
	CD-C	N/A	40,459.74	40,458.98	40,458.40
	C-F	40,463.21	40,464.29	40,463.72	40,463.24
	C-C	N/A	40,463.55	40,463.54	40,463.43

On the other hand, it is also observed that (i) a flexible charging rate enables more benefits than a constant charging rate, and (ii) the discharging ability exhibits more profits than charging-only cases in reducing charging costs and flattening daily load.

For more comparison to show the properties of the ISS, a box-plot for CD_C and CD_F mode with the OF1 objective is illustrated in Figure 6. From the distribution of the optimized outcome, it demonstrates that an ISS can achieve more consistent results than that of the other two methods. The robustness and good convergence of this novel algorithm are thus demonstrated.

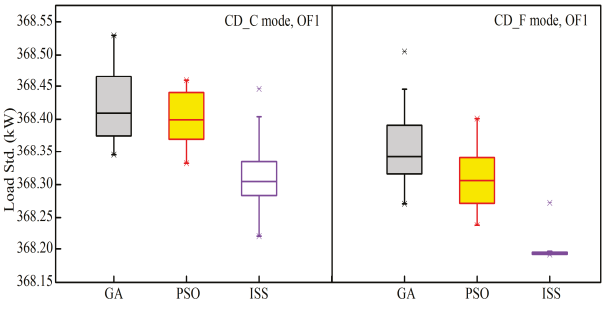

Figure 6. Box-plot for CD_C and CD_F mode with objective OF1.

Table 5 gives the average computational time of the respective algorithms for performing 50 simulations. It is clearly shown that the computational time of ISS is significantly shorter than that of the GS, GA, and PSO, which is the main advantage of the proposed algorithm. Furthermore, it can also be observed that the computational time is generally longer for (i) bidirectional charging cases as compared to the charging-only cases, and (ii) a flexible charging rate as compared to constant charging rate.

To examine the computational efficiency of the ISS scheduling algorithm, the iteration behaviors of GA, PSO and ISS, with trial simulations for the three objective functions under CD-F mode and CD-C mode are shown in Figures 7 and 8. The convergence behaviors of C-F mode and C-C mode present similar properties respective to that of the CD-F and CD-C modes, hence their iteration figures are omitted here. As demonstrated in Figures 7 and 8, despite the strong global search ability, the convergence process of both GA and PSO methods are very slow and may easily get trapped into local optima, whereas ISS always converges with far fewer iterations.

In terms of robustness, convergence, and efficiency, the proposed ISS method has adapted very well to single EV charging cases.

Table 5. Computational time for a single EV for the methods under four charging modes (In seconds).

Objective Function	Type	GS	GA	PSO	Proposed ISS
OF1	CD-F	93.16	11.67	8.51	1.18
	CD-C	N/A	9.38	6.24	0.98
	C-F	49.39	12.07	7.43	1.22
	C-C	N/A	9.97	5.98	0.86
OF2	CD-F	80.39	11.13	6.88	1.14
	CD-C	N/A	9.77	6.15	0.95
	C-F	21.41	12.31	7.32	1.03
	C-C	N/A	9.62	6.47	0.81
OF3	CD-F	43.61	12.65	6.42	1.25
	CD-C	N/A	9.38	5.97	0.94
	C-F	31.43	13.81	6.26	1.12
	C-C	N/A	8.88	5.83	0.83

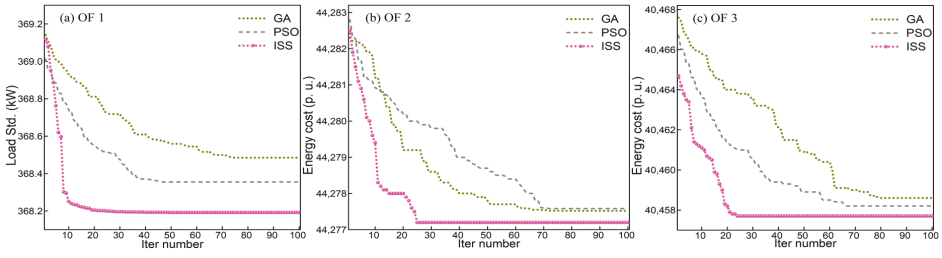

Figure 7. Iteration map for single EV with different objectives under CD-F mode. (**Left**) Load standard deviation with OF1; (**Center**) Energy cost with OF2; (**Right**) Energy cost with OF3.

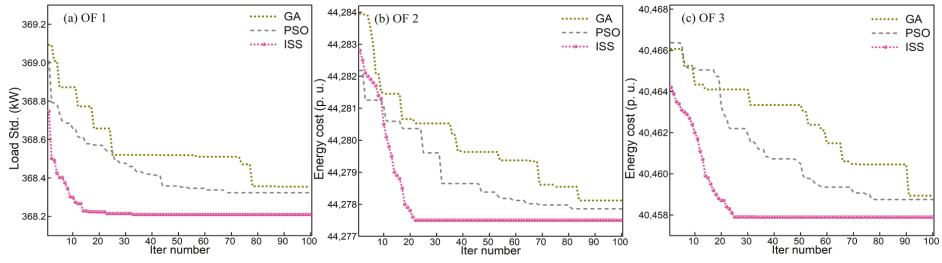

Figure 8. Iteration map for single EV with different objectives under CD-C mode. (**Left**) Load standard deviation with OF1; (**Center**) Energy cost with OF2; (**Right**) Energy cost with OF3.

(2) Group EV charging

For massive amounts of EVs connecting to a charging station or regulated by an aggregator, the proposed GA-ISS hybrid method can help smooth the load profile or minimize the overall charging cost. For illustration purpose, CD-F mode with the aforementioned three objectives is utilized as the testing scenario for the group EV charging case. The desired SOC for all EVs is set to 90%. The maximum running time of the ISS at the initial phase is set as 0.8 s for an individual EV. For comparison and highlighting the benefit of scheduling for massive EVs:

a. The dumbing control method (DCM), which charges all EVs as soon as they are plugged in, is tested;
b. A GA-PSO hybrid method from [41] is chosen for comparison, since it can obtain better solutions along with less variation and processing time in comparison to other common heuristic methods. The population size and iteration number for GA-PSO and GA-ISS are set to be 20 and 50, respectively. Moreover, during the inner optimization for EV scheduling of GA-PSO and GA-ISS, the determination of a single EV state via PSO/ISS is set to be stopped when the minimum criteria of the solution quality is satisfied. In Table 6, the detailed parameters of the algorithms utilized for group EV charging are displayed.
c. A commercial CVX [42] toolbox is also simulated to perform the EV charging scheduling method, since it can simultaneously calculate all the variables and constraints and obtain the global optimized result. This approach is herein named global control.

Table 6. Parameters of the algorithms utilized for group EV charging.

Parameter	DCM	GA-PSO	Global Control	GA-ISS
Mutation rate	N/A	0.2	N/A	0.2
Crossover rate	N/A	0.4	N/A	0.4
Population size	N/A	20	N/A	20
Iteration number	N/A	50	N/A	50

Figure 9 demonstrates the simulation load profiles of these approaches with different optimization goals, chosen from one simulation result. As can be seen, the dumbing method can amplify the peak, indicating the necessity of EV charging scheduling. On the other hand, it is also shown that the proposed GS-ISS method obtains far better results than that of the GA-PSO method, and it can deliver a performance comparable to global control solved through the CVX solver, which requires a commercial licensing payment.

In addition, the final load profile of TOU price (OF2) is more fluctuated when compared to the LP price case (OF3), as shown in Figure 9b,c. As a matter of fact, the LP price load curve is almost the same as the OF1 one, which is obtained with the aim of load curve flattening. This suggests that an appropriate pricing strategy can help smooth the daily load curve with EV charging/discharging.

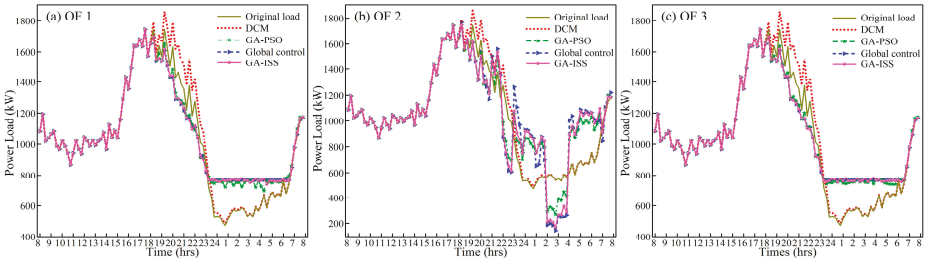

Figure 9. Load profiles for group EV charging of DCM, GA-PSO, Global Control, and GA-ISS under CD-F mode.

The average computational time as well as the optimization results for 20 simulations are listed in Table 7. It can be seen that the time spent by the hybrid GA-ISS approach is comparable to that of the global control, but outperforms the GA-PSO method. This verifies the effectiveness of the GA-ISS method for large scale EV scheduling. However, it should also be noted that the CVX solver may become stalled when more EVs are involved (e.g., when the EV number of the fleet changes to be 200, the computer may run out of memory with the tested PC), and hence solution may not be guaranteed for the global control.

Table 7. Outcomes of different solving methods.

Method	OF1		OF2		OF3	
	Result	**Time**	**Result**	**Time**	**Result**	**Time**
GA-PSO	298.02	337.6	44,615.2	291.2	41,274.5	359.7
Global Control	289.39	92.6	44,538.1	87.7	41,222.2	94.2
GA-ISS	291.75	112.9	44,558.5	105.9	41,229.2	117.1

5. Conclusion and Future Work

This paper presents the detailed derivation of two algorithms: an ISS framework to deal with single EV charging, and a hybrid GA-ISS method comprised of GA theory and the proposed ISS approach for handling a large-scale EV fleet. The main contribution is that the proposed algorithms can support both V2G and G2V, with either a flexible or constant charging power rate. It has been demonstrated that the ISS algorithm is the most computationally efficient way to obtain attractive performances among other methods including GS, GA, and PSO for a single EV charging scenario. On the other hand, for group EV charging, the GA-ISS approach has also been shown to be an extremely effective approach.

The proposed ISS algorithm and GA-ISS hybrid method are shown to be promising in terms of both efficiency and accuracy, thus providing potential techniques for the implementation of EV

charging controls. The proposed algorithms are suitable to be implemented to schedule EV charging in many occasions, such as home charging, EV aggregations (stations), at power companies, etc. It should also be noted that this paper is focused on the issue of EV charging scheduling. Currently, energy storage is increasingly applied in power grids. The charging powers of energy storages are normally much higher than that of EVs, thus can exhibit a greater impact than EVs. Many characteristics of energy storage are similar to EVs and it is valuable to upgrade the algorithm for a wider usage, including the issue of energy storage.

Future work can be performed to incorporate more considerations for EVs, such as the various charging rates of a single EV battery, advanced modeling for SOC impacts on the EV charging rate, EV battery degradations, etc. Studies on the essential coordination between EVs and other power system components (renewable energy resources, home appliances, etc.) can be also addressed to accomplish more comprehensive and practical EV charging algorithms.

Author Contributions: T.M. and X.Z. were responsible to the conceptualization of the algorithms; T.M. conducted the investigation, designed the methodology and completed the original draft; X.Z. and B.Z. gave suggestions on the proposed idea and simulation cases; T.M. and X.Z. revised the paper based on comments from the reviewers.

Funding: This paper was supported by the project "Study on intelligent simulation technologies and panoramic simulation platform design for power market" of China Southern Power Grid (Project number: ZBKJXM20170082).

Conflicts of Interest: The authors declare no conflict of interest.

Nomenclature

ST	Time interval set
SE	EV set
i	Time index
j	EV index
n	Total number of timeslots
$P^{i}_{EV,j}$	Charging power value for EV j in time i
$P^{\min}_{EV,j}$	Lower charging power limit for EV j
$P^{\max}_{EV,j}$	Upper charging power limit for EV j
$Soc_{j,i}$	SOC for EV j in time i
$Soc_{j,start}$	SOC value at the beginning for EV j
$Soc_{j,\text{end}}$	SOC value at the end for EV j
$Soc_{j,\min}$	Minimum allowed SOC value for EV j
$Soc_{j,\max}$	Maximum allowed SOC value for EV j
$E_{\text{exp},j}$	Expectation level for the SOC of EV j
$E_{RC,j}$	Nominal battery SOC of EV j
P^{i}_{total}	Total load demand in time i
P^{i}_{ld}	Active base load in time i
P^{i}_{g}	Maximum supply power in time i
C^{i}_{e}	Electricity tariff in time i
C^{i}_{TOU}	TOU price at time interval i
C^{i}_{LP}	Linear price rate at time interval i
ψ	Linear term of linear price
γ	Constant term of linear price
$C_{EV,j}$	Nominal capacity of EV j

References

1. Haidar, A.M.A.; Muttaqi, K.M.; Sutanto, D. Technical challenges for electric power industries due to grid-integrated electric vehicles in low voltage distributions: A review. *Energy Convers. Manag.* **2014**, *86*, 689–700. [CrossRef]

2. De Quevedo, P.M.; Muñoz-Delgado, G.; Contreras, J. Impact of electric vehicles on the expansion planning of distribution systems considering renewable energy, storage and charging stations. *IEEE Trans. Smart Grid* **2017**. [CrossRef]
3. Morais, H.; Sousa, T.; Vale, Z.; Faria, P. Evaluation of the electric vehicle impact in the power demand curve in a smart grid environment. *Energy Convers. Manag.* **2014**, *82*, 268–282. [CrossRef]
4. Tang, D.; Wang, P. Nodal impact assessment and alleviation of moving electric vehicle loads: From traffic flow to power flow. *IEEE Trans. Power Syst.* **2016**, *31*, 4231–4242. [CrossRef]
5. Beaude, O.; Lasaulce, S.; Hennebel, M.; Mohand-Kaci, I. Reducing the impact of EV charging operations on the distribution network. *IEEE Trans. Smart Grid* **2016**, *7*, 2666–2679. [CrossRef]
6. Zhang, X.; Zhong, Q.; Kadirkamanathan, V.; He, J.; Huang, J. Source-side Series-virtual-impedance Control to Improve the Cascaded System Stability and the Dynamic Performance of Its Source Converter. *IEEE Trans. Power Electron.* **2018**. [CrossRef]
7. Jian, L.; Zhu, X.; Shao, Z.; Niu, S.; Chan, C.C. A scenario of vehicle-to-grid implementation and its double-layer optimal charging strategy for minimizing load variance within regional smart grids. *Energy Convers. Manag.* **2014**, *78*, 508–517. [CrossRef]
8. Xie, D.; Chu, H.; Gu, C.; Li, F.; Zhang, Y. A novel dispatching control strategy for EVs intelligent integrated stations. *IEEE Trans. Smart Grid* **2017**, *8*, 802–811. [CrossRef]
9. Panwar, L.K.; Reddy, K.S.; Kumar, R.; Panigrahi, B.K.; Vyas, S. Strategic Energy Management (SEM) in a micro grid with modern grid interactive electric vehicle. *Energy Convers. Manag.* **2015**, *106*, 41–52. [CrossRef]
10. Sun, B.; Huang, Z.; Tan, X.; Tsang, D.H.K. Optimal scheduling for electric vehicle charging with discrete charging levels in distribution grid. *IEEE Trans. Smart Grid* **2018**, *9*, 624–634. [CrossRef]
11. García-Álvarez, J.; González, M.A.; Vela, C.R. Metaheuristics for solving a real-world electric vehicle charging scheduling problem. *Appl. Soft Comput. J.* **2018**, *65*, 292–306. [CrossRef]
12. Mohamed, A.; Salehi, V.; Ma, T.; Mohammed, O. Real-time energy management algorithm for plug-in hybrid electric vehicle charging parks involving sustainable energy. *IEEE Trans. Sustain. Energy* **2014**, *5*, 577–586. [CrossRef]
13. Deilami, S.; Masoum, S.A.; Moses, S.P.; Masoum, A.S.M. Real-time coordination of plug-in electric vehicle charging in smart grids to minimize power losses and improve voltage profile. *IEEE Trans. Smart Grid* **2011**, *2*, 436–467. [CrossRef]
14. Wang, B.; Yang, J. Optimal electric vehicle charging scheduling with time varying profits. In Proceedings of the 2018 52nd Annual Conference on Information Sciences and Systems (CISS), Princeton, NJ, USA, 21–23 March 2018; pp. 1–6.
15. Mao, T.; Lau, W.H.; Shum, C.; Chung, H.S.H.; Tsang, K.F.; Tse, N.C.F. A regulation policy of EV discharging price for demand scheduling. *IEEE Trans. Power Syst.* **2018**, *33*, 1275–1288. [CrossRef]
16. Zhang, X.; Zhong, Q. Improved Adaptive-Series-Virtual-Impedance Control Incorporating Minimum Ripple Point Tracking for Load Converters in DC Systems. *IEEE Trans. Power Electron.* **2016**, *31*, 8088–8095. [CrossRef]
17. Bourass, A.; Cherkaoui, S.; Khoukhi, L. Secure optimal itinerary planning for electric vehicles in the smart grid. *IEEE Trans. Ind. Inform.* **2017**, *13*, 3236–3245. [CrossRef]
18. Zhao, T.; Peng, Y.; Nehorai, A. An optimal and distributed demand response strategy with electric vehicles in the smart grid. *IEEE Trans. Smart Grid* **2014**, *5*, 861–869.
19. Leterme, W.; Ruelens, F.; Claessens, B.; Belmans, R. A flexible stochastic optimization method for wind power balancing with PHEVs. *IEEE Trans. Smart Grid* **2014**, *5*, 1238–1245. [CrossRef]
20. Malikopoulos, A.A. Supervisory power management control algorithms for hybrid electric vehicles: A survey. *IEEE Trans. Intell. Transp. Syst.* **2014**, *15*, 1869–1885. [CrossRef]
21. Soares, J.; Morais, H.; Sousa, T.; Vale, Z.; Faria, P. Day-ahead resource scheduling including demand response for electric vehicles. *IEEE Trans. Smart Grid* **2013**, *4*, 596–605. [CrossRef]
22. Yu, J.J.Q.; Li, V.O.K.; Lam, A.Y.S. Optimal V2G scheduling of electric vehicles and unit commitment using chemical reaction optimization. In Proceedings of the IEEE Cong. Evolutionary Computation (CEC), Cancun, Mexico, 20–23 June 2013; pp. 392–399.
23. Kang, Q.; Wang, J.; Zhou, M.; Ammari, A.C. Centralized charging strategy and scheduling algorithm for electric vehicles under a battery swapping scenario. *IEEE Trans. Intell. Transp. Syst.* **2016**, *17*, 659–669. [CrossRef]

24. Alonso, M.; Amaris, H.; Germain, J.G.; Galan, J.M. Optimal charging scheduling of electric vehicles in smart grids by heuristic algorithms. *Energies* **2014**, *7*, 2449–2475. [CrossRef]
25. Yilmaz, M.; Krein, P.T. Review of the impact of vehicle-to-grid technologies on distribution systems and utility interfaces. *IEEE Trans. Power Electron.* **2013**, *28*, 5673–5689. [CrossRef]
26. Fang, X.; Misra, S.; Xue, G.; Yang, D. Smart grid—The new and improved power grid: A survey. *IEEE Commun. Surv. Tutor.* **2012**, *14*, 944–980. [CrossRef]
27. Glover, F.; Laguna, M.; Martí, R. Fundamentals of scatter search and path relinking. *Control Cybern.* **2000**, *29*, 653–684.
28. Yu, K.; Pu, D. A nonmonotone filter trust region method for nonlinear constrained optimization. *J. Comput. Appl. Math.* **2009**, *233*, 230–239.
29. Exler, O.; Schittkowski, K. A trust region SQP algorithm for mixed-integer nonlinear programming. *Optim. Lett.* **2007**, *1*, 269–280. [CrossRef]
30. Charging Lithium-Ion. Available online: http://batteryuniversity.com (accessed on 25 December 2018).
31. Tsui, K.M.; Chan, S.C. Demand response optimization for smart home scheduling under real-time pricing. *IEEE Trans. Smart Grid* **2012**, *3*, 1812–1821. [CrossRef]
32. Nebro, A.J.; Luna, F.; Alba, E.; Dorronsoro, B.; Durillo, J.J.; Beham, A. AbYSS: Adapting scatter search to multiobjective optimization. *IEEE Trans. Evol. Comput.* **2008**, *12*, 439–457. [CrossRef]
33. McKay, M.D.; Beckman, R.J.; Conover, W.J. A comparison of three methods for selecting values of input variables in the analysis of output from a computer code. *Technometrics* **2000**, *42*, 55–61. [CrossRef]
34. Egea, J.A.; Balsa-Canto, E.; Garcia, M.-S.G.; Banga, J.R. Dynamic optimization of nonlinear processes with an enhanced scatter search method. *Ind. Eng. Chem. Res.* **2009**, *48*, 4388–4401. [CrossRef]
35. Qian, K.; Zhou, C.; Allan, M.; Yuan, Y. Modeling of load demand due to EV battery charging in distribution Systems. *IEEE Trans. Power Syst.* **2011**, *26*, 802–810. [CrossRef]
36. Vagropoulos, S.I.; Bakirtzis, A.G. Optimal bidding strategy for electric vehicle aggregators in electricity markets. *IEEE Trans. Power Syst.* **2013**, *28*, 4031–4041. [CrossRef]
37. Goldberg, D.E. *Genetic Algorithms in Search, Optimization, and Machine Learning*; Addison-Wesley: Reading, MA, USA, 1989.
38. Kennedy, J.; Eberhart, R. Particle swarm optimization. In Proceedings of the IEEE International Conference on Neual Networks, IV, Perth, Australia, 27 November–1 December 1995; pp. 1942–1948.
39. Kearfott, R.B. *Rigorous Global Search: Continuous Problems*; Kluwer: Dordrecht, The Netherlands, 1996.
40. Kennedy, J.; Eberhart, R. A discrete binary version of the particle swarm algorithm. In Proceedings of the IEEE International Conference on Systems, Man, and Cybernetics, Orlando, FL, USA, 12–15 October 1997; pp. 4104–4108.
41. Sheikhalishahi, M.; Ebrahimipour, V.; Shiri, H.; Zaman, H.; Jeihoonian, M. A hybrid GA-PSO approach for reliability optimization in redundancy allocation problem. *Int. J. Adv. Manuf. Technol.* **2013**, *68*, 317–338. [CrossRef]
42. Michael, G.; Stephen, B. CVX: Matlab Software for Disciplined Convex Programming. Available online: http://cvxr.com/cvx (accessed on 25 December 2018).

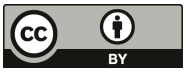

energies

MDPI

Article

Optimal Decision-Making to Charge Electric Vehicles in Heterogeneous Networks: Stackelberg Game Approach

Shijun Chen [1], Huwei Chen [2,*] and Shanhe Jiang [1]

[1] School of Physics and Electronic Engineering, Anqing Normal University, Anqing 246133, China; ch_sh_jun@sina.com (S.C.); jshxlxlw@163.com (S.J.)
[2] Department of Computer Science and Technology, Tsinghua University, Beijing 100084, China
* Correspondence: chenhuwei2008@163.com

Received: 20 November 2018; Accepted: 14 January 2019; Published: 21 January 2019

Abstract: Electric vehicles (EVs) are designed to improve the efficiency of energy and prevent the environment from being polluted, when they are widely and reasonably used in the transport system. However, due to the feature of EV's batteries, the charging problem plays an important role in the application of EVs. Fortunately, with the help of advanced technologies, charging stations powered by smart grid operators (SGOs) can easily and conveniently solve the problems and supply charging service to EV users. In this paper, we consider that EVs will be charged by charging station operators (CSOs) in heterogeneous networks (Hetnet), through which they can exchange the information with each other. Considering the trading relationship among EV users, CSOs, and SGOs, we design their own utility functions in Hetnet, where the demand uncertainty is taken into account. In order to maximize the profits, we formulate this charging problem as a four-stage Stackelberg game, through which the optimal strategy is studied and analyzed. In the Stackelberg game model, we theoretically prove and discuss the existence and uniqueness of the Stackelberg equilibrium (SE). Using the proposed iterative algorithm, the optimal solution can be obtained in the optimization problem. The performance of the strategy is shown in the simulation results. It is shown that the simulation results confirm the efficiency of the model in Hetnet.

Keywords: electric vehicles; heterogeneous networks; demand uncertainty; power optimization; Stackelberg game

1. Introduction

Recently, electric vehicles (EVs) with low gas emission and environment protection have attracted much attention and have been widely applied in some countries when harsh environment problems are exposed in the world, such as energy shortage, air pollution, and the greenhouse effect [1–4]. Considering the increasing number of EVs, many more charging stations have been built to supply charging service. However, charging stations always have to confront the overload problem of charging EVs with a large amount of charging power demand. Then, EVs cannot be charged in time, which will restrict EV users' quality of experience (QoE) [5,6].

Due to the limited capacity of batteries, EVs usually have to be charged with low SOC. Recently, charging stations have attracted much attentions and have been recognized as an available approach to supply charging service [7]. However, confronting the growing number of EV users, both waiting time and the power bill account for a major part of their payment. Though some different incentive mechanisms have been developed so far, there are still some problems, i.e., the optimal strategy of power management is usually designed based on the demand-side of EV users, which neglects the

performance of wireless communication, e.g., wireless sensor networks (WSN) and vehicular-grid networks (V2G) [8].

With the development of communication technology, more and more wireless communication technology has been used in EVs and charging stations, e.g., vehicular ad-hoc networks (VANETs) and cognitive radio networks are applied to make the routing choice for EV users [9,10]. Different from the existing works, we study how to control the power supply among EV users, charging station operators (CSOs), and smart grid operators (SGOs) in the heterogeneous networks (Hetnet). Through Hetnet, there are many advantages for the charging system: (i) CSOs can exchange the real-time information with EV users, by which it helps EV users avoid the charging peak periods and reduce the expenditure of charging service. (ii) The power efficiency can be improved based on the optimal strategy to be designed in Hetnet, which can solve the problem of limited power supply. (iii) It can conveniently supply power to EV users and improve the profits of SGOs with less gas emission [11].

However, in order to improve the quality of experience (QoE), there are still some challenges to be improved and studied in the charging system when adopting the wireless communication [12,13]. These challenges include how to design the optimal strategy for CSOs, while benefiting both EV users and power retailers, respectively. At the same time, few works have been performed to make the optimal strategy in Hetnet [14–16]. Currently, many different power management approaches have been developed in the literature, aiming for scheduling the power supply with high efficiency [17–19]. In the existing works, the proposed approaches cannot directly be used in our paper, which have been designed without consideration of the performance of wireless communication.

In this paper, we propose the optimal incentive decision-making scheme to charge EVs in Hetnet. Firstly, the network model is designed in Hetnet, through which EV users can conveniently be supplied by CSOs. Then, based on the trading relationship among EV users, CSOs, and SGOs, we design the utility function for each of them in this charging system, respectively. In this function, the performance of Hetnet is integrated with the waiting time of EV users. Taking the bit error ratio (BER) in Hetnet, the load uncertainty is also analyzed and studied. In addition, in order to obtain the optimal strategy, we propose a four-stage Stackelberg game scheme. Namely, this charging power problem is formulated as an optimization problem. Through the back induction method, we get the Stackelberg equilibrium (SE), in which we also analyze and prove its existence. With less computation, we present an iterative search algorithm to obtain the optimal solution. Finally, simulation results demonstrate the effectiveness of our proposal.

The contributions of our paper are summarized as follows:

- In order to supply convenient charging service for EV users, the network model is designed. Through Hetnet, the information of each one in this charging system can be obtained. Here, as an important criterion in Hetnet, BER is taken into account, by which power loss is brought about.
- Based on the interaction among EV users, CSOs, and SGOs, we develop the utility function of each one in the charging system, respectively. Simultaneously, load uncertainty is studied and analyzed, by confronting BER in Hetnet. In order to schedule the power supplied from SGOs, we propose a four-stage Stackelberg game scheme. Then, the charging problem is formulated as an optimization problem. Through the theoretical analysis, we prove the existence and uniqueness of Stackelberg equilibrium (SE) in the proposed scheme.
- With less calculation, we present an iterative search algorithm to achieve SE with maximum profits of each in the charging system. At last, the simulation results verify the effectiveness of our proposed algorithm.

The rest of the paper is organized as follows. Section 2 presents a brief overview of the related work. In Section 3, we design the system model and reveal how to exchange the information in Hetnet. In Section 4, a Stackelberg game model is proposed to schedule the power supply. Meanwhile, an iterative search algorithm is presented to achieve optimal solutions. Both simulation results and related analysis are provided in Section 5, and then, the conclusions are given in Section 6.

2. Related Work

Based on the development of wireless communication, both charging service for EV users and advanced communication technologies have been integrated. Through this approach, the QoE of EV users can be greatly improved with the efficiency of supplying power. Manshadi et al. in [20] studied how to operate the charging station based on the relationship between the electricity network and the transportation network. In order to supply the efficient and stable charging service to EV users, Sun et al. in [21] designed a novel software-defined framework. Yang et al. in [22] proposed a flexible real-time power management protocol for charging EVs based on the cooperation of each EV. In the process of managing power, the charging and discharging decision of each EV could be chosen in real time. Considering the charging problem based on the wireless sensor network, Zhang et al. in [23] formulated the wireless charging problem as an NP-hard scheduling problem. Hu et al. in [24] designed an energy management scheme for charging stations to utilize energy efficiently in the software-defined V2G network. However, the proposed algorithm in the above works mainly focused on how to schedule the power for EV users and power retailers, neglecting the power supply from the power grid. The performance of wireless communication is not taken into account, which is very important in scheduling the power for EV users.

Due to the performance of EV users' stochastic arrival and departure from charging stations, the queuing model is widely used to analyze this problem [25]. In order to solve the charging schedule, researchers studied many methods based on the different objectives. N. Liu et al. in [13] proposed a novel heuristic algorithm to schedule the power in the commercial building microgrid. The state of charge (SOC) of EV batteries was considered with the output of PV and the charging rate. W. Yuan et al. in [19] studied the charging strategy to maximize users' utility based on the two-stage Stackelberg model by using the queue model of $\mathcal{M}/\mathcal{G}/\mathcal{K}$, in which the location of charging facility and electrical price were discussed at the same time. I. Bayram et al. in [26] presented the pricing strategy to satisfy EV users' power demand based on the QoS, while shifting the power supply shortage during peak hours. M. Karbasioun et al. in [27] proposed the control policy with the minimal cost for the operator based on the real-time pricing scheme. C. Jin et al. in [28] investigated the charging schedule of the electric vehicles with the energy storage in the electricity market under the real-time price. M. Ismail et al. in [29] studied the profits of operators with queue theory and the proposed search algorithm to find the optimal outlets and capacity size in the charging facility. A. Ovalle et al. in [30] presented the charging schedule of EVs with the forward dynamic programming and game theory approach with the given constraints related to EVs. In addition, considering the driving routing of EV users with its corresponding constraints, artificial intelligence algorithms are usually used to decide the optimal strategy in power management [27]. In the existing works, they only considered that the dynamic event triggering affected the charging power, except the queue waiting time. Though the optimal solution could be obtained, they neglected users' different interests with the waiting space size [31,32].

In contrast, to the best of our knowledge, there are few works on power management with Hetnet. In this paper, we take EVs with recharged batteries into account and present the optimal strategy in Hetnet. Firstly, considering the relationship among them composed of EV users, CSOs, and SGOs, we develop different utility functions with the load uncertainty and BER in Hetnet. In order to obtain the optimal strategy, we propose a four-stage Stackelberg game scheme, in which SGO is set as the leader, while both EV users and CSOs are set as followers. Through a back induction method, we get the SE in the proposed game scheme, by proving its existence and uniqueness. Using the presented iterative search algorithm, the optimal solutions are achieved with maximum profits in this charging system. The performance of our proposed algorithm is shown in the simulation results. It demonstrates the effectiveness of our proposal, through which it can benefit each player in the game.

3. System Model

3.1. Network Model

In this section, we design the network model in Hetnet to describe the communication in the charging system. Then, based on the trading relationship among EV users, CSOs, and SGOs, we develop the utility function of each. Driven by maximum profits, a four-stage Stackelberg game scheme is proposed to study the optimal strategy.

As shown in Figure 1, we assume that EV users equipped with on-board units (OBU) can communicate with each other, while they can share real-time information by road side units (RSU). In order to serve EV users conveniently, the base station (BS) deployed by CSOs is also used to communicate with EV users in Hetnet, including the power price, power demand, and total power supply. Based on Hetnet, EV users can be charged with less waiting time than that without communication technology. In this charging system, we assume that EV user k will be charged by COS m, which is supplied by SGO i, denoted as $\forall k \in \mathcal{J}_m, \mathcal{J}_m = \{1, \ldots, J_m\}$, and $\forall m \in \mathcal{M}, \mathcal{M} = \{1, \ldots, M\}$, respectively. In this paper, SGO i is assumed to supply power to multiple CSOs.

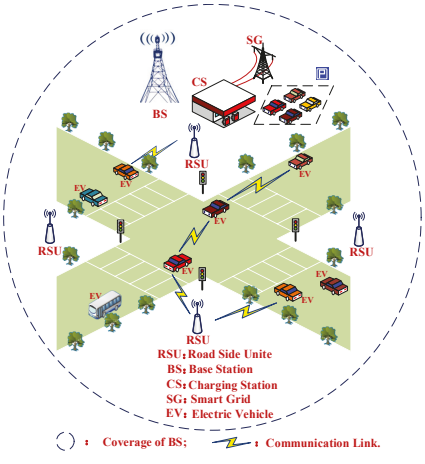

Figure 1. Network model in the heterogeneous network.

3.2. Utility Model for Electric Vehicles

In the power market, one of the economic criteria is clients' satisfaction with respect to the supplied power. Here, we suppose that the utility function can be defined by the difference between EVs' satisfaction and the payment for COS m, which is expressed by:

$$G_{EV}(\boldsymbol{X}) = \sum_{k=1}^{J_m} \left(U_1(x_{k,m}, p_m^i) - C_1(x_{k,m}, p_m^i) \right) \tag{1}$$

$$s.t. \;\; x_{k,m}^{\min} \leq x_{k,m} \leq x_{k,m}^{\max} \tag{2}$$

Here, p_m^i denotes the power price offered by CSO m; $\boldsymbol{X}$ is the set of power demands, $\boldsymbol{X} = (x_{1,m}, \ldots, x_{J_m,m})$; $U_1(x_{k,m}, p_m^i)$ denotes the satisfaction; $C_1(x_{k,m}, p_m^i)$ denotes the payment for charging service. $x_{k,m}$ denotes the power demand of EV user k with the constraints of a proper upper limit $x_{k,m}^{\max}$ and a proper lower limit $x_{k,m}^{\min}$.

Based on the requirement of charging service, EV users can acquire higher satisfaction with less waiting time and a lower power price. Thus, $U_1(x_{k,m}, p_m^i)$ should monotonically decrease on waiting

time W_m and p_m^i, respectively. In contrast, it will increase on the amount of charging power $x_{k,m}$. According to [33], we design $U_1(x_{k,m}, p_m^i)$ as a logarithmic function shown by:

$$U_1(x_{k,m}, p_m^i) = \overline{\gamma}_1 \frac{x_{k,m}}{\varsigma_m} + (A_k - \frac{W_m}{W_{\max}} p_m^i) \ln(1 + x_{k,m}) \tag{3}$$

where $\overline{\gamma}_1$ denotes the preset economic parameter; ς_m is the discount of charging service; A_k is a preset parameter to ensure this function is non-negative; W_m is the waiting time in CSO m, which is bounded by the maximum waiting time $W_{\max}$.

Meanwhile, EV user k will pay for the charging power supplied from CSOs, including the cost in the driving distance. Therefore, $C_1(x_{k,m}, p_m^i)$ is defined by:

$$C_1(x_{k,m}, p_m^i) = p_m^i x_{k,m} + \delta_{k,m} d_{k,m} \tag{4}$$

where $\delta_{k,m}$ denotes the average economic parameter for EV user k; $d_{k,m}$ is EV user k's driving distance to CSO m in Hetnet.

Then, substituting (2) and (3) into (1), we have:

$$G_{EV}(\boldsymbol{X}) = \sum_{k=1}^{J_m} \left[\overline{\gamma}_1 \frac{x_{k,m}}{\varsigma_m} + (A_k - \frac{W_m}{W_{\max}} p_m^i) \ln(1 + x_{k,m}) - p_m^i x_{k,m} - \delta_{k,m} d_{k,m} \right] \tag{5}$$

3.3. Utility Model for Charging Station Operators

Meeting the power demand, each CSO can acquire profits through selling the power to EV users. In order to maximize their profits, CSOs will analyze how to decide the optimal strategy. Here, we assume that the unstable communication in Hetnet leads to the loss of power in transmission, which implies that the power demand of EV users received by CSOs will be $\hat{x}_{k,m} = (1 - \zeta_m) x_{k,m} + \zeta_m \theta_m$. ζ_m is the probability of the loss of power and θ_m denotes the load uncertainty in this charging system. θ_m is supposed to be a zero-mean random variable with variance σ_θ^2. The utility function of CSO m with its constraints is defined by:

$$G_{CS}(\boldsymbol{Y}) = \sum_{m=1}^{M} \left(\sum_{k=1}^{J_m} R_{k,m}(p_m^i, x_{k,m}) - C_2(y_{m,i}, p_i) \right) \tag{6}$$

$$s.t. \quad \sum_{k=1}^{J_m} \hat{x}_{k,m} \leq y_{m,i} \tag{7}$$

Here, the set of CSOs' power demand is $\boldsymbol{Y}$, denoted by $\boldsymbol{Y} = (y_{1,i}, y_{2,i}, \ldots, y_{M,i})$. $C_2(y_{m,i}, p_i)$ denotes the cost for the power supply $y_{m,i}$ from SGO i, which can be designed by:

$$R_{k,m}(p_m^i, x_{k,m}) = (p_m^i - \frac{\overline{\gamma}_1}{\varsigma_m}) \hat{x}_{k,m} \tag{8}$$

$$C_2(y_{m,i}, p_i) = p_i y_{m,i} \tag{9}$$

In order to ensure the balance between the power demand and supply, we define that the probability of charging power supplied to EV users exceeding the power bought will be less than a small requirement level, in which a threshold is used to denote the amount of EV users' power demand beyond the power supply. Thus, according to (7), it can be further expressed by:

$$\Pr\left\{\sum_{k=1}^{J_m}(\eta_m x_{k,m}+\zeta_m\theta_m)-y_{m,i}\geq\tau_m\right\}\leq\vartheta_m \tag{10}$$

Here, η_m is the quality of service in Hetnet QoS, denoted by $\eta_m = 1-\zeta_m$; τ_m is the threshold value; ϑ_m is a smaller value as the requirement level.

Therefore, substituting (8) and (9) into (6), we have:

$$G_{CS}(\boldsymbol{Y})=\sum_{m=1}^{M}\left[(p_m^i-\frac{\overline{\gamma}_1}{\varsigma_m})\sum_{k=1}^{J_m}(\eta_m x_{k,m}+\zeta_m\theta_m)-p_i y_{m,i}\right] \tag{11}$$

3.4. Utility Model for Smart Grid Operators

Based on the above statement, SGOs can also obtain the payoff through selling power to CSOs, besides the necessary investment in generating electricity. We formulate the utility function as the difference between the payoff and investment, expressed by:

$$G_{SG}(p_i,\boldsymbol{Y})=\sum_{m=1}^{M}\Big(R_{m,i}(p_i,y_{m,i})-C_3(y_{m,i})\Big) \tag{12}$$

$$s.t.\ \sum_{m=1}^{M}y_{m,i}\leq\Theta \tag{13}$$

where p_i is the power price offered by SGO i; $R_{m,i}(p_i,y_{m,i})$ is SGO i's payoff; $C_3(y_{m,i})$ denotes the investment for power supply $y_{m,i}$. Based on (8) and [24,25], we have:

$$R_{m,i}(p_i,y_{m,i})=p_i y_{m,i} \tag{14}$$

$$C_3(y_{m,i})=\frac{a_i}{2}y_{m,i}^2+b_i y_{m,i}+\varpi_i \tag{15}$$

where a_i denotes the variable acceleration of the cost function curve; b_i is the rate of the variety of the cost function curve; ϖ_i denotes the fixed cost.

Therefore, substituting (14) and (15) into (12), it can be rewritten as:

$$G_{SG}(p_i,\boldsymbol{Y})=\sum_{m=1}^{M}\Big(p_i y_{m,i}-\frac{a_i}{2}y_{m,i}^2-b_i y_{m,i}-\varpi_i\Big) \tag{16}$$

3.5. A Four-Stage Stackelberg Game Model

We study and analyze the trading interaction among EV users, CSOs, and SGOs, while the utility function of each in this charging system is developed, respectively. Due to selfishness, each of them in this system aims to maximize its own profits without consideration of others' payoff. However, with rationality, each of them studies how to maximize its own profits, based on others' decisions in this system. Therefore, in order to decide the optimal strategy, we adopt game theory to study the charging problem, where a four-stage Stackelberg game scheme is developed in Figure 2. In Stage I, SGO i as the leader will determine the power price p_i and broadcast this information to CSOs. The proper amount of power $y_{m,i}$ ($\forall m\in\mathcal{M}$) will be decided by each CSO in Stage II, given p_i in Stage I. Then, in order to obtain higher revenue, CSO m will decide its price $p_{m,i}$ and the supply power to EV users in Stage III. At last, in Stage IV, EV user k ($\forall k\in\mathcal{J}_m$) will decide its power demand $x_{k,m}$ based on $p_{m,i}$.

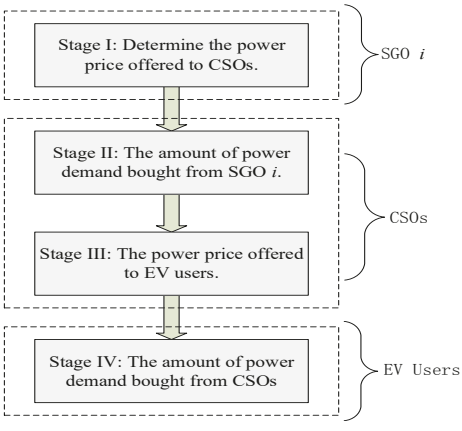

Figure 2. Four-stage Stackelberg game scheme. CSO, charging station operator; SGO, smart grid operator.

For EV users, the relationship among them is non-cooperative and competitive. The objection of each EV user is to maximize its profits based on the price offered by CSOs. Thus, this problem can be formulated as an optimization problem shown by:

$$\boldsymbol{X}_m^* = \arg\max G_{EV}(\boldsymbol{X}_m) \tag{17}$$

Here, the set of optimal power demand supplied by CSO m is $\boldsymbol{X}_m^*$, denoted by $\boldsymbol{X}_m^* = (x_{1,m}^*, x_{2,m}^*, \ldots, x_{J_m,m}^*)$.

Then, CSOs aim to make the optimal pricing plans, with consideration of EV users' power demand bounded by the constraints shown in (2). Similarly, this optimization problem is formulated as:

$$p_m^{i*} = \arg\max G_{CS}(\boldsymbol{Y}, p_m^i) \tag{18}$$

where p_m^{i*} is the optimal pricing strategy offered by CSO m.

In addition, each CSO will determine the amount of power supplied from SGOs with maximum profits. Following the optimal pricing strategy p_m^{i*}, CSO m studies how to obtain the power demand from SGO i, given the power price p_i. In this case, the optimization problem is formulated as:

$$y_{m,i}^* = \arg\max G_{CS}(\boldsymbol{Y}, p_m^i) \tag{19}$$

where $y_{m,i}^*$ is the optimal power demand strategy for CSO m powered by SGO i.

Finally, driven by maximum profits, SGOs analyze how to make decisions on the optimal pricing strategy. Following (19), this problem is formulated as an optimization problem shown by:

$$p_i^* = \arg\max G_{SG}(p_i, \boldsymbol{Y}) \tag{20}$$

where p_i^* is the optimal pricing plan of SGO i offered to CSOs.

Through the above analysis, the optimal solution can be decided by the proposed four-stage game-theoretical scheme. In this game, SE will be solved to maximize their own profits. In this case, each of them will not tend to change its optimal decisions.

4. Four-Stage Stackelberg Game Analysis

In this section, we will analyze the game-theoretical scheme and obtain the SE through backward induction. First of all, we discuss how EV users adjust their power demand to maximize their profits

in Stage IV. Then, based on EV users' power demand, we will analyze how CSOs make decisions on the power pricing for EV users and the amount of power demand from SGO in Stages III and II, respectively. At last, we exploit how SGO decides the powering strategy in Stage I.

4.1. Power Demand of EV Users in Stage IV

Based on the price broadcast by CSOs, EV users make optimal decisions to maximize their profits, besides the necessary payment for power demand. In order to determine the optimal strategy, this can be achieved through solving the following optimization problem shown by:

$$\begin{aligned}&\max_{\forall k\in J_m, x_{k,m}\geq 0} G_{EV}(\boldsymbol{X})\\&=\sum_{k=1}^{J_m}\left[\overline{\gamma}_1\frac{x_{k,m}}{\varsigma_m}+(A_k-\frac{W_m}{W_{\max}}p_m)\ln(1+x_{k,m})\right.\\&\left.-p_m x_{k,m}-\delta_{k,m}d_{k,m}\right]\end{aligned}\tag{21}$$

Here, without loss of generality, p_m is usually decided to be larger than $\frac{\overline{\gamma}_1}{\varsigma_m}$, e.g., $p_m > \frac{\overline{\gamma}_1}{\varsigma_m}$. Thus, we take the first derivation of $G_{EV}(\boldsymbol{X})$ with respect to $x_{k,m}$ as follows.

$$\frac{\partial G_{EV}(\boldsymbol{X})}{\partial x_{k,m}}=\sum_{k=1}^{J_m}\left(\frac{A_k-\frac{W_m}{W_{\max}}p_m}{1+x_{k,m}}+\frac{\overline{\gamma}_1}{\varsigma_m}-p_m\right)\tag{22}$$

Then, taking the second derivation of $G_{EV}(\boldsymbol{X})$ with respect to $x_{k,m}$, we have:

$$\frac{\partial^2 G_{EV}(\boldsymbol{X})}{\partial x_{k,m}^2}=-\sum_{k=1}^{J_m}\frac{A_k-\frac{W_m}{W_{\max}}p_m}{(1+x_{k,m})^2}\tag{23}$$

Since $A_k-\frac{W_m}{W_{\max}}p_m$ is larger than zero in (3), we can know that $\frac{\partial^2 G_{EV}(\boldsymbol{X})}{\partial x_{k,m}^2}<0$, which implies that the first derivation of $G_{EV}(\boldsymbol{X})$ is strictly decreasing on $x_{k,m}$. Thus, we divide it into two cases to analyze the optimal strategy.

Case 1: CSOs will announce the lower price to EV users to be charged.

If the power price p_m is lower than $\frac{(A_k\varsigma_m+\overline{\gamma}_1)W_{\max}}{(W_m+W_{\max})\varsigma_m}$ in (22), we have:

$$\lim_{x_{k,m}\to 0}\frac{\partial G_{EV}(\boldsymbol{X})}{\partial x_{k,m}}=\sum_{k=1}^{J_m}\left[A_k+\frac{\overline{\gamma}_1}{\varsigma_m}-p_m(\frac{W_m}{W_{\max}}+1)\right]>0\tag{24}$$

$$\lim_{x_{k,m}\to\infty}\frac{\partial G_{EV}(\boldsymbol{X})}{\partial x_{k,m}}=-\sum_{k=1}^{J_m}\left(p_m-\frac{\overline{\gamma}_1}{\varsigma_m}\right)<0\tag{25}$$

Therefore, based on the results in (24) and (25), this implies that the utility function is firstly increasing with the increase of $x_{k,m}$. Then, it continuously decreases with the increase of $x_{k,m}$. It will prove that the utility function in (21) is a concave function and that the optimal strategy exists. Correspondingly, we can obtain the optimal strategy.

Case 2: CSOs will announce the larger price to EV users to be charged.

If the power price p_m is not less than $\frac{(A_k\varsigma_m+\overline{\gamma}_1)W_{\max}}{(W_m+W_{\max})\varsigma_m}$, similar to the method used in Case 1, we have:

$$\lim_{x_{k,m}\to 0}\frac{\partial G_{EV}(\boldsymbol{X})}{\partial x_{k,m}}=\sum_{k=1}^{J_m}\left[A_k-p_m(\frac{W_m}{W_{\max}}+1)-\frac{\overline{\gamma}_1}{\varsigma_m}\right]\leq 0 \tag{26}$$

$$\lim_{x_{k,m}\to \infty}\frac{\partial G_{EV}(\boldsymbol{X})}{\partial x_{k,m}}=-\sum_{k=1}^{J_m}\left(p_m-\frac{\overline{\gamma}_1}{\varsigma_m}\right)<0 \tag{27}$$

From (26) and (27), we can know that the utility function in (21) decreases with the increase of $x_{k,m}$, which implies that the optimal strategy also exists. The optimal strategy for EV users is:

$$x^*_{k,m}=0 \tag{28}$$

Based on the above analysis, we can know that $G_{EV}(\boldsymbol{X})$ is a strictly concave function on $\boldsymbol{X}$. The optimal strategy will be obtained through solving $\frac{\partial G_{EV}(\boldsymbol{X})}{\partial x_{k,m}}=0$, and we have:

$$x^*_{k,m}=\begin{cases}\frac{(A_kW_{\max}-p_mW_m)\varsigma_m}{(\varsigma_m p_m-\overline{\gamma}_1)W_{\max}}-1, & if\ p_m<\frac{(A_k\varsigma_m+\overline{\gamma}_1)W_{\max}}{(W_m+W_{\max})\varsigma_m}\\ 0, & others\end{cases} \tag{29}$$

Due to the requirement of protecting batteries' healthy, each EV user's power demand is larger than zero, which means that the power demand of EV users is larger than zero. As a result, the optimal strategy is obtained as follows.

$$x^*_{k,m}=\frac{(A_kW_{\max}-p_mW_m)\varsigma_m}{(\varsigma_m p_m-\overline{\gamma}_1)W_{\max}}-1 \tag{30}$$

4.2. Power Price Offered by Charging Station Operators in Stage III

In this subsection, we will study how CSOs make pricing decisions to improve their profits, on the condition that the power demand of EV users can be decided in Stage IV. Considering the fixed expense and the power price offered by SGO, CSOs should adjust their power price for EV users driven by more profits. Due to the impact of uncertain load, we have:

$$\begin{aligned}&\mathbb{E}\{G_{CS}(\boldsymbol{Y},\boldsymbol{P}^i)\}\\&=\sum_{m=1}^{M}\left\{\sum_{k=1}^{J_m}\eta_m\left[\frac{A_kW_{\max}-p_m(W_m+W_{\max})}{W_{\max}}+\frac{\overline{\gamma}_1}{\varsigma_m}\right]-p_iy_{m,i}-\epsilon_mL_m\right\}\end{aligned} \tag{31}$$

$$s.t.\ \Pr\left\{\sum_{k=1}^{J_m}\left[\eta_mx^*_{k,m}+\zeta_m\theta_m\right]-y_{m,i}\geq\tau_m\right\}\leq\vartheta_m \tag{32}$$

Here, it is worthy to note that (31) implies that the utility function of CSOs is monotonically decreasing with the increase of p_m, which means that the optimal strategy will exist on the condition that the constraints can be known. Substituting (30) into (32), we have:

$$\begin{aligned}
&\Pr\left\{\sum_{k=1}^{J_m}(\eta_m x_{k,m}^* + \zeta_m \theta_{k,m}) - y_{m,i} \geq \tau_m\right\} \leq \vartheta_m \\
&\Longrightarrow \Pr\left\{\sum_{k=1}^{J_m}\theta_{k,m} \geq \frac{1}{\zeta_m}(y_{m,i} + \tau_m - \sum_{k=1}^{J_m}\eta_m x_{k,m}^*)\right\} \leq \vartheta_m \\
&\Longrightarrow \frac{1}{2}\Pr\left\{\zeta_m|\sum_{k=1}^{J_m}\theta_{k,m}| \geq y_{m,i} + \tau_m - \sum_{k=1}^{J_m}\eta_m x_{k,m}^*\right\} \leq \vartheta_m \\
&\Longrightarrow \frac{1}{2}\frac{(\zeta_m\sigma_\theta)^2 J_m}{(y_{m,i} + \tau_m - \sum_{k=1}^{J_m}\eta_m x_{k,m}^*)^2} \leq \vartheta_m \\
&\Longrightarrow p_m \geq \frac{\eta_m \sum_{k=1}^{J_m}\left(A_k - \frac{\overline{\gamma}_1 W_m}{\zeta_m W_{\max}}\right)}{y_{m,i} + \tau_m - \sqrt{\frac{J_m}{2\vartheta_m}}\zeta_m\sigma_\theta + \eta_m J_m(\frac{W_m + W_{\max}}{W_{\max}})} + \frac{\overline{\gamma}_1}{\zeta_m}
\end{aligned} \tag{33}$$

which implies that the optimal price is shown by:

$$p_m^* = \frac{\overline{\gamma}_1}{\zeta_m} + \frac{\eta_m \sum_{k=1}^{J_m}\left(A_k - \frac{\overline{\gamma}_1 W_m}{\zeta_m W_{\max}}\right)}{y_{m,i} + \tau_m - \sqrt{\frac{J_m}{2\vartheta_m}}\zeta_m\sigma_\theta + \eta_m J_m(\frac{W_m + W_{\max}}{W_{\max}})} \tag{34}$$

4.3. Power Supply of Charging Station Operators in Stage II

Based on the price and power demand for EV users, the objection of operators will improve their profits besides the payment for electricity retailers. In this stage, CSOs decide the power supply to be procured from SGO. Substituting (34) into (11), we have:

$$\begin{aligned}
&\mathbb{E}\{G_{CS}(\boldsymbol{Y}, \boldsymbol{P}^i)\} \\
&= \sum_{m=1}^{M}\left\{\sum_{k=1}^{J_m}\left[\eta_m A_k - \frac{\eta_m^2 \sum_{k=1}^{J_m}\left(A_k - \frac{\overline{\gamma}_1 W_m}{\zeta_m W_{\max}}\right)}{\frac{y_{m,i} + \Omega_m}{W_m + W_{\max}} W_{\max}}\right]\right. \\
&\quad \left. - \frac{\overline{\gamma}_1 \eta_m J_m (W_m + W_{\max})}{\zeta_m W_{\max}} - p_i y_{m,i}\right\}
\end{aligned} \tag{35}$$

where:

$$\Omega_m = \tau_m - \sqrt{\frac{J_m}{2\vartheta_m}}\zeta_m\sigma_\theta + \eta_m J_m(\frac{W_m + W_{\max}}{W_{\max}}) \tag{36}$$

In order to obtain the optimal solution in (35), we should exploit and discuss its existence given the price offered by SGO. Similar to the method in Stage IV, we take the first derivative of $\mathbb{E}\{G_{CS}(\boldsymbol{Y}, \boldsymbol{P}^i)\}$ with respect to $y_{m,i}$ as follows.

$$\frac{\partial \mathbb{E}\{G_{CS}(\boldsymbol{Y}, \boldsymbol{P}^i)\}}{\partial y_{m,i}} = \sum_{m=1}^{M} \left[\frac{\eta_m^2 J_m (W_m + W_{\max}) \sum\limits_{k=1}^{J_m} \left(A_k - \frac{\overline{\gamma}_1 W_m}{\varsigma_m W_{\max}} \right)}{W_{\max} (y_{m,i} + \Omega_m)^2} - p_i \right] \tag{37}$$

Following, taking the second derivative of $\mathbb{E}\{G_{CS}(\boldsymbol{Y}, \boldsymbol{P}^i)\}$ with respect to $y_{m,i}$, we have:

$$\frac{\partial^2 \mathbb{E}\{G_{CS}(\boldsymbol{Y}, \boldsymbol{P}^i)\}}{\partial y_{m,i}^2} = - \sum_{m=1}^{M} \left[\frac{2\eta_m^2 J_m (W_m + W_{\max}) \sum\limits_{k=1}^{J_m} \left(A_k - \frac{\overline{\gamma}_1 W_m}{\varsigma_m W_{\max}} \right)}{W_{\max} (y_{m,i} + \Omega_m)^3} \right] \tag{38}$$

Since $A_k > \frac{W_m}{W_{\max}} p_m$ and $p_m > \frac{\overline{\gamma}_1}{\varsigma_m}$, we can know that $A_k > \frac{\overline{\gamma}_1 W_m}{\varsigma_m W_{\max}}$. In addition, due to the non-negative parameters in (35), it means that the second derivative of $\mathbb{E}\{G_{CS}(\boldsymbol{Y}, \boldsymbol{P}^i)\}$ is less than zero. Based on (35)–(38), this implies that the optimal solution can be achieved when the following conditions is satisfied.

$$\begin{aligned} &\lim_{y_{m,i} \to 0} \frac{\partial \mathbb{E}\{G_{CS}(\boldsymbol{Y}, \boldsymbol{P}^i)\}}{\partial y_{m,i}} > 0 \\ &\Longrightarrow \sum_{m=1}^{M} \left[\frac{\eta_m^2 J_m (W_m + W_{\max}) \sum\limits_{k=1}^{J_m} \left(A_k - \frac{\overline{\gamma}_1 W_m}{\varsigma_m W_{\max}} \right)}{W_{\max} \Omega_m^2} \right] - M p_i > 0 \\ &\Longrightarrow p_i < \frac{1}{M} \sum_{m=1}^{M} \left[\frac{\eta_m^2 J_m (W_m + W_{\max})}{W_{\max} \Omega_m^2} \left(\sum_{k=1}^{J_m} A_k - \frac{\overline{\gamma}_1 J_m W_m}{\varsigma_m W_{\max}} \right) \right] \end{aligned} \tag{39}$$

and:

$$\lim_{y_{m,i} \to \infty} \frac{\partial \mathbb{E}\{G_{CS}(x_{k,m}, p_{k,m})\}}{\partial y_{m,i}} = -M p_i < 0 \tag{40}$$

Thus, the utility function of $\mathbb{E}\{G_{CS}(\boldsymbol{Y}, \boldsymbol{P}^i)\}$ is a concave function when both the inequalities (39) and (40) are satisfied. It proves that the optimal strategy exists, which can be achieved as follows.

$$\begin{aligned} &\frac{\partial \mathbb{E}\{G_{CS}(\boldsymbol{Y}, \boldsymbol{P}^i)\}}{\partial y_{m,i}} = 0 \\ &\Longleftrightarrow \frac{\eta_m^2 J_m (W_m + W_{\max}) \sum\limits_{k=1}^{J_m} \left(A_k - \frac{\overline{\gamma}_1 W_m}{\varsigma_m W_{\max}} \right)}{W_{\max} (y_{m,i} + \Omega_m)^2} = p_i \\ &\Longleftrightarrow y_{m,i}^* = \sqrt{\frac{\eta_m^2 J_m (W_m + W_{\max}) \sum\limits_{k=1}^{J_m} \left(A_k - \frac{\overline{\gamma}_1 W_m}{\varsigma_m W_{\max}} \right)}{W_{\max} p_i}} - \Omega_m \end{aligned} \tag{41}$$

Meanwhile, based on (34) and (41), we can obtain the following results.

$$\begin{aligned} & p_m^* < \frac{(A_k\varsigma_m + \overline{\gamma}_1)W_{\max}}{(W_m + W_{\max})\varsigma_m} \\ \Longrightarrow & \frac{\overline{\gamma}_1}{\varsigma_m} + \frac{\eta_m \sum_{k=1}^{J_m}\left(A_k - \frac{\overline{\gamma}_1 W_m}{\varsigma_m W_{\max}}\right)}{y_{m,i} + \Omega_m} < \frac{(A_k\varsigma_m + \overline{\gamma}_1)W_{\max}}{(W_m + W_{\max})\varsigma_m} \\ \Longrightarrow & \frac{\eta_m\varsigma_m(W_m + W_{\max})\sum_{k=1}^{J_m}\left(A_k - \frac{\overline{\gamma}_1 W_m}{\varsigma_m W_{\max}}\right)}{A_k W_{\max}\varsigma_m - \overline{\gamma}_1 W_m} - \Omega_m < y_{m,i}^* \\ \Longrightarrow & p_i < \frac{J_m(\varsigma_m W_{\max}\min A_k - \overline{\gamma}_1 W_m)^2}{\varsigma_m^2 W_{\max}(W_m + W_{\max})\sum_{k=1}^{J_m}\left(A_k - \frac{\overline{\gamma}_1 W_m}{\varsigma_m W_{\max}}\right)} \end{aligned} \tag{42}$$

In addition, driven by more profits, the power price for EV users to be charged is larger than that offered by SGO when the same amount of power procured from CSO will be sold to EV users by CSOs, e.g., $p_m \geq p_i$.

4.4. Power Price Offered by the Smart Grid Operator in Stage I

Given the power price and power demand offered by CSOs, SGO should decide the power price for CSOs to obtain more profits. This pricing problem can be formulated as an optimization problem. Based on (16), (41) and (42), this optimization problem can be expressed by:

$$\max G_{SG}(\boldsymbol{P}) = \sum_{m=1}^{M}\left(p_i y_{m,i}^* - \frac{a_i}{2}y_{m,i}^{*2} - b_i y_{m,i}^* - \varpi_i\right) \tag{43}$$

$$s.t. \sum_{m=1}^{M} y_{m,i}^* \leq \Theta \tag{44}$$

Substituting (41) into (43), we take the second derivative of $G_{SG}(\boldsymbol{P})$ with respect to p_i, and we have:

$$\begin{aligned} & \frac{\partial^2 G_{SG}(\boldsymbol{P})}{\partial p_i^2} \\ & = -\sum_{m=1}^{M}\sqrt{\frac{\eta_m^2 J_m(W_m + W_{\max})\sum_{k=1}^{J_m}\left(A_k - \frac{\overline{\gamma}_1 W_m}{\varsigma_m W_{\max}}\right)}{W_{\max}}} \\ & \times\left[\frac{a_i}{4}\left(4p_i^{-3}\sqrt{\frac{\eta_m^2 J_m(W_m + W_{\max})\sum_{k=1}^{J_m}\left(A_k - \frac{\overline{\gamma}_1 W_m}{\varsigma_m W_{\max}}\right)}{W_{\max}}}\right.\right. \\ & \left.\left. - 3p_i^{-\frac{5}{2}}\Omega_m\right) + \frac{1}{4}p_i^{-\frac{3}{2}} + \frac{3b_i}{4}p_i^{-\frac{5}{2}}\right] \end{aligned} \tag{45}$$

Then, based on the requirement of CSOs' power supply obtained in Stage II, we have:

$$\begin{aligned} y_{m,i}^{*} &= \sqrt{\frac{\eta_m^2 J_m (W_m + W_{\max}) \sum\limits_{k=1}^{J_m} \left(A_k - \frac{\overline{\gamma}_1 W_m}{\varsigma_m W_{\max}} \right)}{W_{\max} p_i}} - \Omega_m \geq 0 \\ \Longrightarrow p_i &\leq \frac{\eta_m^2 J_m (W_m + W_{\max}) \sum\limits_{k=1}^{J_m} \left(A_k - \frac{\overline{\gamma}_1 W_m}{\varsigma_m W_{\max}} \right)}{W_{\max} \Omega_m^2} \\ \Longrightarrow & \frac{\partial^2 G_{Ret}(p_i)}{\partial p_i^2} < 0 \end{aligned} \tag{46}$$

As a result, this implies that $G_{SG}(\boldsymbol{P})$ is a concave function on p_i, and it also proves that the optimal strategy exists. Similar to the method above, the optimal strategy can be obtained as follows.

$$\begin{aligned} & \frac{\partial G_{SG}(\boldsymbol{P})}{\partial p_i} = 0 \\ \Longleftrightarrow & \frac{1}{2} \sum_{m=1}^{M} p_i^{-\frac{1}{2}} \sqrt{\frac{\eta_m^2 J_m (W_m + W_{\max}) \sum\limits_{k=1}^{J_m} \left(A_k - \frac{\overline{\gamma}_1 W_m}{\varsigma_m W_{\max}} \right)}{W_{\max}}} \\ & \times \left(1 + b_i p_i^{-1} \right) + \frac{p_i^{-2} a_i \eta_m^2 J_m (W_m + W_{\max})}{2 W_{\max}} \sum_{k=1}^{J_m} \left(A_k - \frac{\overline{\gamma}_1 W_m}{\varsigma_m W_{\max}} \right) \\ & = \sum_{m=1}^{M} \frac{a_i}{2} p_i^{-\frac{3}{2}} \sqrt{\frac{\eta_m^2 J_m (W_m + W_{\max}) \sum\limits_{k=1}^{J_m} \left(A_k - \frac{\overline{\gamma}_1 W_m}{\varsigma_m W_{\max}} \right)}{W_{\max} \Omega_m^2}} + \Omega_m \end{aligned} \tag{47}$$

Then, by solving (47), the SGO can make the optimal pricing strategy with maximum profits.

In conclusion, based on the proposed game-theoretical scheme, we obtain the optimal solutions in the charging system. Due to the analysis mentioned above in the four-stage game, it holds that $G_{EV}(\tilde{x}_{k,m}^{*}) < G_{EV}(x_{k,m}^{*})$ for random $\tilde{x}_{k,m}^{*}$ in Stage IV, satisfying $\forall k \in J_m$ and $\forall m \in M$; for random $\tilde{p}_m^{*}$, it holds that $G_{CS}(\tilde{p}_m^{*}) < G_{CS}(p_m^{*})$ in Stage III, satisfying $\forall m \in M$; for random $\tilde{y}_{m,i}^{*}$, it holds that $G_{CS}(\tilde{y}_{m,i}^{*}) < G_{CS}(y_{m,i}^{*})$ in Stage II, satisfying $\forall m \in M$; for random $\tilde{p}_i^{*}$, it holds that $G_{SG}(\tilde{p}_i^{*}) < G_{SG}(p_i^{*})$ in Stage I. Here, $\tilde{x}_{k,m}^{*}$, $\tilde{p}_m^{*}$, $\tilde{y}_{m,i}^{*}$, and $\tilde{p}_i^{*}$ denote other different values, except $x_{k,m}^{*}$, p_m^{*}, $y_{m,i}^{*}$, and p_i^{*}, respectively. Therefore, it proves that SE exists in our proposed game-theoretical scheme with the optimal solutions shown by (30), (34), (41), and (47), respectively.

4.5. Algorithm Design to Obtain Stackelberg Equilibrium

According to the above analysis, it is proven that there is a unique SE in our proposed Stackelberg game, which can be able to maximize the profits in the charging system composed of EV users, CSOs, and SGO. We adopt the backward method to obtain the optimal solutions. In order to simplify the calculation, we propose an iterative algorithm to achieve the SE, which is shown in Algorithm 1. In this presented iterative algorithm, we induce the convergence criteria $\frac{||p_i^t - p_i^{t-1}||}{||p_i^{t-1}||} \leq \varrho$ to obtain the precise solutions, in which ϱ is a small threshold value, i.e., $\varrho = 10^{-4}$.

Algorithm 1 : An iterative algorithm for SE.

Input: For SGO i, a random price p_i is announced to CSOs with the maximum power supply $y_{m,i} < \Theta$.
Initialization: $p_i^0 = p_i$.
Repeat the iteration.
for $t = 0 : 1 : t_{\max}$ **do**
  if p_i^t is satisfied based on (42) **then**
    We will calculate the revenue for SGO i and power supply for CSOs.
    if The constraints in (32) and (42) are satisfied. **then**
      Power price for EV users are able to be obtained based on (34).
      if The power price offered by CSO m is satisfied based on (42), which is also smaller than $\frac{\overline{\gamma}_1}{\varsigma_m}$.
      then
        We can calculate the amount of power supply for EV user k based on (30).
      else
        Break the loop.
      end if
    else
      Break the loop.
    end if
  else
    Break the loop.
  end if
  SGO i will update its power price based on the following equations:

$$r_t = p_i^t - \hbar \frac{G_{SG}^{'}(p_i^t)}{G_{SG}^{''}(p_i^t)} \tag{48}$$

$$p_i^{t+1} = p_i^t - G_{SG}^{'}(p_i^t) / \left[\frac{1}{\nu} G_{SG}^{''} \left(p_i^t + \frac{\nu}{2}(r_t - p_i^t) \right) + (1 - \frac{1}{\nu}) G_{Ret}^{''}(p_i^t) \right] \tag{49}$$

  Here, $G_{SG}^{'}(p_i^t) = \partial G_{SG}(p_i^t)/\partial p_i^t$, $G_{SG}^{''}(p_i^t) = \partial^2 G_{SG}(p_i^t)/\partial (p_i^t)^2$. $\hbar$ and ν denote the iterative step, in which $\hbar$ is a very small value and ν is bounded by $0 < \nu < 1$.
end for
Until $||p_i^t - p_i^{t-1}||/||p_i^{t-1}|| \leq \varrho$.
Output the SE including $x_{k,m}^*$, p_m^*, $y_{m,i}^*$, and p_i^*, which can be achieved.

5. Simulation

5.1. Simulation Scenario

In this section, we demonstrate numerical results to verify the performance of the strategy proposed in this paper. Based on [34], we suppose that BER will be no more than 0.1. The cost for waiting to be charged is 0.3 \$/h and 0.4 \$/h in CSO 1 and CSO 2, respectively. Here, assuming that for EV users to be charged arriving at the charging station, λ = 4.8/h, μ = 1.2/h. Other parameters are set in Table 1. The total number of EV users to be charged by CSO 1 is 15, in which $A_k (k = 1, 2, 3)$ is equal to 40. For the rest of the EV users, A_k is equal to 50. The average driving distance for each EV user and CSOs is 10 km and 15 km, respectively. Similarly, the total number charged by CSO 2 is 10, in which $A_k \{k = 1, 2, 3\}$ is equal to 45. For the rest of the EV users, A_k is equal to 50. Other parameters are set as follows: $\tau_1 = 0.02$ MW·h, $\tau_2 = 0.01$ MW·h, $\sigma_1 = \sigma_2 = 2$, $\vartheta_1 = \vartheta_2 = 0.1$.

Table 1. Simulation parameters.

Parameter	Value
$W_{\max}$ for EV users to be charged	{0.7 h, 0.7 h}
The minimum power demand for EV users	0 MW·h
The maximum power demand for EV users	0.5 MW·h
$\overline{\gamma}_1$ for each CSO	2 \$/h
$\overline{\gamma}_2$ for each CSO	0.3 \$/h
Discount charging amount for each EV user	{10 MW·h}
a_i for SGO i	0.5
b_i for SGO i	0.1
c_i for SGO i	80

5.2. Simulation Results

Given the preset parameters above, through the proposed game-theoretical scheme strategy, we study how BER plays an important role in the decisions on the optimal strategy. Figure 3 shows the relationship between the optimal price decided by electricity retailer i and BER in Hetnet. Obviously, from the simulation in Figure 3, this demonstrates that the price becomes smaller with the increase of BER, which implies that BER affects the pricing decision.

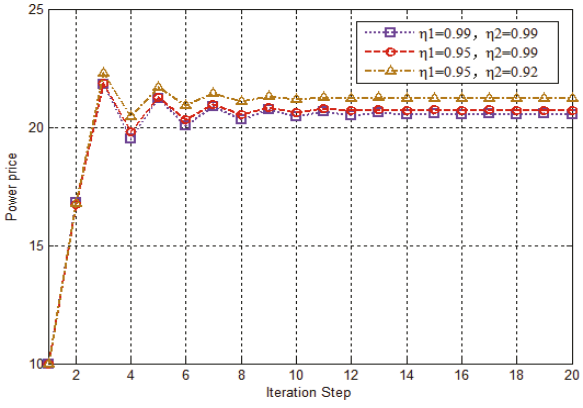

Figure 3. Power price offered by SGO i versus the iteration step, in which its initial price $p_i = 10$, $C_1 = C_2 = 3$, and $S_1 = 6$, $S_2 = 7$, respectively.

For the same example with $\eta_1 = 0.95$ and $\eta_2 = 0.99$ set in Figure 3, Figure 4 illustrates the pricing strategy of electricity retailer i with respect to the iteration step. We can observe that the value of price will converge to a stable value through several iteration steps. In Figure 4, we can also know that the optimal price will be obtained in various cases with different waiting capacities. Similar to Figure 4, Figure 5 illustrates that the power price will be smaller with the increase in the number of outlets supplied by CSOs. This implies that the waiting time will be smaller compared with smaller waiting capacities, which will monotonically increase the optimal price. On the contrary, the power price will decrease with the decreasing waiting time, based on the number of outlets supplied by CSOs.

In order to evaluate how SGO i makes decisions on the optimal pricing strategy with various initial prices, we get the simulation shown in Figure 6 through the proposed game-theoretical strategy. Figure 6 illustrates that the power price offered by SGO i will be adjusted to a higher ideal value through several iteration steps when it is initially set as a smaller value, such as $p_i = 5$ and $p_i = 10$, respectively. On the contrary, the power price will converge to a smaller ideal value through several iteration steps when it is initially set as a higher value. From Figures 3–6, we see that it will converge to a stable value as long as the initial price is offered.

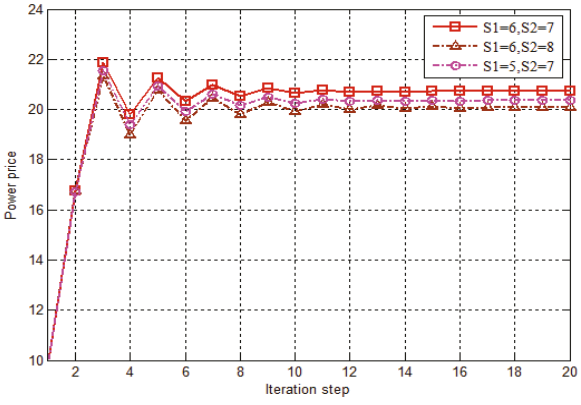

Figure 4. Power price offered by SGO i versus the iteration step, in which its initial price $p_i = 10$ \$/MW·h, $\eta_1 = 0.95$, $\eta_2 = 0.99$, and $C_1 = C_2 = 3$, respectively.

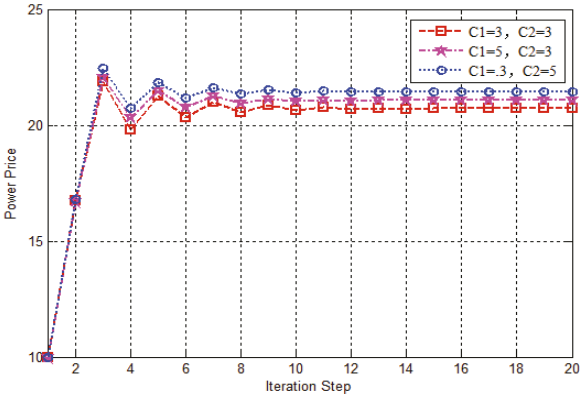

Figure 5. Power price offered by SGO i versus the iteration step, in which its initial price $p_i = 10$ \$/MW·h, $\eta_1 = 0.95$, $\eta_2 = 0.99$, and $S_1 = 6$, $S_2 = 7$, respectively.

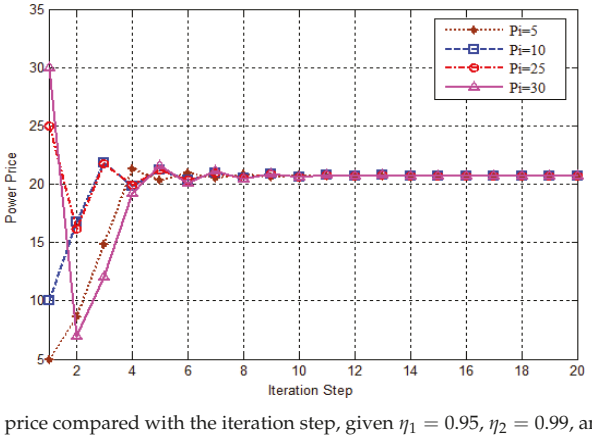

Figure 6. SGO's price compared with the iteration step, given $\eta_1 = 0.95$, $\eta_2 = 0.99$, and $C_1 = C_2 = 3$, $S_1 = 6$, $S_2 = 7$.

In addition, we investigate the optimal strategy for EV users to be charged based on the price given by CSOs. Following the price given by CSOs, Figure 7 demonstrates how EV users adjust their power demand to maximize their benefits. From Figure 7, we can observe that the value of power demand converges to the optimal value through several iteration steps, by using the proposed strategy. Meanwhile, we can also obtain that the amounts of power demand are different from each other. For example, power demand for EV users with $A_k = 40$ is smaller than that with $A_k = 50$, when all of them will be charged by CSO 1. The results for EV users charged by CSO 2 is the same as the above. This implies that power demand for EV users with a higher satisfaction degree is larger than that with a lower satisfaction degree. From the simulation results in Figures 5 and 6, we can know that it matches the existence of SE for our proposed game-theoretical scheme in Section 5, through which it also can be obtained.

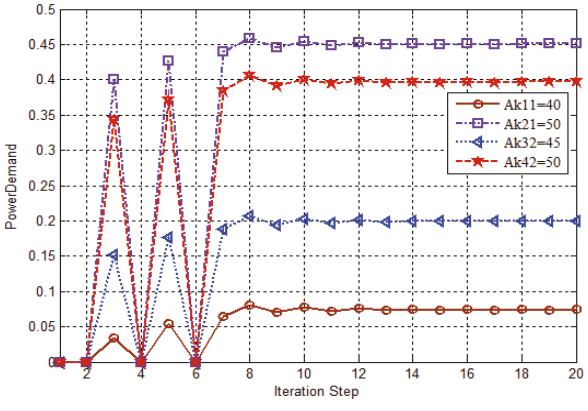

Figure 7. CSOs' power demand brought from CSOs compared with the iteration step, in which $\zeta_1 = 0.05$ and $\zeta_2 = 0.01$, and its initial price $p_i = 10$ \$/MW·h, $W_{m1} = 0.3$ h, $W_{m2} = 0.4$ h, respectively.

From the results in Figures 2 and 3, we investigate the effect of BER and the outlets on the power price. This imposes that it can benefit both CSOs and EV users through adjusting the outlets and improving the performance of wireless communication. According to the simulation results in Figures 4–6, this means that both EV users and CSOs can also obtain the optimal solution, while a random initial power price offered by SGO is given.

Based on the above simulation results, we can know that our algorithm mainly focuses on the power supply in SGO. It also describes that the total utility of all parts in the charging system will be fixed, which cannot be affected with the increasing total power supply from SGO. This proves the existence and uniqueness of SE in our proposed game-theoretical scheme, which imposes the effectiveness of our proposal.

Finally, we compare the performance of the proposed optimal strategy with the existing scheme, with the same parameter setting in the simulations above. We adopt a uniform allocation scheme and a random allocation scheme to calculate the benefits of all EV users, respectively. Based on the utility function of EV users, we calculate the benefits of EV users with various total power demand supplied by SGO i, shown in Figure 8, using these three different methods. From Figure 8, we can observe that the benefits in the proposed scheme are higher than those in the other two schemes with increasing total power demand. This proves the effectiveness of our proposed algorithm in this paper.

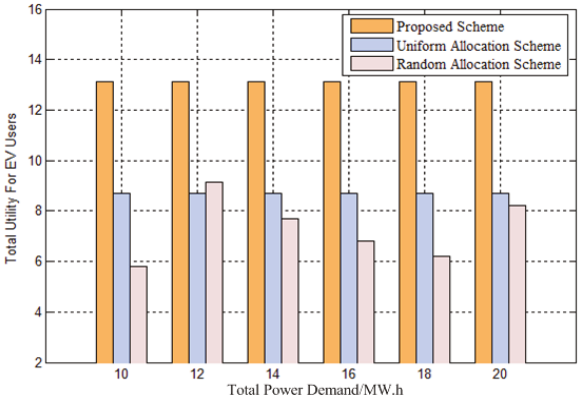

Figure 8. Total utility for EV users with different schemes, in which $\zeta_1 = 0.05$ and $\zeta_2 = 0.01$, and its initial price $P_i = 10$, $W_{m1} = 0.3$, $W_{m2} = 0.4$, respectively.

In order to integrate the study in our paper with the practical application, it will be interesting to develop a smart power decision system (SPDS) to charging the service according to the limited power supply from SGO. The smart decision system is divided into two parts: (1) software: our proposed algorithm is designed as the major part of the optimal strategy, including the analysis of the data processing; (2) hardware: in order to satisfy many more EV users' power demand, the online information of EV users, CSOs, and SGOs is seen as the input of software in SPDS, respectively. At the same time, both the waiting time in CS and delay in Hetnet are taken into account. Further, it would be interesting to modify our proposed algorithm associated with the dynamic renewable power in the smart grid.

6. Conclusions

This work presents a game-theoretical approach to provide EVs with charging services supplied by CSOs, considering BER in Hetnet. A four-stage Stackelberg game scheme is developed to make optimal decisions for this charging system, composed of EV users, CSOs, and SGO. Considering the interaction among them, the utility function of each one is designed, while the load uncertainty is taken into account. Then, the SE can be obtained through the proposed iteration search algorithm, matching its existence and uniqueness in our proposed algorithm. Simulation results have been presented to demonstrate the performance of our proposal. For future work, it is interesting for us to extend our proposed algorithm with virtual technology, confronting realistic problems, i.e., the dynamic arrival of EV users and the delay of charging power in the queue.

Author Contributions: Conceptualization, S.C. and H.C.; Methodology, H.C.; Software, S.C.; Validation, S.C., H.C. and S.J.; Formal analysis, H.C.; Investigation, S.C.; Supervision, S.C.; Project administration, H.C.; Funding acquisition, S.J.

Funding: This research was funded by the National Natural Science Foundation of China under Grant No. 61572238 and the Key Project of Natural Science Research of the Anhui Provincial Department of Education under Grant No. KJ2016A431.

Acknowledgments: The author would like to thank the staff of Department of Computer Science and Technology, Tsinghua University, for their support during this study. Authors would like to thanks School of Physics and Electronic Engineering, Anqing Normal University for their generosity in financial assistance.

Conflicts of Interest: The authors declare no conflict of interest.

References

1. Bayram, I.S.; Michailidis, G.; Devetsikiotis, M.; Granelli, F. Electrical Power Allocation in a Network of Fast Charging Stations. *IEEE J. Sel. Areas Commun.* **2015**, *31*, 1235–1246. [CrossRef]

2. Zhao, S.; Lin, X.; Chen, M. Robust Online Algorithms for Peaking-minimizing EV Charging under Multistage Uncertainty. *IEEE Trans. Autom. Control* **2017**, *62*, 5739–5754. [CrossRef]
3. Rakhymbay, A.; Khamitov, A.; Bagheri, M.; Alimkhanuly, B.; Lu, M.; Phung, T. Precise Analysis on Mutual Inductance Variation in Dynamic Wireless Charging of Electric Vehicle. *Engergies* **2018**, *11*, 624. [CrossRef]
4. Ma, T.; Wu, J.; Hao, L.; Yan, H.; Li, D. A Real-Time Pricing Scheme for Energy Management in Integrated Energy Systems a Stackelberg Game Approach. *Engergies* **2018**, *11*, 2858. [CrossRef]
5. De Hoog, J.; Alpcan, T.; Brazil, M.; Thomas, D.A.; Mareels, I. Optimal Charging of Electric Vehicles Taking Distribution Network Constraints into Account. *IEEE Trans. Power Syst.* **2015**, *30*, 365–375. [CrossRef]
6. Wang, M.; Liang, H.; Zhang, R.; Deng, R.; Shen, X. Mobility-aware Coordinated Charging for Electric Vehicles in VANET-enhanced Smart Grid. *IEEE J. Sel. Areas Commun.* **2014**, *32*, 1344–1360. [CrossRef]
7. Lee, W.; Schober, R.; Wonga, V. An Analysis of Price Competition in Heterogeneous Electric Vehicle Charging Stations. *IEEE Trans. Smart Grid* **2018**. [CrossRef]
8. Sisinni, E.; Saifullah, A.; Han, S.; Jennehag, U.; Gidlund, M. Industrial Internet of Things: Challenges, Opportunities, and Directions. *IEEE Trans. Ind. Inform.* **2018**, *14*, 4724–4734. [CrossRef]
9. Xiong, H.; Xiang, T.; Zhu, Y.; Song, X.; Chen, H.; Chen, H. Electric Vehicle Public Charging Stations Location Optimal Planning. *Autom. Electr. Power Syst.* **2012**, *36*, 65–70.
10. Luan, T.; Shen, X.; Bai, F. Integrity-oriented content transmission in highway vehicular ad hoc networks. In Proceedings of the 2013 IEEE INFOCOM, Turin, Italy, 14–19 April 2013; Volume 12, pp. 2562–2570.
11. Cordeschi, N.; Amendola, D.; Baccarelli, E. Reliable Adaptive Resource Management for Cognitive Cloud Vehicular Networks. *IEEE Trans. Veh. Technol.* **2015**, *64*, 2528–2537. [CrossRef]
12. Jia, L.; Hu, Z.; Song, Y.; Luo, Z. Optimal Siting and Sizing of Electric Vehicle Charging Stations. In Proceedings of the 2012 IEEE International Electric Vehicle Conference, Greenville, SC, USA, 4–8 March 2012; pp. 1–6.
13. Liu, N.; Chen, Q.; Liu, J.; Lu, X.; Li, P.; Lei, J.; Zhang, J. A Heuristic Operation Strategy for Commercial Building Microgrids Containing EVs and PV System. *IEEE Trans. Ind. Electron.* **2014**, *62*, 2560–2570. [CrossRef]
14. Wang, F.; Han, L.; Wen, B. Substation Optimization Planning based on the Improved Orientation Strategy of Voronoi Diagram. In Proceedings of the 2nd International Conference on Information Science and Engineering, Hangzhou, China, 4–6 December 2010; pp. 1563–1566.
15. An, J.; Huang, B.; Kang, Q.; Zhou, M. PSO-based Method to Find Electric Vehicle's Optimal Charging Schedule under Dynamic Electricity Price. In Proceedings of the 2013 10th IEEE International Conference on Networking, Sensing and Control (ICNSC), Evry, France, 10–12 April 2013; pp. 913–918.
16. Mohsenian-Rad, H.; Ghamkhari, M. Optimal Charging of Electric Vehicles with Uncertain Departure Times: A Closed-form Solution. *IEEE Trans. Smart Grid* **2015**, *6*, 940–942. [CrossRef]
17. Lee, W.; Xiang, L.; Schober, R.; Wong, V.W. Electric Vehicle Charging Stations With Renewable Power Generators: A Game Theoretical Analysis. *IEEE Trans. Smart Grid* **2015**, *6*, 608–617. [CrossRef]
18. Guo, S.; Zhao, H. Optimal Site Section of Electric Vehicle Charging Station by Using Fuzzy TOPSIS based on Sustainability Perspective. *Appl. Energy* **2015**, *158*, 390–402. [CrossRef]
19. Yuan, W.; Huang, J.; Zhang, Y. Competitive Charging Station Pricing for Plug-in Electrical Vehicles. *IEEE Trans. Smart Grid* **2014**, *8*, 668–673.
20. Manshadi, S.D.; Khodayar, M.E.; Abdelghany, K.; Üster, H. Wireless Charging of Electric Vehicles in Electricity and Transportation Networks. *IEEE Trans. Smart Grid* **2017**, *9*, 4503–4512. [CrossRef]
21. Sun, Y.; Hu, X.; Liu, X.; He, X.; Wang, K. A Software-defined Green Framework for Hybrid EV-charging Networks. *IEEE Commun. Mag.* **2017**, *55*, 62–69. [CrossRef]
22. Yang, J.; Chou, L.; Chang, Y. Electric-vehicle Navigation System based on Power Consumption. *IEEE Trans. Veh. Technol.* **2015**, *65*, 5930–5943. [CrossRef]
23. Zhang, R.; Cheng, X.; Yangg, L. Flexible Energy Management Protocol for Cooperative EV-to-EV Charging. *IEEE Trans. Intell. Transp. Syst.* **2019**, *20*, 172–186. [CrossRef]
24. Hu, X.; Wang, K.; Liu, X.; Sun, Y.; Li, P.; Guo, S. Energy Management for EV Charging in Software-defined Green Vehicle-to-grid Network. *IEEE Commun. Mag.* **2018**, *56*, 156–163. [CrossRef]
25. Adan, I.; Resing, J. *Queueing Theory*; Eindhoven University of Technology: Eindhoven, The Netherlands, 2002.
26. Bayram, I.S.; Ismail, M.; Abdallah, M.; Qaraqe, K.; Serpedin, E. A Pricing-based Load Shifting Framework for EV Fast Charging Stations. In Proceedings of the 2014 IEEE International Conference on Smart Grid Communications (SmartGridComm), Venice, Italy, 3–6 November 2014; pp. 680–685.

27. Karbasioun, M.M.; Lambadaris, I.; Shaikhet, G.; Kranakis, E. Optimal Charging Strategies for Electric Vehicles under Real Time Pricing. In Proceedings of the 2014 IEEE International Conference on Smart Grid Communications (SmartGridComm), Venice, Italy, 3–6 November 2014; pp. 746–751.
28. Jin, C.; Tang, J.; Ghosh, P. Optimal Electric Vehicle Charging with Energy Storage in Electricity Market. *IEEE Trans. Smart Grid* **2013**, *4*, 311–320. [CrossRef]
29. Ismail, M.; Bayram, I.; Abdallah, M.; Qaraqe, K. Optimal Planning of Fast Charging Facilities. In Proceedings of the 2015 First Workshop on Smart Grid and Renewable Energy (SGRE), Doha, Qatar, 22–23 March 2015; pp. 1–6.
30. Ovalle, A.; Hably, A.; Bacha, S. Optimal Management and Integration of Electric Vehicles to the Grid: Dynamic Programming and Game Theory Approach. In Proceedings of the 2015 IEEE International Conference on Industrial Technology (ICIT), Seville, Spain, 17–19 March 2015; pp. 2673–2679.
31. You, P.; Hsieh, Y. A Hybrid Heuristic Approach to the Problem of the Location of Vehicle Charging Station. *Comput. Ind. Eng.* **2014**, *70*, 195–204. [CrossRef]
32. Huang, S.; He, L.; Gu, Y.; Wood, K.; Benjaafar, S. Design of A Mobile Charging Service for Electric Vehicles in An Urban Environment. *IEEE Trans. Intell. Transp. Syst.* **2015**, *16*, 787–798. [CrossRef]
33. Lee, J.; Guo, J.; Choi, J.K.; Zukerman, M. Distributed Energy Trading in Microgrids: A Game Theoretic Model and Its Equilibrium Analysis. *IEEE Trans. Ind. Electron.* **2015**, *62*, 1–10. [CrossRef]
34. Molisch, A. *Wireless Communications*; Wiley: West Sussex, UK, 2005.

energies

MDPI

Article

A Cross-Entropy-Based Hybrid Membrane Computing Method for Power System Unit Commitment Problems

Min Xie [1], Yuxin Du [2], Peijun Cheng [3], Wei Wei [1,*] and Mingbo Liu [1]

[1] School of Electric Power, South China University of Technology, Guangzhou 510640, China; minxie@scut.edu.cn (M.X.); epmbliu@scut.edu.cn (M.L.)
[2] State Grid Ganzhou Electric Power Supply Company, Ganzhou 341000, China; xinzi6726@163.com
[3] Guangzhou Power Supply Bureau Co., Ltd., Guangzhou 510620, China; 201621012001@mail.scut.edu.cn
* Correspondence: epweiwei@mail.scut.edu.cn

Received: 7 January 2019; Accepted: 31 January 2019; Published: 2 February 2019

Abstract: The cross-entropy based hybrid membrane computing method is proposed in this paper to solve the power system unit commitment problem. The traditional unit commitment problem can be usually decomposed into a bi-level optimization problem including unit start-stop scheduling problem and dynamic economic dispatch problem. In this paper, the genetic algorithm-based P system is proposed to schedule the unit start-stop plan, and the biomimetic membrane computing method combined with the cross-entropy is proposed to solve the dynamic economic dispatch problem with a unit start-stop plan given. The simulation results of 10–100 unit systems for 24 h day-ahead dispatching show that the unit commitment problem can be solved effectively by the proposed cross-entropy based hybrid membrane computing method and obtain a good and stable solution.

Keywords: power system unit commitment; hybrid membrane computing; cross-entropy; the genetic algorithm based P system; the biomimetic membrane computing

1. Introduction

The unit commitment (UC) problem is a typical optimization problem for power systems. The main goal of UC is to schedule the start-stop state of units and generate power according to the load forecasting curve during the dispatch period, with the corresponding constraints so that the cost is minimized [1]. Usually the UC problem can be broken down into two sub-problems: the unit start-stop plan and economic dispatch [2].

Mathematically, the UC problem is a high-dimensional, non-convex and mixed-integer nonlinear programming problem. Its discrete and continuous variables, non-convex objective function and network constraints enhance its non-convexity and complex [3]. Moreover, with the increase in unit and calculation scale, it is difficult to obtain an accurate feasible solution in a reasonable time frame. Therefore, many methods have been proposed by scholars to solve the UC problem, which can be roughly divided into three categories: heuristic methods, mathematical optimization methods, and intelligent optimization methods.

Heuristic methods are represented by the priority list method [4], the earliest method applied to solve the UC problem, which generally sorts by some economic indicators with small and simple calculations, usually relies on the actual scheduling experience.

Mathematical optimization methods include mixed integer nonlinear programming, the Lagrangian relaxation (LR) method [5], etc. Mixed integer nonlinear programming methods include the branch-and-bound (BB) [6], Benders decomposition [7], and other methods, with the decomposition technique generally used to simplify the problem; the solving efficiency has been rapidly improved

with improvements in mathematical optimization software [8]. For the dynamic programming method, the global optimal solution can be obtained with no special requirements on the behavior of the objective function; however, there will be a "dimensionality disaster" [9] when the number of units is large, and to simplify the problem, the optimal solution will be lost when the approximation method adopted. Moreover, it is difficult to consider time-dependent constraints such as the ramp rate constraint. Compared with the dynamic programming method, the LR method has an advantage for large-scale problems since the calculation complexity is approximately proportional to the unit scale; in addition, the Lagrangian multiplier is of practical economic significance, but it cannot prove whether the solution is optimal due to the dual gap. It is also inflexible when considering some kinds of constraints, such as the ramp rate limit, and the possible oscillation and singularity during iteration may lead to convergence difficulties [10].

Bioinspired optimization methods are algorithms that simulate biological evolution or its behavior, and include genetic algorithms (GA) [11], particle swarm algorithm (PSO) [12], and memetic algorithm (MA) [13]. An approximate optimal solution can be obtained with no special requirements on the behavior of the objective function, and feasible solutions can be obtained even when the unit scale is large where no feasible solution can be obtained by other methods; however, the solving efficiency is affected by how the constraints are processed since these methods are essentially unconstrained.

Membrane computing is a computational framework inspired by the living cell and its organization in tissues and other higher order structures, and was first proposed by Gheorghe Păun, an academic at the European Academy of Sciences. In recent years, optimization problems such as image processing [14], robot path planning [15], DNA sequence design [16], gasoline blending scheduling [17], the travelling salesman problem [18], and the minimum storage problem [19] have been successfully solved by this framework. In this paper, we propose a cross-entropy-based hybrid membrane computing (CEHMC) method to solve the UC problem by combining the genetic algorithm-based P system (GAPS) with the biomimetic membrane computing (BMC) method. The GAPS is based on the binary genetic algorithm. It is nested by multiple membranes with the unit start-stop state (0,1 binary variables) as evolution objects. The evolution rules adopt the crossover and mutation rules of binary coded genetic algorithms. The difference between GAPS and GA is the communication of optimal objects in different membranes, which means the optimization results of the outer membrane can be transmitted into the inner membranes constantly when genetic rules are executed in each membrane. The calculation method of biomimetic membrane is inspired by the important role of Golgi apparatus in living cells. With the inner membrane system as the calculation carrier, the required regional structure is designed to simulate the static or dynamic membrane structure, the biochemical or physical reactions in the inner membrane system are simulated by various evolutionary rules, so that the top-ranking evolution objects after evaluation are selected for transmission according to the permeability of substances in the transporting through the membrane. Based on the combination of GAPS with the biomimetic membrane computing method, the cross-entropy (CE) optimization method is introduced to strengthen the searching ability during the optimization.

Because the UC problem is not fully standardized and specified, we will not attempt to give a definitive algorithmic solution to the problem. Instead, our goal in this paper is to demonstrate that the proposed CEHMC approach is viable. We include a case study showing than our method outperforms other nonlinear optimization alternatives for a case study. Therefore, our formulation of the UC problem and its solution algorithm are for illustration purposes only. For that purpose and for the ease of exposition and understanding, the classical UC formulation which has been commonly used in the past decades is used in this paper. The simulation results of 10–100 unit systems for 24 h day-ahead dispatching showed that the UC problem could be solved effectively by the proposed method, and a satisfactory and stable solution was obtained.

2. The Mathematical Model for UC Problems

2.1. Objective Function

The total generation cost F_C during the dispatching period is taken as the optimization goal, including fuel cost and startup cost of all units. Thus, the objective function is:

$$\min F_C = \sum_{t=1}^{T}\sum_{i=1}^{N}\left[I_{i,t}F_{i,t} + (I_{i,t} - I_{i,t-1})^2 C_{i,t}\right] \tag{1}$$

where T is the total dispatch period; N is the number of generators; $I_{i,t}$ is the state of unit i at tth hour; value 1 represents startup, while 0 represents shutdown; $F_{i,t}$ and $C_{i,t}$ are the fuel cost and startup cost, respectively, of unit i at t-th hour; and the fuel cost $F_{i,t}$ can be expressed by the quadratic function as follows:

$$F_{i,1} = A_{i,2}P_{i,t}^2 + A_{i,1}P_{i,t} + A_{i,0} \tag{2}$$

where $P_{i,t}$ is the generation of unit i at t-th hour; and $A_{i,2}$, $A_{i,1}$, and $A_{i,0}$ are the unit cost coefficients of unit i.

Startup cost $C_{i,t}$ is related to the unit OFF time, which can be expressed by the following step function:

$$C_i = \begin{cases} C_{hot,i} & \underline{T}_i^{off} \le T_{i,t}^{off} \le \underline{T}_i^{off} + T_i^{cold} \\ C_{cold,i} & T_{i,t}^{off} > \underline{T}_i^{off} + T_i^{cold} \end{cases} \tag{3}$$

where $C_{hot,i}$ and $C_{cold,i}$ are the hot start cost and cold start cost, respectively, of unit i; $\underline{T}_i^{off}$ is the minimum downtime of unit i; $T_{i,t}^{off}$ is the OFF time of unit i at t-th hour; and T_i^{cold} is the cold start time of unit i.

2.2. Constraints

The constraints of the UC problem usually include the system power balance, system spinning reserve requirement, generation limits, ramp rate limits, and minimum up and down time limits.

- System power balance:

$$\sum_{i=1}^{N} P_{i,t} = D_t \tag{4}$$

- System spinning reserve requirement:

$$\sum_{i=1}^{N} \overline{P}_i I_{i,t} \ge D_t + R_t \tag{5}$$

- Generation limits:

$$\underline{P}_i I_{i,t} \le P_{i,t} \le \overline{P}_i I_{i,t} \tag{6}$$

- Ramp rate limits:

$$\begin{cases} P_{i,t} - P_{i,t-1} \le P_i^{up} I_{i,t-1} + P_i^{start}(I_{i,t} - I_{i,t-1}) \le \overline{P}_i(1 - I_{i,t}) \\ P_{i,t-1} - P_{i,t} \le P_i^{down} I_{i,t} + P_i^{shut}(I_{i,t-1} - I_{i,t}) \le \overline{P}_i(1 - I_{i,t-1}) \end{cases} \tag{7}$$

- Minimum up and down time limits:

$$\begin{cases} (T_{i,t-1}^{on} - \underline{T}_i^{on})(I_{i,t-1} - I_{i,t}) \ge 0 \\ (T_{i,t-1}^{off} - \underline{T}_i^{off})(I_{i,t} - I_{i,t-1}) \ge 0 \end{cases} \tag{8}$$

Here, D_t is the system load demand at t-th hour; $\overline{P}_i$ and $\underline{P}_i$ are the maximum and minimum generation limits, respectively, of unit i; R_t is the system reserve demand, typically 5–10% of the system load demand; P_i^{up} and P_i^{down} are the up and down ramp rate limit, respectively; P_i^{start} and P_i^{shut} are the start and stop rate limit, respectively; $T_{i,t-1}^{off}$ is the OFF time of unit i at the $(t-1)$-th hour; and $\underline{T}_i^{on}$ is the minimum up time.

3. Unconstrained UC Model for CEHMC Method

As mentioned above, the traditional UC model is a multi-constrained nonlinear optimization problem, yet natural computing frameworks such as membrane computing are essentially unconstrained optimization methods, which are commonly used to solve unconstrained optimization problems. As for the complex multi-constrained optimization problem, using the penalty function is usually a good choice [20]. To facilitate the proposed method, the quadratic penalty function was used to deal with the constraints, transforming the UC problem into an unconstrained model without providing any initial feasible solution. Since GAPS is for the unit start-stop plan with embedded generic rules. These rules are design to screen the unit start-stop plans, i.e., testing whether the system spinning reserve requirement and minimum up and down time limits are satisfied, which determines the feasible unit state combination. Consequently, for the unconstrained UC model, only system power balance and ramp rate limits need to be transformed. The objective function can be rewritten as a penalty function as follows:

$$\begin{aligned} \min Q = F_C &+ \mu_1 \sum_h \max\left(\left| \sum_{i=1}^{N} P_{i,t} - D_t \right| - \delta, 0 \right)^2 \\ &+ \mu_2 \sum_g \max \left\{ \begin{array}{l} \left[P_{i,t} - P_{i,t-1} - P_i^{up} I_{i,t-1} - P_i^{start}(I_{i,t} - I_{i,t-1}) - \overline{P}_i(1 - I_{i,t}), 0 \right]^2 \\ + \left[P_{i,t-1} - P_{i,t} - P_i^{down} I_{i,t} - P_i^{shut}(I_{i,t-1} - I_{i,t}) - \overline{P}_i(1 - I_{i,t-1}), 0 \right]^2 \end{array} \right\} \end{aligned} \tag{9}$$

Here, the penalty factors μ_1, $\mu_1 > 0$; $\delta > 0$ is the acceptable violation domain when converting the equality constraint into an inequality constraint. In fact, the value of penalty factors is related to the magnitude of objective function and constraints. If the value is too large, it is likely to get bad solutions, and if the value is too small, the searching direction might be far away from the feasible region. Therefore, the method of testing is usually used to make the penalty item have the same or larger magnitude as the objective function so as to determine the penalty factors.

4. CEHMC Method Applied to Solve UC Problem

Three basic elements of membrane computing are membrane structure, evolution object, and evolution rules. The membrane structure and evolution rules can be designed according to requirements [21]. Taking an intracellular membrane system as the computational framework, the main procedures of the membrane computing method are as follow: first design the membrane structure, then evolve objects according to evolution rules, and lastly select the optimal objects for transmission and communication.

When using the CEHMC method for solving the UC problem, we utilize GAPS to schedule the unit start-stop plan since the start-stop states of generators are discrete variables. While for the dynamic economic dispatch problem, the generation of units is a continuous variable. Since the evolutionary objects (solution vectors) of biomimetic membrane computing is only required to be a real number, not limited to discrete variables. If the evolutionary rules are set to apply to continuous variables, biomimetic membrane computing can used to solve continuous variable optimization problems, such as the dynamic economic dispatch problem in UC. Then, the cross-entropy optimization method is introduced combined with biomimetic membrane computing to improve the searching ability during iteration. Finally, the minimum generation cost is taken as the optimal result of the UC problem.

4.1. GAPS for Unit Start-Stop Plan

Figure 1 shows the membrane structure of GAPS; it is a nested structure [22], where the symbol N represents the N-th nested genetic membrane (i.e., the variable N in Table 1). In practice, it needs to be determined synthetically according to unit size, number of constraints, calculation time and convergence effect, etc. The start-stop states of generators are taken as the evolution objects $\boldsymbol{I}$, and the crossover and mutation rules of the binary encoding GA are the evolution rules.

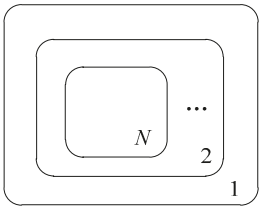

Figure 1. Structure of genetic membrane.

Table 1. Initial parameters of the proposed method.

Unit		10	20	40	60	80	100
GAPS	N	20	20	40	50	60	60
	N_o	10	16	20	20	30	30
	N_{co}	2	2	4	4	6	6
	P_c	0.9	0.9	0.9	0.9	0.9	0.9
	P_m	0.5	0.5	0.5	0.5	0.5	0.5
HMC	N_c'	10	20	30	30	40	50
	N_b'	10	20	20	30	40	50
	N_o'	10	10	10	10	12	12
	N_{co}'	4	4	4	4	6	6
	P_c'	0.95	0.95	0.95	0.95	0.95	0.95
	P_m'	0.5	0.5	0.5	0.5	0.5	0.5
	P_t'	0.9	0.9	0.9	0.9	0.9	0.9

4.2. Biomimetic Membrane Computing Method for Dynamic Economic Dispatch

Figure 2 shows the membrane structure of the biomimetic membrane computing method used in this paper. It is a reticular structure including an outermost membrane, m basic membranes, and a quasi-Golgi membrane [23] represented by G, and the output of generators is taken as the evolution objects $\boldsymbol{P}$, that is, $\boldsymbol{P} = (p_1, p_2, \ldots, p_l)$, $p_k \in \{P_{i,t},\ i = 1, 2, \ldots, N;\ t = 1, 2, \ldots, T\}$. In addition, m is corresponding to the variable N_b in Table 1, which is usually determined synthetically according to unit size, number of constraints, calculation time and convergence effect, etc.

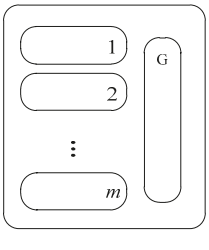

Figure 2. Structure of biomimetic membrane.

The evolution rules can be divided into two categories according to the environment, that is, rules in the basic membranes, and rules in the quasi-Golgi membrane. Besides, correction rules can be used

in all conditions. All the basic rules are set with the calculation probability as the execution condition. When the calculation probability is satisfied, the rule will be executed immediately. The evolution rules are as follows:

(1) Crossover rules

- Numerical crossover rule. Each element on both evolution object is numerically crossed, and the cross ratio of each element is different, which can be described as follows:

$$\begin{left} \boldsymbol{P}_a, \boldsymbol{P}_b \rightarrow \boldsymbol{P}'_a, \boldsymbol{P}'_b \\ \begin{cases} \boldsymbol{P}'_a = \boldsymbol{\eta} \times \boldsymbol{P}_a + (1 - \boldsymbol{\eta}) \times \boldsymbol{P}_b \\ \boldsymbol{P}'_b = (1 - \boldsymbol{\eta}) \times \boldsymbol{P}_a + \boldsymbol{\eta} \times \boldsymbol{P}_b \end{cases} \end{left} \tag{10}$$

  where $\boldsymbol{P}$ and $\boldsymbol{P}'$ are the original and new object, respectively, generated after executing evolution rule; and $\boldsymbol{\eta}$ is a vector whose value is a random number uniformly distributed on [0,1].
- Interval crossover rule. First, select the interval to be randomly exchanged, and then swap the elements in the same interval for two objects. This is described as follows:

$$\begin{left} \boldsymbol{P}_a, \boldsymbol{P}_b \rightarrow \boldsymbol{P}'_a, \boldsymbol{P}'_b \\ \begin{cases} \boldsymbol{P}_a = (p_{a1}, \cdots, p_{ap}, \cdots, p_{aq}, \cdots, p_{al}) \\ \boldsymbol{P}_b = (p_{b1}, \cdots, p_{bp}, \cdots, p_{bq}, \cdots, p_{bl}) \\ \boldsymbol{P}'_a = (p_{a1}, \cdots, p_{bp}, \cdots, p_{bq}, \cdots, p_{al}) \\ \boldsymbol{P}'_b = (p_{b1}, \cdots, p_{ap}, \cdots, p_{aq}, \cdots, p_{bl}) \end{cases} \end{left} \tag{11}$$

  where $p, q \in [1, l]$, $[p, q]$ is the interval to be swapped; and l is the length of object. The procedure of crossover can be divided into two or three steps according to the length of the object. When the length is short, two-step crossover is preferred: first, execute the numerical crossover rule on two selected adjacent objects, and then execute the interval crossover rule on two randomly selected objects. Conversely, when the length of object is long, three-step crossover is preferred: first, execute the numerical crossover rule on two randomly selected objects, then execute the interval crossover rule on the two objects, and lastly execute the numerical crossover rule on two adjacent objects.

(2) Mutation rule

A random increment vector is added to the original object, which can be described as follows:

$$\begin{left} \boldsymbol{P} \rightarrow \boldsymbol{P}' \\ \begin{cases} \boldsymbol{P}' = \boldsymbol{P} + \boldsymbol{\varphi} \\ \boldsymbol{\varphi} = h \times \boldsymbol{r} \times (\overline{\boldsymbol{P}} - \underline{\boldsymbol{P}}) \end{cases} \end{left} \tag{12}$$

where $\boldsymbol{\varphi}$ is the mutation vector; $\overline{\boldsymbol{P}}$ and $\underline{\boldsymbol{P}}$ are the upper and lower limits of $\boldsymbol{P}$, respectively; h is the mutation coefficient; and $\boldsymbol{r}$ is the random vector that follows the standard normal distribution.

(3) Correction rule

After some certain rules, such as the mutation rule, some elements of the new object may exceed their limits and must be modified, that is:

$$p' = \begin{cases} \overline{p} & p > \overline{p} \\ \underline{p} & p < \underline{p} \end{cases} \tag{13}$$

For the quasi-Golgi membrane, activation conditions are set, which means the following rules are executed only if the quasi-Golgi membrane is activated:

- Target indication rule

The communication objects sent into the quasi-Golgi are sorted by their function value, and then each communication object is subtracted from the former stored object by this order. Thus, a direction vector is generated, and the new target indication vector is the sum of this direction vector and last target indication vector. Regardless of whether the quasi-Golgi is activated, the direction vector and target indication vector should be calculated, and the target indication vector should be reserved. Furthermore, the target indication object can be generated only if the quasi-Golgi is activated. This is described as follows:

$$\begin{cases} \boldsymbol{P} \rightarrow \boldsymbol{P}_{S1}, \boldsymbol{P}_{S2} \\ \overrightarrow{\lambda} = \overrightarrow{\lambda} + (\boldsymbol{P}_{sort}^{new} - \boldsymbol{P}_{sort}^{old}) \\ \boldsymbol{P}_{S1} = \boldsymbol{P} + w \times \overrightarrow{\lambda} \\ \boldsymbol{P}_{S2} = \boldsymbol{P} - w \times \overrightarrow{\lambda} \end{cases} \tag{14}$$

where $\overrightarrow{\lambda}$ is the target indication vector; $\boldsymbol{P}_{sort}^{new}$ and $\boldsymbol{P}_{sort}^{old}$ are the sorted communication objects stored in the quasi-Golgi this time and the last time; $\boldsymbol{P}_{S2}$ and $\boldsymbol{P}_{S1}$ both are the new target indication objects; and w is the indication coefficient.

- Transition rule

First select two elements of the selected object randomly, and then swap these elements if they are in the range of the other's value, that is:

$$\begin{cases} \boldsymbol{P} \rightarrow \boldsymbol{P}' \\ \boldsymbol{P} = (p_1, \cdots, p_p, \cdots, p_q, \cdots, p_l) \\ \boldsymbol{P}' = (p_1, \cdots, p_q, \cdots, p_p, \cdots, p_l) \\ p_q \leq p_p \leq \overline{p_q} \wedge p_p \leq p_q \leq \overline{p_p} \end{cases} \tag{15}$$

- Abstraction rule

The abstraction rule is designed only for optimal and suboptimal objects, where each element of the optimal object is replaced by the element on the same position of the suboptimal object, one after another. Then, the element from the suboptimal object is reserved if the new object is better than the old optimal one; otherwise, the old optimal object remains:

$$\begin{cases} \boldsymbol{P}_a, \boldsymbol{P}_b \rightarrow \boldsymbol{P}' \\ \boldsymbol{P}_a = (p_{a1}, \cdots, p_{aj}, \cdots, p_{al}) \\ \boldsymbol{P}_b = (p_{b1}, \cdots, p_{bj}, \cdots, p_{bl}) \\ \boldsymbol{P}' = (p_1, \cdots, p_j, \cdots, p_l) \quad p_j \in \left\{ p_{aj}, p_{bj} \right\} \end{cases} \tag{16}$$

When using the biomimetic membrane computing method, there is an iterative calculation and communication for each basic membrane, and the good objects in the basic membrane can be reserved and sent to the quasi-Golgi for local optimization and evolution. However, with the increment of unit scale, the searching ability and stability of the method is reduced, and thus we added the CE optimization method to the membrane computing method to enhance its searching ability and stability.

4.3. CE Optimization Method

The CE method is an optimization method proposed by Rubinstein and Kroese, who estimated probabilities of rare events for stochastic networks [24]. It was first used to solve combinatorial optimization problems, and then also applied to solve continuous optimization problems [25]. Cross-entropy is a measurement for the similarity degree of two probability distributions. The main

idea of CE is to get a probability distribution whose difference with the unknown optimal probability distribution is minimal [26].

For the dynamic dispatch problem:

$$\gamma^* = \min_{\boldsymbol{P}\in\rho} F(\boldsymbol{P}) \tag{17}$$

where γ^* represents the optimization result of γ for economic dispatching; ρ is the probability space. Obviously, Equation (17) is a minimization problem. When generation $\boldsymbol{P}$ obeys the distribution of $f(\circ;\boldsymbol{u})$, the original optimization problem can be transformed into an optimization problem of finding the optimal probability density function $f(\circ;\boldsymbol{u})$. Moreover, when we define $\boldsymbol{S}_{\{F(\boldsymbol{P})\leq\gamma\}}$ as a set of different indicator functions on ρ with value γ, the optimization problem of $f(\circ;\boldsymbol{u})$ can be further transformed into a corresponding probability estimation problem as follows. The indicator functions in $\boldsymbol{S}_{\{F(\boldsymbol{P})\leq\gamma\}}$ is used to describe the characteristics of a stochastic process, usually formulated as mean function, variance function and correlation function, etc.:

$$l(\gamma) = \boldsymbol{H}_{\boldsymbol{u}}(F(\boldsymbol{P}) \leq \gamma) = \sum_{P} \boldsymbol{S}_{\{F(\boldsymbol{P})\leq\gamma\}} f(\boldsymbol{P};\boldsymbol{u}) = \boldsymbol{E}_{\boldsymbol{u}}\boldsymbol{S}_{\{F(\boldsymbol{P})\leq\gamma\}} \tag{18}$$

where $\boldsymbol{H}_{\boldsymbol{u}}$ and $\boldsymbol{E}_{\boldsymbol{u}}$ are the probability measure and expectation, respectively, of the optimal probability distribution $f(\circ;\boldsymbol{u})$.

Usually the importance sampling method is used to calculate $l(\gamma^*)$: sampling the generation $\boldsymbol{P}_i (i = 1, 2, \ldots, N)$ based on the probability distribution g on $\boldsymbol{P}$:

$$\hat{l} = \frac{1}{N}\sum_{i=1}^{N} \boldsymbol{S}_{\{F(\boldsymbol{P}_i)\leq\gamma\}} \frac{f(\boldsymbol{P}_i;\boldsymbol{u})}{g(\boldsymbol{P}_i)} \tag{19}$$

when the probability distribution g is:

$$g^*(\boldsymbol{P}) = \frac{\boldsymbol{S}_{\{F(\boldsymbol{P})\leq\gamma\}} f(\boldsymbol{P};\boldsymbol{u})}{l} \tag{20}$$

where $\hat{l}$ is the value of l after the importance sampling method; g^* is the assumed value of g for the importance sampling method.

There is an unbiased estimated zero variance with only one sample needed. Therefore, it is difficult to calculate g^* since its value is related to l, and the probability distribution g can usually be selected from the probability distribution cluster $\{f(\circ;\boldsymbol{v})\}$. In this way, the original optimization problem is finally transformed into a determination of parameter $\boldsymbol{v}$ that minimizes the difference between the probability distribution of generation $f(\circ;\boldsymbol{v})$ and optimal g^*. In this paper, parameter $\boldsymbol{v}$ includes the mean value $\boldsymbol{\mu}$ and standard deviation $\boldsymbol{\sigma}$ of samples.

Relative-entropy (i.e., Kullback-Leibler distance) and cross-entropy are commonly used measures for the similarity degree of two probability distributions [27]. In this paper, we used the CE method, as the following formula shows:

$$\min_{\boldsymbol{v}} -\int g^*(\boldsymbol{P}) \ln f(\boldsymbol{P};\boldsymbol{v}) dP \tag{21}$$

Combining Equations (18) and (20), $\boldsymbol{v}^*$ can be calculated by Equation (22):

$$\hat{\boldsymbol{v}}* = \operatorname{argmax}_{\boldsymbol{v}} \frac{1}{N}\sum_{i=1}^{N} \boldsymbol{S}_{\{F(\boldsymbol{P}_i)\leq\gamma\}} \ln f(\boldsymbol{P}_i;\boldsymbol{v}) \tag{22}$$

Moreover, through the smoothing technique, the parameter estimation form $\hat{\boldsymbol{v}}$ of $\boldsymbol{v}^*$ can be expressed as follows:

$$\hat{\boldsymbol{v}}_k = \alpha\widetilde{\boldsymbol{v}}_k + (1-\alpha)\hat{\boldsymbol{v}}_{k-1} \tag{23}$$

where "~" represents the parameter of elite samples. The top-ranking dispatching solutions after evaluation are chosen as the elite samples. "^" represents the parameter of total samples. α is the smoothing factor (typically between 0.7 and 1); and $\widetilde{v}_k$ is the value v of the elite sample after the kth smoothing. Therefore, it is easier to approach the optimal solution with the correction of $\hat{v}$ through the elite sample.

In short, when using the CE optimization method, first predefine the parameter v and generate the candidate solution set according to the probability density function $f(\circ; v)$, and then update the value of v through the elite sample. Thus, the searching direction continues to approximate the optimal solution in the iteration.

4.4. Procedures of CEHMC Method for UC Problem

The main steps of the CEHMC method are in detail as follows, and illustrated in Figure 3.

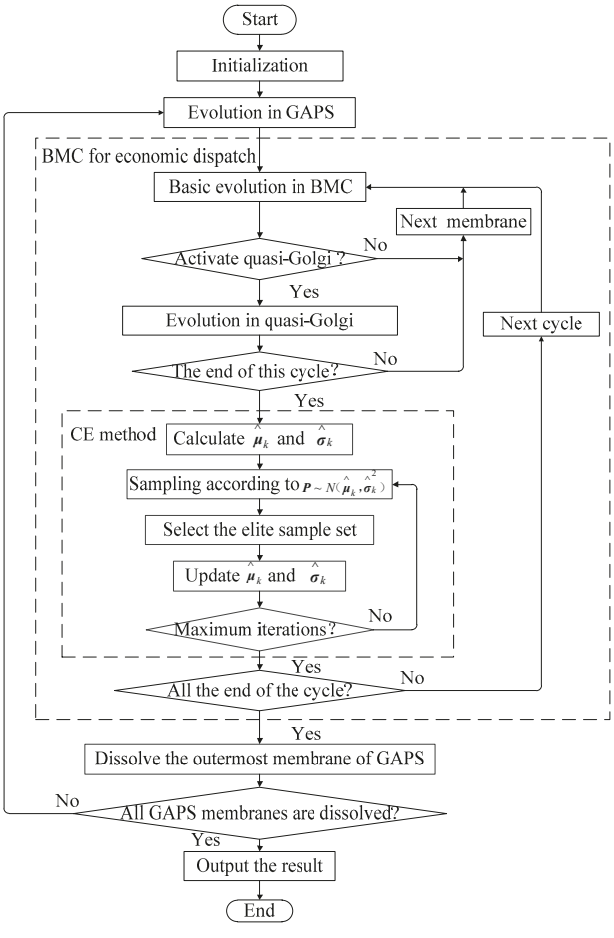

Figure 3. Flowchart of cross-entropy-based hybrid membrane computing (CEHMC)-based unit commitment (UC) problem.

Step 1: Initialization. Set the initial parameters, construct the genetic membrane structure, and generate the initial binary object $\boldsymbol{I_o}$ in each membrane (i.e., generate the start-stop states).

Step 2: Evolution. Execute the evolution rules for all objects $\boldsymbol{I}$ in each membrane.

Step 3: Evaluation. For all start-stop states, solve the economic dispatch part with the CEHMC method. The numerical result *F(**P**)* is taken as the evaluation indicator to replace the old objects. In this dispatch part, the evolution object $\boldsymbol{P}$ is the generation of units, and the main steps are as follows:

3.1 *Initialization*. Set the initial parameters, construct biomimetic membrane structure, and create N_{co} initial communication objects $\boldsymbol{P_{co}}$ in the outermost membrane and send them to the first basic membrane.

3.2 *Computation in the basic membrane*. Create N_o initial objects $\boldsymbol{P_o}$ in the current membrane, and execute the basic evolution rules in order for N_o optimal objects to be selected in this membrane. Then, select N_{co} optimal objects $\boldsymbol{P_{best}}$ as the communication objects $\boldsymbol{P_{co}}$ and N_s suboptimal objects as the reservation objects. Finally, remove the remaining objects, and send the communication objects $\boldsymbol{P_{co}}$ into the quasi-Golgi membrane.

3.3 *Computation in the quasi-Golgi membrane*. Update the target indicator vector, and check whether the activate condition of quasi-Golgi is satisfied. If not, the communication objects $\boldsymbol{P_{co}}$ are sent to the next basic membrane directly, and return to step 3.2; if satisfied, execute evolution rules in the quasi-Golgi for communication objects $\boldsymbol{P_{co}}$, and then select the new communication objects $\boldsymbol{P_{co}}$.

3.4 *Check whether the current computation cycle is completed*. If not, send the communication objects $\boldsymbol{P_{co}}$ into the next basic membrane and return to step 3.2; if completed, start the CE optimization steps:

- Initialization. Calculate the mean and standard deviation for all communication objects $\boldsymbol{P_{co}}$ in the current cycle as the initial sample.
- Sampling. Take generation samples $\boldsymbol{P}_1, \boldsymbol{P}_2, \ldots, \boldsymbol{P}_N$ based on the $\boldsymbol{P} \sim N(\hat{\mu}_k, \hat{\sigma}_k^2)$.
- Evaluation. Select the elite sample set, and then calculate its mean and standard deviation.
- Update parameters. Update the mean $\widetilde{\boldsymbol{\mu}}_k$ and standard deviation $\widetilde{\sigma}_k$ according to Equations (24) and (25):

$$\hat{\boldsymbol{\mu}}_k = \alpha\widetilde{\boldsymbol{\mu}}_k + (1-\alpha)\hat{\boldsymbol{\mu}}_{k-1}, \tag{24}$$

$$\hat{\boldsymbol{\sigma}}_k = \beta_k\widetilde{\boldsymbol{\sigma}}_k + (1-\beta_k)\hat{\boldsymbol{\sigma}}_{k-1} \tag{25}$$

  The standard deviation is usually updated by dynamic smoothing, that is, $\beta_k = \beta_0 - \beta_0(1-\frac{1}{k})^r$, where β_0 is the smoothing factor (typically between 0.8 and 0.99), k is the iteration number, and r is an integer (typically between 5 and 10).
- Judgment of the termination condition. If the iteration was over, output the optimal object P_{best}; if not, return to Step 3.2.

3.5 *Judgment of termination conditions*. Check whether all computation cycles are completed. If not, send the communication objects Pco to the first basic membrane and return to step 3.2; if completed, output the function value of the optimal object Pbest.

Step 4: Communication. Select N_e optimal objects $\boldsymbol{I_{best}}$, and send them to the adjacent (sub-outer) membrane. At the same time, the outermost membrane is dissolved, and thus the previous sub-outer membrane becomes the new outermost membrane.

Step 5: Judgment of termination conditions. If all membranes are dissolved, output the best result $\boldsymbol{I_{best}}$ of the UC problem; if not, return to Step 3.2.

5. Case Study

The 10-unit 24 h standard thermal power test system was taken as the test example to verify the effectiveness of the proposed method. The unit characteristics and load demand are detailed in the literature [28], and the ramp rate limits of units 1, 3, and 4 are all as follows [29]: $P_i^{up} = P_i^{down}$ = 40 MW/h, $P_i^{start} = P_i^{shut} = 2\underline{P}_i$. The initial parameters of the proposed method are list in Table 1. The quasi-Golgi activate condition is that the multiplication of current computation cycle and current basic membrane can be divided by 3 after the second computation cycle.

In order to analyze the performance of the proposed method, 20 complete independent simulations are conducted on each system. Two cases of the UC problem are simulated: (1) UC problem without ramp constraints; (2) UC problem with ramp constraints. The characteristics, including the number of continues and integer variables and number of constraints for these two cases are list in Table 2, which contribute to depict the magnitude and complexity of the investigated UC problem.

Table 2. Computation characteristics of the UC problem.

Unit	Variables		Constraints	
	Integer	Continuous	Without Ramp	With Ramp
10	240	240	748	886
20	480	480	1448	1724
40	960	960	2848	3400
60	1440	1440	4248	5076
80	1920	1920	5648	6752
100	2400	2400	7048	8428

In the following sections, the corresponding simulation results for these two cases are discussed and compared. Moreover, the simulation of the proposed method is programmed by MATLAB 2014a (The MathWorks, Inc, Natick, MA, USA) on the PC with Intel Core i5-3470 CPU, 3.20 GHz, 4 GB Ram (Intel, Santa Clara, CA, USA).

5.1. Simulation Results of UC Problem without Ramp Constraints

The generation of a 10–100-unit 24 h system is shown in Figure 4, where the area of each unit is the generation value.

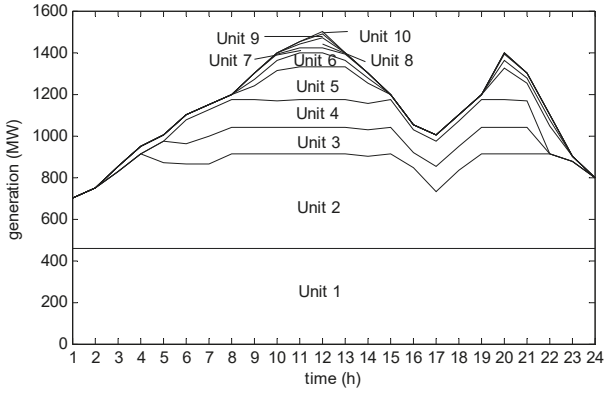

Figure 4. Generation of the 10 units (not considering unit ramp rate constraint).

Comparison of the proposed CEHMC with six bioinspired optimization methods (EPSO, MRCGA, GA, MA, EP, HMC) and three mathematical optimization methods (SOCP, IPL, C&B) is shown in Table 3. To be more illustrative, the normalized comparison results of different algorithms are plotted in Figure 5. For the bioinspired optimization methods, the best and mean solutions of them are plotted as Figure 5a,b, respectively.

Table 3. Comparison of different algorithms (not considering unit ramp rate constraint), unit: $.

Methods		Unit					
		10	**20**	**40**	**60**	**80**	**100**
SOCP [4]		564,531	1,124,713	2,244,369	3,363,758	4,484,357	5,603,728
IPL [7]		563,977	1,123,795	2,243,546	3,360,764	4,481,411	5,600,108
C&B [30]		563,938	1,123,783	2,243,687	3,363,593	4,484,497	5,603,976
EPSO [31]	best	563,938	1,123,232	2,243,407	3,365,480	4,488,601	5,612,742
	mean	563,969	1,124,127	2,246,800	3,373,859	4,501,254	5,620,785
	worst	564,206	1,125,815	2,250,364	3,381,947	4,510,984	5,633,447
MRCGA [11]	best	564,244	1,125,035	2,246,622	3,367,366	4,489,964	5,610,031
	mean	564,467	1,126,199	2,249,609	3,371,036	4,497,346	5,616,957
	worst	565,756	1,128,326	2,252,076	3,375,815	4,505,511	5,623,248
GA [13]	best	565,866	1,128,876	2,252,909	3,377,393	4,507,692	5,626,362
	mean	567,329	1,130,106	2,262,585	3,394,044	4,525,204	5,669,362
	worst	571,336	1,131,565	2,269,282	3,401,847	4,552,982	5,690,086
MA [13]	best	565,827	1,127,254	2,252,937	3,388,676	4,501,449	5,640,543
	mean	566,453	1,128,824	2,262,477	3,394,830	4,527,779	5,665,803
	worst	566,861	1,130,916	2,270,316	3,408,275	4,545,305	5,698,039
EP [32]	best	564,551	1,125,494	2,249,093	3,371,611	4,498,479	5,623,885
	mean	565,352	1,127,257	2,252,612	3,376,255	4,505,536	5,633,800
	worst	566,231	1,129,793	2,256,085	3,381,012	4,512,739	5,639,148
HMC	best	564,541	1,127,594	2,250,328	3,388,056	4,522,491	5,654,987
	mean	564,716	1,128,188	2,251,504	3,390,237	4,525,342	5,659,001
	worst	564,949	1,128,953	2,260,989	3,392,445	4,527,762	5,664,080
CEHMC	best	563,930	1,123,206	2,243,314	3,360,779	4,479,720	5,600,004
	mean	564,027	1,123,309	2,249,388	3,369,956	4,480,122	5,602,334
	worst	564,796	1,126,712	2,260,684	3,391,698	4,497,391	5,609,585

Note: SOCP: second-order cone programming; IPL: improved priority list; C&B: cut and branch; EPSO: elite particle swarm optimization; MRCGA: matrix real-coded genetic algorithm; EP: evolutionary programming; HMC: hybrid membrane computing.

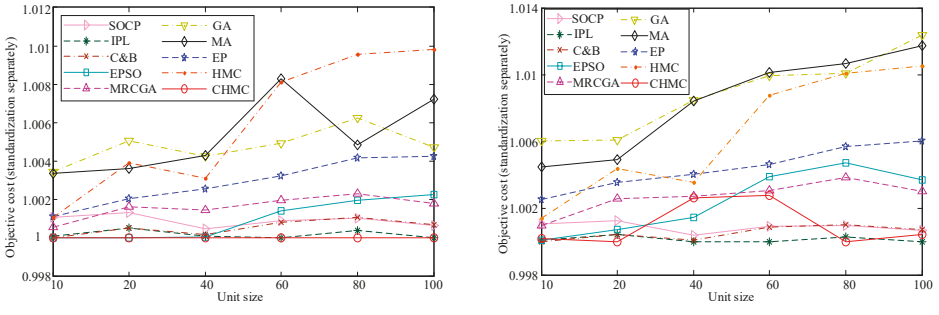

(**a**) best (**b**) mean

Figure 5. Normalized comparison results of different algorithms (not considering unit ramp rate constraint).

From the best solutions, it can be seen that CEHMC has the best performance in all the seven intelligent methods. Compared with the three mathematical optimization methods, the best solutions of CEHMC are lightly larger than IPL (with the smallest objective cost) when unit size is 60 and 80. In other cases of unit size, CEHMC gets the best results. That means, the proposed CEHMC has stable optimization process when unit size increases. Comparing the results of CEHMC and HMC, the solution

of CEHMC is much better than HMC. It is shown that the hybrition of cross-entropy and membrane computing theory can significantly improve the optima searching ability and optimization efficiency.

5.2. Simulation Results of UC Problem with Ramp Constraints

The generation of a 10-unit 24 h system is shown in Figure 6, where the area of each unit is the generation value. Comparison of the proposed CEHMC with two intelligent optimization methods (PSO, HMC) and six mathematical optimization methods (MISOCP, OO, BB, HCMIP, SHCMIP, MILP) is shown in Table 4. To be more illustrative, the normalized comparison results of different algorithms are also plotted in Figure 7. For PSO, HMC and CEHMC, the best solutions of them are plotted as Figure 7a,b, respectively.

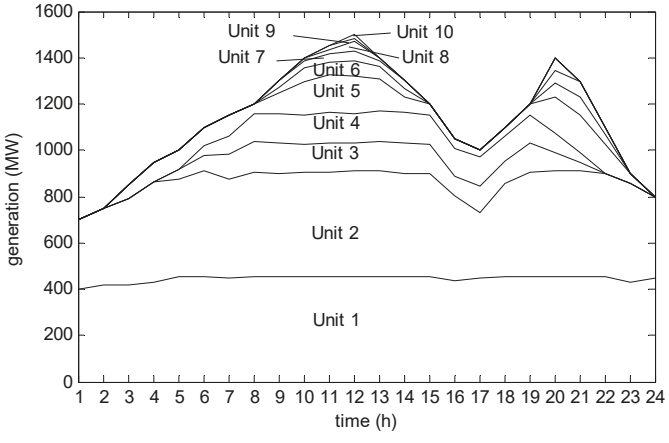

Figure 6. Generation of 10 units (considering unit ramp rate constraint).

Table 4. Comparison of different algorithms (considering unit ramp rate constraint), unit: $.

Methods		Unit					
		10	**20**	**40**	**60**	**80**	**100**
MISOCP [32]		565,777	1,130,647	2,259,203	3,382,470	4,511,813	5,638,456
OO [33]		569,751	1,139,504	2,261,900	3,401,850	4,570,808	5,697,510
BB [33]		568,710	1,136,650	2,260,214	3,383,489	4,531,817	5,658,458
HCMIP [34]		566,084	1,129,241	2,257,269	3,379,852	4,508,689	5,633,984
SHCMIP [35]		565,397	1,127,437	2,251,617	3,376,821	4,501,420	5,625,531
MILP [36]		566,188	1,127,218	2,252,810	3,375,967	4,501,532	5,623,814
PSO	best	571,766	1,141,430	2,285,074	3,436,205	4,590,027	5,730,530
	mean	572,216	1,142,604	2,307,258	3,439,609	4,592,237	5,732,596
	worst	572,623	1,144,225	2,328,432	3,441,807	4,593,553	5,733,525
HMC	best	568,639	1,134,835	2,269,523	3,402,549	4,542,599	5,679,389
	mean	569,396	1,136,139	2,271,292	3,404,612	4,545,670	5,683,837
	worst	570,513	1,137,804	2,273,074	3,406,002	4,548,406	5,687,362
CEHMC	best	565,398	1,127,217	2,251,620	3,375,960	4,501,300	5,623,716
	mean	565,408	1,127,882	2,252,030	3,376,309	4,501,976	5,623,975
	worst	5,654,812	1,130,861	2,256,933	3,380,629	4,503,035	5,624,019

Note: MISOCP: mixed integer second-order cone programming; OO: ordinal optimization method; BB: branch and bound method; HCMIP: hyper-cube mixed integer programming; SHCMIP: sub hyper-cube mixed integer programming; MILP: mixed integer linear programming.

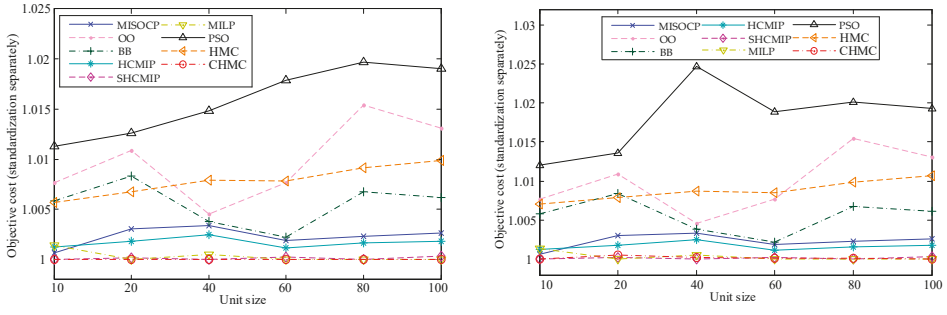

(**a**) best (**b**) mean

Figure 7. Normalized comparison results of different algorithms (considering unit ramp rate constraint).

It is found that, with the unit size larger than 40, CEHMC has the best performance in all the nine optimization methods. In other cases of unit size, the best result of CEHMC is lightly larger than the optima of all the nine optimization algorithms. The introduction of cross-entropy theory greatly improves the optima searching ability, which makes the results of CEHMC generally much better than HMC.

5.3. Influences of the Membrane Number to Convergence

For ease of explanation, the case of 10-unit without ramp constraints is taken as an example to analyze the influences of membrane number to approximation of optimal solution for the proposed CEHMC method.

5.3.1. GAPS

The effect of membrane number in GAPS on the objective value is simulated and illustrated in Figure 8. It is found that N_o and N_{co} may have little influence on the convergence with all those curves have similar shapes. Considering the computation cost and matching with other parameters, N_o is set as 10, and N_{co} is 10.

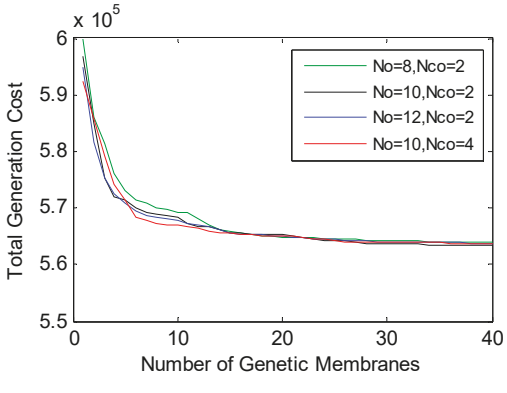

Figure 8. Influence of membrane number to convergence (GAPS).

5.3.2. BMC

BMC is for the dynamic dispatching problem with continuous variables. The influence of membrane number to convergence for BMC is based on a certain unit start-stop plan. The number

of membranes is the product of N_c' and N_b', which can also represent the iteration number. Figure 9 shows the penalty value curves changing with membrane number of BMC. It is found that when the abscissa is 100, the curve is almost gentle. Therefore, N_c' is set as 10, and N_b' is 10.

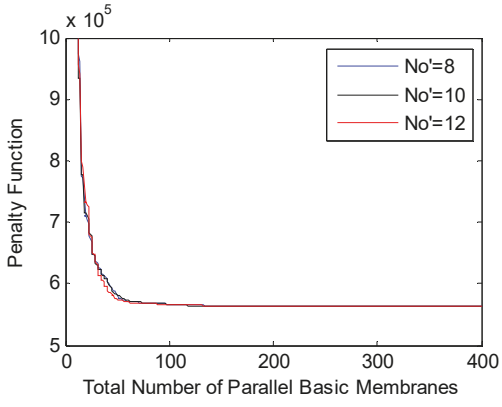

Figure 9. Influence of membrane number to convergence (BMC).

5.4. Analysis of Calculation Efficiency

Figure 10 shows how N_{co}' influences the approaching to the optimal solution. It is found that N_{co}' have effect on convergence. When N_{co}' is set 6, the convergence rate is fastest. when N_{co}' is set 2, the convergence rate is the slowest. After comprehensive consideration, the value of N_{co}' is set 4.

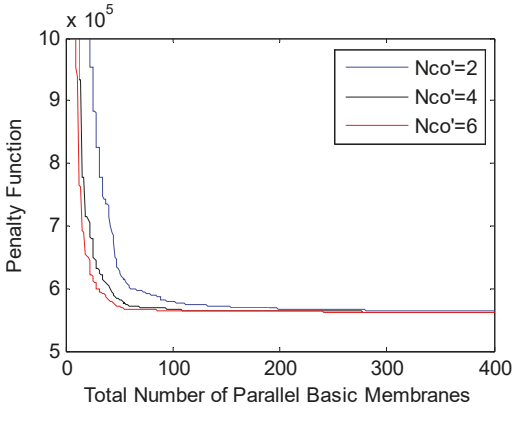

Figure 10. The sensitivity of *Nco*′ to convergence (BMC).

In order to verify the calculation efficiency of the proposed method, the calculation efficiency for the proposed CEHMC method and the other methods (in Table 4) are analysed and compared. The unit ramp rate constraints are considered. The computation time growth rate curves with the unit size increasing from 10 to 100 are illustrated in Figure 11. The computation time growth rate is based on the time consumed for the case of 10-unit.

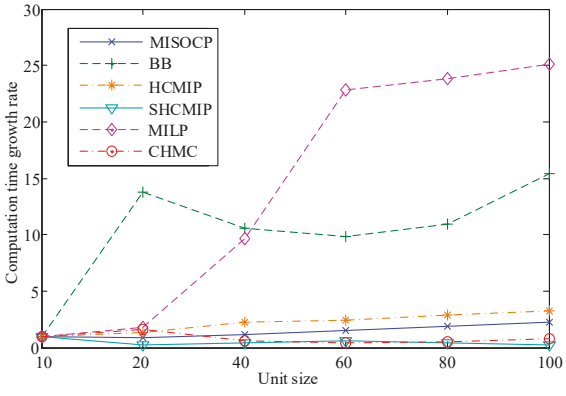

Figure 11. Computation time growth rate curves (considering unit ramp rate constraint).

It can be seen that only SHCMIP has a little better calculation efficiency than the proposed CEHMC method as the unit size increases. The time growth rate of CEHMC is significantly lower than the other four methods (MISOCP, BB, HCMIP, MILP) for large-scale UC problems.

6. Conclusions

In this paper, a cross-entropy-based hybrid membrane computing method is proposed to solve the UC problem which is inspired by living cells and their organization in tissues and other higher order structures. In the proposed method, the genetic algorithm-based P system is applied for the unit start-stop plan with embedded generic rules, which can transmit the outer optima into the inner membranes. The biomimetic membrane computing method combined with the cross-entropy is proposed to solve the dynamic economic dispatch problem with strengthened searching ability, which is inspired by the important role of Golgi apparatus in living cells. The 10–100 unit systems for 24 h day-ahead dispatching simulation results showed that the UC problem could be solved by the proposed method with good efficiency and stability. In future research, network constraints will be considered, and the method will be further improved to optimize simulation results.

Author Contributions: Conceptualization, M.X.; methodology, Y.D.; software, Y.D. and P.C.; validation, W.W.; writing—original draft preparation, Y.D.; writing—review and editing, M.X.; supervision, M.X. and M.L.; funding acquisition, M.X.

Funding: The financial supports for this research, from Guangdong Natural Science Foundation Free Application Project (2018A0303130134), are gratefully acknowledged.

Conflicts of Interest: The authors declare no conflict of interest.

References

1. Pandžić, H.; Dvorkin, Y.; Qiu, T.; Wang, Y.; Kirchen, D. Toward cost-efficient and reliable unit commitment under uncertainty. *IEEE Trans. Power Syst.* **2016**, *31*, 970–982. [CrossRef]
2. Mohammad, J.F.; Mitch, C.; Shabbir, A.; Ahmed, S.; Grijalva, S. Large-scale decentralized unit commitment. *Int. J. Electr. Power Energy Syst.* **2015**, *73*, 97–106.
3. Bai, Y.; Zhong, H.; Xia, Q.; Kang, C. A decomposition method for network-constrained unit commitment with AC power flow constraints. *Energy* **2015**, *88*, 595–603. [CrossRef]
4. Quan, R.; Jian, J.; Yang, L. An improved priority list and neighborhood S. Arch method for unit commitment. *Int. J. Electr. Power Energ. Syst.* **2015**, *67*, 278–285. [CrossRef]
5. Yuan, W.; Zhai, Q. Power-based transmission constrained unit commitment formulation with energy-based reserve. *IET Gener. Trans. Distrib.* **2017**, *11*, 409–418. [CrossRef]

6. Zheng, H.; Jian, J.; Yang, L.; Quan, R. A deterministic method for the unit commitment problem in power systems. *Comput. Oper. Res.* **2016**, *66*, 241–247. [CrossRef]
7. Nasri, A.; Kazempour, S.J.; Conejo, A.J.; Ghandhari, M. Network-constrained AC unit commitment under uncertainty: A benders decomposition approach. *IEEE Trans. Power Syst.* **2015**, *31*, 412–422. [CrossRef]
8. GAMS Development Corporation. GAMS, the Solvers' Manual, 2015. Available online: http://www.gams.com/solvers (accessed on 1 December 2018).
9. Rouhi, F.; Effatnejad, R. Unit commitment in power system t by combination of dynamic programming (DP), genetic algorithm (GA) and particle swarm optimization (PSO). *Indian J. Sci. Technol.* **2015**, *8*, 134. [CrossRef]
10. Magnússon, S.; Weeraddana, P.C.; Rabbat, M.G.; Fischione, C. On the convergence of alternating direction Lagrangian methods for nonconvex structured optimization problems. *IEEE Trans. Control Netw. Syst.* **2016**, *3*, 296–309. [CrossRef]
11. Sun, L.; Zhang, Y.; Jiang, C. A matrix real-coded genetic algorithm to the unit commitment problem. *Electr. Power Syst. Res.* **2006**, *76*, 716–728. [CrossRef]
12. Shukla, A.; Singh, S.N. Multi-objective unit commitment using search space-based crazy particle swarm optimisation and normal boundary intersection technique. *IET Gener. Trans. Distrib.* **2016**, *10*, 1222–1231. [CrossRef]
13. Valenzuela, J.; Smith, A.E. A seeded memetic algorithm for large unit commitment problems. *J. Heuristics* **2002**, *8*, 173–195. [CrossRef]
14. Wang, H.; Peng, H.; Shao, J.; Wang, T. A thresholding method based on P systems for image segmentation. *ICIC Express Lett.* **2012**, *6*, 221–227.
15. Wang, X.; Zhang, G.; Zhao, J.; Rong, H.; Ipate, F.; Lufticaru, R. A modified membrane-inspired algorithm based on particle swarm optimization for mobile robot path planning. *Int. J. Comput. Comm. Control* **2015**, *10*, 732–745. [CrossRef]
16. Xiao, J.H.; Zhang, X.Y.; Xu, J. A membrane evolutionary algorithm for DNA sequence design in DNA computing. *Chin. Sci. Bull.* **2012**, *57*, 698–706. [CrossRef]
17. Zhao, J.; Wang, N. A bio-inspired algorithm based on membrane computing and its application to gasoline blending scheduling. *Comput. Chem. Eng.* **2011**, *35*, 272–283. [CrossRef]
18. Zhang, G.X.; Cheng, J.X.; Gheorghe, M. A membrane-inspired approximate algorithm for traveling salesman problems. *Rom. J. Inf. Sci. Technol.* **2011**, *14*, 3–19.
19. Leporati, A.; Pagani, D. A membrane algorithm for the min storage problem. In *International Workshop on Membrane Computing*; Springer: Berlin/Heidelberg, Germany, 2006; pp. 443–462.
20. Pereira, S.; Ferreira, P.; Vaz, A.I.F. A simplified optimization model to short-term electricity planning. *Energy* **2015**, *9*, 2126–2135. [CrossRef]
21. Păun, G. Computing with membranes. *J. Comput. Syst. Sci.* **2000**, *61*, 108–143. [CrossRef]
22. Păun, A. *On P Systems with Active Membranes. Unconventional Models of Computation*; UMC'2K; Springer: London, UK, 2001; pp. 187–201.
23. Rubinstein, R. The cross-entropy method for combinatorial and continuous optimization. *Methodol. Comput. Appl. Probab.* **1999**, *1*, 127–190. [CrossRef]
24. Kroese, D.P.; Porotsky, S.; Rubinstein, R.Y. The cross-entropy method for continuous multi-extremal optimization. *Methodol. Comput. Appl. Probab.* **2006**, *8*, 383–407. [CrossRef]
25. Quinn, A.; Kárný, M.; Guy, T.V. Fully probabilistic design of hierarchical Bayesian models. *Inf. Sci.* **2016**, *369*, 532–547. [CrossRef]
26. Yang, Z.; Gao, K.; Fan, K.; Lai, Y. Sensational headline identification by normalized cross entropy-based metric. *Comput. J.* **2015**, *58*, 644–655. [CrossRef]
27. Senjyu, T.; Shimabukuro, K.; Uezato, K.; Funabashi, T. A fast technique for unit commitment problem by extended priority list. *IEEE Trans. Power Syst.* **2003**, *18*, 882–888. [CrossRef]
28. Guo, S.; Guan, X.; Zhai, Q. The necessary and sufficient conditions for determining feasible solutions to unit commitment problems with ramping constraints. *IEEE Power Eng. Soc. Gen. Meet.* **2005**, *1*, 344–349.
29. Yuan, X.; Tian, H.; Zhang, S.; Ji, B.; Huo, Y. Second-order cone programming for solving unit commitment strategy of thermal generators. *Energy Convers. Manag.* **2013**, *76*, 20–25. [CrossRef]
30. Roy, P.K. Solution of unit commitment problem using gravitational search algorithm. *Int. J. Electric. Power Energy Syst.* **2013**, *53*, 85–94. [CrossRef]

31. Juste, K.A.; Kita, H.; Tanaka, E.; Hasegava, J. An evolutionary programming solution to the unit commitment problem. *IEEE Trans. Power Syst.* **1999**, *14*, 1452–1459. [CrossRef]
32. Quan, R.; Hua, W.; Jian, J. Solution of large scale unit commitment by second-order cone programming. *Proc. CSEE* **2010**, *30*, 101–107.
33. Xie, M.; Zhu, Y.; Wu, Y.; Yan, Y.; Liu, M. Application of ordinal optimization theory to solve large-scale unit commitment problem. *Control Theory Appl.* **2016**, *33*, 542–551.
34. Yang, L.; Jian, J.; Han, D.; Zheng, H. A hyper-cube cone relaxation model and solution for unit commitment. *Trans. China Electrotech. Soc.* **2013**, *28*, 252–261.
35. Yang, L.; Jian, J.; Zheng, H.; Dan, D. A sub hyper-cube tight mixed integer programming extended cutting plane method for unit commitment. *Proc. CSEE* **2013**, *33*, 99–108.
36. Liu, S.; Jian, J. Research on unit commitment considering emission trading. *Power Syst. Technol.* **2013**, *3*, 3558–3563.

energies

MDPI

Article

A Two-Stage Feature Selection Method for Power System Transient Stability Status Prediction

Zhen Chen [1,*], Xiaoyan Han [2], Chengwei Fan [1], Tianwen Zheng [3,4] and Shengwei Mei [4]

1 State Grid Sichuan Electric Power Research Institute, Chengdu 610041, China; chengwei_fann@163.com
2 State Grid Sichuan Electric Power Company, Chengdu 610041, China; hanxy3343@sc.sgcc.com.cn
3 Sichuan Energy Internet Research Institute, Tsinghua University, Chengdu 610213, China; tianwenscu@163.com
4 Department of Electrical Engineering, Tsinghua University, Beijing 100084, China; meishengwei@tsinghua.edu.cn
* Correspondence: chenzhen5840@163.com

Received: 10 January 2019; Accepted: 13 February 2019; Published: 20 February 2019

Abstract: Transient stability status prediction (TSSP) plays an important role in situational awareness of power system stability. One of the main challenges of TSSP is the high-dimensional input feature analysis. In this paper, a novel two-stage feature selection method is proposed to handle this problem. In the first stage, the relevance between features and classes is measured by normalized mutual information (NMI), and the features are ranked based on the NMI values. Then, a predefined number of top-ranked features are selected to form the strongly relevant feature subset, and the remaining features are described as the weakly relevant feature subset, which can be utilized as the prior knowledge for the next stage. In the second stage, the binary particle swarm optimization is adopted as the search algorithm for feature selection, and a new particle encoding method that considers both population diversity and prior knowledge is presented. In addition, taking the imbalanced characteristics of TSSP into consideration, an improved fitness function for TSSP feature selection is proposed. The effectiveness of the proposed method is corroborated on the Northeast Power Coordinating Council (NPCC) 140-bus system.

Keywords: transient stability; two-stage feature selection; particle encoding method; fitness function

1. Introduction

With the continual enlargement in scale of power grid interconnections and the increasing large-scale integration of renewable power generation, the dynamic characteristics of power systems have become more and more complex, resulting in higher requirements for power system stability analysis [1,2]. In recent years, due to the wide application of wide-area measurement systems and rapid development of artificial intelligence (AI) methods, power system transient stability status prediction (TSSP) based on AI methods has attracted extensive attention. Generally, TSSP is treated as a two class classification problem, including the stable class and the unstable class [3]. Offline, the mapping relationship between the input features and the stability status is established by using the strong nonlinear mapping abilities of AI methods. Online, the upcoming transient stability status of the system can be quickly predicted by feeding the input features into the established classification model.

The input features are important factors that affect the performance of the classification model. However, the existing feature sets applied to TSSP are often manually selected according to experience, which can significantly degrade the performance of the classification model due to the existence of irrelevant and redundant features [4].

Feature selection, which refers to the process of filtering out the optimal feature subset from the original feature set, can eliminate irrelevant and redundant features and improve classification

performance [5]. Therefore, it has become a basic data preprocessing method, and it is of great significance to study the feature selection method for TSSP.

The existing methods for TSSP feature selection can be divided into two main categories [6]: the filter method and the wrapper method.

The filter method ranks the original features by calculating the importance of each individual feature, and it selects a predefined number of top-ranked features as the input features for classification models. Different filter methods are generated according to different importance metrics. In [7,8], the Fisher criterion is utilized to evaluate features comprehensively, considering both the intra-class distance and the inter-class distance. Information measure-based feature selection methods are utilized to select important features in [9,10]. Other methods, such as the relief method [11] and the rough set method [12], are also adopted for TSSP feature selection. The filter method is computationally efficient since it ranks features individually, but it is less effective due to the lack of a classification model in the search process.

The wrapper method considers the feature selection as an optimization problem, and evaluates the feature subset by using certain search strategies and classification algorithms. Based on different search strategies, the wrapper method can be classified into the greedy search technique and the heuristic search technique. The former includes sequence forward search (SFS) methods and sequence backward search (SBS) methods, and the latter mainly includes genetic algorithms (GA) [13], binary particle swarm algorithms (PSO) [14], etc. Since the wrapper method combines the feature selection problem with the classification model, it often has a better performance than the filter method [15]. However, as the feature dimension increases, the wrapper method is usually preferred to obtain the local optimal solution of the problem.

From the above analysis, it can be concluded that both the filter method and the wrapper method have their own merits and demerits, and a more effective feature selection approach should be developed for TSSP problem.

In this paper, a novel two-stage feature selection method is proposed for TSSP problem. In the first stage, normalized mutual information (NMI) is utilized for measuring the relevance between individual feature and classes, and the features are ranked based on the NMI values. Then, the top-ranked features are selected to form the strongly relevant feature subset (SRFS), and the remaining features are described as the weakly relevant feature subset (WRFS). The results obtained in the first stage will be used as the prior knowledge for the next stage. In the second stage, binary particle swarm optimization (BPSO) is utilized as the search algorithm for feature selection, and a new particle encoding strategy that considers population diversity and prior knowledge is proposed. In addition, fitness function plays a very important role in controlling the search direction of BPSO. By taking the imbalanced characteristic of the TSSP problem into consideration, an improved fitness function composed of the geometric mean index and feature subset length is proposed. In this paper, k-nearest neighbor (KNN) is chosen as the classifier to evaluate the classification performance of the candidate feature subset because of its simplicity and rapidity.

The rest of the paper is organized as follows. Section 2 introduces the methodologies used in the paper. Section 3 describes the process of initial feature set construction and data generation. In Section 4, the proposed two-stage feature selection method is provided. The case study is shown in Section 5 and the conclusion is drawn in Section 6.

2. Methodology

2.1. Normalized Mutual Information

Mutual information represents the information shared by two variables, which can be utilized for measuring the correlation degree of two variables [16].

Entropy is the measure of the uncertainty of a random variable. If the probabilities of different output classes C are $P(c_i)$, $i = 1, \ldots, N_c$, then the entropy $H(c)$ is defined as follows:

$$H(C) = -\sum_{i=1}^{N_c} P(c_i) \log_2(P(c_i)) \tag{1}$$

The joint entropy of feature vector F and output class C is defined as:

$$H(C;F) = -\sum_{i=1}^{N_c} \sum_{j=1}^{N_f} P(c_i, f_j) \log_2(P(c_i, f_j)) \tag{2}$$

When the feature vector F is known, the residual uncertainty in the output class C is measured by the conditional entropy:

$$\begin{aligned} H(C|F) &= -\sum_{j=1}^{N_f} P(f_j) \sum_{i=1}^{N_C} P(c_i|f_j) \log_2(P(c_i|f_j)) \\ &= -\sum_{i=1}^{N_c} \sum_{j=1}^{N_f} P(c_i, f_j) \log_2(P(c_i|f_j)) \end{aligned} \tag{3}$$

The relationship between the conditional entropy, entropy, and joint entropy can be demonstrated as below:

$$H(C|F) = H(C;F) - H(F) \tag{4}$$

The mutual information between two variables C and F is defined as [16]:

$$MI(C;F) = H(C) - H(C|F) \tag{5}$$

From the above equation, it can be concluded that mutual information measures the reduction amount of class uncertainty after proving the knowledge of feature vectors.

The mutual information is symmetric and can be reduced to the following equation:

$$MI(C;F) = MI(F;C) = \sum_{i=1}^{N_c} \sum_{j=1}^{N_f} P(c_i, f_j) \log_2 \frac{P(c_i, f_j)}{P(c_i)P(f_j)} \tag{6}$$

In order to normalize the mutual information value into [0, 1], the normalized mutual information (NMI) [17] is denoted as:

$$NMI(C;F) = \frac{2MI(C;F)}{H(C) + H(F)} \tag{7}$$

The larger the NMI value is, the stronger the relevance between features and classes will be, and vice versa. If the NMI value is 0, it means that the feature vector and classes are totally irrelevant or independent of each other. If the NMI value is 1, it indicates that the feature vector and classes are completely relevant.

After ranking the features based on the NMI values, the predefined number of top-ranked features can be selected to form the SRFS, and the remaining features are described as WRFS.

2.2. Binary Particle Swarm Optimization

Among the heuristic intelligent optimization algorithms, the particle swarm optimization (PSO) algorithm, which is easy to implement and has few parameters to tune, is superior to other algorithms in terms of success rate and solution quality. The binary version of PSO (BPSO) is employed for TSSP feature selection since it is a discrete optimization problem with binary solution space [18].

In BPSO, every possible solution to this optimization problem is presented by a particle, which has the two attributes of position and velocity. The next particle velocity is determined by the current particle velocity and particle position. Specifically, during each iteration, particles will be updated based on the distance from the individual best position and the distance from the global best position. The velocity updating formulas of PSO are provided as follows:

$$v_{id}^{k+1} = \omega v_{id}^{k} + c_1 r_1 (pbest_{id}^{k} - x_{id}^{k}) + c_2 r_2 (gbest_{d}^{k} - x_{id}^{k})]\mathrm{a} = 1 \tag{8}$$

$$\omega = \omega_{\max} - \frac{k}{N_k} \times (\omega_{\max} - \omega_{\min}) \tag{9}$$

where x_{id}^{k} and v_{id}^{k} are velocity and position of the particle i in dimension d at iteration k, respectively; *pbest* indicates the best position of the particle i in dimension d at iteration k, while *gbest* is the best position in the swarm so far; c_1 and c_2 represent the acceleration coefficients; r_1 and r_2 are the random numbers from a uniform distribution within the range of [0, 1]. The inertia weight ω is used to control the impact of the last velocity to the current velocity, which is linearly decreased from $\omega_{\max}$ to $\omega_{\min}$ to balance the global and local search [19], as shown in Equation (9). N_k is the maximum number of iterations.

The particle position in BPSO algorithm is updated based on the velocity value, and the transfer function should be employed to map the real valued velocity to a probability value between [0, 1] to change the binary position.

The velocity value in the BPSO algorithm means the difference between the current particle and the optimal particle. If the absolute value of velocity is relatively large, it means that the difference between the current particle and the optimal particle is large, and at this time, the transfer function should provide a higher possibility to change the position status of the current particle. Conversely, if the absolute value of the velocity is small, the difference between the current particle and the optimal particle is small. Then the transfer function should provide a higher probability to maintain the current position status. Therefore, v-shaped transfer functions designed in [20,21] is utilized for converting the velocity value to the changing probability of position status, as shown below:

$$T(v_{id}^{k+1}) = \begin{cases} \frac{2}{1+\exp(-v_{id}^{k+1})} - 1 \text{ if } v_{id}^{k+1} \geq 0 \\ 1 - \frac{2}{1+\exp(-v_{id}^{k+1})} \text{ if } v_{id}^{k+1} < 0 \end{cases} \tag{10}$$

After calculating the probability value, the binary position is then updated with the following formula:

$$x_{id}^{k+1} = \begin{cases} 1 - x_{id}^{k+1} & \text{if } r_3 \leq T(v_{id}^{k+1}) \\ x_{id}^{k+1} & \text{otherwise} \end{cases} \tag{11}$$

where r_3 is a random number uniformly distributed between [0, 1].

According to Equation (11), the particle position will be changed to the opposite status when the random number is smaller than $T(v_{id}^{k+1})$, and when the random number is larger than $T(v_{id}^{k+1})$, the status of particle position will be maintained.

The main steps of BPSO for solving binary optimization problem are describe below:

Step 1: Set the parameters of BPSO including population size, maximum iteration number, velocity range, learning factors, and inertia weight range.

Step 2: Initialize the binary position and velocity of each particle randomly.

Step 3: Calculate the fitness function of each particle, and update the values of individual best position *pbest* and global best position *gbest*.

Step 4: Update the velocity by using Equation (8) and the binary position by using Equations (10) and (11).

Step 5: Terminate the optimization process when the maximum iteration number is reached, and go on to step 6. Otherwise, increase the iteration number and return to step 3.

Step 6: Save the global best position as the ultimate solution for the binary optimization problem.

2.3. New Particle Encoding Strategy

Before using the heuristic search method for feature selection, the population initialization should be carried out first. Figure 1 is an encoding schematic diagram of a particle with 9-dimensional features, where 1 indicates that the feature is selected, and 0 indicates that the feature is discarded.

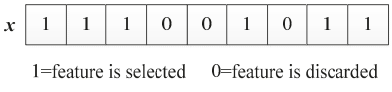

Figure 1. The encoding of a particle for feature selection.

The binary status of the dimension d of particle i is encoded by the following formula:

$$x_{id} = \begin{cases} 1 & r_4 \leq p \\ 0 & \text{otherwise} \end{cases} \tag{12}$$

where r_4 is a random number uniformly distributed between [0, 1], and p is a value between [0, 1].

The value of p indicates the probability that the dimension d is set to 1. In the conventional particle encoding method, each feature is selected by a completely random way, and the p is set to 0.5. The advantage of this particle encoding method is that it can increase the population diversity, but the disadvantages are that it can slow down the convergence speed and easily lead to local optimal solution, especially when the dimensions of feature selection problem is large.

As described in Section 2.1, the initial feature set can be divided into SRFS and WRFS based on the value of NMI. A feature in SRFS means that this feature has a higher probability to be chosen as the ultimate input feature, and a feature in WRFS means that this feature has a lower probability to be chosen as the ultimate input feature. The information obtained in Section 2.1 can be embedded into the particle encoding process as prior knowledge, which can guide the search direction of particles, and improve the efficiency and effectiveness of the feature selection results.

Based on the analysis above, a new particle encoding strategy considering the population diversity and priori knowledge is proposed, whose flowchart is shown in Figure 2.

From Figure 2, the main steps of the proposed particle encoding are listed below:

Step 1: Generate a random number r_5 uniformly distributed in [0, 1], and compare the random number with p_s. If the random number r_5 is smaller than p_s, go to step 2; otherwise, go to step 3. The value of p_s determines the proportion of completely random particle encoding and the particle encoding with prior knowledge, and p_s is set to 0.5 in this paper to balance two different particle encoding methods.

Step 2: Encode the particles considering the prior knowledge which is obtained from Step 1. For the feature in SRFS, the value of p in Equation (12) is set to p_m, and the p_m is bigger than 0.5, meaning that these kinds of features have higher probabilities to be selected. For the feature in WRFS, the value of p in Equation (12) is set to $p_n = 1 - p_m$, meaning that the p_n is smaller than 0.5 and these kinds of features have higher probabilities to be discarded. Then, go to step 4.

Step 3: Encode the particles in a completely random way. All the features are encoded with the original way, meaning that the value of p_r is set to 0.5, and each feature has the same probability to be selected. The purpose of this operation is to increase the diversity of populations. Then, go to step 4.

Step 4: Check whether the number of particles is enough. If yes, stop the particle encoding process, otherwise, back to step 1.

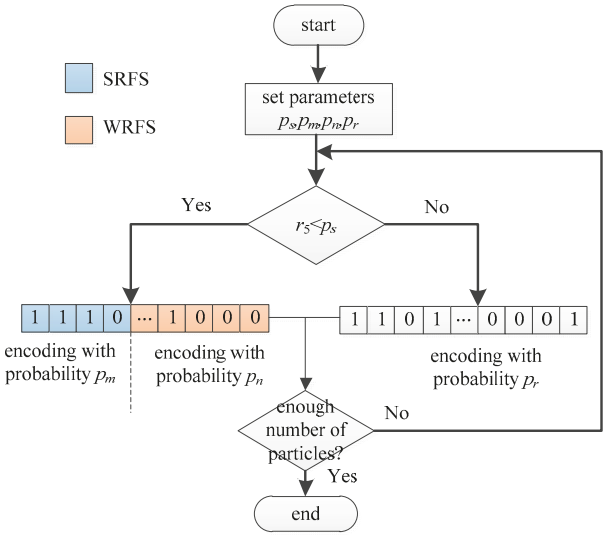

Figure 2. Flowchart of the new particle encoding strategy.

2.4. Geometric Mean (Gmean)-Based Fitness Function

For TSSP feature selection, classification performance and feature number are two inevitable aspects which should be taken into consideration in fitness function. In the existing research, the overall classification accuracy (OCA) is always utilized as the index of classification performance. However, since power systems are scheduled to operate under stable conditions most of the time, the sample numbers of stable class and unstable class are usually highly imbalanced [13]. In this situation, the OCA tends to obscure the classification performance of the unstable class with a small sample number, which does not meet the actual operational requirements of the power system. Therefore, it is not suitable to use the OCA as the classification performance index for TSSP feature selection.

In general, the classification performance of TSSP can be represented by a confusion matrix, which is shown below.

In Table 1, *TS* represents the sample number of stable classes classified as stable class, *TU* represents the sample number of unstable classes classified as unstable class, *FU* represents the sample number of stable classes misclassified as unstable class, and *FS* represents the sample number of unstable classes misclassified as stable class.

Table 1. Confusion Matrix.

Real Status	Predicted Status	
	Stable	**Unstable**
stable	*TS*	*FU*
unstable	*FS*	*TU*

The true stable class rate (TSR) represents the proportion of the sample number of stable classes truly classified as stable class in the total number of stable classes, as shown below:

$$TSR = \frac{TS}{TS + FU} \tag{13}$$

The true unstable class rate (TUR) indicates the proportion of the sample number of unstable classes truly classified as unstable class in the total number of unstable classes, as shown below:

$$TUR = \frac{TU}{TU + FS} \tag{14}$$

To cope with the class-imbalance problem of TSSP, the geometric mean (Gmean) [22,23] of TSR and TUR is employed as the overall performance of classification model in lieu of conventional classification accuracy, which can be expressed as:

$$Gmean = \sqrt{TSR \times TUR} \tag{15}$$

It can be seen from the above formula that the larger the Gmean is, the better the classification performance will be. When both TSR and TUR are 1, Gmean is 1.

In order to further illustrate that Gmean is more suitable for evaluating classification model performance than the traditional accuracy for TSSP, comparison of these two indexes are done below.

The formula of OCA can be expressed as below:

$$OCA = \frac{TS + TU}{N} = \frac{N_s}{N} \times TSR + \frac{N_u}{N} \times TUR \tag{16}$$

where N_s, N_u, and N are the sample number of stable class, the sample number of unstable class and total sample number, respectively.

The OCA index can be considered as the linear weighting of TSR and TUR, and the weight factor is related to the sample number of stable class and unstable class. Assuming that the sample number ratio of stable class and unstable class is 9:1, the comparison of OCA and Gmean is shown in Figure 3.

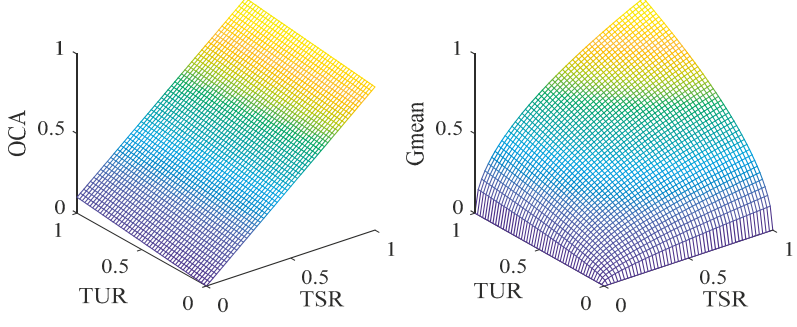

Figure 3. Comparison of overall classification accuracy (OCA) and geometric mean (Gmean).

It can be seen from the Figure 3 that OCA is biased toward stable class classification performance, which has more samples, and Gmean is not biased towards the classification performance of stable class and unstable class since it is independent of the sample number. Specifically, when TUR is 0 and TSR is 1, OCA is about 90%, but Gmean is 0. Therefore, Gmean is more suitable for evaluating TSSP classification performance than OCA.

Considering both the TSSP classification performance and the number of features, the Gmean-based fitness function is defined below:

$$\uparrow Fitness = Gmean - \lambda \frac{N_C}{N_F} \tag{17}$$

where N_C is the number of selected features and N_F is the total number of features. λ is the weight factor to balance these two terms, which is very small to ensure that the classification performance is more important than feature subset length.

3. Data Preparation

3.1. Initial Feature Set

The initial feature set considers the electrical variables closely related to the power system transient stability characteristics, including power flow characteristics before fault occurrence and generator response characteristics after fault occurrence. The former contains load level, generator active power output, and bus voltage level, and the latter includes imbalanced active power, rotor angle, angular velocity, angular acceleration, and kinetic energy [24–26].

In addition, from the aspects of system-level and single-machine level, the initial feature set is going to describe the overall and the partial transient characteristics of the power system. Among them, the system-level features are the statistical values of electrical variables, including extreme value difference, mean absolute value and variance value. The single-machine level features are the electrical variables of each generator. The constructed initial feature set is shown in Table 2. It is worth noting that the rotor angle, angular velocity, and angular acceleration in the feature set are converted to the values relative to the center of inertia.

Table 2. Initial feature set.

Feature Type	t	Number	Feature Description
System level features	t_0	F_1	system load level
		F_2	mean value of generator active power
		F_3	mean value of bus voltage magnitude
	t_f	$F_4 - F_6$	extreme value difference, mean absolute and variance of generator acceleration
		F_7	rotor angle difference of generators with max and min rotor angular acceleration
		$F_8 - F_{10}$	extreme value difference, mean absolute and variance of imbalanced active power
	t_c	$F_{11} - F_{13}$	Inertia center reference of rotor angle, angular velocity, and angular acceleration
		$F_{14} - F_{25}$	extreme value difference, mean absolute, variance of generator rotor angle, angular velocity, angular acceleration and kinetic energy, respectively
		$F_{26} - F_{27}$	rotor angle difference and angular velocity difference of generators with max and min kinetic energy
		$F_{28} - F_{29}$	rotor angle difference and angular velocity difference of generators with max and min angular acceleration
		F_{30}	total energy adjustment of the system
Single-machine level features	t_f	$F_{31} - F_{30} + n_g$	imbalanced active power of each generator
	t_c	$F_{31} + n_g - F_{30} + 2n_g$	rotor angle difference between t_c and t_f of each generator
		$F_{31} + 2n_g - F_{30} + 3n_g$	angular velocity of each generator
		$F_{31} + 3n_g - F_{30} + 4n_g$	angular acceleration of each generator
		$F_{31} + 4n_g - F_{30} + 5n_g$	kinetic energy of each generator

In Table 2, t_0, t_f, and t_c indicate before fault occurrence time, fault occurrence time, and fault clearing time, respectively. The initial feature set contains 30-dimensional system level features and $5n_g$-dimensional single-machine level features, where n_g is the number of generators. The total feature dimension is related to the number of system generators, which means that the size of the power grid directly affects the number of feature dimensions, and the larger the number of generators is, the higher the total feature dimension will be.

3.2. Database Generation

In order to generate a typical and statistical database, large numbers of power system operating conditions (OCs) should be generated by adding random disturbances on the basic power flow [6,27]. The active power and reactive power of load buses are varied randomly within ±20% of the basic value, as shown below:

$$P_{Li} = P_{Li0}[1 + \Delta P_L(1 - 2r_6)] \tag{18}$$

$$Q_{Li} = Q_{Li0}[1 + \Delta Q_L(1 - 2r_7)] \tag{19}$$

where P_{Li} and Q_{Li} are generated active power and reactive power of load i, respectively. P_{Li0} and Q_{Li0} are basic value of active power and reactive power of load i, respectively. ΔP_L and ΔQ_L are both set at 20%.

Without considering slack bus, the active power and terminal voltage of generator buses are varied randomly within ±20% and ±2% of the basic value, respectively.

$$P_{Gi} = P_{Gi0}[1 + \Delta P_G(1 - 2r_8)] \tag{20}$$

$$V_{Gi} = V_{Gi0}[1 + \Delta V_G(1 - 2r_9)] \tag{21}$$

where P_{Gi} and V_{Gi} are generated active power and terminal voltage of generator i, respectively. P_{Gi0} and V_{Gi0} are the basic value of active power and terminal voltage of generator i, respectively. ΔP_G is 20% and ΔV_G is 2%. r_6-r_9 are all random numbers uniformly distributed between [0, 1].

In order to ensure the convergence and availability of randomly generated OC, power flow results needed to be checked. If the power flow converges and all electrical variables are within the normal range, the OC is retained, otherwise it is discarded.

Fault conditions should be provided before time domain simulation. In this paper, the fault type is considered as three-phase permanent short-circuit, and fault duration time is set to 0.12 s. The end of one transmission line is randomly selected as the fault location. Time domain simulation is executed with the available OC and the fault condition, and power flow results and generator response curves are collected to construct the initial feature set. The stability status is determined by the following index:

$$\sigma = \frac{360^\circ - \Delta\delta_{\max}}{360^\circ + \Delta\delta_{\max}} \tag{22}$$

where $\Delta\delta_{\max}$ is the maximum rotor angle deviation at the end of simulation time. If $\sigma < 0$, the system is deemed transiently unstable, and the class label is set at 1, otherwise, the system remains stable and the class label is set at 0. The features and corresponding class labels are utilized to form a sample.

The above process is repeated until a predefined number of samples are generated.

4. Proposed Two-Stage Feature Selection Method

In this section, two-stage feature selection method for the TSSP problem is proposed, which is described briefly below.

The collected data is normalized and randomly divided into training set and testing set. The training set is employed for feature selection and the testing set is utilized to check the quality of the selected feature subset.

In the first stage, the NMI value is calculated with the training set and utilized for measuring the relevance between features and classes, and the features are ranked from large to small based on the NMI values. Then, the classification performance of the ranked features is calculated by using the KNN model to determine the SRFS and WRFS.

In the second stage, the population of BPSO is initialized with the new particle encoding strategy, and the improved fitness value of the particle is calculated with KNN. The values of individual best position and global best position are updated, and the velocity and binary position of particles are updated. The above process is repeated until the terminal condition is met.

After finishing the feature selection process, the classification performance of the selected feature subset is calculated on the testing set.

The flowchart of the proposed two-stage feature selection method is depicted in Figure 4.

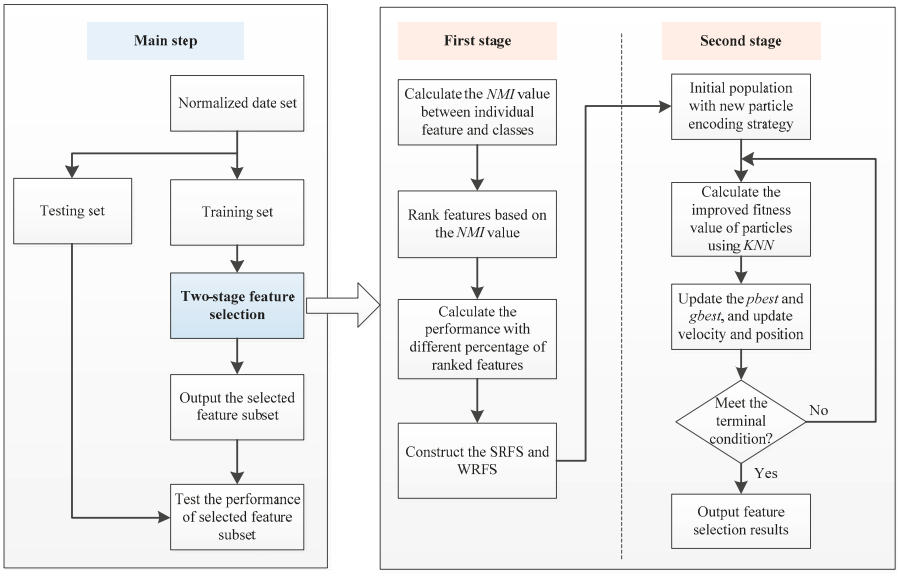

Figure 4. Flowchart of the proposed feature selection method.

5. Case Study

5.1. Basic Description

The proposed methodology is examined on the NPCC 140-bus system including 48 generators and 140 buses, which represents the backbone transmission of the Northeast region of the U.S. Eastern Interconnection power grid [28]. In addition, since the number of generators in this power system is 48, the dimension of the initial feature set is 270. To examine the proposed model on the test system, 8000 samples are generated by time-domain simulations utilizing the scheme in Section 3.2. Randomly, 70% of total samples are selected as the training set, and the remaining 30% are the testing set. Furthermore, 25% of the training set is randomly allocated as the validation set. The detailed description of sample sets is tabulated in Table 3.

Table 3. Training set and testing set.

Dataset	Total Number of Samples	Number of Stable Samples	Number of Unstable Samples
Training set	5600	4625	975
Testing set	2400	1961	439

It can be observed from Table 3 that the sample number ratio of unstable class and stable class is about 1:5, showing apparent imbalanced characteristics between classes.

5.2. Parameter Setting

5.2.1. Construction of Strongly Relevant Feature Subset (SRFS) and Weakly Relevant Feature Subset (WRFS)

The individual feature ranking results based on the NMI values are shown in Figure 5a. Furthermore, different percentages of top-ranked features are respectively selected as the input features of KNN. The classification performance of these feature subsets with the training data is presented in Figure 5b.

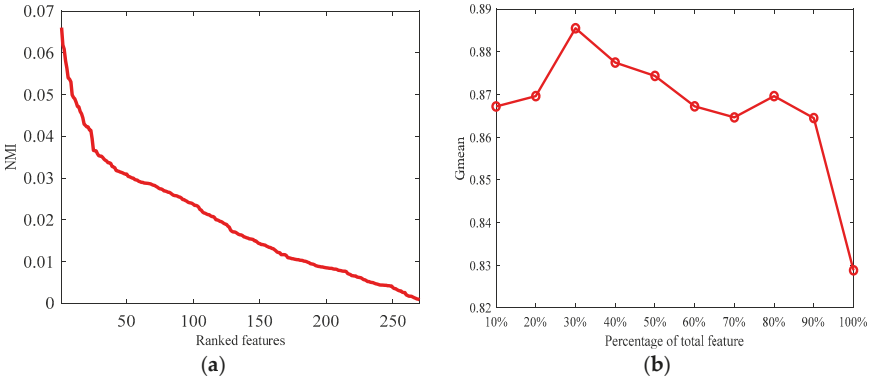

Figure 5. Feature selection results in the first stage: (**a**) Ranked features results; (**b**) Performances with different percentages of total feature.

It can be observed that the best Gmean value can be achieved when the top 30% of ranked features are input features. Therefore, in this study, the top 30% of ranked features are selected as SRFS, and the remaining features are recognized as WRFS.

5.2.2. Other Parameters

The main BPSO parameters utilized in the second stage are given in Table 4.

Table 4. Parameter settings in the proposed method.

Parameters	Settings
Population size	30
Maximum iterations	100
$\omega_{\max}$, $\omega_{\min}$	0.9, 0.4
c_1, c_2	2, 2
λ	0.002

KNN with $k = 1$ [29,30] is employed as the classification model to evaluate the performance of the feature subset. In addition, considering the randomness of the proposed method, ten trials of repeated experiments on the same training and testing set are conducted to obtain the representative results.

In addition, in order to determine the value of p_m, the performance with different p_m values, including {0.6, 0.7, 0.8, 0.9, 1}, is evaluated on the training set. The results are shown in Table 5.

Table 5. Performance with different p_m values.

p_m	Gmean (%)	Number of Selected Features
0.6	91.94	120.7
0.7	91.95	115
0.8	92.09	105.6
0.9	**92.25**	**93.6**
1	92.11	93.8

It can be seen from Table 5 that when p_m value is set to 0.9, the best performance is achieved, and p_n value is equal to 0.1.

5.3. Comparison of Different Particle Encoding Strategies

Under different particle encoding strategies, the best and average convergence curves on the training set are compared, respectively, as depicted in Figure 6.

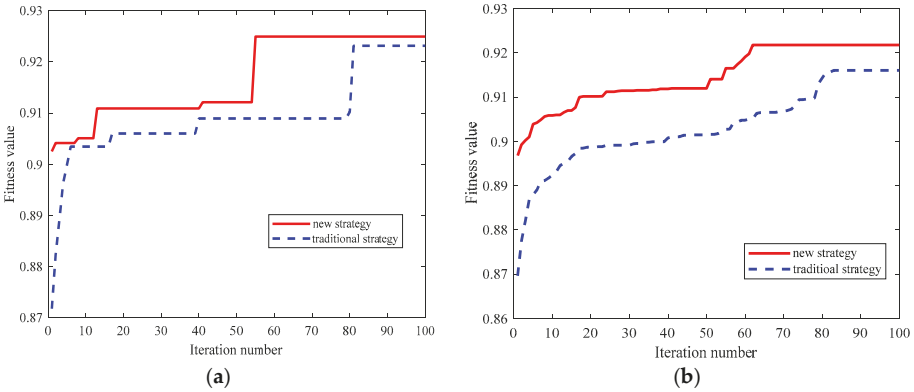

Figure 6. Comparison of convergence curves. (**a**) Best convergence curves; (**b**) Average convergence curves.

From Figure 6, compared with the traditional completely random particle encoding strategy, the new particle encoding strategy that considers the prior knowledge has better initial solution and convergence characteristics.

Under different strategies, the best and average classification results on the testing set are compared, respectively, as presented in Table 6.

Table 6. Comparison of the results of different particle encoding strategies.

Performance Index	Best Results		Average Results	
	Traditional Strategy	New Strategy	Traditional Strategy	New Strategy
TSR (%)	96.43	**96.58**	96.25	**96.56**
TUR (%)	77.45	**83.14**	76.56	**82.30**
Gmean (%)	86.94	**89.61**	85.84	**89.15**
Number of selected features	133	**87**	129.9	**93.6**

In Table 6, the classification performance of the new strategy is superior to the traditional strategy, both in best results and average results. At the same time, the number of selected features of the new strategy is less than that of the traditional strategy. The results illustrate that the new particle encoding strategy proposed in this paper is more effective than the traditional strategy.

5.4. Comparison of Different Fitness Functions

To verify the effectiveness of the improved fitness function, the average results of the OCA-based fitness function and Gmean-based fitness functions are compared on the training set and the testing set, as shown in Table 7.

Table 7. Comparison of the average results of different fitness functions.

Performance Index	Training Set		Testing Set	
	OCA-Based Fitness Function	**Gmean-Based Fitness Function**	**OCA-Based Fitness Function**	**Gmean-Based Fitness Function**
TSR (%)	**97.97**	97.05	**0.9673**	0.9656
TUR (%)	85.65	**87.69**	0.8032	**0.8230**
Gmean (%)	91.60	**92.25**	0.8814	**0.8915**

As seen in Table 7, compared with the OCA-based fitness function, the Gmean-based fitness function achieves better performance on TUR and Gmean on the training set and the testing set. It shows that the Gmean-based fitness function is inclined to select the feature subset having stronger recognition ability for the unstable class, which is more suitable for actual power system TSSP problem.

5.5. Comparison with Other Feature Selection Methods

In this section, some state-of-the-art feature selection methods, including Fisher Score, Relief, NMI, and BPSO, are employed with the same database. The average results comparison of these methods are presented in Table 8.

Table 8. Comparison of the results of different feature selections.

Methods	TSR (%)	TUR (%)	Gmean (%)
All features	96.48	74.03	84.51
Fisher Score	**96.74**	79.27	87.57
Relief	96.63	73.58	84.32
NMI	96.33	79.50	87.91
BPSO	96.25	76.56	85.84
Proposed method	96.56	**82.30**	**89.15**

As seen in Table 8, compared with other feature selection methods, the proposed two-stage method achieves significantly better performance results in terms of TUR and Gmean, and similar results in TSR, which indicates that the proposed method is a better solution for TSSP feature selection.

The running time of different feature selection methods are compared in Table 9. The experiments are performed in a MATLAB (R2017b) environment, running on a personal computer with an Intel core i5-6200 CPU processor with 2.3 GHz and 4 GB memory.

Table 9. Running time comparison.

Methods	Running Time (s)
Fisher Score	0.05
Relief	70.24
NMI	0.95
BPSO	1501.71
Proposed method	1514.92

As seen in Table 9, since Fisher Score, Relief, and NMI belong to the filter method, they are computationally efficient. BPSO belongs to the wrapper method, and it needs longer running time

than the filter methods. The proposed method belongs to the hybrid method combining the filter method and the wrapper method, therefore, its running time is almost the same as that of BPSO.

It is worth noting that the feature selection process of TSSP is done offline, so the relatively larger running time is acceptable. In addition, other techniques, such as parallel computation, can be employed to reduce the running time of the proposed method.

6. Conclusions

This paper proposed a new two-stage feature selection algorithm for TSSP. In the first stage, all the features are divided into SRFS and WRFS based on the NMI values, and in the second stage, a new particle encoding strategy considering both population diversity and prior knowledge is presented. Additionally, considering the imbalanced characteristics of TSSP, an improved fitness function is utilized. The following conclusions can be made from experimental results: (1) compared with the traditional completely random particle encoding method, the proposed particle encoding method can obtain better feature selection results, (2) compared with the OCA-based fitness function, the proposed Gmean-based fitness function tends to select the feature subset having stronger recognition ability for unstable class, and (3) compared with some state-of-the-art feature selection methods, the proposed two-stage feature selection achieves significantly better performance results in terms of TUR and Gmean, and similar results in TSR, which shows that the proposed feature selection method is more suitable for actual power system TSSP problem.

Future work will focus on the improvement of classification model to better handle the imbalanced characteristics of power system TSSP problem.

Author Contributions: Z.C. and X.H. developed the idea of this research and performed simulation verification; C.F. collected and processed the data; Z.C. and T.Z. wrote this paper; S.M. checked and polished this paper.

Funding: This research received no external funding.

Conflicts of Interest: The authors declare no conflict of interest.

References

1. Kundur, P.; Paserba, J.; Ajjarapu, V.; Andersson, G.; Bose, A.; Canizares, C.; Hatziargyriou, N.; Hill, D.; Stankovic, A.; Taylor, C.; et al. Definition and classification of power system stability. *IEEE Trans. Power Syst.* **2004**, *19*, 1387–1401.
2. Edrah, M.; Lo, K.L.; Anaya-Lara, O. Impacts of high penetration of DFIG wind turbines on rotor angle stability of power systems. *IEEE Trans. Sustain. Energy* **2015**, *6*, 759–766. [CrossRef]
3. Kamwa, I.; Samantaray, S.R.; Joos, G. Catastrophe predictors from ensemble decision-tree learning of wide-area severity indices. *IEEE Trans. Smart Grid* **2010**, *1*, 144–158. [CrossRef]
4. Ji, L.Y.; Wu, J.Y.; Zhou, Y.Z.; Hao, L.L. Using trajectory clusters to define the most relevant features for transient stability prediction based on machine learning method. *Energies* **2016**, *9*, 898. [CrossRef]
5. Li, Y.; Yang, Z. Application of EOS-ELM with binary jaya-based feature selection to real-time transient stability assessment using PMU data. *IEEE Access* **2017**, *5*, 23092–23101. [CrossRef]
6. Zhou, Y.Z.; Wu, J.Y.; Ji, L.Y.; Yu, Z.H.; Lin, K.J.; Hao, L.L. Transient stability preventive control of power systems using chaotic particle swarm optimization combined with two-stage support vector machine. *Electr. Power Syst. Res.* **2018**, *155*, 111–120. [CrossRef]
7. Jensen, C.A.; El-Sharkawi, M.A.; Marks, R.J. Power system security assessment using neural networks: Feature selection using fisher discrimination. *IEEE Trans. Power Syst.* **2001**, *16*, 757–763. [CrossRef]
8. Xu, Y.; Dong, Z.Y.; Meng, K.; Zhang, R.; Wong, K.P. Real-time transient stability assessment model using extreme learning machine. *IET Gener. Transm. Distrib.* **2011**, *5*, 314–322. [CrossRef]
9. Amjady, N.; Keynia, F. Day-ahead price forecasting of electricity markets by mutual information technique and cascaded neuro-evolutionary algorithm. *IEEE Trans. Power Syst.* **2009**, *24*, 306–318. [CrossRef]
10. Śmieja, M.; Warszycki, D. Average information content maximization—a new approach for fingerprint hybridization and reduction. *PLoS ONE* **2016**, *11*, e0146666. [CrossRef]

11. Xu, Y.; Dong, Z.Y.; Zhao, J.H.; Zhang, P.; Wong, K.P. A reliable intelligent system for real-time dynamic security assessment of power systems. *IEEE Trans. Power Syst.* **2012**, *27*, 1253–1263. [CrossRef]
12. Li, B.Y.; Xiao, J.M.; Wang, X.H. Feature reduction for power system transient stability assessment based on neighborhood rough set and discernibility matrix. *Energies* **2018**, *11*, 185. [CrossRef]
13. Moulin, L.S.; Alves da Silva, A.; El-Sharkawi, M.A.; Marks, R.J. Support vector machines for transient stability analysis of large-scale power systems. *IEEE Trans. Power Syst.* **2004**, *19*, 818–825. [CrossRef]
14. Zhang, Y.D.; Wang, S.H.; Phillips, P.; Ji, G.L. Binary PSO with mutation operator for feature selection using decision tree applied to spam detection. *Knowl. Based Syst.* **2014**, *64*, 22–31. [CrossRef]
15. Xue, B.; Zhang, M.J.; Browne, W.N.; Yao, X. A survey on evolutionary computation approaches to feature selection. *IEEE Trans. Evol. Comput.* **2016**, *20*, 606–626. [CrossRef]
16. Battiti, R. Using mutual information for selecting features in supervised neural net learning. *IEEE Trans. Neural Net.* **1994**, *5*, 537–550. [CrossRef] [PubMed]
17. Yao, Y.Y.; Wong, S.K.M.; Butz, C.J. On information-theoretic measures of attribute importance. In Proceedings of the Third Pacific-Asia Conference on Knowledge Discovery and Data Mining, Beijing, China, 26–28 April 1999.
18. Kennedy, J.; Eberhart, R.C. A discrete binary version of the particle swarm algorithm. In Proceedings of the IEEE International Conference on System, Man, and Cybernetics, Orlando, FL, USA, 12–15 October 1997.
19. Moradi, P.; Gholampour, M. A hybrid particle swarm optimization for feature subset selection by integrating a novel local search strategy. *Appl. Soft Comput.* **2016**, *43*, 117–130. [CrossRef]
20. Mirjalili, S.; Lewis, A. S-shaped versus V-shaped transfer functions for binary particle swarm optimization. *Swarm Evol. Comput.* **2013**, *9*, 1–14. [CrossRef]
21. Rahman, N.H.A.; Zobaa, A.F. Integrated mutation strategy with modified binary PSO algorithm for optimal PMUs placement. *IEEE Trans. Ind. Inform.* **2017**, *13*, 3124–3133. [CrossRef]
22. Chen, Z.; Xiao, X.Y.; Li, C.S.; Zhang, Y.; Hu, Q.Q. Real-time transient stability status prediction using cost-sensitive extreme learning machine. *Neural Comput. Appl.* **2017**, *27*, 321–331. [CrossRef]
23. He, H.B.; Garcia, E.A. Learning from imbalanced data. *IEEE Trans. Knowl. Data Eng.* **2009**, *21*, 1263–1284.
24. Zhou, Y.Z.; Wu, J.Y.; Yu, Z.H.; Ji, L.Y.; Hao, L.L. A hierarchical method for transient stability prediction of power systems using the confidence of a SVM-based ensemble classifier. *Energies* **2016**, *9*, 778. [CrossRef]
25. Wang, B.; Fang, B.W.; Wang, Y.J.; Liu, H.S.; Liu, Y.L. Power system transient stability assessment based on big data and the core vector machine. *IEEE Trans. Smart Grid* **2016**, *7*, 2561–2570. [CrossRef]
26. Gu, X.P.; Li, Y.; Jia, J.H. Feature selection for transient stability assessment based on kernelized fuzzy rough sets and memetic algorithm. *Int. J. Electr. Power Energy Syst.* **2015**, *64*, 664–670. [CrossRef]
27. Geeganage, J.; Annakkage, U.D.; Weekes, T.; Archer, B.A. Application of energy-based power system features for dynamic security assessment. *IEEE Trans. Power Syst.* **2015**, *30*, 1957–1965. [CrossRef]
28. Ju, W.Y.; Qi, J.J.; Sun, K. Simulation and analysis of cascading failures on an NPCC power system test bed. In Proceedings of the 2015 IEEE PES General Meeting, Denver, CO, USA, 26–30 July 2015.
29. Tran, B.; Xue, B.; Zhang, M.J. A new representation in PSO for discretisation-based feature selection. *IEEE Trans. Cybern.* **2018**, *48*, 1733–1746. [CrossRef] [PubMed]
30. Oh, I.S.; Lee, J.S.; Moon, B.R. Hybrid genetic algorithms for feature selection. *IEEE Trans. Pattern Anal. Mach. Intell.* **2004**, *11*, 1424–1437.

energies

MDPI

Article

Quadrature Current Compensation in Non-Sinusoidal Circuits Using Geometric Algebra and Evolutionary Algorithms

Francisco G. Montoya *, Alfredo Alcayde, Francisco M. Arrabal-Campos and Raul Baños

Department of Engineering, University of Almeria, 04120 Almeria, Spain; aalcayde@ual.es (A.A.); fmarrabal@ual.es (F.M.A.-C.); rbanos@ual.es (R.B.)

* Correspondence: pagilm@ual.es; Tel.: +34-950-214-501

Received: 10 January 2019; Accepted: 18 February 2019; Published: 21 February 2019

Abstract: Non-linear loads in circuits cause the appearance of harmonic disturbances both in voltage and current. In order to minimize the effects of these disturbances and, therefore, to control the flow of electricity between the source and the load, passive or active filters are often used. Nevertheless, determining the type of filter and the characteristics of their elements is not a trivial task. In fact, the development of algorithms for calculating the parameters of filters is still an open question. This paper analyzes the use of genetic algorithms to maximize the power factor compensation in non-sinusoidal circuits using passive filters, while concepts of geometric algebra theory are used to represent the flow of power in the circuits. According to the results obtained in different case studies, it can be concluded that the genetic algorithm obtains high quality solutions that could be generalized to similar problems of any dimension.

Keywords: power factor compensation; non-sinusoidal circuits; geometric algebra; evolutionary algorithms

1. Introduction

The introduction of distributed generation and microgrids in power networks allow an efficient energy management and integration with renewable energy sources [1]. However, these grids include an increasing number of power electronic devices and non-linear electronic loads, such as power inverters, cycloconverters, speed drives, batteries, household appliances, among others. These non-linear loads increase the harmonic disturbances both in voltage and current, causing detrimental effects to the supply system and user equipment [2]. In consequence, these grids are seriously affected by events that degrade the power quality [3], and provoke excessive heating, protection faults, and inefficiencies in the transmission of energy [4], hence it becomes a critical task to determine precisely the electrical energy balances on the microgrid.

Different authors have presented models and theories in the past [5–7], but while all of them coincide in the study of the sinusoidal case, there is some controversy in the analysis of non-sinusoidal systems with a high harmonic content, such as modern microgrids. In particular, well-known theories, such as those proposed by Budeanu [8] and Fryze [9], have been questioned by different authors after demonstrating inconsistency and errors [10–12]. Therefore, it is important to investigate how to improve the compensation of the power factor in non-sinusoidal systems in the presence of harmonics. Some investigations have highlighted that algorithms for calculating the parameters of filters have rarely been discussed [13], although in recent years some authors have applied computational optimization methods, including meta-heuristic approaches, for optimizing filter parameters in circuits having harmonic distortion [2,14–16]. More specifically, genetic algorithms have been successfully applied in [17–19].

In this paper, an evolutionary algorithm is used to optimize the type and characteristics of passive filters for power factor compensation. The rest of the paper is organized as follows: Section 2 introduces some basic ideas about geometric algebra and its application to power systems. Section 3 describes the problem at hand and the genetic algorithm used as solution method. Section 4 presents the empirical study, while the main conclusions obtained are detailed in Section 5.

2. Geometric Algebra and Power Systems

Traditionally, electrical engineers have been taught to solve sinusoidal electrical circuits using complex number algebra, exactly as Steinmetz theory [20] introduced in the 19th century. It stated that differential equations in time domain can be transformed into algebra equations in complex domain. Under these assumptions, the apparent power can be expressed as:

$$\vec{S} = \vec{U}\vec{I}^{*} = P + jQ \tag{1}$$

where P is the active power, Q is the reactive power, and j is unit imaginary number.

The limitations of the algebra of complex numbers and the impossibility to apply the principle of conservation of energy to the apparent power quantity [21] have caused some researchers to propose alternative circuit analysis techniques, including those based on geometric algebra [22].

2.1. Basic Definitions of Geometric Algebra

Geometric algebra has its origins in the work of Clifford and Grassman in the 19th century and is considered as a unified language for mathematics and physics. It is based on the notion of an invertible product of vectors that captures the geometric relationship between two vectors, i.e., their relative magnitudes and the angle between them [23]. Some investigations have defined the properties of geometric algebra [24,25] applied to physics and engineering. Traditional concepts such as vector, spinor, complex numbers, or quaternions are naturally explained as members of subspaces in geometric algebra. It can be easily extended in any number of dimensions, this being one of its main strengths. Because these are geometrical objects, they all have direction, sense, and magnitude. The basics of GA properties are based on well established definitions around vectors. For example, a vector $\boldsymbol{a} = \alpha_1 \boldsymbol{e_1} + \alpha_2 \boldsymbol{e_2}$ (a segment with direction and sense) can be multiplied by a vector $\boldsymbol{b} = \beta_1 \boldsymbol{e_1} + \beta_2 \boldsymbol{e_2}$ in different ways, so the result has different meanings. In (2), the inner product is defined and the result is a scalar.

$$\boldsymbol{a} \cdot \boldsymbol{b} = \|\boldsymbol{a}\| \|\boldsymbol{b}\| \cos\varphi = \sum \alpha_i \beta_i \tag{2}$$

In (3) a new product is defined, the wedge product. The main difference with its cousin the outer product (see Figure 1) is that the result is neither a scalar nor a vector, but a new quantity called **bivector**.

$$\boldsymbol{a} \wedge \boldsymbol{b} = \|\boldsymbol{a}\| \|\boldsymbol{b}\| \sin\varphi \, \boldsymbol{e_1 e_2} \tag{3}$$

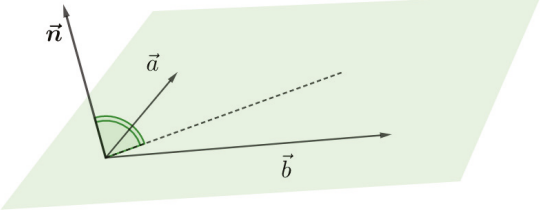

Figure 1. Outer product of vectors $\boldsymbol{a}$ and $\boldsymbol{b}$. The result is a vector $\boldsymbol{n}$, perpendicular to the plane formed by $\boldsymbol{a}$ and $\boldsymbol{b}$.

A bivector is known to have direction, sense and magnitude in the same way a vector has. It defines an area enclosed by the parallelogram formed by both vectors (see Figure 2). This product complies with the anti-commutative property, i.e., $\boldsymbol{a} \wedge \boldsymbol{b} = -\boldsymbol{b} \wedge \boldsymbol{a}$. A bivector is a key concept in geometrical algebra and cannot be found in linear algebra or vector calculus. The outer product of two vectors produces a new entity in a plane that can be operated like vectors, i.e., addition, product, or even inverse. Like vectors, a bivector can be written as the linear combination of a base of bivectors.

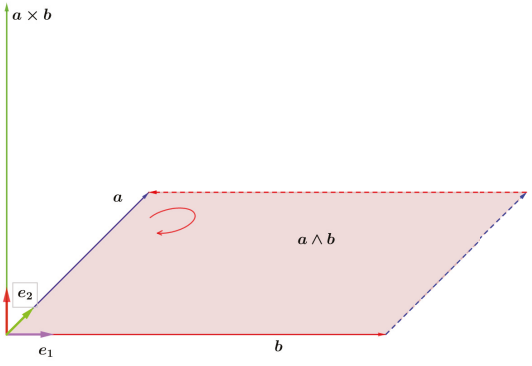

Figure 2. Representation of a bivector $\boldsymbol{a} \wedge \boldsymbol{b}$.

Finally, the third product between vectors is defined in (4) as the **geometric product** and can be described as one of the major contributions in geometric algebra. Not only can vectors be multiplied geometrically, but bivectors and other entities, in general, can be used.

$$\boldsymbol{ab} = \boldsymbol{a} \cdot \boldsymbol{b} + \boldsymbol{a} \wedge \boldsymbol{b} \tag{4}$$

The result is a linear combination of the inner product and the wedge product. Equation (4) can be expanded to further find out new insights.

$$\boldsymbol{A} = \boldsymbol{ab} = \langle \boldsymbol{A} \rangle_0 + \langle \boldsymbol{A} \rangle_2 = (\alpha_1\beta_1 + \alpha_2\beta_2) + (\alpha_1\beta_2 - \alpha_2\beta_1)\boldsymbol{e_1 e_2} \tag{5}$$

where $\langle \boldsymbol{A} \rangle_0$ is the scalar part and $\langle \boldsymbol{A} \rangle_2$ is the bivector part.

2.2. Application of Geometric Algebra to Power Systems

Recently, several researches have proven that geometric algebra or Clifford algebra is a powerful and flexible tool for representing the flow of energy or power in electrical systems [22,26]. Some authors have motivated the use of power theory based on geometric algebra as Physics' unifying language, such that electrical magnitudes can be interpreted as Clifford multivectors [27]. More specifically, Clifford algebra is a valid mathematical tool to address the multicomponent nature of power in non-sinusoidal contexts [28–30] and has been used for analysis of harmonics [31].

The concept of non-active, reactive, or distorted power acquires a meaning that is more in line with its mathematical significance, making it possible to better understand energy balances and to verify the principle of energy conservation. Nevertheless, some authors have highlighted that the verification of the energy conservation law is only possible in sinusoidal situations [32]. To overcome these drawbacks, these authors proposed a new circuit analysis approach using geometric algebra to develop the most general proof of energy conservation in industrial building loads, with capability of calculating the voltage, current, and net apparent power in electrical systems in non-sinusoidal situations.

Different authors have proposed definitions to represent non-active power for distorted currents and voltages in electrical systems, although no single representation has been universally accepted.

For example, in [33] a non-active power multivector from the most advanced multivectorial power theory based on the geometric algebra with the aim of analyzing the compensation of disturbing loads is presented, including the harmonic load compensation, identification, and metering between other applications. Other researches have shown that geometric algebra can be applied to analyze the apparent power defined in a poly-phase system having transmission lines with frequency-dependency under non-sinusoidal conditions [34].

Geometric Apparent Power

As several authors have shown, the use of apparent power loses its meaning under non-sinusoidal conditions, involving erroneous calculation of energy flows between the load and source. In contrast, [35] proposes the use of a new term called net apparent power or geometric apparent power $\boldsymbol{M}$. This concept is the result of the geometric product of voltage and current in $\mathcal{G}_{\mathcal{N}}$ domain (6).

$$\boldsymbol{M} = \boldsymbol{ui} = \boldsymbol{u} \cdot \boldsymbol{i} + \boldsymbol{u} \wedge \boldsymbol{i} \tag{6}$$

which results in a scalar and a bivector when the voltage and current are sinusoids

$$\boldsymbol{M} = \langle \boldsymbol{M} \rangle_0 + \langle \boldsymbol{M} \rangle_2 \tag{7}$$

It can be easily shown from (1) and (7) that

$$\begin{aligned} P &= \langle \boldsymbol{M} \rangle_0 \\ Q &= \| \langle \boldsymbol{M} \rangle_2 \| \end{aligned} \tag{8}$$

so $\langle \boldsymbol{M} \rangle_0$ is the active power derived from the scalar part and $\| \langle \boldsymbol{M} \rangle_2 \|$ is the reactive power derived from the bivector part of the net apparent power multivector.

For the non-sinusoidal case, i.e., when harmonics are present in the voltage and/or current, the apparent power loses its validity and only $\boldsymbol{M}$ can reflect the exact flow of energy in the circuit. Consider a general voltage waveform $u(t)$

$$u(t) = \sum_{i=1}^{n} u_i(t) = \alpha_1 \cos(\omega t) + \beta_1 \sin(\omega t) + \sum_{h=2}^{l} \alpha_h \cos(h\omega t) + \sum_{h=2}^{k} \beta_h \sin(h\omega t) \tag{9}$$

that we can transfer to the geometric domain using [35]

$$\begin{aligned} \varphi_{c1}(t) &= \sqrt{2} \cos \omega t \quad \longleftrightarrow \quad \boldsymbol{e_1} \\ \varphi_{s1}(t) &= \sqrt{2} \sin \omega t \quad \longleftrightarrow \quad -\boldsymbol{e_2} \\ \varphi_{c2}(t) &= \sqrt{2} \cos 2\omega t \quad \longleftrightarrow \quad \boldsymbol{e_2 e_3} \\ \varphi_{s2}(t) &= \sqrt{2} \sin 2\omega t \quad \longleftrightarrow \quad \boldsymbol{e_1 e_3} \\ &\vdots \\ \varphi_{cn}(t) &= \sqrt{2} \cos n\omega t \quad \longleftrightarrow \quad \bigwedge_{i=2}^{n+1} \boldsymbol{e_i} \\ \varphi_{sn}(t) &= \sqrt{2} \sin n\omega t \quad \longleftrightarrow \quad \bigwedge_{\substack{i=1 \\ i \neq 2}}^{n+1} \boldsymbol{e_i} \end{aligned} \tag{10}$$

where $\bigwedge \boldsymbol{e_i}$ represents the product of n vectors and the subscripts c and s denote cosine and sine, respectively. Using (10), any waveform $x(t)$ can be translated to the geometric domain $\mathcal{G}_{\mathcal{N}}$, so the final result for the voltage is

$$\boldsymbol{u} = \alpha_1 \boldsymbol{e_1} - \beta_1 \boldsymbol{e_2} + \sum_{h=2}^{l} \left[\alpha_h \bigwedge_{i=2}^{h+1} \boldsymbol{e_i} \right] + \sum_{h=2}^{k} \left[\beta_h \bigwedge_{i=1, i\neq 2}^{h+1} \boldsymbol{e_i} \right] \tag{11}$$

In (11), the transformation given in [35] has been used and is reproduced here to make this paper more readable. [35] also demonstrates that the admittance of typical passive load is $\boldsymbol{Y_h} = G_h + B_h \boldsymbol{e_1 e_2}$, so the harmonic current associated to h-th voltage harmonic is

$$\boldsymbol{i_h} = (G_h + B_h \boldsymbol{e_1 e_2}) \boldsymbol{u_h} \tag{12}$$

and the total current

$$\boldsymbol{i} = \sum_{h=1}^{n} \boldsymbol{i_h} = \boldsymbol{i_g} + \boldsymbol{i_b} \tag{13}$$

where $\boldsymbol{i_g}$ is the in-phase current where $\boldsymbol{i_b}$ is the quadrature current. The geometric apparent power is then

$$\boldsymbol{M} = \boldsymbol{ui} = \boldsymbol{M_g} + \boldsymbol{M_b} = P + \boldsymbol{CN_d} + \boldsymbol{M_b} \tag{14}$$

where $\boldsymbol{M_g}$ is the *in-phase* geometric apparent power, $\boldsymbol{CN_d}$ is the degraded power (summation of cross-frequency products between voltage and current) and $\boldsymbol{M_b}$ is the quadrature geometric apparent power.

Based on Equations (8) and (14), the power factor in $\mathcal{G}_N$ domain can be defined as

$$pf = \frac{P}{\|\boldsymbol{M}\|} = \frac{\langle M \rangle_0}{\sqrt{\langle M^{\dagger} M \rangle_0}} \tag{15}$$

in contrast to the clasical approach where $\boldsymbol{S}$ is used. As demonstrated by [21], $\boldsymbol{S}$ and $\boldsymbol{M}$ are different concepts for non-sinusoidal scenarios, but reduces to the same in the sinudoidal case. Other power theories like Czarnecki's based their power factor definition on the concept of apparent power $\boldsymbol{S}$, so it leads to different power factor results in non-sinusoidal situations.

3. Problem Description and Solution Strategy

This section describes the proposed problem in this research and details the characteristics of the genetic algorithm used to solve it.

3.1. Problem Description

Power systems operating under harmonic distortion must be optimized to reduce power losses and improve power quality [36,37]. Whether the system is linear or non-linear, it is necessary to provide reactances in parallel with the load in order to reduce these harmonics. The typical design of compensators is based on the knowledge of the susceptances of the system to different frequencies [38], something that is not easy to achieve when you have highly distorted systems. The main objective of non active power compensation is to minimize the source root mean square (RMS) current [5]. However, it is not a trivial task since it involves to determine which type of filter and characteristics of their components is more suitable for compensation purposes in a given circuit. For example, a capacitor with an optimal value connected in parallel to the load is an easy solution but this does not produce the absolute minimum of the distortion power [39], while other alternatives could improve it.

Some studies have highlighted that algorithms for calculating the parameters of filters has not been studied in detail [13], although some authors have implemented optimization algorithms for optimizing the configuration of the filters in circuits having harmonic distortion. For example, in [15] it was proposed a genetic algorithm to minimize current total harmonic distortion using LC passive

harmonic filters. Other recent studies have applied swarm intelligence methods to comparatively evaluate single-tuned, double-tuned, triple-tuned, damped-double tuned, and C-type filters in order to improve the loading capability of a set of transformers under non-sinusoidal conditions [16]. In addition to the use of passive filters, some studies proposed algorithms for estimating the optimal parameters of active and hybrid filters. For example, in [2] it was proposed the use of direct neural intelligent techniques to improve performance of a shunt active filters. In other recent studies, it has been proposed the use of differential evolution (DE) algorithms to optimize the parameters of hybrid filters (combining active and passive filters) in order to minimize harmonic pollution [14]. The problem to be solved involves the determination of the most suitable type of passive filter and its parameters to minimize the source RMS current I_s in order to get the optimal value I_{scp}.

3.2. Solution Approach

Genetic algorithms are optimization methods based on principles of natural selection and genetics [40]. Figure 3 shows the flowchart describing the operation of the genetic algorithm. It consists of a set (population) of solutions, each of which is called individual or phenotype, that evolve to reach solutions of high quality in terms of a fitness function. As an initialization step, a genetic algorithm randomly generates a set of solutions to a problem (a population of genomes). As Figure 4 shows, each individual is represented by a string of real numbers. Specifically, the data structure of each individual consists of three possible values for inductors L (Henry) and three possible values for capacitors C (Farad). All or some of these values will be considered in the optimization process depending on the filter choosed, which will be specified in the FT field (filter type), as described below. The actual values that can be assigned to inductors and capacitors are preset between two limits (upper and lower), so that the search space of the evolutionary algorithm is limited within reasonable margins. After calculating the fitness values for all solutions in a current population, the individuals for mating pool are selected using the operator of reproduction according to a given fitness function defined for the problem to be solved. In our problem the fitness function is

$$min \quad f(L, C) = I_s(L, C) \tag{16}$$

where I_s is the source current calculated according to geometric algebra operations. These selection strategies aim to introduce a certain degree of elitism in the population. These solutions evolve by applying mutation and crossover operators that modify the genotype of the individuals. Offspring solutions substitute some old solutions of the population, and the new generation of individuals repeats the evolution process until a termination criterion is fulfilled (e.g., a maximum number of generations has been reached).

In this paper we have adapted a genetic algorithm solver for mixed-integer or continuous-variable optimization, constrained or unconstrained, included in the MATLAB Global Optimization Toolbox [41]. This toolbox allows to solve smooth or non-smooth optimization problems with constraints using different mutation and crossover operators. The original source code has been adapted to deal with the problem at hand. It also has been adapted to take into account the particularities of the proposed problem through GA. More specifically, an opensource implementation of GA "Clifford multivector toolbox" has been used, available at https://sourceforge.net/projects/clifford-multivector-toolbox/. A preliminary sensitivity analysis has been performed to determine the parameters of the algorithm, such that the values used in our study are: Population size: 100 individuals; crossover rate: 0.8; mutation rate: 0.2; selection criteria: roulette wheel selection; termination criteria: 50 iterations.

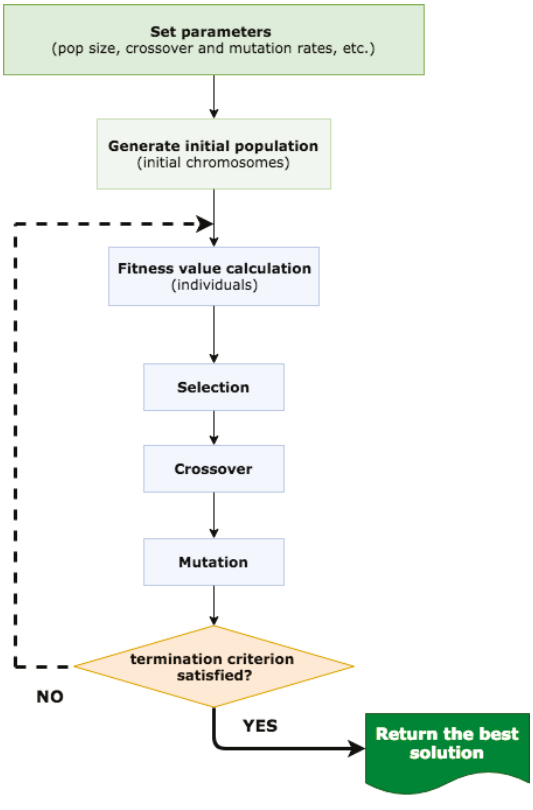

Figure 3. Flowchart of the genetic algorithm.

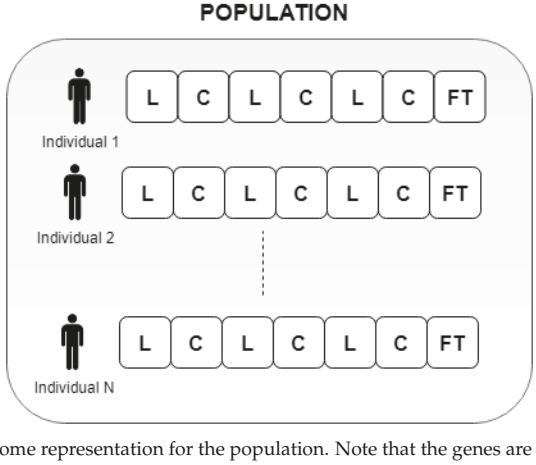

Figure 4. Chromosome representation for the population. Note that the genes are real values for L, C, and integer for FT (Filter Type).

4. Empirical Study

This section presents the results obtained by the genetic algorithm in three different case studies.

4.1. Case Studies

- Czarnecki's case study [39]: this example consists of simple circuit with a harmonic polluted ideal voltage source of normalized frequency $\omega = 1$ rad/s

$$u(t) = 100\sqrt{2}\cos t + 50\sqrt{2}\cos 2t + 30\sqrt{2}\cos 3t \tag{17}$$

with an active power $P = 344.23$ W. Figure 5a shows the circuit load, while Figure 5b shows the solution found by Czarnecki with $L_1 = 5.906$H, $L_2 = 19$H, $C_1 = 0.034$F, and $C_2 = 0.012$F, who compensates the reactive power of the harmonic components by the 1-port X of a precalculated admitance. The method proposed by Czarnecki was able to compensate the source RMS current to 3.10 A from the initial 12.24 A [39].

Using (10), the voltage in $\mathcal{G}_N$ domain can be expressed as

$$\boldsymbol{u} = 100\boldsymbol{e_1} + 50\boldsymbol{e_{23}} + 30\boldsymbol{e_{234}} \tag{18}$$

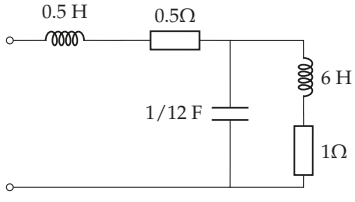

(**a**) Circuit proposed by Czarnecki

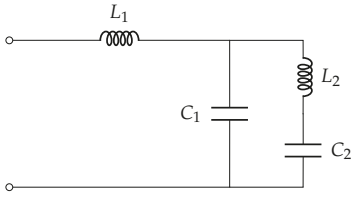

(**b**) Compensator layout

Figure 5. Load and compensator used by Czarnecki in [39].

- Castro-Nuñez and Castro-Puche's case study [26]: this example (already studied by Czarnecki) consists of a circuit with a highly distorted voltage source with fundamental plus 2 harmonics and a linear load, being the voltage

$$u(t) = 100\sqrt{2}\sin t + \frac{100}{11}\sqrt{2}\sin 11t + \frac{100}{13}\sqrt{2}\sin 13t \tag{19}$$

which translates to

$$\boldsymbol{u} = -100\boldsymbol{e_2} + \frac{100}{11}\bigwedge_{i=1,i\neq 2}^{12}\boldsymbol{e_i} + \frac{100}{13}\bigwedge_{i=1,i\neq 2}^{14}\boldsymbol{e_i} \tag{20}$$

where the uncompensated current is 44.72 A. Figure 6a shows the circuit with the distorted voltage source and the linear load, while Figure 6b displays the compensator for this linear load. The compensator design by Castro-Nuñez reduced the source RMS current to 20.10 A [22].

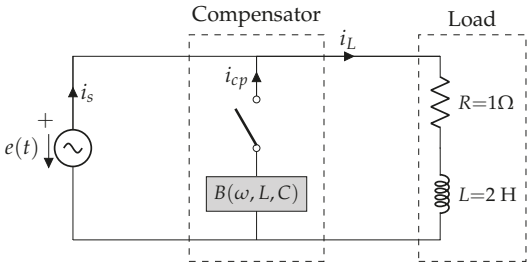

(**a**) Circuit proposed by Castro-Nuñez

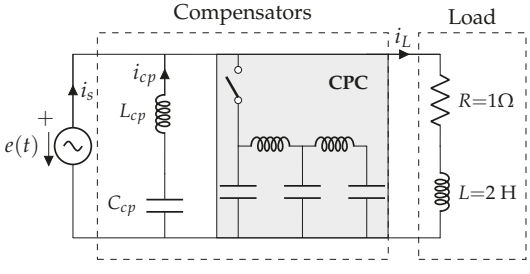

(**b**) Compensators proposed by Castro-Nuñez ($L_{cp}C_{cp}$) and Czarnecki (CPC)

Figure 6. Circuit with distorted voltage source and a linear load used by Castro-Nuñez and Castro-Puche [22].

- Castilla's case study [33]: this example consists of a circuit with a distorted voltage source with three harmonics given by:

$$u(t) = 200\sqrt{2}\cos\omega t + 200\sqrt{2}\cos(3\omega t - 30) + 100\sqrt{2}\cos(5\omega t + 30). \tag{21}$$

which translates to

$$\boldsymbol{u} = 200\boldsymbol{e_2} + 100\sqrt{3}\boldsymbol{e_{234}} + 100\boldsymbol{e_{134}} + 50\sqrt{3}\boldsymbol{e_{23456}} - 50\boldsymbol{e_{13456}} \tag{22}$$

with an uncompensated RMS current of $\|I\| = 4.21$ A. Although the structure of this compensator was not described in the paper published by Castilla [33], this author indicated that it reduced the source RMS current to 3.21 A.

4.2. Filter Optimization

The genetic algorithm has been adapted to manage different types of filters widely used in the literature for compensating purposes and mitigation of current harmonics. Based on Equation (12), the admittance for a general load Y_l and harmonic h, is equal to

$$Y_{l_h} = G_{l_h} + B_{l_h}\boldsymbol{e_1 e_2} = G_{l_h} + B_{l_h}\boldsymbol{e_{12}} \tag{23}$$

If we connect a pure reactive impedance in parallel with the load for current compensation, its admittance Y_{cp_h} will be

$$Y_{cp_h} = B_{cp_h}\boldsymbol{e_{12}} \tag{24}$$

For example, if we choose a simple LC series compensator, we have

$$\begin{aligned} \boldsymbol{Z_h} &= \boldsymbol{X_{L_h}} + \boldsymbol{X_{C_h}} = -hL\omega \boldsymbol{e_{12}} + \frac{1}{h\omega C}\boldsymbol{e_{12}} \\ \boldsymbol{Y_h} &= \frac{1}{\boldsymbol{Z_h}} = \frac{1}{\left(-hL\omega + \frac{1}{h\omega C}\right)\boldsymbol{e_{12}}} = \frac{hwC}{h^2\omega^2 LC - 1}\boldsymbol{e_{12}} \end{aligned} \tag{25}$$

So we need to make equal $B_{cp} = -B_l$ for every harmonic h to fully compensate the quadrature term. For the opmital case, the total current $\boldsymbol{i}$ is reduced to $\boldsymbol{i_g}$ since $\boldsymbol{i_b} + \boldsymbol{i_{cp}}$ is equal to 0 after applying Kirchhoff laws.

Figures 7–12 show the configurations used based on very well-known type of filters:

- C-type filter: it is is mainly used for suppressing the low order of harmonics [13].

Figure 7. C-type filter.

- Series LC-type filter: this filter is also considered to reduce line current harmonics [42].

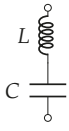

Figure 8. Series LC-type filter.

- Parallel LC-type filter: it provides low impedance shunt branches to the load's harmonic current, which allows to reduce the harmonic current flowing into the line [42].

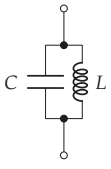

Figure 9. Parallel LC-type filter.

- Triple tuned filter: this type of filter is electrically equivalent to three parallel tuned filters connected in series [43].

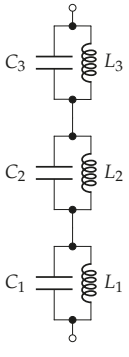

Figure 10. Triple tune filter.

- Foster's filter: this filter combines in parallel single L-type and C-type filters and also parallel LC-type filters.

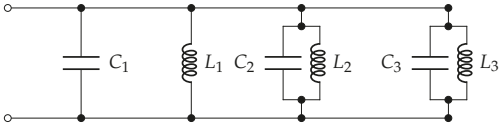

Figure 11. Foster's filter.

- Czarnecki's 4-elements filter: it is a filter that combines two L and two C elements using a series/parallel configuration [39].

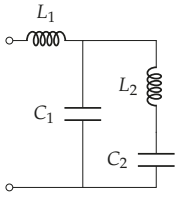

Figure 12. Czarnecki's 4-elements filter.

4.3. Simulation Results

Tables 1–3 show the results obtained by the genetic algorithm in the three case studies described above, being the RMS current through the supply source the objective to be minimized. The best, mean, and standard deviation of 10 independent runs are provided.

Table 1. Compensated root mean square (RMS) current (I_{scp}) obtained by the genetic algorithm in Czarnecki's case study [39].

	Type of Filter					
	C	**Series LC**	**Parallel LC**	**Triple Tune**	**Foster**	**Czarnecki 4**
Best (A)	12.2409	7.5015	12.7235	3.0954	**3.0948**	3.0987
Mean (A)	12.2415	7.5017	12.7249	3.1040	3.1079	3.1454
Std. dev.	0.0008	0.0002	0.0011	0.0124	0.0155	0.0468

Table 2. Compensated RMS current (I_{scp}) obtained by the genetic algorithm in Castro-Nuñez and Castro-Puche's case study [22].

	Type of Filter					
	C	**Series LC**	**Parallel LC**	**Triple Tune**	**Foster**	**Czarnecki 4**
Best (A)	38.0511	20.0275	75.5999	20.0288	**20.0094**	20.0271
Mean (A)	38.0513	20.0313	75.7476	20.5668	20.0807	20.0415
Std. dev.	0.0003	0.0030	0.1411	0.7039	0.0617	0.0150

Table 3. Compensated RMS current (I_{scp}) obtained by the genetic algorithm in Castilla's case study [33].

	Type of Filter					
	C	**Series LC**	**Parallel LC**	**Triple Tune**	**Foster**	**Czarnecki 4**
Best (A)	3.7938	3.5236	3.8242	**3.2024**	3.2131	3.5268
Mean (A)	3.7938	3.5437	3.8242	3.2613	3.2722	3.5313
Std. dev.	0.0000	0.0210	0.0000	0.0369	0.0304	0.0067

As it can be seen in Table 1, in the case study proposed by Czarnecki [39], the filters "Triple tune", "Foster", and "Czarnecki 4" obtain high quality results, while "C-type", "Series LC", and "Parallel LC" filters are far from the optimal solution. Some similar conclusions are obtained when analyzing the date from Table 2, corresponding to the circuit proposed by Castro-Nuñez and Castro-Puche [22]. It is important to point out that better results are obtained in the case of Castro-Nuñez with the same choice of compensator (20.02 A vs. 20.10 A), although Castro-Nuñez does not specify the criterion for choosing the values of the L and C components, apart from discretionary choosing an LC series type compensator. Finally, the analysis of the results provided in Table 3 regarding to the filter proposed by Castilla [33], indicate that "Triple tune", "Foster", "Czarnecki", and the series LC-type filter obtain high quality solutions. In summary, the genetic algorithm is able not only to equal but also to slightly improve the results obtained in these three case studies, which demonstrates that evolutionary approaches can be used to compensate the source current in different circuits using a variety of filters.

Table 4 shows the optimal values achieved for the 3 cases of study and the 6 proposed filters. The optimal current is also included for readability purposes.

Table 5 shows a summary comparison for each of the problems solved showing current values without compensation I_s, the optimum current that a passive filtering can achieve I_{opt}, provided by each author I_{auth}, and the optimum current obtained by applying the technique used in this work $I_{GA_{cp}}$. The value of the power factor for each of the above situations is also indicated plus the power factor without compensation using GA, PF_{GA}. It should be noted that the power factor may differ between what is calculated by complex numbers and what is calculated by geometric algebra due to the different nature of the apparent power $\boldsymbol{S}$ and the geometric apparent power $\boldsymbol{M}$. For the first case, the power factor is calculated as $P/\boldsymbol{S}$ while for the second case it is $P/\boldsymbol{M}$. For example, for the Czarnecki case study, the apparent power $\boldsymbol{S}$ without compensating is worth 1417 VA while compensated is worth 358.8 VA. However, using geometric algebra the power $\boldsymbol{M}$ is worth 1842 VA and compensated is worth 359.25 VA. It should be noted that the final result of the compensation is quite similar since the proposed example is of low complexity as it only has 3 harmonics and low order. If we take into account the case of Castro-Nuñez or Castilla, the power of the proposed method is verified since with only 2 elements (LC filter series) or 3 elements, an almost optimal compensated current is obtained, unlike the original proposal of the author where the filter involved has many more elements and, therefore, much less economic. It should also be noted that the methodology proposed by Castro-Núñez indicates the path to follow when it comes to compensate for the correct power terms, $\boldsymbol{M_b}$, which is not possible to cancel with the traditional power theory because it does not account for those terms arising from crossed products between voltage and currents.

Table 4. Optimal values for L, C achieved by the genetic algorithm for the 3 cases of study and the 6 proposed filters.

	Czarnecki						Castro-Nuñez						Castilla					
	C	**Series LC**	**Parallel LC**	**Triple Tune**	**Foster**	**Czarnecki 4**	**C**	**Series LC**	**Parallel LC**	**Triple Tune**	**Foster**	**Czarnecki 4**	**C**	**Series LC**	**Parallel LC**	**Triple Tune**	**Foster**	**Czarnecki 4**
L_1 (H)	-	10.2116	99.995	0.794	17.457	5.906	-	1.953	2.000	0.256	1.511	1.977	-	15.6537	10.000	0.082	10.000	9.998
L_2 (H)	-	-	-	0.724	6.555	19.000	-	-	-	0.063	1.641	-	-	-	-	0.072	6.651	9.903
L_3 (H)	-	-	-	1.920	5.945	-	-	-	-	0.020	1.198	0.320	-	-	-	0.021	0.660	-
C_1 (μF)	0.010	43,373.492	13.0128	264,930.386	2991.689	34,530.000	135,667.470	224,040.6422	304,711.7123	650,723.116	21,800.000	172,388.219	7.157	0.636	7.291	20.098	5.797	2.079
C_2 (μF)	-	-	-	106,280.564	59,192.627	12,880.000	-	-	-	985,889.243	366,000.000	50,406.350	-	-	-	165.469	1.451	16.065
C_3 (μF)	-	-	-	586,142.767	26,682.668	-	-	-	-	89,338.809	107,600.000	-	-	-	-	21.464	0.844	-
I_{opt} (A)	**12.240**	**7.501**	**12.723**	**3.095**	**3.094**	**3.098**	**38.051**	**20.027**	**75.599**	**20.028**	**20.009**	**20.027**	**3.793**	**3.523**	**3.824**	**3.202**	**3.213**	**3.526**

Table 5. Comparison table for currents and power factor.

	Current				**Power Factor**				
	I_s	I_{opt}	I_{auth}	$I_{GA_{cp}}$	PF_s	PF_{opt}	PF_{auth}	PF_{GA}	$PF_{GA_{cp}}$
Czarnecki	12.24	3.09	3.10	3.09	0.243	0.959	0.959	0.186	0.959
Castro-Nuñez	44.72	20.00	20.10	20.00	0.445	0.993	0.988	0.445	0.992
Castilla	4.21	3.20	3.21	3.20	0.630	0.829	0.829	0.630	0.829

5. Conclusions

In recent years, different authors have shown that geometric algebra, also known as Clifford algebra, can be applied to analyze electric circuits. Having in mind that different studies have shown that geometric algebra is more appropriate than the algebra of complex numbers for the analysis of circuits with non-sinusoidal sources and linear loads, this investigation is an important contribution in estimating the type of filter and its parameters to optimize the quadrature current in electrical circuits. This leads to the compensation of new power terms like quadrature apparent power $\boldsymbol{M_b}$ not included in the commonly accepted definition of electrical power standards. The traditional compensation of reactive power is exceeded by the compensation of cross products between current and voltage that have not been previously taken into account. The proposed approach is based on the use of a genetic algorithm, which is able to optimize the parameters of different types of passive filters. In particular, six widely used filters (single-tuned, double-tuned, triple-tuned, damped-double tuned, and C-type) were compared by regarding their contribution on the loading capability improvement of the transformers under non-sinusoidal conditions.

The results obtained in three test circuits found in the literature show that the application of genetic algorithms based on geometric algebra representations are powerful methods that are able to equal or even improve the results previously obtained by other authors using analytical methods. These results open the door to investigate the use of computational optimization methods for compensating the reactive power in complex circuits. As future work, it is planned to extend the analysis to larger circuits using these and other type of filters. Furthermore, multi-objective optimization methods will be considered to simultaneously optimize the reactive power compensation and to minimize the economic cost of the filters.

Author Contributions: Conceptualization, F.G.M. and R.B.; Methodology, R.B.; Software, A.A. and F.M.A.-C.; Validation, A.A., R.B. and F.M.A.-C.; Formal Analysis, F.G.M.; Investigation, F.G.M. and A.A.; Resources, F.M.A.-C.; Data Curation, R.B.; Writing—Original Draft Preparation, R.B., F.G.M. and F.M.A.-C.; Writing—Review & Editing, F.G.M., A.A., F.M.A.-C. and R.B.; Visualization, F.G.M.; Supervision, F.G.M.; Project Administration, F.G.M. and A.A.

Funding: This research received no external funding.

Acknowledgments: The authors want to acknowledge the CEIA3 campus for the support on this work.

Conflicts of Interest: The authors declare no conflict of interest.

Appendix A. General Concepts

Given an ortho-normal base $\{\sigma_k\}$ with $k = 1, ..., N$ for a vector space $\mathbb{R}^N$, it is possible to define a new space called geometrical algebra $\mathcal{G}_\mathcal{N}$. This new space is characterized by bases not only composed of $\{\sigma_k\}$, but also of external products between these vectors. For example, in the case of a 3D Euclidean space, there is an ortho-normal base $\{\sigma_1, \sigma_2, \sigma_3\}$ where $\sigma_n^2 = 1$. Applying the concept of Grassmann product or exterior product, you get

$$\sigma_l \wedge \sigma_m = \sigma_l \sigma_m = \sigma_{lm} \tag{26}$$

which is a new entity, different from a scalar or a vector because

$$\begin{aligned}(\sigma_l \wedge \sigma_m)^2 = (\sigma_l\sigma_m)(\sigma_l\sigma_m) = \sigma_l(\sigma_m\sigma_l)\sigma_m = \sigma_l(-\sigma_l\sigma_m)\sigma_m = \\ = -(\sigma_l\sigma_l)^2(\sigma_m\sigma_m)^2 = -(1)(1) = -1\end{aligned} \tag{27}$$

$\sigma_l\sigma_m$ squares to -1 so we can conclude that we are facing a new element, which is called a bivector. In the same way, the external product of more than 3 vectors is called trivector, and in general, the product of k vectors is called k-vector. In this way, algebra $\mathcal{G}_3$ can be developed with the base

$$\{1, \sigma_1, \sigma_2, \sigma_3, \sigma_{12}, \sigma_{13}, \sigma_{23}, \sigma_{123}\} \tag{28}$$

Generally speaking, the elements of a geometric algebra are called multivectors ($\boldsymbol{M}$) and can be expressed as a linear combination of the different bases

$$\boldsymbol{M} = \langle \boldsymbol{M} \rangle_0 + \langle \boldsymbol{M} \rangle_1 + \langle \boldsymbol{M} \rangle_2 + ... + \langle \boldsymbol{M} \rangle_n = \sum_{k=0}^{n} \langle \boldsymbol{M} \rangle_k \tag{29}$$

where each $\langle \boldsymbol{M} \rangle_k$ is an element of grade k, representing scalars (grade 0), vectors (grade 1), bivectors (grade 2), or in general k-vectors (grade k).

Appendix B. Geometric Operations

The geometric product is the cornerstone of geometric algebra and is indebted to the contributions of Grassman and Clifford. It is defined as the sum of the scalar product and the external product, and for the case of 2 vectors v_i and v_j

$$\boldsymbol{v_i v_j} = \boldsymbol{v_i} \cdot \boldsymbol{v_j} + \boldsymbol{v_i} \wedge \boldsymbol{v_j} \tag{30}$$

for the base vectors σ_i and σ_j with $i \neq j$, we get bivectors

$$\boldsymbol{\sigma_i \sigma_j} = \boldsymbol{\sigma_i} \cdot \boldsymbol{\sigma_j} + \boldsymbol{\sigma_i} \wedge \boldsymbol{\sigma_j} = \boldsymbol{\sigma_i} \wedge \boldsymbol{\sigma_j} = \boldsymbol{\sigma_{ij}} \tag{31}$$

base vectors anticommute for $i \neq j$ because

$$\boldsymbol{\sigma_i \sigma_j} = \boldsymbol{\sigma_i} \wedge \boldsymbol{\sigma_j} = -\boldsymbol{\sigma_j} \wedge \boldsymbol{\sigma_i} = -\boldsymbol{\sigma_{ji}} \tag{32}$$

On the other hand, unlike vectors which square to 1, bivectors square to -1

$$\sigma_{ij}\sigma_{ij} = \sigma_i\sigma_j\sigma_i\sigma_j = -\sigma_j\sigma_i\sigma_i\sigma_j = -\sigma_j\sigma_j = -1 \tag{33}$$

Finally, we detail some important operations that are used extensively in multivector operations. One of these properties is the *reversion* or $\boldsymbol{M}^{dagger}$ which consists of

$$\boldsymbol{M}^{\dagger} = \sum_{k=0}^{n} \langle \boldsymbol{M}^{\dagger} \rangle_k = (-1)^{k(k-1)/2} \langle \boldsymbol{M} \rangle_k \tag{34}$$

The norm of a multivector $\boldsymbol{M}$ ($\|\boldsymbol{M}\|$) is always a scalar and can be obtained

$$\|\boldsymbol{M}\| = \sqrt{\langle M^{\dagger} M \rangle_0} = \sqrt{\langle M M^{\dagger} \rangle_0} = \sum_k \langle \langle M \rangle_k \langle M^{\dagger} \rangle_k \rangle_0 \tag{35}$$

References

1. Fang, X.; Misra, S.; Xue, G.; Yang, D. Smart grid—The new and improved power grid: A survey. *IEEE Commun. Surv. Tutor.* **2012**, *14*, 944–980. [CrossRef]
2. Merabet, L.; Saad, S.; Abdeslam, D.O.; Merckle, J. Direct neural method for harmonic currents estimation using adaptive linear element. *Electr. Power Syst. Res.* **2017**, *152*, 61–70. [CrossRef]
3. Bollen, M.H.; Das, R.; Djokic, S.; Ciufo, P.; Meyer, J.; Rönnberg, S.K.; Zavodam, F. Power quality concerns in implementing smart distribution-grid applications. *IEEE Trans. Smart Grid* **2017**, *8*, 391–399. [CrossRef]
4. Bouzid, A.M.; Guerrero, J.M.; Cheriti, A.; Bouhamida, M.; Sicard, P.; Benghanem, M. A survey on control of electric power distributed generation systems for microgrid applications. *Renew. Sustain. Energy Rev.* **2015**, *44*, 751–766. [CrossRef]
5. Czarnecki, L.S.; Pearce, S.E. Compensation objectives and currents' physical components-based generation of reference signals for shunt switching compensator control. *IET Power Electron.* **2009**, *2*, 33–41. [CrossRef]

6. Willems, J.L. Budeanu's reactive power and related concepts revisited. *IEEE Trans. Instrum. Meas.* **2011**, *60*, 1182–1186. [CrossRef]
7. De Léon, F.; Cohen, J. AC power theory from Poynting theorem: Accurate identification of instantaneous power components in nonlinear-switched circuits. *IEEE Trans. Power Deliv.* **2010**, *25*, 2104–2112. [CrossRef]
8. Budeanu, C. *Puissances Reactives Et Fictives*; Number 2; Impr. Cultura Nationala: Bouchares, Romania, 1927.
9. Staudt, V. Fryze-Buchholz-Depenbrock: A time-domain power theory. In Proceedings of the 2008 International School on Nonsinusoidal Currents and Compensation (ISNCC 2008), Lagow, Poland, 10–13 June 2008; pp. 1–12.
10. Czarnecki, L.S. What is wrong with the Budeanu concept of reactive and distortion power and why it should be abandoned. *IEEE Trans. Instrum. Meas.* **1987**, *1001*, 834–837. [CrossRef]
11. Czarnecki, L. Budeanu and Fryze: Two frameworks for interpreting power properties of circuits with nonsinusoidal voltages and currents. *Electr. Eng.* **1997**, *80*, 359–367. [CrossRef]
12. Czarnecki, L.S. Currents' physical components (CPC) concept: A fundamental of power theory. In Proceedings of the 2008 International School on Nonsinusoidal Currents and Compensation (ISNCC 2008), Lagow, Poland, 10–13 June 2008; pp. 1–11.
13. Xiao, Y.; Zhao, J.; Mao, S. Theory for the design of C-type filter. In Proceedings of the 2004 11th International Conference on Harmonics and Quality of Power, Lake Placid, NY, USA, 12–15 September 2004; pp. 11–15.
14. Biswas, P.P.; Suganthan, P.N.; Amaratunga, G.A. Minimizing harmonic distortion in power system with optimal design of hybrid active power filter using differential evolution. *Appl. Soft Comput.* **2017**, *61*, 486–496. [CrossRef]
15. Li, W.; Man, Y.; Li, G. Optimal parameter design of input filters for general purpose inverter based on genetic algorithm. *Appl. Math. Comput.* **2008**, *205*, 697–705. [CrossRef]
16. Karadeniz, A.; Balci, M.E. Comparative evaluation of common passive filter types regarding maximization of transformer's loading capability under non-sinusoidal conditions. *Electr. Power Syst. Res.* **2018**, *158*, 324–334. [CrossRef]
17. Chen, Y.M. Passive filter design using genetic algorithms. *IEEE Trans. Ind. Electr.* **2003**, *50*, 202–207. [CrossRef]
18. Klempka, R. Passive power filter design using genetic algorithm. *Praz. Elektrotech.* **2013**, *5*, 294–301.
19. Lachichi, A.; Junyent-Ferre, A.; Green, T. filter design optimization for LV modular multilevel converters in hybrid ac/dc microgrids application. In Proceedings of the 2018 International Conference on Electrical Sciences and Technologies in Maghreb (CISTEM), Algiers, Algeria, 28–31 October 2018; pp. 1–5.
20. Steinmetz, C.P. *Theory and Calculation of Alternating Current Phenomena*; McGraw-Hill Book Company, Inc.: New York, NY, USA, 1916; Volume 4.
21. Castro-Núñez, M.; Londoño-Monsalve, D.; Castro-Puche, R. M, the conservative power quantity based on the flow of energy. *J. Eng.* **2016**, *2016*, 269–276. [CrossRef]
22. Castro-Nunez, M.; Castro-Puche, R. The IEEE Standard 1459, the CPC power theory, and geometric algebra in circuits with nonsinusoidal sources and linear loads. *IEEE Trans. Circuits Syst. I Regul. Pap.* **2012**, *59*, 2980–2990. [CrossRef]
23. Sangston, K.J. Geometry of complex data. *IEEE Aerosp. Electr. Syst. Mag.* **2016**, *31*, 32–69. [CrossRef]
24. Hestenes, D.; Sobcyk, G. *Clifford Algebra to Geometric Calculus: A Unified Language for Mathematics and Physics (Fundamental Theories of Physics)*; Kluwer Academic Publishers: Aarhus, Denmark, 1987.
25. Chappell, J.M.; Drake, S.P.; Seidel, C.L.; Gunn, L.J.; Iqbal, A.; Allison, A.; Abbott, D. Geometric algebra for electrical and electronic engineers. *Proc. IEEE* **2014**, *102*, 1340–1363. [CrossRef]
26. Castro-Nunez, M.; Castro-Puche, R. Advantages of geometric algebra over complex numbers in the analysis of networks with nonsinusoidal sources and linear loads. *IEEE Trans. Circuits Syst. I Regul. Pap.* **2012**, *59*, 2056–2064. [CrossRef]
27. Petroianu, A.I. A geometric algebra reformulation and interpretation of Steinmetz's symbolic method and his power expression in alternating current electrical circuits. *Electr. Eng.* **2015**, *97*, 175–180. [CrossRef]
28. Menti, A.; Zacharias, T.; Milias-Argitis, J. Geometric algebra: A powerful tool for representing power under nonsinusoidal conditions. *IEEE Trans. Circuits Syst. I Regul. Pap.* **2007**, *54*, 601–609. [CrossRef]
29. Castilla, M.; Bravo, J.C.; Ordonez, M. Geometric algebra: A multivectorial proof of Tellegen's theorem in multiterminal networks. *IET Circuits Devices Syst.* **2008**, *2*, 383–390. [CrossRef]

30. Castilla, M.; Bravo, J.C.; Ordonez, M.; Montaño, J.C. Clifford theory: A geometrical interpretation of multivectorial apparent power. *IEEE Trans. Circuits Syst. I Regul. Pap.* **2008**, *55*, 3358–3367. [CrossRef]
31. Gilbert, J.E.; Gilbert, J.; Murray, M. *Clifford Algebras and Dirac Operators in Harmonic Analysis*; Cambridge University Press: Cmabridge, UK, 1991; Volume 26.
32. Bravo, J.C.; Castilla, M.V. Energy conservation law in industrial architecture: An approach through geometric algebra. *Symmetry* **2016**, *8*, 92. [CrossRef]
33. Castilla, M.V. Control of disturbing loads in residential and commercial buildings via geometric algebra. *Sci. World J.* **2013**, *2013*. [CrossRef]
34. Jeon, S.J. Representation of apparent power of non-sinusoidal multi-line power system using geometric algebra. *Trans. Korean Inst. Electr. Eng.* **2009**, *58*, 2064–2070.
35. Castro-Núñez, M.; Castro-Puche, R.; Nowicki, E. The use of geometric algebra in circuit analysis and its impact on the definition of power. In Proceedings of the 2010 International School on Nonsinusoidal Currents and Compensation (ISNCC), Lagow, Poland, 15–18 June 2010; pp. 89–95.
36. Henderson, R.D.; Rose, P.J. Harmonics: The effects on power quality and transformers. *IEEE Trans. Ind. Appl.* **1994**, *30*, 528–532. [CrossRef]
37. De La Rosa, F. *Harmonics and Power Systems*; CRC Press: Boca Raton, FL, USA, 2006.
38. El-Saadany, E.; Zeineldin, H. An optimum reactance one-port compensator for harmonic mitigation. *Electr. Power Qual. Util. J.* **2005**, *11*, 77–82.
39. Czarnecki, L.S. Minimisation of distortion power of nonsinusoidal sources applied to linear loads. In *IEE Proceedings C-Generation, Transmission and Distribution*; IET Digital Library: Hertfordshire, UK, 1981; Volume 128, pp. 208–210.
40. Holland, J.H. *Adaptation in Natural and Artificial Systems: An Introductory Analysis with Applications to Biology, Control, and Artificial Intelligence*; The MIT Press: Cambridge, MA, USA; London, UK, 1975.
41. Mathworks. Genetic algorithm solver. *MATLAB Global Optimization Toolbox*; The MathWorks, Inc.: Natick, MA, USA, 2018.
42. Peng, F.Z.; Su, G.J.; Farquharson, G. A series LC filter for harmonic compensation of AC drives. In Proceedings of the 30th Annual IEEE Power Electronics Specialists Conference (PESC 99), Charleston, SC, USA, 1 July 1999; IEEE: Piscataway, NJ, USA, 1999; Volume 1, pp. 213–218.
43. Bartzsch, C.; Huang, H.; Roessel, R.; Sadek, K. Triple tuned harmonic filters-design principle and operating experience. In Proceedings of the International Conference on Power System Technology (PowerCon 2002), Kunming, China, 13–17 October 2002; IEEE: Piscataway, NJ, USA, 2002; Volume 1, pp. 542–546.

energies

MDPI

Article

Optimization of the Contracted Electric Power by Means of Genetic Algorithms

Alfredo Alcayde, Raul Baños, Francisco M. Arrabal-Campos and Francisco G. Montoya *

Department of Engineering, University of Almería, 04120 Almería, Spain; aalcayde@ual.es (A.A.); rbanos@ual.es (R.B.); fmarrabal@ual.es (F.M.A.-C.)
* Correspondence: pagilm@ual.es; Tel.: +34-950-214501

Received: 28 February 2019; Accepted: 1 April 2019; Published: 2 April 2019

Abstract: An adequate selection of an energy provider and tariff requires us to analyze the different alternatives to choose one that satisfies your needs. In particular, choosing the right electricity tariff is essential for reducing company costs and improving competitiveness. This paper analyzes the energy consumption of large consumers that make intensive use of electricity and proposes the use of genetic algorithms for optimizing the tariff selection. The aim is to minimize electricity costs including two factors: the cost of power contracted and the heavy penalties for excess of power demand over the power contracted in certain time periods. In order to validate the proposed methodology, a case study based on the real data of energy consumption of a large Spanish university is presented. The results obtained show that the genetic algorithm and other bio-inspired approaches are able to reduce the costs associated to the electricity bill.

Keywords: electric power contracts; electric energy costs; cost minimization; evolutionary computation; bio-inspired algorithms

1. Introduction

Electricity market liberalization has been a major challenge for the power systems in different countries [1,2]. This situation has been a genuine step forward to improve competitiveness by offering new tariffs from electricity companies. Usually, consumers are free to choose the energy provider and tariff according to the norms of the country. In any case, it should be guaranteed the stability, quality and security of supply required by users [3,4]. This is not a trivial issue, especially in smart grids, which has implied that some authors have suggested managing databases with information on usage patterns of loads and electricity price tariffs, among other factors [5]. In practice, governments may establish certain restrictions to competition or charges and taxes in the electricity tariff. For example, access charges [6] reflect costs related to the maintenance of the transmission and distribution network infrastructure or costs related to regulated activities.

Generally speaking, the cost-structure usually takes into account many factors related to the type of consumer (domestic, industrial, etc.), quality of service, voltage level, location or season [7]. However, the vast majority of electrical systems base their tariff structure on three main foundations:

- Charges for capacity or access, based on the amount of electrical power (€/kW) demanded from the grid and expected by the user to be guaranteed.
- Charges for active energy consumed, based on the cost of the price of the energy (€/kWh) demanded by the end user.
- Other charges, such as taxes, environmental commitments, penalties, etc.

In this case, the charges for capacity or access play an important role since they can be an important component in the bill of large consumers. In addition, these charges are subject to an hourly variability

within the day and a daily variability within the season of the year. Time-of-use (ToU) is a term that refers to the application of different charges for energy use in different time periods in a way that reflects generation costs and encourages energy consumption in periods that are less critical to the system. Time differentiation (hourly–seasonal) is practised by most countries. For example, in Australia some charges vary by time of use; in United Kingdom peak and off-peak along with seasonal periods are available; France has two seasons and peak/off-peak periods; Italy has four periods as peak, high, medium and off-peak; in the Netherlands, for consumers the kWh charge can be split in off-peak and regular hours; in Norway, where the energy component is time- and regionally-differentiated in winter day, winter night/weekend and summer; while in California the prices vary by season and period [8].

In the case of Spain, it is common to make different charges depending on the time of day, the day of the week, and even the month of the year due to the underlying costs of the system and the need to rationalize the uses of energy by users [9]. As Figure 1 shows, consumers with voltage higher than 1 kV and power contracted higher than 450 kW have six periods (P1, P2, P3, P4, P5, and P6) with different energy and power prices. In the case of consumers having a voltage lower than 1 kV, different tariffs apply where one or three periods can be selected (e.g., three periods option include peak, valley and off-peak hours depending on the time of day).

MONTHS	HOURS																						
	1	2	3	4	5	6	7	8	9	10	11	12	13	14	15	16	17	18	19	20	21	22	23	24
January	6	6	6	6	6	6	6	6	2	2	1	1	1	2	2	2	2	2	1	1	1	2	2	2
February	6	6	6	6	6	6	6	6	2	2	1	1	1	2	2	2	2	2	1	1	1	2	2	2
March	6	6	6	6	6	6	6	6	4	4	4	4	4	4	4	4	3	3	3	3	3	3	4	4
April	6	6	6	6	6	6	6	6	5	5	5	5	5	5	5	5	5	5	5	5	5	5	5	5
May	6	6	6	6	6	6	6	6	5	5	5	5	5	5	5	5	5	5	5	5	5	5	5	5
1st half June	6	6	6	6	6	6	6	6	4	3	3	3	3	3	3	4	4	4	4	4	4	4	4	4
2nd half June	6	6	6	6	6	6	6	6	2	2	2	1	1	1	1	1	1	1	1	2	2	2	2	2
July	6	6	6	6	6	6	6	6	2	2	2	1	1	1	1	1	1	1	1	2	2	2	2	2
August	6	6	6	6	6	6	6	6	6	6	6	6	6	6	6	6	6	6	6	6	6	6	6	6
September	6	6	6	6	6	6	6	6	4	3	3	3	3	3	3	4	4	4	4	4	4	4	4	4
October	6	6	6	6	6	6	6	6	5	5	5	5	5	5	5	5	5	5	5	5	5	5	5	5
November	6	6	6	6	6	6	6	6	4	4	4	4	4	4	4	4	3	3	3	3	3	3	4	4
December	6	6	6	6	6	6	6	6	2	2	1	1	1	2	2	2	2	2	1	1	1	2	2	2

6 — Including weekends and holidays (all day)

Figure 1. Spanish tariff structure (tariff 6.1. A: six periods for consumers with >1 kV and >450 kW).

All of the above leads to a clear conclusion, which is that the electricity system should encourage the use of energy in less critical or grid-loaded time periods, i.e., periods in which the load curve is low and the generating plants are more unloaded, as opposed to peak periods in which the variation in system capacity is very limited. Therefore, the price for access capacity, as well as the price of energy will change according to the restrictions referred to above, being the price much more expensive for the power and energy demanded in peak periods versus off-peak periods. Due to these differences in usage times, as well as the different prices that utility companies charge for energy and power, there may be significant charges on the electricity bill for large consumers based on their consumption habits. For example, a large company may incur large costs because its production takes place during expensive periods (e.g., P1 or P2). This implies that strategies that minimize costs in the most expensive periods must be tackled in favour of those where the system is less loaded, and therefore it is cheaper to consume electricity. The problem is that, in many cases, large consumers cannot change their consumption habits either because their production process does not allow for changes in production schedules or because the provision of services must take place at a certain time. For example, in the case of a University, there are administrative and teaching activities that must be carried out in a specific time interval. This does not imply that there are no other mechanisms that allow us to face a reduction in costs based on the contracted electricity power in each of the hourly periods that make up the selected tariff. Normally, users contract a certain amount of power with the utilities for each

of the periods of use, but this power may not be suitably adjusted, so that it may be excessively high involving large costs, or lower than the value required so that the utility will apply large penalties. A clear example of this inefficient situation often occur in countries such as Spain, where, as shown in Figure 1, there are up to six different tariff periods, from P1 (which would be the most expensive) to P6 (which would be the cheapest). The difference in price for both energy and power can be up to seven times higher in period P1 than in P6. Table 1 contains a summary of the current prices according to the Spanish Ministerial Order IET/2444/2014 for the contracted electric power of the six periods above mentioned. Note the important difference between the most expensive period P1 where the power is about 39 €/kW, as opposed to the cheapest period P6 where the energy is worth about 6.5 €/kW. For energy, the difference is even more evident, reaching almost 10 times the price for period P1 comapred to period P6.

Table 1. Yearly prices of contracted electricity power and energy for tariff 6.1A (HV) in Spain. P1 is the most expensive period, while P6 is the cheapest one.

	P1	P2	P3	P4	P5	P6
Power (€/kW year)	39.139427	19.586654	14.334178	14.334178	14.334178	6.540177
Energy (€/kWh)	0.026674	0.019921	0.010615	0.005283	0.003411	0.002137

Due to the frequent use of penalties for excess power demand, as well as the high costs of this power in certain time bands, it is suitable to implement cost saving strategies for large consumers, such as factories, universities, hospitals, etc. These organizations often have a large number of employees and/or users, so it is not always possible to effectively manage the loads to ensure that the maximum demand value will never exceed the contracted power. This problem is not so critical in the case of domestic or residential consumers, who are not normally subject to seasonal or periodical tariffs due to the fact that the contracted electric power is usually considerably lower than that of a large consumers. This is why some studies have shown that Spanish people at risk of energy poverty, are largely unaware of energy-supply contract types or details. In the case of large customers, a little attention has been paid to the optimal selection of electric supply tariff. A previous investigation [8] proposed methods for posteriori choice of contracted capacities, but to our knowledge the paper here presented is the first one that studies the possibility of applying bio-inspired algorithms for optimizing the contracted electric power in real case studies.

2. Problem Description

This paper presents a working methodology to determine the value of the contracted electric power for an annual period of a standard high voltage multiperiod tariff for the different time periods. The aim of this procedure is to benefice the user to pay a minimum electricity bill, i.e., this operation leads to cost savings that make the consumer more competitive. Note that this has nothing to do with the way of consuming electrical energy and may be the subject of a future research. In the specific case of Spain, certain limitations must also be taken into account due to national regulations. For example, there are restrictions to change the contracted electric power within the current year, so that a consumer may not allowed to change this power or tariff more than once a year.

Electricity tariffs often have two main terms: energy term and power term. The energy term is the variable part of the energy bill that represents the price for the energy consumption (kWh) according to use of electrical energy made by the consumer. The power term accounts for the price of electric energy availability at the consumer side in units of power (kW), that will be paid independently of the use of electricity made by the customer. The sum of these two terms constitutes the basic tariff that will always appear in all invoicing, regardless of the type of tariff contracted by the subscriber. There are some complementary factors that can be applied to the above terms, including: hourly discrimination; reactive energy; seasonality; interruptibility. Moreover, there are other additional concepts for the

Spanish case, such as the electric tax, the energy meter rental (if the customer is not the owner), and VAT tax (21%).

As commented above, most large Spanish consumers use the tariff 6.1A, which is organized into six daily periods. This division traditionally reflects the power load level of the system, so that the P1 period is the most overloaded, while the P6 period is the least loaded. A characteristic of tariff 6.1A is that the contracted electric power must respect the restriction given in the Equation (1), i.e., those customers should contract higher power in those periods where the price is cheaper (see Table 1).

$$\mathrm{P1} \leq \mathrm{P2} \leq \mathrm{P3} \leq \mathrm{P4} \leq \mathrm{P5} \leq \mathrm{P6} \tag{1}$$

On the one hand, the costs for contracting power are linear and correspond to a typical expression such as that given in the Equation (2) for each of the hourly periods considered.

$$C_{Pcont} = \sum_{i=1}^{N} c_i P_i, \tag{2}$$

where C_{Pcont} is the cost of the annual contracted electric power, P_i is the contracted electric power for the period i, c_i is the cost of the power for that period i and N is the number of periods to be considered ($N = 6$ in the case of tariff 6.1A).

On the other hand, it is necessary to consider the excess of power demand. This term may vary from one country to another according to the specific regulations, but it is common to find penalties if the power demanded exceeds the contracted electric power. A maximum demand register processes the maximum power value, usually the average of 15 minutes (this average time may vary depending on the country) reached during the billing period, such that when the value is higher than the contracted power, the customer will pay a penalty on the electricity bill. This penalty may also vary according to the hourly period. In the case of Spain, the penalty is proportional to the sum of the square differences between the contracted power and the power consumed for each quarter-hour segment of each billing period. The other penalty often applied in several countries is the excessive consumption of reactive energy (kVArh).

Equation (3) represents the total invoice to be paid by the consumer for the terms power, energy (active and reactive) and taxes. In this paper, the aim is to minimize the term "power" included in Equation (3), while the terms corresponding to active energy, reactive energy and taxes will not be taken into account as they are not subject to optimization.

$$\text{Invoice} = \underbrace{\sum_{m=1}^{12}\sum_{i=1}^{6} t_{pi} p_{fi} + \sum_{m=1}^{12}\sum_{i=1}^{6} 1.4064 k_i A_{ei}}_{\text{Power}} + \underbrace{\sum_{m=1}^{12}\sum_{i=1}^{5} kR_i + \sum_{m=1}^{12}\sum_{j=1}^{N_m} E_{jm} C_{jm}}_{\text{Energy}} + \text{taxes}, \tag{3}$$

where

m : months (from January to December)
N_m : number of hours of month m
E_{jm} : consumed energy in hour j of month m
C_{jm} : cost of consumed energy in hour j of month m
i : tariff schedule (from P1 to P6 in tariff 6.1A)
t_{pi} : monthly price of power component for period i
p_{fi} : contracted power for period i
$k_i : k_1 = 1 \quad k_2 = 0.5 \quad k_3 = k_4 = k_5 = 0.37 \quad k_6 = 0.17$

$$A_{ei} : \begin{cases} \sqrt{\sum_{k=1}^{n} (P_{d_{ki}} - P_{c_i})^2} & \text{if} \quad P_{d_{ki}} > P_{c_i} \\ 0 & \text{if} \quad P_{d_{ki}} \leq P_{c_i} \end{cases}$$

where $P_{d_{ki}}$ is the demanded power every 15 min
k of period i and P_{c_i} is the contracted power for period i
k : constant of value 0.04155 if the reactive energy is 33% greater than active energy for period i and 0.062332 if greater than 50%
R_i : reactive energy surplus for period i.

Therefore, the total cost of the power term is obtained on the basis of costs per contracted power and penalties for excess power demand. Figure 2 shows how adding surplus power (green color) plus contracted power (black color) gives the billed power (orange color). The surplus curve has that shape because it corresponds to the term A_{ei}, which is a quadratic term, as can be seen in Equation (3). The goal here is to reduce the total cost by optimizing the contracted power (term "power" included in Equation (3)) in each of the six periods while satisfying the restriction given in Equation (1).

This optimization process can be carried out using non-linear quadratic optimization or, alternatively, by means of approximated methods such as meta-heuristics. Meta-heuristic algorithms provide greater flexibility since it is not necessary to have prior information of the problem at hand in order to find optimal or quasi-optimal solutions while satisfying a set of constraints.

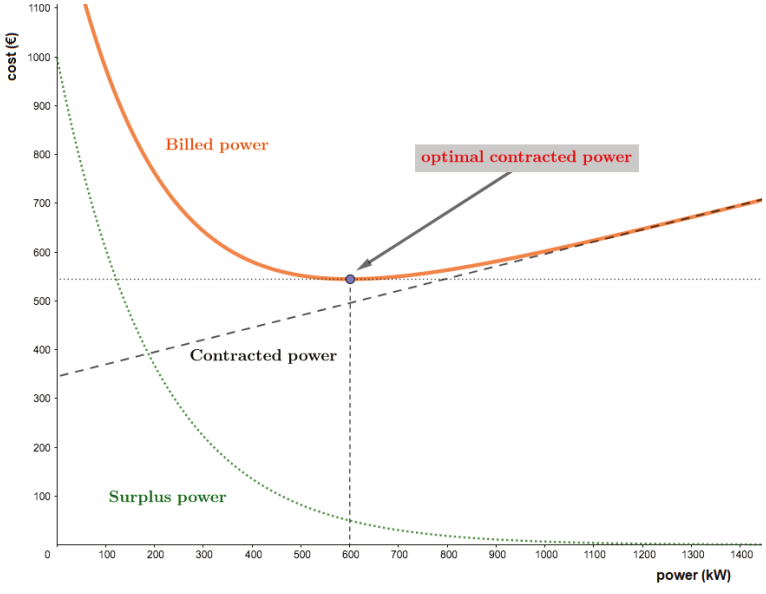

Figure 2. Example of the contribution of surplus power and contracted electric power to final power cost.

3. Solution Method

Having in mind the difficulty of selecting the contract electric power, it is necessary to provide efficient procedures that obtain high quality solutions. Many authors have proposed exact and approximated methods for solving a large variety of problems. The main drawback of Lagrangian relaxation, branch and bound, and other exact approaches is that the runtime increases with the size of the problem instance, being not suitable to solve very large-sized problems. On the contrary, approximated methods sacrifice the guarantee of finding the optimum results in favor of providing an acceptable solution within a reasonable runtime. Among the approximated methods, meta-heuristics are commonly used since they provide quasi-optimal solutions in a fast way. A large number of meta-heuristics have been proposed in the past, including single point search (simulated annealing, tabu search, variable neighborhood search, etc.) and population-based approaches (evolutionary algorithms, particle swarm optimization, ant colony optimization, etc.) [10,11]. Evolutionary algorithms have shown to be efficient methods, and are probably the most commonly used since they are problem-solving procedures that include evolutionary processes as the key design elements, such that a population of individuals is continually and selectively evolved until a termination criteria is fulfilled. Genetic algorithms (GAs) [12] are possibly the most widely used evolutionary techniques for solving a large variety of problems in the field of electrical systems [13,14]. As it can be seen in Figure 3, a genetic algorithm mimics natural selection by evolving over time a population of individual solutions to the problem at hand until a termination condition is fulfilled and the best individual is returned as result of the algorithm.

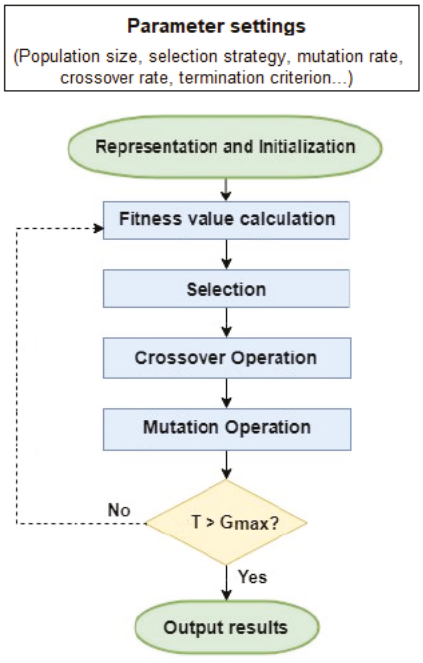

Figure 3. Flowchart of the genetic algorithm.

In this paper, it is proposed to apply a genetic algorithm to solve the problem of selecting the contracted electric power. Although randomized, GAs exploit historical information to direct the search into the region of better performance within the search space. The basic techniques of the GAs are designed to simulate processes in natural systems necessary for evolution. A genetic algorithm has several strategy parameters, including the population size, mutation operator and mutation rate, the crossover operator and crossover rate, the selection mechanism and selective pressure, etc. An adequate parameter setting can be determinant to obtain high quality solutions. The parameters used in our implementation were:

- Population size: This parameter controls the sample size for each population. 100 individuals.
- Crossover operator and crossover rate: The crossover operator creates a new chromosome by combining parts of two (or more) parent chromosomes. In this paper, linear crossover, which consists of taking two chromosome (treating it as vectors) and creating a linear combination of this vectors as result, was used. The crossover rate used here was 0.8 (80%).
- Mutation operator and mutation rate: the mutation operator mutates a specific gene over the whole population, and prevents a population from converging to a local minimum by stopping the solution to become too close to one another. Although most of the search was performed by crossover, mutation can be vital to provide the diversity to the population. The mutation rate used here was 0.03 (3%).
- Selection mechanism: selectors are responsible for selecting a given number of individuals from the population, then obtaining survivors and offspring. The selection mechanism used here was the roulette-wheel selector, which is a fitness proportional selector that applies less selective pressure over than other strategies such as tournament selector.
- Termination condition: termination condition is the criteria to determine when the genetic algorithm should end. The termination condition used here was that the algorithm to stop

its steady state. In our case, the algorithm stopped when it reached the 100th generation without improvement.

In particular, a custom adaptation of the open-source Jenetics library [15] written in Java2, which provides the genetic algorithm, and genetic programming implementations was used. It has no runtime dependencies to other libraries, except the Java 8 runtime. Jenetics allows you to minimize or maximize a given fitness function without tweaking it. Since it is an open source library, it was possible to include the necessary modifications and adapt the source code to the problem at hand.

Although the aim of the paper was not to present a new genetic algorithm, but to use the implementation of the Jenetics library [15] to solve a specific problem, some comments about the performance of the genetic algorithm are provided using typical considerations [16]. On one hand, the space complexity of an algorithm is the amount of memory space required to solve an instance of a problem as a function of the size of the input. In our case, the space complexity of the genetic algorithm was linear since it did not use a cost matrix, but a cost array of length equal to the population size. On the other hand, time complexity of an algorithm is the amount of processing time it needs to run to completion. According to [17], when computing the time complexity, the impact of decision variables and objectives are generally ignored as they are much smaller than the population size. In our case, the time complexity of the genetic algorithm was determined by measuring the maximum number of fitness function evaluations. If the population size, maximum number of generations, and other parameters are fixed, then the maximum number of fitness function evaluations will not change when the size of the input is doubled (e.g., considering data of two years instead of one), although the time needed to evaluate a single fitness function call will be twice as long. Therefore the time complexity was determined to be linear.

4. Empirical Study

In this section, the genetic algorithm described above was used to optimize the contracted electric power using data from a Spanish university.

4.1. Case Study: A Spanish University

In this section the case study of a large public Spanish university is analyzed. The 15 min average power values were stored in the utility's database of the electrical company and are accessible through the consumer web portal. The start and end dates can be selected, enabling the system to download a CSV or Excel file showing the power values and timestamps for each value. In this study, data from a complete year was considered. With this information, the genetic algorithm described above determined the power to be contracted in order to minimize the cost of power contracted and the penalties for excess of power demand over the power contracted. Certainly, the restrictions associated with the tariff were coded and observed by the genetic algorithm.

Figure 4 displays the average day electric load curve, which includes the data of the entire year of 2018. As it can be observed, most energy consumption is reached during mornings. Figure 5 shows how during some hours of a day of activity the power consumption exceeds the contracted electric power, i.e., there is a excess of power demand over the power contracted that will be penalized. Figure 6 shows the 15 min average power values of the entire year, while Figure 7 shows the daily average power values of the entire year. Figure 8 displays the the histogram of power demanded during the year considering 1 h intervals.

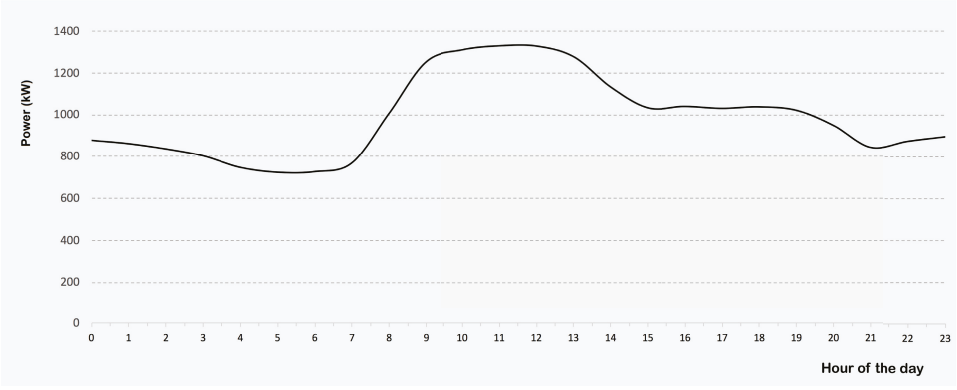

Figure 4. Average day electric load curve of the university analyzed (year 2018).

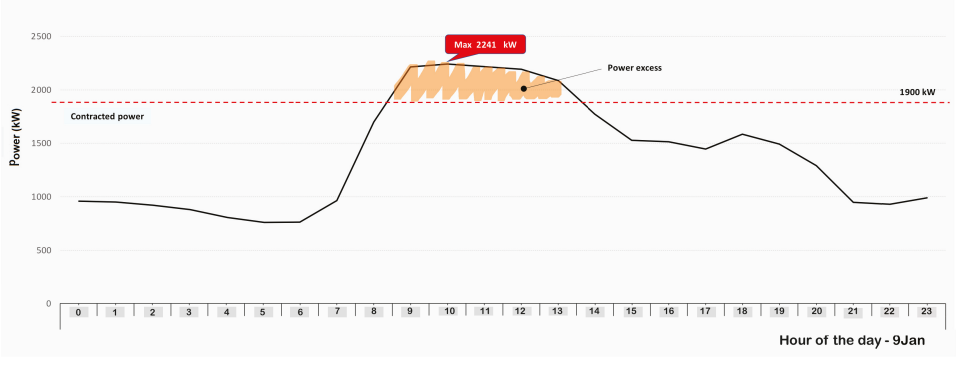

Figure 5. Typical load curve for a day of activity of the university analyzed (year 2018).

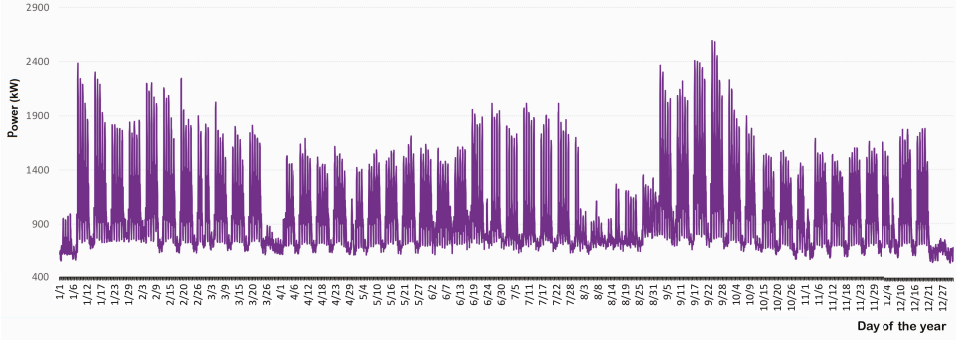

Figure 6. Annual load curve of the university analyzed (year 2018).

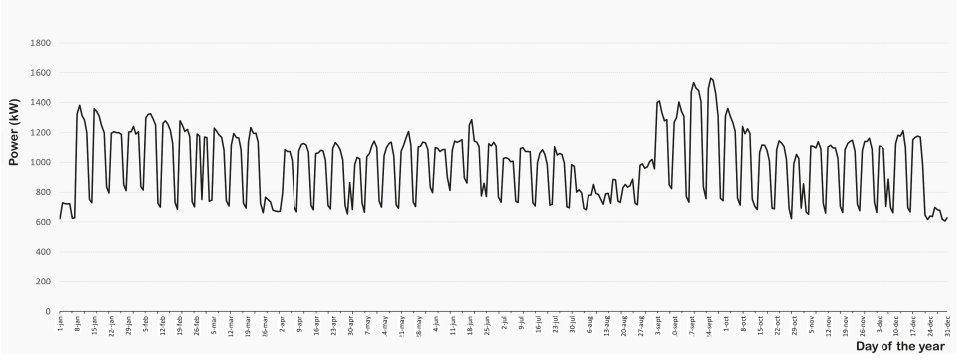

Figure 7. Average load curve of the university analyzed (year 2018).

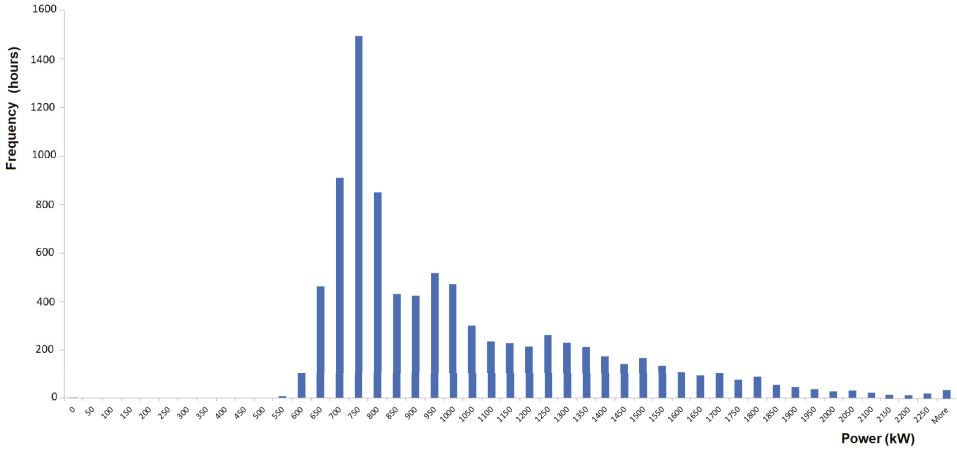

Figure 8. Histogram of power (kW) demanded of the university analyzed (year 2018).

4.2. Results and Discussion

In order to solve the optimization problem, the genetic algorithm has been implemented using the Jenetics library [15]. The algorithm was executed on a laptop computer with an Intel i7-7700HQ processor (quad-core 2.8 GHz), 16 GB RAM, and Windows 10 operating system.

The feasibility region of the optimization problem was set to the range (0,K) kW in each of the six periods. The value of K should be sufficiently large to avoid unfeasible solutions (i.e., solutions that do not cover the contracted power in the six periods), while the bio-inspired algorithms will automatically reduce these values to the optimal ones. In our case, the value of K was set to K = 2592.0 kW, the maximum power demand in the input data (one year dataset). Table 2 shows the statistical results obtained after 50 independent runs of the genetic algorithm (GA) considering the input data described above. In terms of the fitness value, all the independent runs of the GA obtained the same result (215,563.42 €), which denotes the robustness of the algorithm. As Figure 9 shows, the trendlines of the best solutions obtained by the 50 independent runs of the genetic algorithm indicate that all them converged after a given number of generations. Regarding to the execution time, the mean runtime was 0.629 s, with a standard deviation about 0.1 s, which shows that the algorithm converges fast and enhances its search accuracy. On the other hand, Table 2 also shows a comparison of GA with

other two well-known bio-inspired algorithms: particle swarm optimization (PSO) and differential evolution (DE). PSO is based on the collective group behaviour of organisms such as birds flocking, whereby the group attempts to meet the collective objective of the group based on the feedback from the other members [18]. On the other hand, DE algorithms are based on self-adapting capabilities at different stages of the search process such that during the initial stages of the search process the perturbations are large, but in mature stages the members of the population converge to a small region and the DE adapts accordingly [19]. PSO and DE implementations included in the jMetal library have been used to study the performance of these meta-heuristics in the problem at hand. jMetal [20] is an object-oriented Java-based framework for experimentation and study of meta-heuristic optimization algorithms. As it can be observed in Table 2, PSO and DE also obtain the best solution found by GA (215,563.42 €) in some but not all runs.

Table 2. Results obtained by the genetic algorithm, particle swarm optimization (PSO) and differential evolution (DE) (50 independent runs).

	GA		PSO		DE	
	Fitness (€)	**Time (ms)**	**Fitness (€)**	**Time (ms)**	**Fitness (€)**	**Time (ms)**
Min	215,653.4	506	215,653.4	101	215,653.4	4073
Mean	215,653.4	629	215,653.6	200	215,823.2	4491
Max	215,653.4	1165	215,661.1	905	217,356.6	7487
Std. dev	0.00	106	1.09	119	516.11	694

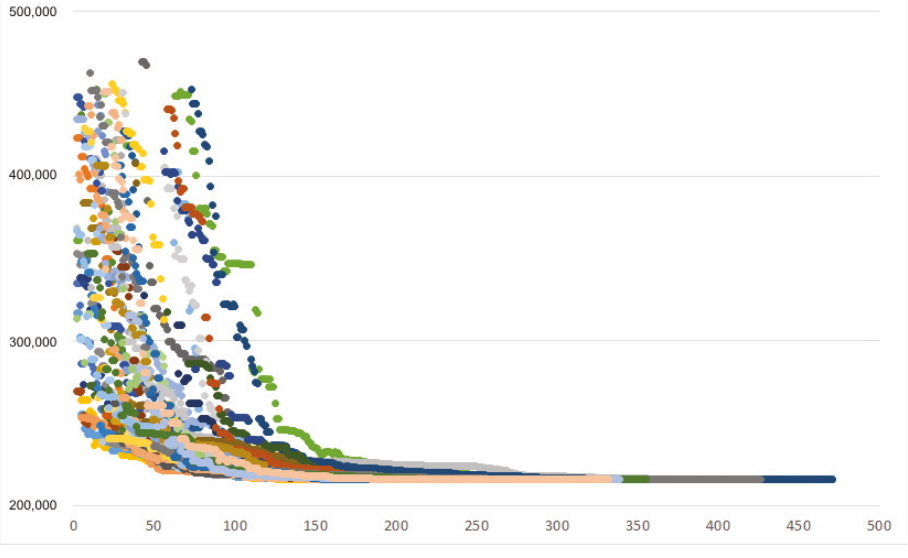

Figure 9. Convergence history of feasible solutions obtained by the 50 independent runs of the genetic algorithm. Numer of executions in horizontal axis and fitness in vertical axis. Every run has a different color.

The results obtained by the genetic algorithm are compared with the (real) electricity bill paid by the university here considered. As Table 3 shows, the solution found by the genetic algorithm [P1,P2,P3,P4,P5,P6]= [1729.0, 1729.0, 1729.0, 1729.0, 1729.0, 1729.0] reduced the sum of the total cost associated to the two components analyzed: power term and penalties for excess of power demand

(energy consumption costs are not displayed). Thus, the contracted electric power proposed by the genetic algorithm significantly reduced the power term, although it increased the penalties for excess of power demand. Overall, the solution provided by the genetic algorithm allowed us to reduce the electricity bill by almost 8000€ with respect to the electricity bill paid by the university studied.

Table 3. Comparison between current contracted power and results obtained by the genetic algorithm.

		Solution	
		Genetic Algorithm	**Real Electricity Bill**
Cost (€)	Contracted power (P1 to P6)	[1729,1729,1729,1729,1729,1729]	[1900,1900,1900,1900,1900,2500]
	Power term	187,196.82	209,634.91
	Excess power	28,456.60	13,988.33
	Total	215,653.42	223,623.24

5. Conclusions

Contracted electric power must consider that time differentiation (hourly-seasonal) is practised by most countries. This is an important fact that should be considered by companies when scheduling their activity, so that their main consumption tend to be distributed by the least economically damaging schedule. This paper proposes the use of computational optimization algorithms in order to select the power contracted by consumers. The novelty of this paper is to evaluate the usefulness of genetic algorithms and other bio-inspired approaches (particle swarm optimization and differential evolution) for optimizing the contracted electric power. Results obtained considering the data of a large Spanish university show that the genetic algorithm significantly reduces the cost of the electric bill. The proposed method also allows applications to tariffs with other hourly periods configurations, as well as tariffs that are applied in other countries and that may differ from the Spanish one. PSO and DE algorithms also obtain high quality solutions in a few seconds. As future work, we plan to analyze the use of these and other computational methods to optimize the contracted electric power considering the particular characteristics of the tariffs in different countries.

Author Contributions: Conceptualization, F.G.M. and R.B.; methodology, R.B.; Software, A.A. and F.M.A.-C.; validation, A.A., R.B. and F.M.A.-C.; Formal Analysis, F.G.M.; investigation, F.G.M. and A.A.; Resources, F.M.A.-C.; data curation, R.B.; writing—original draft preparation, R.B., F.G.M. and F.M.A.-C.; writing—review and editing, F.G.M., A.A., F.M.A.-C. and R.B.; visualization, F.G.M.; supervision, F.G.M.; project administration, F.G.M. and A.A.

Funding: This research received no external funding.

Acknowledgments: The authors want to acknowledge the CEIA3 campus for the support of this work.

Conflicts of Interest: The authors declare no conflict of interest.

References

1. Jamasb, T.; Pollitt, M. Electricity market reform in the European Union: Review of progress toward liberalization and integration. *Energy J.* **2005**, *26*, 11–41. [CrossRef]
2. Joskow, P.L. *Lessons Learned from the Electricity Market Liberalization*; MIT Center for Energy and Environmental Policy Research, Massachusetts Institute of Technology: Cambridge, MA, USA, 2008.
3. Gómez San Román, T. *Electricity Economics: Regulation and Deregulation*; Wiley-IEEE Press: Piscataway, NJ, USA, 2003.
4. Conejo, A.J.; Carrión, M.; Morales, J.M. *Decision Making Under Uncertainty in Electricity Markets*; Springer: Berlin/Heidelberg, Germany, 2010; Volume 1.
5. Fallah, S.; Deo, R.; Shojafar, M.; Conti, M.; Shamshirband, S. Computational intelligence approaches for energy load forecasting in smart energy management grids: State of the art, future challenges, and research directions. *Energies* **2018**, *11*, 596. [CrossRef]

6. Wu, Y.K. Comparison of pricing schemes of several deregulated electricity markets in the world. In Proceedings of the 2005 IEEE/PES Transmission and Distribution Conference and Exhibition: Asia and Pacific, Dalian, China, 18 August 2005; IEEE: Piscataway, NJ, USA, 2005; pp. 1–6.
7. Ma, J. On-grid electricity tariffs in China: Development, reform and prospects. *Energy Policy* **2011**, *39*, 2633–2645. [CrossRef]
8. Fernández, M.; Zorita, A.; García-Escudero, L.; Duque, O.; Moríñigo, D.; Riesco, M.; Muñoz, M. Cost optimization of electrical contracted capacity for large customers. *Int. J. Electr. Power Energy Syst.* **2013**, *46*, 123–131. [CrossRef]
9. Berrie, T.W. *Electricity Economics and Planning*; Number 16; IET: Stevenage, UK, 1992.
10. Glover, F.W.; Kochenberger, G.A. *Handbook of Metaheuristics*; Springer Science and Business Media: Berlin, Germany, 2006; Volume 57.
11. Martí, R.; Pardalos, P.M.; Resende, M.G. *Handbook of Heuristics*; Springer: Berlin/Heidelberg, Germany, 2018.
12. Goldberg, D.E. *Genetic Algorithms*; Pearson Education India: Chennai, India, 2006.
13. Guerrero, M.; Montoya, F.G.; Baños, R.; Alcayde, A.; Gil, C. Community detection in national-scale high voltage transmission networks using genetic algorithms. *Adv. Eng. Inf.* **2018**, *38*, 232–241. [CrossRef]
14. Montoya, F.G.; Alcayde, A.; Arrabal-Campos, F.M.; Baños, R. Quadrature Current Compensation in Non-Sinusoidal Circuits Using Geometric Algebra and Evolutionary Algorithms. *Energies* **2019**, *12*, 692. [CrossRef]
15. Wilhelmstötter, F. *JENETICS Library User's Manual*; Franz Wilhelmstötter: Wien, Austria, 2018.
16. Kaya, H.; Gündüz-Öğüdücü, Ş. SAGA: A novel signal alignment method based on genetic algorithm. *Inf. Sci.* **2013**, *228*, 113–130. [CrossRef]
17. Lin, Q.; Li, J.; Du, Z.; Chen, J.; Ming, Z. A novel multi-objective particle swarm optimization with multiple search strategies. *Eur. J. Oper. Res.* **2015**, *247*, 732–744. [CrossRef]
18. Kar, A.K. Bio inspired computing—A review of algorithms and scope of applications. *Expert Syst. Appl.* **2016**, *59*, 20–32. [CrossRef]
19. Suganthi, S.; Devaraj, D.; Ramar, K.; Thilagar, S.H. An improved differential evolution algorithm for congestion management in the presence of wind turbine generators. *Renew. Sustain. Energy Rev.* **2018**, *81*, 635–642. [CrossRef]
20. Durillo, J.J.; Nebro, A.J. jMetal: A Java framework for multi-objective optimization. *Adv. Eng. Softw.* **2011**, *42*, 760–771. [CrossRef]

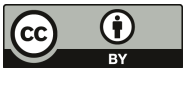

energies

MDPI

Article

Data Analytics-Based Multi-Objective Particle Swarm Optimization for Determination of Congestion Thresholds in LV Networks

Javier Leiva [1,2,*], Rubén Carmona Pardo [1] and José A. Aguado [2]

[1] Endesa, 28042 Madrid, Spain; ruben.carmona@enel.com
[2] Department of Electrical Engineering, University of Málaga, 29016 Málaga, Spain; jaguado@uma.es
* Correspondence: javier.leiva@enel.com

Received: 26 February 2019; Accepted: 2 April 2019; Published: 4 April 2019

Abstract: A growing presence of distributed energy resources (DER) and the increasingly diverse nature of end users at low-voltage (LV) networks make the operation of these grids more and more challenging. Particularly, congestion and voltage management strategies for LV grids have usually been limited to some elemental criteria based on human experience, asset oversizing, or grid reinforcement. However, with the current massive deployment of sensors in modern LV grids, new approaches are feasible for distribution network assets operation. This article proposes a multi-objective particle swarm optimization (MOPSO) approach, combined with data analytics through affinity propagation clustering, for congestion threshold determination in LV grids. A real case study from the smart grid of Smartcity Malaga Living Lab is used to illustrate the proposed approach. Within this approach, distribution system operators (DSOs) can take decisions in order to prevent situations of risk or potential failure at LV grids.

Keywords: congestion management; low-voltage networks; multi-objective particle swarm optimization; affinity propagation clustering; optimal congestion threshold

1. Introduction

Conventional development of the distribution networks has been driven by a worst-case fit-and-forget principle to tackle most of medium-voltage (MV) and low-voltage (LV) congestion challenges due to the long lifetime of their assets and planning horizon [1–4]. This led to limited distributed energy resources (DER) capacity allowed to be connected and costly network reinforcements, although peak loads generally occur only for a few hours in a year [1]. It is definitely recommendable to stop operating the distribution networks as static black boxes [5,6].

Despite promising examples of voltage and reactive power regulation that have been implemented in Germany and Italy according to national standards VDE 4105 and CEI 0-2 respectively [7], congestion management is normally approached dynamically only in transmission networks [8], for example by rescheduling and readjusting set points in generation units [9,10]. Nonetheless, the threats posed by the intermittent and dynamic nature of distributed generators, electric vehicles (EVs), or energy storage systems, to cite some of the most relevant DER technologies [11,12], require new means to help distribution system operators (DSOs) in their key function of congestion management in those complex scenarios [10]. This is the case of control algorithms proposed for operations such as curtailment of MV wind generators [13] or EV smart charging [14]. Therefore, flexibility in distribution networks is an active research question, including DER units and end users in market models that exploit their capabilities to relieve congestion [15] and improve security of supply [16].

However, in the case of LV networks, other means that can be considered as an alternative to those commonly widespread, such as asset oversizing or reinforcement, are scarce [17]. In addition

to this, congestion limits are not clearly defined for LV distribution network assets, such as MV/LV power transformers or LV feeders, apart from conventional criteria initially designed for static network planning [18,19] or the maximum admissible power determined by their nominal characteristics.

Determining what we have defined here as optimal congestion threshold may help DSOs in their dynamic operation of the LV networks. These thresholds provide them with technical references for the value of current measured individually in a certain distribution network element. Thereby, DSOs may enable preventive actions, by means of their own controllable network assets or with the help of other participating agents such as demand aggregators, before congestion definitively takes place and potential risk of failure may severely increase. Consequently, those thresholds must be optimized, as detailed in Section 3, considering not only the highest values of current experienced in the distribution network elements and their admissible congestion limits, but also the time duration and repetition of those congested or close to congestion situations over time.

Congestion management is addressed by classical methods by means of market mechanisms, as in the case of demand side management models [20], or by means of network planning-based methodologies, as in hosting capacity models [21], to cite some relevant examples, but limitations may arise at the time of their implementation on LV networks. Indeed, these models may be adapted to this new paradigm, with the help of present innovative solutions such as LV network-monitoring technologies and MV/LV state estimation algorithms [22]. Particularly, hosting capacity approaches are strongly conditioned by the nominal admissible limits on the network element of study [21] or the number and characteristics of scenarios considered [23], while demand side management requires the development of models oriented to facilitate end users' decision-making [24] and read locational market signals in order to boost participation in LV networks [20].

The methodology proposed here is especially designed for LV networks and seeks a compromise between the subjective human-based criteria and the precise but limited, as explained before, classical models. A data analysis is proposed here to address this challenge by means of clustering a significant group of distribution network elements. The aim is to provide insight into underlying patterns of data, to accelerate knowledge discovery, elements' classification, and subsequent computational efforts [25,26]. In addition to this, an optimization problem is formulated in order to help make decisions for preventing and managing congestion in heterogeneous massive sets of distribution network elements [27]. This provides DSOs with enriched objective criteria for the proactive preventive operation and maintenance of their assets, unlike the mentioned precedents based on their subjective, conservative, and generalized experience. In particular, particle swarm optimization (PSO) is proposed here thanks to its applicability to solve multi-objective optimization problems, and to its capability to avoid finding solutions biased by predetermined human initial decisions [28].

Authors in Reference [9] surveyed some applications of PSO on power systems, emphasizing its capabilities in facing issues such as uncertainty in load demand incorporating distributed generation, EV charging management, or economical dispatch to determine generation operating conditions while network constraints are met. Other relevant applications are those oriented to optimal power flow calculation and congestion management [10]. PSO-based algorithms can also deal with non-smooth functions, especially those related to frequency regulation and voltage constraints [10]. Further approaches are outlined in Reference [9], such as balancing loads between feeders or deciding on the optimal configuration, size, and topology of the distribution system.

PSO bears similarities to other advanced optimization algorithms, such as evolutionary computation techniques, where genetic and ant colony algorithms stand out for their popularity. Nevertheless, those techniques are more complex and present some serious restrictions to be applied in our methodology. Genetic algorithms may be faster than PSO and restrict the reproduction of weak solutions, but their crossover and mutation operations result as incompatible with our optimization problem [29], since it is formed by load duration curves, with individuals defined by non-independent characteristics [30]. Ant colony algorithms, despite of being based on swarm behavior [31] as in the case of PSO, assure convergence in problems where source and destination are predefined and

specific [32], unlike in the congestion threshold determination problem proposed here. The objective of this article is threefold: (1) To determine optimal technical thresholds to prevent congestion in distribution network assets, such as MV/LV power transformers and LV feeders; (2) to contribute with an optimization methodology not based on subjective previous experience and replicable in any kind of network, by employing clustering and multi objective particle swarm optimization (MOPSO); and (3) to apply the methodology to a real dataset obtained from Smartcity Malaga Living Lab, an area with more than 15,000 real end users, where 750 sensors installed in 56 MV/LV secondary substations are measuring current, voltage, power, and energy every 5 min [33].

This article is organized as follows. Section 2 addresses the congestion management problem in LV distribution networks, presenting the limitations of the DSOs to tackle saturation problems. In Section 3, the methodology for optimal congestion threshold determination is presented, detailing the data analytics-based and optimization algorithm developed, as well as its objectives, formulation, constraints, and pseudocode. The results of this methodology are discussed in Section 4 thanks to its application on power transformers and LV feeders from a real case of study from Smartcity Malaga Living Lab. Finally, Section 5 presents the conclusions and the fundamental ideas discussed in the article.

2. Congestion in LV Distribution Networks

Distribution networks have their end users spread, distributed in any form, independently if regarding a LV feeder and its phases, or among different feeders connected to the same power transformer in a secondary substation [4,34,35]. Moreover, each end user, whether consumer, prosumer, or generator, has its own arbitrary pattern, even more diverse with the proliferation of DER technologies.

A clear example of this highly heterogeneous distribution of clients of the LV networks can be seen in Figure 1 for two MV/LV (medium voltage/low voltage) secondary substations of Smartcity Malaga Living Lab [36], despite being located in the same geographical area, having the same number of LV feeders and nominal rating in their power transformers, and also the same number of predominantly residential single-phase end users, which is slightly above 500 in each case.

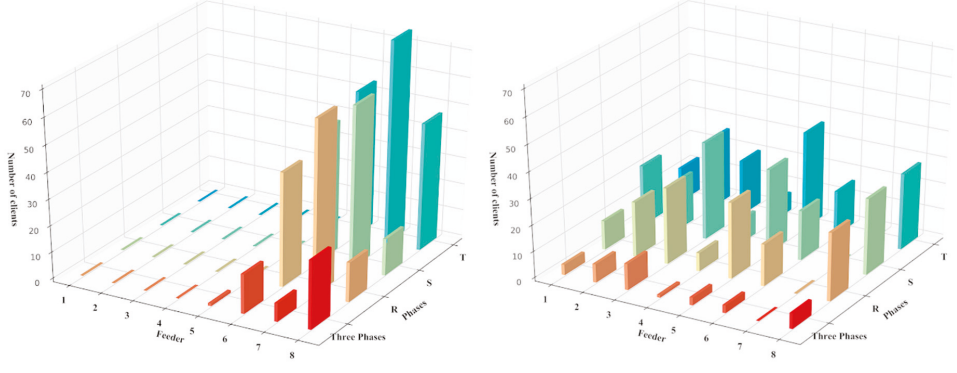

Figure 1. An example of single-phase (in orange, green, and blue) and three-phase (in red) client distribution per low-voltage (LV) feeder in two secondary substations (**a**,**b**) of Smartcity Malaga Living Lab.

This heterogeneity influences severe congestion and voltage in the network. In order to compensate for the voltage drop and to avoid subsequent undervoltage at the end of the feeder, the voltage at the LV side of a MV/LV power transformer has been traditionally set over 1 p.u. [1] with

a conventional off-line fixed setting [37]. Meanwhile, conventional options to tackle congestion go predominantly through network oversizing and extension, as in the case of rating upgrade of power transformer or construction of new secondary substations to overcome critical situations that take place in short periods of time [38,39], as can be seen in the load duration curves of a set of Smartcity Malaga power transformers displayed in Figure 2.

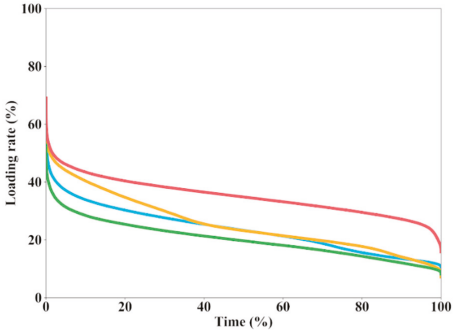

Figure 2. Load duration curves in power transformers in four secondary substations over a period of a year of Smartcity Malaga Living Lab.

Furthermore, congestion variations experienced in adjacent LV feeders and their phases, as displayed in Figure 3, evidence a totally decoupled unbalanced performance, leading to highly diverse characteristic values. Therefore, this means having situations close to congestion along a LV feeder, or particular phase, at the same moment the neighbor ones may not.

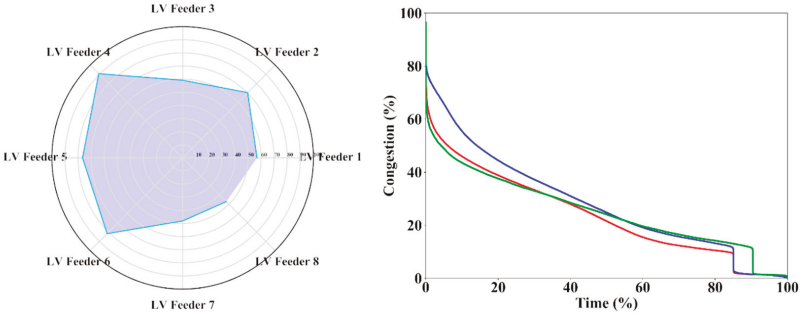

(**a**) (**b**)

Figure 3. (**a**) Maximum current measured in the LV feeders with respect to their nominal admissible currents, and (**b**) load duration curves of the three phases in its LV feeder 5, of a power transformer of Smartcity Malaga Living Lab over a period of a year.

Unlike voltage, network congestion limits are not clearly defined by international grid codes, such as in EN50160 [40], which states that voltage on MV and LV distribution network nodes must remain within ±10% for 95% of the week, and between +10% and −15% for all time. Apart from the maximum limit determined by the nominal admissible power of each asset of the network, other values commonly used to set maximum congestion thresholds are 95% by the transmission system operator in Spain for their cables [18], or 75% by the regulator of the electric sector in Peru for both cables and power transformers [19], to cite some examples. However, these values are based on their local experience.

Power transformers are critical expensive assets in distribution networks, hence special attention must be given to their operation and maintenance [41,42]. Nonetheless, detailed information is scarce at the LV network level, such as the particular phase where a single-end user or DER unit is connected [43], despite successful smart grid pilot projects such as Smartcity Malaga [44], INTEGRIS [5], IDE4L [45], or MONICA [46] have dedicated special efforts in distribution network digitalization and state estimation. Therefore, technical solutions are available today to address congestion in singular elements such as LV feeder phases, avoiding bottlenecks that may arise even earlier in the case of significant DER penetration or demand growth [47,48], since technical constraint violations may occur at an earlier stage [49].

Therefore, DSOs may operate the distribution networks by means of a permanent dynamic supervision of the congestion level, taking into account the optimal congestion threshold assigned by this methodology to any particular network element. As pointed out in Section 1, those thresholds provide DSOs with technical references that prevent them before congestion definitively takes place in a particular distribution network element and, consequently, potential risk of failure increases. This lets them leave behind corrective processes and act before an incident occurs, therefore optimizing budget allocation and the quality of service provided to end users [50] by means of preventive actions, such as adjusting on-load tap changing (OLTC) MV/LV power transformers [51] or interacting with DER units so that they adjust their operating regime to the existing network conditions [7].

3. Proposed Approach for LV Congestion Determination

The proposed methodology consists of three stages, as displayed in Figure 4. Firstly, data acquisition allows for the creation of the search space, which is formed in this problem by load duration curves of distribution network elements. They may represent a numerous diverse dataset for modern DSOs, hence, data analysis techniques must be applied. On the one hand, this allows for the classification of assets by grouping them regarding their similarities. On the other hand, the most representative elements can be identified, so deeper studies can be performed on them, and later be extrapolated to the rest of similar assets for the sake of the efficiency of the analysis.

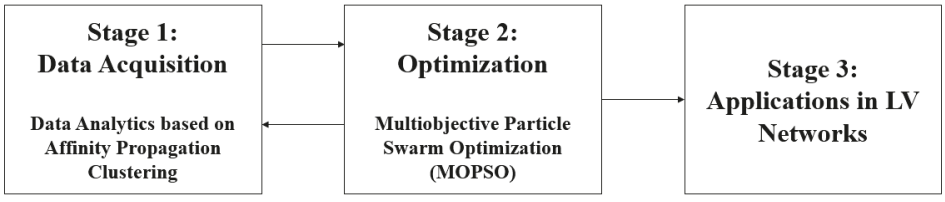

Figure 4. Stages of the methodology proposed.

Data analytics is approached here by means of an affinity propagation clustering technique [25]. Apart from initially considering any of those distribution network elements as potential cluster centers, this technique is characterized by not requiring any previous specification about the number of clusters to be formed, in addition to exchanging messages iteratively between elements until a high-quality set of exemplars and clusters emerges, doing so in less than one hundredth the time and at a lower error rate than other exemplar-based methods [25,52]. Consequently, only a basic identification and characterization of those assets to be clustered is needed to initiate the analytics.

The second stage focuses on determining the optimal congestion thresholds. For this, a particle swarm optimization (PSO) problem is formulated, which is a stochastic-based artificial intelligence search technique inspired on natural life [28]. A population of particles, called *swarm*, formed by points, *flows* through the search space taking into consideration the historical best position for each particle itself and the rest as a whole, naturally orienting the search towards an optimal or near-optimal solution [9,17].

Multi-objective PSO (MOPSO) is proposed here due to its capacity for simultaneous resolution of multiple conflicting objectives in congestion threshold determination [17]. In addition to this, MOPSO presents a low computational cost to provide a set of solutions, that, unlike classical multi-objective methods, are diverse and spread enough [17]. This allows for finding the best, non-trivial trade off among more than one objective, since no single solution may simultaneously optimize the whole search objective [53].

The affinity propagation clustering previously executed allows for the application of MOPSO only on the most representative element of each cluster. Then, the third stage addresses the extrapolation of the result obtained in the optimization process to the rest of assets.

3.1. Data Analytics based on Affinity Propagation Clustering

The affinity propagation algorithm [25] applied here is set with a dumping factor of 0.9 in order to avoid high numerical oscillations and favor the convergence of the clustering process, and is trained with a dataset formed by the characteristics listed on Table 1.

Table 1. Characteristic values of each network element of the dataset.

Criteria	Characteristic
Loading	Maximum congestion value measured
Repetition	Maximum congestion value measured after the 3 most critical days in a year Maximum congestion value measured after the 10 most critical days in a year Maximum congestion value measured after the 15 most critical days in a year
Time duration	Maximum congestion value measured after the 0.01% most critical scenarios in a year Maximum congestion value measured after the 0.1% most critical scenarios in a year Maximum congestion value measured after the 1% most critical scenarios in a year
Geographical	Number of points of delivery Total length of the element [1]
End users	Number of clients Percentage of domestic clients
Power	Nominal admissible power Total power contracted

[1] Total length of the element: 0 in the case of power transformers; including any segment downstream associated in the case of power lines.

Standardization in the clustering process is important, since the values of those characteristics are often measured in different units, meaning that some of them could be dominating other ones, hence influencing the course of the cluster analysis [54]. To overcome this, the characteristic values considered in this methodology are re-scaled by using min-max standardization.

In addition to the nominal admissible power or the maximum congestion value for each asset, such as power transformers or LV feeder, the time duration of those congested situations experienced has to be carefully considered, as in the case of Spain, where the annual maximum demand is denoted by the congestion level reached around the 100 most critical hours [55], about 0.01% of the year. Furthermore, here it is proposed to consider the number of different days where the maximum congestion levels took place in order to take into consideration the degree of repetition of those risky situations.

Other key aspects, such as the number and type of end users connected to every distribution network element, its length (which is zero in the case of power transformers, but includes any segment downstream associated in the case of LV feeder phases), or the total power contracted, are also considered. Hence, the clustering process provides a data analysis based not only on graphical features of each load duration curve, but also based on physical parameters of the corresponding asset.

3.2. Multi-Objective Particle Swarm Optimization

The determination of the optimal congestion threshold is a constrained optimization problem where a specific multi-objective function is minimized. The aim is to find the optimal characteristic value of congestion in the load duration curve of a distribution network element considered, valid for the longest time scenarios of operation and being the closest to the maximum demand level experienced on it.

The multi-objective function is formed by three subfunctions. The first objective subfunction F_{obj_1} aims to minimize the standard deviation of the congestion characteristic values ϕ of the load duration curve, leading to select groups of points that are more concentrated around a certain congestion level. This diminishes the influence of abrupt changes in congestion characteristic values, exceptionally unconnected with neighboring values, and typically corresponding to the highest demand scenarios.

The second objective subfunction F_{obj_2} tackles the percentage of time scenario characteristic values ρ of the load duration curve. Having the maximum standard deviation here aims to find a solution far from unrepresentative short time variations. This subfunction is characterized by the inverse of the standard deviation in order to fit it in the minimization of the multi-objective problem.

Finally, the third objective subfunction F_{obj_3} addresses the inclination angle φ by scoring linearly between 0 and 10 points of the linear regression of any group of points forming a particle of the load duration curve. An inclination angle of 45° presents the best compromise between congestion measurements and time scenarios, namely, between its vertical and horizontal projections. However, with the aim of not losing the influence of the highest demand experienced, a favorable inclination angle, called φ_{fav}, must be set above 45°, helping the optimization problem converge towards more stabilized congestion characteristic values but without being too close to 90° and then falling into unrepresentative, extremely brief, and highest-congestion scenarios. A band of the most favorable angles, φ_{band}, is also set in order to help define diverse punctuation areas, as shown in Figure 5. This objective subfunction is characterized by the inverse, as expressed in Equation (7), in order to fit it in the minimization of the multi-objective problem, as in the case of objective subfunction 2.

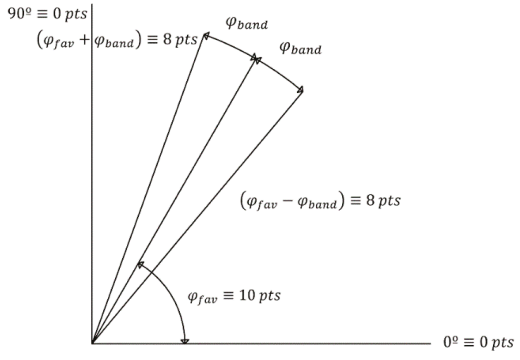

Figure 5. Representation of value assignation according to the favorable inclination angle set.

Therefore, the formulation of this multi-objective is stated as follows:

$$\begin{gathered} \text{Minimize}: \; F_{obj}(\phi,\, \rho,\, \varphi) = \; f\Big(F_{obj_1}(\phi),\, F_{obj_2}(\rho),\, F_{obj_3}(\varphi)\Big) \\ \text{Subject to}: \; \phi \geq \phi_{limit} \end{gathered} \tag{1}$$

The problem constraint $\phi \geq \phi_{limit}$ refers to all those congestion characteristic values above a particular value, which is considered to represent a realistic, considerable, potential risk of saturation of the distribution network elements. It is recommended to consider a wider range of congestion states

than in traditional criteria, as mentioned in Section 2 for 95% [18] and 75% [19], in order to cover a broader set of representative scenarios and then to avoid extremely singular transient states.

By checking compliance with this restriction, MOPSO is not applied in the case of those clusters whose elements are not satisfying the problem constraints for none of the points of their load duration curves, since they are not considered to be above a minimum level of potential risk.

In our methodology, and according to MOPSO algorithm, the *swarm* is formed by N particles, each of them composed by n points, as displayed in Figure 6, that move along the search space, that is to say, in a certain load duration curve. Consequently, each particle j is characterized by the congestion ϕ_j and the corresponding percentage of time scenarios ρ_j of its center, and its position $x_j(t)$ in a moment of time t along the load duration curve depends on its previous position $x_j(t-1)$ and its velocity $v_j(t)$ [27]:

$$x_j(t) = x_j(t-1) + v_j(t). \tag{2}$$

This velocity $v_j(t)$ is composed by terms related to the inertia ω_j and the velocity of the particle in the previous state $v_j(t-1)$ to represent its tendency to continue in the same direction, and the attraction towards the best position $p_{j_{best}}$ ever found by the particle and by any of the particles of the swarm $p_{global\ best}$ [27]:

$$v_j(t) = \omega_j \cdot v_j(t-1) + \psi_1 \cdot rand_1 \cdot \left(p_{j_{best}} - x_j(t-1)\right) + \psi_2 \cdot rand_2 \cdot \left(p_{global\ best} - x_j(t-1)\right). \tag{3}$$

Authors in Reference [27] pointed that the sum of constants ψ_1 and ψ_2 should be 4.0, meaning $\psi_1 = \psi_2 = 2$ to give the same weight to the individual and group experience. $rand_1$ and $rand_2$ are random values between 0 and 1 [27], and the inertia of the particle ω_j is given by:

$$\omega_j = \omega_{max} - \frac{\omega_{max} - \omega_{min}}{iter_{max}} \cdot iter_i \tag{4}$$

where ω_{max} and ω_{min} are also constant values set at 1 and 0 respectively, in order to reach an initial high value near to 0.9 as pointed in Reference [27], hence moving fast towards the global optimum.

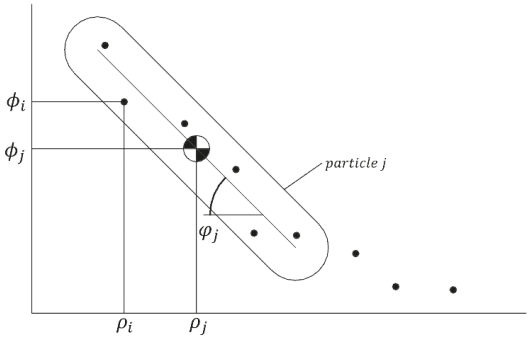

Figure 6. Representation of congestion, time scenarios, and inclination characteristic values of a generic particle formed by a series of points.

Therefore, in each iteration, every ϕ_j and ρ_j corresponding to the center of each particle, in addition to ϕ_i, ρ_i and the inclination angle of the linear regression φ_j of their n points, will be evaluated in the following subfunctions of the multi-objective function, leading to a solution:

$$F_{obj_1}(\phi_j) = \sqrt{\frac{1}{n-1}\sum_{i=1}^{n}\left(\phi_i - \overline{\phi}_j\right)^2} \tag{5}$$

$$F_{obj_2}(\rho_j) = \frac{1}{\sqrt{\frac{1}{n-1}\sum_{i=1}^{n}\left(\rho_i - \overline{\rho}_j\right)^2}} \tag{6}$$

$$\frac{1}{F_{obj_3}(\varphi_j)} = \begin{cases} 8 \cdot \frac{\varphi_j}{\left(\varphi_{fav} - \varphi_{band}\right)} \; if \; \varphi_j \leq \varphi_{fav} - \varphi_{band} \\ 8 + 2 \cdot \frac{\varphi_j - \left(\varphi_{fav} - \varphi_{band}\right)}{\varphi_{band}} \; if \; \varphi_j \in \left(\varphi_{fav} - \varphi_{band}, \varphi_{fav}\right) \\ 10 \; if \; \varphi_j = \varphi_{fav} \\ 8 + 2 \cdot \frac{\left(\varphi_{fav} + \varphi_{band}\right) - \varphi_j}{\varphi_{band}} \; if \; \varphi_j \in \left(\varphi_{fav}, \; \varphi_{fav} + \varphi_{band}\right) \\ 8 \cdot \frac{90 - \varphi_j}{90 - \left(\varphi_{fav} + \varphi_{band}\right)} \; if \; \varphi_j \geq \varphi_{fav} + \varphi_{band} \end{cases} \tag{7}$$

where: $\overline{\phi}_j$ is the mean congestion value in the particle j; $\overline{\rho}_j$ is the mean percentage time scenario value in the particle j.

Pareto dominance must be checked every time the position of a swarm is updated, storing those non-dominated solutions among the obtained for the N particles after their evaluation on the mentioned subfunctions of the multi-objective function, in order to approximate the Pareto front [9].

In relation to this, the first stopping criterion is determined for the algorithm developed here: The global optimum results from the best particle of the swarm after a certain number of consecutive iterations without any progress in the Pareto front. In addition to this, the second stopping criterion consists of a maximum number of iterations.

As pointed out in Section 1, other advanced optimization algorithms, such as genetic and ant colony algorithms, apart from being more complex than this PSO-based approach, present serious restrictions to be applied in our methodology due to the impossibility to cross and mutate points defined by non-independent congestion and time characteristics [29,30], and to the absence of a clear, predefined optimal solution area [32].

3.3. Applications in LV Networks

This methodology can be applied on wide groups of distribution network elements by means of the ratio between the optimal congestion threshold $\phi_k^{opt\_calc}$ determined by the MOPSO algorithm and the maximum congestion value measured ϕ_k^{max} for each cluster center k. Therefore, this so-called *threshold ratio*$_k$ can be employed individually on any of the members m belonging to that cluster k in order to determine its particular optimal congestion threshold ϕ_m^{opt}, where:

$$threshold\ ratio_k(\%) = \frac{\phi_k^{opt\_calc}}{\phi_k^{max}} \cdot 100 \tag{8}$$

$$\phi_m^{opt} = threshold\ ratio_k \cdot \phi_m^{max} \tag{9}$$

Moreover, the use of the threshold ratio reflects the existing differences among the congestion experienced in each element, instead of simply imposing the optimal of the cluster center. Thus, the application of the methodology follows the flowchart described in Figure 7.

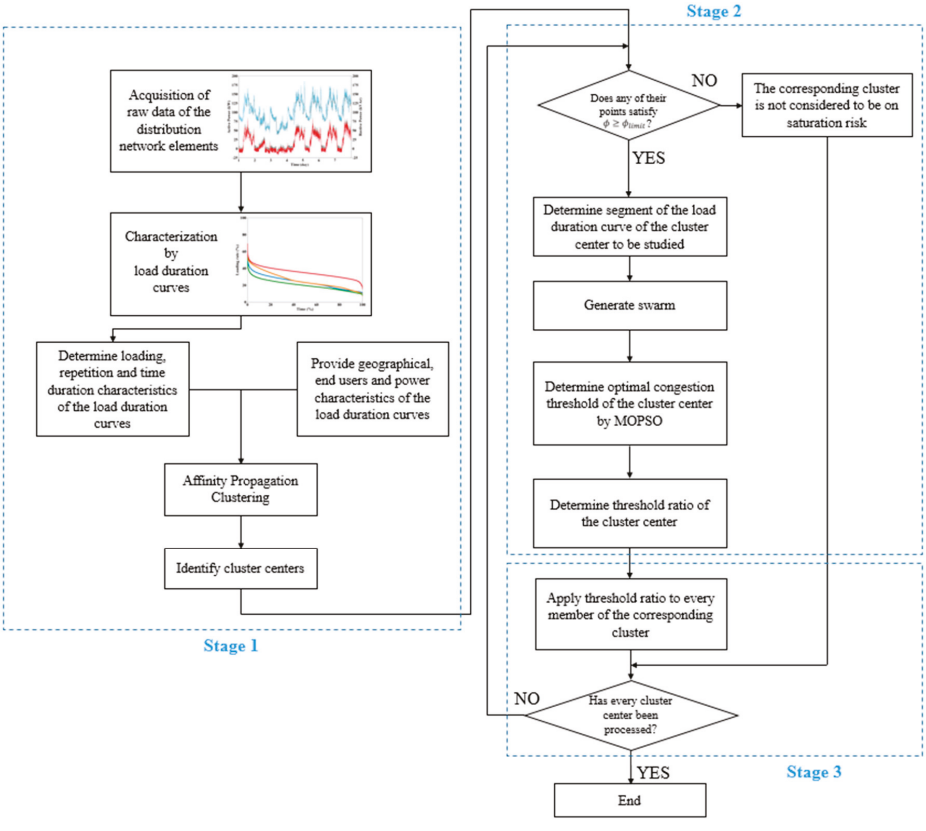

Figure 7. General flowchart of the methodology.

4. Results and Discussion

This methodology has been applied on real data obtained from Smartcity Malaga Living Lab. In particular, data from five MV/LV secondary substations are considered here, including a total of six power transformers and their 18 corresponding LV side phases. In addition to this, as displayed in Table 2, their corresponding 45 LV feeder lines, with three phases in each case, are also here considered, therefore taking into account their highly dispersed and heterogeneous distribution of clients, as shown in Figure 1. Consequently, this methodology has been implemented on load duration curves from 153 distribution network elements, a group of elements linked to around 5000 out of the 15,000 real end users of the Living Lab.

Table 2. Distribution network elements of the group considered in the case study.

Secondary Substation	Power Transformers	LV Feeders	Distribution Network Elements
A	1	7	24
B	1	7	24
C	1	7	24
D	2	12	42
E	1	12	39

4.1. Data Analytics for Data Pre-Processing

Every distribution network element has been characterized by 5-min data acquisition during a whole year period, meaning more than 109,000 current measurements in each case. Thus, this group formed by a total of 153 elements involves handling around 16,000,000 data. Consequently, the size of this dataset provides a wide, varied dataset to reflect the reality of the operation and maintenance of the distribution networks, not only because of the number of assets considered, but also because of the time interval, including summertime, wintertime, working days, and holidays.

According to the methodology detailed in Section 3, the first stage is data analytics. Applying affinity propagation to cluster those 153 elements results in the composition of four different clusters, as shown in Figures 8–10, and the identification of their corresponding cluster centers listed in Table 3.

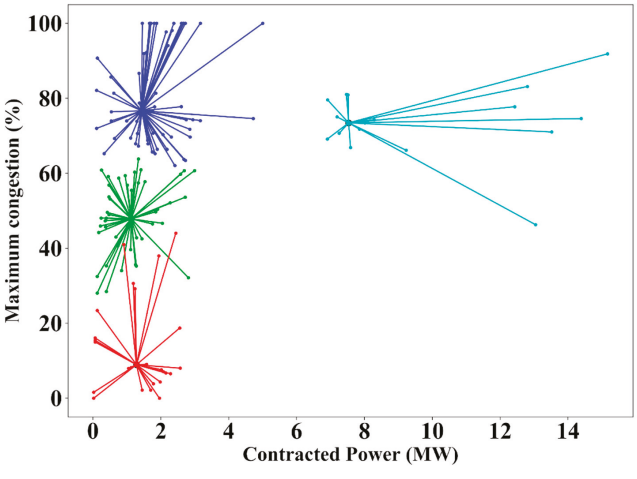

Figure 8. Maximum congestion in relation to the total contracted power in the case study.

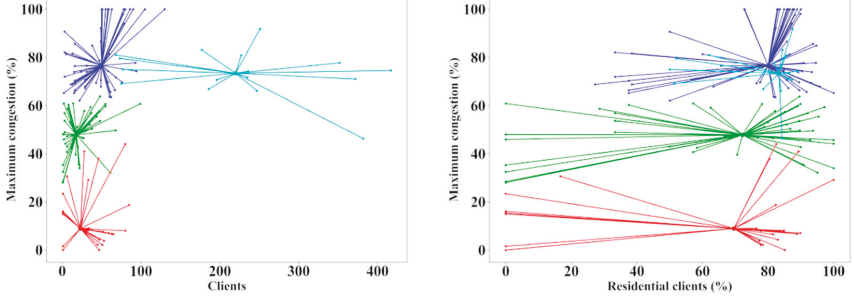

(**a**) (**b**)

Figure 9. (**a**) Maximum congestion in relation to the number of clients and (**b**) in relation to the proportion of residential clients in the case study.

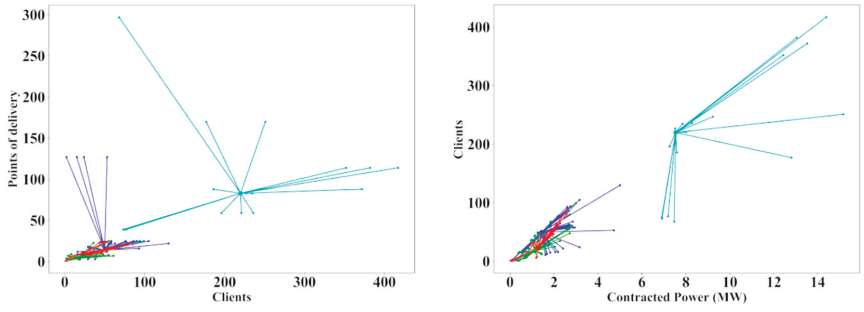

(**a**) (**b**)

Figure 10. (**a**) Number of clients in relation to the number of points of delivery and (**b**) in relation to the contracted power in the case study.

Table 3. Composition of the clusters.

Cluster	Cluster Center	Color	Cluster Members
1	Secondary Substation D LV Feeder 7 Phase T	Dark blue	61
2	Secondary Substation D LV Feeder 14 Phase S	Green	47
3	Secondary Substation D Transformer 2 Phase S	Light blue	18
4	Secondary Substation E LV Feeder 9 Phase T	Red	27

The lowest values obtained at the maximum congestion characteristic can be found in the members of cluster 4. Although all the power transformers of the group belong to cluster 3, which has the least number of members, clusters 1, 2, and 4 are highly heterogeneous since they have LV feeder phases belonging to every secondary substation of the group. In addition to this, three out of the four cluster centers belong to the same secondary substation, which evidences the diversity among elements that can be found even in the same asset of the distribution network.

Regarding maximum congestion, 16 distribution network elements have measured values over 95% of their maximum admissible power [18], and 14 out of them reached their nominal maximum congestion of 100%. Regarding the conventional congestion threshold of 75% [19], 40 elements experienced congestion over that limit, and only 10 out of them remain over it at 1% of time scenarios. At the same time, 29 elements present a maximum congestion value measured below 35%, representing almost the fifth part of the group, and 17 out of them remained below 10%.

The highest number of clients in a secondary substation, by grouping those connected to the three LV sides of its power transformer, is around 1300 clients, and the lowest is 225, while the average per LV feeder phase is 37 clients, ranging from 1 to 130. Despite the area being predominantly residential, representing 50% or more of the clients in 100 LV feeder phases, only 15 LV feeder phases present 100% industrial clients.

Geographically, more than 600 points of delivery are included in the group of elements, ranging from 1 to 25 per LV feeder phase and with an average of 14 per each of them. The average length per LV feeder phase is 200 m. The clustering executed here makes it possible to identify differences that are not easily discernible a priori, as can be seen in Figure 10, where most of the elements from clusters 1, 2, and 4 are coincident for the represented characteristics.

4.2. Optimization

The second stage of the methodology is optimization. To evaluate the different cluster centers obtained, a particular $\phi_{limit} = 35\%$ is set in order to focus the analysis only on potentially risky congestion states, according to the reality observed in the real electrical network of study of Smartcity

Malaga Living Lab. In addition to this, ϕ_{limit} adapts the methodology to the search space without rejecting any predetermined proportion or number of assets.

Once ϕ_{limit} restrictions have been checked, it is observed that the cluster center 4, in red in Figures 8–10, does not satisfy it for any of its points. Therefore, this cluster is out of the following optimization process because of not being in a situation of risk minimally considerable. At the same time, applying ϕ_{limit} to the cluster centers 1, 2, and 3 allow for the focus of the optimization problem in a limited set of points of their load duration curves, listed in Table 4, corresponding to the most saturated scenarios.

Table 4. Number of points considered for the execution of the multi-objective particle swarm optimization (MOPSO) algorithm.

Cluster Center	Points in Raw Load Duration Curve	Points above ϕ_{limit}
1	1196	600
2	1772	117
3	597	195

MOPSO is then applied on cluster centers 1, 2, and 3, where a favorable inclination angle $\varphi_{fav} = 75°$, a tolerance band $\varphi_{band} = 5°$, a maximum number of iterations without any progress in Pareto front $iter_{Pareto\ front} = 10$, and a maximum number of iterations $iter_{max} = 100$ have been set. The initialization of the population is carried out by means of a random stochastic process that distributes them arbitrarily along the search space. The optimization algorithm that has been executed for the series of particles and their corresponding points is shown in Table 5.

Table 5. Populations considered for the execution in the MOPSO algorithm.

Case	Particles	Points per Particle
1	15	3
2	20	3
3	30	3
4	30	5
5	20	5
6	15	5

The results obtained from the MOPSO algorithm developed are displayed in Table 6 showing a good robustness of the method, with a low standard deviation despite being a stochastic-based method. Therefore, the methodology can be considered to be slightly dependent on the size of the population.

Table 6. Optimal congestion thresholds of the cluster centers.

Cluster Center	Maximum Congestion Measured	Optimal Congestion Threshold						
		Case 1	Case 2	Case 3	Case 4	Case 5	Case 6	Standard Deviation
1	76.65%	68.00%	66.62%	66.00%	67.15%	66.00%	66.00%	0.01
2	47.84%	34.97%	35.55%	35.90%	35.65%	39.62%	37.49%	0.04
3	73.44%	60.97%	64.30%	55.15%	64.57%	64.57%	65.68%	0.05

A representation of the evolution in the values obtained in the three objective subfunctions is displayed in Figure 11. Particularly, those are the values obtained by the best particle in each iteration of the algorithm in the Case 1, which is formed by a swarm of 15 particles with 3 points each, applied to cluster center 1. It must be noted that the role of the best particle can be played by different particles of the swarm along the different iterations, according to Pareto compliance.

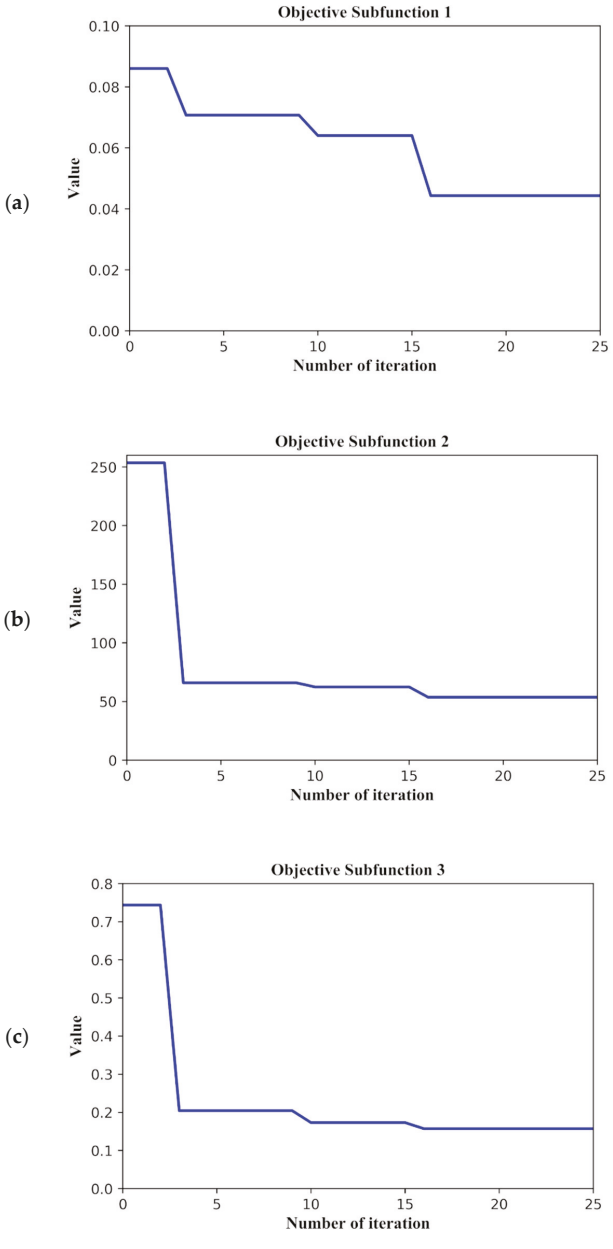

Figure 11. Evolution in the values obtained, for the best particle of each iteration, in case 1 applied to cluster 1, in the objective subfunctions of (**a**) congestion characteristic values, (**b**) time scenario characteristic values, and (**c**) inclination angle.

The example displayed in Figure 11 shows how values obtained for objective subfunctions 1, 2, and 3 are decreasing progressively, but not continuously, towards the minimum, leading to identifying a particle with the corresponding optimal congestion characteristic value of 68.00% displayed in Table 6. The global optimum finally results after 25 iterations, meaning that the stopping criterion of

10 consecutive iterations without any progress in the Pareto front has been applied; hence, the other stopping criterion of a maximum number of iterations of 100 has not been reached.

Apart from considering a favorable inclination angle of 75° ± 5°, the MOPSO algorithm has also been executed for 70° ± 5° and 65° ± 5°. As shown in the results displayed in Figure 11 for cluster center 2, the algorithm presents a good stability in the results obtained and therefore a low dependence on this parameter, as evidenced in Figure 12, despite the varied characteristics of the swarms employed. In addition to this, it evidences that higher values of favorable inclination angles result in higher optimal values due to the greater influence of the maximum congestion values measured in the element.

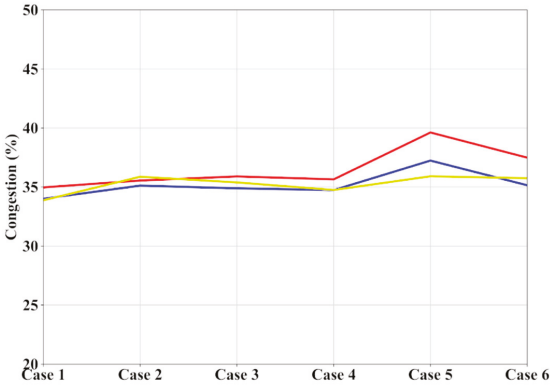

Figure 12. Optimal congestion thresholds for cluster center 2 considering favorable inclination angles of 75° (in red), 70° (in blue), and 65° (in yellow).

4.3. Application on the Distribution Network of the Case Study

The third and last stage of the methodology is its application in LV networks. To do so, once the congestion thresholds have been determined for each cluster center, the mean threshold ratio is calculated for each cluster center of the case study, as shown in Table 7.

Table 7. Threshold ratios calculated for the cluster centers.

Cluster Center	Threshold Ratio						
	Case 1	**Case 2**	**Case 3**	**Case 4**	**Case 5**	**Case 6**	**Mean**
1	88.71%	86.91%	86.11%	87.61%	86.11%	86.11%	**86.93%**
2	73.10%	74.31%	75.04%	74.52%	82.82%	78.37%	**76.36%**
3	83.02%	87.55%	75.10%	87.92%	87.92%	89.43%	**85.16%**

Therefore, by applying the corresponding mean threshold ratio, an individual, particular optimal congestion threshold is set for 135 out of the 153 distribution network elements of Smartcity Malaga Living Lab belonging to clusters 1, 2, and 3. To cite some relevant figures, 22 distribution network elements have been set with optimal thresholds over the conventional 75% [19] of their maximum admissible power, 63 elements over 60%, and 78 over 50%.

The numerical results here obtained, as displayed in Figure 13, provide the network operators with an objective, individual determination of the optimal congestion threshold in order to establish supervision and control strategies such as those mentioned in Sections 1 and 2. In addition to this, as shown in Table 8 in the case of the cluster centers, this methodology provides the time scenarios corresponding to those optimal congestion thresholds.

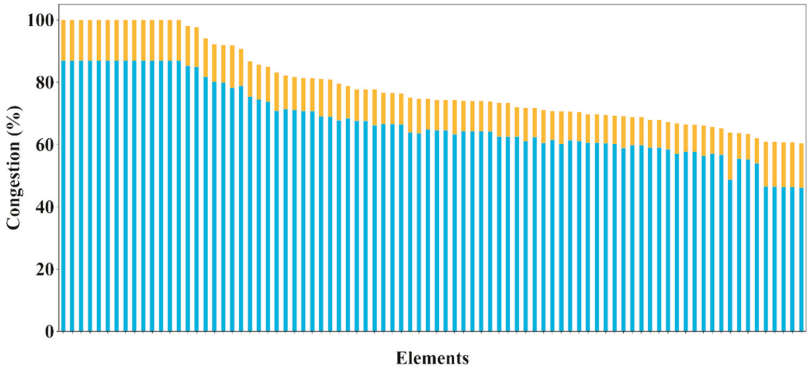

Figure 13. Maximum congestion measured (in orange) and optimal congestion threshold assigned (in blue) in the most saturated elements in the case study.

Table 8. Threshold ratios and time characteristics of the cluster centers.

Cluster Center	Maximum Congestion Measured	Optimal Congestion Threshold	Threshold Ratio	Optimal Percentage of Time Scenario	Optimal Number of Time Scenarios	Different Days of Occurrence
1	76.65%	66.63%	86.93%	0.025%	27	13
2	47.84%	36.53%	76.36%	0.038%	40	22
3	73.44%	62.54%	85.16%	0.050%	53	28

For instance, in the case of cluster center 1, the optimal congestion threshold determined at 66.63% potentially means intervening in 0.025% of the year of time considered in this dataset. Even more, 27 different scenarios experienced congestion above that threshold, each one of a 5-min duration, taking place over 13 different days. In this way, the distribution network elements of the group can be ranked according to their optimal congestion threshold but also considering the number of congested time scenarios, as displayed in Figure 14, given the useful additional information provided.

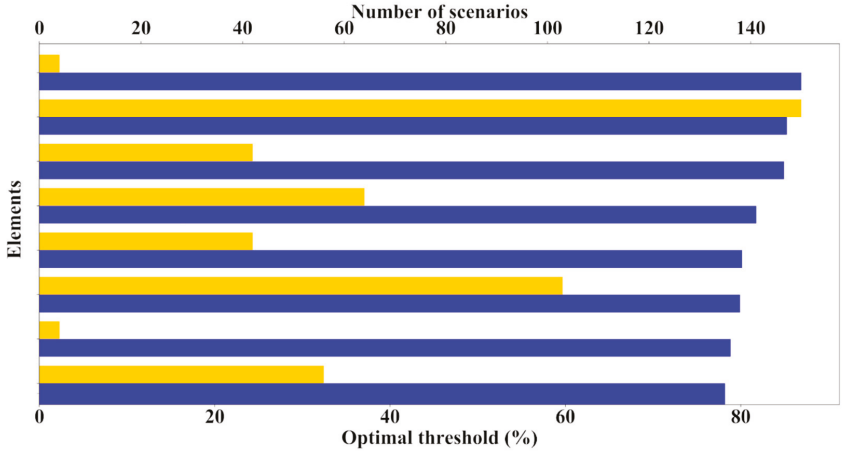

Figure 14. Optimal congestion threshold (in blue) and number of time scenarios (in orange) in a set of elements in the case study.

Moreover, the previous set of distribution network elements can also be ranked according to their optimal congestion threshold but considering now the number of different days presenting congestion, as displayed in Figure 15; hence, a totally different ranking can be composed, since there is not a direct relation between them.

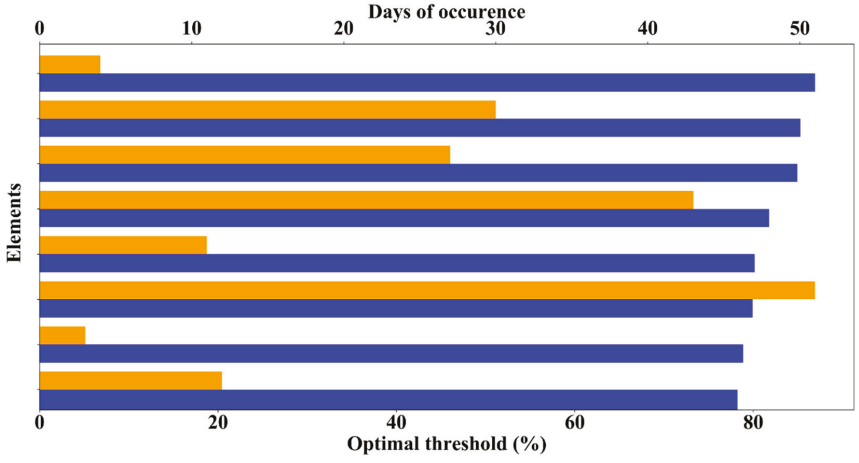

Figure 15. Optimal congestion threshold (in blue) and days of occurrence (in orange) in a set of elements in the case study.

Consequently, this methodology allows DSOs to tackle potential congestion states in their assets by prioritizing the operation of those distribution network elements which are closer to saturation according to both the optimal threshold determined and the expected congested situations.

5. Conclusions

This methodology provides a tool that supports DSOs in making decisions to manage congestion in any of the elements of the distribution network, such as MV/LV power transformers or LV feeders and their corresponding phases. It allows them to operate and maintain their assets in a preventive way beyond the classic planning criteria traditionally used, hence bringing an alternative to oversizing and reinforcements, and not based on previous, subjective precedents. Moreover, the methodology has been validated with real data obtained from Smartcity Malaga Living Lab, under real operating conditions.

Due to the means available today for the digitalization of the network, the large volumes of data to be handled far outweigh human experience, as in the case study presented here, based on a dataset formed by more than 16,000,000 data for a single year from a network related to around 5000 real end users. The pre-processing performed by means of affinity propagation clustering results in a more efficient computational analysis. Thus, the 153 distribution network elements considered here were divided into four clusters, with three of them meeting the restrictions of the optimization problem. In the case of the fourth cluster, formed by 18% of the distribution network elements, their congestion levels were not considered to be over a minimum level of risk.

The optimization process carried out provides enriched criteria with respect to traditional methods, such as considering a fixed threshold of 75%, which implies only 26% of the elements were considered to be over a minimum risky saturation level, and even less in the case of 95% fixed threshold. Meanwhile, our MOPSO algorithm not only takes into account congestion, but also time scenarios, in order to determine an optimal congestion threshold to 82% of the elements of the group of study, characterizing them individually and under an objective basis. Furthermore, 41% of the elements of the case study were provided with optimal congestion thresholds over 60% of their nominal admissible power,

evidencing that using this methodology gives an expanded view of congestion situations that are not negligible under preventive operation and maintenance standards.

The methodology can be applied to online processing. Nonetheless, an adaptation of the methodology may be necessary. The computational time required, and the granularity and size of the dataset considered, must be carefully assessed, having in mind that, as in the case of the clustering process considered here, data analytics techniques may help in handling those massive datasets. In addition to this, the availability of online data is a major issue, since proper data acquisition, processing, and provision to the methodology must be designed, for example by means of big data techniques [56], since, as the network conditions change, the optimization solution and clusters might change as well.

Author Contributions: Conceptualization, J.L. and J.A.A.; methodology, J.L. and R.C.P.; software, J.L. and R.C.P.; supervision, J.A.A.; validation, J.L.; writing—original draft, J.L.; writing—review and editing, R.C.P. and J.A.A.

Funding: This work has been partially funded by the project ENE2016-80638-R granted by *Ministerio de Economía y Competitividad* of the Government of Spain.

Conflicts of Interest: The authors declare no conflict of interest.

References

1. Hague, A.N.M.M.; Nguyen, P.H.; Vo, T.H.; Bliek, F.W. Agent-based unified approach for thermal and voltage constraint management in LV distribution network. *Electr. Power Syst. Res.* **2017**, *143*, 462–473. [CrossRef]
2. You, S.; Segerberg, H. Integration of 100% micro-distributed energy resources in the low voltage distribution network: A Danish case study. *Appl. Therm. Eng.* **2014**, *71*, 797–808. [CrossRef]
3. Chua, K.H.; Wong, J.; Lim, Y.S.; Taylor, P.; Morris, E.; Morris, S. Mitigation of Voltage Unbalance in Low Voltage Distribution Network with High Level of Photovoltaic System. *Energy Procedia* **2011**, *12*, 495–501. [CrossRef]
4. Kadam, S.; Bletterie, B.; Gawlik, W. A Large Scale Grid Data Analysis Platform for DSOs. *Energies* **2017**, *10*, 1099. [CrossRef]
5. Lu, S.; Repo, S.; Della, G.; Della Gustina, D.; Álvarez-Cuevas, F.; Löf, A.; Pikkarainen, M. Real-Time Low Voltage Network Monitoring-ICT Architecture and Field Test Experience. *IEEE Trans. Smart Grid* **2015**, *6*, 2002–2012. [CrossRef]
6. Li, R.; Gu, C.; Li, F.; Shaddick, G.; Dale, M. Development of Low Voltage Network Templates-Part I: Substation Clustering and Classification. *IEEE Trans. Power Syst.* **2015**, *30*, 3036–3044. [CrossRef]
7. Caldon, R.; Coppo, M.; Turri, R. Distributed voltage control strategy for LV networks with inverter-interfaced generators. *Electr. Power Syst. Res.* **2014**, *107*, 85–92. [CrossRef]
8. Håberg, M.; Bood, H.; Doorman, G. Preventing Internal Congestion in an Integrated European Balancing Activation Optimization. *Energies* **2019**, *12*, 490. [CrossRef]
9. Zhang, Y.; Wang, S.; Ji, G. A Comprehensive Survey on Particle Swarm Optimization Algorithm and Its Applications. *Math. Probl. Eng.* **2015**, *2015*, 931256. [CrossRef]
10. Hazra, J.; Sinha, A.K. Congestion Management Using Multiobjective Particle Swarm Optimization. *IEEE Trans. Power Syst.* **2007**, *22*, 1726–1734. [CrossRef]
11. Reihani, E.; Motalleb, M.; Ghorbani, R.; Saoudb, L.S. Load peak shaving and power smoothing of a distribution grid with high renewable energy penetration. *Renew. Energy* **2016**, *86*, 1372–1379. [CrossRef]
12. Tuballa, M.L.; Abundo, M.L. A review of the development of Smart Grid technologies. *Renew. Sustain. Energy Rev.* **2016**, *59*, 710–725. [CrossRef]
13. Vandoorn, T.L.; de Vyver, J.V.; Gevaert, L.; Degroote, L.; Vandevelde, L. Congestion Control Algorithm in Distribution Feeders: Integration in a Distribution Management System. *Energies* **2015**, *8*, 6013–6032. [CrossRef]
14. Cao, C.; Wang, L.; Chen, B. Mitigation of the Impact of High Plug-in Electric Vehicle Penetration on Residential Distribution Grid Using Smart Charging Strategies. *Energies* **2016**, *9*, 1024. [CrossRef]
15. Romero-Ruiz, J.; Pérez-Ruiz, J.; Martín, S.; Aguado, J.A.; de la Torre, S. Probabilistic Congestion Management using EVs in a Smart Grid with intermittent Renewable Generation. *Electr. Power Syst. Res.* **2016**, *137*, 155–162. [CrossRef]

16. Esmat, A.; Usaola, J.; Moreno, M.A. Distribution-Level Flexibility Market for Congestion Management. *Energies* **2018**, *11*, 1056. [CrossRef]
17. Lalwani, S.; Singhal, S.; Kumar, R.; Gupta, N. A comprehensive survey: Applications of multi-objective particle swarm optimization (MOPSO) algorithm. *Trans. Comb.* **2013**, *2*, 39–101. [CrossRef]
18. Spanish Electricity System 2017 Report. Red Eléctrica de España. Available online: https://www.ree.es/en/statistical-data-of-spanish-electrical-system/annual-report/spanish-electricity-system-2017-report (accessed on 25 February 2019).
19. Instalaciones en Alerta. Organismo Supervisor de la Inversión en Energía y Minería de Perú. Available online: http://www.osinergminorienta.gob.pe/web/rcc/catalogos (accessed on 25 February 2019).
20. Siano, P.; Sarno, D. Assessing the benefits of residential demand response in a real time distribution energy market. *Appl. Energy* **2016**, *161*, 533–551. [CrossRef]
21. Sherif, I.; Shady, A.A.; Almoataz, A.; Ahmed, Z. State-of-the-art of hosting capacity in modern power systems with distributed generation. *Renew. Energy* **2019**, *130*, 1002–1020. [CrossRef]
22. Abdel-Majeed, A.; Braun, M. Low Voltage System State Estimation Using Smart Meters. In Proceedings of the 47th International Universities Power Engineering Conference (UPEC), London, UK, 4–7 September 2012; pp. 1–6. [CrossRef]
23. Niederhuemer, W.; Schwalbe, R. Increasing PV hosting capacity in LV grids with a probabilistic planning approach. In Proceedings of the 2015 International Symposium on Smart Electric Distribution Systems and Technologies (EDST), Vienna, Austria, 8–11 September 2015; pp. 537–540.
24. Roldán-Blay, C.; Escrivá- Escrivá, G.; Roldán-Porta, C. Improving the benefits of demand response participation in facilities with distributed energy resources. *Energies* **2019**, *169*, 710–718. [CrossRef]
25. Frey, B.J.; Dueck, D. Clustering by passing messages between data points. *Science* **2007**, *315*, 972–976. [CrossRef] [PubMed]
26. Zhang, X.; Furtlehner, C.; Germain-Renaud, C.; Sebag, M. Data Stream Clustering With Affinity Propagation. *IEEE Trans. Knowl. Data Eng.* **2014**, *26*, 1644–1656. [CrossRef]
27. del Valle, Y.; Venayagamoorthy, G.K.; Mohagheghi, S.; Hernandez, J.C.; Harley, R.G. Particle Swarm Optimization: Basic Concepts, Variants and Applications in Power Systems. *IEEE Trans. Evol. Comput.* **2008**, *12*, 171–195. [CrossRef]
28. Kennedy, J.; Eberhart, R. Particle swarm optimization. In Proceedings of the ICNN'95—International Conference on Neural Networks, Perth, Australia, 27 November–1 December 1995; pp. 1942–1948. [CrossRef]
29. Jones, K.O. Comparison of Genetic Algorithm and Particle Swarm Optimisation. In Proceedings of the International Conference on Computer Systems and Technologies, Varna, Bulgaria, 16–17 June 2005; Section IIIA.
30. Bai, Q. Analysis of Particle Swarm Optimization Algorithm. *Comput. Inf. Sci.* **2010**, *3*, 180–184. [CrossRef]
31. Chen, R.M.; Shen, Y.M.; Wang, C.T. Ant Colony Optimization Inspired Swarm Optimization for Grid Task Scheduling. In Proceedings of the International Symposium on Computer, Consumer and Control (IS3C), Xian, China, 4–6 July 2016; pp. 461–464. [CrossRef]
32. Selvi, V.; Umarani, R. Comparative Analysis of Ant Colony and Particle Swarm Optimization Techniques. *Int. J. Comput. Appl.* **2010**, *5*, 1–6. [CrossRef]
33. Endesa desarrolla un sistema para controlar en tiempo real la red de distribución. Available online: https://www.endesa.com/es/prensa/news/d201811-endesa-desarrolla-un-sistema-para-controlar-en-tiempo-real-la-red-de-distribucion.html (accessed on 25 February 2019).
34. Sathiskumar, M.; Kumar, A.N.; Lakshminarasimman, L.; Thiruvenkadam, S. A self adaptive hybrid differential evolution algorithm for phase balancing of unbalanced distribution system. *Int. J. Electr. Power Energy Syst.* **2012**, *42*, 91–97. [CrossRef]
35. Velez, V.M.; Hincapie, R.A.; Gallego, R.A. Low voltage distribution system planning using diversified demand curves. *Int. J. Electr. Power Energy Syst.* **2014**, *61*, 691–700. [CrossRef]
36. Smartcity Málaga Living Lab: A laboratory to create the city of the future. Available online: https://www.endesa.com/en/projects/a201801-living-lab-malaga-city-future.html (accessed on 25 February 2019).
37. Calderaro, V.; Conio, G.; Galdi, V.; Piccolo, A. Reactive power control for improving voltage profiles: A comparison between two decentralized approaches. *Electr. Power Syst. Res.* **2012**, *83*, 247–254. [CrossRef]

38. Soyster, A.L.; Eynon, R.T. The Conceptual Basis of the Electric Utility Sub-model of Project Independence Evaluation System. In Proceedings of the Seminar of the United Nations Economics Commission for Europe, Washington, DC, USA, 24–28 March 1980; Energy Modelling Studies and Conservation, 1982; pp. 417–429. [CrossRef]
39. Wu, A.; Ni, B. *Line Loss Analysis and Calculation of Electric Power Systems*, 2nd ed.; Wiley: Hoboken, NJ, USA, 2016. [CrossRef]
40. AENOR. *Standard UNE-EN 50160:2011/A1:2015*; AENOR: Madrid, Spain, 2015.
41. Zhao, Z.Y.; Tang, C.; Zhou, Q. Identification of Power Transformer Winding Mechanical Fault Types Based on Online IFRA by Support Vector Machine. *Energies* **2017**, *10*, 2022. [CrossRef]
42. Tenbohlen, S.; Coenen, S.; Djamali, M.; Müller, A.; Samimi, M.H.; Siegel, M. Diagnostic measurements for power transformers. *Energies* **2016**, *9*, 347. [CrossRef]
43. Wang, K.; Skiena, S.; Robertazzi, T.G. Phase balancing algorithms. *Electr. Power Syst. Res.* **2013**, *96*, 218–224. [CrossRef]
44. Carillo-Aparicio, S.; Heredia-Larrubia, J.R.; Perez-Hidalgo, F.M. Smart City Málaga, a real-living lab and its adaptation to electric vehicles in cities. *Energy Policy* **2013**, *62*, 774–779. [CrossRef]
45. Barbato, A.; Dede, A.; Della Giustina, D.; Massa, G.; Angioni, A.; Lipari, G.; Ponci, F.; Repo, S. Lessons learnt from real-time monitoring of the low voltage distribution network. *Sustain. Energy Grids Netw.* **2018**, *15*, 76–85. [CrossRef]
46. Gomez-Exposito, A.; Arcos-Vargas, A.; Maza-Ortega, J.M.; Rosendo-Macías, J.A.; Alvarez-Cordero, G.; Carillo-Aparicio, S.; González-Lara, J.; Morales-Wagner, D.; González-García, T. City-Friendly Smart Network Technologies and Infrastructures: The Spanish Experience. *Proc. IEEE* **2018**, *106*, 626–660. [CrossRef]
47. Navarro-Espinosa, A.; Mancarella, P. Probabilistic modeling and assessment of the impact of electric heat pumps on low voltage distribution networks. *Appl. Energy* **2014**, *127*, 249–256. [CrossRef]
48. Nijhuis, M.; Gibescu, M.; Cobben, S. Gaussian Mixture Based Probabilistic Load Flow for LV-Network Planning. *IEEE Trans. Power Syst.* **2017**, *32*, 2878–2886. [CrossRef]
49. Rodriguez-Calvo, A.; Cossent, R.; Frias, P. Integration of PV and EVs in unbalanced residential LV networks and implications for the smart grid and advanced metering infrastructure deployment. *Int. J. Electr. Power Energy Syst.* **2017**, *91*, 121–134. [CrossRef]
50. Tehrani, M.K.; Fereidunian, A.; Lesani, H. Financial planning for the preventive maintenance of power distribution systems via fuzzy AHP. *Complexity* **2016**, *21*, 36–46. [CrossRef]
51. Long, C.; Ochoa, L.F. Voltage Control of PV-Rich LV Networks: OLTC-Fitted Transformer and Capacitor Banks. *IEEE Trans. Power Syst.* **2016**, *31*, 4016–4025. [CrossRef]
52. Qian, Y.; Yao, F.; Jia, S. Band selection for hyperspectral imagery using affinity propagation. *IET Comput. Vis.* **2009**, *3*, 213–222. [CrossRef]
53. Das, S.; Mullicka, S.S.; Suganthan, P.N. Recent advances in differential evolution—An updated survey. *Swarm Evol. Comput.* **2016**, *27*, 1–30. [CrossRef]
54. Trebuňa, P.; Halčinová, J.; Fil'o, M.; Markovič, J. The importance of normalization and standardization in the process of clustering. In Proceedings of the 12th International Symposium on Applied Machine Intelligence and Informatics (SAMI), Herl'any, Slovakia, 23–25 January 2014; pp. 381–385. [CrossRef]
55. Elías, X.; Bordas, S. *Energía, Agua, Medioambiente, Territorialidad y Sostenibilidad*, 1st ed.; Díaz de Santos: Madrid, Spain, 2011.
56. Jiang, Z.; Liu, K. Real Time Interpretation and Optimization of Time Series Data Stream in Big Data. In Proceedings of the 3rd IEEE International Conference on Cloud Computing and Big Data Analysis (ICCCBDA), Chengdu, China, 20–22 April 2018; pp. 243–247.

energies

MDPI

Review

A Survey on Optimization Techniques Applied to Magnetic Field Mitigation in Power Systems

Juan Carlos Bravo-Rodríguez [1,*], Juan Carlos del-Pino-López [1] and Pedro Cruz-Romero [2]

[1] Escuela Politécnica Superior, Universidad de Sevilla, c/ Virgen de África 9, 41011 Sevilla, Spain; vaisat@us.es
[2] Escuela Técnica Superior de Ingeniería, Universidad de Sevilla, Avd. de los Descubrimientos s/n, 41092 Sevilla, Spain; plcruz@us.es
* Correspondence: carlos_bravo@us.es; Tel.: +34-954-552-847

Received: 28 February 2019; Accepted: 1 April 2019; Published: 8 April 2019

Abstract: With the continuous increase in the number and relevance of electric transmission lines and distribution networks, there is a higher exposure to the magnetic fields generated by them, leading to more cases of human electrosensitivity, which greatly necessitates the design and development of magnetic field mitigation procedures and, at the same time, the need to minimize both performance degradation and deterioration in the efficiency as well. During the last four decades, fruitful results have been reported about extremely low frequency magnetic field mitigation, giving a wide variety of solutions. This survey paper aims to give a comprehensive overview of cost-effective optimization techniques destined to magnetic field mitigation in power systems, with particular attention to the results reported in the last decade.

Keywords: optimization; magnetic field mitigation; overhead; underground; passive shielding; active shielding; MV/LV substation

1. Introduction

As is known, many electrical installations, mainly overhead transmission lines (OHL), underground power cables (UPC), medium voltage/low voltage (MV/LV) substations, and building's electrical distribution systems, are the source of extremely low frequency (ELF) (50/60Hz) magnetic fields (MF). This has led to an ever-increasing demand on the safety of people exposed to the potentially adverse health effects of MF [1]. On the electromagnetic compatibility side, the interferences coming from ELF MFs may affect the performance of electrical and electronic devices (problems in medical electric equipment due to their sensitivity [2], electromagnetic interferences caused by transmission and distribution lines on communication cables [3], etc.).

The exposure to ELF MFs may increase the overall risk of many diseases [4,5] for MF intensity values higher than certain threshold levels, capable of inducing harmful currents in the human tissues [6]. However, after more than 40 years of research, the scientific community has not yet reached an agreement on whether long exposure to MF, at levels lower than those of the international recommendations, can have an effect on human health. In this sense, international bodies, like the Council of the European Union, and international agents of experts as the International Commission on Non-Ionizing Radiation Protection (ICNIRP) [7] as well as the Institute of Electrical and Electronics Engineers (IEEE) [8], have proposed some MF reference levels. Specifically, ICNIRP establishes limits of MF exposure at 50 Hz, according to the following two typical scenarios: A total of 200 μT for general public and 1000 μT for occupational exposure [7]. These limits are based only on short-term effects on human health after exposure to considerably higher MF values, incorporating safety margins to provide adequate protection for acute effects when they are kept. In any case, no convincing evidence about chronic effects associated with acute effects for exposures below the established threshold for has yet been found. Even more, there is no clear understanding if and how ELF MFs, at the low

levels emitted by common appliances, might affect human health. Thus, until this moment, any possible cause–effect relationship between the exposure to ELF MFs and derived human diseases remains unknown. Only a few studies suggest that exposures in the order of 0.4 μT may be related to childhood leukemia, although recent studies found no material association between ELF MF and this disease [9]. Due to this fact, in 2002, the International Agency for Research on Cancer (IARC), which is part of the World Health Organization (WHO), just classified ELF MFs among the "possibly carcinogenic" physical agents (Group 2B) [1], so a precautionary principle (PP) is recommended [5,9], especially in sensitive places such as hospitals, schools, and playgrounds [10]. Thus, this uncertain panorama has led some countries or local authorities to set up, frequently, much lower exposure limits than the reference levels of ICNIRP and IEEE [11], as reported in Table 1. For example, some US states, such as Florida and New York, have settled MF limits at 15 μT, for up to 230 kV, and 20 μT in higher voltages [12]. Additionally, more stringent limits have been imposed in some European countries, including Italy (where the maximum limits are 3 or 10 μT for new and existing facilities, respectively), Slovenia and Flanders (with a maximum of 10 μT), or Switzerland (with the strongest limit of 1 μT [12]).

Table 1. Reference values for both general public and occupational exposure (μT) at 50/60 Hz.

Scope	ICNIRP 2010 [7]	IEEE 2002 [8]
General public	200	904
Occupational	1000	2710

This survey paper aims to give a comprehensive overview of optimization techniques applied to the design of ELF MF mitigation solutions in power systems, with particular attention given to the results reported in the last decade. All this work is summarized in Table 2, categorized in terms of years and methods/applications.

Table 2. A timeline of applications for MF mitigation and related optimization techniques.

MF Mitigation Method	Years			Optimization Technique	MF Mitigation Applications
	1990s	2000s	2010s		
Conductor arrangement	■	■	■	Parametric analysis	OHL/UPC
		■		Multi-objective OPF	OHL
		■		Genetic Algorithm	OHL/UPC
			■	Particle Swarm Optimization	OHL
			■	Statistical approach	UPC
			■	Differential Evolution	OHL
Passive loops	■	■	■	Parametric Analysis	OHL/UPC/Subst.
		■		Augmented Lagrangian	OHL
		■	■	Genetic Algorithm	OHL/UPC
			■	Particle Swarm Optimization	OHL
Active loops	■	■	■	Parametric analysis	OHL/UPC/Subst.
		■		Annealing optimization	OHL
		■	■	Genetic Algorithm	OHL/UPC/Subst.
			■	Multiagent Swarm Stochastic	OHL
Passive shields	■	■	■	Parametric analysis	OHL/UPC/Subst.
		■		Continuum Gradient	UPC
			■	Genetic Algorithm	UPC

The rest of the paper is organized as follows. Following the introduction section, the principles of MF mitigation in electrical appliances are first presented in Section 2, highlighting the most commonly used solutions and the need for optimization tools in their design. Sections 3 and 4 present a detailed survey on the optimization algorithms related to both intrinsic and extrinsic methods more often used

in the last decades, emphasizing the main advances in this field as a result of their use. This paper ends with final remarks in Section 5.

2. Mitigation of Low-Frequency Magnetic Fields

Generally, ELF MF mitigation methods can be categorized into two different groups, that may be applied to both OHL and UPC, as well as in MV/LV substations [13]. These are intrinsic techniques and extrinsic techniques.

2.1. Intrinsic Techniques

In the first kind of techniques, the geometrical and electrical parameters of the MF source, are modified for lowering the global MF (or magnetic flux density). The most extended solutions in this category are the following [13]:

- Layout and compaction [13]: It is well-know that, when the relative positions of the conductors are rearranged (layout), for example from linear to equilateral triangle disposition, the MF decays faster as the distance to conductors increases (Figure 1). A further MF reduction can be obtained by reducing the phase-to-phase clearance (compaction). For example, by installing compactors along overhead line spans (realized through rod insulators forming equilateral triangles), a 56% reduction of the maximum ground-level MF is achievable, in comparison to an overhead transmission line realized with compacted towers (the solution that, at present, minimizes the magnetic field without compactors) [14]. However, this solution also entails a new problem, which includes higher voltage gradients on conductors and insulators, resulting in higher audible noise, radio interference, and increased hardware corona [15–18]. Additionally, the mitigation achieved can be limited, especially in UPC, where the current rating (ampacity) may be affected by these techniques [19].
- Distance management [13]: Since the intensity of a MF decreases naturally, as a function of distance from the source, it is possible to achieve the appropriate reduced level of MF by simply increasing this distance of separation from the sources (Figure 2). This solution is limited by technical constraints (maximum height for OHL or maximum possible depth for UPC, for example).
- Phase splitting [20,21]: Each phase of an electric power supply can be split in several conductors, forming quadrupoles, which results in a low-field configuration (Figure 3). However, this makes the installation more complex and more expensive, since additional equipment and material is required.
- Phase cancellation [22]: Unlike in the phase splitting method, in the phase cancellation method the phases are just rearranged accordingly into an existing configuration. As no new material has to be added, this method is cost effective. This technique is only interesting in the case of more than one circuit. Thus, a representative phase cancellation solution is the low reactance configuration in a double circuit line (Figure 4). The greatest effectiveness of this method is limited almost exclusively to super-bundle double circuit vertical configurations, where the higher and lower phases are interchanged in the second circuit.

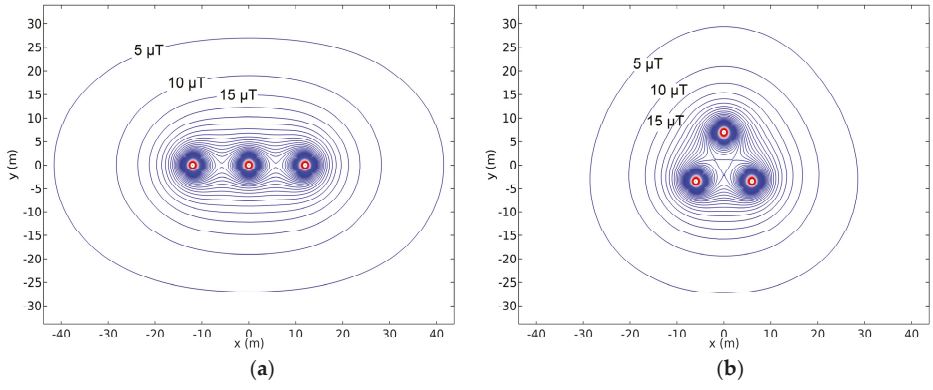

Figure 1. MF levels for a three-phase line in (**a**) flat configuration and in (**b**) triangular configuration (based on [13], CIGRÉ 2009).

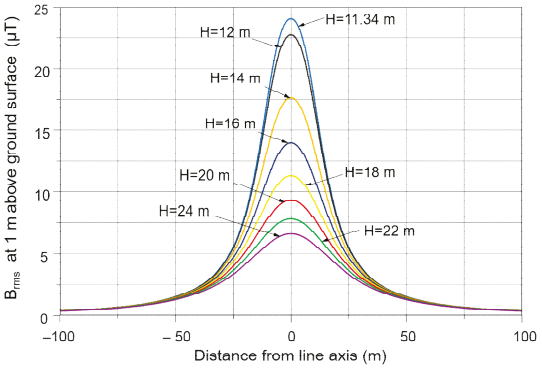

Figure 2. MF at 1 m above ground surface for various heights (H) for a three-phase line (based on [13], CIGRÉ 2009).

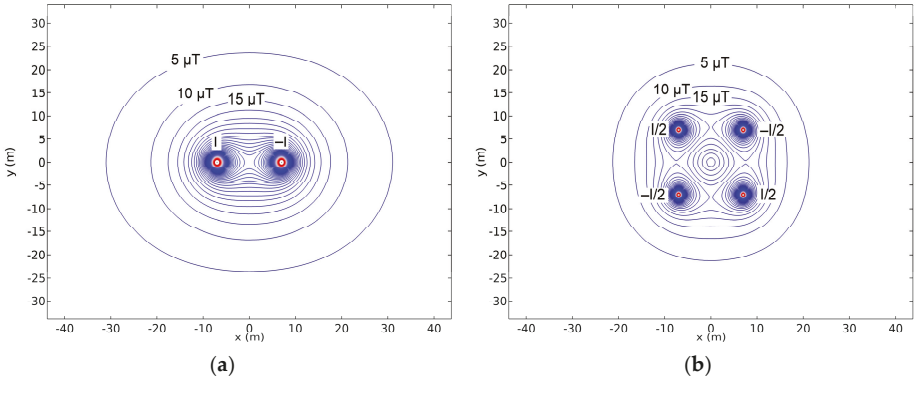

Figure 3. MF levels for a line arranged as a (**a**) dipole and (**b**) a quadrupole line (based on [13], CIGRÉ 2009).

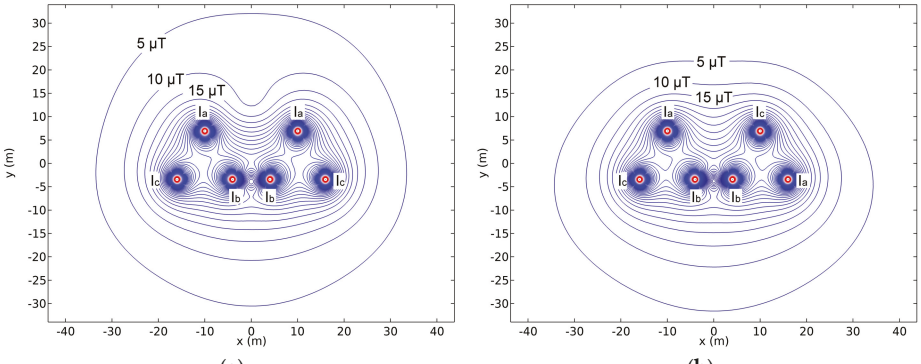

Figure 4. MF levels for a double circuit line in two phase arrangements, (**a**) super-bundle and (**b**) low reactance line (based on [13], CIGRÉ 2009).

In addition to these solutions, and particularly for the case of UPC, a proper electrical connection of the metallic sheaths may also provide a significant reduction in the MF. In this sense, solid bonding may achieve great levels of mitigation, but with an important impact on the ampacity of the UPC.

At this point, it should be noted that the mitigation levels achieved by most of the previous techniques are usually limited and may not always meet the MF mitigation requirements for a specific location. In these situations, extrinsic techniques provide a good alternative since they are able to provide a much higher mitigation effect when needed.

2.2. Extrinsic Techniques

These techniques are based on placing additional apparatuses (mitigation system) close to the source of ELF MF or the region to be protected and can be classified as passive and active techniques [13], depending on the mechanism used to provide the mitigation effect:

- Passive techniques [23–25]: In this case, the MF mitigation is obtained because the mitigation system acts in response to the MF generated by the source. For example, a typical situation is when currents are induced in these elements due to Faraday's Law, which, in turn, generate a new MF that partially cancels the one from the source. Typical mitigation solutions in this group are passive loops [23,24] (Figure 5a) and conductive shields [25] (Figure 5b). Another case is when ferromagnetic materials are used in the mitigation system, since they have the property to attract and trap the MF flux lines thanks to their high permeability. This way, the MF flux lines are moved away from the region to be protected, resulting in a MF mitigation in that area. A good example is the use of ferromagnetic shields [25] (Figure 5c).
- Active techniques [26]: In contrast to previous solutions, active techniques require the use of external power sources to inject appropriate currents (magnitude and phase) in the mitigation system to provide the required mitigation effect (Figure 5d), and, as such, are able to provide a much higher mitigation reduction [26–30]. This is usually used in the so-called active loops. Nonetheless, this requires a more complex mitigation system, as it is necessary to install expensive equipment apart from MF sensors, such as the power sources, and a monitoring system to continuously adjust the injected current to achieve the required mitigation at any time [26,27,30]. All this makes this solution much more expensive than passive ones.

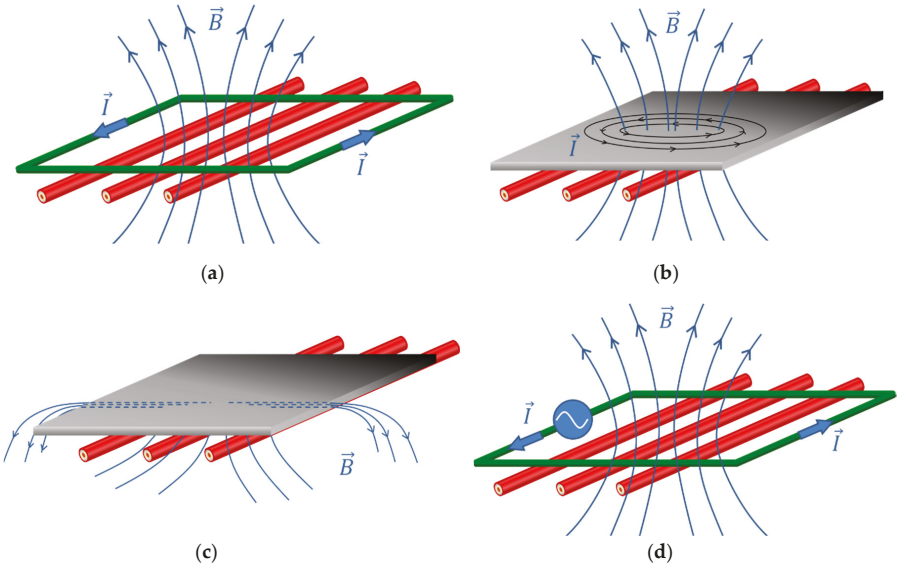

Figure 5. Passive and active techniques as follows: (**a**) Passive loop, (**b**) conductive shield, (**c**) ferromagnetic shield, and (**d**) active loop.

It should be remarked that combinations of different techniques are usually used to reduce ELF MF below a certain threshold when required. In any case, there are multiple parameters in any of the mentioned solutions that need to be adequately defined to achieve the mitigation requirements, for example, distances and clearances to the MF source, dimensions of the mitigation system and the positions of its elements, and electrical parameters or magnitude and phase for the currents to be injected. There are also a number of technical and operational constrains that must be included in the design procedure to go beyond MF minimization and incorporate other important features, such as thermal aspects, forbidden regions where the mitigation system cannot be installed, induced voltages in nearby infrastructures, failure risks, mitigation system costs, etc. In this sense, it is important to include the thermal problem in the mitigation system design procedure, since it may affect the ampacity of the mitigated system [19], especially in UPC. In this situation, the two following techniques are the most extended ones: The international standard analytical approach (IEC 60287) [31,32] and the 2-D finite-element analysis approach (FEM) [33,34]. The first line of thought is the most frequently used reference by engineers for cable sizing. In this line, considerable research efforts have been expended in modifying and enhancing its modelling capabilities under both steady-state and variable loading conditions [35–37]. Thus, this traditional method can be used for the thermal analysis of most of the intrinsic and extrinsic mitigation techniques, when applied to UPC. However, it is not suitable when dealing with conductive or ferromagnetic shields. The complexity of the geometry and the material properties requires a more powerful tool, like FEM [34,38,39]. With this procedure it is possible to calculate the steady-state temperatures at various points of the cable system when the mitigation system is installed and, hence, the overall cable ampacity corresponding to a specified maximum conductor temperature can be determined too [19].

All this clearly shows the need for optimization tools to obtain effective designs for the mitigation system. In the following sections a detailed survey regarding the optimization algorithms frequently used in ELF MF mitigation system design is developed.

3. Optimization Applied to Intrinsic Techniques

An optimal MF mitigation design is characterized by the MF sources and the position of the regions to be shielded. Usually, combinations of different strategies may be used to reduce the MF in an affected area. Thus, once the sources and the mitigation strategies are defined, the resulting MF can be assessed by analytical methods, usually by means of the Biot–Savart law [13,40,41]. This way, the MF mitigation performance provided by the intrinsic techniques presented earlier can be easily evaluated and optimized. In this sense, each mitigation technique has its own set of parameters that have to be optimized for minimizing the MF at the area of interest. The way in which some studies have tackled this problem for OHL and UPC, as well as in MV/LV substations, is presented next, where optimization algorithms, such as particle swarm optimization (PSO), genetic algorithms (GA), and evolutionary multi-objective optimization (EMO), are the most extended ones.

3.1. Conductor Arrangement

As mentioned previously, conductor management turns out to be a very effective way for reducing ELF MFs. Various options within this strategy can be used to reduce the field of the source by playing on the geometry of the conductors that produce such a field, e.g., three phase conductor rearrangements and phase currents split into several conductors. In the following, the main optimization techniques applied to OHL and UPC and MV/LV substations are summarized.

3.1.1. Overhead Transmission Lines

Optimal arrangement of double-circuit OHL conductors for the minimization of the ELF MF strengths constitutes a specific issue that has been the subject of numerous studies. The influence of rearranging the double-circuit overhead phase succession on ELF MF emissions was evaluated in [42,43]. In [44], it was concluded that the optimum arrangement can be easily applied to already constructed high voltage transmission lines by properly interchanging the phase conductors at the substations. A comparative studio of the ELF MF distribution in conventional and compact power line configurations is analyzed in [45–47].

The GA is a useful tool for determining optimal arrangements of parallel independent OHL, aimed to decrease both electric and MF emissions. In [15,48], the Monte Carlo approach implemented in GA allows for the consideration of uncertain phase shifts between independent OHL. In [49], a method for an accuracy calculation of MF under OHL is achieved by considering optimal phasing transposition for double circuit transmission lines, adding the losses in ground wire(s) and the associates side effects.

Often, optimization methods aimed to minimize ELF MF strengths join different ELF MF objective functions into a single fitness function. Typical optimization techniques are generally applied, including GA-based techniques [50], differential evolution stochastic search algorithms [44], and PSO [51]. The single fitness function for all of these optimization techniques is obtained by weighting both electric field strength and MF strength with a certain utility function. The choice of the weight or utility function is a crucial key for optimizing phase arrangements of double-circuit OHL. Moreover, the different parameters of the selected weight or utility function for minimizing the MF strengths yield different optimal solutions [52] that may involve certain side effects, as follows: Surface gradient (surface electric field) of the conductors, audible noise, apparent power losses, radio interferences, corona losses, phase inductance, phase inductance and capacitance, etc.

Developing this idea still further, the issue of the optimum phase arrangements for double-circuit OHL can be seen as a multiple-objective problem. The multi-objective optimization methods are proposed for helping in the determination of solutions that are not limited to a single optimum design, but rather to a simultaneous optimization of the MF strengths. In [53], the mitigation is obtained by solving a multi-objective optimal power flow (MO-OPF) problem with a specific objective function for the MFs. Recently, the optimization problem approach is broadened to include additional assessment criteria, such as apparent power losses, surface gradients of the conductors, and audible noise [53],

obtaining an optimum set of solutions to minimize the MF strengths based on the controlled elitist GA (a variant of the algorithm Non-dominated Sorting Genetic Algorithm II (NSGA-II) [54].

3.1.2. Underground Power Lines

UPC produce ELF MF that may have a greater impact on human health than in the case of overhead lines due to the lower distance between cables and persons. In this sense, the need of restricting this MF becomes a significant task, mostly in urban areas, at the connections of cables to substations, and in mining and railway systems.

The optimal arrangement of a multi-circuit UPC system, at specified locations and supporting unbalanced loads, was initially obtained by means of an algorithm developed in 1998 [55]. Alternatively, and also considering prefixed selected positions, the optimal phase arrangement is achieved by using GA [56] and, recently, considering both minimum construction cost and limitation on the maximum MF as parameters of the optimization procedure [12]. A different approach is presented in [57] for an underground power system composed of several parallel subconductors, where a deterministic procedure, based on a geometrical indicator, is employed for identifying the optimal sequence arrangement with the lowest MF emissions, showing an important improvement regarding GA computational time. Alternatively, some studies substitute the use of GA in favor of other techniques, such as Sequential Quadratic Programming (SQP) [58], reducing the number of unknowns by using symmetric layouts for the power cables.

On the other hand, parametrical investigations are also conducted in the phase configurations of the cables in order to reduce the MF in the vicinity of the cables and to determine the configurations which produce the minimum values of the MF (optimum configurations) [59].

Most of optimal above-mentioned cable arrangements are calculated assuming fixed currents. However, usually, in real applications, the electrical currents in cables are not constant, but time varying. In order to obtain an optimal design, this stochastic nature of the currents in the cables should be considered. In [60], multiple-circuit UPC feeders, allocated in a tunnel with randomly changing loads, are analyzed. The optimal disposition of cable bundles and phases from fixed selected positions is obtained using a GA. The authors of [12] proposed new algorithms to obtain optimal disposition of cables and dimensions of tunnels, minimizing construction costs and MF for both the general and the occupational public. Time changing currents are considered, resulting in a so-called statistical approach.

It should be remarked that few studies have been reported coupling intrinsic MF mitigation techniques and the thermal formulation [19]. Thus, in [61], the magnetic eddy-current and transient thermal problems are joined for modeling UPC. Such problems in 2-D cases have been solved by FEM and the resulting formulation is applied to three-phase multi-circuit UPC, considering different phase rearrangements in order to reduce the MF levels above the ground surface.

3.1.3. Substations

The best, and also the most cost-effective mitigation method for the MF in substations consists of in phase management [13], by keeping the phases mixed as soon as they leave the transformer (Figure 6). This can provide high shielding factors. For this reason, phase cancellation should be the first technique to attempt before trying other techniques that can complement this one, such as the extrinsic techniques that are reviewed in the next section.

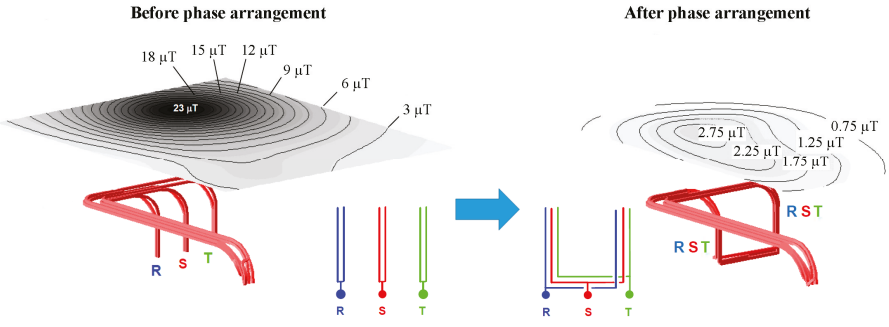

Figure 6. MF before and after mixing phases on the LV connections in a MV/LV substation (based on [13], CIGRÉ 2009).

In any case, with the aim of improving the overall mitigation when considering the MF emission level of the substations, the first steps to be made refer to a proper organization of the LV conductors in order to decrease the loops provided by the current path [62]. From a practical viewpoint, this objective can be covered by several easy points as follows:

- Preventing useless separation between conductors of different phases;
- Using plaited conductors, with all four conductors, as often as possible;
- Minimizing the length of the cables within the substation;
- Possibly using a compact busbar system, if available, between the transformer and the main LV switchboard.

4. Optimization Applied to Extrinsic Techniques

In the following, the most used optimization techniques applied to extrinsic MF mitigation solutions are presented.

4.1. Passive Loops

In this technique, one or several coils, or loops, are placed appropriately so that currents are induced by the source of the MF, in accordance with Faraday's Law [13]. This way, the MF generated by the coils partially compensates the original source MF [23,24,63–65]. To achieve better results, many studies have proposed different configurations and arrangements for the loops (independent loops, common conductor loops, enchained loops, etc.), as well as series-compensation of the coils by means of capacitors to increase the induced currents (Figure 7), hence, improving the MF reduction [64,66–73].

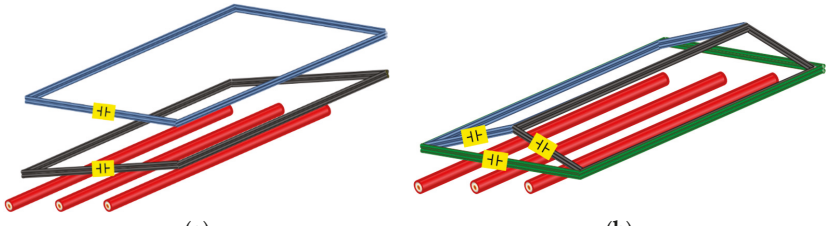

(**a**) (**b**)

Figure 7. Two examples of passive loops arrangements, as follows: (**a**) Independent series-compensated loops and (**b**) enchained series-compensated loops over a power line.

Thus, the main aspects to be considered when designing passive loops are (Figure 8) the following: The number and arrangement of the coils, the number of loops on each coil, the cross section of the

conductors to be used in the loops, the clearance between loops ($d(i,k)$), their position relative to the MF source ($d(k,p_3)$), the presence of forbidden regions, and the capacitors for series-compensation, if required. All this implies a number of parameters that should be defined adequately for each particular situation. Therefore, the need for applying optimization algorithms, to define all these parameters for maximizing the MF reduction in any situation, is clear. In this sense, the MF level in such systems can be computed by means of analytical methods [27,64–66,73,74], leading to efficient and fast optimization procedures.

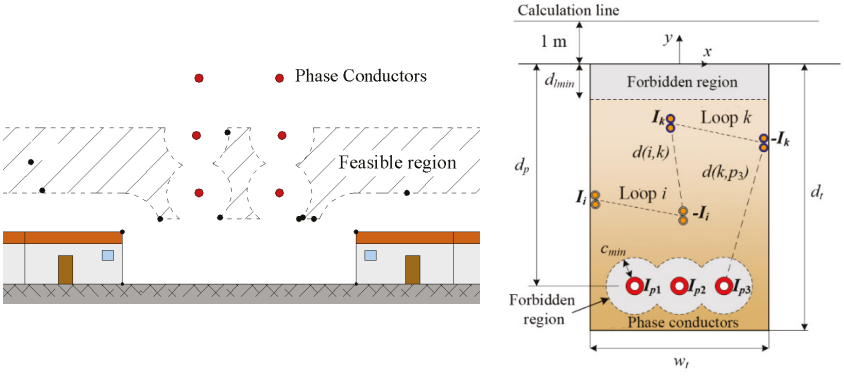

Figure 8. Some parameters and constraints involved in the design of (**a**) passive loops in OHL and (**b**) enchained loops for an UPC.

A first example is shown in [69], where a semiheuristic optimization procedure, based on an augmented Lagrangian, for obtaining the optimal location of the passive loops when mitigating the MF generated by an overhead power line is presented. The proposed procedure first requires the determination of the shield location that maximizes the induced currents in the loops. Then, a second optimization is applied to minimize the MF in a certain region, far or close to the power line. Some constraints should be included to limit the line conductor-to-loop conductor clearance. The main conclusions are that the optimal loop arrangements depend on the line configuration and the location of the area to be protected.

In [74,75] a new procedure, based on genetic algorithms (GA), is presented. By means of this new procedure, the optimal location and main properties of the loops are obtained for different arrangements (flat, alternate, and super-bundle) and voltage levels in OHL. Thanks to the flexibility of the GA, two scenarios are considered in relation to the location of the region to be protected, minimizing the MF at one side from the power line (unilateral mitigation) and minimizing the MF at both sides from the power line (bilateral mitigation). In both scenarios, new constraints are implemented for limiting the loop conductor-to-ground clearance and the loop's maximum height, as well as other restrictions to define forbidden regions due to the presence of dwellings, trainways, etc. The main results show an increase in the MF reduction achieved by the optimized loops, in comparison to previous studies. Additionally, it is observed that the mitigation efficiency achieved depends mainly on the line configuration, followed by the loop design and the voltage levels. Optimal loops are also analyzed in terms of sensitivity, concluding that its mitigation performance may be influenced by small variations in loop's position, resistance, and compensation capacitance, this effect being more intense in some situations. Eventually, it is also concluded that bilateral mitigation should be avoided if possible, since the mitigation performance is worse in this scenario.

As a consequence of these results, in [76] a new procedure based on GA is presented for more complex situations, such as the mitigation of the MF in UPC by means of passive loops. To this

aim, some revisions are applied to the objective function that now maximize the reduction factor (RF), defined as the ratio between the original MF and the mitigated one, at 1 m above ground surface and located at one side of the trench axis. Results show that, for different configuration of series-compensated loops, the mitigation performance of the optimized loops can be much greater than that provided by other passive techniques (such as conductive shields). However, it is also remarked that these optimal solutions are quite sensitive to small variations in loop position and electrical parameters. For this reason, the semiheuristic procedure is improved to obtain the less sensible solution, which ensures a minimum RF in the area of interest.

In any case, all these studies conclude that a better performance is obtained when loops are placed closer to the phase conductors. Nevertheless, this is critical, especially in the case of UPC, since the power losses generated in the loops my affect the current rating of the line. In this sense, [77] goes a step further by including the thermal problem in the semiheuristic optimization procedure proposed in [76]. This way, new constraints may be included to limit the maximum temperature of line conductors so that loops can be closer to them, with no effect on the line current rating. Additionally, the objective function in the GA is also modified to maximize the ratio RF_{min}-*Cost*, where RF_{min} is the RF provided by the optimal loop, in the worst situation after considering variations of $\pm 5\%$ in loop positions and electrical parameters, and *Cost* is the total cost of the loops, including the operational cost. This way, new constraints are included to consider both technical and economic aspects in the optimization procedure. Consequently, the optimized loops obtained are able to guarantee a minimum RF in the area of interest, and all this with the minimum possible cost.

It should be remarked that passive loops have been also applied to more specific situations, such as joint bays in UPC. In this sense, [78] proposes the optimization of passive loops by means of GA, comparing its performance to the one provided by other typical loop arrangements that are usually used in these installations [71]. As a result, this comparison clearly shows how the mitigation performance of the loops can be noticeably increased by means of an optimized design.

More recently, new studies have used other optimization algorithms that have paid much attention in optimization research today. One example are nature-inspired meta-heuristic algorithms, like PSO, that have shown to be faster than GA [79]. In this sense, [65] presents a new optimization procedure, based on PSO, for obtaining the loop position for minimizing the induced voltages in aerial pipes installed close to 400 kV OHL. For this purpose, one or two passive loops, made of conductive or ferromagnetic conductors, are installed. From this study it is concluded that a better performance is obtained if conductors have a permeability greater than 1.

4.2. Active Loops

Unlike passive loops, active loops are supplied by external power sources to inject the required current (magnitude and phase) at any moment, being able to provide a much higher mitigation reduction. This solution has been analyzed mainly in OHL [26,27,80,81] and MV/LV substations [28,82,83]. However, this mitigation system may be much more complex and more expensive than passive ones. Thus, apart from the type of loops, its number, position, and cross section, new variables should be included in the optimization problem, such as the magnitude and phase of the injected currents. Consequently, the use of an optimization procedure is very helpful for obtaining the optimal configuration and position of the active loops that require the smallest power source for providing a certain MF mitigation. To this aim, and thanks to the simple geometry of the shielding system, the evaluation of the MF can be addressed by means of analytical expressions, mainly based on the Biot–Savart Law [13], so that different optimization procedures can be implemented easily, as described next.

Regarding its application to OHL, a first approach in active loop optimization is developed in [27], where the position of the active loop is first obtained by means of an annealing optimization algorithm, considering the loops as passive loops. Then, the current that minimizes the MF at a certain region is calculated. However, it is concluded that further optimization is required for selecting the optimum conductor for the loops.

A full optimization procedure is presented later in [29], where the positions and currents of active loops are optimally obtained, by means of a GA, for mitigating the MF of an overhead line. This way, the mitigation system can be optimized in an easy way for any line configuration and area of interest.

As shown in the passive techniques design, the advantages presented by the GA makes this optimization algorithm the most employed when designing mitigation systems. In this sense, [84] presents the design and optimization procedure of an active loop system based on a GA, employing a low-cost hardware, such as Arduino. In this work, the model of the MF source is obtained first and then the position and current of the active loop is derived by means of the GA, for a particular loading condition of the MF source. Finally, the control system ensures the suitable current to be injected in the loops at any loading conditions. The performance of this prototype is later improved by implementing a "Perturb and Observe" algorithm in the control system [85].

Recently, for the case of OHL, new advances have been developed through the means of a different optimization algorithm. In particular, in [81,86–88] the number, configuration, arrangement, and loop currents are derived by means of a multi-objective optimization problem that is solved by multi-agent multiswarm stochastic optimization, based on Pareto optimal solutions. In [88] this procedure is improved to take into account uncertainties in the parameters of the loops (positions, currents, etc.) as well as in other parameters related to the area to be protected and the location to be installed at. This is done by the analysis of the space-time characteristic of the MF generated by the source. Finally, this procedure is validated experimentally in [81], showing differences lower than 20% between the MF values derived from simulations and experimental measurements. Additionally, it is observed that, as expected, the mitigation efficiency depends on the location of the MF sensors.

Nonetheless, active loops have also been optimized for the MF mitigation generated by MV/LV substations. In this sense, in [28] an optimization design based on GAs is presented for minimizing the MF levels in a target value outside the cabin. The procedure is applied to a full 3D model of the substation, wherein all its elements need to be adequately modeled first. Then, the location of the active loop inside the cabin is derived from the optimization algorithm.

A similar procedure is later presented in [82,83], where GA is used to optimize different active loop configurations for the MF mitigation in different volumes around and above a MV/LV substation. Opposite to [28], in this work, the active system is composed of three pairs of loops installed in the walls of the volume to be protected, with each pair supplied by one power source. The position of each loop and the currents to be injected are then derived for minimizing the average MF inside a particular inspection area, inside the volume to be shielded. The main conclusions show that a great reduction can be obtained. Furthermore, unlike other passive mitigation systems, this procedure helps focus the maximum MF mitigation efficiency in any region inside the target volume (Figure 9).

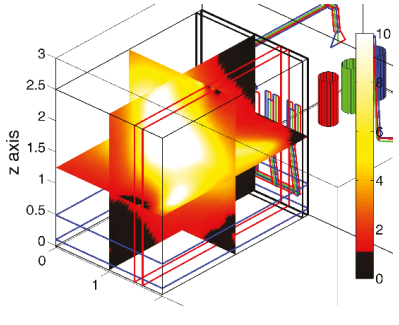

Figure 9. Optimal location for the active loops and RF (color bar) achieved in the center of the target volume outside a MV/LV substation.

4.3. Passive Shields

The use of metallic shields is one of the passive solutions presented earlier and has been extensively used on its own, or in combination with other mitigation systems, for mitigating the MF in buildings close to OHL [13] and in the mitigation of the MF generated by UPC [38,71,72,89–91] and MV/LV substations [92–95]. In literature in the last decades, different geometries have been proposed and analyzed concerning their application for electrical applications, employing conductive and/or ferromagnetic materials [25,38,91,94–99]. Thus, for each shield geometry and for a particular location, a number of parameters must be specified for ensuring the required MF mitigation (shield dimensions, position relative to the source, and material properties). In this sense, there are no analytical expressions for evaluating the MF reduction provided by every possible shielding configuration, due to its complex geometric and material properties. There are only few cases where analytical expressions are derived [96,97,100,101], but these are usually based on simplified situations (infinite width shields, perfect magnetic or perfect electric materials, ferromagnetic cylindrical shields, etc.). So, numerical methods, such as FEM, are frequently preferred to address this problem [38,89,91,94,99,102,103]. Nevertheless, from the optimization point of view, this may imply more computational requirements and longer computation time, depending on the complexity of the analyzed system, so obtaining new analytical formulae for more realistic situations would lead to faster and more efficient optimization procedures for this mitigation technique. Nonetheless, new numerical approaches have been presented recently that may help in this task in the near future [104–107] since they drastically reduce the number of unknowns when dealing with thin shields, in comparison with FEM.

In the literature there are many studies focused on optimizing shields for industrial applications, such as induction heating [108] and shielding electronic equipment [109]. However, few studies can be found regarding the optimization of magnetic shields applied to power systems. Thus, for power installations, most of the studies have tackled this problem by means of parametric analyses [25,38,90,91,96,98], where the main conclusions highlight that better a mitigation performance is obtained when the shield is larger and closer to the MF source. However, in some situations, like UPC, the closer the shield the higher the induced losses and, hence, the temperature. As a consequence, the presence of the shield may affect the current rating of the line [19,38,91]. Therefore, the need for an optimization process for optimizing the shield, not only in terms of MF mitigation efficiency but also in total cost (including operation cost) and limited impact on the current rating of the MF source, is clear. However, shielding optimization has only been considered for UPC. In this sense, a first approach is presented in [102], where a continuum gradient-based shape optimization procedure for conductive shields installed over UPC is proposed. Its main objective is to optimize the shape of the plates for maximal MF reduction and a minimal amount of material for the shield. For this tasks, numerical simulations are performed by FEM and additional constrains are included to obtain symmetric shapes for the shield. The main results conclude that the optimal shields achieve high MF mitigation reduction. However, obtained shapes are complex, making its placement in actual locations very difficult. Additionally, thermal effects are not considered in the optimization procedure.

On the other hand, [89] proposes an optimization process, based on a GA, for the minimization of the cost of ferromagnetic and conductive shields when applied to UPC duct banks, reducing the MF above ground to below a certain level without limiting the current rating of the cables. The proposed procedure starts by obtaining the conductor arrangement which provides the minimum MF at the region to be shielded (located above ground and at one side of the trench). Then, the optimization algorithm determines the shield dimensions and positions with the lowest possible cost. Here, the thermal problem is considered to limit the impact on the current rating of the lines to be shielded (Figure 10). Additionally, non-linear properties are considered for the ferromagnetic plates, so simulations are performed by means of FEM. The conclusions highlight that better results, in terms of efficiency and cost, are obtained for certain combinations of shield shape, shield material, and conductor arrangement. Furthermore, results show a good performance when additional circuits are installed sometime later in the shielded duct bank.

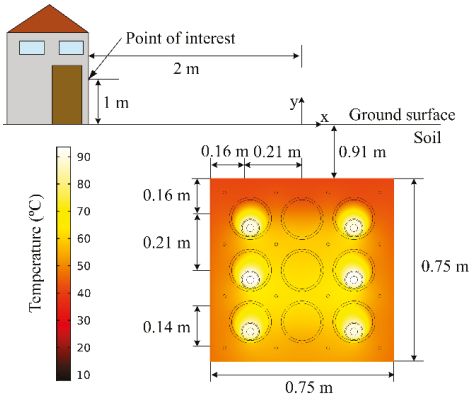

Figure 10. Temperature distribution in shielded cable duct bank.

5. Conclusions

The motivation for this work stems from challenges facing the electrical facilities in determining optimal, cost-effective, and safety measures to avoid non-desirable magnetic field exposures. In this way, this paper addresses optimization methods for minimizing extremely low frequency (50/60Hz) magnetic fields. Specifically, optimization methods are reviewed in accordance with their application to overhead transmission lines, underground power cables, and MV/LV substations. Meanwhile, the optimization methods are surveyed following the classification of intrinsic techniques and extrinsic techniques. Despite that no single optimization algorithm can solve all optimization problems on this topic, the overview of the different available algorithms, typically applied for mitigating magnetic fields, will help to select the appropriate algorithm for the problem at hand.

It can be concluded that most of the optimization proposals to achieve optimal cost-effective magnetic field mitigation are mainly based on parametric studies. Alternatively, a great variety of optimization algorithms (differential evolution, augmented Lagrangian, continuum gradient, etc.) have also been used. Among all of them, the genetic algorithm is highlighted by its efficiency but, in recent times, it is progressively being replaced by the particle swarm optimization technique.

Finally, it is also concluded that the use of numerical methods, when dealing with passive shields, may burden the computation time and efficiency of any optimization procedure and it may be more appropriate to use analytical expressions when possible.

Author Contributions: J.C.B.-R. and J.C.d.-P.-L. conceived the topic, conducted the literature survey, and wrote a preliminary version in combination with P.C.-R., who provided valuable data, gave helpful comments, and revised the paper. All the authors were involved in preparing the final version of this manuscript. J.C.d.-P.-L. supervised the whole work.

Funding: This research was funded by the Agencia Estatal de Investigación and Fondo Europeo de Desarrollo Regional (AEI/FEDER, UE) under the project ENE2017-89669-R and by the Universidad de Sevilla (VI PPIT-US) under grant 2018/00000740.

Conflicts of Interest: The authors declare no conflict of interest.

References

1. WHO/IARC. *Monograph 80: Non-Ionising Radiation, Static and Extremely Low-Fequency Electric and Magnetic Fields*; WHO/IARC: Lyon, France, 2002; Volume 80.
2. Rao, S.; Sathyanarayanan, A.; Nandwani, U. EMI problems for medical devices. In Proceedings of the International Conference on Electromagnetic Interference and Compatibility, Bangalore, India, 23 February 2002; IEEE: New Delhi, India, 1999; pp. 21–24.

3. Shwehdi, M.H. A practical study of an electromagnetic interference (EMI) problem from Saudi Arabia. In Proceedings of the Large Engineering Systems Conference on Power Engineering (IEEE Cat. No.04EX819), Halifax, NS, Canada, 28–30 July 2004; pp. 162–169.
4. Bontá, D.M.; Director, D.; Richard Neutra, R.; Vincent DelPizzo, D.; Geraldine Lee, G.M.; Lee, S.; Shen Liu, K.; Shaw, G.; Smith, D.; Marilyn Underwood, D.C.; et al. *An Evaluation of the Possible Risks from Electric and Magnetic Fields (EMFS) from Power Lines, Internal Wiring, Electrical Occupations, and Appliances*; California Department of Industrial Relations: Oakland, CA, USA, 2002.
5. Van Loock, W. Elementary effects in humans exposed to electromagnetic fields and radiation. In Proceedings of the IEEE 2009 5th Asia-Pacific Conference on Environmental Electromagnetics, Xian, China, 16–20 September 2009; pp. 221–224.
6. Florea, G.A.; Dinca, A.; Gal, S.I.A. An original approach to the biological impact of the low frequency electromagnetic fields and proofed means of mitigation. In Proceedings of the 2009 IEEE Bucharest PowerTech, Bucharest, Romania, 28 June–2 July 2009; pp. 1–8.
7. ICNIRP (International Commission on Non-Ionizing Radiation Protection). Guidelines for Limiting Exposure to Time-Varying Electric and Magnetic Fields (1 Hz to 100 kHz). *Health Phys.* **2010**, *99*, 818–836. [CrossRef]
8. *IEEE PC95.1 Draft Standard for Safety Levels with Respect to Human Exposure to Electric, Magnetic and Electromagnetic Fields, 0 Hz to 300 GHz*; IEEE: Piscataway, NJ, USA, 2018.
9. Amoon, A.T.; Crespi, C.M.; Ahlbom, A.; Bhatnagar, M.; Bray, I.; Bunch, K.J.; Clavel, J.; Feychting, M.; Hémon, D.; Johansen, C.; et al. Proximity to overhead power lines and childhood leukaemia: An international pooled analysis. *Br. J. Cancer* **2018**, *119*, 364–373. [CrossRef] [PubMed]
10. Hossam-Eldin, A.; Youssef, K.; Karawia, H. Measurements and evaluation of adverse health effects of electromagnetic fields from low voltage equipments. In Proceedings of the IEEE 2008 12th International Middle-East Power System Conference, Aswan, Egypt, 12–15 March 2008; pp. 436–440.
11. Swanson, J. *EMF Exposure Standards Applicable in Europe and Elsewhere: Environment & Society Working Group*; Connecticut Siting Council: New Britain, CT, USA, 2006.
12. Hernández Jiménez, V.J.; Castronuovo, E.D.; Sánchez, I. Optimal statistical calculation of power cables disposition in tunnels, for reducing magnetic fields and costs. *Int. J. Electr. Power Energy Syst.* **2018**, *103*, 360–368. [CrossRef]
13. CIGRÉ Working Group C4.204. *Mitigation Techniques of Power-Frequency Magnetic Fields Originated from Electric Power Systems. CIGRÉ Technical Brochure*; CIGRÉ: Paris, France, August 2009; ISBN 978-2-85873-060-5.
14. Bignucolo, F.; Coppo, M.; Savio, A.; Turri, R. Use of rod compactors for high voltage overhead power lines magnetic field mitigation. *Energies* **2017**, *10*, 1381. [CrossRef]
15. Ranković, A. Novel multi-objective optimization method of electric and magnetic field emissions from double-circuit overhead power line. *Int. Trans. Electr. Energy Syst.* **2017**, *27*, e2243. [CrossRef]
16. Hedtke, S.; Pfeiffer, M.; Franck, C.M.; Zaffanella, L.; Chan, J.; Bell, J. Audible noise of hybrid AC / DC overhead lines: Comparison of different prediction methods and conductor arrangements. *Epri's High-Volt. Direct Curr. Flex. Ac Transm. Syst. Conf.* **2015**, *1*, 1–8.
17. Electric Power Research Institute. *EPRI Transmission Line Reference Book: 115–345-kV Compact Line Design: The "Blue Book"*; EPRI: Palo Alta, CA, USA, 2008.
18. Straumann, U.; Straumann, U.; Franck, C.M. *Discussion of Converting a Double-Circuit AC Overhead Line to an AC/DC Hybrid Line with Regard to Audible Noise*; CIGRÉ: Paris, France, 2011.
19. CIGRÉ Working Group B1.23. *Impact of EMF on Current Ratings and Cable Systems*; CIGRÉ Technical Brochure; CIGRÉ: Paris, France, 2013; ISBN 978-2-85873-254-8.
20. Cruz Romero, P.; Izquierdo Mitchell, C.; Burgos Payan, M. Optimal split-phase configurations. In Proceedings of the 2001 IEEE Porto Power Tech Proceedings (Cat. No.01EX502), Porto, Portugal, 10–13 September 2001; Volume 3, p. 5. [CrossRef]
21. Pettersson, P. Principles in transmission line magnetic field reduction. *IEEE Trans. Power Deliv.* **1996**, *11*, 1587–1593. [CrossRef]
22. Dawoud, M.M.; Habiballah, I.O.; Farag, A.S.; Firoz, A. Magnetic field management techniques in transmission underground cables. *Electr. Power Syst. Res.* **1999**, *48*, 177–192. [CrossRef]
23. Shperling, B.; Menemenlis-Hopkins, L.; Fardanesh, B.; Clairmont, B.; Child, D. Reduction of magnetic fields from transmission lines using passive loops. In Proceedings of the CIGRÉ Session, Paris, France, 25–31 August 1996; pp. 36–103.

24. Yamazaki, K.; Kawamoto, T.; Fujinami, H. Requirements for power line magnetic field mitigation using a passive loop conductor. *IEEE Trans. Power Deliv.* **2000**, *15*, 646–651. [CrossRef]
25. Farag, A.S.; Dawoud, M.M.; Habiballah, I.O. Implementation of shielding principles for magnetic field management of power cables. *Electr. Power Syst. Res.* **2002**, *48*, 193–209. [CrossRef]
26. Reta-Hernández, M.; Karady, G.G. Attenuation of low frequency magnetic fields using active shielding. *Electr. Power Syst. Res.* **1998**, *45*, 57–63. [CrossRef]
27. Cruz Romero, P.; Izquierdo, C.; Burgos, M.; Ferrer, L.F.; Soto, F.; LLanos, C.; Pacheco, J.D. Magnetic field mitigation in power lines with passive and active loops. In Proceedings of the CIGRÉ Session, Paris, France, 25–30 August 2002.
28. Garzia, F.; Geri, A. Active shielding design in full 3D space of indoor MV/LV substations using genetic algorithm optimization. In Proceedings of the 2003 IEEE Symposium on Electromagnetic Compatibility. Symposium Record (Cat. No.03CH37446), Boston, MA, USA, 18–22 August 2003; Volume 1, pp. 197–202.
29. Celozzi, S.; Garzia, F. Active shielding for power-frequency magnetic field reduction using genetic algorithms optimisation. *IEE Proc. Sci. Meas. Technol.* **2004**, *151*, 298–304. [CrossRef]
30. Barsali, S.; Giglioli, R.; Poli, D. Active shielding of overhead line magnetic field: Design and applications. *Electr. Power Syst. Res.* **2014**, *110*, 55–63. [CrossRef]
31. IEC-60287-1-1 Standard. *Electric Cables–Calculation of Current Rating–Part 1: Current Rating Equations (100% Load Factor) and Calculation of Losses, Section 1: General*; International Electrotechnical Commission: Geneva, Switzerland, 2006.
32. IEC-60287-2-1 Standard. *Electric Cables–Calculation of Current Rating–Part 2: Thermal Resistance–Section 1: Calculation of Thermal Resistance*; International Electrotechnical Commission: Geneva, Switzerland, 2015.
33. de León, F.; Anders, G.J. Effects of backfilling on cable ampacity analyzed with the finite element method. *IEEE Trans. Power Deliv.* **2008**, *23*, 537–543. [CrossRef]
34. Naskar, A.K.; Bhattacharya, N.K.; Sarkar, D. Transient thermal analysis of underground power cables using two dimensional finite element method. *Microsyst. Technol.* **2018**, *24*, 1279–1293. [CrossRef]
35. Holyk, C.; Anders, G.J. Power Cable Rating Calculations-A Historical Perspective [History]. *IEEE Ind. Appl. Mag.* **2015**, *21*, 6–64. [CrossRef]
36. Hoerauf, R. Ampacity application considerations for underground cables. *IEEE Trans. Ind. Appl.* **2016**, *52*, 4638–4645. [CrossRef]
37. Mozan, M.A.; El-Kady, M.A.; Mazi, A.A. Advanced thermal analysis of underground power cables. In Proceedings of the Fifth International Middle East Power Conference MEPCON'97, Alexandria, Egypt, 4–6 January 1997; pp. 506–510.
38. del-Pino-López, J.C.; Cruz-Romero, P. Influence of different types of magnetic shields on the thermal behavior and ampacity of underground power cables. *IEEE Trans. Power Deliv.* **2011**, *26*, 2659–2667. [CrossRef]
39. del-Pino-López, J.C.; Cruz-Romero, P.; Serrano-Iribarnegaray, L. Impact of electromagnetic losses in closed two-component magnetic shields on the ampacity of underground power cables. *Prog. Electromagn. Res.* **2013**, *135*, 601–625. [CrossRef]
40. Abdurakhmanov, A.M.; Zimin, K.A.; Ryabchenko, B.N.; Tokarskiy, A.Y.; Rubtsova, N.B. Solving the Environmental Electromagnetic Safety Issues in 110–500 kV AC Cable Power Lines. In Proceedings of the CIGRÉ Session, Paris, France, 26–31 August 2018.
41. Kladas, A.; Diamantis, A.; Damatopoulou, T.; Dikaiakos, C.; Papaioannou, G.; Michos, D. Over Head Transmission Lines and High Voltage Substations Electromagnetic Field Analysis and Design Considerations for Minimizing External Impacts. In Proceedings of the CIGRÉ Session, Paris, France, 26–31 August 2018; pp. 1–14.
42. Stewart, J.R.; Dale, S.J.; Klein, K.W. Magnetic field reduction using high phase order lines. *IEEE Trans. Power Deliv.* **1993**, *8*, 628–636. [CrossRef]
43. Tsalemis, D.; Tsanakas, D.; Milias-Argitis, J.; Agoris, D. Optimum arrangements of the phase conductors of overhead transmission lines for the electric field minimization. In Proceedings of the International Symposium on High Voltage Engineering ISH 97, Montreal, QC, Canada, 25–29 August 1997; pp. 97–100.
44. Deželak, K.; Jakl, F.; Štumberger, G. Arrangements of overhead power line phase conductors obtained by Differential Evolution. *Electr. Power Syst. Res.* **2011**, *81*, 2164–2170. [CrossRef]

45. Farag, A.S.; Bakhashwain, J.M.; Al-Shehri, A.; Cheng, T.C.; Gao, Y. Bundled conductor configuration optimization for compact transmission lines incorporating electromagnetic fields management. *Energy Convers. Manag.* **1998**, *39*, 1053–1071. [CrossRef]
46. Tsanakas, D.; Filippopoulos, G.; Voyatzakis, J.; Kouvarakis, G. Compact and optimum phase conductor arrangement for the reduction of electric and magnetic fields of overhead lines. In Proceedings of the CIGRÉ Session, Paris, France, 25–30 August 2000; pp. 36–103.
47. Dahab, A.A.; Amoura, F.K.; Abu-Elhaija, W.S. Comparison of Magnetic-Field Distribution of Noncompact and Compact Parallel Transmission-Line Configurations. *IEEE Trans. Power Deliv.* **2005**, *20*, 2114–2118. [CrossRef]
48. Ranković, A.; Mijailović, V.; Rozgić, D.; Cetenović, D. Optimization of electric and magnetic field emissions produced by independent parallel overhead power lines. *Serb. J. Electr. Eng.* **2017**, *14*, 199–216. [CrossRef]
49. Costea, M.; Băran, I. Side effects of the power frequency magnetic field mitigation. In Proceedings of the 2017 10th International Symposium on Advanced Topics in Electrical Engineering, ATEE 2017, Bucharest, Romania, 23–25 March 2017; pp. 330–335.
50. El Dein, A.Z. Optimal Arrangement of Egyptian Overhead Transmission Lines' Conductors Using Genetic Algorithm. *Arab. J. Sci. Eng.* **2014**, *39*, 1049–1059. [CrossRef]
51. Salameh, M.S.H.A.; Nejdawi, I.M.; Alani, O.A.; Commission, E.R.; Contracting, B.G. Using the Nonlinear Particle Swarm Optimization (PSO) Algorithm To Reduce the Magnetic Fields From Overhead High Voltage Transmission Lines. *IJRRAS* **2010**, *4*, 18–31.
52. Konak, A.; Coit, D.W.; Smith, A.E. Multi-objective optimization using genetic algorithms: A tutorial. *Reliab. Eng. Syst. Saf.* **2006**, *91*, 992–1007. [CrossRef]
53. Ippolito, L.; Siano, P. Using multi-objective optimal power flow for reducing magnetic fields from power lines. *Electr. Power Syst. Res.* **2003**, *68*, 93–101. [CrossRef]
54. Kalyanmoy, D. *Multi-Objective Optimization Using Evolutionary Algorithms*; John Wiley Sons, Inc.: New York, NY, USA, 2001; ISBN 047187339X.
55. Karady, G.G.; Nunez, C.V.; Raghavan, R. The feasibility of magnetic field reduction by phase relationship optimization in cable systems. *IEEE Trans. Power Deliv.* **1998**, *13*, 647–654. [CrossRef]
56. Lai, G.G.; Huang, H.M. Optimal Connection of Power Transmission Lines With Underground Power Cables to Minimize Magnetic Flux Density Using Genetic Algorithms. *IEEE Trans. Power Deliv.* **2008**, *23*, 1553–1560. [CrossRef]
57. Giaccone, L. Optimal layout of parallel power cables to minimize the stray magnetic field. *Electr. Power Syst. Res.* **2016**, *134*, 152–157. [CrossRef]
58. Almeida, M.E.; Maló Machado, V.; Guerreiro das Neves, M. Mitigation of the magnetic field due to underground power cables using an optimized grid. *Eur. Trans. Electr. Power* **2011**, *21*, 180–187. [CrossRef]
59. Mimos, E.I.; Tsanakas, D.K.; Tzinevrakis, A.E. Optimum phase configurations for the minimization of the magnetic fields of underground cables. *Electr. Eng.* **2010**, *91*, 327–335. [CrossRef]
60. Lai, G.G.; Yang, C.; Su, C.-T. Estimation and management of magnetic flux density produced by underground cables in multiple-circuit feeders. *Eur. Trans. Electr. Power* **2010**, *20*. [CrossRef]
61. Rachek, M.; Larbi, S.N. Magnetic eddy-current and thermal coupled models for the finite-element behavior analysis of underground power cables. *IEEE Trans. Magn.* **2008**, *44*, 4739–4746. [CrossRef]
62. Fulchiron, D.; Delaballe, J. Reduction of the Low Frequency EMF Emission of MV/LV Substations. In Proceedings of the 17th International Conference on Electricity Distribution (CIRED), Barcelona, Spain, 12–15 May 2003.
63. Saied, M.M. Canceling the Power Frequency Magnetic and Electric Fields of Power Lines. *IETE J. Educ.* **2014**, *54*, 90–99. [CrossRef]
64. Rebolini, M.; Forteleoni, M.; Capra, D. Passive cancellation loops: Case study, model simulation and field test on a real HV overhead line in Italy: Electromagnetic computation and optimization. In Proceedings of the 2017 AEIT International Annual Conference: Infrastructures for Energy and ICT: Opportunities for Fostering Innovation, AEIT 2017, Cagliari, Italy, 20–22 September 2017; pp. 1–6.
65. Djekidel, R.; Bessedik, S.A.; Spiteri, P.; Mahi, D. Passive mitigation for magnetic coupling between HV power line and aerial pipeline using PSO algorithms optimization. *Electr. Power Syst. Res.* **2018**, *165*, 18–26. [CrossRef]

66. Walling, R.; Paserba, J.J.; Burns, C.W. Series-capacitor compensated shield scheme for enhanced mitigation of transmission line magnetic fields. In Proceedings of the 1991 IEEE Power Engineering Society Transmission and Distribution Conference, Dallas, TX, USA, 22–27 September 1991; pp. 769–775.
67. TR-105571. *Magnetic Field Management of Overhead Transmission Lines: Field Reduction Using Cancellation Loops*; EPRI: Palo Alto, CA, USA, 1995.
68. Larsson, A.; Jonsson, U.; Sjödin, J. Design, test and cost of a magnetic field cancellation loop near swedish 400 kV line. In Proceedings of the Power Tech, Stockholm, Sweden, 18–22 June 1995.
69. Cruz-Romero, P.; Izquierdo, C.; Burgos, M. Optimum passive shields for mitigation of power lines magnetic field. *IEEE Trans. Power Deliv.* **2003**, *18*, 1357–1362. [CrossRef]
70. Cruz-Romero, P.; Hoeffelman, J.; del-Pino-López, J.C. Passive loop-based mitigation of magnetic fields from undergound power cable. *IEEE Latin Am. Trans.* **2008**, *6*, 59–65. [CrossRef]
71. Canova, A.; Bavastro, D.; Freschi, F.; Giaccone, L.; Repetto, M. Magnetic shielding solutions for the junction zone of high voltage underground power lines. *Electr. Power Syst. Res.* **2012**, *89*, 109–115. [CrossRef]
72. Frezzi, P.; Hug, R.; Grant, J.; Klingler, A. Passive magnetic field compensation of existing underground cables. In Proceedings of the IEEE International Symposium on Electromagnetic Compatibility, Wroclaw, Poland, 5–9 September 2016; pp. 876–881.
73. Brandão Faria, J.A.; Almeida, M.E. Accurate calculation of magnetic-field intensity due to overhead power lines with or without mitigation loops with or without capacitor compensation. *IEEE Trans. Power Deliv.* **2007**, *22*, 951–959. [CrossRef]
74. Cruz-Romero, P.; Riquelme-Santos, J.; del-Pino-López, J.C.; de-la-Villa-Jaén, A.; Ramos, J.L.M. A comparative analysis of passive loop-based magnetic field mitigation of overhead lines. *IEEE Trans. Power Deliv.* **2007**, *22*, 1773–1781. [CrossRef]
75. Cruz-Romero, P.; Riquelme-Santos, J.; de-la-Villa-Jaén, A.; Martínez, J.L. Ga-based passive loop optimization for magnetic field mitigation of transmission lines. *Neurocomputing* **2007**, *70*, 2679–2686. [CrossRef]
76. del-Pino-López, J.C.; Cruz-Romero, P. The effectiveness of compensated passive loops for mitigating underground power cable magnetic fields. *IEEE Trans. Power Deliv.* **2011**, *26*. [CrossRef]
77. del-Pino-López, J.C.; Cruz-Romero, P. Thermal Effects on the Design of Passive Loops to Mitigate the Magnetic Field Generated by Underground Power Cables. *IEEE Trans. Power Deliv.* **2011**, *26*, 1718–1726. [CrossRef]
78. Canova, A.; Freschi, F.; Giaccone, L.; Guerrisi, A.; Repetto, M. Magnetic field mitigation by means of passive loop: Technical optimization. *Compel Int. J. Comput. Math. Electr. Electron. Eng.* **2012**, *31*, 870–880. [CrossRef]
79. Król, K.; Machczyński, W. Optimization of electric and magnetic field intensities in proximity of power lines using genetic and particle swarm algorithms. *Arch. Electr. Eng.* **2018**, *67*, 829–843. [CrossRef]
80. Jonsson, U.; Larsson, A.; Sjodin, J.-O. Optimized reduction of the magnetic field near Swedish 400 KV lines by advanced control of shield wire currents. Test results and economic evaluation. *IEEE Trans. Power Deliv.* **1994**, *9*, 961–969. [CrossRef]
81. Bovdui, I.; Kuznetsov, B.; Voloshko, A.; Nikitina, T. Experimental Research of Effectiveness of Active Shielding System of Overhead Transmission Lines Magnetic Field with Various Control Algorithms. In Proceedings of the 2018 IEEE 3rd International Conference on Intelligent Energy and Power Systems (IEPS), Kharkiv, Ukraine, 10–14 September 2018; pp. 151–154.
82. del-Pino-López, J.C.; Giaccone, L.; Canova, A.; Cruz-Romero, P. Design of active loops for magnetic field mitigation in MV/LV substation surroundings. *Electr. Power Syst. Res.* **2015**, *119*, 337–344. [CrossRef]
83. del-Pino-López, J.C.; Giaccone, L.; Canova, A.; Cruz-Romero, P. Ga-based active loop optimization for magnetic field mitigation of MV/LV substations. *IEEE Lat. Am. Trans.* **2014**, *12*, 1055–1061. [CrossRef]
84. Canova, A.; del-Pino-López, J.C.; Giaccone, L.; Manca, M. Active shielding system for ELF magnetic fields. *IEEE Trans. Magn.* **2015**, *51*. [CrossRef]
85. Canova, A.; Giaccone, L. Real-time optimization of active loops for the magnetic field minimization. *Int. J. Appl. Electromagn. Mech.* **2018**, *56*, 97–106. [CrossRef]
86. Kuznetsov, B.I.; Turenko, A.N.; Nikitina, T.B.; Voloshko, A.V.; Kolomiets, V.V. Method of synthesis of closed-loop systems of active shielding magnetic field of power transmission lines. *Tekhnichna Elektrodynamika* **2016**, *4*, 8–10. [CrossRef]

87. Voloshko, A.V.; Bovdyj, I.V.; Nikitina, T.B.; Vinichenko, E.V.; Kuznetsov, B.I.; Kobilyanskiy, B.B. Synthesis of Active Screening System of Magnetic Field of High Voltage Power Lines of Different Design Taking Into Account Spatial and Temporal Distribution of Magnetic Field. *Electr. Eng. Electromec.* **2017**, *0*, 29–33. [CrossRef]
88. Kuznetsov, B.; Voloshko, A.; Bovdui, I.; Vinichenko, E.; Kobilyanskiy, B. High Voltage Power Line Magnetic Field Reduction by Active Shielding Means with Single Compensating Coil. In Proceedings of the 2017 International Conference on Modern Electrical and Energy Systems (MEES), Kremenchuk, Ukraine, 15–17 November 2017; pp. 196–199.
89. del-Pino-López, J.C.; Cruz-Romero, P.; Serrano-Iribarnegaray, L.; Martínez-Román, J. Magnetic field shielding optimization in underground power cable duct banks. *Electr. Power Syst. Res.* **2014**, *114*, 21–27. [CrossRef]
90. Ippolito, M.G.; Puccio, A.; Ala, G.; Ganci, S. Attenuation of low frequency magnetic fields produced by HV underground power cables. In Proceedings of the 2015 50th International Universities Power Engineering Conference (UPEC), Stoke on Trent, UK, 1–4 September 2015; pp. 1–5.
91. Souza, D.S.C.; Caetano, C.E.F.; De Paula, H.; Lopes, I.J.S.; Boaventura, W.D.C.; Paulino, J.O.S.; Evo, M.T.A. Experimental Investigation of Magnetic Field Shielding Techniques and Resulting Current Derating of Underground Power Cables. *IEEE Trans. Ind. Appl.* **2018**, *54*, 1146–1154. [CrossRef]
92. Grbic, M.; Canova, A.; Giaccone, L. Magnetic field in an apartment located above 10/0.4 kV substation: Levels and mitigation techniques. *CIRED—Open Access Proc. J.* **2017**, 752–756. [CrossRef]
93. Grbić, M.; Canova, A.; Giaccone, L. Levels of magnetic field in an apartment near 110/35 kv substation and proposal of mitigation techniques. In Proceedings of the Mediterranean Conference on Power Generation, Transmission, Distribution and Energy Conversion (MedPower 2016), Belgrade, Serbia, 6–9 November 2016; pp. 1–8.
94. Hasselgren, L.; Moller, E.; Hamnerius, Y. Calculation of Magnetic Shielding of a Substation at Power Frequency Using Fem. *IEEE Trans. Power Deliv.* **1994**. [CrossRef]
95. Canova, A.; Giaccone, L. High Performance Magnetic Shielding Solution for Elf Sources. In *CIRED*; IET: Glasgow, UK, 2017; pp. 686–690.
96. Hasselgren, L.; Luomi, J. Geometrical aspects of magnetic shielding at extremely low frequencies. *IEEE Trans. Electromagn. Compat.* **1995**, *37*, 409–420. [CrossRef]
97. Canova, A.; Manzin, A.; Tartaglia, M. Evaluation of different analytical and semi-analytical methods for the design of ELF magnetic field shields. *IEEE Trans. Ind. Appl.* **2002**, *38*, 788–796. [CrossRef]
98. del-Pino-López, J.C.; Cruz-Romero, P. Magnetic field shielding of underground cable duct banks. *Prog. Electromagn. Res.* **2013**, *138*, 1–19. [CrossRef]
99. Cho, I.H.; An, H.S.; Lim, Y.S.; Lee, B.W. Application Study on High Permeability Metal Magnetic Material for the Magnetic Field Shielding of Underground Cable. In Proceedings of the CIGRÉ Session, Paris, France, 26–31 August 2018.
100. Moreno, P.; Olsen, R.G. A simple theory for optimizing finite width ELF magnetic field shields for minimum dependence on source orientation. *IEEE Trans. Electromagn. Compat.* **1997**, *39*, 340–348. [CrossRef]
101. Gomes, N.; Almeida, M.E.; Machado, V.M. Series Impedance and Losses of Magnetic Field Mitigation Plates for Underground Power Cables. *IEEE Trans. Electromagn. Compat.* **2018**, *60*, 1761–1768. [CrossRef]
102. Liu, Y.; Sousa, P.; Salinas, E.; Cruz Romero, P.; Daalder, J. Continuum gradient-based shape optimization of conducting shields for power frequency magnetic field mitigation. *IEEE Trans. Magn.* **2006**, *42*, 1215–1218. [CrossRef]
103. Sun, G.Y.; Blasiis, C.D.; Corsaro, P. Study of magnetic shielding for high-voltage cables: A comparison between an experiment and FEM simulation. Proceedings of CIGRÉ Session, Paris, France, 26–31 August 2018.
104. Canova, A.; Freschi, F.; Giaccone, L.; Repetto, M. Numerical Modeling and Material Characterization for Multilayer Magnetically Shielded Room Design. *IEEE Trans. Magn.* **2018**, *54*. [CrossRef]
105. Freschi, F.; Repetto, M. A general framework for mixed structured/unstructured PEEC modelling. *Appl. Comput. Electromagn. Soc. J.* **2008**, *23*, 200–206.
106. Giaccone, L.; Ragusa, C.; Khan, O.; Manca, M. Fast magnetic field modeling for shielding systems. *IEEE Trans. Magn.* **2013**, *49*, 4128–4131. [CrossRef]
107. Freschi, F.; Giaccone, L.; Repetto, M. Algebraic formulation of nonlinear surface impedance boundary condition coupled with BEM for unstructured meshes. *Eng. Anal. Bound. Elem.* **2018**, *88*, 104–114. [CrossRef]

108. Crevecoeur, G.; Sergeant, P.; Dupre, L.; Van de Walle, R. Two-Level Response and Parameter Mapping Optimization for Magnetic Shielding. *IEEE Trans. Magn.* **2008**, *44*, 301–308. [CrossRef]
109. Ziolkowski, M.; Gratkowski, S.R. Genetic Algorithm and Bezier Curves-Based Shape Optimization of Conducting Shields for Low-Frequency Magnetic Fields. *IEEE Trans. Magn.* **2008**, *44*, 1086–1089. [CrossRef]

MDPI
St. Alban-Anlage 66
4052 Basel
Switzerland
Tel. +41 61 683 77 34
Fax +41 61 302 89 18
www.mdpi.com

Energies Editorial Office
E-mail: energies@mdpi.com
www.mdpi.com/journal/energies

MDPI
St. Alban-Anlage 66
4052 Basel
Switzerland

Tel: +41 61 683 77 34
Fax: +41 61 302 89 18

www.mdpi.com

ISBN 978-3-03921-157-9